59th Scientific Conference for Students of Physics and Natural Sciences

Open Readings 2016

March 15-18, 2016

Vilnius, LITHUANIA

Programme and Abstracts

Faculty of Physics
Vilnius University
Saulėtekio Ave. 9-III, LT-10222 Vilnius
LITHUANIA

www.ff.vu.lt
www.openreadings.eu

ISSN 2029-4425

Contents

Conference programme

15 March, TUESDAY

09:00	**Prof. Clemens F. Kaminski**, University of Cambridge, United Kingdom **PRINCIPLES AND APPLICATIONS OF SUPERRESOLUTION MICROSCOPY**		
	ORAL SESSION O1		
10:00	Ilya Yakovets, Igor Yankovsky, Vladimir Zorin, Lina Bezdetnaya **THE ALTERATION OF mTHPC INTRATUMORAL DISTRIBUTION IN HT-29 SPHEROIDS BY CYCLODEXTRINS**	O1-1	**18**
10:15	Valentin Natarov, Anna Vasilevskaya, Dzmitry Kotsikau, Vladimir Survilo, Vladimir Pankov, Elena Petrova **LOW COST SYNTHESIS OF IRON OXIDE–SiO_2 NANOCOMPOSITES FOR ISOLATION OF PCR-ACCEPTABLE NUCLEIC ACIDS**	O1-2	**19**
10:30	Greta Jarockytė, Vitalijus Karabanovas, Ričardas Rotomskis **UPTAKE AND DISTRIBUTION OF NANOPARTICLES IN 3D SPHEROID CELL CULTURE**	O1-3	**20**
10:45	Dominyka Dapkutė, Simona Steponkienė, Juras Kišonas, Danutė Bulotienė, Līga Saulīte, Una Riekstiņa, Ričardas Rotomskis **TUMOR TROPIC DELIVERY OF QUANTUM DOTS USING MESENCHYMAL STEM CELLS**	O1-4	**21**
11:00	COFFEE BREAK		
	ORAL SESSION O2		
11:30	Mikalojus Brazdžiūnas, Jessica Erin Koehne **OPTIMIZATION OF CTNI BINDING TO CNT ELECTRODES ON A PAPER BASED BIOSENSOR**	O2-1	**24**
11:45	Lluís Hernández-Navarro, Javier Gómez Orlandi, Benedetta Cerruti, Eduard Vives, Jordi Soriano **A RANDOM FIELD ISING MODEL FOR ASSESSING CONNECTIVITY IN CULTURED NEURONAL NETWORKS**	O2-2	**25**
12:00	Asta Lučiūnaitė, Miranda Mele, Carlos B. Duarte **CHANGES IN GABAergic SYNAPSES INDUCED BY STATUS EPILEPTICUS**	O2-3	**26**
12:15	Tatjana Pladere, Diana Bete, Jurgis Skilters, Gunta Krumina **IMPACT OF MENTAL FATIGUE ON VISUAL GROUPING OF ISOLUMINANT STIMULI**	O2-4	**27**
12:30	BREAK		
13:00-15:00	**POSTER SESSION P1**		
15:00	**Dr. Javier García de Abajo**, ICFO Institute of Photonic Sciences, Spain **GRAPHENE METAMATERIALS**		
	ORAL SESSION O3		
16:00	Migle Kazlauskiene, Gintautas Tamulaitis, Ceslovas Venclovas, Virginijus Siksnys **PROGRAMMABLE RNA AND DNA CLEAVAGE BY A CRISPR-CAS SYSTEM**	O3-1	**30**
16:15	Róża Hamera-Fałdyga, Katarzyna Urbaniak, Małgorzata Celeda, Grzegorz Mlostoń **NEW APPLICATION OF LAWESSON'S REAGENT (LR) FOR THE PREPARATION OF DIHETARYL AND ARYL/FERROCENYL SUBSTITUTED TRIFLUOROMETHYLENE THIOLS**	O3-2	**31**
16:30	Marta Głodek, Anna Makal, Janusz Zakrzewski, Damian Plażuk **NAZAROV CYCLISATION REACTION OF IN SITU GENERATED α,β-ALKENOYLPERYLENES**	O3-3	**32**
16:45	Dovilė Lengvinaitė, Francesca Mocci, Kęstutis Aidas **MD SIMULATIONS OF 1-DECYL-3-METHYL-IMIDAZOLIUM CHLORIDE IONIC LIQUID AND ITS MIXTURES WITH WATER**	O3-4	**33**
17:00	Dovile Baziulyte, Marius Stalnionis, Ignas Jurciukonis, Vitalijus Karabanovas, Simas Sakirzanovas **HYDROPHILIC, UPCONVERTING LANTHANIDE-DOPED $NaGdF_4$:Yb,Er@$NaGdF_4$ CORE-SHELL NANOPARTICLES AS POTENTIAL MULTIFUNCIONAL BIOPROBES**	O3-5	**34**
17:15	Elena Petrova, Dzmitry Kotsikau, Valentin Natarov, Vladimir Pankov, Ekaterina Kravchenko **STRUCTURAL AND MAGNETIC CHARACTERISTICS OF $Mg_xZn_{1-x}Fe_2O_4$ NANOPARTICLES, OBTAINED BY DIFFERENT METHODS**	O3-6	**35**
17:30	BREAK		
	OSA WELCOME EVENING		
19:00	**Dr. John C. Mather**, NASA Goddard Space Flight Center, USA **FROM THE BIG BANG TO NOW, OBSERVING THE UNIVERSE WITH JWST**		

16 March, WEDNESDAY

9:00	**Prof. Ursula Keller**, ETH Zürich, Switzerland **ATTOSECOND SCIENCE: RECENT HIGHLIGHTS AND FUTURE TRENDS**		
	ORAL SESSION O4		
10:00	Magdalena Woinska, Simon Grabowsky, Dylan Jayatilaka, Paulina Dominiak, Krzysztof Wozniak **QUANTUM CHEMISTRY IN THE SERVICE OF MODERN CRYSTALLOGRAPHY – TESTING NEW REFINEMENT METHODS ON A SET OF CRYSTAL STRUCTURES OF AMINO ACIDS AND TRIPEPTIDES**	O4-1	**38**
10:15	Urszula A. Budniak, Paulina M. Dominiak **THERMAL ANALYSIS OF 2,6-DIAMINOPURINE CRYSTALS WITH THE HELP OF CHARGE DENSITY**	O4-2	**39**
10:30	Monika Nowakowska, Sharmin Nadkarni, Narasimha Rao Bolla, Andrzej Kutner, Krzysztof Woźniak **CRYSTAL STRUCTURES AND SYNTHESIS OF VITAMIN D ANALOGUES**	O4-3	**40**
10:45	Andrius Merkys, Antanas Vaitkus, Mykolas Okulič-Kazarinas, Saulius Gražulis **SPOTTING THE GEOMETRIC PROPERTIES IN THE CRYSTALLOGRAPHY OPEN DATABASE**	O4-4	**41**
11:00	COFFEE BREAK		
	ORAL SESSION O5		
11:30	Tingting Weng, Daniel DeBrincat, Vaida Arcisauskaite, John McGrady **IN SEARCH OF STRUCTURE-FUNCTION RELATIONSHIPS IN MOLECULAR RECTIFIERS**	O5-1	**44**
11:45	Linas Jonušauskas, Marcus Lau, Peter Gruber, Bilal Gökce, Stephan Barcikowski, Mangirdas Malinauskas, Aleksandr Ovsianikov **3D MICROFABRICATION OF GOLD NANOPARTICLE DOPED HYBRID POLYMER VIA FEMTOSECOND LASER PULSES**	O5-2	**45**
12:00	Lukas Stankevičius, Tomas Tamulevičius **SIMULATION OF HIGH DIFFRACTION EFFICIENCY TRANSMISSION GRATINGS**	O5-3	**46**
12:15	Juliusz Chojenka, Mariusz Hajdyła, Alexey Maximenko, Marta Marszałek **INFLUENCE OF THE SUBSTRATE ELECTRIC CONDUCTIVITY ON THE MORPHOLOGY OF ANODIZED POROUS ALUMINA**	O5-4	**47**
12:30	BREAK		
13:00-15:00	**POSTER SESSION P2**		
15:00	**Prof. habil. Dr. Audrius Dubietis**, Vilnius university, Lithuania **SPATIOTEMPORAL LIGHT BULLETS**		
	ORAL SESSION O6		
16:00	Laura Paulina Sinkunaite, Michael Landry, Keita Kawabe **CAVITY ALIGNMENT USING FRINGE SCANNING**	O6-1	**50**
16:15	Jakub Boguslawski, Maciej Kowalczyk, Grzegorz Sobon, Rafal Zybala, Jan Tarka, Krzysztof M. Abramski, Jaroslaw Sotor **ANTIMONY TELLURIDE SATURABLE ABSORBERS FOR ULTRAFAST FIBER LASERS**	O6-2	**51**
16:30	Jan Szczepanek, Tomasz M. Kardaś, Yuriy Stepanenko **INFLUANCE OF SPECTRAL FILTRATION ON PULSE-SHAPE IN AN ALL NORMAL DISPERSION FIBER OSCILLATOR**	O6-3	**52**
16:45	Edvinas Skliutas, Ieva Gendvilienė, Vygandas Rutkūnas, Mangirdas Malinauskas **FILAMENT FARBRICATION OF BIODEGRADABLE POLYLACTIC ACID THREE-DIMENSIONAL MICROSTUCTURES**	O6-4	**53**
17:00	Nick Van Steerteghem, Stijn Van Cleuvenbergen, Steven Deckers, Chanaka Kumara, Amala Dass, Hannu Häkkinen, Koen Clays, Thierry Verbiest, Stefan Knoppe **SYMMETRY BREAKING IN GOLD SUPERATOM COMPLEXES: A NONLINEAR OPTICAL STUDY**	O6-5	**54**
17:15	Karolis Adomavičius, Ernestas Žeimys **RESEARCH OF SPATIAL AND SPECTRAL PROPERTIES OF TERAHERTZ RADIATION GENERATED IN AIR**	O6-6	**55**
17:30	BREAK		
18:00	SOCIAL EVENT		

17 March, THURSDAY

9:00	**Prof. Gintaras Valušis**, Center for Physical Sciences and Technology, Lithuania **MATERIALS SOLUTIONS FOR TERAHERTZ TECHNOLOGY**		
	ORAL SESSION O7		
10:00	Joanna Symonowicz **THE AGING PROCESSES IN THE P3HT:PCBM SOLAR CELLS**	O7-1	**58**
10:15	Augustas Vaitkevičius, Mikhail Korjik, Paulius Baronas, Ekaterina Trusova, Darius Dobrovolskas, Gintautas Tamulaitis **INFLUENCE OF THE COMPOSITION ON EMISSION OF GLASSES AND GLASS CERAMICS DOPED WITH RARE EARTH IONS**	O7-2	**59**
10:30	Karolina H. Markiewicz, Iwona Misztalewska, Agnieszka Z. Wilczewska, Krzysztof Winkler **FORMATION OF NEW FUNCTIONAL NANOHYBRIDS BY RAFT/MADIX POLYMERIZATION**	O7-3	**60**
10:45	Iwona Misztalewska, Olga Wojtasik, Karolina H. Markiewicz, Agnieszka Z. Wilczewska **NEW MAGNETIC SEPARABLE POLYMERIC NANOHYBRIDS WITH CHELATING PROPERTIES**	O7-4	**61**
11:00	COFFEE BREAK		
	ORAL SESSION O8		
11:30	Mindaugas Kamarauskas, Vladimir Agafonov, Kinan E. Nasser, Marius Treideris, Arunas Setkus **NICKEL ASSISTED SILICON ETCHING**	O8-1	**64**
11:45	Simona Streckaite, Renata Karpicz, Alytis Gruodis, Saulius Grigalevicius, Vidmantas Gulbinas **FLUORESCENCE QUENCHING OF INDOLO[3,2-b]CARBAZOLE COMPOUNDS BY CONFORMATIONAL MOTIONS OF ATTACHED SUBSTITUENTS**	O8-2	**65**
12:00	Paulius Baronas, Tobias Harlang, Villy Sundström, Saulius Juršėnas **ULTRAFAST DYNAMICS OF PHOTO INDUCED ELECTRON TRANSFER IN IRON COMPLEX BASED SOLAR CELLS**	O8-3	**66**
12:15	Sergejus Balčiūnas, Maksim Ivanov, Jūras Banys, Vladimir Shvartsman **DIELECTRIC PROPERTIES OF ORGANIC-INORGANIC LEAD HALIDE PEROVSKITES $CH_3NH_3PbX_3$ (X = I, Br, Cl)**	O8-4	**67**
12:30	BREAK		
13:00-15:00	**POSTER SESSION P3**		
15:00	**Dr. Lorenzo Pavesi**, University of Trento, Italy **SILICON NANOCRYSTALS AS ENABLER FOR SILICON PHOTONICS**		
	ORAL SESSION O9		
16:00	Ieva Beleckaitė, Ramūnas Adomavičius, Andrius Arlauskas, Renata Butkutė, Vaidas Pačebutas, Algirdas Selskis, Virginijus Bukauskas, Arūnas Krotkus **TERAHERTZ EMISSION FROM NON-STOICHIOMETRIC Ga-RICH GaAs LAYER**	O9-1	**70**
16:15	Andrius Rimkus, Evelina Pozingytė, Ramūnas Nedzinskas, Bronislovas Čechavičius, Julius Kavaliauskas, Gintaras Valušis, Lianhe Li, Edmund H. Linfield **OPTICAL STUDY OF VERTICALLY ELONGATED InGaAs QUANTUM DOTS**	O9-2	**71**
16:30	Evelina Pozingytė, Andrius Rimkus, Ramūnas Nedzinskas, Bronislovas Čechavičius, Julius Kavaliauskas, Lianhe Li, Edmund Linfield **OPTICAL STUDY OF TWO-COLOUR QUANTUM RING INFRARED PHOTODETECTOR**	O9-3	**72**
16:45	Ignas Nevinskas, Sandra Stanionytė, Vaidas Pačebutas, Arūnas Krotkus **TERAHERTZ EMISSION FROM SEMICONDUCTOR SURFACES**	O9-4	**73**
17:00	Kazimieras Nomeika, Ramūnas Aleksiejūnas **CARRIER DIFFUSIVITY AS THE KEY PARAMETER BEHIND THE QUANTUM EFFICIENCY DROOP IN (IN,GA)N QUANTUM STRUCTURES**	O9-5	**74**
17:15	Žydrūnas Podlipskas **TWO-WAY CONNECTION BETWEEN QUALITY OF LAYERS IN AlGaN/GaN TEMPLATE**	O9-6	**75**

18 March, FRIDAY

9:00	**Prof. Andris Ambainis**, University of Latvia, Latvia **QUANTUM COMPUTERS - THE STORY OF A WILD IDEA**		
	ORAL SESSION O10		
10:00	Janis Smits, Florian Gahbauer, Andris Berzins, Juris Prikulis, Krisjanis Smits, Ruvin Ferber, Donats Erts, Marcis Auzinsh, Dmitry Budker, Andrey Jarmola **LONGITUDINAL SPIN-RELAXATION IN NITROGEN-VACANCY CENTERS IN DIAMOND IRRADIATED BY LOW ENERGY ELECTRONS**	O10-1	**78**
10:15	Lukas Razinkovas, Audrius Alkauskas **THEORETICAL ANALYSIS OF THE VIBRATIONAL STRUCTURE OF DEFECTS IN 3C-SIC**	O10-2	**79**
10:30	Tomas Marčiulionis, Vladimir Chorošajev, Darius Abramavičius **QUANTUM DYNAMICS OF NONLINEAR COUPLED OSCILLATORS**	O10-3	**80**
10:45	Mažena Mackoit, Audrius Alkauskas **AB-INITIO STUDIES OF POINT DEFECTS IN h-BN**	O10-4	**81**
11:00	COFFEE BREAK		
	ORAL SESSION O11		
11:30	Giedrius Tušinskis, Juozas Bučinskas **ELECTROMAGNETIC WAVE SCATTERING BY A 2D PHOTONIC CRYSTAL SUBMERGED IN A MATERIAL CYLINDER**	O11-1	**84**
11:45	Aidas Medžiūnas, Jonas Venius **MATHEMATICAL MODEL OF BOLUS SURFACE FOR VARIOUS ANGLES IN ELECTRON CANCER THERAPY**	O11-2	**85**
12:00	Žygimantas Vosylius, Algirdas Novičkovas, Vincas Tamošiūnas **SIMULATION OF IRRADIANCE AND PHOTORESPONSE DISTRIBUTIONS IN CASE OF LARGE (>1M^2) SOLAR SIMULATORS EMPLOYING ARRAYS OF LIGHT-EMITTING DIODES**	O11-3	**86**
12:15	Monika Venčkauskaitė, Andrius Juodagalvis, Adrian Perieanu **PROSPECTS FOR THEW-BOSON ASSOCIATED HIGGS BOSON PRODUCTION WITH THREE MUONS IN THE FINAL STATE AT 13 TeV WITH CMS**	O11-4	**87**
12:30	BREAK		
13:00-15:00	**POSTER SESSION P4**		
15:00	**Dr. Sergei Nayakshin**, University of Leicester, United Kingdom **FORMATION OF PLANETS FAR AND NEAR: A REVOLUTION IN SIGHT**		
	ORAL SESSION O12		
16:00	Marta Dziełak, Anna Bartkiewicz **SEARCHING FOR WEAK METHANOL MASER EMISSION AT 6.7 GHz**	O12-1	**90**
16:15	Katarzyna Rusinek, Andrzej Marecki **CORE-DOMINATED TRIPLE BLAZARS AS (NEWBORN) X-SHAPED SOURCES**	O12-2	**91**
16:30	Bartosz Tułaza **SPATIAL ORIENTATION AND PHOTOIONIZATION OF PLANETARY NEBULAE**	O12-3	**92**
16:45	Laimons Začs, Faig A.Musaev, Bogdan Kaminskyi, Yakiv Pavlenko, Aija Grankina, Julius Sperauskas, Bruce J. Hrivnak **SPECTROSCOPIC VARIABILITY OF IRAS 22272+5435**	O12-4	**93**
17:00	Iaroslav Iakubivskyi, Hendrik Ehrpais, Erik Ilbis, Karl Reinkubjas, Pekka Janhunen, Petri Toivanen, Jouni Envall, Andris Slavinskis **ESTCUBE-2 MISSION ANALYSIS: PLASMA BRAKE EXPERIMENT FOR DEORBITING**	O12-5	**94**
17:15	John Holt, Kamil Ciesielski **NOVEL ROCK SAMPLING TECHNIQUE FOR USE ON MARS**	O12-6	**95**
17:30	BREAK		
19:00	CONFERENCE PARTY and AWARD CEREMONY		

List of poster presentations

15 March, TUESDAY

13:00-15:00 **POSTER SESSION P1**

Justas Dainys, Žilvinas Pūtys, Linas Ložys **ENERGETIC COST OF SPAWNING MIGRATION: DO STOCKED EELS FROM LITHUANIA CAN REACH THE SPAWNING GROUNDS AT SARGASSO SEA**	P1-01	**98**
Genrik Mordas, Vadimas Dudoitis, Kristina Plauškaitė, Nina Prokopčiuk, Vidmantas Ulevičius **ASSESSMENT OF NEW PARTICLE FORMATION EVENTS ON THE COAST OF BALTIC SEA**	P1-02	**99**
Viktorija Mačiulytė **REMOTE SENSING OF DROUGHTS**	P1-03	**100**
Julija Pauraitė, Genrik Mordas, Steigvilė Byčenkienė, Vidmantas Ulevicius **SPATIAL AND TEMPORAL ANALYSIS OF ORGANIC AND BLACK CARBON MASS CONCENTRATIONS IN LITHUANIA**	P1-04	**101**
Laurynas Krikščikas, Šarūnas Jacevičius, Andrius Garbaras **CARBON CONCENTRATION AND STABLE ISOTOPE RATIOS IN PM1 AEROSOL PARTICLES IN VILNIUS, LITHUANIA**	P1-05	**102**
Marina Valentukeviciene **IRON COMPOUNDS IN WATER SUPPLY SYSTEMS, SOURCES AND ACCUMUALTION**	P1-06	**103**
Yuliya Kunitskaya, Elena Golubeva, Tatiana Kochetkova, Elizaveta Kavalenka, Pavel Bulai **INFLUENCE OF PROLONGED EXTERNAL ELECTRIC FIELD STIMULATION OF C6 CELLS ON RESTING PLASMA MEMBRANE POTENTIAL AND MITOCHONDRIAL MEMBRANE IPOTENTIAL**	P1-07	**104**
I. Sadauskienė, I. Stanevičienė, K. Adomaitytė, A. Liekis, R. Naginienė, V. Šimakauskienė, D. Baranauskienė **SUPEROXIDE DISMUTASES ACTIVITY IN MICE BRAIN UNDER SELENIUM AND/OR ALIUMINIUM IONS TREATMENT**	P1-08	**105**
Nikita Vasilyeu, Elena Golubeva, Tatsiana Kulahava, Mikhail Shuba, Alesya Paddubskaya **THE INFLUENCE OF DNA-WRAPPED SINGLE-WALLED CARBON NANOTUBES ON THE PROLIFERATIVE ACTIVITY OF C6 RAT GLIOMA CELLS**	P1-09	**106**
Yuliya Leonik, Tatsiana Kulahava, Elena Golubeva, Mikhail Shuba, Alesya Paddubskaya **THE INFLUENCE OF CARBON NANOTUBES ON REDOX PROCESSES IN MODEL SYSTEMS AND NEUTROPHILS**	P1-10	**107**
Inga Songailiene, Tomas Sinkunas, Marius Rutkauskas, Ralf Seidel, Virginijus Siksnys **CASCADE COMPLEX RECONSTITUTION IN VITRO AND R-LOOP FORMATION BY SINGLE MOLECULE EXPERIMENTS**	P1-11	**108**
Artis Brasovs, Kaspars Ērglis **MICRORHEOLOGICAL MEASUREMENTS OF BACTERIOPHAGE Pf1 WITH AN OPTICAL LASER TWEEZERS**	P1-12	**109**
Agnieška Mackoit, Kristina Daniūnaitė, Sonata Jarmalaitė **DNA METHYLATION ANALYSIS OF ANGIOGENESIS-RELATED GENES ADAMTS12 AND FILIP1L IN PROSTATE CANCER**	P1-13	**110**
Julija Fadejeva, Dovilė Šiuškaitė, Saulius Cicėnas, Diana Schveigert **ERCC1 AND RRM1 GENES AS PREDICTIVE BIOMARKERS IN NON-SMALL CELL LUNG CANCER**	P1-14	**111**
Mantas Stankevičius, Živilė Cibulskaitė, Nijolė Kazlauskienė, Ričardas Rotomskis **ACCUMULATION OF QUANTUM DOTS IN RAINBOW TROUT (Oncorhynchus mykiss) EMBRYOS**	P1-15	**112**
Akvile Slektaite, Sonata Adomaviciute, Ricardas Rotomskis **POLYVINYLPYRROLIDONE STABILIZED GOLD NANOPARTICLES: SYNTHESIS AND PHARMACOKINETICS IN VIVO**	P1-16	**113**
Laurynas Karpus, Dovilė Baziulytė, Simas Šakirzanovas, Vitalijus Karabanovas, Ričardas Rotomskis **OPTICAL PROPERTIES OF $NaGdF_4$:Yb,Er@$NaGdF_4$ UPCONVERTING NANOPARTICLES AND THEIR APPLICATION IN CANCER DIAGNOSTICS**	P1-17	**114**
Eglė Daugėlaitė, Marius Stašys, Dovilė Baziulytė, Ričardas Rotomskis **UPCONVERSION NANOPARTICLES IN MAGNETIC RESONANCE IMAGING**	P1-18	**115**
Matas Damonskis, Judita Puišo, Paulius Danilovas **CARROTS EXTRACT FOR SILVER NANOPARTICLES SYNTHESIS BY PHOTOREDUCTION METHOD**	P1-19	**116**
Anna Matsukovich, Elena Shabunya-Klyachkovskaya, Mikhail Smirnov, Alexey Perepelitsa **LUMINESCENCE PROPERTIES OF CdS QUANTUM DOTS NEAR Ag NANOPARTICLES**	P1-20	**117**
Laima Budėnaitė, Marija Matulionytė-Safinė, Greta Jarockytė, Dominyka Dapkutė, Ričardas Rotomskis **CELLULAR UPTAKE AND BIOLOGICAL EFFECT OF MES- AND BSA- COATED PHOTOLUMINESCENT GOLD NANOCLUSTERS IN VITRO**	P1-21	**118**
Agata Mlynska, Simona Kavaliauskienė, Petras Juzėnas, Dalia Kaškelytė, Roaldas Gadonas, Mikhail Samtsov, Aleksandr Lugovsky, Elena Bakienė **PHOTOTOXIC ANTIBACTERIAL AND ANTITUMORAL ACTIVITY OF CARBOCYANINE DYE TICS NO. 150**	P1-22	**119**
Michail Yekelchyk, Darya Nosan **DIFFERENTIAL FLUORESCENT PROTEOMIC IDENTIFICATION OF DIAGNOSTICALLY IMPORTANT PROTEINS OF BREAST CANCER**	P1-23	**120**
Vilmantas Gėgžna, Ignas Čiplys, Darius Varanius, Rūta Kurtinaitienė, Gunaras Terbetas, Aurelija Vaitkuvienė, Juozas Vidmantis Vaitkus **CHEMOMETRIC ANALYSIS WITH CROSS-VALIDATION FOR SPECTROSCOPIC SIGNALS OBTAINED FROM MEDICAL SPECIMENS**	P1-24	**121**
Sabina Brazevic, Magdalena Grajek **THE TOBACCO INFLUENCE ON THE ELECTRIC POTENTIAL OUTCOME IN PATIENTS AFTER MYOCARDIAL INFARCTION**	P1-25	**122**
Dmitri Dormeshkin, Andrei Gilep, Sergey Usanov **QUANTIFICATION AND LOCALIZATION STUDIES OF RECOMBINANT ANTIBODIES USING CYTOCHROME b5 FUSION PARTNER**	P1-26	**123**
Yaroslav Dichenko, Mikita Bokshyts, Sergey Usanov **KINETIC PROPERTIES OF HUMAN OXYSTEROL 7α-HYDROXYLASE CYP7B1**	P1-27	**124**
Andrei Svirid, Andrei Gilep, Sergey Usanov **IN VITRO BIOTINYLATION ON MAGNETIC PARTICLES FOR BIO-ORTHOGONAL CONJUGATION**	P1-28	**125**
Inga Šileikaitė, Rimantas Šiekštelė, Inga Matijošytė **FUNCTIONAL ANALYSIS OF METAGENOMIC GENE CLUSTER WITH EXPOSED LIPOLYTIC ACTIVITY**	P1-29	**126**

16 March, WEDNESDAY

13:00-15:00 **POSTER SESSION P2**

17 March, THURSDAY

13:00-15:00 **POSTER SESSION P3**

Dovydas Banevičius, Bronė Lenkevičiūtė-Vasiliauskienė, Sigita Višniakova, Albinas Žilinskas **CHINOLINE DERIVATIVES WITH AMINO SUBSTITUENTS: AN INVESTIGATION OF PHOTOLUMINESCENCE AND ELECTROLUMINESCENCE PROPERTIES IN THE OLEDs**	P3-01	**210**
Ernesta Bužavaitė, Sigita Višniakova, Bronė Lenkevičiūtė - Vasiliauskienė **OLEDS WITH QUINOLINE DERIVATIVES AS EMISSIVE LAYER: AN INVESTIGATION OF LUMINESCENCE AND ELECTRICAL PROPERTIES**	P3-02	**211**
Karolis Gesevičius, Bronė Lenkevičiūtė-Vasiliauskienė, Ieva Mikalauskaitė **ORGANIC SOLAR CELLS WITH UP-CONVERTERS: LAYER BY LAYER FABRICATION AND INFLUENCE OF THE UP-CONVERSION LAYER TOWARDS SOLAR CELL EFFICIENCY**	P3-03	**212**
Gleb Gorokhov, Anton Moiseenko, Dzmitry Bychanok, Polina Kuzhir **IMPROVED ABSORPTION PROPERTIES OF NANOCARBON/MAGNETITE COMPOSITES IN 26-37 GHz**	P3-04	**213**
Meldra Kemere, Janis Sperga, Uldis Rogulis, Jurgis Grube **LUMINESCENCE PROPERTIES OF EUROPIUM AND DYSPROSIUM CO-DOPED OXYFLUORIDE GLASSES**	P3-05	**214**
Davis Conka, Roberts Zarins, Liga Avotina, Gunta Kizane **INVESTIGATION OF POSSIBILITIES OF DETERMINATION OF LONG-CHAIN HYDROCARBONS IN CARBON-BASED DUST FROM FUSION REACTOR**	P3-06	**215**
Ieva Igaune, Elīna Pajuste, Gunta Ķizāne, JET Contributors **TRITIUM ACCUMULATION IN JOINT EUROPEAN TORUS BERYLLIUM WALL MATERIALS**	P3-07	**216**
Oskars Valtenbergs, Arturs Zarins, Gunta Kizane, Arnis Supe, Larisa Baumane **RADIOLYSIS OF LITHIUM ORTHOSILICATE PEBBLES WITH ADDITION OF TITANIUM DIOXIDE**	P3-08	**217**
Oleksandr Maretskii, Anatoliy Titenko, Lesya Demchenko **THE EFFECT OF ANNEALING IN MAGNETIC FIELD ON FERROMAGNETIC NANOPARTICLES PRECIPITATION IN Cu-Al-Mn ALLOY WITH INDUCED MARTENSITIC TRANSFORMATION**	P3-09	**218**
Alina Muravitskaya **PLASMON-ENHANCED RAMAN SCATTERING BY ZnO NANOCRYSTALS**	P3-10	**219**
Danas Sakalauskas, Simas Sakirzanovas **SYNTHESIS OF $Sr_{1-x}Y_xF_{2+x}$ VIA CO – PRECIPITATION METHOD USING DIFFERENT CAPPING AGENTS**	P3-11	**220**
Aleksandra Kravchenko, Dmitriy Guschik, Aleksandra Yurkova **CONSOLIDATION OF POWDERED QUASICRYSTALLINE Al–Fe–Cr ALLOY UNDER QUASI-HYDROSTATIC PRESSURE**	P3-12	**221**
Marta Roman, Judyta Strychalska, Tomasz Klimczuk **SUPERCONDUCTIVITY ON THE EDGE OF FERROMAGNETISM – PHYSICAL PROPERTIES OF La3Co COMPOUND**	P3-13	**222**
Mindaugas Juodėnas, Dainius Virganavičius, Tomas Tamulevičius, Viktoras Grigaliūnas, Morten Madsen, Sigitas Tamulevičius **DIRECTED ASSEMBLY OF MICRO PARTICLES INTO WELL-ORGANIZED ARRAYS**	P3-14	**223**
Paula Jankovska, Valdis Korsaks, Baiba Berzina **OXYGEN GAS SENSING PROPERTIES OF AlN NANOPOWDER**	P3-15	**224**
Simonas Ramanavicius, Arunas Jagminas **EFFECT OF ADDITIVES ON THE HYDROTHERMAL SYNTHESIS OF MANGANESE FERRITE NANOPARTICLES**	P3-16	**225**
Donatas Dargis **CARRIER DYNAMICS IN InGaN QUANTUM WELLS WITH GROSS WELL WIDTH FLUCTUATIONS**	P3-17	**226**
Evelina Pozingytė, Andrius Rimkus, Simona Paurazaitė, Saulius Tumėnas, Ramūnas Nedzinskas, Liuwen Chang, Mitch M.C. Chou **TEMPERATURE-DEPENDENT PHOTOLUMINESCENCE OF NONPOLAR ZnO/ZnMgO QUANTUM WELLS**	P3-18	**227**
Tadas Bučiūnas, Lina Skardžiūtė, Jelena Dodonova, Sigitas Tumkevičius, Saulius Juršėnas **TRIPLET ANNIHILATION AND THERMALLY ACTIVATED DELAYED FLUORESCENCE IN PYRROLE PYRIMIDINE DERIVATIVES**	P3-19	**228**
Przemyslaw Dziegielewski, J. Antonowicz, A. Pietnoczka, O. Mathon, I. Kantor, S. Pascarelli, T. Shinmei, T. Irifune **POLYAMORPHSIM IN METALLIC GLASSES ASSESSED BY EXAFS METHOD**	P3-20	**229**
Agnė Kalpakovaitė, Tomas Grinys, Rytis Dargis, Andrew Clarck, Kazimieras Badokas, Tadas Malinauskas **GROWTH KINETICS OF NON-POLAR GaN GROWN ON SI SUBSTRATE WITH AN ERBIUM OXIDE INTERLAYER**	P3-21	**230**
Kazimieras Badokas, Tadas Malinauskas, Tomas Grinys **GROWTH OF NON-POLAR GaN ON Si WITH RARE-EARTH OXIDE INTERLAYERS**	P3-22	**231**
Henrikas Svidras, Darius Dobrovolskas **SPATIAL DISTRIBUTION OF PHOTOLUMINESCENCE IN GAN NANORODS WITH INGAN/GAN MULTIPLE QUANTUM WELLS**	P3-23	**232**
Marek Kolenda, Tadas Malinauskas, Jūras Mickevičius, Jonas Jurkevičius, Darius Dobrovolskas, Arūnas Kadys **BGaN GROWTH ON 6H-SiC AND AlN BY MOVPE AND CHARACTERIZATION**	P3-24	**233**
Justinas Glemža, Jonas Matukas, Sandra Pralgauskaitė **LOW-FREQUENCY NOISE SPECTROSCOPY AND THRESHOLD CHARACTERISTICS OF LASER DIODES**	P3-25	**234**
Sergey Aplesnin, Maksim Sitnikov, Aliona Zhivulko, Kazimir Yanushkevich **INTERRELATION OF MAGNETIC AND ELECTRIC PROPERTIES GDXMN1-XSE SEMICONDUCTORS**	P3-26	**235**
Austeja Galvelyte, Zheng Tang, Olle Inganas **INVESTIGATION OF MORPHOLOGY AND PERFOMANCE IN TQ1:[60]PCBM:[70]PCBM STANDARD GEOMETRY SOLAR CELLS**	P3-27	**236**
Alexander Fedotov, Sergey Perevoznikov **TRANSPORT PROPERTIES OF POLYCRYSTALLINE BISMUTH FILMS**	P3-28	**237**
Justinas Aleknavičius, Darius Dobrovolskas, Gintautas Tamulaitis **CORRELATION BETWEEN SPATIAL DISTRIBUTION OF PHOTOLUMINESCENCE AND SURFACE MORPHOLOGY IN GaBiAs EPITAXIAL LAYERS AND QUANTUM WELLS**	P3-29	**238**

18 March, FRIDAY

13:00-15:00 **POSTER SESSION P4**

Ilze Laicane, Jurgis Skilters, Vsevolod Liakhovetckii, Astra Kulite, Gunta Krumina **PERCEPTION OF BIOLOGICAL MOTION AND PERCEPTUAL GROUPING IN CENTRAL AND PERIPHERAL VISUAL FIELD**	P4-01	**266**
Saulius Pakalka, Aušra Kynienė, Šarūnas Masys, Valdas Jonauskas **ELECTRON-IMPACT IONIZATION CROSS SECTIONS FOR W(25+) ION**	P4-02	**267**
Grigory Rusetsky, Oleg Khasanov, Olga Fedotova, Eugenijus Gaižauskas **SOLITON REGIMES FOR TERAHERTZ AND SECOND HARMONIC PULSES GENERATION IN PERMANENT DIPOLE MOMENT MEDIUM**	P4-03	**268**
Olga Kozlova, Maria Zelenina, Veranika Burko **ELECTRONIC PROPERTIES STUDY OF QUASI-TWO- DIMENSIONAL HETEROSTRUCTURES BASED ON SILICON AND GERMANIUM**	P4-04	**269**
Olga Kozlova, Victor Stempitsky **INVESTIGATION OF THE INFLUENCE OF TITANIUM DISULFIDE DEFORMATION ON ITS STABILITY**	P4-05	**270**
Anton Yermalovich, Aleksandr Danilyuk **INTERACTION OF NOBLE METAL NANOPARTICLES WITH ELECTROMAGNETIC RADIATION AT PLASMON RESONANCE FREQUENCIES**	P4-06	**271**
Dovilė Čibiraitė, Alvydas Lisauskas, Jonas Matukas **PLASMON DISPERSION RELATION IN GATED TWO DIMENSIONAL ELECTRON GAS**	P4-07	**272**
Monika Bijeikyte, Audrius Alkauskas **DYNAMICS OF CARRIER RECOMBINATION IN InGaN/GaN QUANTUM WELLS: KINETIC MONTE-CARLO STUDIES**	P4-08	**273**
Veranika Skachkova, Maryia Zialenina **BLACK PHOSPHORUS: A PERSPECTIVE LAYERED MATERIAL**	P4-09	**274**
Alfonsas Juršėnas, Sergejus Orlovas, Gediminas Račiukaitis **VECTOR ELECTROMAGNETIC FIELDS IN ABSORBING MEDIUM FOR LASER MICROFABRICATION APPLICATIONS**	P4-10	**275**
Domas Linkevičius, Aušra Saudargienė, Bruce Graham **NEURONAL EXCITABILITY CHANGES UNDER ACH MODULATION IN A MULTI-COMPARTMENTAL HIPPOCAMPAL CA1 PYRAMIDAL NEURON MODEL**	P4-11	**276**
Vytautas Dudenas, Thomas Gajdosik **RENORMALIZATION OF PROPAGATORS OF WEYL SPINORS IN THE SEESAW EXTENSION OF THE STANDARD MODEL**	P4-12	**277**
Jogundas Armaitis, Gediminas Juzeliūnas **THREE-DIMENSIONAL SPIN HALL EFFECT**	P4-13	**278**
Anton Kuncinas, Thomas Gajdosik **TWO HIGGS DOUBLET MODELS AS EXTENSIONS TO THE STANDARD MODEL: DIFFERENT BASIS CHOICES**	P4-14	**279**
Jonas R. Umaras, Adrian Perieanu, Andrius Juodagalvis **MONTE CARLO SIMULATION STUDIES OF THE TAU LEPTON POLARISATION IN THE Z AND H BOSON DECAYS IN PP COLLISIONS**	P4-15	**280**
Alexey Pavlov, Maxim Belov **SPHERICAL TRIANGLE TO FIND THE COORDINATES OF CELESTIAL BODIES**	P4-16	**281**
Azem Hysa, Dhurata Hysa **MOTION NEAR THE LIBRATION POINT L4 (SUN-JUPITER SYSTEM)**	P4-17	**282**
Laimons Začs, Julius Sperauskas, Aija Grankina, Viktoras Deveikis, Bogdan Kaminskyi, Yakiv Pavlenko, Faig A.Musaev **THE EVOLVED PULSATING CEMP STAR HD 112869**	P4-18	**283**
Sylwia Plenzner, Gracjan Maciejewski **HOT EXOPLANETS ON NON-CIRCULAR ORBITS**	P4-19	**284**
Algimantas Bikulčius, Liudas Tumonis **DEVELOPMENT AND TESTING OF CUBESAT ROCKET ENGINE TEST STAND**	P4-20	**285**
Liutauras Ričkus, Romas Baronas **MODELLING BIOSENSORS UTILIZING ALLOSTERIC ENZYME ACTIVITY**	P4-21	**286**
Ignas Kazakevičius, Evaldas Maceika **RADIONUCLIDES DISPERSION MODELING IN LIGHT WATER REACTOR BUILDING COMPARTMENTS DURING HYPOTHETICAL NUCLEAR INCIDENT**	P4-22	**287**
Gintaras Kerevičius **IDENTIFICATION OF THE ENERGY SPECTRUM OF AUTOIONIZING STATES OF BARIUM EXCITED BY ELECTRON IMPACT**	P4-23	**288**
Augustinas Stepšys, Saulius Mickevičius, Darius Germanas, Ramutis Kazys Kalinauskas **CALCULATION OF FIVE PARTICLE HARMONIC-OSCILLATOR TRANSFORMATION BRACKETS IN TRANSLATIONAL INVARIANT BASIS**	P4-24	**289**
Ada Gajauskaitė, Sergej Orlov, Gediminas Račiukaitis **THEORETICAL STUDY OF NEW TYPE OF VECTOR BESSEL BEAMS**	P4-25	**290**
Rytis Kazakevičius, Julius Ruseckas **ANOMALOUS DIFFUSION AND POWER LAW STATISTICS**	P4-26	**291**
Yakovleva Marina **ABSORPTION ENHANCING OF ELECTROMAGNETIC WAVE IN GRAPHENE BY PERIODIC GRATING**	P4-27	**292**
Małgorzata Domagała, Marcin Palusiak **HALOGEN BOND, HYDROGEN BOND – NONCOVALENT INTERACTIONS IN THE Cl-, Br-COMPLEXES**	P4-28	**293**
Maryia Zhuk, Irina Doroshenko, Valery Pogorelov, Valdas Sablinskas, Vitas Balevicius, Lars G. M. Pettersson, George Pitsevich **RELATIVE RAMAN LINE INTENSITIES OF BENDING HOH VIBRATIONS AS IMPORTANT FACTOR OF LOCAL WATER STRUCTURE**	P4-29	**294**
Rokas Skaisgiris, Arūnas Miasojedovas, Alytis Gruodis, Dalius Gudeika, Juozas V. Gražulevičius, Saulius Juršėnas **TWISTED INTERNAL CHARGE TRANSFER IN 1,8-NAPHTHALIMIDE DERIVATIVES WITH DIMETHYLAMINOBENZENE MOIETIES**	P4-30	**295**
Linas Litvinas, Romas Baronas, Antanas Žilinskas **OPTIMISATION OF BIOSENSOR UTILIZING SYNERGISTIC SUBSTRATES CONVERSION**	P4-31	**296**

Oral session 1

Molecular biology

THE ALTERATION OF mTHPC INTRATUMORAL DISTRIBUTION IN HT-29 SPHEROIDS BY CYCLODEXTRINS

Yakovets Ilya[1,2,3*], Yankovsky Igor[1,2,3], Zorin Vladimir[1], Bezdetnaya Lina[2,3]

[1] Department of Biophysics, Belarussian State University, Minsk, Belarus
[2] Centre de Recherche en Automatique de Nancy, CNRS, Université de Lorraine, Nancy, France
[3] Institut de Cancérologie de Lorraine, Vandoeuvre-lès-Nancy, France
**viprorok@gmail.com*

Photodynamic therapy (PDT) is a treatment that uses special drugs, called photosensitizes (PS), along with light to kill cancer cells. The distribution of anticancer drugs is an important factor in the success of treatment. The distribution of molecules into the tumor is governed by at least three phenomena: the extravasation from the blood vessels, diffusion through the extravascular tissue and interaction with intracellular targets within the tumor environment. In the present study we used multicellular spheroids to investigate the modification of intratumoral transport of PS via complexation with cyclodextrins.

Multicellular spheroids are spherical aggregates of tumor, which reflect many properties of solid tumors, such as tight junctions between epithelial cells, gradients of nutrient concentrations and cell proliferation from the exterior to the center. By incubating spheroids in a medium that contains an anticancer drug it is possible to examine the kinetics of drug penetration in tumor tissue.

The photosensitizer used in the study is 5,10,15,20-tetra(*m*-hydroxyphenyl)chlorin (mTHPC). It is one of the most potent second-generation clinically approved photosensitizer [1]. The main limitation of its application in PDT is a low water-solubility. To prevent mTHPC aggregation several special formulations, such as liposomes, polymer solutions and bioconjugates were designed. An application of specialized pharmacological formulations supposes a development of new experimental techniques to control photosensitizer distribution in biological media. Cyclic oligosaccharides, cyclodextrins, are also considered as perspective formulation for tetrapyrrolic photosensitizers.

Cyclodextrins (CDs) are macrocyclic oligosaccharides that combine a hydrophobic nano-sized cavity with a hydrophilic surface. The cavity enables the partial or total incorporation of lipophilic molecules. Cyclodextrins as carriers of various drug molecules can be vehicles of photosensitizers (PS) via complexation [2].

In the present study we have shown, that effect of cyclodextrins on spheroids strongly depends on concentration and type of CD. Low concentrations of CDs result in an increase of mTHPC accumulation in spheroids with a maximal uptake at 4.4 μM for Methyl-β-cyclodextrin and 88.2 μM for 2-Hydroxypropyl-β-cyclodextrin. Further increase in CDs concentrations is accompanied by a gradual decrease of mTHPC uptake. Another observation is related to the increased mTHPC penetration depth into the tumor spheroids in the presence of CD. Microscopic analysis demonstrated that the presence of CDs results in significant changes of the distribution profiles of mTHPC in spheroids.

We suggest that CDs increase a diffusion rate of mTHPC between biological transporters and cellular targets at the low concentrations (causing less than 50% binding of CD to mTHPC). At the same time, higher CDs concentrations that provide almost complete binding of mTHPC molecules inhibit the accumulation of mTHPC in spheroids.

The data obtained confirm the interest of CDs in mTHPC-PDT.

Acknowledgements. This study was supported by Belarussian Republican Foundation for Fundamental Research, the Ministry of Education of the Republic of Belarus and French "Ligue National contre le Cancer". We thank Biolitec Research GmbH (Jena, Germany) for providing us with mTHPC.

[1] Senge, M.O. mTHPC – A Drug on Its Way from Second to Third Generation Photosensitizer? Photodiagnosis and Photodynamic Therapy **9** (2), 170-179 (2012).
[2] Yang R., Li, K., Wang, K., Liu F., Li, N., Zhao F. Cyclodextrin-porphyrin supramolecular sensitizer for mercury (II) ion, Anal. Chem. Acta **469**, 285-293 (2002).

LOW COST SYNTHESIS OF IRON OXIDE–SiO_2 NANOCOMPOSITES FOR ISOLATION OF PCR-ACCEPTABLE NUCLEIC ACIDS

Valentin Natarov[1], Anna Vasilevskaya[2], Dzmitry Kotsikau[1], Vladimir Survilo[3], Vladimir Pankov[1], Elena Petrova [1]

[1] Department of Physical Chemistry, Belarusian State University, Belarus
[2] Institut of Bioorganic Chemistry of The National Academy of Sciences of Belarus
[3]Ltd. InterLabService, Russian Fediration
che.natarov@bsu.by

In the past decade, magnetic nanocomposites have attracted considerable attention due to their promising biomedical applications [1]. One of such applications is nucleic acids isolation from biological specimens [2]. This operation is an integral part of any research in molecular biology, biotechnology or medical diagnostics and also very important because isolated DNA can be used in polymerase chain reaction (PCR). Magnetic separation using iron oxide (γ-Fe_2O_3 and Fe_3O_4) and silica-based nanocomposite sorbents represents a well-proven method for highly pure nucleic acids isolation. To be applied in bioseparation, the materials have to meet a number of requirements: high adsorption/desorption yield, chemical stability and compatibility with other components of nucleic acids isolation kit (chaotropic agent, organic solvents and buffer solutions). Nanocomposite particles also have to be monodisperse and form sufficiently stable water suspension with proper magnetic response (time to separate magnetic phase from liquid using NdFeB bar magnet). Thus, the development of these materials has both scientific and commercial values.

Sodium silicate represents a non-toxic and inexpensive alternative of widely used tetraethyl orthosilicate (TEOS) for synthesis of silica coated nanomaterials. Iron oxide–SiO_2 nanocomposite was obtained via conventional surfactant-free sol-gel method using two different silica precursors: sodium silicate and TEOS. Initial magnetite (Fe_3O_4) was prepared by co-precipitation of ferrous and ferric salts with ammonia aqueous solution. The obtained Fe_3O_4/SiO_2 specimens (34-36 Wt.% SiO_2) were also thermally processed at different temperatures (50 and 500°C). Water suspension of nanocomposite particles (40 mg/ml) was used as magnetic sorbent in bioseparation of nucleic acids from human saliva and blood. The DNA was investigated by UV-spectroscopy and used in traditional and real-time PCR.

The size of iron oxide-SiO_2 nanoparticles was estimated by electron microscopy (SEM) to vary from 30 to 60 nm. In solution, nanoparticles have a tendency to form stable aggregates with 0,8–1,2 μm hydrodynamic size and ~ -26 mV zeta-potential determined by dynamic laser scattering. Such suspension possesses proper sedimentation stability (>3 min) and magnetic response less 1 min. According to X-ray diffraction and IR-spectroscopy, the nanocomposite consists of spherical well-crystalline spinel-type iron oxide nanoparticles distributed in amorphous silica matrix. The powdered nanocomposites show a soft-ferromagnetic behavior with saturation magnetization of about 35-40 emu/g.

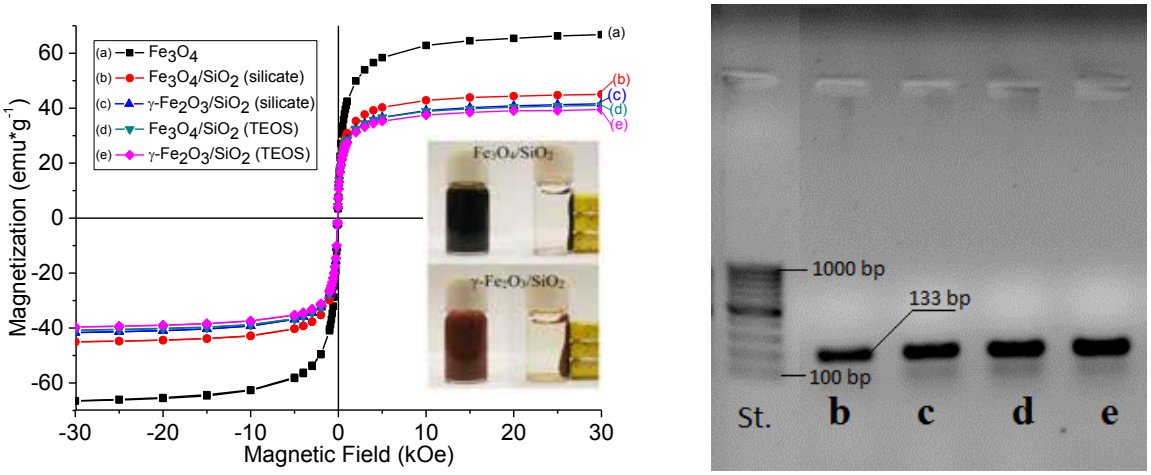

Fig. 1. Magnetization curves for Fe_3O_4 and nanocomposites at 300 K. Inset pictures: magnetic response of nanocomposite particles (left) and gel-electrophoresis of products obtained in PCR of isolated human DNA (right)

Through synthesis optimization, nanocomposites obtained via different precursors were quite similar. Also, there was an increase of effectiveness for calcined (500°C) nanocomposites, which can be attributed to degradation of amorphous silica surface and changes in pore structure. DNA isoplated from human saliva has A260/A280 parameter nearly 1,8 and was secsessfuly used in PCR (ACE gene polymorphisms). According to real-time PCR test, synthesized nanocomposites demonstrate results comparable with commercial isolation kit (Allrun AllMag®, Chania).

[1] L. Zhou, J. Yuan, Y. Wei, Core-shell structural iron oxide hybrid nanoparticles: from controlled synthesis to biomedical applications, Journal of materials chemistry **21**, 2823-2840 (2011).
[2] X. Li, J. Zhang, H. Gu, Adsorption and desorption behaviors of DNA with magnetic mesoporous silica nanoparticles, Langmuir **27**, 6099-6106 (2011)

UPTAKE AND DISTRIBUTION OF NANOPARTICLES IN 3D SPHEROID CELL CULTURE

Greta Jarockytė[1], Vitalijus Karabanovas[1, 2], Ričardas Rotomskis[1, 3]

[1] Biomedical Physics Laboratory of National Cancer Institute, Baublio 3B, LT08406, Vilnius, Lithuania;
[2]Department of Chemistry and Bioengineering, Vilnius Gediminas Technical University, LT-10223 Vilnius, Lithuania.
[3]Biophotonics group of Laser Research Centre, Vilnius University, Saulėtekio 9, c.3, LT-10222, Vilnius, Lithuania
greta.jarockyte@nvi.lt

The rapidly evolving nanotechnology field in cancer researches requires a better understanding of nanoparticles uptake into solid tumors. However, there is not enough information about relationship between nanoparticle properties and nanoparticle transport to the tumor [1]. Nowadays two-dimensional (2D) cell cultures are most frequently used cellular model for the study of cancer biology and treatment. However, a lot of cellular functions and responses that are present in natural tissues are lost in 2D cell cultures. Three-dimensional (3D) cell cultures show a higher degree of morphological and functional similarity to the tissues. Spheroid formation is one of the most well characterized models for 3D cell culture. In cancer research, spheroids could be used as tumor models. Spheroids are self-assembled spherical clusters of cell colonies cultured in environments where cell-cell interactions dominate over cell-substrate interactions, and they naturally mimic avascular tumors with inherent metabolic (oxygen) and proliferative (nutrient) gradients [2].

The aim of our study was to investigate accumulation of quantum dots in 3D spheroid cell culture.

Mouse embryonic fibroblasts (NIH3T3) were used for experiments. 3D cells spheroids were formed using hanging drop technique. NIH3T3 cells were seeded in 96-well hanging drop plate (Biomatrix, USA) and cultivated in 37ºC incubator. After 48 h of incubation, 10 % of cell culturing media in each well were changed to a fresh media containing carboxyl quantum dots (Qdot® 625 ITK™, Invitrogen, USA). The final concentration of quantum dots in each well was 8 nM. After 24 h of incubation with quantum dots, 3D cells spheroids were transferred from hanging drop plate to 8-well microscopy plate. The accumulation of quantum dots were observed using Nikon Eclipse Te2000-U confocal microscope (Nikon, Japan).

3D cell culture at different moments of spheroid formation is represented in Fig. 1. After 24 h of incubation, quantum dots accumulated only in cells which were in the periphery of spheroid. There was not accumulation of quantum dots in the center part of 3D spheroid cell culture. It means that cells do not transfer nanoparticles from one to another. The distribution of quantum dots in each peripheral cell was the same as accumulation of quantum dots in 2D cell culture: nanoparticles accumulated in perinuclear region via endocytosis.

3D spheroid cell culture could be used as avascular tumor model to investigate the uptake and distribution of nanoparticles in the tumor cells. Our results showed that cells in 3D spheroid cell culture do not transfer nanoparticles to each other.

Acknowledge: this work was financially supported by the joint Lithuanian-Latvian-Taiwanese Tripartite Cooperation Programme, Grant No. TAP-LLT-13-016.

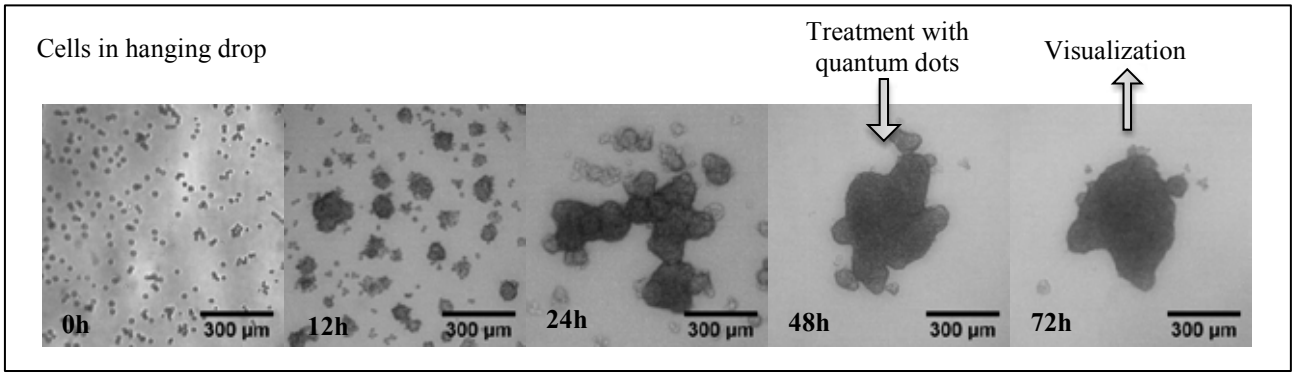

Fig. 1. Formation of 3D spheroid cell culture.

[1] F. Sambale, A. Lavrentieva, F. Stahl, C. Blume, M. Stiesch, C. Kasper, D. Bahnemann, T. Schepera. Three dimensional spheroid cell culture for nanoparticle safety testing. Journal of Biotechnology 205, 120–129 (2015).

[2] Y.-C. Tung, A. Y. Hsiao, S. G. Allen, Y. Torisawa, M. Hoc, S. Takayama. High-throughput 3D spheroid culture and drug testing using a 384 hanging drop array. Analyst 136, 473–478 (2011).

TUMOR TROPIC DELIVERY OF QUANTUM DOTS USING MESENCHYMAL STEM CELLS

Dominyka Dapkutė[1], Simona Steponkienė[1], Juras Kišonas[1], Danutė Bulotienė[1], Līga Saulīte[2], Una Riekstiņa[2], Ričardas Rotomskis[1,3]

[1] Biomedical Physics Laboratory, National Cancer Institute, Vilnius, Lithuania
[2] Faculty of Medicine, University of Latvia, Riga, Latvia
[3] Biophotonics group of Laser Research Center, Vilnius University, Vilnius, Lithuania
dominyka.dapkute@nvi.lt

Mesenchymal stem cells (MSCs) are multipotent cells possessing transdifferentiation, self-renewal and immunomodulatory properties. It was noticed that MSCs preferentially migrate toward tumors due to chemokine signaling [1]. Because of their inherent tumor tropism, MSCs could be used as nanoparticle delivery vehicles [2]. Quantum dots (QDs) are fluorescent semiconductor nanoparticles. They have unique optical properties and can be easily modified with proteins, drugs, antibodies and other molecules for targeted drug delivery [3]. These characteristics enable QDs to be used as multifunctional anti-cancer nanoagents. However, knowledge about the influence of QDs on skin MSCs is still limited.

In this study, we investigated the effect of QDs on intrinsic properties of MSCs. We used human dermal MSCs and commercially available Invitrogen Qdot® 625 ITK™ Carboxyl QDs. Cell migration assay kit containing polycarbonate inserts with 8 μm pores was used to detect MSCs *in vitro* migration toward MDA-MB-231 breast cancer cells and MCF-10A mammary epithelial cells. CB17 SCID immunodeficient mice with human breast cancer xenografts were used to evaluate *in vivo* migration of MSCs. *In vitro* results showed that MSCs selectively migrate toward cancer cells and QDs do not reduce the migration of the cells (Fig. 1.). The experiments with immunodeficient mice revealed that MSCs localize in the sites of tumor and metastasis. While co-culturing QD-loaded MSCs and unlabeled cancer cells, we detected that the exchange of nanoparticles between the cells is minimal. It shows that MSCs could safely transport QDs through the body. Our results show promising potential of MSCs to be used as nanoparticle carriers to the tumors.

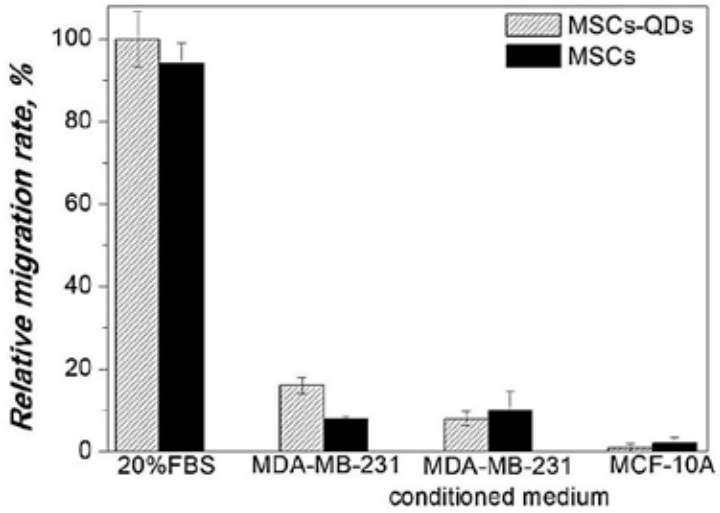

Fig. 1. MSCs *in vitro* migration after the incubation with QDs.

This work was supported by the project „Mesenchymal stem cell and cancer stem-like cell response to nanoparticle treatment“ (TAP LLT 03/2014) funded by Joint Lithuanian–Latvian–Taiwanese Research Program.

[1] Lourenco S, Teixeira VH, Kalber T et al., Macrophage migration inhibitory factor-CXCR4 is the dominant chemotactic axis in human mesenchymal stem cell recruitment to tumors, Journal of immunology **194**, 3463-74 (2015).
[2] Huang X, Zhang F, Wang H et al., Mesenchymal stem cell-based cell engineering with multifunctional mesoporous silica nanoparticles for tumor delivery, Biomaterials **34(7)**, 1772-80 (2013).
[3] Smith AM, Duan H, Mohs AM et al., Bioconjugated quantum dots for in vivo molecular and cellular imaging. Advanced Drug Delivery Reviews **60(11)**, 1226-40 (2008).

Oral session 2

Biomedical sciences

OPTIMIZATION OF CTNI BINDING TO CNT ELECTRODES ON A PAPER BASED BIOSENSOR

Mikalojus Brazdžiūnas[1], Jessica Erin Koehne[2]

[1]Faculty of Natural Sciences, Vilnius University, M.K.Čiurlionio st. 21/27, LT-03101, Vilnius, Lithuania
[2]NASA Ames Research Center, Moffett Field, CA 94035, USA
mikalojus.brazdziunas@gf.stud.vu.lt

Monitoring astronauts' cardiac health on the International Space Station requires cheap, simple and easily made biosensors. One possible solution is a fully printable paper based biosensor [1]. The sensor's electrodes and fluidics will be printed using inkjet and stencil printing on standard chromatography paper.

Cardiac troponin-I (cTnI) is used because it is a cardiac health biomarker and an indicator of acute heart failure. The specific binding affinity of these proteins to antibodies probes on the carbon nanotube (CNT) electrode will be characterized to assess the capture efficiency of the biosensor (Fig. 1). A high density mesh of CNT coated paper fibers should improve binding between proteins and ligands if the sample fluid flows through the CNT network and not across it. Scanning electron microscopy (SEM), cyclic voltametry (CV), differential pulse voltammetry (DPV) and electrochemical impedance spectroscopy (EIS) will be used to characterize protein binding and thus detection.

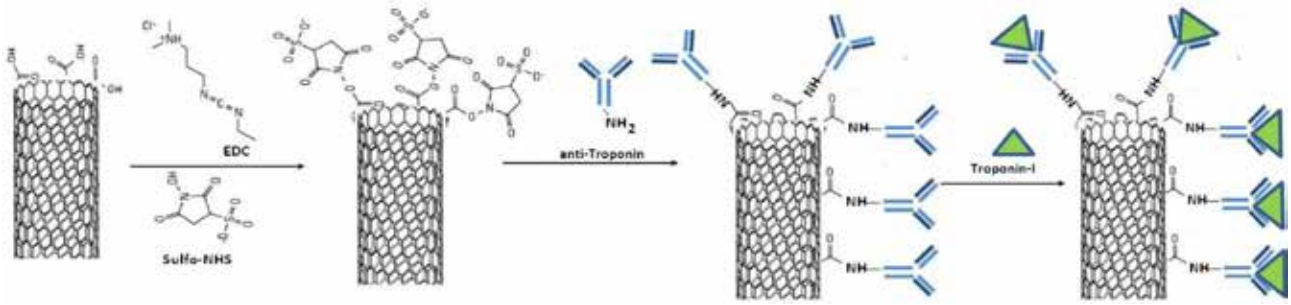

Fig. 1. Basic scheme for troponin ligand immobilization on the surface of CNTs.

Early data from SEM imaging suggest good conductivity of paper fibers covered with CNTs. Further work includes imaging CNTs with a protein and a specifically bound ligand. The purpose of this work is to use a streptavidin-biotin model to optimize the CNT electrode geometry for high cTnI binding by characterizing CNT coating process, protein binding and sensitivity of the electrode.

Binding characterization was done by SEM imaging of CNT coated paper fibers with immobilized streptavidin and bound biotin conjugated with Au nanoparticles. This provided evidence for carbon nanotubes being a suitable electrode material on paper based biosensor. Statistical analysis of SEM imaged Au nanoparticles revealed significant differences between different electrode geometries.

CV and DPV measurements of potassium ferricyanide ($K_4Fe(CN)_6$) solutions assessed the sensitivity of the electrode. The lowest concentration of potassium ferricyanide solution when redox event signal was registered is 1-10 μM which is sensitive enough to detect small myocardial infarction [2].

The results show that this model is suitable to be used for characterizing cTnI binding to the CNT electrode. EIS will be employed as a more sensitive method for protein detection.

[1] R.K. Gupta et al., Label-free detection of C-reactive protein using carbon nanofiber based biosensor, Biosensors and Bioelectronics **59**, 112-119 (2014).
[2] M.F.M. Fathil et al., Diagnostics on acute myocardial infarction: cardiac troponin biomarkers, Biosensors and Bioelectronics **70**, 209-220 (2015).

A RANDOM FIELD ISING MODEL FOR ASSESSING CONNECTIVITY IN CULTURED NEURONAL NETWORKS

Lluís Hernández-Navarro[1], Javier Gómez Orlandi[1], Benedetta Cerruti[2], Eduard Vives[1], Jordi Soriano[1*]

[1] Department of Structure and Constituents of Matter, University of Barcelona, Spain
[2] Department of Physics, University of Roma, Italy
lhernandez@ecm.ub.edu

The connectivity map of a living neuronal network, together with the intrinsic neuronal dynamics, shapes in great measure the collective behavior and functionality of a neuronal circuit [1,2]. While neuronal dynamics can be well analyzed and modeled, accessing the connectivity blueprint of a neuronal network is a highly difficult task, particularly in living circuits. Hence, a major effort has been devoted to seek for strategies to bring to light such information, either as a detailed, neuron-to-neuron connectivity map or through statistical descriptors.

Combining experiments and modeling, we here present an innovative framework in the context of an Ising model to unveil key topological features of neuronal networks in vitro, specifically their average connectivity and distribution of connections. Experimentally, our networks consist of cultures of rat cortical neurons at 14 days of development and with diverse density and spatial distributions. Through electrical stimulation and calcium imaging (Fig. 1), we measure the transition from an ensemble of connected neurons to a disconnected population as the connectivity probability between neurons is gradually reduced. We considered as order parameter the size of the largest group of connected neurons (*giant component*), and investigate the characteristics of both the transition curve and point [3,4,5]. Theoretically, we use Stastical Physics to map the behavior of the neuronal network into a Random Field Ising model (RFIM) [6,7,8] in a mean-field approximation. Percolation is then introduced by reducing the average connectivity strength between neurons. Our model can be solved analytically and the solutions depend just on few parameters that can be ascribed to experimental details. The fitting of the theoretical model to experimental data uncovers two key topological aspects, namely the average connectivity of the network and the degree of heterogeneity of the connectivity map, quantified through the discordance between the mean-field theoretical curves and the actual data.

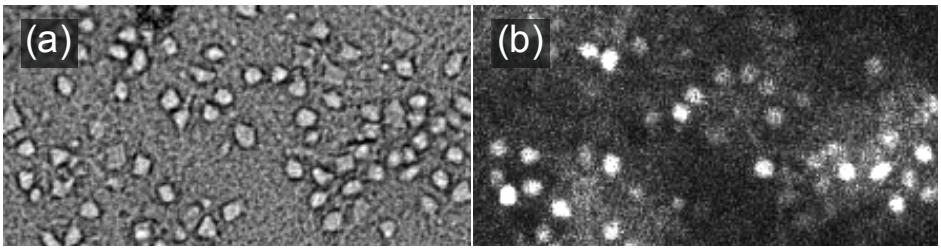

Fig. 1. (a) Optical image of an homogeneous neuronal culture (100x200μm). (b) Fluorescence image of the culture. Active neurons are shown as bright spots, while inactive ones remain darker.

[1] J. G. Orlandi, J. Soriano, E. Alvarez-Lacalle, S. Teller, and J. Casademunt, Nature Physics 9, 582 (2013).
[2] Eckmann, J. P., Feinerman, O., Gruendlinger, L., Moses, E., Soriano, J., and Tlusty, T., The physics of living neural networks. *Physics Reports*, *449*(1), 54-76, (2007).
[3] I. Breskin, J. Soriano, E. Moses, and T. Tlusty, Physical review letters 97, 188102 (2006).
[4] J. Soriano, M. R. Martínez, T. Tlusty, and E. Moses, Proceedings of the National Academy of Sciences 105, 13758 (2008).
[5] O. Cohen, A. Keselman, E. Moses, M. R. Martínez, J. Soriano, and T. Tlusty, EPL (Europhysics Letters) 89, 18008 (2010).
[6] J. P. Sethna, K. Dahmen, S. Kartha, J. A. Krumhansl, B. W. Roberts, and J. D. Shore, Physical Review Letters 70, 3347 (1993).
[7] D. Dhar, P. Shukla, and J. P. Sethna, Journal of Physics A: Mathematical and General 30, 5259 (1997).
[8] X. Illa, P. Shukla, and E. Vives, Physical Review B 73, 092414 (2006).

CHANGES IN GABAergic SYNAPSES INDUCED BY *STATUS EPILEPTICUS*

Asta Lučiūnaitė[1], Miranda Mele[2], Carlos B. Duarte[2]

[1]Institute of Biotechnology, Vilnius University, Vilnius, Lithuania
[2]Center for Neuroscience and Cell Biology, University of Coimbra, Coimbra, Portugal
asta.luciunaite@chf.stud.vu.lt

Inhibitory neurotransmission in the CNS plays an essential role in maintaining the excitatory/inhibitory balance required for correct brain function. Brain inhibitory neurotransmission is largely mediated by γ-aminobutyric acid (GABA), acting through $GABA_A$ receptors ($GABA_AR$), composed of at least 2α-, 2β-, and 1γ-subunits. Deficits in the functional expression of $GABA_AR$ have been implicated in the pathogenesis of several neurological and psychiatric diseases, including brain ischemia, anxiety, depression, schizophrenia, substance abuse and epilepsy. Epilepsy is a condition characterized by recurrent seizures that may include repetitive muscle jerking called convulsions. A seizure is a sudden disruption of the brain's normal electrical activity accompanied by altered consciousness and/or other neurological and behavioral manifestations. During epilepsy alteration in $GABA_AR$ dynamics has been reported [2, 3]. The aim of this project is to characterize the molecular mechanisms underlying the alterations in $GABA_AR$ trafficking in epileptogenesis.

We used *in vitro* system consisting of cultured hippocampal neurons, which were exposed to a solution lacking Mg^{2+} – induced *Status Epilepticus* (SE) conditions. To characterize this experimental model we analysed the alterations in $[Ca^{2+}]_i$ through single cell calcium imaging using the fluorescent dye Fluo4 and spinning disk video microscopy. To investigate the alterations in $GABA_AR$ turnover we used immunocytochemistry approach allowing assessing the internalization and the recycling of $GABA_AR$. To monitor $GABA_AR$ dynamics we used live imaging – fluorescence microscopy technique to observe proteins changes in live cells. Cells were transfected with $GABA_AR$ β3 tagged with a pH sensitive form of GFP, myc-tag for detection with fluorescent antibodies or Gephyrin-FingR for visualization of inhibitory synapses in live neurons.

We observed that SE increases the $[Ca^{2+}]_i$. We also found an enhanced internalization of $GABA_AR$ which was accompanied by a decrease in the recycling of the receptors. Live imaging technique showed the decrease in $GABA_AR$ in cell surface after SE. Moreover, SE conditions induced changes in scaffold protein gephyrin clustering.

Our results showed that SE induces a decrease of $GABA_AR$ recycling and alters $GABA_AR$ surface dynamics. Furthermore, changes in gephyrin clusters were detected. Gephyrin is required for the stabilization of $GABA_AR$ receptors at the synapse, so this correlates with the alteration induced by SE conditions in membrane $GABA_AR$. In conclusion, the alterations of GABAergic neurotransmission observed in SE conditions are related to the alteration of $GABA_AR$ turnover observed in this study.

This research was funded by the grants: PTDC/NEU-NMC/0198/2012 and Bolsa Cientifica LPCE (liga Portuguesa contra a Epilepsia) 2014. The research traineeship was funded by Erasmus exchange program.

[1] E. Sigel, M.E. Steinmann, Structure, function, and modulation of GABA(A) receptors, The Journal of Biological Chemistry **287**, 40224-31 (2012).
[2] T.C. Jacob, S.J. Moss, R. Jurd, GABA(A) receptor trafficking and its role in the dynamic modulation of neuronal inhibition, Nature reviews. Neuroscience **9**, 331-43 (2008).
[3] M.I. González, H.L. Grabenstatter, C.A. Cea-Del Rio, Y. Cruz Del Angel, J. Carlsen, R.P. Laoprasert, A.M. White, M.M. Huntsman, A. Brooks-Kayal, Seizure-related regulation of GABAA receptors in spontaneously epileptic rats, Neurobiology of Disease **77**, 246-56 (2015).

IMPACT OF MENTAL FATIGUE ON VISUAL GROUPING OF ISOLUMINANT STIMULI

Tatjana Pladere[1], Diana Bete[1], Jurgis Skilters[2], Gunta Krumina[1]

[1] Department of Optometry and Vision Science, University of Latvia, Latvia
[2] Center for the Cognitive Sciences and Semantics, University of Latvia, Latvia
tatjana.pladere@iespejamamisija.lv

In the natural world, a visual stimulus is surrounded by a number of other irrelevant stimuli. Due to amount of information and limited capacity of a processing system, visual grouping occurs. Our visual perception prefers certain grouping of information (for instance, proximity, similarity, connectedness, good continuation and common region) [1]. But there is strong evidence that the visual perception can be substantially impaired in the presence of mental fatigue [2]. The question is how selective visual attention, which can be considered a top-down controlled neuronal gain mechanism, is influenced.

The purpose of our research is to determine the influence of mental fatigue on visual grouping of definite information – color and configuration of stimuli in the psychophysical experiment. 101 individual, between 18 and 32 years old, participated in this study. Individuals provided subjective data by filling in the questionnaire about their health and general feeling. The objective evidence was obtained in the specially designed visual search task were chromatic and achromatic stimuli with same luminance were used in order to avoid so called pop-out effect. Each individual was instructed to define the symbols with aperture in the same direction in four tasks. Color component differed according to the goals of study.

The results demonstrate that the visual grouping is completed faster when target visual stimuli have the same color and aperture direction. The average time per target (2.74 ± 0.07 seconds) is significantly different from data which is obtained in other conditions ($p < 0.05$). The shortest reaction time is in the evening (from 5 pm to 10 pm, 2.84 ± 0.06 seconds). What is more, the results of reaction time suggest that the analysis of two grouping processes compete for selective attention in the visual system when similarity in color conflicts with similarity in configuration of stimuli. The described effect increases significantly in the presence of mental fatigue. But it does not have strong influence on the accuracy of task accomplishment.

[1] R. Houtkamp, P. R. Roelfsema. Parallel and serial grouping of image elements in visual perception. Journal of Experimental Psychology: Human Perception and Performance., 36 (6), 1443- 1459 (2010).
[2] L. G. Faber, N. M. Maurits, M. M. Lorist. Mental fatigue affects visual selective attention. PloS one, 7 (10), e48073 (2012).

Oral session 3

Chemistry, chemical physics and biochemistry

PROGRAMMABLE RNA AND DNA CLEAVAGE BY A CRISPR-CAS SYSTEM

Migle Kazlauskiene*, Gintautas Tamulaitis, Česlovas Venclovas, Virginijus Šikšnys

Institute of Biotechnology, Vilnius University, Lithuania
* migle.kazlauskiene@gmail.com

CRISPR-Cas systems are an adaptive prokaryotic defense mechanism set against viral infection and horizontal gene transfer. The sequence-specific degradation of invasive nucleic acids (NA) is carried out by ribonucleoprotein effector complexes. While the cleavage is executed by protein subunits, the recognition of specific target nucleic acid is performed mostly by an RNA molecule called crRNA. This feature allows easy programmability of sequence-specificity of the CRISPR-Cas systems. Effector complexes from Type I and II CRISPR-Cas systems (Cascade and Cas9-RNA, respectively) cleave foreign DNA [1]. Currently they are being developed into precise genome editing tools [2]. On the other hand, Type III-B effector complexes degrade RNA [3]. However, genetic evidence suggested that closely related Type III-A Csm complex targets DNA [4]. Recently DNA cleavage by Csm complex has been reconstituted *in vitro*, although in a complex system involving transcription [5]. Nevertheless, the mechanism nucleic acid interference, mediated by Csm complexes, remains unclear.

Here we aimed to establish the nucleic acid specificity and cleavage mechanism of the Type III-A system Csm-machinery using *Streptococcus thermophilus* as a model system. We expressed the Type III-A CRISPR-Cas locus in *Escherichia coli*, isolated the Csm effector complex and characterized its composition. We showed that Csm complex recognizes target RNA molecules via basepairing with crRNA and Csm3 proteins, present in the Csm complexes in several copies, cleaves them in multiple sites interspaced by 6 nucleotides [6]. Moreover, we discovered that target RNA binding promotes single-stranded DNA hydrolysis by the Csm complex and identified the active center responsible for this activity. We also established that host cell protects its own DNA from degradation both by means of spatiotemporal regulation of Csm complex activity and by recognition of its own transcripts via the sequences flanking the target. Further, we demonstrated that Csm complex may be reprogrammed to cleave the NA substrate of interest *in vitro* and *in vivo* (in *E. coli* cells). This opens new possibilities for a programmable precise RNA cleaving tool as well as cell selection in molecular biology.

[1] D. Rath, L. Amlinger, A. Rath, M. Lundgren, The CRISPR-Cas immune system: Biology, mechanisms and applications, Biochimie **117,** 119-128 (2015).
[2] R.M. Terns, M.P. Terns, CRISPR-based technologies: prokaryotic defense weapons repurposed, Trends in genetics, **30,** 111-118 (2014).
[3] C.R. Hale, P. Zhao, S. Olson, M.O. Duff, B.R. Graveley, L. Wells, R.M. Terns, M.P. Terns, RNA-guided RNA cleavage by a CRISPR RNA-Cas protein complex, Cell, **139,** 945-956 (2009).
[4] L.A. Marraffini, E.J. Sontheimer, CRISPR interference limits horizontal gene transfer in staphylococci by targeting DNA, Science, **322,** 1843-1845 (2008).
[5] P. Samai, N. Pyenson, W. Jiang, G.W. Goldberg, A. Hatoum-Aslan, L.A. Marraffini, Co-transcriptional DNA and RNA Cleavage during Type III CRISPR-Cas Immunity, Cell, **161,** 1164-1174 (2015).
[6] G. Tamulaitis, M. Kazlauskiene, E. Manakova, C. Venclovas, A.O. Nwokeoji, M.J. Dickman, P. Horvath, V. Siksnys, Programmable RNA shredding by the type III-A CRISPR-Cas system of *Streptococcus thermophilus*, Molecular Cell, **56,** 506-517 (2014).

NEW APPLICATION OF LAWESSON'S REAGENT (LR) FOR THE PREPARATION OF DIHETARYL AND ARYL/FERROCENYL SUBSTITUTED TRIFLUOROMETHYLENE THIOLS

Róża Hamera-Fałdyga, Katarzyna Urbaniak, Małgorzata Celeda, , Grzegorz Mlostoń*

Department of Organic & Applied Chemistry, University of Łódź, Poland
Tamka 12, PL-91-403 Łódź
roza.hamera@gmail.com

Alcohols and thiols containing both trifluoromethyl group and ferrocenyl moiety constitute a novel class of relatively little known fluoroorganic compounds. The introduction of the trifluoromethyl group CF_3 into the molecule of an organic compound usually results in a significant modification of its biological and physico-chemical properties [1]. The ferrocenyl substituted thiols and alcohols represent an unique class of practically useful building blocks for the synthesis of biologically active compounds and are extensively studied as potentially interesting compounds for materials and bioorganic chemistry [2]. Fluorinated, ferrocenyl functionalized compounds are rare, however, chiral 2,2,2-trifluoro-1-ferrocenylethanol is an important compound in proteomics research and related medicinal studies. Its synthesis was reported by Cullen et al., as well as by Sokolov et al. via multistep synthesis based on the electrophilic trifluoroacetylation of ferrocene followed by backer's east supported reduction of the C=O bond [3].

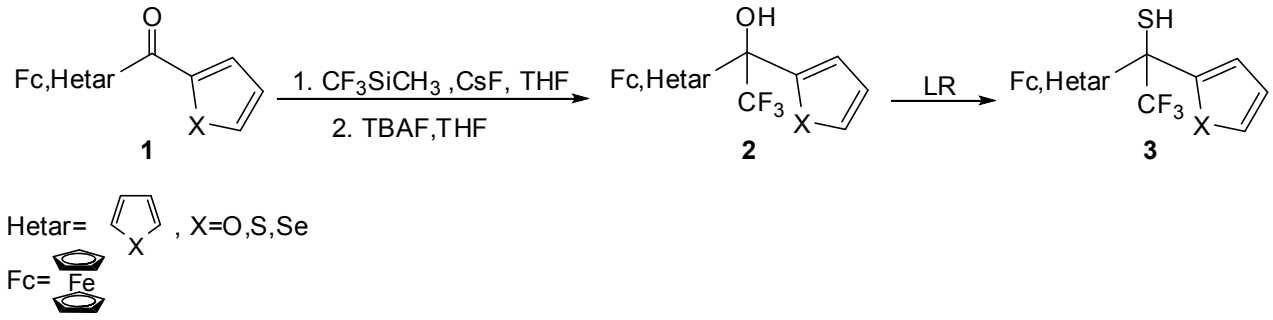

Scheme 1.Synthesis of trifluoromethylated thiols **3** .

The trifluoromethylation of carbonyl derivatives is a valuable method for the C-CF_3 bond construction. The nucleophilic trifluoromethylation with (trifluoromethyl)trimethylsilane (Ruppert-Prakash reagent) offers a convenient protocol for the conversion of ketones and aldehydes into the trifluoromethyl substituted alcohols [4].

Our ongoing studies are focused on the use of Lawesson's reagent (LR) for the synthesis of corresponding trifluoromethyl substituted thiols of type **3**. The presented method offers an innovative approach to the preparation of both alcohols of type **2** and thiols of type **3** functionalized with hetaryl and/or ferrocenyl moieties.

Acknowledgement: *Financial support by the National Science Center (PL-Cracow) within the research grant OPUS–7 (UMO–2014/13/B/ST5/04004) is acknowledged.*

[1] G. Mlostoń, E. Obijalska, H. Heimgartner, J. Fluorine Chem., **131**, 830–844 (2010).
[2] a) P.J. Štěpnička; Ed., Ferrocenes: Ligands, Materials and Biomolecules; Wiley & Sons Ltd: Chichester, U.K. (2008); b) T. Izumi, S. Aratani, J. Chem. Techn. Biotechnol., **63**, 25–32 (1995).
[3] a) W. Cullen, R. William, M. Fishman, Inorg. Chim. Acta, **46**, 85–86 (1980); b) V.I. Sokolov, L.L. Troitskaya, T.I. Rozhkova, Gazz. Chim. Ital., 117, 525–528 (1987).
[4] G. Rubiales, C. Alonso, E. Martinez de Marigorta, F. Palacios, Arkivoc, 362–405 (2014).

NAZAROV CYCLISATION REACTION OF *IN SITU* GENERATED *α,β*-ALKENOYLPERYLENES

Marta Głodek[1], Anna Makal[2], Janusz Zakrzewski[1], Damian Plażuk[1*]

[1] Faculty of Chemistry, Department of Organic Chemistry, University of Łódź, ul. Tamka 12, 91-403 Łódź, Poland
[2] Faculty of Chemistry, Warsaw University, ul. Pasteura 1, 02-093 Warszawa, Poland
martaglodek@vp.pl

Development of new carbon-carbon bond forming reactions is still one of up to date issues in organic chemistry. During last decade numerous new C-C bond forming reactions and new variants of an old C-C bond forming reactions have been described. Friedel-Crafts acylation, which appends alkyl or acyl groups to aromatic rings *via* alkyl or acyl cation intermediates, is still one of the most important reaction in a synthesis of complex molecules [1]. The other important C-C bond forming reaction, allowing to formation of cyclopentanone from divinyl ketones, is Nazarov cyclization [2,3]. In the communication we will disclose a one-step synthesis of fused-perylene ketones *via* tandem Friedel-Crafts acylation reaction and Nazarov cyclization. Scope, limitation, stereochemistry, mechanistic aspects and fluorescent properties on new perylene-based days will be discussed.

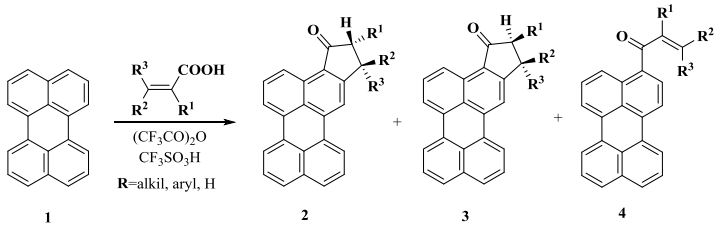

Fig. 1. Reaction of perylene with α,β-alkenoic acids under Friedel-Crafts reaction conditions

Acknowledgement: The authors are grateful for the financial support of The National Science Centre (Poland) based on the decision no DEC-2013/11/B/ST5/01077

[1] Dunach, E., Carbon-carbon bond formation by Lewis superacid catalysis. *Chemistry and Biodiversity* **2014,** *11*, 1752-1763.
[2] Raja, S.; Nakajima, M.; Rueping, M., Experimental and computational study of the catalytic asymmetric 4π-electrocyclization of N-heterocycles. *Angewandte Chemie - International Edition* **2015**, 54, 2762-2765.
[3] Vaidya, T.; Cheng, R.; Carlsen, P. N.; Frontier, A. J.; Eisenberg, R., Cationic cyclizations and rearrangements promoted by a heterogeneous gold catalyst. *Organic Letters* **2014**, 16, 800-803.

MD SIMULATIONS OF 1-DECYL-3-METHYL-IMIDAZOLIUM CHLORIDE IONIC LIQUID AND ITS MIXTURES WITH WATER

Dovilė Lengvinaitė[1,2], Francesca Mocci[2], Kęstutis Aidas[1]

[1] Department of General Physics and Spectroscopy, Faculty of Physics, Vilnius University, Lithaunia
[2] Department of Chemical sciences, University of Cagliari, Italy
dlengvinaite@gmail.com

Molecular dynamics (MD) simulations are valuable tool to study the thermodynamics, structure and dynamics of ionic liquids on the atomistic level. It is noteworthy that these simulations allow to investigate relatively large systems containing thousands of atoms from which all static and dynamic observables can be extracted reasonably well. The main output of a simulation is a phase space trajectory and the specific challenge consists of using the detailed information about the atomic positions, velocities and forces to obtain relevant information about physics of the system studied.[1]

Room-temperature ionic liquids (RTILs), that are salts are liquids at ambient temperatures and pressures, provide desirable features such as very low vapor pressure, thermal stability, high ionic conductivity, non-flammability, and a large temperature range for which they remain liquid. One of the many advantages of RTILs is the ability to tune physicochemical properties such as density, viscosity, conductivity, and hydrogen bonding by selecting appropriate cations, anions, and polar or non-polar solvents. Interactions between different types of RTILs and water solvents are important because RTILs can absorb a large amount of water from the atmosphere.

Molecular dynamics (MD) simulations play an important role in understanding how condensed-phase properties of IL/water mixtures are linked to their microscopic structure and to the network of interactions formed by their components.[2]

The aim of this work are to verify the best setting for the simulations in term of accuracy and computation time and use them to study the structural and dynamical properties of the ionic liquid (1-decyl-3-methyl-imidazolium chloride ([Dmim][Cl])) and how they are affected by the presence of water molecules. The effect of parameter such as the non bonded interactions cut off and time step on the simulation results has been verified.

Using the Amber 14 simulation package[3] we simulated both the pure ionic liquid, and its mixtures of varying water content. Changes in important bulk properties such as the density has been monitored, revealing that long simulation time (> 100 ns) are required to the system to reach equilibrium. An overall view of the structural properties of the investigated systems has been gained from the radial distribution functions g(r) of a selected subset of atoms that have been calculated from the MD trajectories (see Fig. 1). Structural and bonding properties have been further analyzed by calculating spatial distribution functions (SDF). To elucidate the effect of water on the dynamic properties of IL/water mixtures, we computed the translational self-diffusion coefficients.

Detailed account of the results will be presented at the conference.

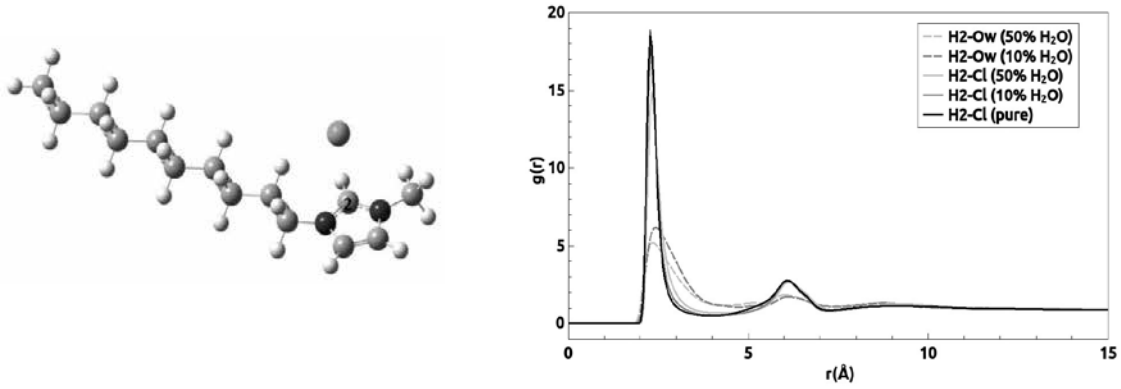

Fig. 1. Structure of the 1-decyl-3-methyl-imidazolium chloride ionic pair (on the left side) and radial distribution functions of [DMim][Cl]/water mixtures (on the right side)

[1] Liu, Z.; Huang, S.; Wang, W.; *J. Phys. Chem. B* **2004**, *108*, 12798.
[2] Niazi, A. A.; Rabideau, B. D.; Ismail, A. E.; *J. Phys. Chem. B* **2013**, *117*, 1378.
[3] Case, D. A.; Berryman, J. T.; Betz, R. M.; **AMBER 2015**, University of California, San Francisco.

HYDROPHILIC, UPCONVERTING LANTHANIDE-DOPED $NaGdF_4$:Yb,Er@$NaGdF_4$ CORE-SHELL NANOPARTICLES AS POTENTIAL MULTIFUNCIONAL BIOPROBES

Dovile Baziulyte[1], Marius Stalnionis[2], Ignas Jurciukonis[2], Vitalijus Karabanovas[2], Simas Sakirzanovas[1]

[1]Vilnius University, Faculty of Chemistry, Lithuania
[2]National Cancer Institute, Biomedical Physics Laboratory, Lithuania
dovile.baziulyte@chf.vu.lt

Upconverting nanoparticles (UCNPs) have found a potential uses in many applications such as biological imaging, cancer-targeting or drug delivery [1]. However, these applications of such nanomaterials are still restricted due to the hydrophobic oleate capping ligand and low upconversion efficiency.

In this study, hydrophobic UCNPs was converted into hydrophilic ones using a commercially available surfactant Tween 80. Furthermore, it is shown that the epitaxial growth of an optically inert $NaGdF_4$ layer around $NaGdF_4$:Yb,Er core nanoparticle effectively prevents surface quenching of excitation energy. Scanning electron microscopy (SEM), powder X-ray diffraction (XRD), and photoluminescence (PL) spectra have been used to characterize the size, crystal structure and emission color of the samples, respectively. Photoluminescence data indicates that the upconverting fluorescent intensity of $NaGdF_4$:Yb,Er@$NaGdF_4$@Tween80 was obviously higher than that of $NaGdF_4$:Yb,Er@Tween80 (Fig. 1). The outer $NaGdF_4$ layer protects the inner core and its crystal structure, thus enhancing the fluorescence. Due to the good water-solubility and strong UC luminescence, these hydrophilic nanocrystals may be used for imaging and detection applications in biological assays.

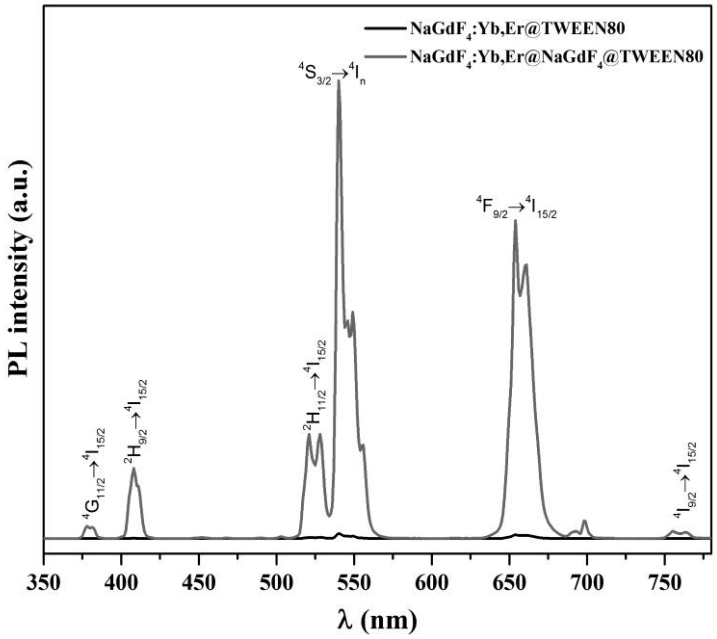

Fig. 1. Upconversion luminescence spectra of Tween 80 coated core and core-shell nanoparticles upon 980 nm excitation.

[1] L. Y. Ang, M. E. Lim, L. C. Ong, et al., Applications of upconversion nanoparticles in imaging, detection and therapy, Nanomedicine **6**, 1273–1288 (2011).

STRUCTURAL AND MAGNETIC CHARACTERISTICS OF $Mg_xZn_{1-x}Fe_2O_4$ NANOPARTICLES, OBTAINED BY DIFFERENT METHODS

Elena Petrova[1], Dzmitry Kotsikau[1], Valentin Natarov[1], Vladimir Pankov[1], Ekaterina Kravchenko[1]

[1] Department of Physical Chemistry, Belarusian State University, Belarus
petrovaeg@bsu.by

Superparamagnetic iron oxide-based nanoparticles are of great interest in medicine as magnetic resonance imaging (MRI) contrast agents, being a good alternative to traditional Gd-containing substances. The main requirements for such nanoparticles to be applicable in MRI are: small size and narrow size distribution, low toxicity and high magnetic properties, i.e. saturation magnetization value. Magnetic iron oxides with spinel structure (γ-Fe_2O_3 and Fe_3O_4) are most commonly used, however, their magnetic properties can still be improved by varying synthesis conditions and substituting some of the iron with other metal (Co, Ni, Mg, Zn etc.) ions, the arrangement of which also playing a big role [1, 2].

$Mg_xZn_{1-x}Fe_2O_4$ (x = 0.25, 0.5, 0.7) nanoparticles were synthesized using different methods: coprecipitation, spray pyrolysis and nitrate-citrate auto-combustion method, the last two being modified by introducing NaCl as inert component. Magnesium and zinc were chosen as doping ions due to relatively low toxicity and well-known ability to increase saturation magnetization of magnetite when placed in octahedral sites in spinel structure [3]. The phase and microstructure of the nanoparticles were studied with XRD and SEM/TEM analysis, and magnetic measurements were conducted at room and low (5-7 K) temperatures. The aim was to establish correlation between synthesis conditions, cation distribution, particle size and magnetic properties of the nanoparticles.

All the techniques used were found to produce single-phased spinel nanomaterials with the average particle size below 100 nm: 70-90 nm for nitrate-citrate, 20-40 nm for spray pyrolysis and 5-10 nm for coprecipitation method. The lattice constants for all methods used were found to be smaller than for bulk materials, with the increase with increasing zinc concentration, but differ for the same composition obtained by different methods. This can be explained by the difference in cation distribution because of the difference in temperatures and times of synthesis.

All the samples show no hysteresis behavior at room temperature which indicates their superparamagnetic state. At room temperature the highest saturation magnetization values for nitrate-citrate and coprecipitation methods were observed for $Mg_{0,5}Zn_{0,5}Fe_2O_4$ (22 and 33 emu/g, respectively). However, for spray pyrolysis method the highest saturation magnetization relates to $Mg_{0,7}Zn_{0,3}Fe_2O_4$ (26 emu/g).

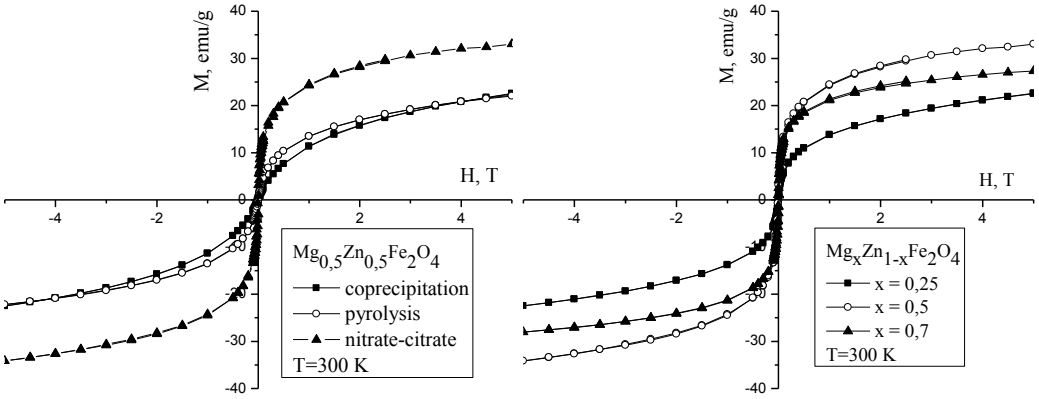

Fig. 1. Magnetization vs. field curves for the $Mg_xZn_{1-x}Fe_2O_4$ powders obtained by different methods, at room temperature.

The inversion degrees for all samples were calculated and found to be around 0,93 for coprecipitation, 0,91 for spray pyrolysis and 0,89 for nitrate-citrate method, which corresponds well with the results of magnetic measurements – the lower the inversion degree, the higher is saturation magnetization. Annealing at high temperatures leads to the increase of saturation magnetization due to cation redistribution in spinel structure, but also results in additional aggregation of nanoparticles due to the sintering. To avoid agglomeration during annealing NaCl was used as a template for spray pyrolysis and nitrate-citrate methods, providing nanosized powders that are potentially applicable for MRI contrasting and other biomedical applications.

[1] K. Nishio, M. Ikeda et al., Preparation of size-controlled (30–100 nm) magnetite nanoparticles for biomedical applications, J. Magn. Magn. Mater. **310**, 2408-2410 (2007).

[2] A.K. Gupta, M. Gupta, Synthesis and surface engineering of iron oxide nanoparticles for biomedical applications, Biomaterials, **26**, 3995-4021 (2005).

[3] A. Daigle, J. Modest, A.L. Geiler et al., Structure, morphology and magnetic properties of $Mg_xZn_{1-x}Fe_2O_4$ ferrites prepared by polyol and aqueous coprecipitation methods: a low-toxicity alternative to $Ni_xZn_{1-x}Fe_2O_4$ ferrites, Nanotech., **22**, 305708-14 (2011).

Oral session 4

Chemistry and chemical physics

QUANTUM CHEMISTRY IN THE SERVICE OF MODERN CRYSTALLOGRAPHY – TESTING NEW REFINEMENT METHODS ON A SET OF CRYSTAL STRUCTURES OF AMINO ACIDS AND TRIPEPTIDES

Magdalena Woińska[1], Simon Grabowsky[2], Dylan Jayatilaka[3], Paulina Dominiak[1], Krzysztof Woźniak[1]

[1] Biological and Chemical Research Centre, Chemistry Department, University of Warsaw, Żwirki i Wigury 101, 02-089 Warsaw, Poland
[2] Institut für Anorganische Chemie und Kristallographie, Fachbereich 2 - Biologie/Chemie, Universität Bremen, Leobener Str. NW2, 28359 Bremen, Germany
[3] School of Chemistry and Biochemistry, The University of Western Australia, 35 Stirling Highway, Perth WA 6009, Australia
mwoinska@chem.uw.edu.pl

X-ray diffraction is the most commonly applied experimental method of investigating structure of substances in the crystal phase. Moreover, high resolution crystallographic measurements allow to reconstruct electron density which is a rich source of information about properties of molecules in crystals and interactions between them. However, extracting reliable information requires not only good quality experimental data, but also advanced data processing methods (i.e. crystallographic refinement methods) based on sophisticated models utilizing the achievements of quantum chemistry. To date, the most popular technique is the multipole refinement (MM) introduced by Hansen and Coppens [1], which, due to insufficient flexibility and not constraining the refined electron density to any physical quantity, is known to yield experimental density characterized by many flaws [2]. Alternative methods presented in this work are two refinement techniques, such as Hirshfeld atom refinement (HAR, refinement of positional parameters of atoms only) and the subsequent fitting of experimentally constrained wave function (XCW, introducing the experimental contribution to the wave function) [3][4], based on Hirshfeld partition of electron density. In this partition each atom in the crystal is ascribed its own contribution to the molecular density, which is proportional to its share in the density of a molecule constructed of spherically averaged atomic densities. On the basis of this procedure the parameters necessary to carry out refinement of crystal structure and electron density are obtained. HAR and XCW use extensively computational chemistry methods, as each refinement step includes *ab initio* calculations of the molecular wave function. For these techniques, the obtained electron density is constrained to the quantum mechanical minimum of energy, unlike for MM. HAR and XCW are therefore free from serious limitations of MM, which for example results in significant improvement of the description of positions and thermal motions of hydrogen atoms in crystals [4].

In this contribution we would like to present the comparison of the described methods of high resolution X-ray data refinement for a set of crystalline structures of 4 amino acids and 6 tripeptides. The quality of electron density in crystals reconstructed with the applied techniques is evaluated basing on the analysis performed within QTAIM formalism [5]. This method allows to partition the space in the crystal into separate fragments belonging to each atom and thus obtain atomic properties such as charge, dipole moment and volume, as well as properties at the bond critical points (BCPs, critical points of electron density present in the vicinity of chemical bonds) such as electron density or its Laplacian. QTAIM properties obtained with MM, HAR and XCW on the basis of the experimental electron density are compared to the benchmark values derived from periodic DFT calculations carried out for all the structures with CRYSTAL06 program. The analysis of bond lengths and thermal motions of atoms in the investigated crystals is also performed. The selected compounds allow to study certain types of C, N, O and H atoms and bonds linking them, which are common not only in molecules of biological importance but also in a variety of organic compounds. Therefore, the analysis of trends revealed by QTAIM properties in the chosen class of compounds facilitates drawing more general conclusions concerning the performance of each of the refinement methods. Our study reveals the advantage of the Hirshfeld partition based methods over MM in the description of electron density in crystals derived from X-ray experiments. MM systematically underestimates atomic charges of N, O and C and also tends to incorrectly describe polar bonds such as C-N or C-O, overestimating electron density and Laplacian at the BCPs and resulting in wrong description of the regions of O lone electron pairs. HAR and XCW eliminate these problems, moreover they yield QTAIM properties being in significantly higher agreement with the theoretical values and also result in better quality of the refined structures compared to MM. It is worth noting that including experimental contribution to the molecular wave function by XCW causes certain divergence from the reference values, thereby making HAR the method best reproducing the results of theoretical calculations.

[1] N. K. Hansen & P. Coppens, Testing aspherical atom refinements on small-molecule data sets, Acta Cryst. **A34**, 909-921 (1978).
[2] J. M. Bąk, S. Domagała, C. Hübschle, C. Jelsch, B. Dittrich & P. M. Dominiak, Verification of structural and electrostatic properties obtained by the use of different pseudoatom databases, Acta Cryst. **A67**, 141-153 (2011).
[3] D. Jayatilaka & B. Dittrich, Acta Cryst. A64, 383-393 (2008).
[4] S. C. Capelli, H.-B. Bürgi, B. Dittrich, S. Grabowsky & D. Jayatilaka, IUCrJ, **1**, 361-379 (2014).
[5] R. F. W. Bader, Atoms in Molecules: A Quantum Theory, 1st ed. No. 22 in the International Series of Monographs on Chemistry. Oxford: Clarendon Press (1990).

THERMAL ANALYSIS OF 2,6-DIAMINOPURINE CRYSTALS WITH THE HELP OF CHARGE DENSITY

Urszula A. Budniak[1,2], Paulina M. Dominiak[1,2]

[1] Department of Chemistry, University of Warsaw, Poland
[2] Biological and Chemical Research Centre, University of Warsaw, Poland
ubudniak@chem.uw.edu.pl

The aim of the project was to analyze temperature evolution of 2,6-diaminopurine (DAP) crystal structure. DAP is a nucleobase, a derivative of adenine present in nucleoacids, which can be used to compare Watson-Crick pairing in DNA. Investigating the properties of analogues of nucleobases may contribute to our knowledge about nucleic acid properties in general and give an opportunity to find novel ligands binding to DNA, what is essential for drug design.

The main part of the project was based on the single-crystal X-ray diffraction experiments. The single crystals of DAP were measured in different temperatures ranging from 100 to 320 K. Due to the temperature rise, subtle, untrivial changes in diffraction pattern were observed. The structures were refined using two methods – Independent Atom Model (IAM) and Multipole Model (MM). IAM is a standard model, in which molecular charge density is described as the sum of spherical, isolated atoms. In turn, Hansen-Coppens MM takes into account also aspherical deformations, what allows to properly model the charge density on molecular bonding and lone pairs.

What essential, charge density is strongly correlated with thermal motion of atoms, thus the proper de-convolution is needed. Measurements in low temperature reduce thermal vibrations and hence increase the resolution limit, up to which the data can be collected. More accurate charge density model allows to obtain better thermal motion model. For this reason, high-resolution charge density measurement at 100 K was conducted. Obtained data were then refined using MM.

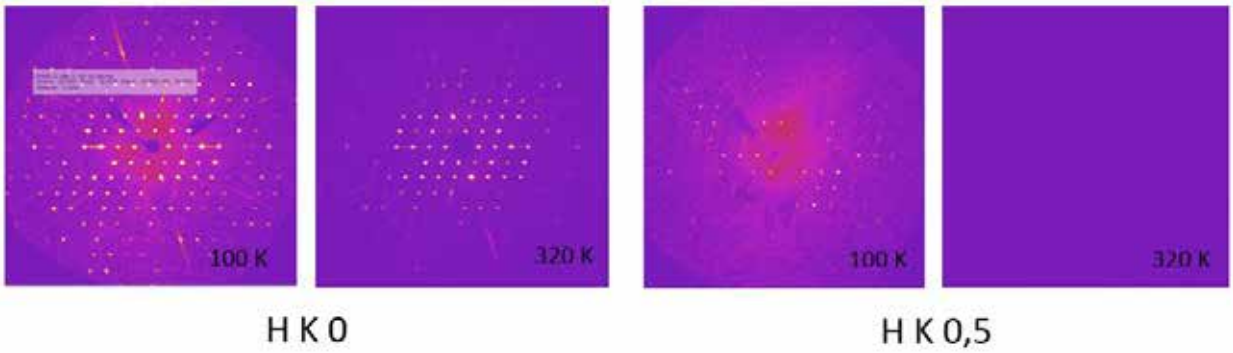

Fig.1 Differences between selected planes in various temperatures.

Unit cell parameters and atomic displacement parameters variations within temperature changes were noticed. The accurate analysis of observed variations was performed using the parameters transferred from MM.

To complement X-ray measurements, differential scanning calorimetry (DSC) and thermogravimetric analysis (TGA) experiments were also performed. These two methods enable to notice phase transitions or dehydration in sample, however existence of phase transition in case of DAP was not confirmed (only dehydration process was definitely proved).

Preliminary results suggest that DAP crystals have commensurate structure, which can be also described as a superstructure.

CRYSTAL STRUCTURES AND SYNTHESIS OF VITAMIN D ANALOGUES

Monika Nowakowska[1,2], Sharmin Nadkarni[3], Narasimha Rao Bolla[3], Andrzej Kutner[3], Krzysztof Woźniak[1]

[1] Faculty of Chemistry, University of Warsaw, Poland
[2]College of Inter-Faculty Individual Studies in Mathematics and Natural Sciences (MISMaP), University of Warsaw, Poland
[3]Pharmaceutical Research Institute, Warsaw, Poland
mnowakowska@chem.uw.edu.pl

The term vitamin D refers to a group of fat-soluble secosteroids. Two major forms of vitamin D are D_2 – ergocalciferol - which is found in plants and yeasts, and D_3 – cholecalciferol - which is found in animals and humans. The Vitamin D Receptor (VDR) also known as NR1I1 is a transcription factor. Due to the activation by calcitriol, the VDR and retinoid-X receptors form a heterodimer which changes its conformation. The heterodimer bonds to hormone response elements on DNA, which enables regulation of transcriptional response.[1] Moreover, VDR is involved in microRNA-directed post-transcriptional mechanism which is connected with the influence of calcitriol on human bones.[2] VDR could be find in many tissues, where plays various roles. So vitamin D has a lot of applications including regulation of calcium-phosphate metabolism, antiproliferation action, decreasing possibility of developing tumor and many others.

The crystal structures of 1,25-dihydroxyergocalciferol and 1,25-dihydroxycholecalciferol analogues have been determined and the result of this research will be presented. The crystal and molecular structures of these compounds were solved and refined using single crystal X-ray diffraction. Three of analogues crystallize in the $P2_12_12_1$ space group of the orthorhombic crystal system with the unit cell parameters: a=9.62082(8) Å, b=14.18309(12) Å, c=31.7987(2) Å; a=6.6492(5) Å, b=9.9013(9) Å, c=38.811(3) Å and a=38.0952(3) Å, b=12.95430(10) Å, c=11.07290(10) Å, respectively. One of analogues (Fig. 1) crystallizes in the C2 space group of the monoclinic system, with the unit cell parameters a= 33.410(2) Å, b=6.3780(4) Å, c=12.2329(8) Å. I will discuss structural differences between the above mentioned analogues and factors influencing these differences.

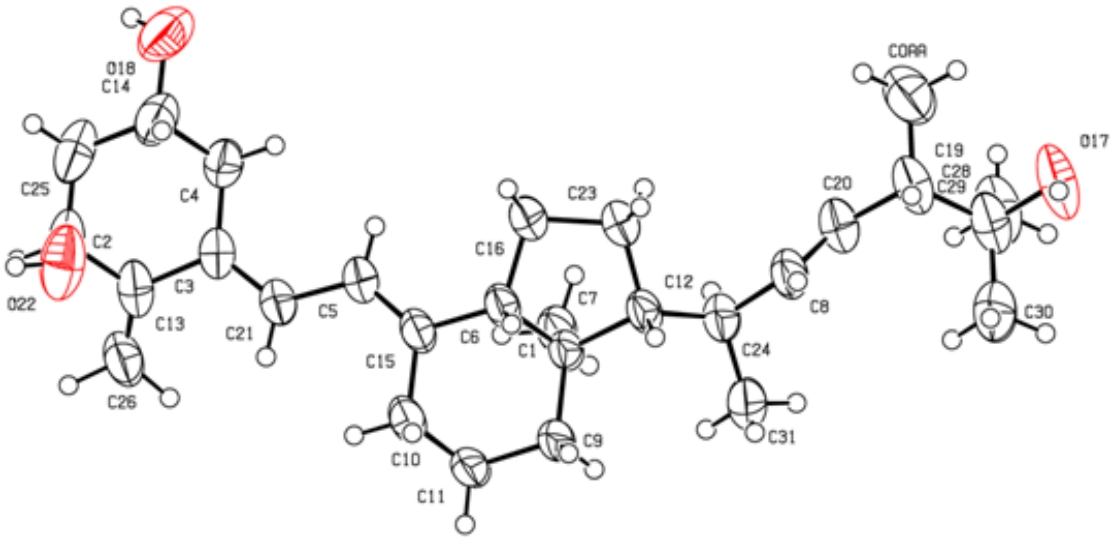

Fig. 1. Structure of 1,25-dihydroxyergocalciferol analogue which will be presented.

[1]Cheskis, B., Freedman, L. P. et al., Ligand modulates the conversion of DNA-bound vitamin D3 receptor (VDR) homodimers into VDR-retinoid X receptor heterodimers. Molecular and cellular biology, **14(5)**, 3329-3338. (1994).
[2] Lisse, T. S., Chun, R. F., Rieger, S., Adams, J. S., Hewison, M., Vitamin D activation of functionally distinct regulatory miRNAs in primary human osteoblasts. Journal of Bone and Mineral Research, **28(6)**, 1478-1488, (2013).

SPOTTING THE GEOMETRIC PROPERTIES IN THE CRYSTALLOGRAPHY OPEN DATABASE

Andrius Merkys[1], Antanas Vaitkus[1], Mykolas Okulič-Kazarinas[1], Saulius Gražulis[1,2]

[1]Vilnius University Institute of Biotechnology, Graiciuno 8, LT-02241 Vilnius, Lithuania
[2]Vilnius University Faculty of Mathematics and Informatics, Naugarduko 24, LT-03225 Vilnius, Lithuania
andrius.merkys@gmail.com

Computational screening of crystal structures vastly reduces the cost of identifying the materials with desired properties. It is a well-known fact that the properties of molecules – building blocks of materials – depend on the features of their geometry. Thus one could quite accurately predict various properties of a material by knowing the coordinates of a molecular structure and using computational chemistry tools. For example, knowledge of crystal contents and densities is sufficient enough to carry out the search of possible hydrogen storage materials [1]. Moreover, the identification of novel graphene-like compounds requires one to screen crystal structures for periodic layered compounds [2]. In order to present a tool for fast and efficient investigation of geometric properties in the Crystallography Open Database (http://www.crystallography.net) [3], the largest open resource of experimentally determined small molecule crystal structures, we have created methods allowing automatic unsupervised extraction of molecular geometry parameters – interatomic bond lengths, bond and dihedral angles, and crystal voids [4]. Our software is capable of automatically drawing conclusions about the geometry of crystal structures that are stored in the COD [5]. Such automatic conclusions could be used to detect geometric outliers in the newly deposited structures. We hope that the new methods and software will be helpful for the spotting of the geometric properties in the COD as well as other structural databases.

[1] Breternitz, J. & Gregory, D. The Search for Hydrogen Stores on a Large Scale; A Straightforward and Automated Open Database Analysis as a First Sweep for Candidate Materials. Crystals, 2015, 5, 617-633, http://www.mdpi.com/2073-4352/5/4/617/htm

[2] Mounet, N.; Schwaller, P.; Cepellotti, A.; Merkys, A.; Castelli, I. E.; Gibertini, M; Pizzi, G. & Marzari, N. In preparation.

[3] Gražulis, S.; Daškevič, A.; Merkys, A.; Chateigner, D.; Lutterotti, L.; Quirós, M.; Serebryanaya, N. R.; Moeck, P.; Downs, R. T. & Le Bail, A. Crystallography Open Database (COD): an open-access collection of crystal structures and platform for world-wide collaboration. Nucleic Acids Research, 2012, 40, D420-D427, http://nar.oxfordjournals.org/content/40/D1/D420.abstract

[4] Gražulis, S.; Merkys, A.; Vaitkus, A. & Okulič-Kazarinas, M. Computing stoichiometric molecular composition from crystal structures. Journal of Applied Crystallography, 2015, 48, 85-91, http://dx.doi.org/10.1107/S1600576714025904

[5] Merkys, A.; Long, F.; Murshudov, G. N. & Gražulis, S. Stereochemical statistics in Crystallography Open Database. Acta Crystallographica Section A, 2013, 69, s388-s389, http://scripts.iucr.org/cgi-bin/paper?S0108767313096621

Oral session 5

Laser physics and optical technologies

IN SEARCH OF STRUCTURE-FUNCTION RELATIONSHIPS IN MOLECULAR RECTIFIERS

Tingting Weng[1,2], Daniel DeBrincat[2], Vaida Arcisauskaite[2*], John McGrady[2*]

[1] Department of Chemistry, University of Wisconsin-Madison, USA
[2] Department of Chemistry, University of Oxford, UK
vaida.arcisauskaite@chem.ox.ac.uk

The recent updates to the International Technology Roadmap for Semiconductors (ITRS) [1] set out the need for fundamentally new technologies to replace existing silicon-based device components. One attractive solution is to develop molecular-scale analogues of key components such as wires, diodes and transistors. For the present, the challenge is to understand the chemistry and physics that controls current flow through molecules. Only then this knowledge is in place can real progress be made in addressing issues related to incorporation of such components into realistic devices.

Much of the recent momentum in the field of molecular electronics has been centred on organic components, where the π conjugated systems typically provide the dominant transport pathways. Transition metal based systems, in contrast, have been somewhat overlooked despite the fact that their innately flexible electronic structure offers enormous potential. Ligand field effects, changes in redox and spin state and metal-metal bonding all play a critical role in determining the nature of the transport channels near the Fermi level in a putative molecular electronic device. Structure-function relationships – principles that can guide synthetic effort towards target molecules – are not as well developed in the context of transition metal electronics as they are in the organic field.

The design of rectifiers, compounds which function is to allow the preferential flow of current in one directions, has been a holy grail since Aviram and Ratner first proposed the concept 40 years ago [2]. It is clear that asymmetry, either in the molecule or in its contacts to the electrodes, precludes the possibility that current flow is rigorously symmetric, but to what extent does the compositional asymmetry actually perturb the transport channels of interest? Arrays of redox-active transition metals are a promising avenue for further study: intramolecular electron transfer can support large internal electric fields which localize channels on one side or other of the molecule. Subtle changes in the left-right delocalization of a channel can then be controlled through spin-polarisation, and this can lead to substantial rectification ratios. In this presentation I will present our computational work [3] that seeks to provide a set of guidelines for electronic structure-function (*viz* rectification) relationships in transition metal atom chains (see Fig. 1).

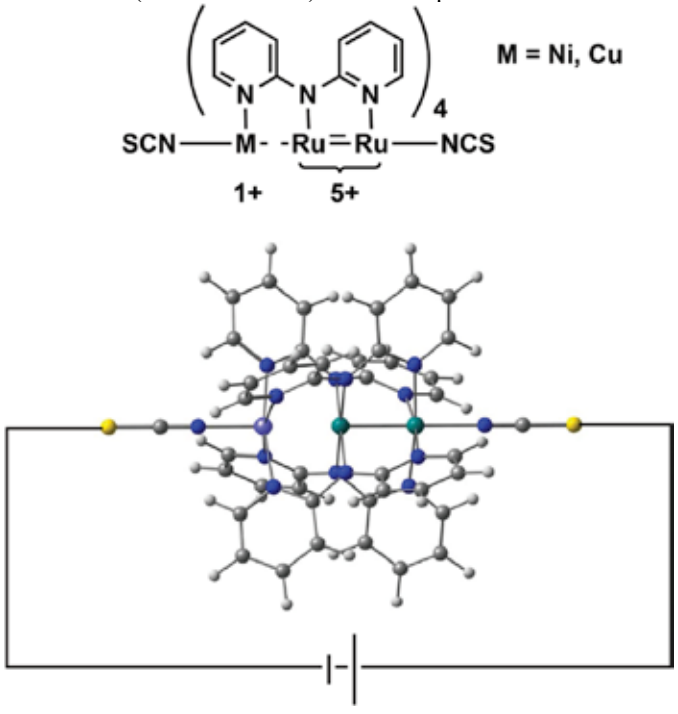

Fig. 1. $Ru_2M(dpa)_4(NCS)_2$, M=Ni, Cu Extended Metal Atom Chains (EMACs) investigated in our computational study [3].

[1] http://www.itrs2.net/itrs-reports.html
[2] A. Aviram, M. A. Ratner, Molecular Rectifiers, Chem. Phys. Lett. **29**, 277-283 (1974).
[3] T. Weng, D. DeBrincat, V. Arcisauskaite, J. E. McGrady, In search of structure-function relationships in transition-metal based rectifiers, Inorg. Chem. Front. **1**, 468-477 (2014).

3D MICROFABRICATION OF GOLD NANOPARTICLE DOPED HYBRID POLYMER VIA FEMTOSECOND LASER PULSES

Linas Jonušauskas[1], Marcus Lau[2], Peter Gruber[3], Bilal Gökce[2], Stephan Barcikowski[2], Mangirdas Malinauskas[1] and Aleksandr Ovsianikov[3]

[1] Department of Quantum Electronics, Vilnius University, Saulėtekio Ave. 9, Vilnius LT-10222, Lithuania
[2] University of Duisburg-Essen and Center for Nanointegration Duisburg-Essen (CENIDE), Technical Chemistry I, Universitaetsstr. 7, 45141 Essen, Germany
[3] Institute of Materials Science and Technology (E308), TU-WIEN (Technische Universitt Wien), Getreidemarkt 9, 1060 Wien, Austria
linas.jon@gmail.com

3D laser lithography (3DLL) [1] of a negative photopolymer (zirconium/silicon hybrid solgel SZ2080) doped with gold nanoparticles (Au NP) is performed employing a 515 nm, 200 kHz and 300 fs amplified laser system. The Au NP are generated via pulsed laser ablation in liquids (PLAL) [2] and sized around ∼7 nm [Fig. 1]. The effect of doping is explored - by varying the nanoparticle concentration from $4.8{\cdot}10^{-6}$ wt% to $9.8{\cdot}10^{-3}$ wt% we find that the fabricated line widths are both enlarged and diminished. The increase in feature size by up to 14.8% (when doped with $3.9{\cdot}10^{-3}$ wt% Au NP) compared to structures achieved in pure SZ2080 is observed. While implicating both positive and negative effect on the photosensitivity, the doping has no adverse impact on the mechanical quality of intricate 3D microstructures produced from the nanocompound [Fig. 2]. Additionally, we found that SZ2080 increases the long term (∼months) colloidal stability of Au NP in isopropanol.

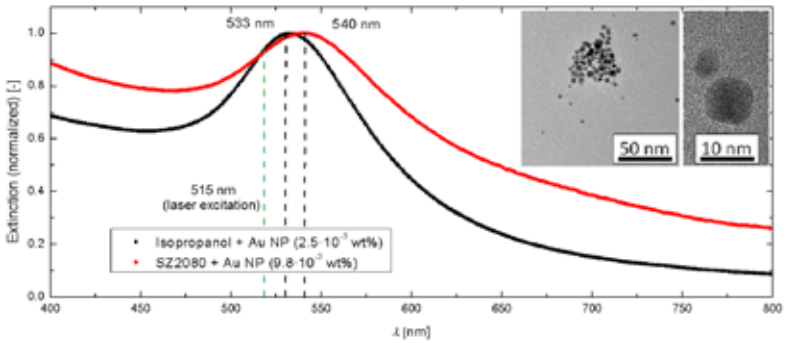

Fig. 1. Normalised extinction spectra of Au NP in isopropanol (peak centered around 533 nm) and SZ2080 doped with Au NP (peak around 540 nm). Concentrations are $2.5{\cdot}10^{-3}$ wt% and $9.8{\cdot}10^{-3}$ wt%, respectively. Green dashed line - laser wavelength applied for excitation (515 nm). Insets show HR-TEM images of particles used in this work.

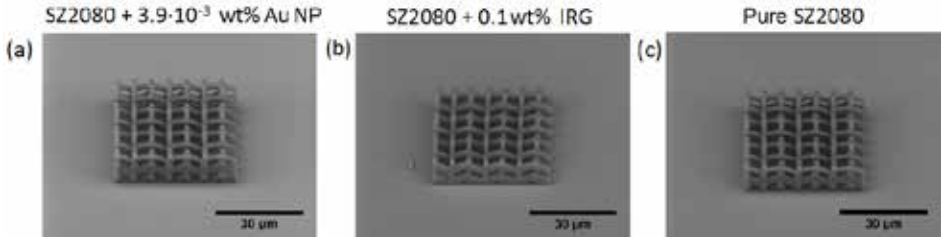

Fig. 2. Comparison of structures produced out of SZ2080 doped with $3.9{\cdot}10^{-3}$ wt% Au NP (a), SZ2080 with 0.1 wt% IRG (b) and pure SZ2080 (c). Fabrication from the material combining polymer and Au NP shows no influence on the mechanical quality of the structure.

Explanation based on Au NP plasmonic properties granting discussed phenomena is given. This knowledge can be used as a base for future work aimed at further examining mechanisms in pulsed laser processing of nanoparticle doped polymers. Also functional devices owning exotic properties [3] granted by combination of 3D micro-architecture and Au NP can be realized by 3DLL and potentially applied in novel photonic devices and biomedical scaffolds to mention a few.

[1] M. Malinauskas, A. Žukauskas, S. Hasegawa, Y. Hayasaki, V. Mizeikis, R. Buividas and S. Juodkazis, Ultrafast laser processing of materials: from science to industry, Light: Sci. Appl., in press (2016).
[2] D. D. Zand, P. Nachev, R. Rosenfeld, P. Wagener, A. Pich, D. Klee and S. Barcikowski, Nanocomposite Fibre Fabrication via in situ Monomer Grafting and Bonding on Laser-generated Nanoparticles, J. Laser Micro. Nanoeng. **7**(1), 21-27 (2012).
[3] S. Eustis and M. A. El-Sayed, Why gold nanoparticles are more precious than pretty gold: Noble metal surface plasmon resonance and its enhancement of the radiative and nonradiative properties of nanocrystals of different shapes, Chem. Soc. Rev. **35**(3), 209-217 (2006).

SIMULATION OF HIGH DIFFRACTION EFFICIENCY TRANSMISSION GRATINGS

Lukas Stankevičius[1,2], Tomas Tamulevičius[1,2]

[1]Institute of Material Science, Kaunas University of Technology
[2] Physics Department, Kaunas University of Technology
lukas.stankevicius@ktu.edu

Many research applications requires high intensity ultrashort laser pulses. Usually they are achieved employing chirped pulse amplification [1] and this requires nearly unit diffraction efficiency (DE = 100%) diffraction gratings. In this work, high efficiency diffraction grating for transmitted light diffraction was simulated.

Simulation was performed employing GSolverV52 software based on rigorous coupled-wave analysis. Two materials, one of high refractive index (Nb_2O_5) and other of low (SiO_2) were forming the antireflection coating and grating layer. Optimization was done for Yb:KGW laser with central wavelength of 1030 nm. Littrow configuration and TE (*Transverse Electric*) polarization case was simulated. Diffraction efficiency of -1T order was optimized varying grating structure parameters (Fig. 1 a).

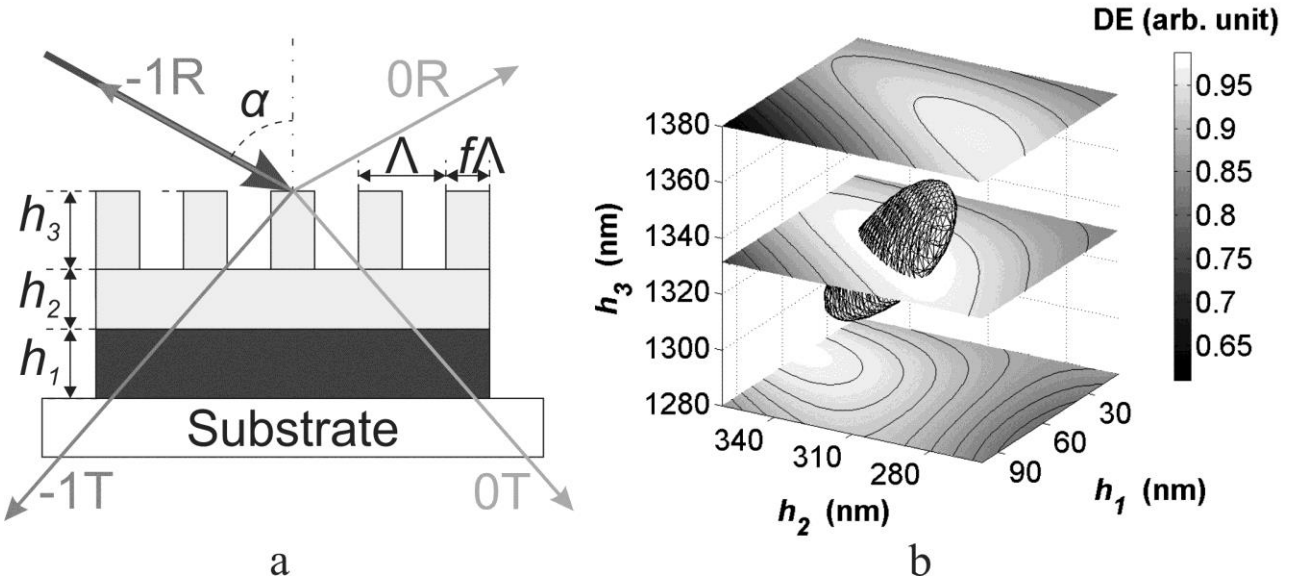

Fig. 1. (a) Simulation model. Light is of TE polarization and α = 61º incidence angle (Littrow). Structure is on fused silica substrate. Grating has filling factor f = 0.5 and period Λ = 588 nm. h_1, h_2 and h_3 corresponds to thickness of shown layers. (b) Simulation diffraction efficiency dependence on structure parameters h_1, h_2 and h_3. Greyscale shows DE value for each point. Ellipse shape in the middle of the graph is closed surface of greater than 0.98 diffraction efficiency values.

It was demonstrated that the highest transmitted light diffraction efficiency is 0.986 for proposed structure parameters h_1=60.2 nm, h_2=315.5 nm and h_3=1331.3 nm. It is noted that grating structure utilizes antireflective properties of two different refractive index layers combination, as they assures 0.999 (0T) at h_1=72.3 nm and h_2=258.4 nm without presence of the grating.

Acknowledgement

We would like to acknowledge dr. L. Giniūnas (Light Conversion), dr. R. Drazdys and dr. K. Juškevičius (Optida) for consultations and information about dielectric coatings. Lukas Stankevičius acknowledge support by project "Promotion of Student Scientific Activities" (VP1-3.1-ŠMM-01-V-02-003) from the Research Council of Lithuania. This project is funded by the Republic of Lithuania and European Social Fund under the 2007-2013 Human Resources Development Operational Programme's priority 3.

[1] A. Dubietis, G. Jonušauskas, A. Piskarskas, Powerful femtosecond pulse generation by chirped and stretched pulse parametric amplification in BBO crystal, Optics Communications, 88(4-6), 1992, pp 437-440

INFLUENCE OF THE SUBSTRATE ELECTRIC CONDUCTIVITY ON THE MORPHOLOGY OF ANODIZED POROUS ALUMINA

Juliusz Chojenka[1], Mariusz Hajdyła[2, 3], Alexey Maximenko[2], Marta Marszałek[2]

[1]Department of Physics, Cracow University of Technology, Poland
[2] Institute of Nuclear Physics, Polish Academy of Sciences, Poland
[3] Faculty of Physics, Astronomy and Applied Computer Science of the Jagiellonian University, Cracow, Poland
chojenka@wp.pl

Some patterning methods use nanoporous anodic alumina membranes as templates in order to obtain ordered arrays of nanostructures (nanodots, antidots and nanowires) [1-3]. Their hexagonally close packed structure can be easily tuned by the type of the electrolyte and the applied voltage. This work presents variations of the morphology of porous Anodic Aluminium Oxide (AAO) templates prepared by anodization of Al films deposited either on metal, or on semiconducting or dielectric substrates which are a barrier between the anode and the anodized film. Metallic Al films were deposited in high vacuum ($\sim 10^{-6}$ mbar) on Ti, Si, and Si/SiO_2 substrates. The anodization was carried out in sulphuric, oxalic and ortho-phosphoric acids at constant voltages of 25 V, 40 V and 185 V, respectively. The current-time dependence during anodization process was registered for each type of substrate. The morphology of the produced membranes was studied by Scanning Electron Microscopy (SEM) and Atomic Force Microscopy (AFM).

It was found that the cell diameter (the distance between the centres of neighbouring pores, D_C) of the fabricated oxide is less sensitive to the type of substrate than to the electrolyte type and the applied voltage. On the other hand, the decrease of pore diameters (D_P) of AAO prepared on semiconducting and dielectric substrates in comparison with AAO prepared on the TiO_2-free Ti substrate turned out to be significant. The latter effect can be explained by the decrease of the anodizing current density, which is detemined by conductivity of the substrate. Besides, it was found that for AAO prepared on the Si/SiO_2 substrate each cell contains a few additional pores with diameter ~15 nm.

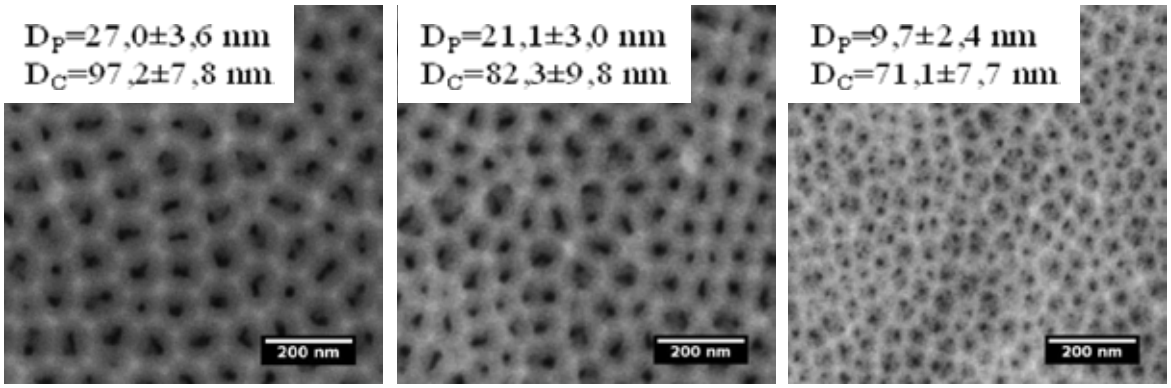

On Ti substrate ***On Si substrate*** ***On Si/SiO_2 substrate***

Fig. 1. Porous AAO templates prepared by anodization in oxalic acid on Ti, Si and Si/SiO_2 substrates.

Electric conductivity of the substrate is additional parameter which allows to adjust not only the diameter of the basic pores of the anodized alumina but also the number and the diameter of additional pores inside the elementary cell.

[1] Y. Lei, W. Cai, G. Wilde, Highly ordered nanostructures with tunable size, shape and properties: A new way to surface nano-patterning using ultra-thin alumina masks, Progress in Materials Science 52 (2007) 465–539
[2] A. Maximenko, J. Fedotova, M. Marszałek, A. Zarzycki, Y. Zabila, Magnetic characteristics of CoPd and FePd antidot arrays on nanoperforated Al_2O_3 templates, J. Mag. Mag. Mat. 400, 200205, 2016
[3] M.T. Rahman, N.N. Shams, C.H. Lai, J. Fidler, D. Suess, Co/Pt perpendicular antidot arrays with engineered feature size and magnetic properties fabricated on anodic aluminum oxide templates, Phys. Rev. B 81, 014418, 2010

Oral session 6

Laser physics and optical technologies

CAVITY ALIGNMENT USING FRINGE SCANNING

Laura Paulina Šinkūnaitė[1,2], Michael Landry[2], Keita Kawabe[2]

[1]School of Physics & Astronomy, University of Glasgow, United Kingdom
[2]LIGO, Hanford, WA, United States of America
sinkunaite.lp@gmail.com

LIGO stands for the Laser Interferometer Gravitational-wave Observatory. There are two identical observatories based approximately 3,000 kilometres apart: one is in Livingston, Louisiana, and its twin is located at the Hanford site, Washington. The latter observatory is where this project has been carried out.

The Hanford-site detector is an interferometer which contains two 4 km-long arm cavities formed into "L" shape. Its optical configuration is a suspended, dual-recycled Michelson interferometer with Fabry-Pérot cavities for arms [1]. They need to be aligned, before they can be locked on a fundamental transverse mode, TEM00. Once the cavity is locked, or controlled on resonance, alignment signals can be derived from wave-front sensors which measure the TEM01 mode content, which is a superposition of Hermite-Gaussian TEM01 and TEM10 modes [3]. However, the alignment state is not always good enough for locking on TEM00 (Fig. 1 and Fig. 2).

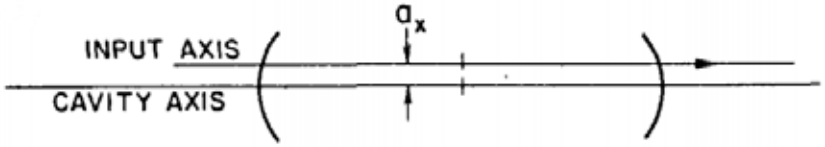

Fig. 1. Example of misalignment: transverse displacement [2].

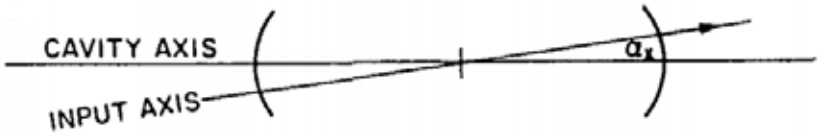

Fig. 2. Example of misalignment: tilt through an angle α [2].

Even when this is the case, the alignment can be evaluated using a free swinging cavity, that shows flashes when higher-order Hermite-Gaussian modes become resonant,

$$u_{nm}(x,y,z) = (2^{n+m+1}n!m!\pi)^{-1/2}\frac{1}{w(z)}exp(i(n+m+1)\Phi(z)) \\ \times H_n\left(\frac{\sqrt{2}x}{w(z)}\right)H_m\left(\frac{\sqrt{2}y}{w(z)}\right)exp\left(-i\frac{k(x^2+y^2)}{2R_C(z)}-\frac{x^2+y^2}{w^2(z)}\right). \quad (1)$$

This requires another round of optimisation: by moving test masses, small changes are made to the mirror orientation, and hence the TEM00 mode can be optimised iteratively. Currently, this is a manual procedure, and thus it is very time-consuming. Therefore, this project is aimed to study another possible way to lock the cavity on the TEM00 mode. Misalignment information can also be extracted from the power of the higher-order modes transmitted through the cavity. This report presents an algorithm for this alternative and faster way to derive the alignment state of the arm cavities.

[1] H. Kogelnik and T. Li, *Laser beams and resonators*, Appl. Opt. **5 (10)**, 1550-1567 (1966).
[2] D. Anderson, *Alignment of resonant optical cavities*, Appl. Opt. **23 (17)**, 2944-2949 (1984).
[3] Y. Hefetz, N. Mavalvala, and D. Sigg, *Principles of calculating alignment signals in complex resonant optical interferometers*, J. Opt. Soc. Am. B **14 (7)**, 1597-1605 (Jul 1997).

ANTIMONY TELLURIDE SATURABLE ABSORBERS FOR ULTRAFAST FIBER LASERS

Jakub Bogusławski[1*], Maciej Kowalczyk[1], Grzegorz Soboń[1], Rafał Zybała[2], Jan Tarka[1], Krzysztof M. Abramski[1], Jarosław Sotor[1]

[1] Laser & Fiber Electronics Group, Faculty of Electronics, Wrocław University of Technology, Wybrzeże Wyspiańskiego 27, 50-370 Wrocław, Poland
[2] Faculty of Materials Science and Engineering, Warsaw University of Technology, Wołoska 141, 02-507 Warsaw, Poland
jakub.boguslawski@pwr.edu.pl

Ultrafast fiber lasers are light sources of choice for many applications, like fluorescence microscopy, laser micromachining or nonlinear optics (including nonlinear frequency or supercontinuum generation). Due to the excellent beam quality, compactness and alignment-free, turn-key operation, they are commonly used not only for scientific, but also for industrial applications. As a consequence, fiber lasers are one of the most intensively developed branches of laser technology. Besides the application-driven research, they are also excellent test bed for basic studies – various kinds of solitons have been discovered in mode-locked fiber lasers as well as some extreme events, like soliton explosions. A femtosecond pulse in a fiber laser is formed as a consequence of interference of thousands oscillating cavity modes. To make this possible, a fixed phase relationship (mode-locking) must be induced through the balance of anomalous dispersion and nonlinearities supported through the use of a saturable absorber. The saturable absorber is a nonlinear optical device which changes its absorption as a function of the intensity of incident light, supporting the formation of the high peak power pulse over the noise. So far, the most common way to realize the saturable absorber is to use a semiconductor saturable absorber mirror (SESAM). The technology is well-established and characteristics of SESAM might be controlled to some extent. However, they suffer from the complicated (and very expensive) fabrication methods and rather narrow operation bandwidth (excluding the use of one SESAM at various operation bandwidths). For those reasons new solutions are constantly sought.

Recently, we have proposed a new material - antimony telluride - as a saturable absorber for fiber lasers [1]. Antimony telluride (Sb_2Te_3) is a V_xVI_y semiconductor with a ~0.3 eV energy gap, which has recently been recognized as a 3D topological insulator [2]. Topological insulators are newly discovered state of matter, characterized by highly conductive, metallic states on their surface and edges, similar to those present in graphene. Additionally, they exhibit high optical nonlinearity, which in connection to a flat transmission characteristic in a wide range in near- and mid-infrared, makes them a promising class of materials for saturable absorber application. Additionally, with the use of a pulsed magnetron sputtering technique (a kind of physical vapor deposition) [3,4], the material might be deposited on the variety of optical surfaces, including glass plate, mirrors, fiber connector tip or side-polished fiber. This material has been long known as a thermoelectric material and therefore the technology is well established. The approach is very straight-forward when compared to the SESAM fabrication. Antimony telluride was successfully used for mode-locking and Q-switching of fiber lasers operating in different spectral regions, including 1 μm, 1.56 μm and 2 μm (ytterbium-, erbium-, and thulium-doped fiber laser), which proves its versatility. The fabrication method and nonlinear optical properties of Sb_2Te_3 as well as various fiber laser configurations will be discussed during the presentation.

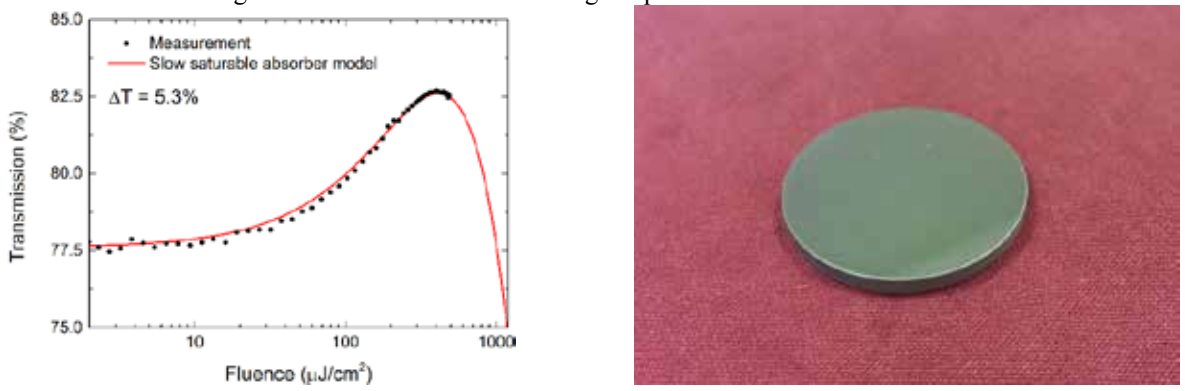

Fig. 1. The exemplary nonlinear transmission of Sb_2Te_3 saturable absorber (a); the inverse slope for higher fluence originates from a two-photon absorption. The photography of a glass plate with Sb_2Te_3 layer (b).

[1] J. Sotor, G. Soboń, W. Macherzyński, P. Paletko, K. Grodecki, K. M. Abramski, "Mode-locking in Er-doped fiber laser based on mechanically exfoliated Sb_2Te_3 saturable absorber," Optical Materials Express **4**, 1-6 (2014).
[2] H. Zhang, C. X. Liu, X. L. Qi, X. Dai, Z. Fang, S. C. Zhang, "Topological insulators in Bi_2Se_3, Bi_2Te_3 and Sb_2Te_3 with a single Dirac cone on the surface," Nature Physics **5**, 438–442 (2009).
[3] J. Bogusławski, G. Soboń, R. Zybała, J. Sotor, "Dissipative soliton generation in Er-doped fiber laser mode-locked by Sb_2Te_3 topological insulator," Optics Letters **40**, 2786-2789 (2015).
[4] J. Bogusławski, G. Soboń, R. Zybała, K. Mars, A. Mikuła, K. M. Abramski, J. Sotor, "Investigation on pulse shaping in fiber laser hybrid mode-locked by Sb_2Te_3 saturable absorber," Optics Express **23**, 29014-29023 (2015).

INFLUANCE OF SPECTRAL FILTRATION ON PULSE-SHAPE IN AN ALL NORMAL DISPERSION FIBER OSCILLATOR

Jan Szczepanek[1*], Tomasz M. Kardaś[1], Yuriy Stepanenko[1,2]

[1] Institute of Experimental Physics, Faculty of Physics, University of Warsaw, Pasteura 5, 02-093 Warsaw, Poland
[2] Institute of Physical Chemistry Polish Academy of Sciences, Kasprzaka 44/52, 01-224 Warsaw, Poland
*jan.szczepanek@fuw.edu.pl

All-fiber ultrashort-pulse lasers are becoming more and more popular not only for their excellent performance, which is now comparable with solid state lasers, but also because of complicated and fascinating nonlinear dynamics that take place within the cavity. All-normal-dispersion cavity fiber lasers are especially interesting because during propagation through the cavity laser pulses become highly chirped and, thus, maximum pulse intensity can reach high levels without the risk of the pulse distortion. This allows achieving pulse energies in nanojoule range with compressed pulse duration below 200 fs. In this paper we will be focused on the pulse propagation in the all-normal dispersion cavity where nonlinear phase accumulation together with normal GDD stretches the pulse [1]. The pulse formation process in such a cavity is known as a dissipative soliton regime. The pulse generation and shaping mechanism in such regime depends not only on the saturable absorber but also on the spectral filtration of the pulse. The narrow band-pass spectral filter cuts off the wings of highly chirped pulse inside the cavity and effectively shortens the pulse in time domain [2]. The spectral filter compensates temporal pulse broadening effect that appears during propagation in the normal dispersion material. We showed experimentally that by using different spectral shapes of the bandpass filter inside the all-fiber cavity one can manipulate to some extent the spectral intensity and spectral phase components of the pulse. Spectral filtration determines the initial pulse temporal envelope before further propagation in the all-fiber cavity.

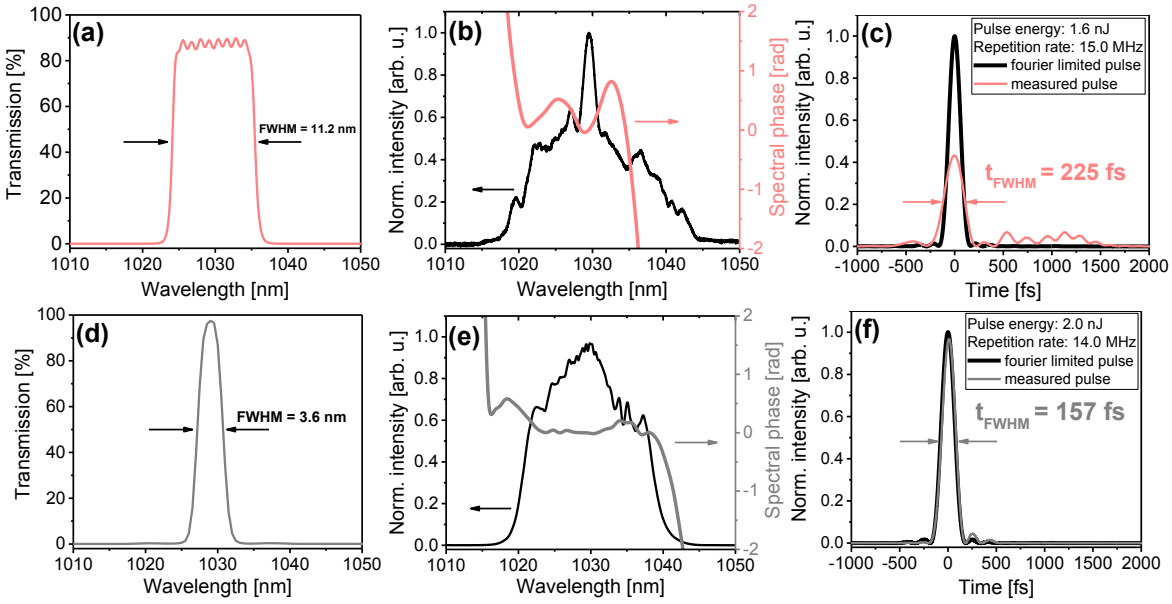

Fig. 1. Pulse parameters for two all-fiber laser configurations with different spectral filters transmission curves. Measured spectral filter transmissions (a), (d), measured spectra and spectral phase for different filters (b), (e), reconstructed pulse intensity (c),(f).

In Fig. 1 we present parameters of pulses from two all-fiber oscillators configurations with different spectral filter used inside the cavity. The (a),(b),(c) graphs present performance of the 15.0 MHz oscillator which delivered 1.6 nJ pulses compressed down to 225 fs [3]. The cavity works with 11.2 nm FWHM super-gaussian spectral filter (a). The (d),(e),(f) graphs show parameters of 2.0 nJ, 157 fs high-quality pulses generated from the oscillator working at 14.0 MHz repetition rate with the gaussian shaped 3.6 nm FWHM spectral filter (d). The results showed that the gaussian profile of spectral filtration (without steep edges) helped to avoid excessive nonlinear phase accumulation. In the configuration with gaussian filter the nonlinear phase of the pulse gained during the propagation in the cavity was compensated by means of standard grating compressor. The pulses were compressed close to their fourier-limited duration. The experimental results are supported by extensive numerical simulations of spectral filtration shape influence on the pulse temporal envelope in the all-fiber cavity.

[1] A. Chong, W. H. Renninger, and F. W. Wise, "Properties of normal-dispersion femtosecond fiber lasers," JOSA B **25**, 140–148 (2008).
[2] B. G. Bale, J. N. Kutz, A. Chong, W. H. Renninger, and F. W. Wise, "Spectral filtering for high-energy mode-locking in normal dispersion fiber lasers," JOSA B **25**, 1763–1770 (2008).
[3] J. Szczepanek, T. M. Kardaś, M. Michalska, C. Radzewicz, and Y. Stepanenko, "Simple all-PM-fiber laser mode-locked with a nonlinear loop mirror," Opt. Lett. **40**, 3500 (2015).

FUSED FILAMENT FABRICATION OF BIODEGRADABLE POLYLACTIC ACID THREE-DIMENSIONAL MICROSTUCTURES

Edvinas Skliutas[1], Ieva Gendvilienė[2], Vygandas Rutkūnas[2], Mangirdas Malinauskas[1]

[1]Department of Quantum Electronics, Vilnius University, Saulėtekio Ave. 9, Vilnius LT-10222, Lithuania
[2]Department of Prosthodontics, Vilnius University, Žalgirio Str. 115, Vilnus LT-08217, Lithuania
edvinas.skliutas@ff.stud.vu.lt

Fused filament fabrication (FFF also known as fused deposition modeling or FDM) allows rapid and accurate materialization of computer aided design (CAD) models into real objects out of biodegradable polylactic acid (PLA). This technology is simple, cheap and flexible, thus can be implemented in a wide range of applications: from rapid sculpting of new product prototypes or custom counterparts to printing of microstructured objects owning internal architecture. The later one is particularly promising for cell culturing research and tissue engineering practice.

Three-dimensional porous micro-woodpile geometry structures can be successfully applied as templates for cell proliferation [1] and further be used as implants for tissue engineering (TE) as well as regenerative medicine applications. TE develops biological substitutes that restore, maintain or improve tissue function or a whole organ [2]. The aim of our research was production of various porosity microstructures for restoration of hard tissue (bone) by employing commercially available low-cost 3D printer and a standard material. It is known, that the pore size usually has to be within the range of 0.1-1 mm to be suitable for osteoblast cell growth. To manufacture such objects we used a widespread 3D printer (3DP) "Ultimaker Original". This device empowers fabrication of free-form shapes out of thermoplastic using FFF technology. Our chosen thermoplastic was biocompatible, biodegradable, optically transparent PLA. Also we applied colored (for additional functionality) and photosensitive PLA (highly luminescent under UV light).

Cell growth in the 3D woodpile depends on its microstructure and porosity, for this reason we decided to continue ours researches with woodpiles having hexagonal inner geometry representing the most balanced architecture in both mechanical and pore spatial distribution perspectives, respectively. To compare hexa-woodpiles with simple and shifted geometry woodpiles, hexa-structure ensures the strongest mechanical properties and characterization [3]. Further, the 5,5 mm diameter circles were subtracted from the manufactured woodpile using laser light filamentation (LLF) in water technology [4]. Their SEM images are described in Fig. 1. Samples of subtracted circles were given for researches from Vilnius University Institute of Biochemistry. The micro-scaffolds were placed into the created standardized defect in rat's skull. 60 days later animals were euthanized and implants were taken for histology analysis. Results of histology show incomplete callus formation. However, a layer of bone was seen surrounding the whole grafted segment and the center of the defect was filled with connective tissue. Micro-scaffolds were partially resorbed as well as there were no inflammatory reactions observed.

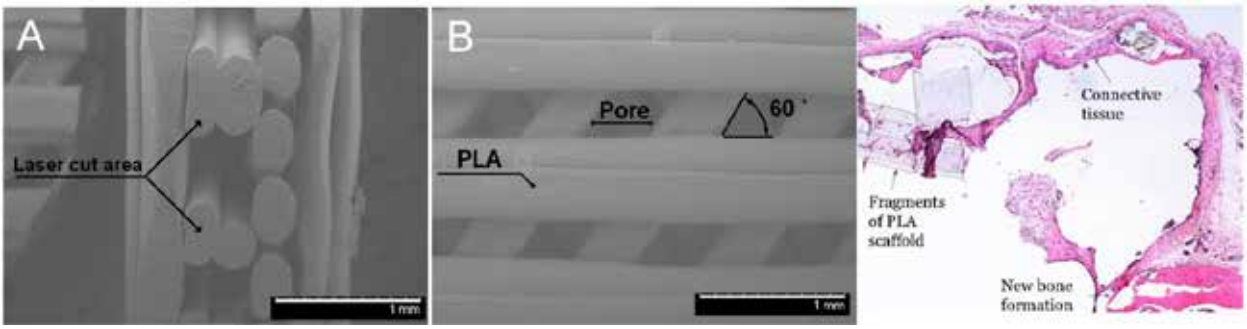

Fig. 1. Micro-woodpile with hexagonal structure. A – a subtracted circle from 3DP woodpile with 0.6 mm pore size, micro-logs are rotated 60 deg angle. B – a 3DP woodpile from top side. A and B images are obtained with SEM. C Histology of bone defect filled with PLA scaffold.

In brief, our proposed approach employing tabletop 3D printer of "hobby" level enables creation of personal microfabrication laboratory at home offering production of custom made 3D structured templates of biocompatible as well as biodegradable PLA thermoplastic material. In comparison to material subtraction (milling) or lithography techniques – FFF additive manufacturing provides possibility of straightforward 100% material usage.

[1] M. Malinauskas, et al., "3D Microporous Scaffolds Manufactured via Combination of Fused Filament Fabrication and Direct Laser Writing Ablation", Micromachines **4**(5), 839–858 (2014).
[2] A. Selimis, et al., "Direct laser writing: Principles and materials for 3D scaffold printing", Microelectronic Engin. **132**, 83-89, (2015).
[3] D. Mizeras, et al., "Tailoring bulk mechanical properties of 3D printed objects of polylactic acid varying internal micro-architecture", Proc. SPIE, **9505**, 95050P (2015).
[4] S. Butkus, et al., "Rapid microfabrication of transparent materials using filamented femtosecond laser pulses", Appl. Phys. A, **114**, 81-90 (2014)

SYMMETRY BREAKING IN GOLD SUPERATOM COMPLEXES: A NONLINEAR OPTICAL STUDY

Nick Van Steerteghem[1], Stijn Van Cleuvenbergen[1], Steven Deckers[1], Chanaka Kumara[2], Amala Dass[2], Hannu Häkkinen[3], Koen Clays[1], Thierry Verbiest[1], Stefan Knoppe[1]

[1] Department of Chemistry, University of K.U. Leuven, Belgium
[2] Department of Chemistry and Biochemistry, University of Mississippi, United States
[3] Department of Chemistry and Department of Physics, University of Jyväskylä, Finland
Nick.vansteerteghem@chem.kuleuven.be

Gold superatom complexes consist of several tens of gold atoms clustered together to form a highly symmetric structure, often an icosahedron although other structures exist. Their electronic structure is characterized by the fact that they form very atom-like orbitals defined by the entire group of atoms, rather than the individual atom separately. Stable electronic configurations are those which consist of a closed shell of electrons, and as such, these structures give rise to complexes containing a *magic number* of atoms. To prohibit them from clustering together and precipitating in solution, they are stabilized by a monolayer of thiolate ligands.

Monolayer-protected gold particles have attracted a considerable interest from a broad range of disciplines. Unique properties emerge as a result of their size and electronic structure. Amongst their many uses, we are investigating them as promising candidates for contrast agents in nonlinear optical imaging applications, such as multi-photon excited fluorescence and second-harmonic generation (SHG) [1].

In SHG, a laser beam of particular frequency interacts with a nonlinear material and produces light of the second-harmonic frequency, or frequency doubled light, of which the efficiency is determined by the hyperpolarizability of the material. Importantly, second-order nonlinear properties can only exist in materials which do not possess inversion symmetry, on the microscopic (molecular) as well as the macroscopic (crystal structure) scale. Measuring the hyperpolarizability of particles in solution is done using the Hyper-Rayleigh scattering technique, the nonlinear variant of Rayleigh scattering [2].

Herein, we demonstrate two new mechanisms to efficiently induce SHG by means of symmetry breaking in a series of thiolate protected gold clusters consisting of 25 and 38 Au atoms; 1) ligand induced symmetry breaking and 2) doping of the central cluster core with foreign metal atoms. These mechanisms show the unique features and tailorability of Au clusters, which can be prepared with atomic definition, in contrast to larger nanoparticles, where SHG mainly arises from spherical defects.

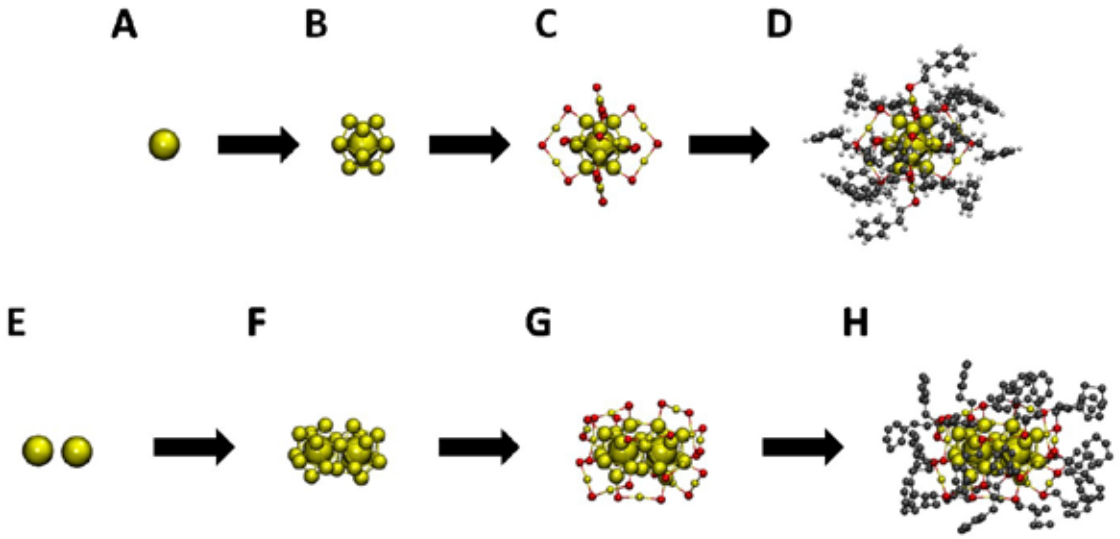

Fig. 1. Structures of the investigated $Au_{25}(2\text{-PET})_{18}$- and $Au_{38}(2\text{-PET})_{24}$ clusters. A, E: Central atom(s) of the core; B,F: icosahedral core(s); C: the full $Au_{25}S_{18}$ and G: $Au_{38}S_{24}$ framework; D,H: the full cluster, hydrogen not shown in H.

[1] Knoppe, S. et al., Non-linear optical properties of Thiolate-protected gold clusters, J. Phys. Chem. C., 6221 – 6226 (2015).
[2] Clays, K. et al., Hyper-Rayleigh scattering in solution, Phys. Rev. Lett., 66, 2980 (1991).

RESEARCH OF SPATIAL AND SPECTRAL PROPERTIES OF TERAHERTZ RADIATION GENERATED IN AIR

Karolis Adomavičius, Ernestas Žeimys

Vilnius University Laser Research Center, Saulėtekio Ave. 10, LT-10223 Vilnius, Lithuania
Karolis.Adomavicius@ff.stud.vu.lt

Terahertz (THz) radiation represents the region in the electromagnetic spectrum between far-infrared and microwave radiation and has frequency between 0.1 THz and 10 THz (wavelength varies from 3 mm to 0.03 mm). The radiation in this region of electromagnetic spectrum is non-ionizing and safe. Moreover, it can easily pass through clothing, wood, paper, various plastics and ceramics. Furthermore, vibrational and rotational transitions of various molecules have energies in THz frequency range. This leads to a wide range of applications, such as spectroscopy, biological and medical imaging, detection of hazardous materials, security screening, etc. For over a decade, scientists and engineers have been investigating this radiation and developing new THz sources and detectors.

In our experiments THz radiation was generated in ambient air by focusing three different wavelength laser pulses. As a pump source the Ti:Sapphire laser system (central wavelength about 790 nm) operating at 1 kHz and delivering 9 mJ pulses of 35 fs (FWHM) duration was used. The pump beam was divided into two beams by using a beam splitter. One beam was used to pump Optical Parametric Amplifier (OPA), which generated tunable in wavelength signal (1140-1600 nm) and idler (1600-2600 nm) waves. These two waves were aligned collinearly with the second laser beam and focused into air. Due to strong nonlinear interaction between these three pulses, THz radiation was effectively produced in the laser-generated air plasma.

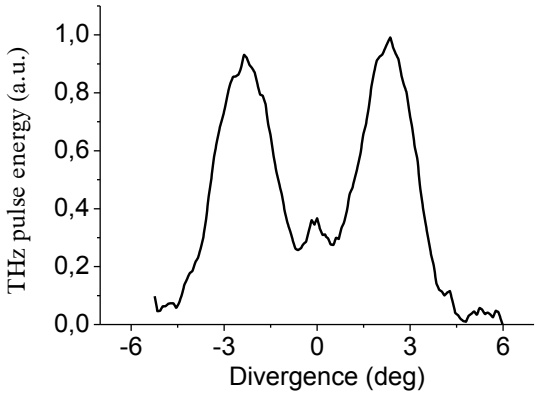

Fig 1. Spatial profile of generated THz beam.

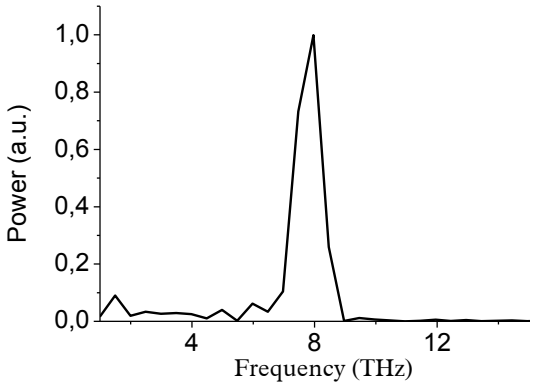

Fig 2. Spectrum of generated THz beam.

The results of the research show that THz radiation spatial profile (Fig. 1.) has typical conical shape with divergence of about 5 degrees. The spectrum of generated THz beam was measured using Michelson interferometer. As shown in the graph above (Fig. 2.), THz spectrum obtained using a sapphire beam splitter is from 0.1 to 9 THz with a maximum at 8 THz. Note that using a nitrocellulose pellicle beam splitter resulted in THz spectrum of up to 115 THz with maximum at 30 THz. In conclusion, spatial and spectral characteristics of THz radiation, generated by three femtosecond laser pulses of different wavelengths focused in the air, have been investigated. The obtained results indicate that a broadband THz emission can be generated using this method.

Oral session 7

Functional materials and derivatives, modern technologies

THE AGING PROCESSES IN THE P3HT:PCBM SOLAR CELLS

Joanna Symonowicz

Faculty of Fundemental Problems of Technology, Wrocław University of Technology, Poland
198590@student.pwr.edu.pl

During the last century the world became completely dependent on the electric energy. Since the non-renewable sources are running out, the attention was moved onto the solar energy. The organic solar cells are its cheapest source as they can be produced by 3D printers. What is more, due to their flexibility they can provide architects with various ideas for reshaping the building facades.

Fig. 1. The Spanish Pavilon at Venice Biennale 2010 equipped with a PV façade (source: onyxgreenbuilding.wordpress.com)

Despite of all the virtues, organic solar cells are not common in everyday usage due to its fast aging-process which result in poor efficiency in less than half a year. In my experiment the fullerene derivate photovoltaics (glass/ITO/ZnO/P3HT:PCBM/MoO3/Ag) were tested a day and a year after the production. The broadband spectroscopy helped to investigate cells' electric structure and, thus, to describe the influence of the oxygen doping on the efficiency decay.

[1] F. Kremer, A. Schonhals, Broadband Dielectric Spectroscopy, Heidelberg: Springer, 59-93 (2003).
[2] O. Armbruster, S. Bauer, C. Lungenschmied, Dielectric response of doped organic semiconductor devices: P3HT:PCBM solar cells, Physical Review B, Condensed Matter **84**, 085208 (2011).
[3] T. Kietzke, Recent Advances in Organic Solar Cells, Advanced OptoElectronics **1**, (2007).

INFLUENCE OF THE COMPOSITION ON EMISSION OF GLASSES AND GLASS CERAMICS DOPED WITH RARE EARTH IONS

Augustas Vaitkevičius[1], Mikhail Korjik[2], Paulius Baronas[1], Ekaterina Trusova[3], Darius Dobrovolskas[1], and Gintautas Tamulaitis[1]

[1] Institute of Applied Research and Semiconductor Physics Department, Vilnius University, Lithuania
[2] Research Institute for Nuclear Problems, Belarus State University, Belarus
[3] Belarusian State Technological University, Belarus
augustas.vaitkevicius@ff.vu.lt

With increasing performance and declining cost, light emitting diodes (LEDs) have seen an increase in adoption for general illumination applications. LEDs are projected to reach an 84 % market share in the general lighting market by 2030. The key issue in the development of high power lighting sources is the search, study and implementation of novel wavelength converters. Due to high thermal and photo stability, the glass ceramics is prospective as a matrix in production of converters in high power white LEDs [1].

We studied the influence of the glass composition and crystallization on emission of glasses doped with different rare earth elements. Barium ($BaO\text{-}2SiO_2$) and lithium ($Li_2O\text{-}2SiO_2$) glasses were selected for the study. The glass samples were doped or co-doped with cerium, dysprosium, terbium or europium ions. The influence of crystallization was studied after transforming the doped glasses into glass ceramics by annealing it at 850° C for 1 hour. The samples were fabricated at the Belarusian State Technological University.

The study was performed by using confocal photoluminescence (PL) spectroscopy. A WITec Alpha 300 S microscopic system coupled to a spectrometer with a thermally cooled CCD camera was used. A CW laser diode emitting at 405 nm was used for excitation. The spatial resolution of 250 nm in plane and 1 μm perpendicularly to the sample surface was achieved. An integrating sphere with a xenon lamp equipped with a monochromator was used to measure the external quantum efficiency. All measurements were performed at room temperature.

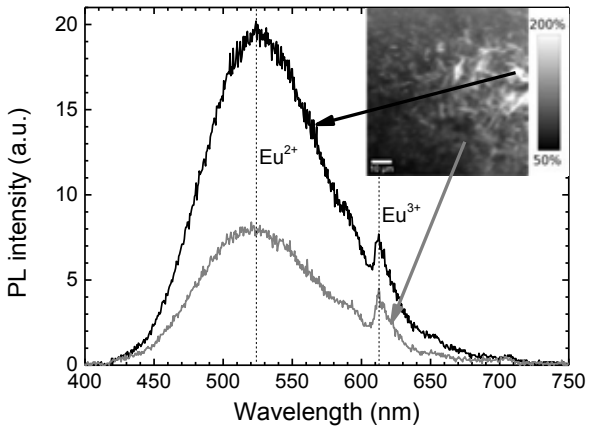

Fig. 1 Photoluminescence spectra from bright and dark areas (indicated) of $BaO\text{-}2SiO_2$:Eu glass ceramics. Inset shows a 80×80 μm^2 image of the spectrally integrated PL intensity.

Though the distribution of PL parameters in the glass samples was found to be homogeneous, the glass ceramic samples exhibited considerable inhomogeneity. In $BaO\text{-}2SiO_2$:Eu glass ceramics, the inhomogeneity of the PL intensity is related with the ratio between emission band due to Eu^{2+} and Eu^{3+}: the ratio is larger in the needle-like bright areas. The different ratio is a result of variation in the crystallinity in the bright and dark areas. We observed that the spectral positions of the PL bands are the same in the needle-like bright areas and the dark background. This is an indication that the crystallization imposed no significant changes to the local surroundings of the europium ions.

The evaluation of chromatic properties of PL from glass samples with different dopants shows that a white light source can be fabricated using glass ceramics crystallized from an appropriate mixture of barium and lithium glasses doped with Eu, Ce, Dy, Tb. The combination of the emission from these four ions allows for optimization and tenability of the chromatic properties. We also observed that the external quantum efficiency of the glass ceramics is higher than that of the corresponding glass.

[1] D. Chen, W. Xiang, X. Liang et al., Advances in transparent glass-ceramic phosphors for white light-emitting diodes – A review, Journal of the European Ceramic Society, **35**, 859-869 (2015).

FORMATION OF NEW FUNCTIONAL NANOHYBRIDS BY RAFT/MADIX POLYMERIZATION

Karolina H. Markiewicz, Iwona Misztalewska, Agnieszka Z. Wilczewska, Krzysztof Winkler

Institute of Chemistry, University of Bialystok, Poland
k.markiewicz@uwb.edu.pl

Materials composed of polymers and nanostructures such as magnetic nanoparticles (MNP) or carbon nanotubes (CNT) due to the combination of their properties (chemical/mechanical/electric/magnetic) are promising candidates for application in many areas of science and industry [1-4].

Controlled radical polymerization (CRP) is a synthetic tool that allows precise and easy control of the chemical composition and architecture of polymers. RAFT/MADIX (reversible addition-fragmentation chain transfer/ macromolecular design via the interchange of xanthates) technique is one of the types of CRP which uses xanthates (dithiocarbonates) to mediate polymerization by reversible chain-transfer process [5]. This method can be used to produce polymers with well-controlled macromolecular properties from numerous monomer types in organic solvents or water under mild pressure and temperature conditions. Important advantage of RAFT/MADIX technique is tolerance of dithiocarbonates towards most of the functional groups present in monomer [6]. The synthesis of polymers on nanoparticles/nanotubes surface using this method allows to control some of the nanohybrids properties i.e. solubility or specific interactions [7].

The formation of polymer-CNT and polymer-MNP nanohybrids by RAFT/MADIX technique using commercially available and synthesized monomers is presented. Various strategies of preparation of these materials ('grafting from', 'grafting to' and formation *in situ*) are discussed.

This project is financially supported by the National Science Centre, Poland, grant no. 2014/13/N/ST5/01563.

[1] A.M. Díez-Pascual, D. Gascón, Carbon nanotube buckypaper reinforced acrylonitrile–butadiene–styrene composites for electronic applications, ACS Applied Materials and Interfaces, **5**, 12107–12119 (2013).

[2] H.R. Rajabi, M. Roushani, M. Shamsipur, Development of a highly selective voltammetric sensor for nanomolar detection of mercury ions using glassy carbon electrode modified with a novel ion imprinted polymeric nanobeads and multi-wall carbon nanotubes. Journal of Electroanalytical Chemistry, **693**, 16–22 (2013).

[3] C. Boyer et al., The design and utility of polymer-stabilized iron-oxide nanoparticles for nanomedicine applications, NPG Asia Materials, **2(1)**, 23–30 (2010).

[4] A.Z.M. Badruddoza et al., Fe_3O_4/cyclodextrin polymer nanocomposites for selective heavy metals removal from industrial wastewater, Carbohydrate Polymers, **91(1)**, 322-332 (2013).

[5] M. Destarac et al., Macromolecular Design via the Interchange of Xanthates (MADIX): Polymerization of Styrene with O-Ethyl Xanthates as Controlling Agents, Macromolecular Chemistry and Physics, **2013(16)**, 2281–2289 (2002).

[6] D. Taton, A.Z. Wilczewska, M.Destarac, Direct synthesis of double hydrophilic statistical di- and triblock copolymers comprised of acrylamide and acrylic acid units via the MADIX Process, Macromolecular Rapid Communication, **22(18)**, 1497-1503 (2001).

[7] M. Beja et al., RAFT/MADIX polymers for the preparation of polymer/inorganic nanohybrids, Progress in Polymer Science, **36**, 845-886 (2011).

NEW MAGNETIC SEPARABLE POLYMERIC NANOHYBRIDS WITH CHELATING PROPERTIES.

Iwona Misztalewska[1], Olga Wojtasik[1], Karolina H. Markiewicz[1], Agnieszka Z. Wilczewska[1]

[1] Institute of Chemistry, Department of Biology and Chemistry, University of Bialystok, Poland
i.misztalewska@uwb.edu.pl

β-Diketones represent one of the oldest classes of versatile chelating ligands forming very stable chelate complexes with various metal ions.[1] One of the best-known compound which belongs to this group is acetylacetone. However, due to bad solubility in water and good solubility in organic solvents, acetylacetonate metal organic complexes are difficult to recover from the organic solution by water wash method. Additionally, these complexes are usually thermally unstable because of their low decomposition temperatures.[2] These problems could be solved by anchoring of acetylacetone ligands/complexes on a solid phase. In this presentation immobilisation of acetylacetone derivatives on surface of superparamagnetic iron oxide nanoparticles will be presented.

Three different chelating monomers (two of them possess acetylacetone moiety) were synthesized and used to form polymeric shells around magnetic cores by RAFT/MADIX (Reversible Addition-Fragmentation Chain Transfer and Macromolecular Design *via* the Interchange of Xanthates) polymerization. Two methods of synthesis of new bifunctional polymeric nanohybrids were applied. These nanohybrids consist of magnetic cores and polymeric shells which are covalently bonded to the surface. Therefore, they are very stable and resistant to washing off. In addition, these polymeric shells possess chelating properties. Also the influence of post-modification of polymeric shell on its properties were investigated. To investigate relation between polymeric shell structure and its chelating activity three types of polymerization were performed on surface of magnetic nanoparticles (MNP): hompolymerization, block copolymerization and random copolymerization (Fig. 1).[3]

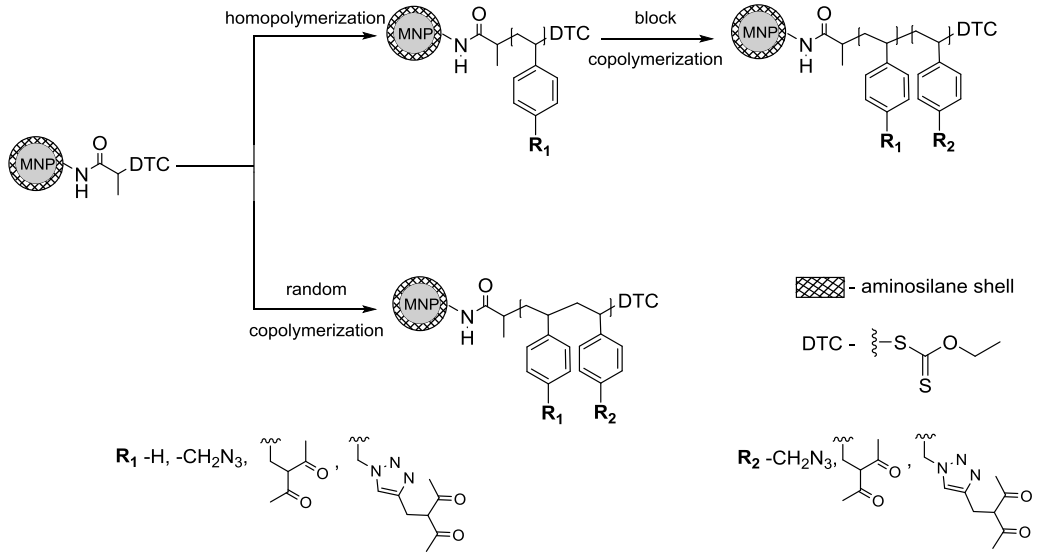

Fig. 1. Synthesis of polymeric shells on the surface of MNP (DTC- dithiocarbonate).

Nanohybrides were fully characterized using variety of methods eg. FTIR, TEM, SEM/EDX, TGA, and fluorimetry.

The project was financially supported by National Science Centre, Poland, grant no. 2011/03/B/ST5/02691
Analyses were performed in Centre of Syntesis and Analisys BioNanoTechno of University of Bialystok.
The equipment in the Centre of Synthesis and Analysis BioNanoTechno of University of Bialystok was funded by EU, as a part of the Operational Program Development of Eastern Poland 2007-2013, project: POPW.01.03.00-20-034/09-00 and POPW.01.03.00-20-004/11.

[1]G. Pawlicki, B. Staniszewski, et al., Complexation studies of 3-substituted β-diketones with selected d- and f-metal ions, Chem. Pap. **65**, 221–225 (2011).
[2]Y. Ishii, S. Sakaguchi, T. Iwahama, Innovation of Hydrocarbon Oxidation with Molecular Oxygen and Related Reactions, Adv. Synth. Catal. **343**, 393–427 (2001).
[3]I. Misztalewska, A. Z. Wilczewska, et al., New acetylacetone-polymer modified nanoparticles as magnetically separable complexing agents, RSC Adv **5**, 100281–100289 (2015).

Oral session 8

Functional materials and derivatives, modern technologies

NICKEL ASSISTED SILICON ETCHING

Mindaugas Kamarauskas, Vladimir Agafonov, Kinan E. Nasser, Marius Treideris, Arunas Setkus

Center for physical science and technology, A. Gostauto 11, 01108, Vilnius
mindaugas.kamarauskas@ftmc.lt

Controllable fabrication of Si nano and microstructures has a lot of practical applications in functional devises fabrication. A big range of methods have been developed to fabricate Si nanostructures, such as vapor-liquid-solid (VLS) growth, reactive ion etching (RIE), electrochemical etching or metal-assisted chemical etching (MACE), all of which aim to control various parameters of the Si structures in functional devices [1]. Metal-assisted chemical etching method uses a thin layer of noble metal (e.g., Au, Pt, or Au/Pd alloy) sputtered on the surface of a Si substrate that catalyzed the etching of Si in a mixed solution containing HF, H_2O_2, and EtOH, resulting in straight pores or columnar structures. Furthermore, as MACE is based on a simple redox process in an etching solution, it produces a very smooth and clean Si surface that is free of the surface damage that typically results when using the RIE process [2]. However high noble metals cost is limiting factor for practical applications and cost reduction with use of cheaper metals is serious task to achieve.

In this work we present nickel (Ni) assisted etching for silicon. Commercially available p-type (100) 1-5 Ohmcm wafers were used. For the investigations Ni layers with different thickness were deposited by magnetron sputtering and electroless plating. Test structures were formed by using lithography and Ni etching in acid solutions for samples with thin magnetron sputtered layers and by electroless plating on opened areas in photoresist by lithography. Silicon etching was carried by immersing samples in $HF:H_2O_2:H_2O$ solution. After etching samples were investigated using atomic force microscopy (AFM) (fig. 1). From AFM images statistical investigations on etched structures was made by using SPIP software.

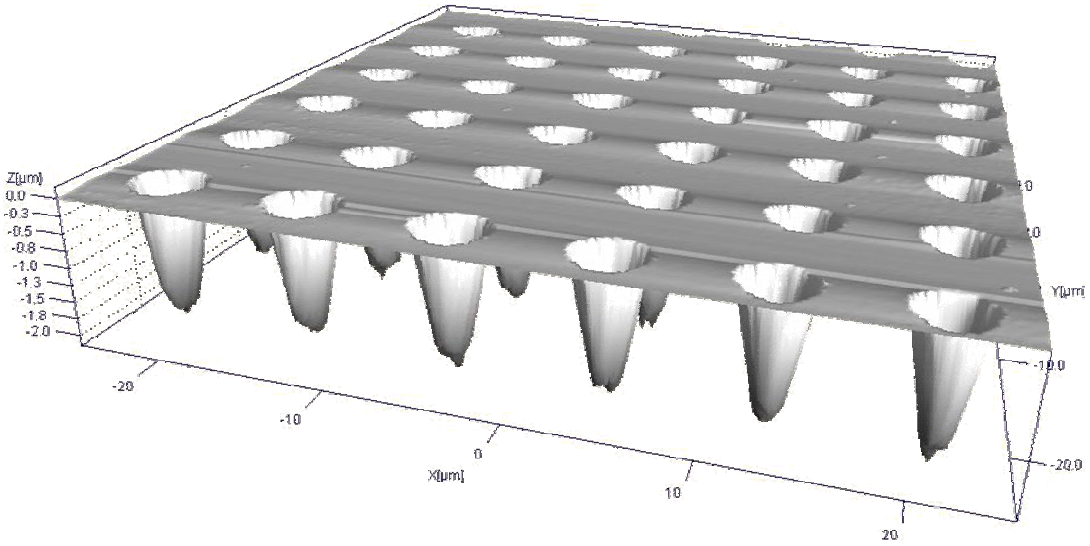

Fig. 1. 3D view of test structures on silicon surface formed by Ni assisted etching

Influence on technological parameters (Ni layer thickness, etching time, etchant ratio) for etched structures was investigated.

Acknowledgement. This research was funded by a grant (No. MIP-70/2015) from the Research Council of Lithuania.

[1] Z.Huang, N.Geyer, P. Werner, J. de Boor, U. Gosele, Metal-Assisted Chemical etching of silicon: A review, Advanced Materials **23**, 285-308 (2011)

[2] H. D. Um, et al., Versatile control of metal-assisted chemical etching for vertical silicon microwire arrays and their photovoltaic application, Scientific Reports **5**, 11277 (2015).

FLUORESCENCE QUENCHING OF INDOLO[3,2-*b*]CARBAZOLE COMPOUNDS BY CONFORMATIONAL MOTIONS OF ATTACHED SUBSTITUENTS

Simona Streckaite[1], Renata Karpicz[1], Alytis Gruodis[2], Saulius Grigalevicius[3], Vidmantas Gulbinas[1]

[1] Center for Physical Sciences and Technology, Savanorių 231, LT-02300 Vilnius, Lithuania
[2] Department of General Physics and Spectroscopy, Vilnius University, Saulėtekio 9-III, LT-10222 Vilnius, Lithuania
[3] Department of Polymer Chemistry and Technology, Kaunas University of Technology, Radvilenų Plentas 19, LT-50254 Kaunas, Lithuania
simona.streckaite@ftmc.lt

Indolo[3,2-*b*]carbazoles (ICZ) is a popular class of organic materials for various electronic applications. They have been used in a number of devices such as organic light-emitting diodes (OLEDs) [1], organic field-effect transistors (OFETs) [2], solar cells [3], etc.. ICZ is an important unit to synthesize various oligomers and polymers with interesting electrical, optical, magnetic and other features. ICZ molecules have ladder-type planar structure, similar as the pentacene, and two nitrogen atoms in the carbazole fragments, which provide electron-donating ability [4]. Moreover, because of high glass transitions temperature, ICZ compounds possess great thermal and morphological stability under ambient conditions [5]. Optimization of chemical, physical and structural characteristics is still important problem which has to be solved. For excellent performance and practical applications it is essential to understand the influence of different substituents to the behavior of ICZ compounds.

In this work, six new ICZ derivatives with different connected substituents were investigated. Steady-state and time-resolved absorption and fluorescence spectroscopy methods were used to study their spectroscopic properties in solutions and in solid films, and to reveal differences among molecules caused by different substituents. Quantum chemical calculations were also performed to support the experimental data.

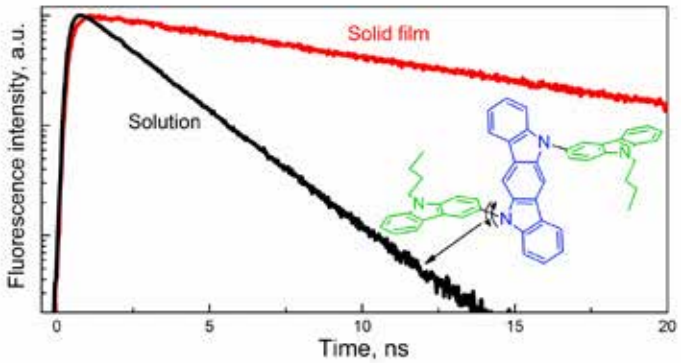

Fig. 1. Fluorescence decay kinetics of one of the investigated ICZ molecules in solution and in thin film. Conformational motions of substituents lead to increased non-radiative relaxation

Absorption and emission spectra of indolo[3,2-*b*]carbazole materials red-shift by extending ICZ core with addition of substituents. The substituents also significantly influence fluorescence yields of these compounds, and their impact is different in solutions and in solid films (Fig. 1). Theoretical calculations demonstrated that charge redistribution during HOMO-LUMO transitions takes place mainly in cores of ICZ compounds, however slightly including substituents, which orientations change in the excited state. We conclude that restricted conformational motions of the substituents in solid films lead to longer fluorescence decays and higher fluorescence yields. Consequently, spectroscopic properties of ICZ compounds may be significantly altered by attaching substituents at different positions of ICZ molecules, however, in order to maintain their high fluorescence yield, conformational motions of the substituents shall be restricted.

[1] Ting H-C, Chen Y-M, You H-W et al., Chaskar A, et al. Indolo[3,2-b]carbazole/benzimidazole hybrid bipolar host materials for highly efficient red, yellow, and green phosphorescent organic light emitting diodes, J. Mater. Chem. **22**, 8399 (2012).
[2] Boudreault P-LT, Virkar A a., Bao Z et al., Synthesis and characterization of soluble indolo[3,2-b]carbazole derivatives for organic field-effect transistors, Org. Electron. **11**, 1649–59 (2010).
[3] Chan L-H, Lin L-C, Yao C-H et al., Synthesis of indolo[3,2-b]carbazole-based random copolymers for polymer solar cell applications, Thin Solid Films **544**, 386–91 (2013).
[4] Zhao H-P, Tao X-T, Wang F-Z et al. Structure and electronic properties of triphenylamine-substituted indolo[3,2-b]carbazole derivatives as hole-transporting materials for organic light-emitting diodes, Chem. Phys. Lett. **439**, 132–7 (2007).
[5] Shi H, Yuan J, Dong X, et al., Synthesis, photophysical and charge-transporting properties of a novel asymmetric indolo [3,2-b]carbazole derivative containing benzothiazole and diphenylamino moieties, Spectrochim. Acta Mol. Biomol. Spectrosc. **133**, 501–8 (2014).

ULTRAFAST DYNAMICS OF PHOTO INDUCED ELECTRON TRANSFER IN IRON COMPLEX BASED SOLAR CELLS

Paulius Baronas[1], Tobias Harlang[2], Villy Sundström[2], Saulius Juršėnas[1]

1 Institute of Applied Research, Vilnius University, Saulėtekio al. 9-III, LT-10222 Vilnius, Lithuania
2 Department of Chemical Physics, Lund University, Getingevägen 60, S-22241 Lund, Sweden
Paulius.Baronas@ff.stud.vu.lt

Dye sensitized solar cells (DSSCs) recently attracted much scientific attention as an alternative light-to-electricity conversion solution. The multiple advantages include inexpensive and simple manufacturing process, device flexibility and transparency, as well as relatively high efficiency and stability. Until this day, the best performing DSSC devices reaching 11.5% efficiency were produced using ruthenium (Ru^{II}) complexes as a light harvesting material, however, limited resources and toxicity of ruthenium initiated the search of alternative materials [1]. Current DSSC studies are aiming at replacing ruthenium with more abundant analogs like iron, which is known to have similar electronic properties [2]. Unfortunately, the characteristic short lived excited states of the iron complexes does not allow to achieve high conversion efficiencies. Nevertheless, injection and recombination mechanisms shown in (Fig. 1) of interfacial electron transfer between metal complexes and the conduction band of titanium dioxide (TiO_2) are still under debate.

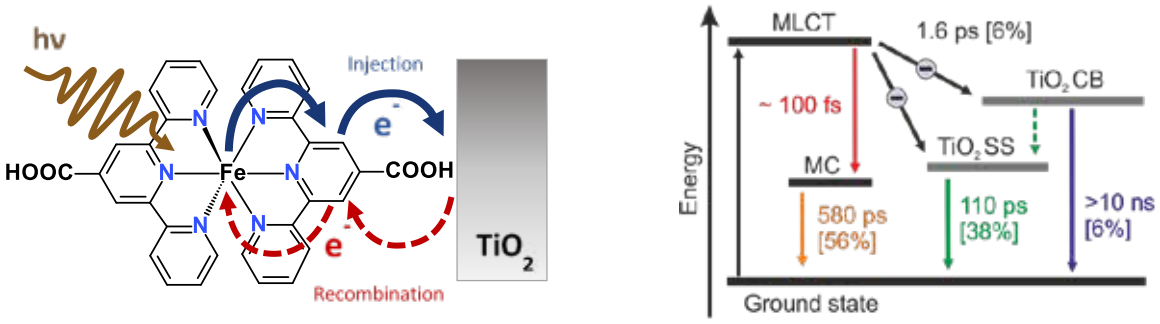

Fig. 1. The visualization of electron transfer processes in Fe^{II}(tpy) - TiO_2 system (left). The energy level diagram of Fe(tpy) on TiO_2 (right), transition lifetimes with their relative amplitudes are indicated.

This work focused on investigation of electron transfer from extremely short-lived metal-to-ligand charge transfer (MLCT) states of iron (Fe^{II}) complex functionalized with terpyridine (tpy) ligands. The spectral and temporal excited state evolution was studied employing transient absorption technique, which allowed to investigate ultrafast processes occurring within timescales as short as femtoseconds. The global data analysis techniques allowed to separate and identify different states with a characteristic lifetime. Isolated iron complexes in dilute acetonitrile solutions exhibited two main excited state species: short-lived (<100 fs) MLCT state and long-lived metal-center (MC) states. Finally, the electron injection properties were investigated in systems, where Fe^{II}(tpy) complexes were sensitized to TiO_2 nanostructured semiconductor. The observed multi-exponential excited state decay with lifetimes ranging from picoseconds to microseconds (see Fig. 1, right) suggested that fast initial electron transfer (1.6 ps) from MLCT state to the conduction band (CB) of TiO_2 is followed by slower electron recombination. Our hypothesis was that electron recombination processes can either occur from the intra-band trap surface states (SS) with a lifetime of 110 ps or from the conduction band, resulting in much longer lifetime, which is also an indication of initial direct electron injection.

Although the observed injection efficiency in studied Fe^{II}(tpy) complexes was found to be low, this work contributes to the development of novel molecular iron based dyes to be employed in efficient DSSC devices. Most recent research is focusing on Fe^{II} complexes modified with N-heterocyclic carbenes (NHC) ligands, which were found to significantly prolong the MLCT lifetime leading to 92% electron injection efficiency [2,3].

[1] B. E. Hardin, H. J. Snaith, and M. D. McGehee, The renaissance of dye-sensitized solar cells, Nature Photonics, **6**, 162–169 (2012).

[2] T. C. B. Harlang, Y. Liu, O. Gordivska, L. A. Fredin, C. S. Ponseca Jr, P. Huang, P. Chábera, K. S. Kjaer, H. Mateos, J. Uhlig, R. Lomoth, R. Wallenberg, S. Styring, P. Persson, V. Sundström, and K. Wärnmark, Iron sensitizer converts light to electrons with 92% yield, Nature Chemistry, **7**, 883–889 (2015).

[3] Y. Liu, T. Harlang, S. E. Canton, P. Chábera, K. Suárez-Alcántara, A. Fleckhaus, D. a Vithanage, E. Göransson, A. Corani, R. Lomoth, V. Sundström, and K. Wärnmark, Towards longer-lived metal-to-ligand charge transfer states of iron(II) complexes: an N-heterocyclic carbene approach., Chem. Commun., **49**, 6412–4, (2013).

DIELECTRIC PROPERTIES OF ORGANIC-INORGANIC LEAD HALIDE PEROVSKITES $CH_3NH_3PbX_3$ (X = I, Br, Cl)

Sergejus Balčiūnas[1], Maksim Ivanov[1], Jūras Banys[1], Vladimir Shvartsman[2]

[1] Faculty of Physics, Vilnius University, Sauletekio 9/3 817k., LT10222 Vilnius, Lithuania
[2] Institute for Materials Science, University Duisburg – Essen, Universitätsstraße 15, Essen, Germany
sergejus.balciunas@gmail.com

In recent years, organic-inorganic hybrid solar cells with perovskite-type pigments have been widely studied. The first lead halide perovskite solar cell was made by Kojima in 2009, showing power conversion efficiency (PCE) of 3.81 % [1], the recent paper by Zhou reported PCE exceeding 19% for $CH_3NH_3PbI_{3-x}Cl_x$ [2]. It is believed that ferroelectricity has important but questionable origin of excellent photovoltaic performance of organic – inorganic lead halide perovskites. Theoretical calculations predict polarization values up to 38 μC/cm^2 [3], but no experimental evidence was found yet.

There are various methods to synthesize organic – inorganic lead halide perovskites, but two typical methods are usually used. Polycrystalline $MAPbX_3$ can be prepared by precipitation from a hydro iodic acid solution or equimolar mixture of CH_3NH_3X and PBX_2. Detailed explanation of synthesizes methods for $CH_3NH_3PbX_3$ can be found in Tom Baikie paper [3].

In this presentation dielectric properties of organic-inorganic lead halide perovskites will be presented. The first order phase transition (from tetragonal to orthorhombic phase [4]) was observed in all three halide perovskite crystals at temperatures around 160K, 150K and 175K for X=I, Br and Cl accordingly. The temperature hysteresis of the first order phase transition is around 5-7 K for all crystals (Fig 1. (a)). Furthermore the dispersion observed in figure 1 (b) suggest that $CH_3NH_3PbX_3$ crystals have order – disorder phase transition.

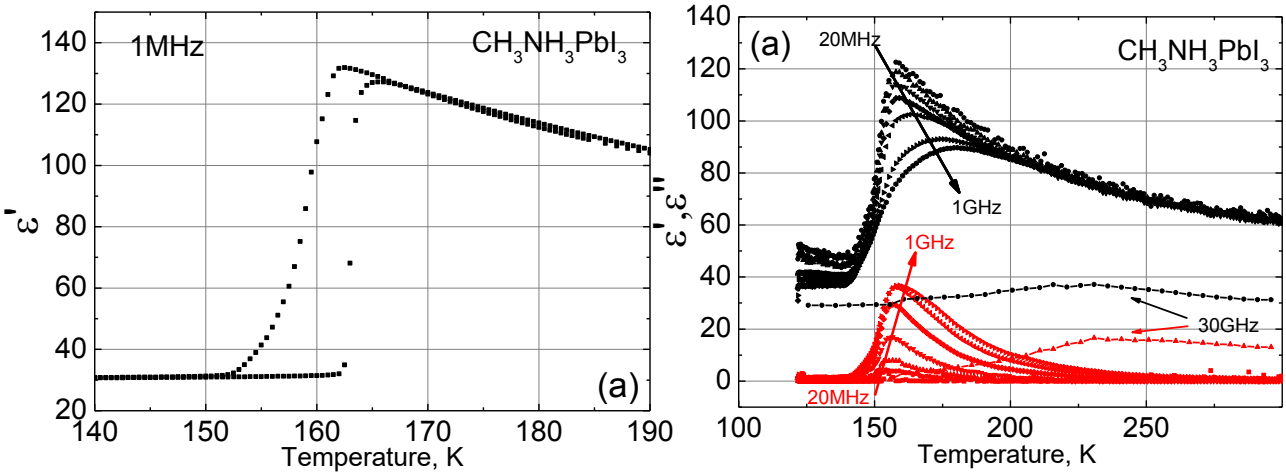

Fig. 1. Temperature dependence of dielectric permittivity for $CH_3NH_3I_3$ single crystals.

[1] A. Kojima, K. Teshima, Y. Shirai, and T. Miyasaka, "Organometal halide perovskites as visible-light sensitizers for photovoltaic cells," Journal of the American Chemical Society, vol. 131, pp. 6050-6051, 2009.
[2] H. Zhou, Q. Chen, G. Li, S. Luo, T.-b. Song, H.-S. Duan, et al., "Interface engineering of highly efficient perovskite solar cells," Science, vol. 345, pp. 542-546, 2014.
[3] T. Baikie, Y. Fang, J. M. Kadro, M. Schreyer, F. Wei, S. G. Mhaisalkar, et al., "Synthesis and crystal chemistry of the hybrid perovskite (CH 3 NH 3) PbI 3 for solid-state sensitised solar cell applications," Journal of Materials Chemistry A, vol. 1, pp. 5628-5641, 2013.
[4] T. Oku, "Crystal Structures of CH3NH3PbI3 and Related Perovskite Compounds Used for Solar Cells," 2015.

Oral session 9

Semiconductor and condensed matter physics, material sciences

TERAHERTZ EMISSION FROM NON-STOICHIOMETRIC Ga-RICH GaAs LAYER

Ieva Beleckaitė, Ramūnas Adomavičius, Andrius Arlauskas, Renata Butkutė, Vaidas Pačebutas, Algirdas Selskis, Virginijus Bukauskas and Arūnas Krotkus

Center for Physical Sciences and Technology, A. Goštauto g. 11, Vilnius, Lithuania
ieva.beleckaite@ftmc.lt

Recently, low-dimensional semiconductor nanomaterials in the forms of nanowires, nanorods, nanotubes, etc., have attracted great attention due to their potential for infrared optoelectronics and photovoltaic applications [1]. These nanomaterials also inspire potential applications in the terahertz (THz) range, for example, as an efficient terahertz emitters [2]. Despite the enhanced THz radiation efficiency, nanostructures like bulk semiconductors have the same limitation due to vertically oriented radiating dipole (i. e. the main part of the radiation propagates in parallel to the surface resulting in the low THz emissivity outside the sample). One way to overcome this problem is to use non-vertically aligned semiconductor nanowires as the electromagnetic dipole is oriented along the nanowire [3]. The other solution could be nanomaterials with more complex geometry or unusual physical properties. In the present work, THz emission from Ga-rich GaAs layer was investigated. It was found that excess gallium originates in submicron scale, elongated and oriented structures which determine unique properties of laser induced THz pulse emission from the layer (Fig. 1).

Investigated GaAs layer was grown by solid source molecular beam epitaxy (MBE) using SVTA reactor equipped with a metallic Ga and two-zone arsenic valved-cracker source to produce As_2 dimers. The semi-insulating (100)-oriented GaAs wafers were used as substrates. GaAs layers were grown at a substrate temperature of 540°C and As_2 and Ga beam equivalent pressure ratio close to 4. The thickness of GaAs layers was about 3.5 μm. Experiments have been performed using Ti:sapphire oscillator generating 150 fs, 800 nm pulses at the repetition rate of 76 MHz. THz electric field transients were detected with a low temperature grown GaAs antenna which was positioned to detect only p polarized THz radiation. THz emission measurements were carried out in transmission and quasi-reflection geometries. During measurements the samples were rotated around the normal to the sample surface – so called azimuthal dependencies were measured. Also THz pulse amplitude dependencies on an angle between the incident laser beam and a normal to the sample surface have been obtained.

In general, a laser beam induces two THz beams at the semiconductor surface: they propagate together with reflected or refracted laser beams. In the case of conventional semiconductor surfaces the intensity ratio between both THz beams is constant regardless of the azimuthal angle. In this context, our investigated sample demonstrates anomalous behavior: depending on the azimuthal angle, THz energy apparently passes between reflection and transmission modes (Fig 2). Such behavior we explain by coexistence of two types of radiating dipoles. Perpendicular to the semiconductor surface dipoles are typical for semiconductor surface emitters, whereas parallel dipoles are very effective and preferable but hardly realizable. Our results demonstrate that nanostructuring of semiconductor surfaces leads to the appearance of the electric fields which force photoexcited carriers to move parallel to the surface. Moreover we introduce measurement techniques which allows us to observe and analyse the generated fields.

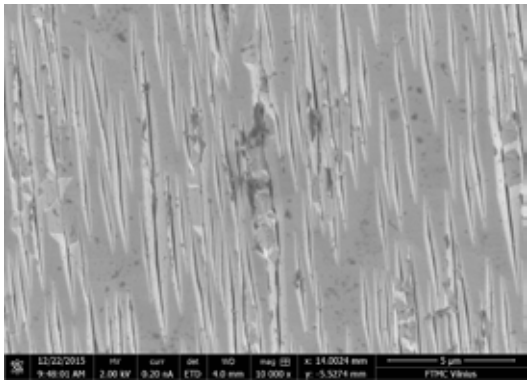

Fig. 1. SEM image of the surface of GaAs layer grown by MBE under Ga-rich conditions. The scale bar at the lower right indicates 5μm

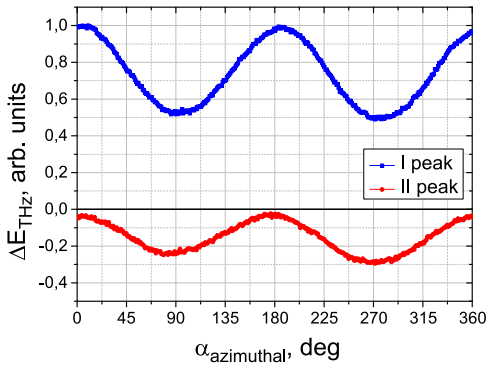

Fig. 2. Amplitude of THz pulse radiated from Ga-rich GaAs layer versus azimuthal angle. I peak corresponds to THz beam propagating in reflected laser beam direction, II peak corresponds to THz beam propagating in opposite direction.

[1] N. P. Dasgupta et al., 25th Anniversary Article: Semiconductor Nanowires - Synthesis, Characterization, and Applications, Advanced Materials, **26**, 2137–2184 (2014).
[2] A. Arlauskas et al., Strong terahertz emission and its origin from catalyst-free InAs nanowire arrays, Nano Letters, **14**, 1508–1514, (2014).
[3] I. Beleckaitė et al., Terahertz emission from non-vertically aligned semiconductor nanowires, 40th International Conference on Infrared, Millimeter, and Terahertz waves (IRMMW-THz) (2015). Available at: http://dx.doi.org/10.1109/irmmw-thz.2015.7327903.

OPTICAL STUDY OF VERTICALLY ELONGATED InGaAs QUANTUM DOTS

Andrius Rimkus[1], Evelina Pozingytė[1], Ramūnas Nedzinskas[1], Bronislovas Čechavičius[1], Julius Kavaliauskas[1], Gintaras Valušis[1], Lianhe Li[2] and Edmund H. Linfield[2]

[1]Center for Physical Sciences and Technology, Semiconductor Optics Laboratory, Vilnius, Lithuania
[2]University of Leeds, School of Electronic and Electrical Engineering, Leeds, United Kingdom
andrius.rimkus@ftmc.lt

Self-assembling quantum dots (QDs) due to atomic-like quantum confinement are particularly attractive for fundamental research and various applications in optoelectronics, such as infrared photodetectors, lasers, optical amplifiers, etc. Alongside material composition the shape engineering of QDs is the key issue to control the electronic and optical properties. Vertically elongated QDs, also referred to as quantum rods (QRs), are novel quantum heterostructures representing the intermediate confinement between 0-D and 1-D [1].

The QR samples studied were grown on a semi-insulating (001) GaAs substrate by molecular beam epitaxy. GaAs buffer layer was followed by 200 nm-thick $Al_{0.2}Ga_{0.8}As$ layer. QRs of different height were then formed by depositing $N = 10–35$ periods of GaAs/InAs SL (3 and 0.64 monolayers of GaAs and InAs, respectively) on the QD layer (Fig. 1a) using either As_2 or As_4 source. Thereby, In-rich InGaAs QRs were embedded within In-reduced InGaAs quantum well (QW) [Fig. 1b] and this structure was sandwiched between two GaAs layers, each 100 nm-thick.

In this work we present an in-depth study of the effect of growth mode by using different As sources along with the impact of height of the QR (number of SL periods deposited) on the optical properties of InGaAs nanorods. Temperature-dependent photoluminescence (TD-PL), photoluminescence excitation (PLE) and photoreflectance (PR) spectroscopy in 3–300 K temperature was used in the study [2].

Optical spectra of QR structures are dominated by excitonic transitions related to ground-state (GS) and excited-state (ES) in the InGaAs QRs, along with optical transitions related to quantum well (QW) states. The TD-PL spectra shows that the PL peak energy has a red-shift that deviate from the Varshni formula. Moreover, we have observed unusual temperature dependence of the GS transition linewidth. The TD-PL spectra are discussed in terms of thermalized redistribution of the carriers among the QRs of different sizes. The PL intensity dependence on temperature plot of the As_2- and As_4-grown QRs shows different quenching for each sample. The origin of PL intensity quenching with temperature is discussed referring to the QR electronic energy structure revealed from PR spectra and calculations performed within the effective mass approximation.

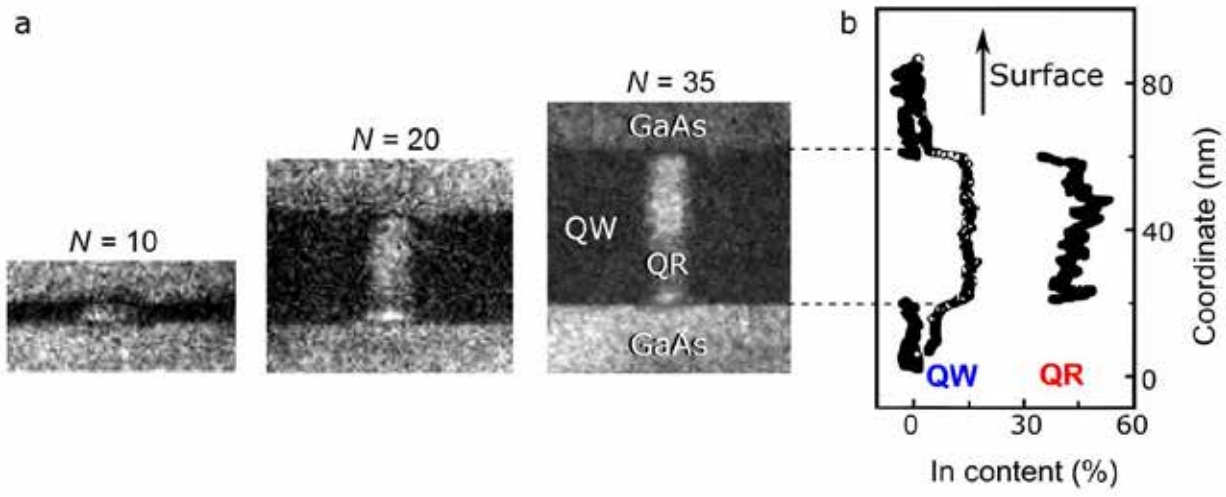

Fig. 1 (a) Micrograph of the QRs with different number of SL periods $N = 10$, 20 and 35 and (b) indium composition profiles across the InGaAs QW and InGaAs QR of the sample with $N = 35$.

[1] L.H. Li, G. Patriarche, M. Rossetti, and A.Fiore, J. Appl. Phys. **102**, 033502 (2007).
[2] R. Nedzinskas, B. Čechavičius, V. Karpus, J. Kavaliauskas, G. Valušis, L. H. Li, S. P. Khanna, and E. H. Linfield, J. Appl. Phys. **109**, 123526 (2011).

OPTICAL STUDY OF TWO-COLOUR QUANTUM RING INFRARED PHOTODETECTOR

Evelina Pozingytė[1], Andrius Rimkus[1], Ramūnas Nedzinskas[1], Bronislovas Čechavičius[1], Julius Kavaliauskas[1], Lianhe Li[2], Edmund Linfield[2]

[1]Semiconductor Optics Laboratory, Center for Physical Sciences and Technology, Lithuania
[2]School of Electronic and Electrical Engineering, University of Leeds, United Kingdom
evelina.pozingyte@ftmc.lt

InAs quantum dot (QD) capped with a thin GaAs layer (CL) and subsequently annealed typically changes the morphology to quantum ring (QR) [1]. The QD transition to QR is schematically presented in Fig. 1. The optical and electronic properties of QRs are similar to those of the small QDs. QR provides a small confined-to-conduction band transitions that can be applied to photodetectors in a far-infrared range (FIR). Also, QR infrared photodector (QRIP) combines the advantages of quantum well and QD photodetectors: it provides size controllability and detects normal incidence light [2, 3]. However, a deeper knowledge about electronic and optical properties of such nanostructures is important for the development of QR-based optoelectronic devices.

Fig. 1. The morphology transition from QD to QR (adapted from [1]).

In this work, electronic states and optical interband transitions of QR are investigated using photoluminescence (PL) and photoreflectance (PR) techniques. Several QR structures with different thickness of GaAs CL are tested in order to reveal the influence of CL on optical response of QR. InAs QDs were capped with 1.5 nm, 2 nm and 2.5 nm-thick GaAs CL and then 30 s growth interruption (annealing) was performed. Spectroscopic study showed a blue-shift ($\sim$ 200 meV) of QR ground state (GS) transition energy in respect to QDs. This GS shift is observed due to significantly smaller vertical confinement (height) of rings. Also, the PL spectra demonstrate multi-peak bands, which signify a formation of different ring size groups after capped QD are annealed.

Finally, an optical study of hybrid nanostructure, which contains QR and dots-in-a-well (DWELL) layers, is presented. This structure was intentionally designed as a two-colour infrared photodetector. PR and PL spectra of the studied complex QR-DWELL heterostructure revealed a variety of optical transitions. Optical features in PL and PR spectra were attributed to GS and excited state transitions within InAs QDs and In(Ga)As QRs. Also, PR spectra showed an optical transitions between states of a binary InAs/InGaAs QW and InAs QR wetting layer.

[1] J.-H. Dai,J.-H. Lee, S.-C. Lee, Transition mechanism of InAs quantum dot to quantum ring revealed by photolu,inescence spectra, IEEE Photonics Technology Letters 20(**16**), 1372-1374 (2008).
[2] H. S. Ling, S. Y. Wang, C. P. Lee, M. C. Lo, Characteristics of In(Ga)As quantum rings infrared photodetectors, Journal of Applied Physics **105**, 034504 (2009).
[3] R. Samadzadeh, M. Zavvari, R. Hosseini, Tunable far infrared detection using quantum rings-in-well intersubband photodetectors **47**, 3555-3565 (2015).

TERAHERTZ EMISSION FROM SEMICONDUCTOR SURFACES

Ignas Nevinskas, Sandra Stanionytė, Vaidas Pačebutas and Arūnas Krotkus

Optoelectronics Lab., Center for Physical Sciences and Technology, Vilnius
ignas.nevinskas@ftmc.lt

When semiconductors such as GaAs, InAs or InGaAs are illuminated with femtosecond laser pulses, they emit electromagnetic waves in the range from 0.1 to 10 THz namely the Terahertz Gap. Such radiation is non-damaging, so it is attractive for medical uses or identification of explosives for safety purposes. Some molecules have distinct chemical 'fingerprint' in this region allowing their recognition in substances.

Generally, one of the main mechanisms contributing to terahertz generation is rapidly changing conductivity on a timescale of a few picoseconds. High currents are achieved by accelerating the photocarriers with external electric fields in the case of Photoconductive Antennas, however, a more technologically compelling solution would be to use intrinsic electric fields, which is the case for surface terahertz emitters.

It has been known for 11 years that the bulk *p*-InAs (10^{16} – 10^{17} cm^{-3}) is the most efficient surface THz emitter [1]. *p*-InAs exhibits a natural surface charge accumulation due to high density of donor surface states which pin the Fermi level above its conduction band edge forming a space charge region. An analogy to this phenomenon are *p*-*n* or, more versatile, *p*-*i*-*n* junctions.

An InAs *p*-*n* junction has been MBE grown following an AlInAs buffer layer on an InP:S substrate. The thickness of *n*-type and *p*-type layers are 600 nm and 50 nm respectively. At wavelengths longer than ~1.8 μm the detected THz pulse amplitude is comparable to that of *p*-InAs. Two GaInAs *p*-*i*-*n* junction samples of different thicknesses of -*i*- i.e. 200 nm and 400 nm have also been grown. The *p*-type and *n*-type layers are of 50 nm of GaInAs:Be and 50 nm of GaInAs:Si respectively. From Fig. 1 it is seen that the THz field amplitude generated by the diode is ~75% larger than that obtained from the laser excited surface of the *p*-InAs single crystal [2].

Future goals are focused on investigation of InAs *p*-*i*-*n* structures.

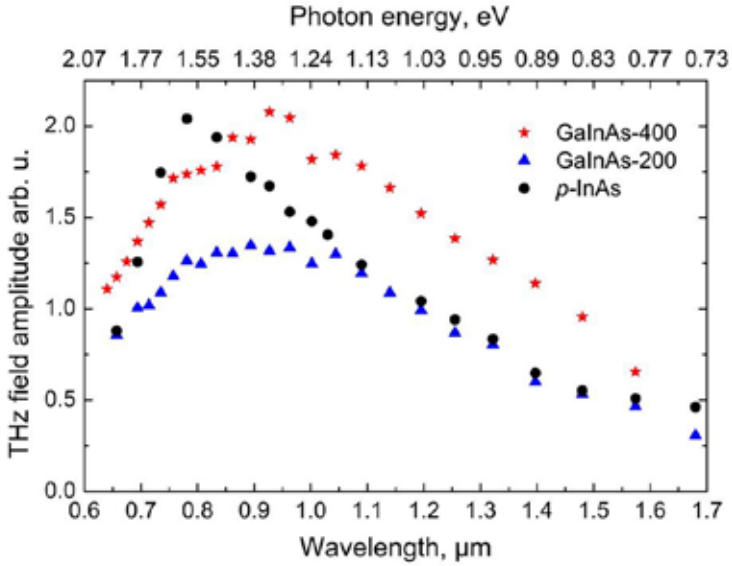

Fig. 1. THz excitation spectra for samples GaInAs-200 and GaInAs-400 compared with a similar dependence measured on *p*-type InAs crystal surface.

[1] R. Adomavičius, A. Urbanowicz, G. Molis, A. Krotkus and E. Šatkovskis, Appl. Phys. Lett., **85**, 13, p. 2463 (2004).
[2] I. Nevinskas, S. Stanionytė, V. Pačebutas, and A. Krotkus, Lithuanian Journal of Physics, **55**, 4, pp. 274-279 (2015).

CARRIER DIFFUSIVITY AS THE KEY PARAMETER BEHIND THE QUANTUM EFFICIENCY DROOP IN (IN,GA)N QUANTUM STRUCTURES

Kazimieras Nomeika, Ramūnas Aleksiejūnas

Department of Semiconductor Optoelectronics, Institute of Applied Research, Vilnius University, Saulėtekis Avenue 9-3, Vilnius 10222, Lithuania
Kazimieras.Nomeika@tmi.lt

The efficiency of InGaN light-emitting diodes (LEDs) becomes limited at high carrier densities, the effect known as the efficiency droop. There is an ongoing debate as to the physical origin of the non-radiative recombination mechanism, which is responsible for this effect [1]. This task is burdened by many variables usually present in the studies so having fewer parameters would be favorable. In this work, we study a large number of InGaN quantum well structures with varying thickness, composition and quality. We demonstrate that there is a strong negative correlation between the carrier diffusion coefficient and quantum efficiency, regardless of the structure details. It proves that the carrier mobility is a governing parameter in the efficiency droop process.

The investigation was carried out in more than 30 different multilayered quantum well (QW) structures, emitting light in 410-580 nm spectral region. All samples were grown by metalorganic chemical vapor deposition (MOCVD) on c-plane sapphire substrates. Samples were grown by five different growers in several separate reactors, and have different indium content (from 5% to more than 25%), number of quantum wells (from 1 to 10), quantum well width (from 2 to 6 nm), etc. Photoluminescence (PL) and light-induced transient gratings (LITG) [2] techniques were used in this study. For the evaluation of PL quantum efficiency (QE), the three-measurement approach with an integrating sphere was applied [3]. The selective excitation at 393-405 nm of the samples allowed to monitor processes directly in QWs, but not in GaN barriers.

The results show a decrease in PL peak quantum efficiency with the increase in diffusivity (Fig. 1a). The value of diffusion coefficient *D* in each sample was measured at the excitation energy fluence at which efficiency droop (i.e. the peak QE) occurs. This trend proves that although samples are different, diffusivity is one of the key parameters governing the peak quantum efficiency. This can be explained with the density activated defect recombination (DADR) model [4]. In this model as the excitation energy fluence rises, the saturation of localized states leads to the excitation of charge carriers into the extended states where they have greater mobility and can reach non-radiative recombination centers more easily. Hence, higher mobility of these extended states results in bigger non-radiative losses. Fig. 2b shows that excitation energy fluence threshold at which droop occurs directly correlates with diffusivity (with Pearson's r= 0.92). Higher thresholds in the samples with lower QE (which in turn is generally ascribed to higher density of defects, what increases the rate of non-radiative recombination) compliment the correlation seen in Fig. 1a.

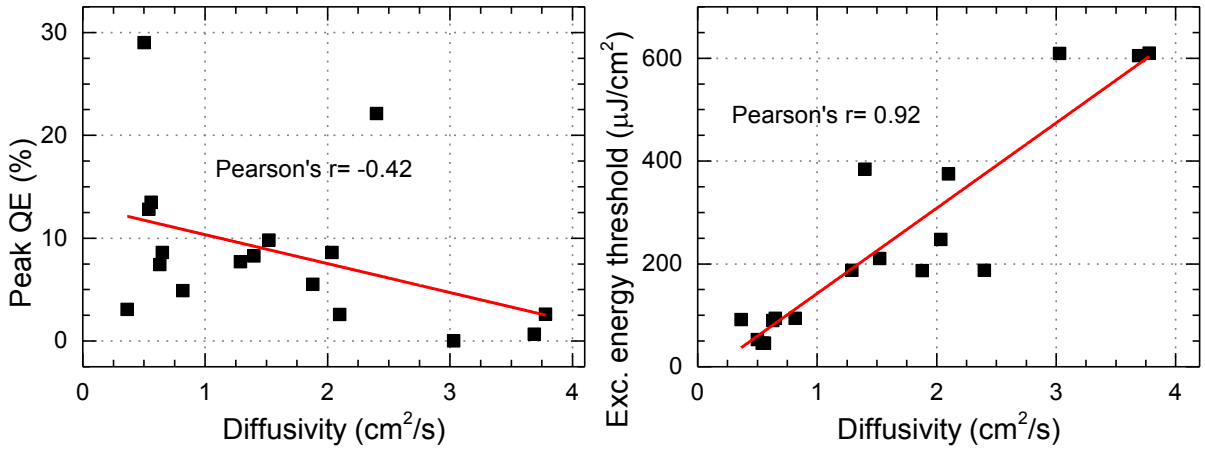

Fig. 1. Peak quantum efficiency dependence on diffusivity (a) and correlation between the droop threshold energy fluence and diffusivity (b).

[1] J. Piprek, Efficiency droop in nitride-based light-emitting diodes, physica status solidi (a), **207** (10), pp. 2217-2225 (2010).
[2] K. Nomeika, M. Dmukauskas, R. Aleksiejūnas et al., Enhancement of quantum efficiency in InGaN quantum wells by using superlattice interlayers and pulsed growth, Lith. J. Phys. **55** (4), pp. 255–263 (2015).
[3] S. Leyre, E. Coutino-Gonzalez, J. J. Joos et al., Absolute determination of photoluminescence quantum efficiency using an integrating sphere setup, Review of Scientific Instruments **85** (12), 123115 (2014).
[4] J. Hader, J.V. Moloney, and S.W. Koch, Density-activated defect recombination as a possible explanation for the efficiency droop in GaN-based diodes, Appl. Phys. Lett. **96** (22), 221106 (2010).

TWO-WAY CONNECTION BETWEEN QUALITY OF LAYERS IN AlGaN/GaN TEMPLATE

Žydrūnas Podlipskas

Institute of Applied Research and Semiconductor Physics Department, Vilnius University, Vilnius, Lithuania
Zydrunas.podlipskas@ff.stud.vu.lt

The main purpose of GaN buffer in any nitride-based heterostructure is reduction of lattice strain and damping of threading dislocations. Both functions decrease the defect density in upper layers and increase overall quality of the heterostructure, implying that the quality of all subsequent layers is determined by an underlying layer. In this report, I demonstrate a reverse effect – the influence upper layer has to base layer properties.

For the study, a set consisting of eleven 130 – 300 nm thick AlGaN epilayers was grown using metalorganic chemical vapor deposition (MOCVD) on c-plane GaN/sapphire templates. GaN buffer for every sample was grown at identical conditions, and initially was of the same quality. Al content x in $Al_xGa_{1-x}N$ epilayers varied from 11% to 28%, as determined from XRD measurements. Nonradiative carrier lifetime was used as a measure of quality, and was extracted from kinetics of light induced transient gratings (LITG). 25 ps duration pulses of 263 nm and 355 nm wavelength were used for excitation of AlGaN epilayers and GaN buffers, respectively.

Analysis of LITG results indicated that nonradiative carrier lifetime τ in AlGaN epilayers was strongly influenced by Al content x: τ decreased from 0.9 to 0.2 ns with increasing x (see solid lines in Fig. 1. (a) and abscissa axis of Fig. 1. (b)). This outcome could be determined by two processes: (i) deterioration of crystal quality (increasing density of nonradiative centers); (ii) increasing carrier diffusivity D (from 1.2 to 2.3 cm^2/s with increasing x). Carrier diffusivity can govern their lifetime since carriers have to diffuse to nonradiative centers to recombine. Meanwhile, diffusivity can increase with Al content due to interchange of upper valence subbands: crystal field band CH of lower effective mass emerges above heavy holes band HH ($m_{HH} = 3.57m_0$, $m_{CH} = 0.26m_0$) at $x = 0.04 – 0.6$ (depending on strain).

Carrier lifetime measurements in GaN buffer revealed unconventional τ variation from sample to sample in the range of $\tau = 0.5 – 0.9$ ns (see dashed lines in Fig. 1. (a) and ordinate axis of Fig. 1. (b)). This result should not be expected since GaN buffers in every sample were grown at identical conditions. The correlation between carrier lifetimes in GaN and AlGaN layers (Fig. 1. (b)) implies that during the growth, defects of AlGaN penetrated interface of AlGaN/GaN and deteriorated the very surface of GaN buffer at that interface. This result is particularly important in development of AlGaN/GaN high-electron-mobility transistors (HEMTs), since underlying GaN layer in HEMT determines the performance of a whole device.

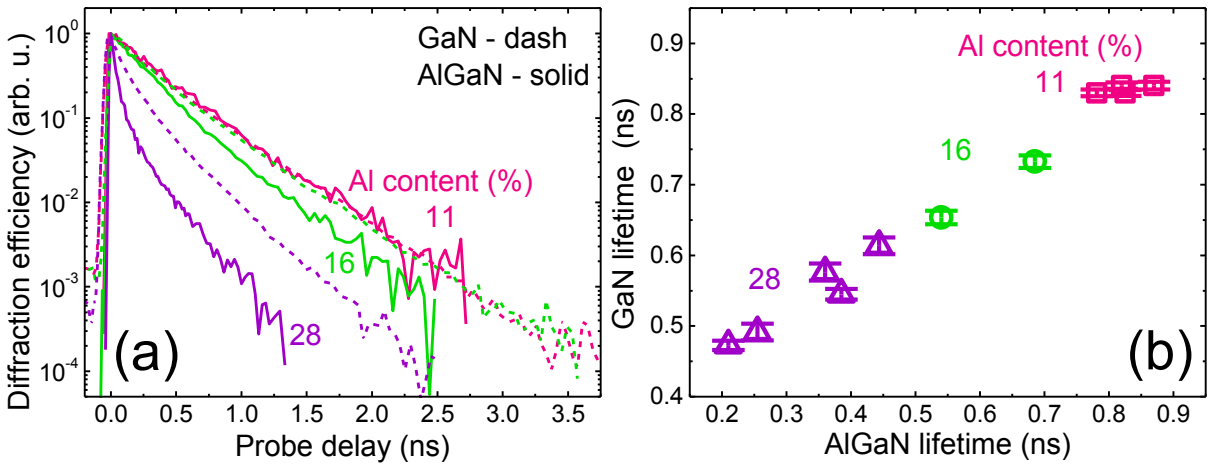

Fig. 1. (a) Normalized LITG transients recorded in $Al_xGa_{1-x}N$ epilayers of various Al content x and their respective GaN buffer; **(b)** nonradiative carrier lifetime in the very surface of GaN buffer as a function of carrier lifetime in the respective AlGaN epilayer.

Oral session 10

Theoretical physics

LONGITUDINAL SPIN-RELAXATION IN NITROGEN-VACANCY CENTERS IN DIAMOND IRRADIATED BY LOW ENERGY ELECTRONS

Janis Smits[1], Florian Gahbauer[1], Andris Berzins[1], Juris Prikulis[3], Krisjanis Smits[2], Ruvin Ferber[1], Donats Erts[3], Marcis Auzinsh[1], Dmitry Budker[4], Andrey Jarmola[4]

[1]Laser Center, University of Latvia, 25 Zellu street, LV-1586 Riga, Latvia
[2]Institute of Solid State Physics, 8 Kengaraga Street, LV-1063 Riga, Latvia
[3]Institute of Chemical Physics, University of Latvia, 19 Rainis Blvd., LV-1586 Riga, Latvia
[4]Physics Department, University of California, Berkeley, Berkeley, CA 94720-7300, USA
smitsjanis@gmail.com

Nitrogen-vacancy (NV) centers are powerful instruments in many areas of reasearch, including quantum information, magnetometry and nanoscale sensing. They have been used to detect individual electron spins and spin ensembles, measure the magnetic field distributions in biological signals and measure temperature and electric fields [1]. However successful use of NV centers demands understanding of the interactions between these centers and the environment.

This motivates recent efforts of the longitudinal relaxation time (also known as T_1 relaxation time). It characterizes the population relaxation from a polarized state back to thermal equilibrium. Previous work has shown that T_1 depends on the NV concentration [2] which means that not only phonons but cross-relaxation between NV centers play a role in the process.

In this work we examined the T_1 dependence on the NV concentration as well as applied magnetic field for NV centers prepared by electron irradiation with varying dosage. A stretched exponential $e^{-(\frac{t}{\tau_1})^{\beta}}$ is used to describe the data in order to account for a wide range of relaxation processes and the obtained τ_1 and β parameters are plotted as a function of NV concentration (figure 1). Strain splitting and zero field splitting were also measured for different NV concentrations as well.

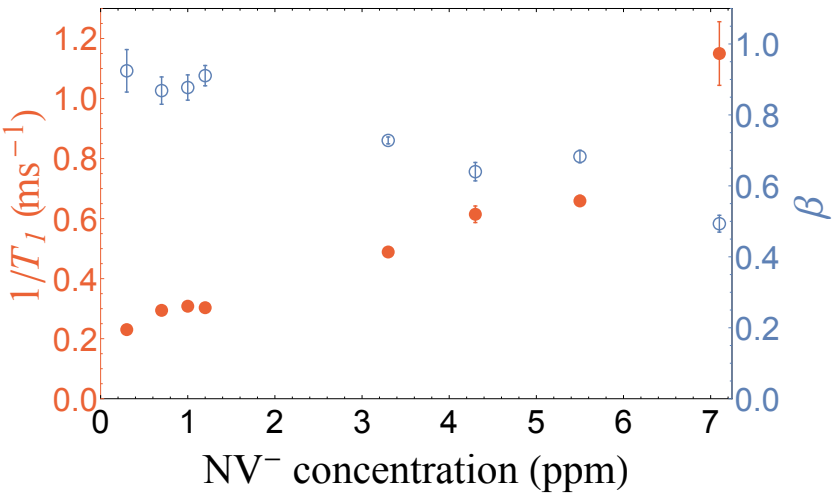

Fig. 1. Relaxation rate $1/T_1$ and stretching parameter β as a function of NV concentration with a splitting field of 30G.

The main conclusions obtained in this work are that with higher concentrations of NV centers the relaxation becomes more "stretched" which means that there are more relaxation channels than at lower concentrations. Also the T_1 time decreased with increasing NV concentration and could be used as a proxy (among other parameters such as luminosity) for determining NV concentration. We also observed a correlation between strain splitting E and NV concentration but no change in zero field splitting D which means that the N-V distance does not change with increasing defect concentration.

Acknowledgments
This work has been supported by M-ERA.NET project MyND no. Z/15/1366.

[1] L. Rondin et al., Magnetometry with nitrogen-vacancy defects in diamond, Reports on Progress in Physics, **77**, 056503 (2014), arXiv:1311.5214
[2] M. Mrozek et al., Longitudinal spin relaxation in nitrogen-vacancy ensembles in diamond, EPJ Quantum Technology **2**, 22 (2015), arXiv:1505.02253.

THEORETICAL ANALYSIS OF THE VIBRATIONAL STRUCTURE OF DEFECTS IN 3C-SIC

Lukas Razinkovas, Audrius Alkauskas

Center for Physical Sciences and Technology, Lithuania
lukas.razinkovas@gmail.com

Recently a new computational methodology was developed for the theoretical analysis of the vibrational structure of optical transitions in deep-level defects [1]. It combines established theoretical results with modern electronic structure techniques. However, the correct description of the luminescence band can be obtained only if calculations are performed in a rather large isolated defect system for which direct electronic structure calculations are computationally too demanding. This new methodology allows us to simulate such system by combining results from smaller defect system with the properties of the bulk lattice. Such computations were applied to study the phonon sideband pertaining to the spin-triplet transition at NV centers in diamond [1].

To apply the same methodology for defect centers in silicon carbide, we performed phonon structure analysis of ground-state 3C-SiC bulk and defect systems. The plane-wave pseudopotencial approach to density-functional theory has been applied to perform electronic structure calculations. To calculate vibrational modes and frequencies for bulk and defect suppercells we used PBE and hybrid HSE density-functionals. The finite difference method has been used to obtain lattice dynamical properties. Calculated phonon-dispersion curves for bulk system agree with experimental results and are used to study the range of the dynamical matrix in cubic SiC. Obtained results will be used to construct dynamical matrix of a large defect system, from which electron-phonon coupling properties will be determined.

[1] A. Alkauskas, B. B. Buckley, D. D. Awschalom, C. G. Van de Walle, First-principles theory of the luminescence lineshape for the triplet transition in diamond nv centres, New Journal of Physics 16(7), 073026 (2014).

QUANTUM DYNAMICS OF NONLINEAR COUPLED OSCILLATORS

Tomas Marčiulionis, Vladimir Chorošajev, Darius Abramavičius

[1] Department of Theoretical Physics, Vilnius University, Lithuania
marciulionis.tomas@gmail.com

Theoretical methods proposed by Redfield and Förster describe non equilibrium system dynamics due to interaction between environment and the quantum system in the spirit of the perturbation theory. [1,2,3.] However, these methods are limited and cannot be applied in certain conditions. When the interaction between the environment and system is strong that intermolecular interactions and energies of electronic excitations considerably change, the perturbation theory cannot be applied any longer. New alternative methods have been introduced to solve this issue. In this work we are analyzing Dirac – Frenkel variational method. Variational method is used to model spectral characteristics of molecular complexes in the finite temperature. We postulate the form of wave function of the quantum system. This form is called *Ansatz*. Parameters of this functions are varied and the residue of solution is minimized [4]. Davydov ansatz [5] is used to describe the exciton – environment interaction for the bath of harmonic oscillators, however this form is not optimal to model the realistic quantum system.

Empirically it was proven that width and intensity of the peaks in optically excited photosynthetic complexes spectrum is temperature dependent [6]. Such phenomena appear because of the anharmonicity of the potential energy of quantum oscillators, which represents environmental phonons. Due to the anharmonicity the width of wave packet must depend on the packet's position in coordinate – momentum phase space. As it follows, in order to describe such behavior it must be assured that wave packet becomes displaced and squeezed in the phase space of position and momentum of oscillator. To achieve such behavior with time – dependent Dirac – Frenkel variational method, the Ansatz proposed by Davydov must be modified to contain squeezing parameter.

$$|\psi_{D1}(t)\rangle = \sum_n \left(\alpha_n(t)\hat{a}_n^\dagger \exp \sum_q \left(\lambda_{qn}(t)\hat{b}_q^\dagger - \lambda_{qn}^*(t)\hat{b}_q\right)\right) \exp\left(\frac{1}{2}\sum_q \left(\xi_{qn}^*(t)\hat{b}_q^2 - \frac{1}{2}\xi_{qn}(t)\hat{b}_q^{\dagger 2}\right)\right)|0\rangle, \quad (1)$$

Here α_n are the electronic excitation states, $\hat{a}_n^\dagger$ - electronic excitation creation operator, λ_q – displacement maginitude, ξ_{qn} is the complex squeeze parameter and $\hat{b}_q^\dagger(\hat{b}_q)$ – creation (annihilation) operators.

In this work we apply time dependent Dirac – Frenkel variational method in order to analyze the simple anharmonic quantum system using this new Ansatz. The anharmonic quantum oscillator interacting with electronic degrees of freedom was chosen as model system.

Our model has proven the hypothesis that the width of wave packet dynamically changes only in the anharmonic quantum oscillator case and we have proven that *Ansatz* proposed by the Davydov cannot fully describe the dynamics of anharmonic quantum oscillator.

[1] A. G. Redfield, „On the theory of relaxation processes", IBM J. Res. Develop., vol. 1, no. 1, pp. 19-31, 1957.
[2] V. Balevičius Jr., A. Gelžinis, D. Abramavičius, T. Mančal and L. Valkunas, „Excitation dynamics and relaxation in a molecular heterodimer", Chem. Phys., vol. 404, no. 0, pp. 94-102, 2012
[3] T. Förster, „Zwischenmolekulare energiewanderung und fluoreszenz", Ann. Phys., vol. 437, no. 1-2, pp. 55-75, 1948.
[4] Chorosajev, V.; Gelzinis, A.; Valkunas, L.; Abramavicius, D., "Dynamics of exciton-p olaron transition in molecular assemblies: the variational approach", J. Chem. Phys., vol. 140, pp 244108, 2014.
[5] W. Förner, „Davydov solitons in proteins," Int. J. Quantum Chem., vol. 64, no. 3, pp. 351-377, 1997.
[6] Freiberg, A.; Rätsep, M.; Timpmann , K.; Trinkunas, G. & Woodbury, N.W. "Self-Trapped Excitons in LH2 Antenna Complexes between 5K and Ambient Temperature", J. Phys. Chem. B., 2003, 107, 11510-11515

AB-INITIO STUDIES OF POINT DEFECTS IN h-BN

Mazena Mackoit, Audrius Alkauskas

Center for Physical Sciences and Technology, Lithuania
mazena.mackoit@ftmc.lt

In recent years, a lot of attention started shifting towards the investigation of point defects in view of their potential applications in quantum information processing. Nowadays, one of the most interesting defects is the NV center in diamond. Its quantum state can be optically initialized, manipulated, and measured with high fidelity at room temperature. Despite a big area of possible applications diamond has its technological shortcomings in real world applications, such as high costs and fabrication difficulties. Therefore, it is important to search for defects analogous to the diamond NV center in other wide-bandgap semiconductors [1].

In the last few years, hexagonal boron nitride (*h*-BN) has been attracting more attention with the emergence of two-dimensional atomic crystals and van der Waals heterostructures, initiated by the discovery of graphene. *h*-BN has one of the largest band gaps among III-V compounds. Its value was determined to be 5.955 eV by means of optical spectroscopy [2], so it is expected to host optically active defects that have ground and excited states within the gap. This year scientists were able to measure quantum emission from localized defects in *h*-BN monolayers and multilayers even at room temperature [3]. Another experiment shows possibility of manipulation of individual defects using scanning tunnelling microscopy [4]. However, it is still not clear what defects are a probable source of the measured emission.

Ab initio calculations, which are based on density functional theory (DFT), could bring a lot of valuable information about defects: they can predict whether a desired defect is likely to form in a given material and will be it stable once formed, etc.

In this study we investigate boron vacancy, which is one of the dominating defects in *h*-BN. Boron vacancy defect has C_{3v} point group symmetry. In neutral charge state, V_B has 3 unsaturated dangling bonds. These defect states can be ionized by adding/removing electrons to it. Spin-polarized calculations were performed to examine neutral and positive charge states of this defect. Total spin states were determined and formation energies of these charged defects were calculated with *ab-initio* methods. Additionally first attempts to qualitatively estimate excited states were made. Detailed account of the results will be presented at the conference.

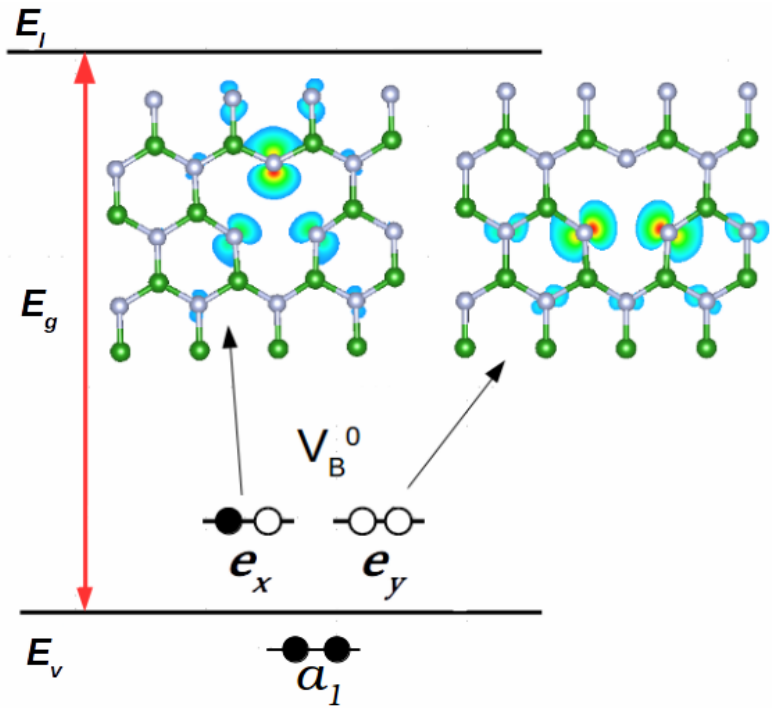

Fig. 1. Electronic band structure diagram depicting the defect levels (e_x, e_y, a_1) of the neutral V_B. Calculated wave functions are presented near the defect area. V_B eigenstates are close to the edge of the valence band. Formed defect levels e_x and e_y are σ type orbitals.

[1] J. R. Weber, W. F. Koehl, J. B. Varley et al., Quantum computing with defects, PNAS **107**, no. 19, 8513 - 8518 (2010).
[2] G. Cassabois, P. Valvin and B. Gil, Hexagonal boron nitride is an indirect bandgap semiconductor, Nature Photonics (2016).
[3] T. T. Tran, K. Bray, M. J. Ford et al., Quantum emission from hexagonal boron nitride monolayers, Nature Nanotechnology, **11**, 37 - 41 (2016).
[4] D. Wong, J. Velasco Jr, L. Ju et al., Characterization and manipulation of individual defects in insulating hexagonal boron nitride using scanning tunnelling microscopy, Nature Nanotechnology, **10**, 949 - 953 (2015).

Oral session 11

Interdisciplinary

ELECTROMAGNETIC WAVE SCATTERING BY A 2D PHOTONIC CRYSTAL SUBMERGED IN A MATERIAL CYLINDER

Giedrius Tušinskis[1], Juozas Bučinskas[1]

[1] Department of Theoretical Physics, Vilnius University, Lithuania
giedrius.tusinskis@ff.stud.vu.lt

A large interest in the electromagnetic (EM) wave scattering problems appeared in the past decade. It was mainly caused by the rapid development in the field of metamaterials and their applications in electronics. The possibility of modelling different type structures renewed the interest in finding new applications for arrays of parallel cylinders in electronics [1]. 2D arrays of cylinders – photonic crystals – are widely used in optics as elements of devices that control a beam. Photonic crystals made of macroscopic size have lower requirements for surface processing and are easy to manipulate [2]. Such 2D arrays are a convenient object to study EM wave scattering, because it is possible to find an analytical solution of Maxwell's equations for such systems. In the analysis of problems of EM wave scattering by structures made of semiconductors the absorption is important because it is highly affected by changes in density and mobility of free charge carriers. The main advantage of such structures is that the concentration and mobility of free charge carriers can be controlled by changing the illumination, temperature and direct magnetic field. Furthermore using arrays of cylinders as a cloak from electromagnetic waves is suggested [3].

Good knowledge of the radial component of Poynting vector $\vec{P} = [\vec{E}, \vec{H}^*]$ is needed since it contains information about radial component of energy flux density of EM wave field. In Fig. 1 we present dependencies of P_ρ for two different type photonic crystals with N_q cylinders placed in a circle and submerged in a material cylinder (see Fig. 1 (d)).

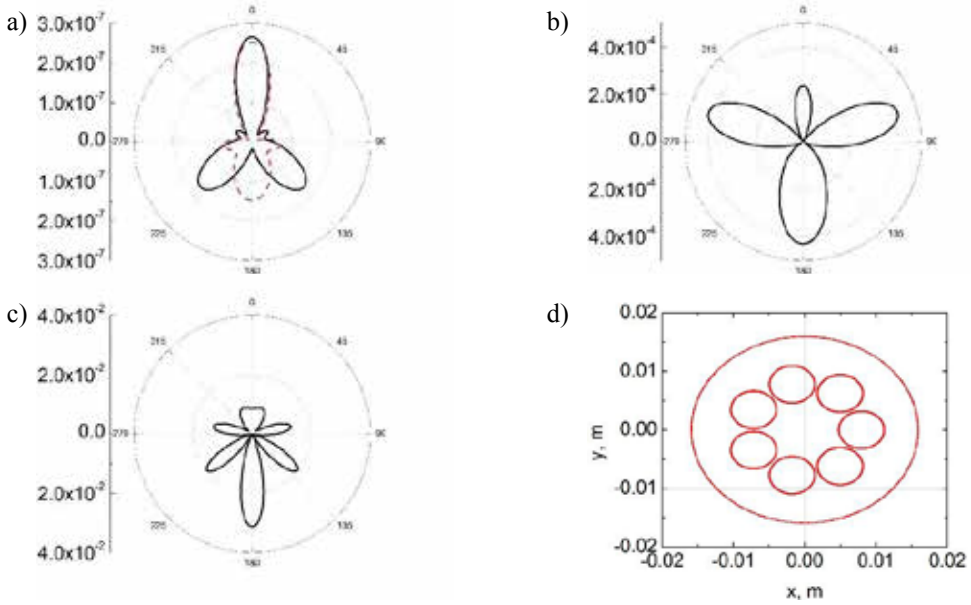

Fig. 1. Dependencies of P_ρ when the polarization vector of incident EM wave $\vec{E}_0 = (0,1,0)$ (a) with $N_q = 4$ (dashed) and $N_q = 7$ (solid), (b) $\vec{E}_0 = (0,0,1)$ with $N_q = 4$, (c) $\vec{E}_0 = (0,0,1)$ with $N_q = 7$ and (d) the placement of the cylinder array.

As seen in Fig. 1 (a) P_ρ is almost independent on the number of submerged cylinders when they are placed in a concentric manner for the polarization $\vec{E}_0 = (0,1,0)$. A completely different behavior is exhibited for polarization $\vec{E}_0 = (0,0,1)$ Fig. 1 (b) and (c). The incident wave is monochromatic linearly polarized plane wave. Inner cylinders are made from silicon submerged in a glass cylinder, with permittivity $\varepsilon_{Si} = 11.8 - i/(\omega\varepsilon_0\rho_{Si})$, $\varepsilon_{Glass} = 4 - 0.001i$, here $\omega = 2\pi f$, $f = 9$ GHz (frequency of the incident wave), ρ - specific resistivity, ρ_{Si} =1 Ωm. The radius of material cylinder R=16 mm, radii of submerged cylinders R_i=3,2mm. Distance from the material cylinder at which P_ρ is calculated – D=53mm.

[1] J. D. Joannopoulos, S. G. Johnson, J. N. Winn, R. D. Meade. 'Photonic Crystals', Princeton university press (2008).
[2] F. J. Valdivia-Valero and M. Nieto-Vesperinas, 'Resonance excitations and light concentration in sets of dielectric nanocylinders in front of a subwavelength aperture. Effects on extraordinary transmission. Optics Express', Vol. 18, No 7, 6740 (2010).
[3] Pekka Alitalo and Sergei Tretyakov, 'Cylindrical Transmission-Line Cloak for Microwave Frequencies', DOI: 10.1109/IWAT.2008.4511309.

MATHEMATICAL MODEL OF BOLUS SURFACE FOR VARIOUS ANGLES IN ELECTRON CANCER THERAPY

Aidas Medžiūnas[1], Jonas Venius[2]

[1]Faculty of Mathematics and Informatics, Vilnius University, Lithuania
[2]National Cancer Institute, Lithuania
aidas.medziunas@mif.stud.vu.lt

Malignant tumors are the second most frequent cause of death in the European Region. The main methods of treatment are surgery, radiation therapy (RT), chemotherapy and combinations of these methods. Up to 60% of cancer patients benefit from RT. X-rays and electrons are by far the most widely used types of beams in RT. However, Electron Beam Radiation Therapy (EBRT) provides unique advantages when superficial (5-6 cm depth) tumors are being treated. In human body electron beams have a finite range depending on their energy, after which dose falls off rapidly. Therefore they spare deeper healthy tissue, which leads to faster patient recovery, less side effects and higher life quality after the treatment.

However, the biggest limitation of EBRT is an inability to adjust the shape and intensity of the beam to the contour of a tumor. This results in either large areas of healthy tissue being irradiated. In order to solve these problems oncologists use *bolus* - standard shaped masses of extra material placed on the irradiated surface with particle absorption properties equivalent to (e.g. loosely packed polythene bags) or higher than (e.g. lead plates) tissue, acting as absorbents of unwanted radiation and correctors of beam shape. Nevertheless, this kind of *boli* is crude and inefficient. Hence, with the advent of 3D printing the need of individualized *bolus* based treatment emerged.

For the solution of this task there are three main criteria of success, which can be described as an optimization problem:

$$\begin{cases} D_{Tumor} \longrightarrow \max, & \text{tumor has to receive the maximum dose of radiation;} \\ D_{Critical} \longrightarrow \min, & \text{critical structures around the tumor have to receive the minimum dose of radiation;} \\ D_{Healthy} \longrightarrow \min, & \text{rest of the healthy tissue has to receive dose according to ALARA priciple.} \end{cases} \tag{1}$$

The goal of this work is development of computer based optimization method, that attempts to satisfy all three optimization criteria Eq. (1) by combining optimum beam angle of incidence and single radiation field *bolus* surface. The theoretical basis for the method is formed by classical radiation therapy[1].

The work result is a computer algorithm, which finds depth dose distribution under standard conditions (perpendicular beam incidence, flat surface and etc.) from experimental data based cubic spline interpolation method. Then this distribution becomes basic template and is passed to contour irregularities correction function (CICF) based on the Effective Source to Surface Distance Method[2]. Once this preparations phase is done algorithm solves Eq. (1) by variation of parameters: beam angle of incidence and *bolus* surface Fig. 1.

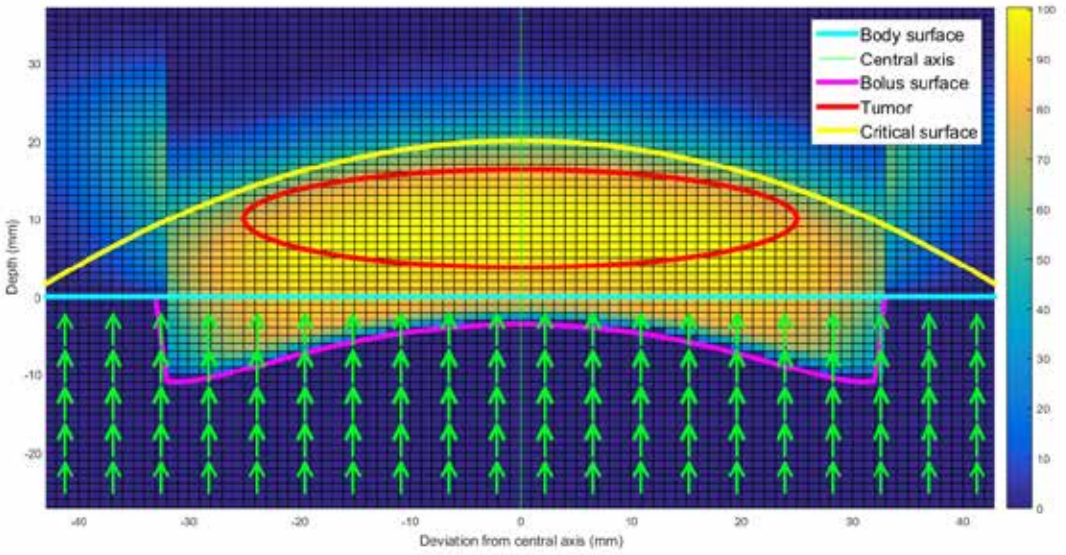

Fig. 1. Depth dose distribution with bolus surface limiting dose up to 50% maximum in critical surface.

[1] Faiz M. Khan, John P. Gibbons, The Physics of Radiation Therapy, Philadelphia, USA, (2014).
[2] E.B. Podgorsak, Radiation Oncology Physics, International Atomic Energy Agency, Vienna, Austria, (2005).

SIMULATION OF IRRADIANCE AND PHOTORESPONSE DISTRIBUTIONS IN CASE OF LARGE (>1M^2) SOLAR SIMULATORS EMPLOYING ARRAYS OF LIGHT-EMITTING DIODES

Žygimantas Vosylius[1], Algirdas Novičkovas[2], Vincas Tamošiūnas[1]

[1] Faculty of Physics, Vilnius University, Saulėtekio al. 9, bldg. III, LT-10222 Vilnius, Lithuania
[2] Institute of Applied Research, Vilnius University, Saulėtekio al. 9, bldg. III, LT-10222 Vilnius, Lithuania
zygimantas.vosylius@ff.vu.lt

Rapid production growth of solar cell and modules also increases a need in novel device characterization equipment. One of quality control stages in solar cell production is device testing under standardized irradiation conditions, provided by solar simulators. The most commonly used irradiance and spectral distributions aim to match so-called AM1.5G conditions [1]. IEC 60904-9 Ed.2.0 [2] standard defines criteria of how A, B or C class can be assigned to solar simulator in three categories: spectral distribution match, temporal stability, irradiance distribution uniformity. Traditionally, Xenon arc lamps were the mostly used light source of solar simulators. However, they suffer from issues related to a relatively short lamp life and stability. Therefore, development of simulators based on light-emitting diodes (LEDs), such as one reported in [3], are getting more and more attention due to stability and long-time performance of light sources.

In this work, simulation results of irradiance and spectrum distributions for large (> 1 m^2) solar simulators employing arrays of light-emitting diodes are presented. Also, photoresponse peculiarities for GaInP/GaAs/GaInAsP/GaInAs and perovskite/Si tandem solar cells were investigated. First of all, irradiance distribution models for all given LEDs were created and ratios between model's arbitrary units and real irradiance were determined by comparing computed values with corresponding experimental data. After computing irradiance distributions in case of 0.5 – 1 m distances between light-emitting diodes and measurement plain, arrays of each LED with AAA class irradiance uniformity were designed. Afterwards, distributions of spectra were computed for the plane of interest. Results of simulations are presented in Fig. 1. Obtained intensity distribution is presented in a left panel of the figure (Fig. 1a). Here one can clearly see that more than 1 × 1 m^2 area would be uniformly illuminated at 1000 W/m^2 irradiance within A-class requirements (within ± 2 %). On the right panel of the figure (Fig. 1a) the resulting spectrum in one of the points of the sample plane is presented.

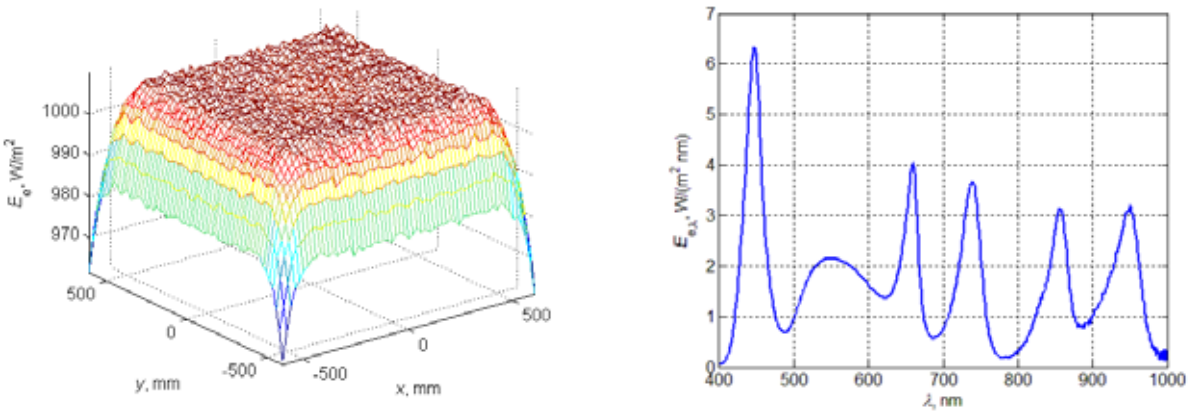

(a) (b)

Fig.1 Simulated irradiance distribution (a) and spectrum (b) for large LED-based solar simulator.

It has been established that 2486 LEDs are needed to build such solar simulator, in order for deviations from mean values of irradiance and photoresponse distributions to be small enough to fulfill all three A-class criteria as defined by AM1.5G standard. However it was determined, that type of simulator would still not be suitable for one of the most demanding applications - GaInP/GaAs/GaInAsP/GaInAs tandem solar cell examination due to the lack of infrared radiation with wavelengths above 1 µm. However, perovskite/Si cell should absorb all spectra effectively while generating photocurrent which should be similar for both active layers - approximately 27 mA/cm^2.

[1] *Photovoltaic Devices–Part 3: Measurement Principles for Terrestrial Pho-tovoltaic (PV) Solar Devices With Reference Spectral Irradiance Data*, IEC 60904-3 Ed.2.0, 2006.
[2] *Photovoltaic Devices–Part 9: Solar Simulator Performance Requirements*, IEC 60904-9 Ed.2.0, 2007.
[3] Algirdas Novickovas, Artūras Baguckis, Algirdas Mekys, and Vincas Tamošiūnas, "Compact Light-Emitting Diode-Based AAA Class Solar Simulator: Design and Application Peculiarities", *IEEE Journal Of Photovoltaics*, VOL. 5, NO. 4, July 2015.

PROSPECTS FOR THE W-BOSON ASSOCIATED HIGGS BOSON PRODUCTION WITH THREE MUONS IN THE FINAL STATE AT 13 TEV WITH CMS

Monika Venčkauskaitė[1], Andrius Juodagalvis[1], Adrian Perieanu[2]

[1]Institute of Theoretical Physics and Astrophysics, Vilnius University, Lithuania
[2]Institute of Experimental Physics, Hamburg University, Germany
monika.venckauskaite@gmail.com

Determining the Higgs boson properties is of high importance in particle physics today. Since the discovery of the Higgs boson it was shown that this particle interacts and decays in many ways predicted by the Standard Model as summarized in [1]. However, more studies are required to confirm that the discovered particle has the properties matching to those predicted by the Standard Model. The study of the fermionic Higgs boson decays provides information about the Higgs boson coupling to the fermions.

For this analysis we selected the Higgs boson decay channel $h \to \tau^+\tau^-$ with τ leptons decaying each into muon and neutrinos. The selected Higgs boson production mechanism is Higgs boson production in association with the W boson. Therefore, the most complicated background process to discriminate is the Z boson production with the W boson where the signature is very similar: $Z \to \tau^+\tau^-$ with τ leptons decaying each into muon and neutrinos. The W boson in both processes decays into muon and neutrino. The goal of this analysis was to find possible discriminating variables for these two processes. The analysis was performed having two levels of events. First level was the generated level. Events at this level were obtained using Monte Carlo generator (PYTHIA 8.2, described in [2]). The second level in the analysis was the reconstructed level. The generated events were reconstructed with CMS software (CMSSW).

In particle physics, the invariant mass m_0 is equal to the mass in the rest frame of the particle. It can be calculated by the particle's energy E and it's momentum p measured in any frame, by the energy-momentum relation:

$$m_0^2 c^2 = \left(\frac{E}{c}\right)^2 - \|\mathbf{p}\|^2 \tag{1}$$

The invariant mass m_0 in equation (1) remains the same in every frame. It can be reconstructed from the decay products of the particle. However, τ leptons cannot be fully reconstructed in the detector. We can only detect their visible decay products - muons. The neutrinos from the $\tau^- \to \mu^- \nu_\tau \bar{\nu}_\mu$ and $\tau^+ \to \mu^+ \bar{\nu}_\tau \nu_\mu$ decays are not measured.

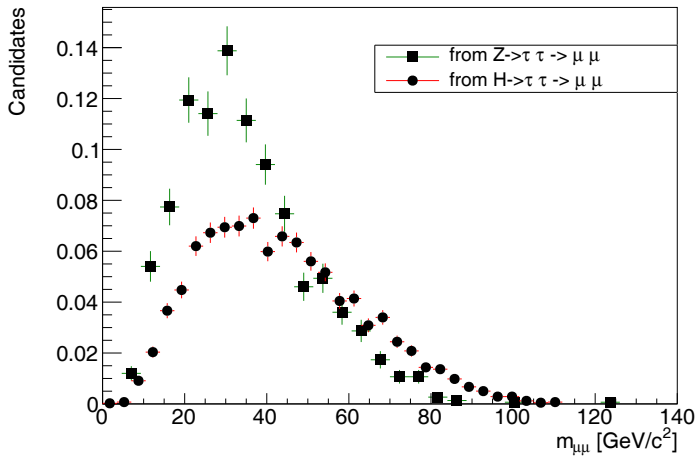

Fig. 1. Invariant mass of the dimuon pair at the reconstructed level for the Z boson (squares) and the Higgs boson (dots).

In the Fig. 1 we can see that there is a difference between reconstructed invariant mass from muon pair for Wh and WZ processes. Therefore, the reconstructed invariant mass is one of the discriminants between these two processes. We also found differences between the Wh and WZ processes in the missing transverse energy and in the various angles between the detected muons. These discriminants and the correlations between them will provide useful information for multivariate analysis using a trained neural network to analyze the data in proton-proton collisions at 13 TeV detected during the LHC Run II.

[1] M. Carena, C. Grojean, M. Kado and V. Sharma, *Status of Higgs boson physics*, (2013). http://pdg.lbl.gov/2015/reviews/rpp2014-rev-higgs-boson.pdf
[2] T. Sjöstrand, S. Mrenna and P. Skands, *A Brief Introduction to PYTHIA 8.1, 2008*, Comput. Phys. Comm. **178** 852,(2008). http://arxiv.org/abs/0710.3820

Oral session 12

Astrophysics and astronomy

SEARCHING FOR WEAK METHANOL MASER EMISSION AT 6.7 GHZ

Marta Dziełak, Anna Bartkiewicz

Toruń Centre for Astronomy, Nicolaus Copernicus University, Poland
dzielak@astri.uni.torun.pl

Methanol maser emission at 6.7 GHz is associated with regions where the formation of massive stars is taking place. [1]

I was searching for objects that have might be undetected in previous surveys toward selected regions with the field-of-view of 4arcmin. I used archival data from eVLA (interferometric network)[2] for 103 cataloged sources. I found 22 objects whose coordinates were not in the input catalogues. 13 of these objects were not found in the literature.

Additionally, owing to a method of looking at the cubes of maps for whole spectra, I found a new emission - the source G25.708+0.030.

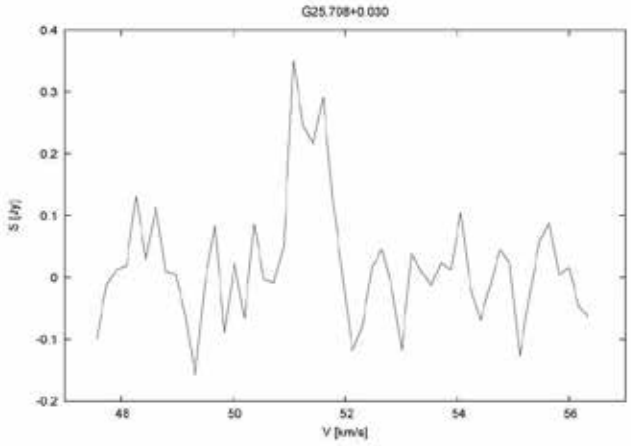

Fig. 1. New emission - the source G25.708+0.030

[1] Szymczak M., Hrynek G., Kus A.J., 2000, A&AS, 143, 269
[2] http://www.vla.nrao.edu/

CORE-DOMINATED TRIPLE BLAZARS AS (NEWBORN) X-SHAPED SOURCES

Katarzyna Rusinek, Andrzej Marecki

Toruń Centre for Astronomy, Nicolaus Copernicus University, Poland
krusinek@astro.umk.pl

Core-dominated triple (CDT) blazars are pretty intriguing sources. Their nearly symmetric FR II-type lobes are faint and diffuse while the compact core is the brightest feature [1]. These radio sources are thus not consistent with the general paradigm of double-lobed extragalactic radio sources, which are normally lobe-dominated. Hence the crucial issue is to learn what is reason behind that fundamental morphological difference between these two classes.

There are three possible explanations of CDTs so far [2]. First of them suggests that a fully fledged X-shaped object is hidden behind simple triple source and the high brightness of the core is caused by orientation of one of arms that is pointed towards the observer. This arm is extremely foreshortened and Doppler-boosted. Another approach assumes the presence of a double-double radio source with enormous ratio of inner to outer linear sizes of the two pairs of lobes. The third scenario involves the unresolved double core that is not aligned with the large-scale double. This might be a newborn X-shaped source.

The image below (Fig. 1) presents an example of a CDT source. In some cases core reveals some distortions which may indicate the existence of extra substructures.

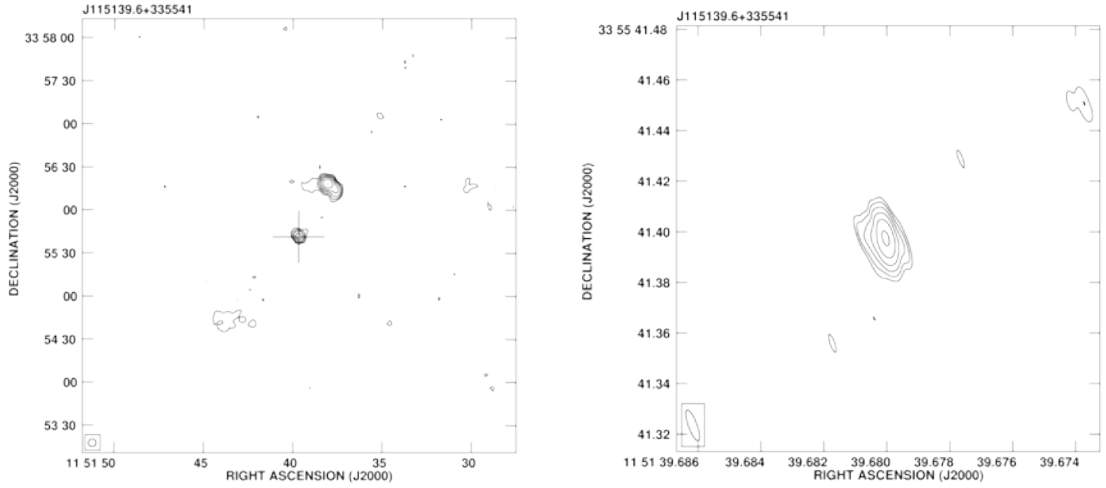

Fig. 1. FIRST (on the left) and EVN (on the right) image of J115139.6+335541 and its core. *Source:* [3]

An example of untypical X-shaped source was probably found in [2]. J1625+2712 is known as CDT object, however the EVN map (Figure 1 therein) shows double core. The ratio of linear sizes of these both pairs of lobes is extremely high ($\sim 3,000$). Moreover, the misalignment between these two pairs is also significant – nearly 50°.

Now we may present first results from new radio maps of J1625+2712 made by VLBA year ago. The core was observed in four frequencies what enabled us to carry out specific research about its morphology and character.

[1] Cseh, D., Frey, S. et al., Radio interferometric observations of two core-dominated triple radio sources at $z > 3$, A&A, 523, A34 (2010).
[2] Marecki, A., X-shaped radio sources as parent population of core-dominated triple blazars, in Proc. of Resolving the Sky-Radio Interferometry: Past, Present, and Future, 2012 April 1720, Manchester, UK, published online at http://pos.sissa.it/cgi-bin/reader/conf.cgi?confid=163, id.24 (arXiv:1212.2072) (2012).
[3] Marecki, A., & Swoboda, B., The transition from quasar radio-loud to radio-quiet state in the framework of the black hole scalability hypothesis, A&A, 525, A6 (2011).

SPATIAL ORIENTATION AND PHOTOIONIZATION OF PLANETARY NEBULAE

Bartosz Tułaza, Krzysztof Gęsicki

[1] Toruń Centre for Astronomy, Nicolaus Copernicus University (Poland)
258287@stud.umk.pl

The aim of my work was the study of planetary nebulae through attempts to create three-dimensional models in program Shape. Created structures enabled expansion of knowledge about the process of mass loss on the asymptotic giant branch and served as an introduction to photoionization modeling of selected objects [2]. The main result of the work is a catalog showing the pictures, models and a brief description of planetary nebulae.

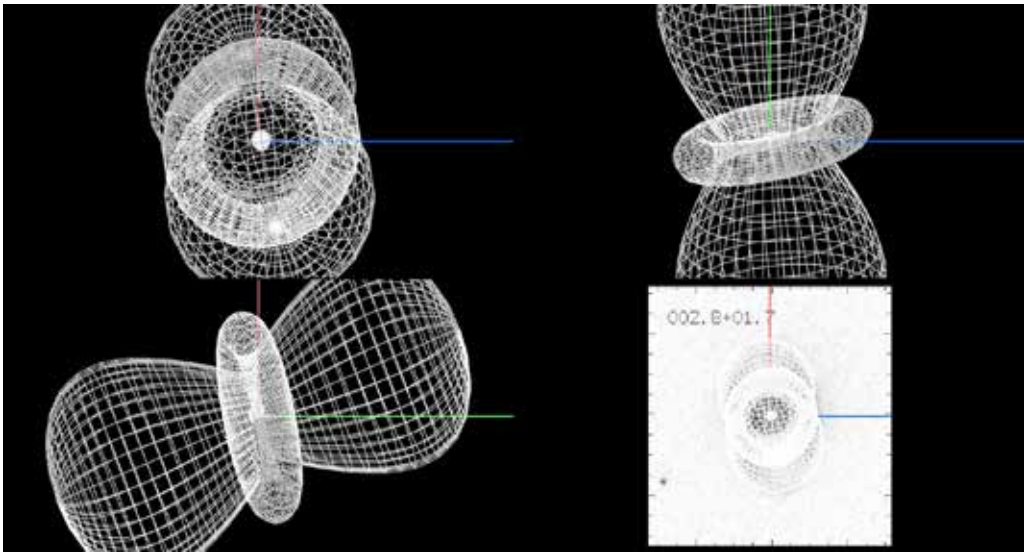

Fig. 1. Example of a three-dimensional model of planetary nebula.

Next step in my work was use of a Monte Carlo method to two- or three-dimensional modeling of radiation transfer with a predetermined shape and distribution [3]. Conclusions contains statistics on the classification of planetary nebulae and evaluation of the research method.

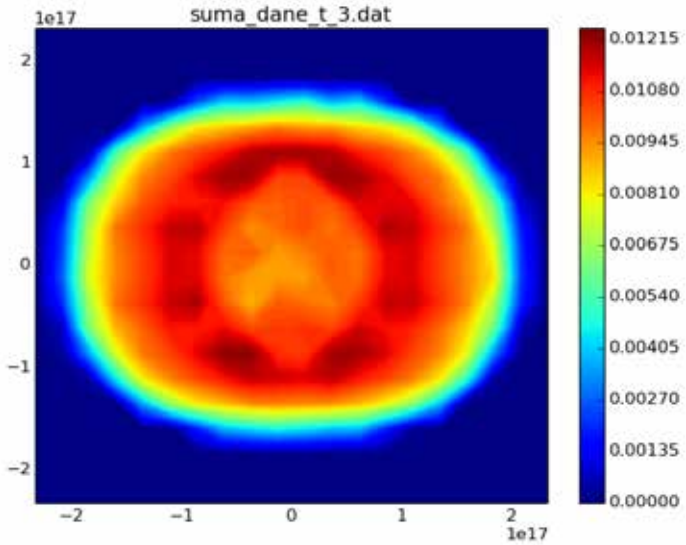

Fig. 2. Example of a two-dimensional photoionization model.

[1] http://bufadora.astrosen.unam.mx/shape

[2] K. Gesicki, A. A. Zijlstra, M. Hajduk, C. Szyszka. Accelerated post-AGB evolution, initial-final mass relations, and the star-formation history of the Galactic bulge. 2014. Astronomy & Astrophysics. Vol. 566. A48

[3] B. Ercolano, M. J. Barlow, P. J. Storey, The dusty MOCASSIN: fully selfconsistent 3D photoionization and dust radiative transfer models, 2005

SPECTROSCOPIC VARIABILITY OF IRAS 22272+5435

Laimons Začs[1,2], Faig A.Musaev[3], Bogdan Kaminskyi[4], Yakiv Pavlenko[4], Aija Grankina[1], Julius Sperauskas[2], and Bruce J. Hrivnak[5]

[1] Laser Center, University of Latvia, Raiņa bulvāris 19, LV-1586 Rīga, Latvia
[2] Vilnius University Observatory, Čiurlionio 29, Vilnius 2009, Lithuania
[3] Special Astrophysical Observatory of the Russian AS, Nizhnij Arkhyz, 369167, Russia
[4] Main Astronomical Observatory of Academy of Sciences of Ukraine, Zabolotnoho 27, Kyiv, 03680, Ukraine
[5]Department of Physics and Astronomy, Valparaiso University, Valparaiso, IN 46383, USA
aija.laure@gmail.com

A time series of high-resolution spectra was observed in the optical wavelength region for the bright proto-planetary nebula IRAS 22272+5435 (HD 235858), along with a simultaneous monitoring of its radial velocity and BV R_C magnitudes.

The object is known to vary in light, color, and velocity due to pulsation with a period of 132 days.

The light and color variations are accompanied by significant changes in spectral features, most of which are identified as lines of carbon-bearing molecules. According to the observations, the C_2 Swan system and CN Red system lines are stronger near the light minimum. A photospheric spectrum of the central star was calculated using new self-consistent atmospheric models. The observed intensity variations in the C_2 Swan system and CN Red system lines were found to be much larger than expected if due solely to the temperature variation in the atmosphere of the pulsating star. In addition, the molecular lines are blueshifted relative to the photospheric velocity. The site of formation of the strong molecular features appears to be a cool outflow triggered by the pulsation. The variability in atomic lines seems to be mostly due variations of the effective temperature during the pulsation cycle. The profiles of strong atomic lines are split, and some of them are variable in a time scale of a week or so, probably because of shock waves in the outer atmosphere [1].

The European Union FP7-PEOPLE-2010-IRSES program is acknowledged for funding exchange visits in the framework of the project POSTAGBinGALAXIES (grant agreement No. 269193).

[1] Začs, L., Musaev, Kaminskyi, B., Pavlenko, Y., Grankina, A., Sperauskas, J., and Hrivnak B.J., Spectroscopic variability of IRAS 22272+5435, The Astrophysical Journal **816**, 3 (2016)

ESTCUBE-2 MISSION ANALYSIS: PLASMA BRAKE EXPERIMENT FOR DEORBITING

Iaroslav Iakubivskyi[1*], Hendrik Ehrpais[1], Erik Ilbis[1], Karl Reinkubjas[1], Pekka Janhunen[2], Petri Toivanen[2], Jouni Envall[2], Andris Slavinskis[1,3]

[1]Insitute of Physics, University of Tartu, Estonia
[2]Finnish Meteorological Institute, Finland
[3]Tartu Observatory, Estonia
[*]*iaroslav.iakubivskyi@estcube.eu*

Here we present the preliminary mission analysis for the ESTCube-2 three-unit CubeSat, which is designed to test the Coulomb drag propulsion. One of the applications of Coulomb drag is the electric solar wind sail (E-sail) that could be used to travel within the Solar System with record speeds due to the solar wind. Another application is deploying a charged tether in low Earth orbit to brake the orbital velocity of the satellite using Coulomb drag. The negatively charged plasma brake tether interacts with the ambient ionospheric plasma ram flow to slow down the satellite.

To test this concept, ESTCube-2 will deploy and charge nominally 300 m tether, which will be used to reduce the orbit altitude of the satellite. Such a tether could deorbit ESTCube-2 from the altitude of 700 km to 500 km in half a year. The experience with ESTCube-1 and Aalto-1 has shown that it is feasible to host a similar payload in ⅓ to ½ of a CubeSat unit. The mass of 300 m long tether is nominally 30 grams according to a conservative estimate. Hence the plasma brake is a lightweight, efficient, cost-effective and scalable deorbiting system with a potential to address the space debris problems in the most critical altitudes of 900 km and less.

ESTCube-2 in-orbit demonstration platform will be designed and developed such that it can be employed for other Coulomb drag propulsion experiments. For example, by demonstrating the electric solar wind sail (E-sail) outside the Earth's magnetosphere which would allow to confirm the analytical, numerical and laboratory estimations of the E-sail force. The main requirements for the satellite bus are to provide the total angular momentum of 23 Nms for centrifugal tether deployment, to provide means of deployment verification, and to provide up to 3000 mW of power for charging the tether. This paper will present mission analysis and system level design of ESTCube-2.

NOVEL ROCK SAMPLING TECHNIQUE FOR USE ON MARS

John Holt[1], Kamil Ciesielski[2]

[1] Space Research Centre, University of Leicester, United Kingdom
[2] Gdansk University of Technology, Faculty of Applied Physics and Mathematics, Poland
kamciesi@student.pg.gda.pl

The Small Planetary Linear Impulse Tool (SPLIT), developed in Space Research Centre, University of Leicester, was started as a response for NASA's Call for Proposals for this mission Mars 2020 (Mars Sample Return). It is a novel geotechnical tool for use on Mars and other rocky or icy planets or moons. Its aim is to sample rocks for biosignature search in an efficient and highly controlled way from as well as scientific, as engineering point of view. SPLIT's main advantages, when compared to currently working devices[1] are minimized contamination of stone's pristine surface, extended depth of penetration and lower usage of energy.

The focus of the interdisciplinary student's project was to use the new prototype in order to learn to search for water traces and morphological biosignatures on pristine rocks' surfaces and look at the dependence of the above on stones' chemical composition and its structure. From the technical point of view, the project was aimed a finding the most efficient way of sampling the rocks.

Results turned out to be very encouraging: with use of a variety of planetary analogues from local sources and Atacama Desert, it was demonstrated that SPLIT is able to deliver its primary function - to uncover perfect location for biosignatures search in Martian conditions. What is more, we learned a few technical issues about its operation modes, and micro-astrobiology, which can improve the science of future planetary missions.

Fig 1. NASA rover Spirit in Martian landscape [2].

[1] Grotzinger, John P., et al. "Mars Science Laboratory mission and science investigation." Space science reviews 170.1-4 (2012): 5-56.
[2] findingdulcinea.com/news/science/2009/may/Spirit-Stuck-in-Martian-Landscape-as-NASA-Tries-to-Help.html

Poster session 1

ENERGETIC COST OF SPAWNING MIGRATION: DO STOCKED EELS FROM LITHUANIA CAN REACH THE SPAWNING GROUNDS AT SARGASSO SEA

Justas Dainys, Žilvinas Pūtys, Linas Ložys

Nature Research Centre, Laboratory of Marine Ecology, Lithuania
dainys@ekoi.lt

In a response to decline in eel stock many European countries are stocking eels to seas and inland waters in order to enhance the production of adult (silver) eels escaping to the sea for spawning migration. However, the degree of contribution to the spawning stock of these eels is poorly known. It is not known yet do stocked eels accumulate enough energy resources (lipids) for successful ~7500 kilometre long spawning migration from Lithuanian coastal waters to Sargasso Sea. Migrating silver eels do not feed during their migration to the spawning grounds; therefore they rely for their energy completely on fat stores [1] which are accumulated during sedentary yellow eel stage in coastal or inland waters.

Current study was carried out to answer the question whether eels translocated from coasts of Western Europe and stocked in Lithuania accumulate enough energy for gonadal development and spawning migration, and have at least theoretical chances to reach the spawning grounds.

Fulton's condition factor is considered to be one of the measures of silver eel quality. This factor is calculated from the relationship between the weight of eel and its length, with the intention of describing the "condition" of that individual. Fish with higher condition factor are considered healthier, having more energy reserves for normal activities, growth and reproduction. However, results of our study suggest that Fulton's condition factor has no significant correlation ($p > 0.05$) with fat content (%) in studied eels. This suggests that eels with higher Fulton's factor does not necessarily have accumulated more lipids.

However, swimming potential, as well as fat content, significantly ($p < 0.05$) correlates with ocular index (OI) and silvering stage according to EELREP (2005) [2]. Average swimming potential of studied silver eels (stages S4, S5 and SMII) is estimated to be 7631 km (average 26.7 %), while eels of the last silvering stage (SMII) had highest fat content (average 31.9%) and highest swimming potential (9046 km on average). The results of this study demonstrates that eels are able to perform spawning migration from Lithuania and cover more than 7500 kilometres in this way contributing to successful spawning and recruitment.

[1] Tesch, F.W. The eel, 5th ed. Blackwell Science, Oxford, England. 408 pp. (2003)
[2] EELREP. Estimation of the reproduction capacity of European eel. Final report. 272 pp. (2005)

ASSESSMENT OF NEW PARTICLE FORMATION EVENTS ON THE COAST OF BALTIC SEA

G. Mordas, V. Dudoitis, K. Plauškaitė, N. Prokopčiuk, and V. Ulevičius

Department of Environmental Research, SRI Center for Physical Sciences and Technology, Lithuania
vadimas.dudoitis@ftmc.lt

This research focuses on new particle formation (NPF) events on the coast of Baltic Sea at Preila (55°55' N; 21°04' E). The continuous measurements of the particle number size distribution (PNSD) (9-840 nm) were held during the whole year 2013. The NPF events were observed in 111 days of the year, which were classified.

The multi-lognormal fitting (Fig. 1) of PNSD provides useful information about the dynamics of NPF events. The modes were characterised by their PNC values, mean geometric diameter (D_g) and geometric standard deviation (σ_g). It was estimated from the observations that the typical NPF event started at 11:00 and lasted for six hours. During this event the nucleation mode D_g shifted from 7 to 26 nm, with the estimated growth rate (GR) of 3.3 nm·h^{-1}. Though the nucleation and Aitken particle modes are overlapping, different processes are behind the aerosol growth. In Aitken mode aerosol particle GR (6.4 nm·h^{-1}) was c.a. twice as fast as for nucleation mode. It can be explained by lower Kelvin effect to condensational growth of Aitken mode particles and by the additional growth due to the coagulation of ultrafine particles.

The aerosol formation rate (J_9), GR and condensation sink (CS) derived at Preila station, were compared in Table 1 with results from other measurement stations in Europe. The J_9 of 0.45 cm^{-3}·s^{-1} at Preila was similar to Utö and Hyytiälä J_{10} values, i.e. 0.45 and 0.70 cm^{-3}·s^{-1}, both stations represent North Baltic Sea region. The CS at Preila was one of the lowest (1.53·10^{-3} s^{-1}) and similar only to Hyytiälä CS values (2.0·10^{-3} s^{-1}).

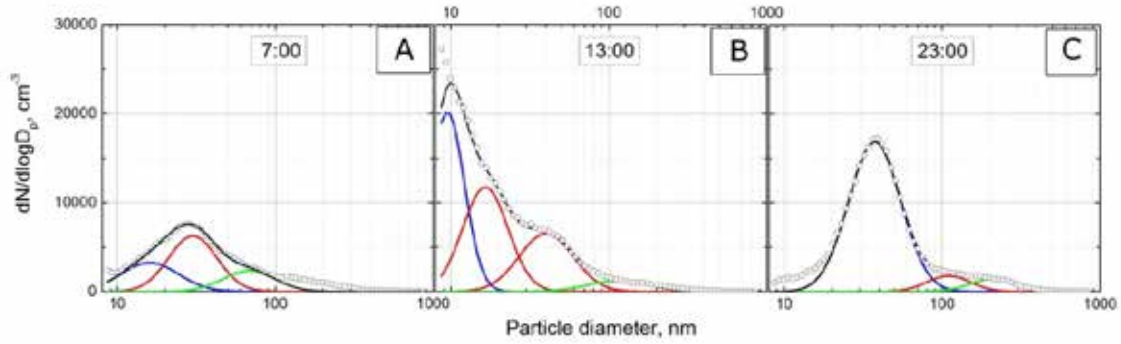

Figure 1. The aerosol particle size distribution modes (1-h averaged values) were fitted on the event day in the morning (A), during the day (B) and in the evening (C). Blue, red and green lines represent the nucleation, Aitken and accumulation modes, respectively. Black line stands for the sum of the modes.

Table 1. The main parameters of the NPF events at Preila and other European stations

Location	J_{10}, cm^{-3}·s^{-1}	GR, nm·h^{-1}	CS, s^{-1}	Reference
Preila (coastal, LT)	0.45 (J_9)	3.8	1.53·10^{-3}	This study
Hyytiälä (rural, FI)	0.70	2.9	2.0·10^{-3}	[1]
Utö (marine, FI)	0.45	2.3	3.8·10^{-3}	[2]
Vavihill (coastal, SE)	1.54	2.5	5.4·10^{-3}	[3]
San Pietro Capofiume (rural, IT)	3.60	6.1	10.0·10^{-3}	[4]
K-puszta (rural, HU)	1.20	6.1	5.0·10^{-3}	[4]

The research leading to these results has received funding from Lithuanian-Swiss cooperation programme to reduce economic and social disparities within the enlarged EU under project agreement No. CH-3-ŠMM-01/08.

[1] A. Jaatinen, A. Hamed, J. Joutsensaari et al., A comparison of new particle formation events in the boundary layer at three different sites in Europe, Boreal Environment Research 14, 481–498 (2009)

[2] A. P. Hyvärinen, M. Komppula, C. Engler et al., Atmospheric new particle formation at Utö, Baltic Sea 2003-2005, Tellus B 60(3), 345-352 (2008)

[3] A. Kristensson, M. Dal Maso, E. Swietlecki et al., Characterization of new particle formation events at a background site in Southern Sweden: relation to air mass history, Tellus B 60(3), 330–344 (2008).

[4] H. E. Manninen, T. Nieminen, E. Asmi et al., EUCAARI ion spectrometer measurements at 12 European sites – analysis of new particle formation events, Atmospheric Chemistry and Physics 10, 7907–7927 (2010).

REMOTE SENSING OF DROUGHTS

Viktorija Mačiulytė

Department of Hydrology and Climatology, Vilnius University, Čiurlionio 21/27, LT-03101, Vilnius, Lithuania
viktorija.maciulyte@gf.vu.lt

Drought is the natural phenomenon and primarily associated with the loss or reduction of agricultural production, forestry and water resources. An analysis of droughts and their impacts assessment can help to choose the measures for drought impact mitigation in vulnerable regions. One of the major problem is the drought diagnostics [1].

Droughts can be diagnosed using different indices like SPI (*standardized precipitation index*), PHDI (*Palmer hydrological drought index)* and HTC (*Selianinov hydrothermal coefficient*) [2]. These indices require special or conventional observations: meteorological, agricultural etc. Data from meteorological stations not always are representative local scale precipitation patterns as well as for specific soil or vegetation areas.

The drought diagnostics uses the remote sensing method. Only satellites sensors that have a high spatial resolution (0.01°) are under consideration. Sensors register the amount of short wave radiation reflected and long wave radiation emitted from the surface objects [3].

In this study *Normalized Difference Vegetation Index* (NDVI) was used (1). It shows the surface vegetation "greenness". Briefly speaking it measures plant reflection of red (R – wavelengths 0.58–0.68 μm) and near-infrared (NIR – wavelengths 0.73–1.10 μm) radiation. Data series covers the period from 1981 to present. NDVI values vary from 0.1 (no vegetation) to 1.0 (perfect greenness).

$$\mathrm{NDVI} = \frac{\mathrm{NIR}-\mathrm{R}}{\mathrm{NIR}+\mathrm{R}} \qquad (1)$$

NDVI was detected by AVHRR and MODIS sensors on board of NOAA, Terra and Aqua series satellites in 1981–2015 year. Areas for analysis were selected according to the different moistening conditions in Lithuania (Fig. 1) [2]. Information about air temperature, precipitation, snow depth, snow cover and ground frost length was included to the analysis to determine relationship between NDVI values and meteorological conditions.

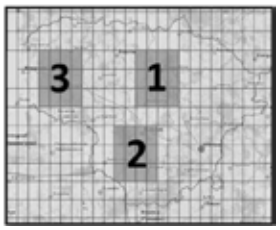

Fig. 1. The areas for analysis.

The negative anomalies (drought conditions; standardized NDVI value below -2) were determined 1.8 times more often than the positive. According to NDVI the vegetation period droughts are most common in the third area (Fig. 1). It was also found that NDVI is able to identify all dry periods as of using HTC [2]. Drought development in 2002 within area 2 is shown in Fig. 2 and Fig 3. Rectangular shows drought period identified by HTC. During this drought (08.03–09.14) the mean air temperature was 2.8 °C higher than 1981–2015 climatology while precipitation amount was less by 44 %. Standardized NDVI values varied from -1.7 till -2.6.

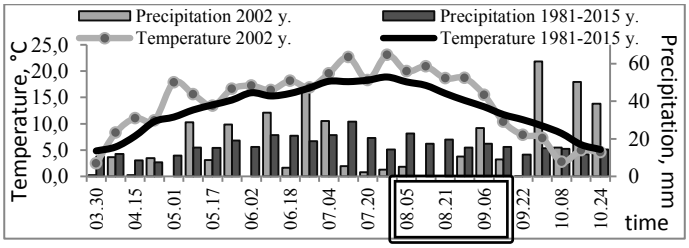

Fig. 2. Mean air temperature and precipitation amount 2002 and 1981–2015 in the *second* area.

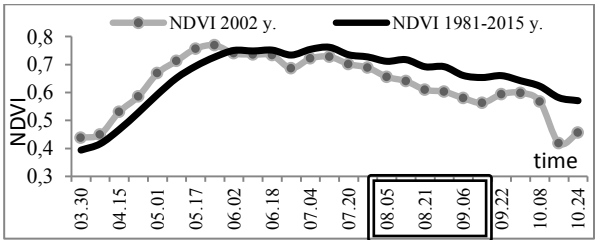

Fig. 3. Mean NDVI 2002 and 1981–2015 in the *second* area.

NDVI capable to diagnose more drought periods during the same time comparing to other indices. Droughts are often localized in small areas due to spatial unevenness of precipitation regime. However, the negative NDVI anomaly not always means a drought conditions. In spring the low NDVI values can be related with prolonged winter season and as a consequence a later than usual start of vegetation. Also late frosts in spring and early frosts in autumn have negative impact on vegetation conditions. The results of this study show that the drought index based on remote sensing method could be the alternative instrument in drought analysis and monitoring.

[1] K. Stahl, I. Kohn et al., Impacts of European drought events: insights from an international database of text-based reports. NHESS (2015).
[2] D. Valiukas, *Sausrų ir sausų laikotarpių Lietuvoje analizė*. Doctor dissertation. Vilnius University (2015).
[3] Alabama Cooperative Extension System, *Basic of crop sensing.* Alabama A&M and Auburn Universities. ANR-1398 (2011).

SPATIAL AND TEMPORAL ANALYSIS OF ORGANIC AND BLACK CARBON MASS CONCENTRATIONS IN LITHUANIA

Julija Pauraitė[1,2], Genrik Mordas[1], Steigvilė Byčenkienė[1] and Vidmantas Ulevicius[1]

[1] Institute of Physics, Center for Physical Sciences and Technology, Savanorių ave. 231, LT-02300 Vilnius, Lithuania

[2]Faculty of Physics, Vilnius University, Saulėtekio Ave 9, build. 3, LT-10222 Vilnius, Lithuania

julijapauraite@yahoo.com

Atmospheric carbonaceous aerosols constitute a significant part of the atmospheric aerosols, while a large part of them consists of organic material (~50%). The carbonaceous atmospheric particulate matter consists of black carbon and a variety of organic compounds. Black carbon (BC) is a primary incomplete combustion-generated carbonaceous aerosol with a graphitic-like structure, while organic carbon (OC) may have both primary and secondary origins. Primary OC may result from fossil fuel emissions, biomass burning or represent biological particles or plant debris while the secondary OC can be formed in the atmosphere by gas-to-particle conversion.

Both organic carbon and black carbon mass concentrations were measured in Lithuania at coastal/marine (Preila), rural (Rūgšteliškis), and urban background (Vilnius) environments have been analyzed to infer the spatial and temporal distributions of the OC/BC ratios from May 2013 to October 2014. OC/BC ratios reflected the location of the different sites, as well as possible different sources influencing air quality. The estimations of OC/BC ratios were made to compare values of parameter α. In this study, parameter α (Fig.1) was determined by coefficient of linear OC/BC fitting curve.

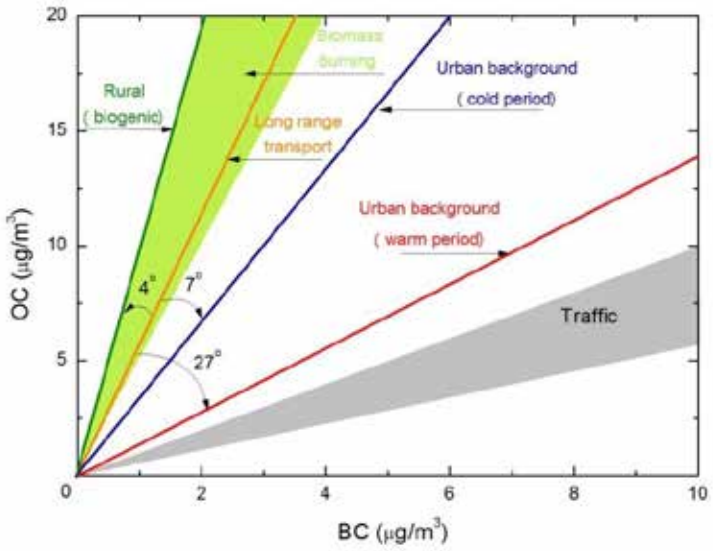

Fig. 1. Alteration of parameter α value for different sources.

The highest hourly BC aerosol mass concentration in urban background environment reached 17.2 $\mu g \cdot m^{-3}$ during the cold period, while the mean BC concentration was found to be 2.34 $\mu g \cdot m^{-3}$, which is about a factor of three higher than mean values in coastal/marine and rural sites (0.84 and 0.77 $\mu g \cdot m^{-3}$, respectively). It was estimated that the mean OC concentrations have distinct seasonal variations with the highest values observed (8.60 $\mu g \cdot m^{-3}$) in urban background and lowest mean concentration (3.01 $\mu g \cdot m^{-3}$) in coastal/marine environment in the cold period. The maximum OC concentrations values during the cold period (75.44 $\mu g \cdot m^{-3}$) were more than four times higher of those in the warm period (17.78 $\mu g \cdot m^{-3}$) in urban background environment. In contrast, the mean OC values measured during the warm period in coastal/marine (4.11 $\mu g \cdot m^{-3}$) and rural (4.56 $\mu g \cdot m^{-3}$) environment was higher compared to the cold period (3.01 and 3.45 $\mu g \cdot m^{-3}$, respectively). Strong influence of local sources of BC in urban environment and long-range transport in rural environments was observed. The carbonaceous aerosol shows a relative enrichment in OC during the warm period in coastal/marine and rural sites (α = 84°–85°). The high values of OC/BC ratio in forested (rural) areas suggest that OC emissions could be derived from biogenic sources. The decrease of the OC/BC ratio in urban environment during the warm period was caused by the vehicle traffic activity and other anthropogenic sources.

Acknowledgement: The research leading to these results has received funding from Lithuanian-Swiss cooperation programme to reduce economic and social disparities within the enlarged EU under project agreement No CH-3-ŠMM-01/08.

[1] J. Pauraitė et al., Spatial and Temporal Analysis of Organic and Black Carbon Mass Concentrations in Lithuania, Atmosphere **6**, 1229-1242 (2015).

CARBON CONCENTRATION AND STABLE ISOTOPE RATIOS IN PM1 AEROSOL PARTICLES IN VILNIUS, LITHUANIA

Laurynas Krikščikas, Šarūnas Jacevičius, Andrius Garbaras

Institute of Physics, Center for Physical Sciences and Technology, Lithuania
laurynas.kr@hotmail.com

Atmospheric aerosols in range of PM1 (aerosol particles smaller than 1 μm) have adverse effects on human health and Earth's climate [1]. To reduce these effects it is necessary to possess the ability to trace atmospheric aerosol sources. Such ability is partially obtained by measuring $\delta^{13}C$ values in aerosol particles because different organic materials (fossil fuel, biomass, etc.) have distinct $\delta^{13}C$ values. The definition of $\delta^{13}C$ is given in equation (1), $(^{13}C/^{12}C)$ represents isotopic carbon ratio of standard and sample, respectively.

$$\delta^{13}C = \left(\frac{\left(\frac{^{13}C}{^{12}C}\right)_{sample}}{\left(\frac{^{13}C}{^{12}C}\right)_{standard}} - 1 \right) \times 1000\ ‰ \qquad (1)$$

Aerosol samples were collected at Institute of Physics, Savanorių ave. 231, Vilnius, Lithuania, during period from 2014-10-22 to 2015-06-26. A high volume automatic air sampler and *Whatman Q-MA* quartz fiber filters were used for aerosol sample collection. Measurements of carbon concentration and $\delta^{13}C$ values in aerosol samples were performed with *EA-IRMS* system (elemental analyzer - isotope ratio mass spectrometer). Meteorological data was obtained from *NOAA Air Resources Laboratory* archives [2].

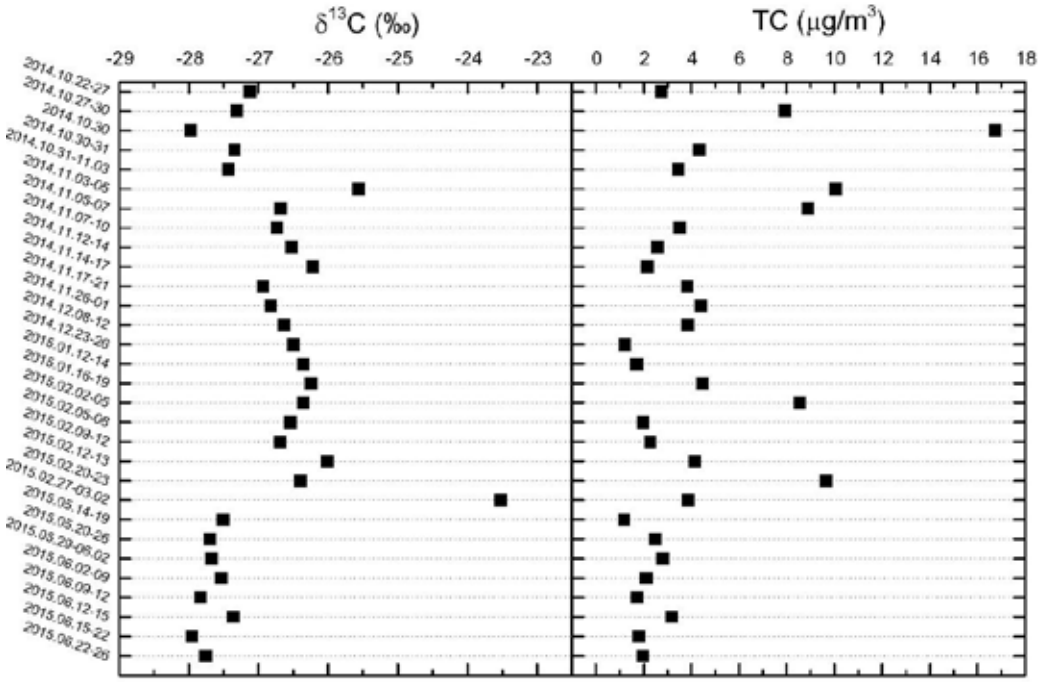

Fig. 1. Temporal distribution of total carbon (TC) concentration and $\delta^{13}C$ in aerosol samples (Vilnius, Lithuania)

Stable isotope ratio mass spectrometry, combined with other analysis techniques, allows distinguishing carbon sources (biogenic from anthropogenic) in the atmosphere.

[1] I. Rimšelytė, J. Ovadnevaitė , D. Čeburnis, K. Kvietkus, E. Pesliakaitė, (2007). *Lith. J. of Phys*., 47(4), 523–529.
[2] Rolph, G.D. (2016). Real-time Environmental Applications and Display sYstem (READY) Website (http://www.ready.noaa.gov). NOAA Air Resources Laboratory, College Park, MD.

IRON COMPOUNDS IN WATER SUPPLY SYSTEMS, SOURCES AND ACCUMUALTION

Marina Valentukeviciene

Department of Water Management, Vilnius Gediminas Technical University, Lithuania
marina.valentukeviciene@vgtu.lt

The material of water supply pipelines plays a central role in the uptake of iron from groundwater into sediments via the formation of biofilm on the internal surface of pipeline. The biofilm enhance nutrient uptake into the microorganism community, both as a consequence of the physical property of the pipe and by the ability of the microorganisms to mobilize nutrients from water solution through the action of extracellular enzymes. In addition to acquiring essential micronutrients, iron bacteria are also very efficient at taking up and accumulating microelements. This ability includes accumulating heavy metals, particularly iron compounds. This can have important consequences for the retention, mobility and availability of these elements in the water intended for human consumption. The aim of the present study was to investigate the behaviour of the iron ions in pipelines sediments, water supply using different materials.

The studied site was located in capital of Lithuania, Vilnius and the experiment was laboratory scaled and carried out at the small size pipelines model consist of different materials (steel and plastic). The experimental pipelines system was made from different material pipes, it included: new galvanized steel pipe, heavily corroded steel pipe and polyethylene (PE) pipe. In certain experimental pipeline system was maintained permanent water circulation. Water circulation rate was 0.3 m/s and in certain experimental model was also involved imitation of night regime. Water and sediments samples were taken from system right after night regime. Iron concentration was rather high at the site with water from raw groundwater sources. The maximum total iron concentration in corroded steel pipe was 2.10 mg/L and in the plastic (PE) pipe approximately equal to 1.35 mg/L. The highest total iron concentration values 0.79 mg/L for the new steel pipe with anticorrosive layer were found after 24 h of water stagnation in the pipelines, while the total iron concentration values in the other short retention time were in the range 0.06-0.25 mg/L. Water turbidity content (NTU) at the study site was also high.

The maximum measured water turbidity in the corroded steel pipe was 55.35 NTU (range 29.0–55.35 NTU), while in the new steel pipe and plastic pipe it was 28 NTU (range 0.1–28.00 NTU). Samples from old steel pipe had very high turbidity values for the 12 and 29 h water retention time (48.38 and 55.35 NTU, respectively).

The total iron concentration and water retention time values were not correlated to the uptake of residual metal in either old or new metallic pipes, but all concentrations in plastic pipes were correlated to water retention time. Stable iron uptake was not correlated with total manganese uptake, suggesting that the uptake mechanisms of these two metal ions by biofilm may differ. No correlation between manganese and total iron in pipelines has been found in studies carried out elsewhere. The preference for pipelines metal depends on the nutritional status of the microorganism, which at least partly explains the differences reported between field experiments [2] and laboratory experiments [1, 3] with a good nutrient supply.

The results provide some new insights into the use of transfer factors or concentration ratios. The transfer of iron from pipelines biofilm to the water supply raised some particular questions about possible transfer mechanisms. The concentrations of the three nitrogen compounds elements NO_3^-, NO_2^- and NH_4^+ and the iron concentration of the supplied water were determined in various components of water retention time– plastic (PE), new steel with anticorrosive layer and corroded old pipes. The biofilm– water interface fraction was found to be distinctly enriched with manganese and iron compared with bulk phase. Iron concentration increased in the order: bulk phase–water stagnation phase, while concentration increased in the order: bulk phase–tap water. Iron was more or less evenly distributed within bulk phase, biofilm and water-biofilm interface fractions, indicating no iron enrichment of those pipes compartments. The uptake of iron, nitrites, nitrates and ammonium during the entire transfer process between biofilm and water found to occur against a concentration gradient. For two nitrogen compounds studied, the levels of nitrates and ammonium were at least one order of magnitude higher in water phase compared with attached biofilm. Iron uptake seemed to be regulated by microorganism's nutritional demands for this element.

[1] Valentukevičienė, M. Applying backwash water in order to enhance removal of iron and ammonia from spent filters with fresh filter media. Environment protection engineering. Vol. 35, no. 3 (2009), p. 135-144.

[2] Valentukevičienė, M; Rimeika, M. Development of a fluidised batch process using natural powdered zeolite (Clinoptilolite). Polish journal of environmental studies. Vol. 16, no. 2 (2007), p. 283-288.

[3] Amosenkienė, A.; Valentukevičienė, M.; Dauknys, Quality changes of drinking water in the water supply network (case study from Lithuania). Annals of Warsaw University of Life Sciences - SGGW. Land reclamation. 2009, No 41 (2), p. 109-118.

INFLUENCE OF PROLONGED EXTERNAL ELECTRIC FIELD STIMULATION OF C6 CELLS ON RESTING PLASMA MEMBRANE POTENTIAL AND MITOCHONDRIAL MEMBRANE POTENTIAL

Yuliya Kunitskaya, Elena Golubeva, Tatiana Kochetkova, Elizaveta Kavalenka, Pavel Bulai

Department of Biophysics, Belarusian State University
yuliya.kunitskaya@gmail.com

Mitochondria play an important role in many cellular processes including calcium signaling, proliferation, apoptosis, etc. Apoptosis is accompanied by the decrease of the mitochondrial membrane potential [1]. Regulation of the mitochondrial membrane potential by physical methods, such as prolonged influence of the external electric fields, can provide effective technique for controlling and operating cells proliferation rate and cell death. The purpose of the present study is to establish external field parameters leading to the regulation of mitochondria membrane and resting plasma membrane potentials and to reveal the interrelationship between mitochondrial and plasma membrane potentials changes, caused by cells exposure to the external electric field.

Uniform alternating electric field was used to carry out electrical stimulation of C6 rat glioma cells. The resting transmembrane potential value was measured using patch-clamp technique. The mitochondrial membrane potential determination was performed using a fluorescent dye JC-1. Two protocols of cells stimulation by the external electric field were developed [2]. Due to the first protocol cells stimulation by the external electric field was launched in 8 hours after cells passaging, due to the second protocol the time-gap between cells passaging and the stimulation itself was 24 hours. Stimulation of cells by the external electric field lasted for 12 hours and the values of mitochondrial membrane potential and resting transmembrane potential of cells were determined 4 hours after the end of stimulation process [2].

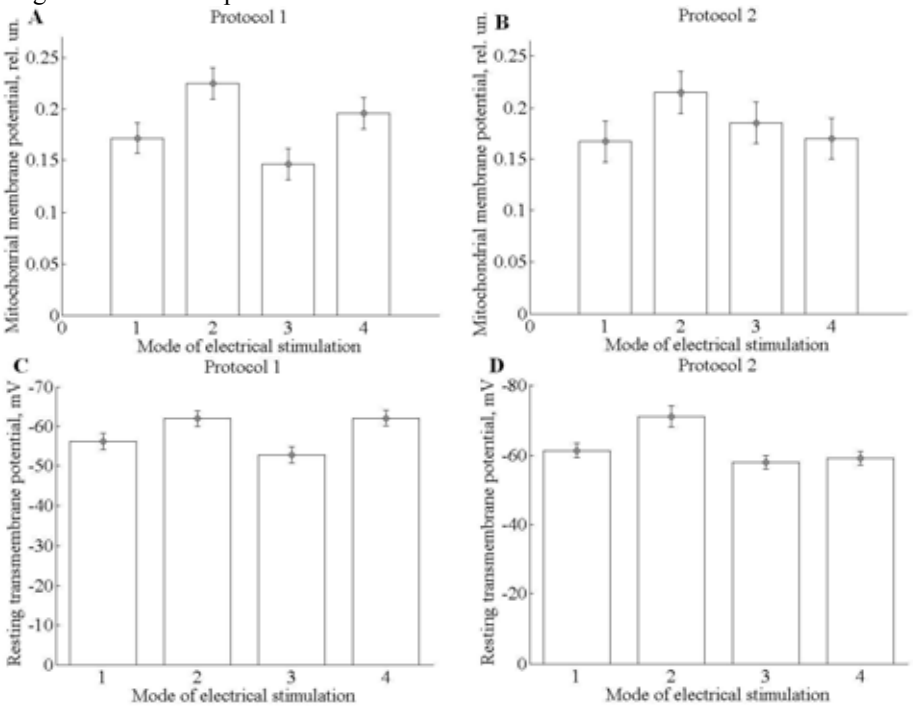

Fig. Modification of mitochondrial membrane (A, B) and resting transmembrane (C, D) potentials in C6 rat glioma cells exposed to external electric field in accordance with protocol 1 (A, C) and protocol 2 (B, D)

It was found, that plasma membrane hyperpolarization occurs in cells exposed to the external electric field with amplitude 20 V / m (1 pulse in stack). Plasma membrane depolarization is observed after cells stimulation by the field with the same set of parameters, but with 3 stimulating pulses in stack. Plasma membrane depolarization (hyperpolarization) is accompanied by the decrease (increase) of the mitochondrial potential (Fig.). The correlation between the mitochondrial potential and the resting transmembrane potential enables to assume the possibility of mitochondrial activity regulation through the external electric field-induced transmembrane potential modification.

[1] E Gottlieb et al., Mitochondrial membrane potential regulates matrix configuration and cytochrome c release during apoptosis, Cell Death andDifferentiation10, 709-717 (2003).

[2] Y.N. Kunitskaya, E.N. Golubeva, P.M. Bulai, Infkuence of chronic electrical stimulation on the resting transmembrane potential value of C6 cells, «MSEP» (2014)

SUPEROXIDE DISMUTASES ACTIVITY IN MICE BRAIN UNDER SELENIUM AND/OR ALIUMINIUM IONS TREATMENT

I. Sadauskienė[1,2], I. Stanevičienė[1,2], K. Adomaitytė[3], A. Liekis[1], R. Naginienė[1], V. Šimakauskienė[1], D. Baranauskienė[1,2]

[1]Neuroscience Institute, Lithuanian University of Health Sciences
[2]Department of Biochemistry, Medical Academy, Lithuanian University of Health Sciences
[3]Department of Neurobiology and Biophysics, Faculty of Natural Sciences, Vilnius University
ilona.sadauskiene@lsmuni.lt

Within a cell superoxide dismutases (SOD) are the first line of defence against reactive oxygen species. The present study was conducted to investigate the influence of Se and/or Al ions on the SOD activity in brain as well as distribution of these elements in the blood and the brain of laboratory mice.

Experiments were done on 4-6 weeks old outbreed mice. SOD activity was determined in brain after 24 h and 14 d. Al and/or Se solution i.p. injections. SOD activity was determined spectrofotometrically. The concentration of protein was measured by the Warburg-Christian method. Se and Al concentrations were determined by inductively coupled plasma mass spectrometer.

It was evaluated the effect of Al on SOD activity in mouse brain after a single i.p. Al injection. The results showed that SOD activity was the same value in control and experimental groups. After a single Se dose injection SOD activity decreased by 28.6% (compared to the control group). Subsequently, were evaluated changes in SOD activity following a single Se+Al mixture injection. It was observed a significant decrease in SOD activity (17.8%).

In further experiments, there was evaluated the effects of Al and/or Se on SOD activity after 14 d. i.p. injections. The results showed that injections of these elements alone did not cause changes of SOD activity. The data of the effect of both elements showed that SOD activity decreased by 41.5% (compared to the control group).

Estimation of the element distribution in brain homogenates showed that after 24 h and 14 d. concentrations did not differ from controls. While in blood: after 24 h exposure levels of Se increased in Se and Se+Al group (22% and 41% respectively) and after 14 d. increased Se and Al concentrations. It is also established in Se+Al group, but Al concentrations are significantly lower.

Our studies revealed that the Se and Al total effect in the mice brain reduce the enzymatic SOD activity after 24 h and 14 d. repeated exposure.

THE INFLUENCE OF CARBON NANOTUBES ON REDOX PROCESSES IN MODEL SYSTEMS AND NEUTROPHILS

Yuliya Leonik[1], Tatsiana Kulahava[1],Elena Golubeva[1], Mikhail Shuba[2], Alesya Paddubskaya[3]

[1] Department of Biophysics, Belarusian State University, Belarus
[2] Research Institute for Nuclear Problems, Belarusian State University,Belarus
[3]Center for Physical Sciences and Technology, Lithuania
yulyaleonik@mail.ru

Carbon nanotubes (CNTs), due to their unique physical and chemical properties, are considered as perspective nanomaterials for various medical and biophysical applications [1]. CNT is a rolled graphene layer without seams. Depending on the layers number CNTs can be divided into the following groups: single-walled (SWCNTs) and multi-walled (MWCNTs) carbon nanotubes [2]. In order to manipulate the physical properties and biological functions of CNTs for their further applications, CNTs could be modified with different functional groups [3].

In the present study the comparison of interaction of SWCNTs and MWCNTs, functionalized by DNA and oligonucleotides (ON) in final concentrations of 50 and 100 ng/mL, with free-radical products in model systems was made. The following model systems were used: myeloperoxidase (MPO) – luminol – hydrogen peroxide (H_2O_2), luminol – H_2O_2, luminol – NaOCl, horseradish peroxidase (HRP) – luminol – H_2O_2. Oxygen-activating capacity of neutrophils under the influence of CNTs was studied. The research was carried out using luminol-enhanced chemiluminescence (CL).

Table – The integral intensity of luminol-enhanced chemiluminescence in model systems

		The integral intensity of luminol-enhanced CL, % relatively to a basic control			
		MPO-H_2O_2	H_2O_2	NaOCl	HRP - H_2O_2
	Basic control	100±10	100±9	100±12	100±10
SWCNTs –COOH	CNTs in water	45 ± 9	98 ± 5	96 ± 3	89 ± 4
MWCNTs –COOH	CNTs in water	74±7	69± 9	52± 11	56± 5
MWCNTs+DNA	Control + DNA	154± 11	122 ±5	14 ±3	106 ± 4
	CNTs+DNA (system)	246 ± 5 (160±7)#	334 ±9 (274±3)#	20±9 (142±8)#	14 ± 11 (13±9)#
SWCNTs +OH	Control+OH	6 ±5	295± 7	165± 9	58 ± 8
	CNTs+OH (system)	30 ± 8	231±7	127± 8	8±9

– % relatively to a sample control

It was revealed, that SWCNTs with COOH-functionalization do not interact with H_2O_2 and NaOCl. However, in presence of MWCNTs-COOH in model systems decrease of the integral intensity of luminol-enhanced CL (IICL) is observed, showing evidence, that MWCNTs-COOH either interact with reactive oxygen species (ROS), or act as CL-quenchers. Decrease of IICL is detected in model systems with enzymes MPO and HRP in the presence of SWCNTs -COOH, SWCNTs-OH and MWCNTs-COOH. Increase of the integral intensity of luminol-enhanced CL during interaction of MWCNTs-DNA with H_2O_2 and MPO is revealed.

60 % and 25 % decrease in oxygen-activating capacity of phagocytes, stimulated by adhesion to glass and chemotaxic peptide N-formyl-methionyl-leucyl-phenylalanine (fMLP) respectively, during cells interaction with SWCNTs-ON was established. This effect is probably caused ON-induced decrease of ROS generation catalised by MPO. MWCNTs-DNA and MWCNTs-COOH had no influence on the integral intensity of luminol-enhanced chemiluminescence of neutrophils. Thus, CNTs with different kinds of functionalization regulate neutrophils redox state.

[1] E. Golubeva et. al., Carbon nanotubes visualization in living cells by means of confocal Raman,Book of Abstracts “Fundamental and Applied Electromagnetics FANEM 2015”, NATO Advanced Research Workshop, Belarusian State University, Minsk, Belarus, 25-27 May, 2015, 76-77.
[2] Abdelbary M. A. Elhissi, W. Ahmed et al., Carbon Nanotubes in Cancer Therapy and Drug Delivery, Journal of Drug Delivery, Vol. 2012, Article ID 837327, 10 pages.
[3] S. Alidori, K. Asqiriba et al., Deploying RNA and DNA with Functionalized Carbon Nanotubes,Phys Chem C Nanomater Interfaces. 2013 Marc 21; 117(11): 5982–5992
[4] G. P. Kotchey, Yong Zhao et al., Peroxidase-mediated Biodegradation of Carbon Nanotubes in vitro and in vivo, *Adv Drug Deliv Rev*. 2013 December, 65(15).

CASCADE COMPLEX RECONSTITUTION *IN VITRO* AND R-LOOP FORMATION BY SINGLE MOLECULE EXPERIMENTS

Inga Songailiene[1], Tomas Sinkunas[1], Marius Rutkauskas[2], Ralf Seidel[2] and Virginijus Siksnys[1]

[1] Department of Protein-DNA Interactions, Vilnius University, Lithuania
[2]Institute of Experimental Physics, University of Leipzig, Germany
inga.songailiene@bti.vu.lt

Clustered, regularly interspaced, short palindromic repeats (CRISPR) with associated Cas genes comprise an adaptive immunity system in bacteria and archaea. In CRISPR systems foreign nucleic acids are targeted in RNA-dependent sequence specific manner. The immunity is acquired by integrating short (21-72 nucleotides (nt)) spacers from foreign nucleic acids in CRISPR region. After the transcription through CRISPR array, the pre-crRNA precursor is formed which undergoes further maturation to the 61 nt crRNA. Cas proteins form an effector complex with matured crRNA which serves as a guide and ensures the target interference [reviewed recently by 1-3]. In Type I CRISPR-Cas systems, invading DNA is detected by a large ribonucleoprotein surveillance complex called Cascade [4]. Guided by crRNA Cascade ribonucleoprotein complex binds to DNA target, if PAM (protospacer adjacent motif) sequence is present, and forms a structure, called R-loop. R-loop is a three-stranded nucleic acid structure that is composed of a RNA:DNA hybrid, leaving the non-target single-stranded DNA. Once stable R-loop is generated, the DNA target degradation is performed by Cas3 nuclease-helicase [5]. While R-loops can play roles in genome instability, recent data has revealed that R-loops can also have positive impact on epigenetic or genetic regulation processes in both prokaryotic and eukaryotic cells. The length of R-loops range widely from 20 bp to 2 kbp [6].

According to the crystal structure of I-E type Cascade complex from *E.coli*, the core of the complex is composed of Cas7 proteins that oligomerize along the crRNA. Structure of the DNA:RNA duplex is underwound and forms kinks that occur in every sixth base pair of the target hybrid (mimicking broken ladder) [7]. Conserved sequences on 3'- and 5'-ends of crRNA are anchored by Cas6e and Cas5e proteins accordingly [7],[8],[9].

Here we aim to investigate *Streptococcus thermophilus* Cascade complex target recognition and R-loop formation by biochemical and biophysical approach. We have shown that Cascade target recognition is unidirectional process starting from PAM sequence. As a full-length R-loop is formed, Cascade becomes "locked" and afterwards triggers DNA target degradation by nuclease-helicase Cas3 [10].

Further, we reconstituted a functional Cascade complex *in vitro* from separate proteins, namely Cse1, Cse2, Cas5, Cas6 and Cas7 and *in vitro* transcribed crRNA. *In vitro* reconstituted Cascade performed the target DNA recognition and triggered DNA cleavage in the same manner as *in vivo* expressed complex. R-loop formation was monitored on single molecule DNA supercoiling setup.

[1] AV. Wright, JK. Nuñez, JA. Doudna. Biology and Applications of CRISPR Systems: Harnessing Nature's Toolbox for Genome Engineering. Cell. 2016 Jan 14;164(1-2):29-44.
[2] LA. Marraffini. CRISPR-Cas immunity in prokaryotes. Nature. 2015 Oct 1;526(7571):55-61.
[3] KS. Makarova *et al*., An updated evolutionary classification of CRISPR-Cas systems. Nat Rev Microbiol. 2015 Nov;13(11):722-36.
[4] JS. Brouns *et al.,* Small CRISPR RNAs guide antiviral defense in prokaryotes. Science. 2008 Aug 15;321(5891):960-4.
[5] T. Sinkunas , G. Gasiunas, C. Fremaux, R. Barrangou, P. Horvath, V Siksnys, Cas3 is a single-stranded DNA nuclease and ATP-dependent helicase in the CRISPR/Cas immune system. EMBO J. 2011 Apr 6;30(7):1335-42.
[6] A. Aguilera, T. García-Muse, R loops: from transcription byproducts to threats to genome stability. Mol Cell. 2012 Apr 27;46(2):115-24.
[7] H. Zhao *et al*., Crystal structure of the RNA-guided immune surveillance Cascade complex in Escherichia coli. Nature. 2014 Nov 6;515(7525):147-50.
[8] S. Mulepati, A. Héroux, S. Bailey, Structural biology. Crystal structure of a CRISPR RNA-guided surveillance complex bound to a ssDNA target. Science. 2014 Sep 19;345(6203):1479-84.
[9] RN. Jackson *et al.*, Structural biology. Crystal structure of the CRISPR RNA-guided surveillance complex from Escherichia coli. Science. 2014 Sep 19;345(6203):1473-9.
[10] M. Rutkauskas, T. Sinkunas, I. Songailiene, MS. Tikhomirova, V. Siksnys, R. Seidel, Directional R-Loop Formation by the CRISPR-Cas Surveillance Complex Cascade Provides Efficient Off-Target Site Rejection. Cell Rep. 2015 Mar 3. pii: S2211-1247(15)00135-7.

DNA METHYLATION ANALYSIS OF ANGIOGENESIS-RELATED GENES *ADAMTS12* AND *FILIP1L* IN PROSTATE CANCER

Agnieška Mackoit[1], Kristina Daniūnaitė[2] and Sonata Jarmalaitė[2]

[1] Faculty of Medicine, Vilnius University, Lithuania
[2]Human Genome Research Centre, Faculty of Natural Sciences, Vilnius University, Lithuania
agnieska.mackoit@mf.stud.vu.lt

Currently, hypoxia-induced angiogenesis is a popular subject in cancer biology research, nevertheless, the molecular mechanisms and regulation of vascularization are still poorly understood. Several recent studies have suggested an association between hypermethylation of angiogenesis-related genes *ADAMTS12* and *FILIP1L* and development of various types of cancer including prostate cancer (PCa) [1].

PCa is an oncological disease, which affects around 3000 men in Lithuania each year [2]. As with other solid tumors, the growth rate and progression of PCa is critically dependent on tumor angiogenesis. The development of novel diagnostic biomarkers' system could enable effective detection of early stages of prostate carcinogenesis and help to choose the most effective treatment.

The main purpose of our study was to analyze promoter methylation of the *ADAMTS12* and *FILIP1L* genes in cancerous and non-cancerous prostate tissues (NPT) in order to identify potential epigenetic markers for PCa detection.

Global DNA methylation profiling by means of microarrays (Agilent Technologies) allowed the identification of angiogenesis-associated genes *ADAMTS12* and *FILIP1L*, which were characterized by aberrant DNA methylation changes in tumors as compared to NPT. Promoter methylation status of selected genes was validated in 130 PCa and 35 NPT by methylation-specific PCR (MSP). Benign prostate hyperplasia (BPH) samples (N = 17) were used as an additional control group.

ADAMTS12 and *FILIP1L* promoter methylation was detected in 109 of 130 (84%) PCa samples for each gene. In NPT, methylation frequencies of *ADAMTS12* and *FILIP1L* were 2 of 35 (6%) and 4 of 35 (11%), respectively. These results showed significant differences of the methylation frequency in PCa versus NPT ($P < 0.001$) or BPH ($P < 0.001$) cases (Fig. 1). According to clinical-pathological parameters of PCa cases, only methylation of *ADAMTS12* gene promoter was significantly associated with biochemical disease recurrence ($P = 0.041$) or higher tumor (pT) stage ($P = 0.045$) and was close to significant ($P = 0.057$), in Gleason score 7 versus 6 cases. No statistically significant correlations were observed between *ADAMTS12* or *FILIP1L* methylation status and prostate-specific antigen (PSA) level, tumor volume, prostate mass, or patients' age.

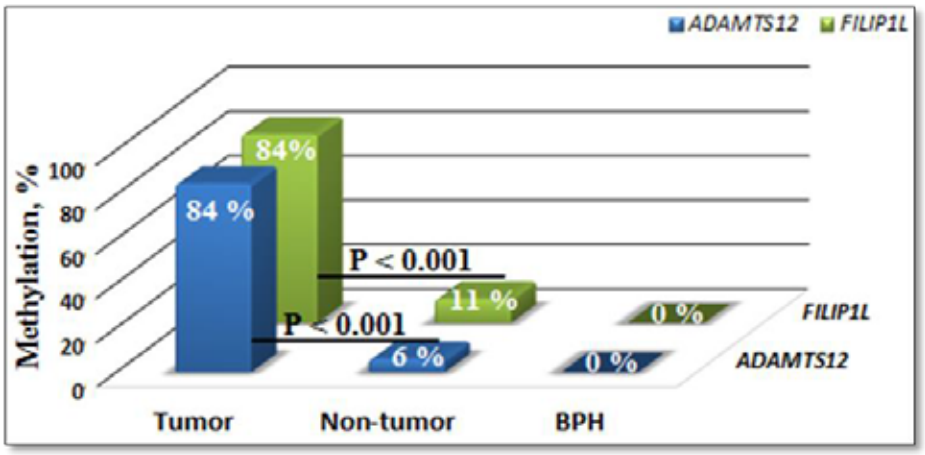

Fig. 1. Aberrant methylation frequencies of *ADAMTS12* and *FILIP1L* genes in prostate tumors (PCa), non-cancerous prostate tissues (NPT), and benign prostatic hyperplasia (BPH) samples.

Our study revealed a significant difference in methylation frequencies of the *ADAMTS12* and *FILIP1L* genes between prostate tumor and non-tumor tissues. Further quantitative research of genes' expression is required to evaluate reliability of these genes as potential biomarkers that are able to accurately distinguish indolent and aggressive PCa tumors.

[1] Desotelle J., Truong M., Ewald J., Weeratunga P., Yang B., Huang W., Jarrard D. *CpG island hypermethylation frequently silences FILIP1L isoform 2 expression in prostate cancer.* J Urol. 2013; 189 (1):329-35.
[2] Ulys A., Vėželis A., Ivanauskas A., Snicorius M. *Treatment methods of prostate cancer recurrence after radiotherapy. Current treatment alternatives and our clinical experience.* Lithuanian Surgery 2013, 12 (3), p. 138–143.

ERCC1 AND *RRM1* GENES AS PREDICTIVE BIOMARKERS IN NON-SMALL CELL LUNG CANCER

Julija Fadejeva[1,2], Dovilė Šiuškaitė[1], Saulius Cicėnas[2], Diana Schveigert[2]

[1] Faculty of Natural Sciences, Vilnius University, Vilnius, Lithuania
[2] National Cancer Institute, Vilnius, Lithuania
siuskaitedovile@gmail.com

INTRODUCTION. Lung cancer is one of the most common oncological diseases and the leading causes of cancer-related deaths worldwide. Platinum-based chemotherapy drugs are used for non-small cell lung cancer (NSCLC) patients' treatment. However, drug resistance in cancer chemotherapy is a major problem that is observed nowadays [1]. Still, there are no reliable molecular biomarkers to predict whether a tumor responds to platinum-based chemotherapy. Potential predictive biomarkers could be *ERCC1* and *RRM1* genes which are involved in nucleotide excision repair system.

AIM. The aim of this study was to identify association between *ERCC1* and *RRM1* gene expression and NSCLC patients' response to treatment.

MATERIALS AND METHODS. The study included 80 NSCLC patients treated at Department of Thoracic Surgery and Oncology, National Cancer Institute (Vilnius, Lithuania). Blood samples of the patients were analyzed before and after treatment. RNA was extracted from whole blood using „QIAamp RNA Blood Mini Kit" (*QIAGEN*, Germany). The analysis of *ERCC1* and *RRM1* expression was done by qRT-PCR method. Each sample was examined in triplicate. Changes in *ERCC1* and *RRM1* expression were calculated using $2^{-\Delta\Delta CT}$ method. Patients were separated into those with low and high gene expression. The statistical analysis was done by IBM SPSS 21 (*Armonk, NY: IBM Corp,* JAV, 2012) software. A $\chi 2$ test was used to analyze *ERCC1* and *RRM1* in relation to patients' clinical-pathological parameters and response to treatment. Results were considered as statistically significant when $p \leq 0,05$. The present study was approved by the Lithuanian Bioethics Committee.

RESULTS. Statistically significant differences were found between *ERCC1* expression in patients' blood before treatment and patients' gender. High *ERCC1* expression was identified more often among men (p=0,044). Moreover, there are trends in the association between *ERCC1* expression after treatment, tumor differentiation grade and response to treatment. High *ERCC1* expression is more common for poor differentiation tumors and stable disease (respectively, p=0,066 and p=0,051). Similarly, there are trends in the association between *RRM1* expression in blood and patients' response to treatment. High *RRM1* expression after treatment was identified more often among NSCLC patients with stable disease (p=0,051).

CONCLUSIONS. *ERCC1* and *RRM1* genes may influence platinum-based chemotherapy treatment of NSCLC patients. In order to improve the effectiveness of treatment it is appropriate to identify *ERCC1* expression changes in the blood. Therefore, NSCLC patients with low *RRM1* expression should be actively followed-up because of quicker disease progression. For the prediction of clinical outcome of NSCLC patients additional studies with larger population group should be done in the future.

---

[1] S. Sun, W. Shi, Z. Wu, G. Zhang, B.O. Yang, S. Jiao. Prognostic significance of the mRNA expression of ERCC1, RRM1, TUBB3 and TYMS genes in patients with non-small cell lung cancer, Experimental and Therapeutic Medicine 10 (3), 937-941 (2015).

ACCUMULATION OF QUANTUM DOTS IN RAINBOW TROUT (*Oncorhynchus mykiss*) EMBRYOS

Mantas Stankevičius[1], Živilė Cibulskaitė[1,3], Nijolė Kazlauskienė[3], Ričardas Rotomskis[1,2]

[1]Biomedical Physics Laboratory, National Cancer Institute, Baublio 3b, LT-08406, Vilnius, Lithuania
[2]Biophotonics group of Laser Research center, Vilnius University, Sauletekio ave. 9, LT-10222, Vilnius, Lithuania
[3]Institute of Ecology of Nature Research Centre, Akademijos st.-2, LT-08412 Vilnius, Lithuania
mantas.stankevicius@gf.stud.vu.lt

Nanoparticles (NP) are widely applied in various areas, including food, household chemistry and cosmetics industry. NP have a great perspective in medicine diagnostics and treatment. However, NP are characterized by unique and poorly known nanotoxicity properties [1]. This represents an environmental problem as the quantum dots (QD) may cause toxicity-dependent results, which might be fatal. Regardless of constant increase of NP concentration in environment the danger of contact and possible passage of NP through living organism's protective barriers are not well understood. In general, it is supposed that the chorion protects the embryos from foreign intrusion during development before hatching.

The aim of the present study was to examine of QD passage through a rainbow trout (*Oncorhynchus mykiss*) embryos chorion and accumulation in embryos structures.

The study was carried out on rainbow trout embryos in "eye-egg" stage. Short–term (2-hour) and long–term (120-hour) exposures and accumulation of QD in embryos structures were performed in climatic camera under static conditions. Embryos were imaged using Nikon ECLIPSE TE2000-U confocal scanning laser microscope equipped with RGB detector with 3 band-pass filters. The 500-530 nm band-pass filter was used for autofluorescence detection and 569-640 nm band-pass filter for QD luminescence detection. Also $4x10^{-9}$ *M* and $28x10^{-9}$ *M* solutions of CdSe/ZnS-COOH (QD ITK 625) QD with fluorescence maxima at 625 nm were applied during the study. Visualization, analysis, segmentation and interpretation of 2D and 3D structures were managed using "Imaris" imaging software.

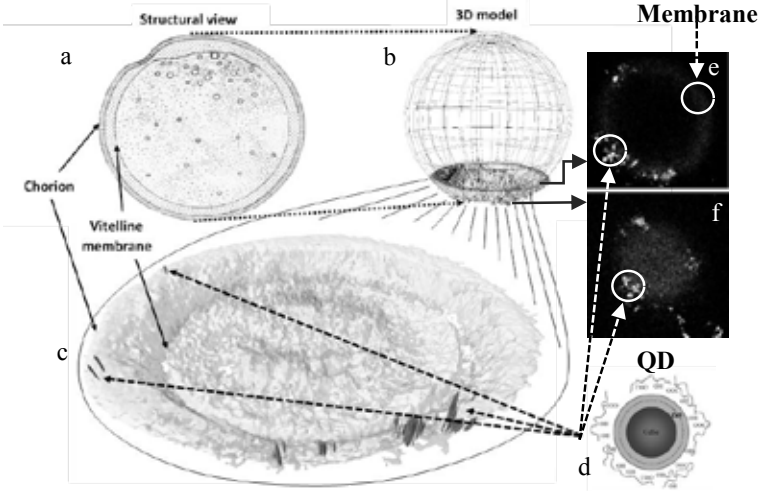

Fig. 1. Structure of rainbow trout embryos and reconstructed 3D view of a small portion of the embryos (b and c): light gray color represents autofluorescence, dark grey color represents fluorescence of QD. Structure of CdSe/ZnS-COOH QD (d). Autofluorescence and fluorescence of QD corresponding to different planes of embryos (e and f): white spots represents fluorescence of QD, grey color represents autofluorescence.

In order to determine accumulation of QD in rainbow trout "eye-egg" stage embryos, incubation of embryos with QD solutions was performed for 2 and 120 hours. To avoid contamination after incubation all embryos were washed using well water. Subsequently, confocal Z-scan imaging of embryos was employed for visualization of embryos at different planes (Fig. 1. e and f). However, we could not see any fluorescence coming from the structures situated deeper than ~ 400 μm. This might occur with regard to weak transparency of embryos. For this reason only a small portion of embryos (~ 350 μm) was imaged (Fig. 1. b and c). Through the filter 569-640 nm red QD fluorescence was detected (Fig. 1. c, e and f). The green autofluorescence was detected through the filter 500-530 nm. Green color represents autofluorescence of embryos membrane as well as integral and internal proteins (Fig. 1. c, e and f). In 2D images several types of QD distributions, corresponding to different planes of embryos can be observed (Fig. 1. e and f). Nevertheless, 2D images (Fig. 1. e and f) are complicated to clearly understand distribution of QD in membrane. Consequently, we use "Imaris" for better understanding of QD distribution in embryos structures. Likewise 2D images "Imaris" 3D reconstruction showed red fluorescence of QD only in those areas where green autofluorescence was detected (Fig. 1. c, e and f). That is to say, QD adhered to the external surface of chorion of embryos and most likely stuck in it. However, QD did not penetrate through it further to the inner structures (vitelline membrane, yolk and embryo) of the embryos (Fig. 1. c, e and f). In this particular case chorion likely restricted QD uptake. Results approve presumption about chorion protective function against NP.

[1] Kahru, A.; Dubourguier, H.C., 2010. From ecotoxicology to nanoecotoxicology. Toxicology, 269, 105–119.

POLYVINYLPYRROLIDONE STABILIZED GOLD NANOPARTICLES: SYNTHESIS AND PHARMACOKINETICS *IN VIVO*

Akvile Slektaite[1], Sonata Adomaviciute[1,2], Ricardas Rotomskis[1,2]

[1] Biomedical Physics Laboratory, National Cancer Institute, Vilnius, Lithuania
[2] Biophotonics group of Laser Research Center, Vilnius University, Vilnius, Lithuania
akvile.slektaite@nvi.lt

Early and accurate detection of cancer might be complicated due to limited efficiency of contrast agents. Gold nanoparticles (AuNP) could be excellent contrast agent for X-ray imaging due to specific properties of gold that overcome some limitations of standard (iodine-based) contrast agents used for imaging *in vivo*. Gold has higher photoelectric effect cross-section of X-rays, significantly lower clearance rate than iodine and are considered to be nontoxic in living systems [1]. Surgical treatment of cancer might be difficult as well because tumour cells and lymph nodes might be obscure in contrast of other tissues even when contrast agents are injected.

In our study, we synthesized polyvinylpyrrolidone (PVP) stabilized gold nanoparticles, assessed their optical properties and compared pharmacokinetics of synthesized AuNP with standard contrast agent *in vivo*. Two methods to purify nanoparticles were used and properties of Au-MES-PVP particles were assessed using TEM microscope images.

Synthesised AuNP were diluted four times and centrifuged for 1 hour with 10 000 G force, after that the supernatant was removed. The other way that we used to separate particles was with the dialysis diaphragm. Purified with both methods, absorption spectrum of AuNP were similar. According to TEM images (Fig. 1) and absorption spectrum of synthesized AuNP (Fig. 2) [2] they are fairly uniform in size with a diameter of about 15 nm.

To determine pharmacokinetics and X-ray imaging contrast *in vivo*, BDF1 hybrid male mice were used. One was injected with a clinically approved contrast agent (Ultravist 300) bolus of 0.1 ml directly into the right leg tissue (control sample). The other with the same bolus of synthesized and purified Au-MES-PVP accordingly. X-ray images were acquired before and after the injection at 0, 5, 10, 15, 30, 45, 60 minutes and 24, 48 hours. Initial distribution of contrast agent in the injected tissue were detected in both cases, but after 10 min Ultravist 300 started accumulating in bladder and after 1 hour almost all contrast agent was concentrated there, after 24 hours no traces of Ultravist 300 was noticed. Different pharmacokinetics were observed with Au-MES-PVP nanoparticles. Significant change of X-ray contrast in leg was not observed 1 hour after the injection. But after 24 hours Au-MES-PVP particles concentrated in the lymph nodes on the right side of a mouse and were still seen even after 48 hours. Afterwards, the autopsy of the mouse showed that the lymph nodes on the right side were black and plain seen in the contrast of other tissues.

Results showed that Au-MES-PVP clearance rate is slower than Ultravist 300. Therefore, repeated injections of contrast agents might not be necessary for imaging. Moreover, Au-MES-PVP nanoparticles accumulate in lymphatic system hence it can be used for distinguishing lymph nodes and tissues. Further investigation in this area will provide a deeper level of understanding the properties and possibilities of PVP stabilized nanoparticles in imaging and, perhaps, removing of tumours.

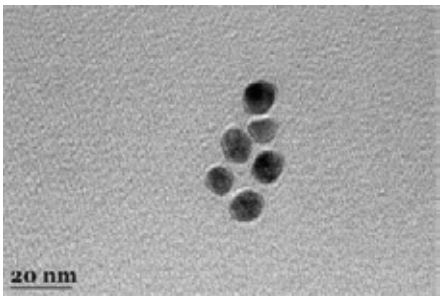

Fig. 1. TEM images of Au-MES-PVP showing spherical nanoparticles about 15 nm in diameter.

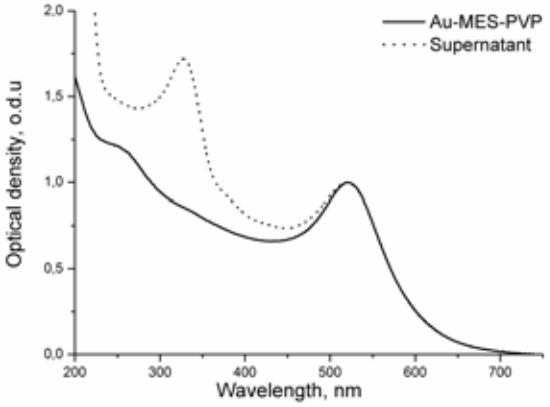

Fig. 2. Normalized absorption spectra of Au-MES-PVP nanoparticles.

[1] J.F Hainfeld, D.N. Slatkin, T.M. Focella, H.M. Smilowitz, *Gold nanoparticles: A new X-ray contrast agent* (Br. J. Radiol. 2006, 79, 248–253)
[2] Wolfgang Haiss, Nguyen T. K. Thanh, Jenny Aveyard, and David G. Fernig, *Determination of Size and Concentration of Gold Nanoparticles from UV-Vis Spectra* (Anal. Chem. 2007, 79, 4215-4221)

OPTICAL PROPERTIES OF $NaGdF_4$:Yb,Er@$NaGdF_4$ UPCONVERTING NANOPARTICLES AND THEIR APPLICATION IN CANCER DIAGNOSTICS

Laurynas Karpus[1], Dovilė Baziulytė[2], Simas Šakirzanovas[2], Vitalijus Karabanovas[1,4], Ričardas Rotomskis[1,3]

[1] Biomedical Physics Laboratory, National Cancer Institute, Lithuania
[2]Department of Applied Chemistry, Faculty of Chemistry, Vilnius University, Lithuania
[3] Biophotonics Laboratory, Laser Research Centre, Vilnius University, Lithuania
[4]Department of Chemistry and Bioengineering, Vilnius Gediminas Technical University, Lithuania
Laurynas.karpus@gmail.com

Upconversion photoluminescence (PL) refers to non-linear optical processes facilitated by multi-absorption of two or more pump photons to convert lower energy photons into higher energy ones. Upconverting nanoparticles (UCNPs) are a promising new generation of imaging agents capable of working as theranostic agents [1]. Compared to traditional photoluminescence agents they offer many advantages, for instance working in optical transparency window (~650-1350nm), deeper light penetration, reduced photodamage of biological tissues due to NIR excitation, narrow bandwidths for multiplexed imaging, possibility to add second imaging source such as MRI. However, current multimodal UCNPs are still not widely used in medical environment because of their low photoluminescence intensity and poor contrast in MRI. In our study we have designed and synthesized hexagonal phase $NaGdF_4$:Yb/Er@$NaGdF_4$ core-shell structure nanoparticles with PL, MRI and drug carrying capabilities. X-ray diffraction, Scanning Electron Microscopy, PL spectroscopy were used to characterize UCNPs. Nanoparticles were phase transferred to water after ligand-exchange with TWEEN 80 in order to make them hydrophilic. Upon 980nm excitation nanoparticles exhibit sharp emission peaks which can be attributed to $^2H_{9/2} \rightarrow {}^4I_{15/2}$, $^2H_{11/2} \rightarrow {}^4I_{15/2}$, $^4S_{3/2} \rightarrow {}^4I_{15/2}$, $^4F_{9/2} \rightarrow {}^4I_{15/2}$ transitions of Er^{3+} ions. These peaks correspond to respective blue (408nm), green (521nm, 540nm) and red emissions (658nm). It was shown that PL intensity increased about 32 times by growing an optically inert $NaGdF_4$ layer around $NaGdF_4$:Yb/Er nanoparticles (Figure 1). To estimate how many photons participated in each energy transition UCNPs intensities were measured as a function of the laser pump power. For the upconversion process, the number of photons required to populate the upper emitting level is described by the relation $I_{UCNP} \sim I^n_{NIR}$ where I_{UCNP} is the fluorescence intensity, I_{NIR} is the pump laser intensity and n is the number of pump photons required. Slopes (n) of the main peaks at 408, 521, 540 and 658nm were 2.6, 1.99, 1.96, 1.87 respectively, suggesting three-photon process at 408nm, and two-photon processes for the remaining wavelengths (Figure 2). Additionally, colloidal stability of UCNPs in different biological media (DMEM, various pH) were investigated. No significant decrease in emission intensity was observed during one month. We have also obtained that $NaGdF_4$:Yb/Er@$NaGdF_4$ UCNPs are photostable and do not degrade even when exposed to high doses of irradiation.

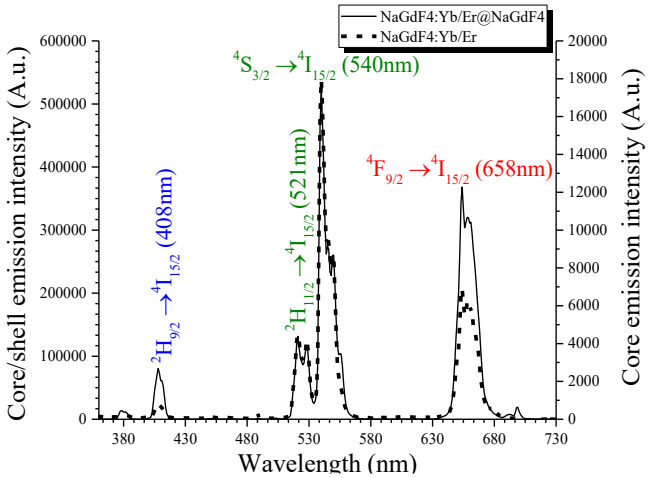

Fig. 1. Emission spectra of $NaGdF_4$:Yb/Er@$NaGdF_4$ compared to $NaGdF_4$:Yb/Er with indicated energy transitions.

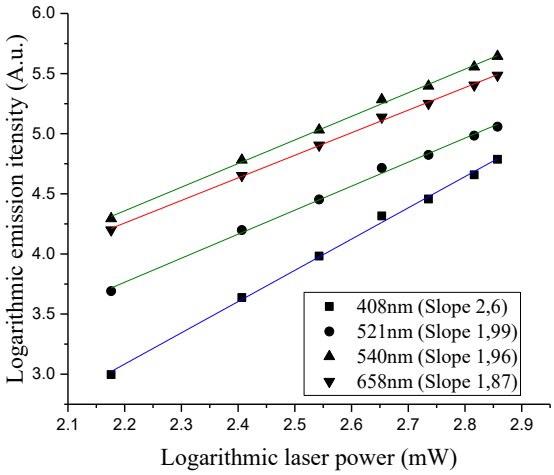

Fig. 2. Log-log plots of $NaGdF_4$:Yb/Er@$NaGdF_4$ emission intensity as a function of 980nm laser excitation power.

Lastly, cell viability assay XTT was performed to measure cellular metabolic activity (with Mda-mb-231, Mcf-7 cancer cell lines) after 24 hours treatment with different concentration of UCNPs. A toxic effect of UCNPs was observed at a concentration of higher then 33μg/ml. Results of our study have shown that core/shell $NaGdF_4$:Yb/Er@$NaGdF_4$ nanoparticles may be effective multimodal theranostic agents in early cancer diagnostics. This work was supported by grant No.MIP-030/2014 from the Research Council of Lithuania.

[1] G. Chen, H. Qiu, P. Prasad, X. Chen, *Upconversion Nanoparticles: Design, Nanochemistry and Applications in Theranostics* (Chemical Reviews 114(10), 5161-5214, 2014).

UPCONVERSION NANOPARTICLES IN MAGNETIC RESONANCE IMAGING

Eglė Daugėlaitė[1,3], Marius Stašys[1,3], Dovilė Baziulytė[2], Ričardas Rotomskis[1,3]

[1] Biomedical Physics Laboratory, National Cancer Institute, Lithuania
[2] Departament of Applied Chemistry, Faculty of Chemistry, Vilnius University, Lithuania
[3]Biophotonics Laboratory, Laser Research Centre, Vilnius University, Lithuania
Egle.daugelaite@ff.stud.vu.lt

Magnetic resonance imaging (MRI) is a widely diagnostic imaging method. MRI provides an excellent spatial resolution, but suffers from poor sensitivity. To improve the latter, MRI contrast agents are used. The most commonly used contrast agents are gadolinium-based. Unfortunately, current contrast agents have several disadvantages such as high toxicity or not sufficient enough contrast [1]. That leads to investigation of the novel MRI contrast agents. Gadolinium (Gd^{3+}) has unique paramagnetic properties, therefore it is preferred in development of a next generation MRI contrast agent. In recent years, rare-earth upconverting nanoparticles (UCNPs), which are composed of $NaGdF_4$:Yb,Er, have received significant attention, as they can be useful for several imaging modalities namely MRI (due to the presence of the Gd^{3+} ion in the host matrix) and optical imaging (due to Yb^{3+}, Er^{3+} co-doped $NaGdF_4$) [2]. The aim of this study is to evaluate the possibility to use in clinic $NaGdF_4$: Yb,Er nanoparticles as an efficient MRI contrast agents.

Magnetical properties of TWEEN 80 modified core $NaGdF_4$: Yb,Er and core-shell $NaGdF_4$:Yb,Er@$NaGdF_4$ upconverting nanoparticles were obtained on a 1.5 T Philips Achieva MRI scanner using Sense Flex-M coil. As shown in Fig.1, core and core-shell UCNPs gives a significant positive contrast in the T1-weighted MR images. Significant differences in MR signal enhancement between different types of UCNPs were not observed. Also we investigated MR signal intensity (SI) versus Gd^{3+} concentration in core-shell UCNPs solution and compared to the clinical contrast agent Magnevist® and Gd^{3+} salt. Results are shown in Fig.2. In all of the cases, the enhancement in MR signal with the increase of the concentration was obtained until concentration reaches a critical value and the signal begins to decrease. Therefore, it is very important to choose the optimal injection dose in order to obtain the maximum contrast and to avoid signal decreasing effect.

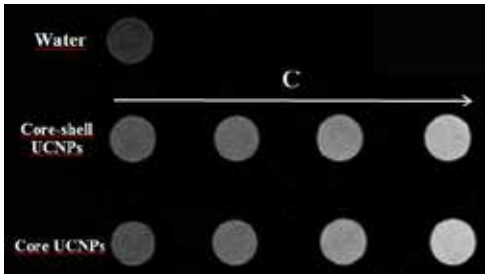

Fig.1. T1W MR in vitro images of core and core-shell UCNPs aqueous solutions.

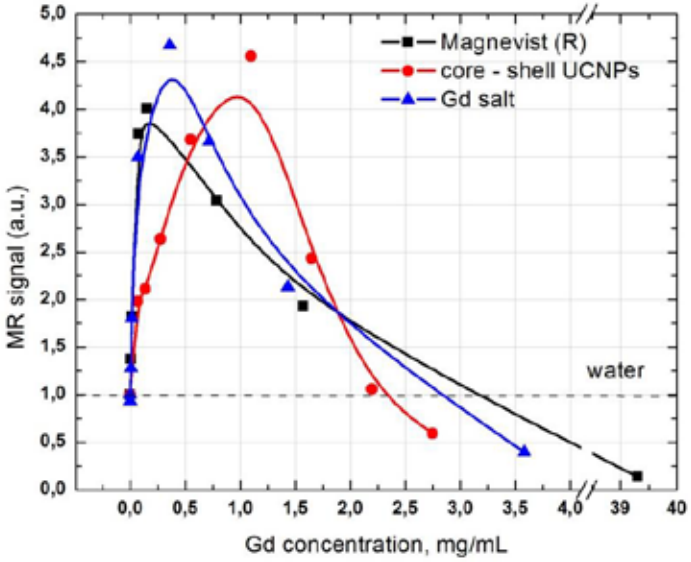

Fig.2. MR signal intensity plot of core-shell UCNPs, Magnevist® and Gd^{3+} salt of different concentration aqueous solutions vs. concentration.

These observations indicate that $NaGdF_4$:Yb,Er upconverting nanoparticles could be applied as an efficient MRI contrast agent. Further investigation is required.

[1] H.Ersoy and F. J. Rybicki, Biochemical Safety Profiles of Gadolinium-Based Extracellular Contrast Agents and Nephrogenic Systemic Fibrosis, J Magn Reson Imaging 26(5) 1190–1197 (2007)
[2] H.Dong, Sh.R.Du et al.,Lanthanide Nanoparticles: From Design toward Bioimaging and Therapy, Chem. Rev., 115, 10725−10815 (2015)

CARROTS EXTRACT FOR SILVER NANOPARTICLES SYNTHESIS BY PHOTOREDUCTION METHOD

Matas Damonskis[1], Judita Puišo[1], Paulius Danilovas[2]

[1]Kaunas University of Technology, Department of Physics, Studentų g. 50, LT-51368 Kaunas, Lithuania
[2]Kaunas University of Technology, Department of Polymer Chemistry and Technology, Radvilėnų pl. 19, LT-50299 Kaunas, Lithuania
matas.damonskis@ktu.edu

Carrots is the one of the most popular root vegetable. Carrots are the natural source of phytonutrients, antioxidants, vitamins with anti-cancer anti-aging, diuretic, free radical-trapping, single oxygen quenching, anti-mutagenic, chemo-preventive, photo-protective and immune-enhancing properties. Carrots contains not only nutrition antioxidants such as vitamins A, C and E, but also non-nutritional antioxidants, such as carotenoids, polyacetylenes, flavonoids, flavones and phenolic compounds. The taste of carrots is influenced on the presence of glutamic acid and buffering action of the free amino acids. Free sugars such as sucrose, glucose, xylose and fructose are accounted in carrots. The total content of sugars varied from 2.71 to 4.53 % in the fresh carrots. The average nitrate and nitrite content in the fresh carrots 40 mg/100 g and 0.41 mg in 100 g. Carrots gets its characteristic bright orange color from the carotenoids. The total carotenoids content of carrot roots range from 6,000 to 54,800 μg/100g [1-2].

Carrots have lost vitamins and carotenoids after storing and processing. Dehydration of carrot is alternative of preservation throughout the year with the minimum loss of carotenoids. Application of dehydrated carrots for green synthesis extract allows enhancing and expanded abilities of natural dyers and biomarkers [3].

This study presents green synthesis of silver nanoparticles using dehydrated carrot extract. The dehydrated carrots extract was used as bio-reductant and bio-capping agent for the synthesis of silver nanoparticles.

Silver nitrate used for the synthesis of silver nanoparticles was procured from Sigma Aldrich, Poland (CAS No 7761-88-8). Dehydrated carrots, produced in Holland were purchased from the local supermarket as spices. 20 g of dehydrated carrots were added to 120 g~ deep UV irradiation solutions (<320 nm) were stored the transparent 20 ml glass bottle.

The reduction of Ag^+ ions to Ag^0 was monitored by measuring the UV-Vis spectrum by sampling of aliquots of (1.5 ml) of Ag nanoparticle solution diluting the sample in 1.5 ml distilled water. UV-VIS absorbance spectra were measured by Ocean Optics USB4000 at the range of 200-800 nm. The active acidity of the juices (control solutions) and the solutions with formed silver nanoparticles was measured by a pH meter "HI 98103Checker® pH Tester" (*Hanna instruments*, USA). pH Analysis: 1 mM aqueous silver nitrate ($AgNO_3$) solution shows 3.8 pH, there is concerned change in pH was determined of silver nanoparticle synthesis using extracts of plant. The size of particles of silver and carrot's extract nanocomposites was investigated by photon correlation spectrometer DelsaNano C (Beckman Coulter) (Dual 30 mW laser, partical size: 0.6 nm to 7 μm). The size and size distribution of colloids of silver nanoparticles were studied using dynamic light scattering (DLS).

Colour of prepared silver nanoparticles solution was reddish brown. The surface plasmon resonance (SPR) peak of colloidal silver nanoparticles position was observed at 412 nm, respectively. According DSL results silver-carrot's nanocomposite particles size varied from 143.7 nm to 765.4 nm. The pH of silver colloidal solution was lightly acid (5.85 - 6.23). The total amount of soluble sugars was less than 3 ºBrix.

Synthesis of silver nanoparticles using carrot's extract through efficiency green chemistry methodology, avoiding the presence of hazardous and toxic solvents and waste. The action of biomolecules as reducing agents was monitored.

[1] http://www.fineli.fi/food.php?foodid=302&lang=en
[2] KD Sharma ,S Karki, NS Thakur, S. Attri, Chemical composition, functional properties and processing of carrot-a review, J Food Sci Technol. 2012 Feb;49(1):22-32 (http://link.springer.com/article/10.1007%2Fs13197-011-0310-7)
[3] M. Umadevi, S.Shalini; M.R. Bindhu, Synthesis of silver nanoparticle using D. carota extract, Adv. Nat. Sci.: Nanosci. Nanotechnol. 3 (2012) 025008 (6pp)

LUMINESCENCE PROPERTIES OF CdS QUANTUM DOTS NEAR Ag NANOPARTICLES

Anna Matsukovich[1], Elena Shabunya-Klyachkovskaya[1], Mikhail Smirnov[2], Alexey Perepelitsa[2]

[1] B.I. Stepanov Institute of Physics, National Academy of Sciences of Belarus, Belarus
[2] Voronezh State University, Russia
a_matsukovich@tut.by

Semiconductor nanocrystals have attracted impressive attention because of their novel optical and electronic properties. Direct and wide bandgap semiconductor nanomaterials are potential candidates for applications in nonlinear optics and optoelectronics [1]. Quantum dots of CdS with the Ag nanoparticles can be used for senesitive detection cancer cells and wound healing in addition to enhancing the tumor-killing effects of anticancer drugs [2].

This work shows the studying of luminescence properties of 2 types of CdS quantum dots (QDs) in the presents of Ag nanoparticles. The sample #1 was a water solution of QDs in thioglycolic acid (TGA). The sample #2 was a solution of QDs, heated at the temperature 95°C and washed through a cellophane membrane. Optical density spectrum of QDs solution has absorption in the ultraviolet range 350-450 nm.

The water solutions of QDs have been deposited on the glass and silver gel-film substrates and dried at the room temperature in the horizontal position. Silver sol was prepared by reduction of silver nitrate with sodium citrate as described in [3]. Polydispersed silver sol formed, average particle size is about 50 nm. Optical density spectrum of silver film has the broad peak of plasmon resonance at 485 nm.

Luminescence spectra were registred with a grating (150 lines/mm) spectrograph S3901 (Solar TII, Belarus) combined with a liquid nitrogen cooled silicon CCD camera (Princeton Instruments, USA). Luminescence excitation was performed a light-emitting diode with the emission spectrum peaking at 404 nm. The luminescence spectra exposure time was 60 s.

The sample #1 on the glass are characterized by the broad bands at 640 and 661 nm. The luminescence spectrum of sample #2 has the broad band at 636 nm. The presence of silver nanoparticles (NPs) led to luminescence quenching in sample #1 (Figure 1a). On the other hand we observed luminescence enhancement for the sample 2 near Ag NPs (Figure 1b).

The decay time of luminescence depends on the probability of radiation and non-radiation transitions. The presence of metallic nanostructures may increase probabilities of both radiative and non-radiative transitions [4]. According to our experimental data the luminescence decay times decreased in the presents of Ag nanoparticles on 2.4 ns and 2 ns for samples #1 and #2, respectively. The decay times acceleration are caused by increasing the probability of non-radiation transitions. However, since sample #2 has a low quantum yield on the glass surface, competitive processes of radiation and non-radiation transitions could be occur in the presents of Ag nanoparticles and led to increasing the luminescence intensity.

So, QDs of CdS heated up to 95 °C are prespective as the markers for cancer treatment with the Ag nanoparticles.

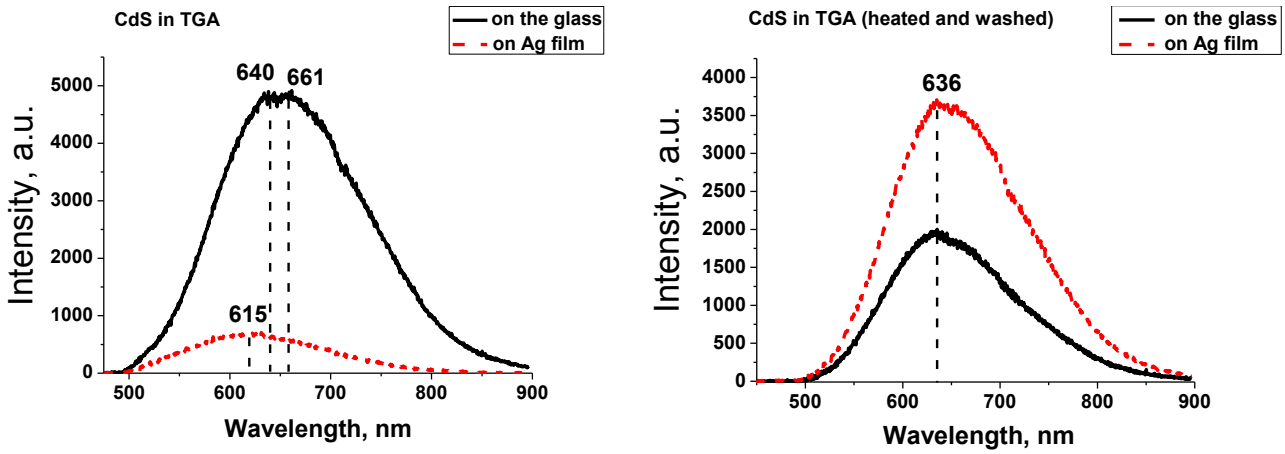

a) b)

Fig. 1. Luminescence spectra of a) CdS QDs in TGA and b) CdS QDs in TGA, heated at the temperature 95°C and washed through a cellophane membrane

[1] L. Saravanan, S. Diwakar et al., Synthesis, Structural and Optical Properties of PVP Encapsulated CdS Nanoparticles, Nanomater. nanotechnol.**1(2),** 42-48 (2011).
[2] M. Yamada et al., Therapeutic gold, silver, and platinum nanoparticles, WIRes: Nanomedicine and Nanobiotechnology, **7(3)**, 428-445 (2015).
[3] P.C. Lee, D. Meisel, J. Phys. J. Phys. Chem**. 86 (17),** 3391–3395 (1982).
[4] Y. Saito, A simple chemical method for the preparation of silver surfaces for efficient SERS, Langmuir. **18(8)**, 2959–2961(2002).

CELLULAR UPTAKE AND BIOLOGICAL EFFECT OF MES- AND BSA-COATED PHOTOLUMINESCENT GOLD NANOCLUSTERS IN VITRO

Laima Budėnaitė[1], Marija Matulionytė-Safinė[1,2], Greta Jarockytė[1], Dominyka Dapkutė[1], Ričardas Rotomskis[1,2]

[1] Biomedical Physics Laboratory, National Cancer Institute, Lithuania
[2] Biophotonics Group of Laser Research Centre, Vilnius University, Lithuania
Marija.matulionyte@nvi.lt

Ultrasmall photoluminescent gold nanoclusters (Au NCs), composed of several atoms with sizes up to a few nanometers have recently stimulated extensive interest. Unique molecule-like behaviors and facile synthesis make Au NCs very promising photoluminescent probes. However, possible application of Au NCs in biomedical area holds a potential risks related to exposure of biomolecules, cells and tissues. In this report we present effect of size and coating of photoluminescent Au NCs on cellular uptake, cytotoxicity and induction of reactive oxygen species (ROS) generation in cancer cells.

Two types of Au NCs that differ in coating were investigated: 2-(N-morpholino) ethanesulfonic acid (MES)-coated gold (Au-MES) NCs and bovine serum albumin (BSA)-encapsulated gold (BSA-Au) NCs. Au-MES NCs were synthesized according to the modified protocol by Bao et al. [1] and BSA-Au NCs were synthesized according to previously reported procedure with slight modifications [2]. The *in vitro* experiments were performed on MCF-7 breast cancer cells and more resistant MDA-MB-231 cells. After 24 hours of incubation BSA-Au NCs were observed accumulated in vesicles distributed mainly at the perinuclear region of cells indicating endocytic uptake. In contrast, Au-MES NCs were distributed homogeneously in total volume of the MCF-7 and MDA-MB-231 cells including nuclei as if they have entered the cells by diffusion. The XTT assay have shown that Au-MES NCs induced incubation-time dependent toxic effect on MCF-7 and MDA-MB-231 cells, 24 hour treatment was critical for cells viability. On the contrary, BSA-Au NCs demonstrated no significant influence on viability of both cell lines. To investigate whether the cytotoxicity is related to increased ROS generation due to the treatment with Au NCs flow cytometry was used. It was observed that Au-MES NCs induce oxidative stress by generating ROS, while after treatment with BSA-Au NCs no increase in ROS production within the cells was determined.

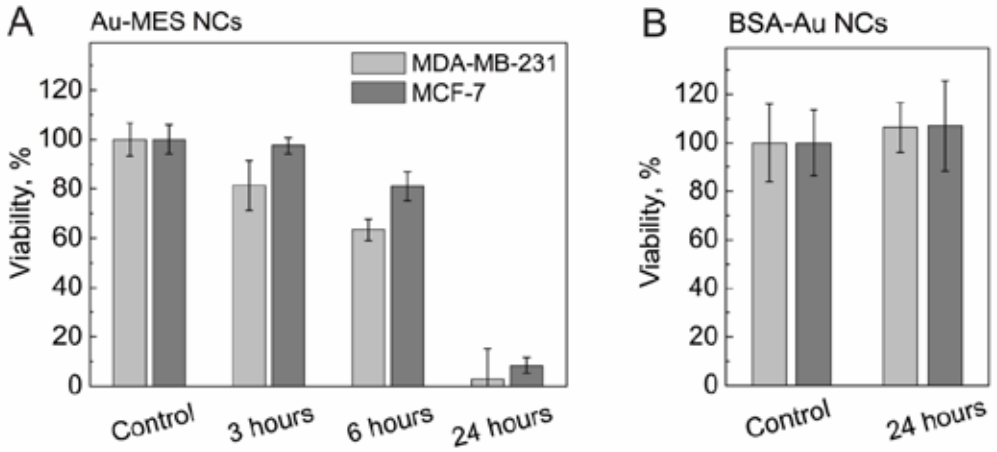

Fig. 1. Cytotoxic effect of Au-MES NCs (A) and BSA-Au NCs (B) on MDA-MB-231 and MCF-7 cancer cells.

Incubation with Au-MES NCs increased levels of cell ROS generation resulting in increased cytotoxicity, however, it may not be the only reason as the ultrasmall size of Au-MES NCs [3] gives them a possibility to interact with DNA or other vital cellular components while BSA-coating ensured biocompatibility and low cytotoxicity of BSA-Au NCs.

[1] Y. Bao, H.-C.Yeh, Ch. Zhonget. al., Formation and Stabilization of Fluorescent Gold Nanoclusters Using Small Molecules, J. Phys. Chem. C 114, 15879–15882 (2010).
[2] J. Xie, Y. Zheng, and J.Y. Ying. Protein-Directed Synthesis of Highly Fluorescent Gold Nanoclusters. J. Am. Chem. Soc., 131 (3): p. 888–889 (2009).
[3] M. Matulionytė, R. Marcinonytė, R. Rotomskis, Photoinduced spectral changes of photoluminescent gold nanoclusters, J. Biomed. Opt. 20(5), (2015).

PHOTOTOXIC ANTIBACTERIAL AND ANTITUMORAL ACTIVITY OF CARBOCYANINE DYE TICS NO. 150

Agata Mlynska[1], Simona Kavaliauskienė[2], Petras Juzėnas[2], Dalia Kaškelytė[3], Roaldas Gadonas[3], Mikhail Samtsov[4], Aleksandr Lugovsky[4], Elena Bakienė[1]

[1]Vilnius University, Faculty of Natural Sciences, Vilnius, Lithuania,
[2]Oslo University Hospital, Institute for Cancer Research, Oslo, Norway,
[3]Vilnius University, Faculty of Physics, Vilnius, Lithuania,
[4]A.N. Sevchenko Research Institute of Applied Physical Problems, Minsk, Belarus.
agata.mlynska@gmail.com

Photodynamic therapy is based on the excitation of cell-accumulated photosensitizer with specific light source, resulting in generation of ROS and free radicals which promote cell death [1]. Clinically approved photosensitizing agents are used for treating cancer or microbial infections. We investigated the phototoxic activity of a novel tricarbocyanine indolenine dye TICS No. 150 (Fig. 1A). Due to its red light absorbance (Fig. 1B), this dye emerged a promising agent for photodynamic therapy [2]. However, its potential phototoxic antimicrobial effect was not explored yet.

We aimed to examine the phototoxic effect of TICS No. 150 in bacterial and cancer cells and investigate its mechanism of action. To address these questions we performed a series of experiments on bacterial Salmonella enterica and eukaryoric prostate cancer cells, ehich were incubated with photosensitizer TICS No. 150 and irradiated with 720 nm laser diode light.

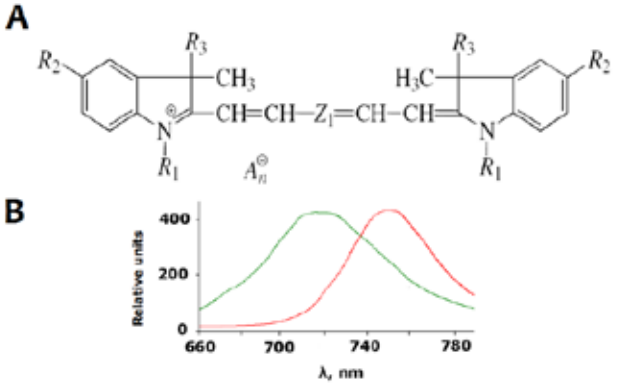

Fig. 1. A – Structural formula of TICS No. 150. B – Excitation and emission spectra of TICS No. 150 in phosphate buffered saline.

We found out that TICS No. 150 is phototoxic to *Salmonella enterica* cells in time- and dose-dependent manner (Fig 2). Mutant bacteria with shorter lipopolysaccharide in outer membrane are more sensitive to TICS No. 150 photodynamic effect. TICS No. 150 remains non-toxic until it enters the cell. The sensitivity of *Salmonella enterica* cells to the dye can be enhanced by increasing the permeability of outer cell membrane.

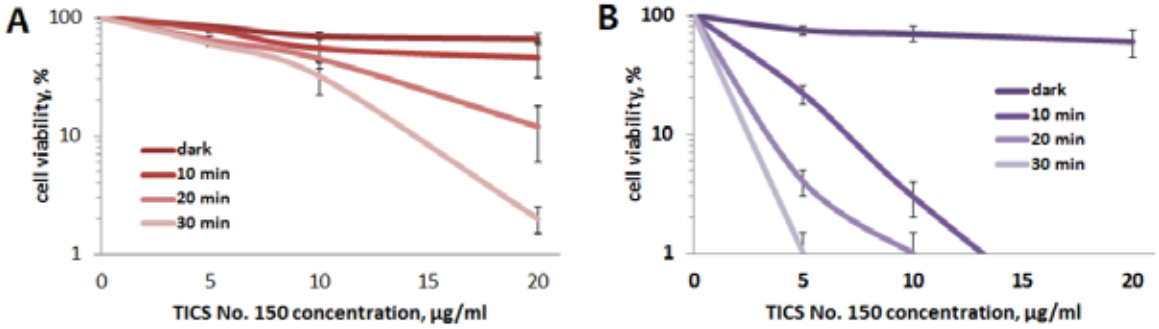

Fig. 2. Phototoxic effect of TICS No. 150 on wild type (A) and mutant (B) *Salmonella enterica* cells.

Moreover, TICS No.150 also showed considerable *in vitro* photoxicity to prostate carcinoma cells in time- and dose-dependent manner. TICS No.150 acts by generating singlet oxygen, which causes cell damage and induces apoptosis.

[1] Dougherty TJ, Gomer CJ, Henderson BW et al., Photodynamic therapy, J. Natl. Cancer. Inst. 90(12), 889-905 (1998).

[2] Istomin YP, Alexandrova EN, Chalov VN et al.,Uptake and phototoxicity of tricarbocyanine indolenine dye covalently bound with glucose (TICS) under acidification of tumor cells environment, Exp Oncol 26, 226-31 (2004).

CHEMOMETRIC ANALYSIS WITH CROSS-VALIDATION FOR SPECTROSCOPIC SIGNALS OBTAINED FROM MEDICAL SPECIMENS

Vilmantas Gėgžna[1,2], Ignas Čiplys[1,2], Darius Varanius[1,2], Rūta Kurtinaitienė[3], Gunaras Terbetas[4], Aurelija Vaitkuvienė[1], Juozas Vidmantis Vaitkus[1,5]

[1] Institute of Applied Research, Vilnius University, Vilnius, Lithuania
[2] Faculty of Natural Sciences, Vilnius University, Vilnius, Lithuania
[3] Vilnius University Hospital Santariskiu Klinikos, Vilnius, Lithuania
[4] Clinics of Neurology and Neurosurgery, Faculty of Medicine, Vilnius University, Vilnius, Lithuania
[5] Faculty of Physics, Vilnius University, Vilnius, Lithuania
Vilmantas.Gegzna@gf.stud.vu.lt

Spectroscopic techniques may be a convenient tool for medical diagnostics as they are non-invasive and can be implemented in modern spectroscopic devices that are small and portable. However, before it is possible to use these techniques in medical diagnostics, there is a challenge to develop an appropriate computational model that allows extracting relevant biomedical information about a certain type of medical conditions from spectroscopic data. Discipline called chemometrics [1] provides a set of mathematical and statistical tools dedicated tho deal with described issue. Thus the aim of this study was to apply chemometrical methods to analyze spectroscopic data obtained from human intervertebral disc (HID) and uterine cervix (UC) specimens and to evaluate if there is an agreement between specroscopic and more conventional biomedical evaluation.

Methods. This investigation was approved by Lithuanian Bioethical Comitee. Samples of HID were obtained during operations of intervertebral disc hernia in Clinics of Neurology and Neurosurgery (Vilnius, Lithuania) and samples of UC were collected in Vilnius University Hospital Santariskiu Klinikos (Vilnius, Lithuania) during patient's examination in doctor's office. All specimens were taken as a part of conventional medical procedure and used in the investigation under written consent of each patient. So called biomedical information (information about samples localization inside a boddy of patient and/or results of biochemical, e. g., quantity of collagen, proteoglycans, as well as medical, e. g., histological and cytological, tests) was collected.

In the experimental part of analysis auto-fluorescence of the samples was excited *in-vitro* with 355 nm radiation (laser "STA-01-TH", Standa, ltd.) and registered with a spectrometer "OceanOptics USB2000" (Ocean Optics, Inc.) through a fiber based optical system.

Chemometric analysis was carried out with software "R" (https://www.R-project.org/). Its packages "alsace"[2], "nmf" [3], "hyperSpec"[4], and "caret" [5] had a key role in spectra manipulation, extraction of spectroscopic features and development of computational spectroscopy-based classification model. An agreement between biomedical and spectroscopic information was evaluated by Cohen's kappa (κ) [6] statistic. The results were verified by k-fold cross-validation [7].

Results. Positive values of kappa ($\kappa>0$) were achieved. This fact indicates that there is at least some degree of agreement between spectroscopic and biomedical data.

[1] K. Varmuza and P. Filzmoser. Introduction to Multivariate Statistical Analysis in Chemometrics. (CRC Press, 2009).
[2] R. Wehrens, et al. Metabolite profiling in LC-DAD using multivariate curve resolution: the alsace package for R. *Metabolomics 11(1):143-54* (2014).
[3] R. Gaujoux, C. Seoighe. A flexible R package for nonnegative matrix factorization. *BMC Bioinformatics* 11:367 (2010).
[4] C. Beleites, C. Krafft, J. Popp and V. Sergo. hyperSpec: working with spectroscopic data. (The R User Conference useR! 2011).
[5] M. Kuhn. Building Predictive Models in R Using the caret Package. *Journal of Statistical Software* 28(5)1-26 (2008).
[6] J.R Landis, G.G. Koch. "The measurement of observer agreement for categorical data". *Biometrics* 33 (1):159–74 (1977).
[7] J.D. Rodríguez et al. Sensitivity Analysis of k-Fold Cross Validation in Prediction Error Estimation. *IEEE Trans Pattern Anal Mach Intell* 32(3):569-575 (2010)

THE TOBACCO INFLUENCE ON THE ELECTRIC POTENTIAL OUTCOME IN PATIENTS AFTER MYOCARDIAL INFARCTION

Sabina Brazevič, Magdalena Grajek

Department of Physics, Adam Mickiewicz University in Poznań, Poland
sabina.brazevic@amu.edu.pl

One of the most important organs of our body is heart. Its main function is to pump blood in a closed system of blood vessels. During contractions and relaxations dipole moments are generated, which we record as an electrocardiographic (ECG) curve using suitable electrode system.

Coronary heart disease (CHD) is one of the greatest threats to humanity, which entails serious consequences ranging from impairment of efficiency, the need to reduce activity, and ending with the premature death, usually caused by a myocardial infarction (MI). This is due to many risk factors responsible for its dissemination and poor prognosis. Its exact cause is not known [1]. On the other hand we identified a number of factors that increase the risk of coronary heart disease, i.e. diabetes, obesity, smoking, physical inactivity, eating high-energy food and stress. But in this paper we would like to concentrate on tobacco and its influence on patient's health. According to American Heart Association (2015 Heart Disease and Stroke Statistics Update) smoking is estimated to cause 10 per cent of cardiovascular disease (CVD) and is the second leading cause of CVD, after high blood pressure [2]. It causes significant narrowing of the coronary arteries, thereby causing the imbalance of oxygen supply that ultimately result in a myocardial infarction, stroke or sudden death.

Cardiovascular diseases are increasing significantly each year. According to official statistical data given by World Heart Federation cardiovascular disease is the leading global cause of death, accounting for 17.3 million deaths per year, a number that is expected to grow to more than 23.6 million by 2030. Moreover, cardiovascular diseases claim more lives than all forms of cancer combined [3]. Therefore, coronary artery disease remains a problem for all humanity, especially in developed countries and it is important to its fast and accurate diagnosis. This will allow for quick implementation of appropriate therapeutic intervention. Irregularities caused by coronary heart disease can be detected in a standard ECG and its analysis can provide useful information on the changes of electric potential, i.e. the proper functioning of the heart muscle.

The main objective of this study was to compare the parameters obtained on the basis of ECG, performed before and after surgery with the time elapsed since the myocardial infarction until the surgery in patients qualified for coronary artery bypass grafting (CABG).

In cooperation with the Faculty of Physics of Adam Mickiewicz University in Poznan and Division of Cardiac Surgery at Josephus Struthius Hospital in Poznan, a group of 140 patients with advanced coronary artery disease was studied. Patients were divided into two groups depending on the time elapsed from the time of MI and in which the operation has been performed, namely:

- Group I – those with less than six months between MI and operation (52 persons)
- Group II – patients with more than six months between MI and operation (88 persons)

An additional objective was to test whether smoking has a negative effect on the patient's condition. Therefore, we classified patients into 3 groups: current smokers (17% of all patients from a studied group), former smokers - more than 1 month without a cigarette (67%) and those who never smoked (16%).

Many statistical calculations and results were obtained using mathematical statistical program - STATISTICA 10, including the fact that pathological changes, such as elevated or depressed ST segment, left axis deviation became a risk factors. For current smokers from a group I the occurrence of ST segment elevation was statistically significant in the ECG record before the surgery ($p = 0.00626$). Also the occurrence of depressed ST segment in patients of I group, who never smoked was found to be statistically significant ($p = 0.01646$). But in the ECG made after the surgery statistically significant elevated ST segment had only smokers from the II group ($p = 0.02284$). Electrocardiogram remains a fundamental and primary research due to its simplicity, availability and diagnostic performance that is why we decided to check which group (according to smoking) has the best prognosis.

[1] A.J. Camm, T.F. Lüscher, P.W. Serruys, *Heart and Vascular Disease* (Volume I, Termedia, Poznań, 2006:38, 81)
[2] Heart Disease and Stroke Statistics – At-a-Glance (American Heart Association/American Stroke Association)
https://www.heart.org/idc/groups/ahamah-public/@wcm/@sop/@smd/documents/downloadable/ucm_470704.pdf (access 04.02.2016)
[3] Tobacco: totally avoidable risk factor of CVD (World Heart Federation)
http://www.world-heart-federation.org/fileadmin/user_upload/documents/Fact_sheets/2012/Tobacco_avoidable_risk_factor_of_CVD.pdf
(access 04.02.2016)

QUANTIFICATION AND LOCALIZATION STUDY OF RECOMBINANT ANTIBODIES USING CYTOCHROME b_5 FUSION PARTNER

Dmitri Dormeshkin, Andrei Gilep, Sergey Usanov

Institute of Bioorganic Chemistry NAS Belarus, Belarus
dormeshkin@gmail.com

Monoclonal antibodies in XXI century became a valuable tool as a therapeutics, parts of immunodiagnostics and as a research tool in the field of proteomics [1]. Recombinant Fab fragments due to their ability of antigen binding in addition to a smaller size and bacterial expression possibility displaced monoclonal antibodies in some applications.

Despite all the advances of recombinant antibody expression in bacteria, a various problems with low expression levels and poor solubility of these proteins still exists. The method most often used to overcome the above is to express the protein of interest as a fusion tag, which increase solubility of fusion protein [2].

The promising candidate as a fusion tag is heme-binding domain of cytochrome b_5. This hemeprotein possesses a great solubility and could be expressed in *Escherichia coli* in extremely high yields. Moreover, due to the Fe-protoporphyrin IX, coordinated with two histidines, cytochrome b_5 has a stable red color with the absorbance maximum in the Soret region at 413 nm and two minor peaks in the Q-band region region at 532 nm and 559 nm. Thus, this protein could be used as a fusion and solubility tag in the same time, but there is no information about its applicability in the case of large proteins with quaternary structure in periplasmic space.

Using the hybridoma cell line 5G-H2, secreting monoclonal antibodies against cortisol, as a source of mRNA and cDNA respectively, V_LC_L and V_HC_{H1} fragments of Fab domain were amplified by the polymerase chain reaction (PCR). Heme-binding domain of rat microsomal cytochrome b_5 was fused to C-end of CH1 heavy chain domain with TEV-protease digestion site and His_6-tag facilitating protein purification between them.

Molecular weight of the obtained fusion protein was confirmed by MALDI-TOF mass-spectrometry. It has been revealed that the most of the purified protein is in the dimeric state in solution with molecular weight well corresponding to the estimated. Binding activities of Fab-b5 fusion and hybridoma secreted immunoglobulin were measured by biolayer interferometry and ELISA. No significant difference between them was revealed.

Noteworthy, fusion protein yield was increased more than three fold in comparison with Fab fragment expression (from 2 mg/L to 7 mg/L in shake flasks cultivation). It confirms our assumption, that cytochrome b_5 could enhance fusion protein expression in periplasmic space in addition to reported cytoplasmic expression enhancement.

Fusion Fab-b5 protein possesses a stable red color and characteristic absorbance spectrum with the maximum at 413 nm (Figure 1).

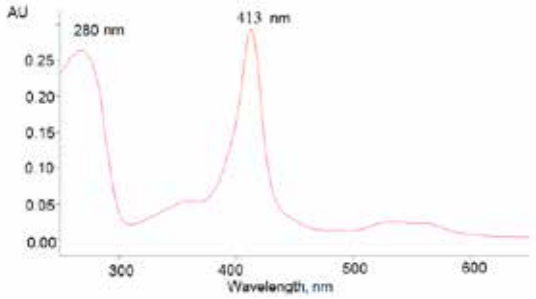

Fig.1. Absorbance spectrum of Fab-b5 fusion protein

Due to this feature it became possible to distinguish fusion protein of interest in complex mixtures and control the process of recombinant proteins expression and purification in real-time. The high value of oxidized cytochrome b_5 molecular extinction coefficient ε_{413} = 117 mM^{-1} cm^{-1} allows precise determination of protein concentration in broad ranges with the lower detection limit of pM concentrations even using the microvolume spectrophotometers. Moreover, difference spectrum measurement allows to minimize the contribution of other chromophores in the samples which could absorb in the same wavelength region. Cytochrome b_5 fusion tag multiples recombinant antibody yield and doesn't affect antigen-binding properties.

The ability of cytochrome b_5 fusion protein to change its absorbance maximum, depending on redox potential or folded state, could promote its usage as a marker of environmental state on the surface of or inside the nanoparticles (denaturating agents, redox potential) in the usage as a part of conjugated on its surface biomolecule. Moreover, it remains quantifiable, so it became possible to estimate bioorthogonal conjugation efficiency in simple and reliable way.

[1] K. Machold, J. Smolen. Adalimumab - a new TNF-alpha antibody for treatment of inflammatory joint disease, Expert Opin Biol Ther 3, 351-360(2003).
[2] R. Finn, et al.Rainbow tags: A visual tag system for recombinant protein expression and purification, BioTechniques 38, 387-392 (2005).
[3] Mitra, A., et al.High level expression of peptides and proteins using cytochrome b5 as a fusion host, Protein Expr Purif. 41, 84-97 (2005).

KINETIC PROPERTIES OF HUMAN OXYSTEROL 7α-HYDROXYLASE CYP7B1

Yaroslav Dichenko[1], Mikita Bokshyts[2], Sergey Usanov[1]

[1] Institute of Bioorganic Chemistry, National Academy of Sciences, Belarus
[2] Faculty of Biology, Belarusian State University, Belarus
dichenko@iboch.bas-net.by

Human oxysterol 7α-hydroxylase CYP7B1 catalyzes the 6α- or 7α-hydroxylation of steroids and oxysterols. The enzyme has different physiological function, but the most interesting is metabolism of neurosteroids [1] – compounds, which are synthesized *de novo* in the brain and other parts of the nervous system and mediate different brain functions [2]. Dysfunction of CYP7B1 is associated with a number of genetic disorders such as liver failure in newborns due to accumulation of toxic oxysterols and spastic paraplegia type 5 in adults [1]. But molecular reasons of such disorders are still unclear due to lacking of information about chemical and physical properties of the enzyme.

In the present study we used highly purified human CYP7B1, expressed in *E. coli* cells, for investigation of kinetic properties of the enzyme.

Purified human CYP7B1 has a typical P450 absorption spectrum with the heme iron in a low-spin state, as evidenced by a Soret region maximum at 418 nm and α, β-bands at 567 and 535 nm, respectively, and a spectrophotometric index $A_{417/280}$=1.4. The protein molecular mass corresponds to the expected value of 58 kDa. Upon reduction with sodium dithionite, followed by CO binding, a ferrous-CO complex is formed with a Soret region maximum at 450 nm, indicating that the reduced, substrate-free form is rather stable.

Application of stopped flow technique allowed us to determine rate constants of binding steroids 25-hydroxycholesterol, 27-hydroxycholesterol, pregnenolone, 21-hydroxypregnenolone, dehydroepiandrosterone, 5-androsten-3β,17β-diol, epiandrosterone and 5α-androstane-3β,17β-diol in CYP7B1 active site. The data obtained show that binding of substrate molecule in all cases is pseudo-first order reversible reaction with the lowest effective rate constants for 5-androsten-3β,17β-diol, epiandrosterone and 5α-androstane-3β,17β-diol. The highest value obtained for pregnenolone and 27-hydroxycholesterol.

Given results are in good agreement with *in silico* data that obtained by us earlier. It was shown that CYP7B1 has big active site cavity in comparison of other cytochromes P450, but due to steric limitations of substrate access channel only androstanes through their small size, in contrast with pregnanes and especially oxysterols, can easy enter the enzyme active site.

So, the data mined explain unique catalytic properties of CYP7B1 in comparison with other steroid 7α-hydroxylases and can cast light on molecular reasons of different neuropathies, connected with mutations of the enzyme.

[1] A.R. Stiles et al, CYP7B1: one cytochrome P450, two human genetic diseases, and multiple physiological functions, J. Biol. Chem. **284(42)**, 28485-28489 (2009).
[2] Y. Akwa et al, Neurosteroid metabolism. 7 alpha-Hydroxylation of dehydroepiandrosterone and pregnenolone by rat brain microsomes, Biochem. J. **288(3)**, 959-964 (1992).

IN VITRO BIOTINYLATION ON MAGNETIC PARTICLES FOR BIO-ORTHOGONAL CONJUGATION

Andrei Svirid, Andrei Gilep, Sergey Usanov

Institute of Bioorganic Chemistry, National Academy of Sciences of Belarus, Republic of Belarus
svirid@iboch.bas-net.by

Biotin labeling is widely used technique because of its extremely high affinity to avidin/streptavidin, promoting effective detection and purification by avidin/streptavidin conjugates [1,2]. Research applications include enzyme-linked immunosorbant assay (ELISA), immunoprecipitation (IP), cell surface labeling, flow cytometry and Western blot analysis. BirA, biotin ligase from *E. coli*, catalyzes the covalent attachment of biotin to the lysine side chain in a 15-mer peptide (Avi-tag), promoting targeted and highly efficient biotinylation.

The use of micro- or nanosized particles (ultrafine particles) in biochemistry and biotechnology became widespread, involving a large number of particle types and affinity mechanisms [3]. Applications include different kinds of isolation and purification of biomolecules and some solid phase applications. Sometimes, affine bound to particle biomolecule can undergo conformational changes and exhibit altered properties. Direct biotinylation of immobilized on particle molecule may benefit from this interaction, moreover this approach can help to streamline process of bio-orthogonal conjugation.

BirA was expressed in a form of fusion with MBP (maltose binding protein) involving consequent release of soluble BirA with TEV (tobacco etch virus) protease. This approach allowed to obtain 10 mg of recombinant BirA per liter of bacterial culture.

Peptide substrate for BirA (sequence: ENLYFQSHHHHHHHHHHGLNDIFEAQKIEWHE) contained Avi-tag, decahistidine tag and recognition site for TEV protease and has a mass 4081 Da. Peptide was bound to Millipore PureProteome Ni^{2+} coated magnetic beads, which are designed for affinity purification of His-tagged fusion proteins.

Activity test was carried out in following conditions: 40mM substrate, 10 mM Tris-HCl pH 8.0, 10 mM $MgSO_4$, 10 mM ATP, 50μM D-biotin and 5μg BirA at 4°C for 16h. Then substrate on beads was washed twice by PBS and eluted by 500mM imidazole. Eluate was purified on Agilent SampliQ C18 Endcapped columns and analyzed on Bruker Microflex MALDI-TOF.

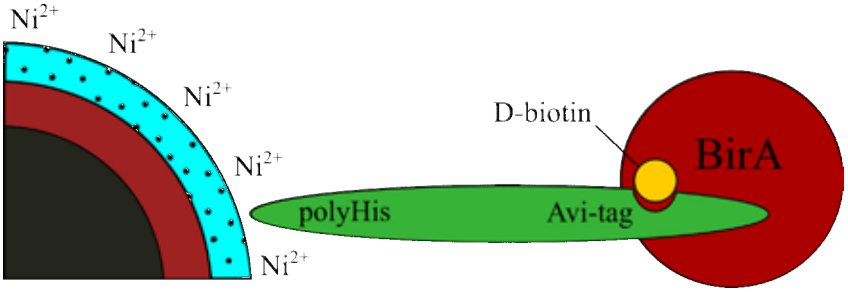

Fig. 1. Biotinylation reaction scheme.

As a result we obtained nearly fully (>95%) biotinylated peptide with a mass 4307 Da. For comparison, the biotinylation reaction in solution proceeded less efficiently. This fact indicates that magnetic particles doesn't interfere with biotinylation reaction and, moreover, somehow improves the yield of biotinylated product.

Thus, we can suggest that this approach will be useful in applications such as bio-orthogonal conjugation, because it involves purification and biotinylation of the molecule of the interest at the same time.

[1] S. Ashraf, R. Benson, E. Payne, C. Halbleib, H. Grøn, A novel multi-affinity tag system to produce high levels of soluble and biotinylated proteins in Escherichia coli, Protein Expr Purif **33**(2), 238-245 (2004).
[2] M. Czerwinski, A. Krop-Watorek, K. Wasniowska et al., Construction of an agglutination tool: recombinant Fab fragments biotinylated in vitro, N Biotechnol **26**(5), 215-221 (2009).
[3] L. Borlido, A. Azevedo, A. Roque et al., Magnetic separations in biotechnology. Biotechol Adv **31**, 1374–1385 (2013).

FUNCTIONAL ANALYSIS OF METAGENOMIC GENE CLUSTER WITH EXPOSED LIPOLYTIC ACTIVITY

Inga Šileikaitė, Rimantas Šiekštelė, Inga Matijošytė

Sector of Applied Biocatalysis, Institute of Biotechnology, Vilnius University
inga.sileikaite@gf.stud.vu.lt

Process of biocatalysis is defined as usage of enzymes for chemical transformations. Industrial demand of enzymes is increasing due to their benefits in comparison with chemical catalysts. Such advantages are mild conditions of reaction environment and stereo-, regioselectivity. [1]

Although, the diversity of microorganism species in nature is large, only 1 % of microorganisms are cultivated in laboratory conditions. This reduces the ability to discover new and novel enzymes. There is necessity to find alternative methods for discovery of biocatalysts. One of such cultivation independent methods is metagenomics, which is based on total DNA extraction from environmental source, construction and screening of DNA library. [2]

Most of known enzymes are encoded by single genes. However, recent investigations indicated that enzymes also could be encoded by gene clusters, which are described as a group of related genes responsible for biosynthesis of biologically active molecules. [3]

The aim of our study was to prove the existence of metagenomic gene cluster and it's lipolytic activity. Sequencing analysis of gene cluster revealed that it was composed of six genes. We have focused on functional analysis of separate genes and variants of gene groups on selective growth medium with tributyrin. The obtained results indicated that only gene cluster as entire unit is responsible for lipolytic activity. More detailed data on investigation of gene cluster will be presented during poster session.

[1] Torrelo G, Hanefeld U, Hollmann F. Biocatalysis. Catal Lett. 2015;1:309-345.
[2] Bashir Y, Singh SP, Konwar BK Metagenomics: An application based perspective. Chin JBiol. 2014; 2014: 1-7.
[3] Osbourn A.Secondary metabolic gene clusters: evolutionary toolkits for chemical innovation. Trends Genet. 2010; 26: 449-457.

INFLUENCE OF ACUTE AND CHRONIC STRESS ON THE RAT BRAIN PROTEOME

Ivanchyk Aliaksandr, Pankratava Alena, Shapira Mihail, Yantsevich Aliaksey

Institute of Bioorganic Chemistry, National Academy of Sciences of Belarus, Minsk
alexivan4ik@gmail.com

Stress is a set of non-specific reactions on the impact of unfavorable factors. These non- specific reactions, are accompanied by changes in the neuro-endocrine functioning, and are known to be non- specific basis for many diseases. So far as stress reactions are triggered and regulated by the nervous and endocrine systems, detailed information about the processes occurring in the nervous system can open up possibilities to minimize the negative effects of stress in the nervous system and the whole organism. Therefore in this study we used rats as a model for understanding acute and chronic stress-induced proteome changes in brain tissue.

We performed a wide range of experiments concerning the analysis of protein profile of rat brain. In the current work we used homogenates of different rat brain regions provided by the Institute of biochemistry of biologically active compounds, National Academy of Sciences of Belarus. Total protein was extracted from the tissue homogenate with methanol-chloroform method and analyzed by «Shot-gun» proteomic approach.

We developed optimized approach for the isolation of proteins from the aggregate of the rat brain tissues. Qualitative and quantitative differences of protein profile in different regions of rat brain obtained from experimental stressed animals. The obtained results could be important for establishment of mechanisms of pathological processes, owls occurring in the brain under stress.

EVALUATION OF PREDICTIVE MARKERS IN THE OVARIAN CANCER MICROENVIRONMENT AND PERIPHERAL BLOOD

Sima Garberytė[1,2], Agata Mlynska[2,3], Karolina Žilionytė[2,3], Birutė Intaitė[4], Vita Pašukonienė[2]

[1]State Research Institute Centre For Innovative Medicine
[2]Laboratory of Immunology, National Cancer Institute
[3]Department of Biochemistry and Molecular Biology, Vilnius University
[4]Department of Oncogynecology, National Cancer Institute
s.garberyte@imcentras.lt

Ovarian cancer is one of the most common causes of cancer death in women. Ovarian cancer (OC) is the sixth most common cancer and the third most common cause of women's death from cancer in Lithuania. Due to the lack of specific symptoms and the lack of an effective screening method for most patients, the disease is detected only later (III and IV) stages, when the five-year survival rate is only 27% [1,2,3,4]. Identification of new predictive markers and their use as anti-cancer therapeutic targets for ovarian cancer may optimize OC diagnostics and therapy.

The aim was to identify predictive stemness (CD24, CD44, CD117, CD133, ESA), resistance (ABCB1, ABCG2, ABCC1) and markers of immunosuppression (immunosuppressive enzyme IDO, PB cytotoxic / suppressant lymphocyte populations) in human ovarian tumor microenvironment as well as in peripheral blood and to determine interactions among them.

The study population consisted of samples from patients with advanced epithelial ovarian cancer (FIGO stage IIIC/IV). Data about PB lymphocytes, stemness and resistance marker expression were obtained using the LSR II flow cytometer (BD Biosciences). IDO expression was detected by ELISA method. Finally, the correlation among these characteristics was evaluated.

We observed differences in stemness, resistance and immunosuppression marker expression in patients. Our results showed that of all the tested markers immunosuppressive enzyme IDO was proved to be versatile, because its expression correlated with increased expression of MDR transporters ABCC1 and ABCG2, with expanded population of immunosuppressive lymphocytes CD4+CD25+FoxP3+ and marker of stemness CD44.

There are significant relationships between different elements of immunosuppression, stemness and drug resistance in ovarian tumors. Further investigations are necessary to validate the significance of the relationships in larger study populations and to prove the prognostic and predictive value of selected multi-biomarker panel.

[1]. Howlader N, Noone AM, Yu M, Cronin KA. Use of imputed population-based cancer registry data as a method of accounting for missing information: application to estrogen receptor status for breast cancer. Am J Epidemiol. 2012; 176(4):347-56.
[2]. Jayson GC, Kohn EC, Kitchener HC, Ledermann JA. Ovarian cancer. Lancet. Priimtas spaudai 2014.
[3]. Syrios J, Banerjee S, Kaye SB. Advanced Epithelial Ovarian Cancer: From Standard Chemotherapy to Promising Molecular Pathway Targets - Where Are we Now? Anticancer Res. 2014; 34(5):2069-77.
[4]. eco.iarc.fr [internetinė svetainė]. Lyon: International Agency for Research on Cancer. Sukurta 2012 [žiūrėta 2014 05 02]. Adresas: http://eco.iarc.fr/eucan/Country.aspx?ISOCountryCd=440

A COMPREHENSIVE STUDY ON DELAMINATION AND RESTACKING OF MAGNESIUM-ALUMINUM LAYERED DOUBLE HYDROXIDE

Szabolcs Muráth[1], Zoltán Somosi[1], Ildikó Tóth[2], Etelka Tombácz[2], Pál Sipos[3], István Pálinkó[1]

[1] Department of Organic Chemistry, University of Szeged, Hungary
[2] Department of Physical Chemistry and Materials Science, University of Szeged, Hungary
[3] Department of Inorganic and Analytical Chemistry, University of Szeged, Hungary
murathsz@chem.u-szeged.hu

Layered double hydroxides (LDHs) are popular and well-studied materials in the field of inorganic chemistry, catalysis and materials science. [1] They have typical lamellar structure with positively charged layers compensated by the so-called intercalated anions situated in the interlamellar space coordinated by water molecules. The layers usually consist of divalent (M^{II}) and trivalent (M^{III}) metal ions with a M^{II}:M^{III} molar ratio between 6 to 1. What makes the layered double hydroxides so diverse is the great variety of the metal ions in the layers and the facile anion exchange process. [2-4] The size and orientation of the compensating anions are the main factors of basal spacing, which is the sum of the thickness of a layer and the interlayer space. The schematic structure of a layered double hydroxide is shown in Fig. 1.

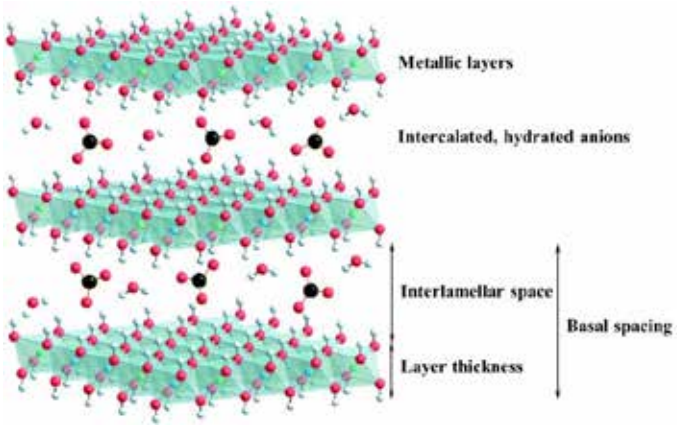

Fig. 1. Schematic structure of the most common LDHs.

One of the most interesting properties of LDHs is delamination; a process, in which we treat the material in (typically) organic liquids in a way that the regular structure collapses and a colloid system of the individual sheets is formed. However, these delaminated/exfoliated layered double hydroxides can be regenerated into their initial form with aqueous treatment. The uncovered potential of the above-mentioned restacking process is the simultaneous anion exchange as the layered structure is rebuilt. The extent of delamination can be measured with dynamic light scattering, a method, which describes the average radii of particles in a colloid system. Although, the diameter of an exfoliated particle is identical with the intact crystal, the thickness is reduced leading to higher velocity in the liquid system. Since the instrumental respond relies on the movement of the particles, thinner ones are interpreted as they have smaller average radius.

The main goals of our work were: (i) the characterization of the exfoliating ability of different types of organic materials towards magnesium-aluminum layered double hydroxide (MgAl-LDH), (ii) selecting the LDH colloids having the smallest average size and treat them with aqueous solution of various anions, (iii) analyzing the solid precipitate after the hydration, and investigating whether ion exchange and restacking can take place simultaneously.

Our study reveals that MgAl-LDH was successfully delaminated in polar amides, as formamide, *N*-methylformamide, *N*-methylacetamide and in long-chained normal alcohols. Usually, delamination was finalised by ultrasonic treatment. Since the amides are miscible with water, we started our restacking experiments with LDHs exfoliated in formamide. As rehydrating solutions, we applied numerous sodium salts with singly-, doubly- and triply charged anions. Recontruction was accomplished using anions with one and two negative charges, but triple-charged ones generally disrupted the rebuilding process, likely, because their salts with the metals of the LDH are very stable, and the thin layers can more readily transform to the salts rather than the ordered materials. The characterization of the samples were performed by several methods: X-ray diffractometry (XRD), infrared spectroscopy (IR), dynamic light scattering (DLS), scanning electron microscopy (SEM) and energy-dispersive spectrometry (EDS).

[1] F. Li, X. Duan, Applications of layered double hxdroxides, Structure and Bonding **119**, 193-223 (2006)
[2] V. Rives, M. A. Ulibarri, Layered double hydroxides (LDH) intercalated with metal coordination compounds and oxometalates, Coordination Chemistry Reviews **181**, 61-120 (1999)
[3] G. R. Williams. D. O'Hare, Towards understanding, control and application of layered double hydroxide chemistry, Journal of Materials Chemistry **16**, 3065-3074 (2006)
[4] J. He, M. Wei, B. Li et al., Preparation of layered double hydroxides, Structure and Bonding **119**, 89-119 (2006)

UNEXPECTED REGIOSELECTIVITY IN THE FRIEDEL-CRAFTS REACTION OF 2,7-DI-*TERT*-BUTYLPYRENE WITH ETHOXYCARBONYL ISOTHIOCYANATE

Marzena Witalewska, Anna Wrona-Piotrowicz, Janusz Zakrzewski

Department of Organic Chemistry, Faculty of Chemistry, University of Lodz, Poland
marzena-witalewska@o2.pl

Friedel-Crafts reaction of pyrene with isothiocyanates affords pyrene-1-carbothioamides in high yields [1]. In this communication we report that this reaction in the case of a sterically congested pyrene derivative, 2,7-di-*tert*-butylpyrene **1**, takes place selectively at the 1-position.

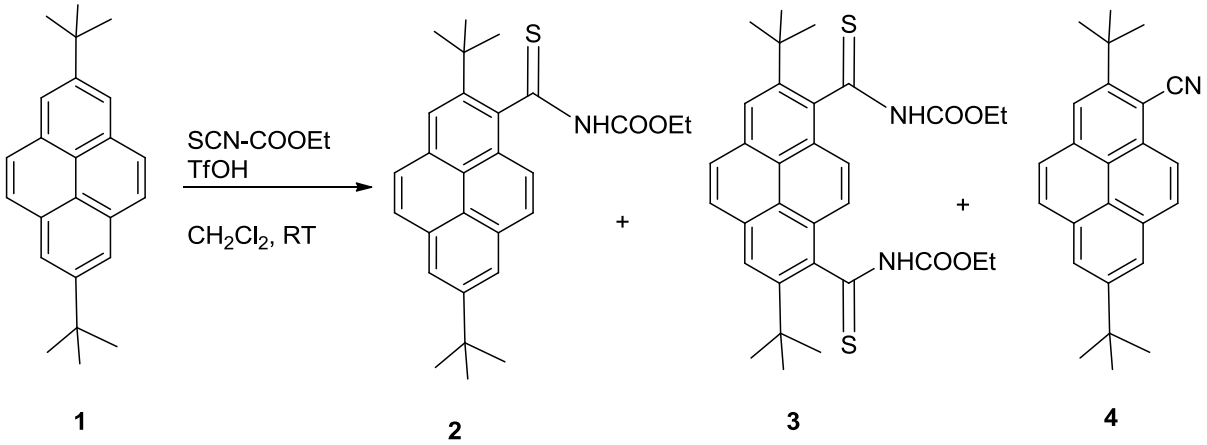

Fig 1. Reaction of **1** with ethoxycarbonyl isothiocyanate in dichlorometane.

Table 1. Reaction of **1** with ethoxycarbonyl isothiocyanate in dichlorometane.

	Time of reaction	**Yield 2**	**Yield 3**	**Yield 4**
1.	2 h	36 %	19 %	-
2.	10 min	82 %	-	-
3.	16 h	15 %	-	37 %
4.	3 days	-	-	39 %
5.	7 days	-	-	58 %

It affords, depending upon the reaction conditions, monothioamide **2**, dithioamide **3** and nitrile **4**. The latter compound is strongly fluorescent in solution and in the solid state. Its photophysical properties have been studied. The X-ray structure of **3** has been determined.

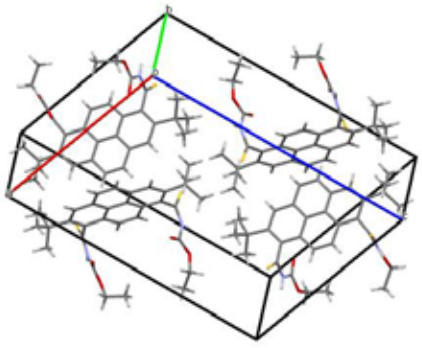

Fig 2. Structure X-ray of compound **3**.

[1] A. Wrona-Piotrowicz, J. Zakrzewski, R. Métivier, A. Brosseau, A. Makal, K. Woźniak, Efficient synthesis of pyrene-1-carbothioamides and carboxamides. Tunable solid-state fluorescence of pyrene-1-carboxamides, RSC Advances, **4**, 56003-12 (2014).

VERTICAL DISTRIBUTION OF ^{239,240}Pu AND ^{238}Pu ANALYTES IN THE SOIL

Laima Nedzveckienė, Benedikta Lukšienė, Šarūnas Buivydas, Rasa Gvozdaitė

Center for Physical Sciences and Technology, Savanorių 231, LT-02300 Vilnius, Lithuania.
laima.nedzveckienė@ftmc.lt

Natural and artificial radionuclides exist in different chemical forms in the natural environment. The presence of plutonium in the geosphere poses a long-term environmental concern due to its toxicity and the long half-lives of several isotopes (e.g., half-life for ^{239}Pu is $2.41 \cdot 10^4$ years). Therefore, understanding the mechanisms responsible for enhancing or retarding the mobility of plutonium in the environment is important for the risk management. The plutonium may exists as Pu(III), Pu(IV), Pu(V) and Pu(VI). Each of these oxidation states exhibits a different geochemical behavior in terms of oxidation/reduction, hydrolysis, complexation, precipitation and sorption. Therefore, the mobility of plutonium in the environment is highly dependent on oxidation states. Surface-mediated reduction of relatively mobile Pu(V) to relatively immobile Pu(IV) has been observed on a variety of surfaces [1-3].

The aim of this work is to adapt the scheme of the radiochemical analysis for the determination of ^{239,240}Pu and ^{238}Pu activity concentrations and to evaluate their distribution in each 1 cm forest soil layer down to the 22 cm depth.

Analysis of experimental results showed that the soil organic matter content and ^{239,240}Pu and ^{238}Pu activity concentrations were gradually declining according to the depth. The maximum activity concentration of ^{239,240}Pu in the 3-5 cm layer was 0.90 to 1.45 Bq/kg, and these values roughly correspond to the ^{239,240}Pu activity levels in forest soil, usually collected to the depth of 5-10 cm. The calculated ^{238}Pu/^{239,240}Pu activity concentration ratio in each layer showed that the plutonium origin was of the global fallout from the nuclear weapon testing. The ^{238}Pu/^{239,240}Pu activity concentration ratio of the global origin deposition is approximately 0.04 to 0.05, and the impact of the Chernobyl nuclear power station accident is characterized by the ratio of ~ 0.4-0.5.

[1] W. Runde, S.D. Conradson, D.W. Efurd, N. Lu, C.E. VanPelt, C.D. Tait, Appl. Geochem **17** 837 (2002).

[2] A.L. Sanchez, J.W. Murray, T.H. Sibley, Geochim. Cocmohim. Acta **49** 2577 (1985)

[3] D. Shaughnessy, H. Nitsche, C.H. Booth, D.K. Shuh, G.A. Waychunas, R.E. Wison, H. Gill, K.J. Cantrell, R.J. Serne, Environ. Sci. Technol. **37** 3367 (2003).

PECULARITIES OF ^{238}Pu AND ^{239,240}Pu ASSESSMENT IN FRESH WATER SYSTEMS

Zita Žukauskaitė, Benedikta Lukšienė

State Research Institute Center for Physical Sciences and Technology, Savanorių ave. 231, LT-02300 Vilnius, Lithuania
zita.zukauskaite@ftmc.lt

Plutonium was deposited in the environment as a result of global fallout and releases from other nuclear activities during the past 70 years. Among 20 isotopes of Pu with mass numbers from 228 to 247 the most studied isotopes of plutonium in the environment are ^{238}Pu (87.7 yr), ^{239}Pu (24110 yr), ^{240}Pu (6563 yr) and ^{241}Pu (14.4 yr), among which ^{239}Pu and ^{240}Pu are the most important ones due to their long half-lives and relatively high abundance. Besides, the atomic ratios of ^{240}Pu/^{239}Pu varying with release conditions of Pu and the type or design of the device can serve as a finger print for tracing the source of plutonium contamination [1].

Measurements of plutonium in fresh water require a very large volume of water sample (300-500 L) due to a very low concentration of plutonium. Plutonium analysis consists of several main stages: pre-concentration, separation, purification, electrodeposition and alpha spectrometric measurement.

Pre-concentration of radionuclides prior to their determination is necessary to avoid difficulties associated with their detection [2]. Radionuclides from large volume of water might be pre-concentrated using chemical precipitation, evaporation, adsorption onto various sorbents.

There is a wide variability of materials, whose sorption capability of removing heavy metals and radionuclides from large volume water samples is investigated [3, 4]. Bentonite [5], mesoporous silica functionalized with copper ferrocyanide [6], zeolite, montmorillonite, aerogel, silica gel [7], hydrous oxides of Mn, Al, Mg and Fe [2], microbial and seaweed biomass (living or dead), cellular products, activated carbons, sewage sludges, clays and clay-like minerals, hybrid materials and ordered mesoporous silica [8] are used as sorbents. Biomaterials such as moss, lichens, pine needles, peat, saw dust, fly ash, etc. can also be used as sorbents. Chemical precipitation can be caried out using multi-stage precipitation with $FeCl_3$, Nd_2O_3 and $KMnO_4$. The plutonium content is precipitated together with the $Fe(OH)_3$, NdF_3 and MnO_2 precipitates.

The easiest and shortest way of plutonium pre-concentration is sorption on various sorbents. It might take from several minutes to one day, compared with chemical precipitation (4-5 days) and evaporation using a water bath (1-2 months).

The aim of this work is to compare a few methods to pre-concentrate plutonium from a large volume of water samples.

The obtained results showed that the easiest way of plutonium pre-concentration was sorption on sorbents. Chemical precipitation carried out using $FeCl_3$ (pH=2) was compared with sorption on sorbent – moss. Results showed that sorption on moss could be used as a cheaper and faster way of the sample pre-concentration method – the obtained ^{239,240}Pu values by compared methods were close to each other.

[1] X.L. Hou, P. Roos, Critical Comparison of radiometric and mass spectrometric methods for the determination of radionuclides in environmental, biological and nuclear waste samples, Analytica Chimica Acta **608** 105-139 (2008).
[2] G. Koulouris, B. Slowikowski et al., Pre-concentration of actinoids from waters: a comparison of various sorbents, Applied Radiation and Isotopes **53,** 279-287 (2000).
[3] Li Ping, Yin Zhuoxin et al., The immobilization of U (VI) on iron oxyhydroxides under various physicochemical conditions, Environmental Science.: Processes Impacts **16**, 2278–2287 (2014).
[4] F.E. Soetaredjo, A.Kurniawan et al., Investigation of the continuous flow sorption of heavy metals in a biomass-packed column: revisiting the Thomas design model for correlation of binary component systems. RSC Adv., 4, 52856–52870 (2014).
[5] J. D. Begg, M. Zavarin, S. J. Tumey, A. B. Kersting, Plutonium sorption and desorption behavior on bentonite, Journal of Environmental Radioactivity **141**, 106-114 (2015).
[6] T. Sangvanich, V. Sukwarotwatb, R. J. Wiacek et al., Selective capture of cesium and thallium from natural waters and simulated wastes with copper ferrocyanide functionalized mesoporous silica, Journal of Hazardous Materials **182**, 225–231 (2010).
[7] S. Shaban, V. Mikulaj, Sorption-desorption of radiocesium on various sorbents in presence of humic acid, Journal of Radioanalytical and Nuclear Chemistry **208(2)**, 593-603 (1996).
[8] F.E. Soetaredjo, A. Kurniawan, L.K. Ong, D.R. Widagdyo, S. Ismadji, Investigation of the continuous flow sorption of heavy metals in a biomass-packed column: revisiting the Thomas design model for correlation of binary component systems RSC Adv. **4**, 52856–52870 (2014).

STRUCTURAL STABILITY OF β-LACTOGLOBULIN VARIANTS

Katažyna Milto[1], Magdalena Tworzydło[1], Joanna Loch[2], Krzysztof Lewiński[2], Piotr Bonarek[1]

[1]Faculty of Biochemistry, Biophysics and Biotechnology Department of Physical Biochemistry, Jagiellonian University, Poland

[2]Faculty of Chemistry, Department of Crystal Chemistry and Crystal Physics, Jagiellonian University, Poland

kasia.milto@gmail.com

Due to increasing level of prescription drug poisoning over the last decades, several techniques were developed to help to remove toxins from the human body. It has been reported that modified lipocalins called anticalins could be used as a carrier molecules for drug poisoning treatment. β-lactoglobulin, small lipocalin protein, is known to have high affinity to hydrophobic compounds. Additionally, it is water soluble, thermally stable and has high stability at low pH. Site-directed mutagenesis of the protein with such properties could make this protein alternative carrier molecule for different compounds.

Here we study structural stability of different β-lactoglobulin variants using urea-induced chemical denaturation. The process was monitored by circular dichroism and intrinsic tryptophan fluorescence spectroscopies. In several cases mutations made in the interior of binding site are significant to protein stability. Furthermore, by analyzing data acquired systematically over a wide range of pH, we are able to show changes in secondary structure fractions of different mutants.

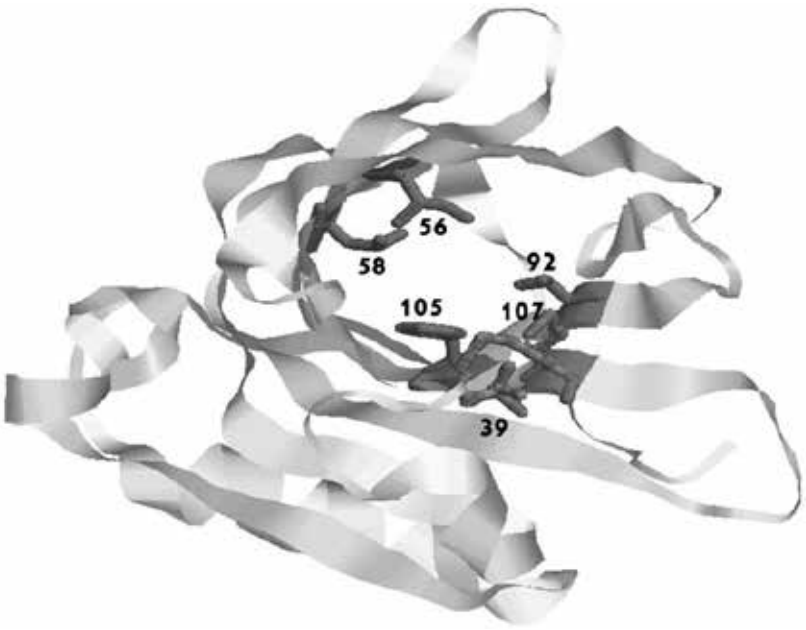

Fig. 1. β-lactoglobulin structure. Numbers indicate amino acid residues at which mutations were introduced.

This study was supported by the Polish National Science Centre, grant number: 2012/05/B/ST5/00278

[1] A. C. J. M. de Pont, Extracorporeal treatment of intoxications, Current Opinion in Critical Care **13**, 668–673 (2007).

[2] A. Skerra, Alternative binding proteins: Anticalins – harnessing the structural plasticity of the lipocalin ligand pocket to engineer novel binding activities, FEBS J. **275**, 2677–2683 (2008).

[3] A. Barbiroli, T. Beringhelli, F. Banomi et al., Bovine β-lactoglobulin acts as an acid-resistant drug carrier by exploiting its diverse binding regions, Biol. Chem. **391**, 21-32 (2010).

IMOBILIZATION OF ANTHOCYANINS ON POLYMERIC MATERIALS

Domynikas Bucinskas, Karolina Almonaityte, Ruta Berenyte

Department of Polymer Chemistry and Technology, Kaunas University of Technology, Lithuania
domynikas.bucinskas@gmail.com

Anthocyanins (ATC) are the most important water-soluble natural pigments of vascular plants [1]. ATC have a high potential for use as natural colorants due to their attractive colours, non-toxicity, and antioxidant activity which plays the vital role in the prevention of various diseases [2]. The European blueberry, also called bilberry (*Vaccinium myrtillus* L.), is one of the most important wild berries due to its delicious taste and high content of beneficial nutrients and bioactive compounds. However, ATC are highly unstable, and their colour stability is strongly affected by the pH, temperature, ATC concentration, light, enzymes and other accompanying substances. For this reason, many studies have been conducted in order to increase the ATC stability. A new approach to stabilizing ATC is their introduction into a complex with anionic biopolymers [3]. Carrageenans (CARG) are natural water-soluble hydrocolloids composed of a linear chain of sulphated galactans and extracted from certain species of red seaweed. There are major varieties of CARG. κ-CARG has only one sulphate group per a disaccharide repeating unit, whereas ι-CARG has two. Due to the existence of anionic sulphate groups, CARG can interact with oppositely charged polymers or drugs [4].

The aim of present work was to form complexes between ATC extracted from *Vaccinium myrtillus* and κ- and ι-carrageenan and to immobilize obtained complexes into a polymeric matrix: hydroxypropylmethylcelullose (HPMC) film, non-woven viscose fabric and wooden sticks. The influence of the complex composition and polymeric matrix on the color yield, amount of incorporated ATC, stability of ATC and antioxidant activity was the further aim of the present study.

Table(1). Influence of CARG/ATC complex on colour and antioxidant activity of wooden sticks

Impregnation solution	Antioxidant activity, %	Colour characteristic		
		Lightness, NBS	Saturation, NBS	Hue
ATC	49	40.5	26.2	352^o
κ-CARG/ATC	30	45.1	18.0	341^o
ι-CARG/ATC	36	45.3	17.7	347^o

During formation of ionic complexes between κ-CARG or ι-CARG and ATC a hypsochromic shifts of the absorbance wavelength was observed along with an increase in the absorbance maximum (hyperchromic effect), e.g. the colour of ATC solution rapidly changed from red with purple shade (colour of ATC solution) to red (colour of CARG/ATC complex solution). Colour of CARG/ATC complex remain after immobilization on polymer matrix (see Table(1)). Formation of CARG/ATC complexes increase the ATC stability and preserved the ATC antioxidant activity. This tendency still persist after immobilization of CARG/ATC complexes into the polymer matrix.

[1] A. Castaneda-Ovando A., L. Pacheco-Hernandez, E. Paez-Hernandez, E et al., Chemical studies of anthocyanins: A review, Food Chemistry, **113**, 859–871 (2009).
[2] R. N. Cavalcanti, D. T. Santos, M. A. A. Meireles, Non-thermal stabilization mechanism of anthocyanins in model and food system – An overview, Food Research International, **44**, 499–509 (2011).
[3] R. Klimaviciute, V. Navikaite, V. Jakstas, L.Ivanauskas, L, Complexes of dextran sulfate and anthocyanins from *Vaccinium myrtillus*: formation and stability, Carbohydrate Polymers, ***129***, 70–78.
[4] L. Li, R. Ni, Y. Shao, S. Mao, Carrageenan and its application in drug delivery, Carbohydrate Polymers, **103**, 1–11 (2014).

THE INFLUENCE OF THE TEMPERATURE ON TERMODYNAMICS OF CREATION THE COMPLEXES OF HP-β-CYCLODEXTRIN WITH SEVERAL SURFACTANTS

Katarzyna Abramczyk[1], Adam Bald[1], Andreas Heintz[2]

[1] Department of Physical Chemistry, University of Łódź, Poland
[2] Abteilung Physikalische Chemie, Institut für Chemie, Universität Rostock, Germany
kasiabramczyk@interia.pl

Research in the field of cyclodextrin chemistry for several decades became increasingly popular [1],[2]. This is due to the unusual shape of the cyclodextrin molecule which gives unique properties cyclodextrins, particularly formation of inclusion complexes [3],[4]. Two methods of determining the stability constants (Kf) of inclusion complexes that kind of connections are the most popular. These are conductometry and calorimetry.

In our group, we focused on determining the formation constants (Kf) of inclusion complexes of carboxylate anions with HP-β-cyclodextrins using full conductivity equation. It let us to determine exact values of stability constants and limiting molar conductivity of inclusion complexes. By the calorimetric method, we determined enthalpies of the process straight from measurements, which can be interesting as a reference methods for values obtained from the conductivity measurements.

In our studies, we use the highest class measuring equipment which provide maximum accuracy (Wayne Kerr "Precision Component Analyzer" type 6430B, Lauda calibration thermostat UB20F etc). The obtained results of molar conductivity of sodium salts of chosen carboxylic acids for different concentrations of cyclodextrin, we used to calculate stability constants of inclusion complex (K_f) in a wide temperature range (283,15K – 318,15K). We determined also the values of Gibbs energy (ΔG_f^0) and other thermodynamic functions (ΔH_f^0 oraz ΔS_f^0) of creation of creation of inclusion complexes

Calorimetric measurements have been made using TAM calorimeter (2277 Thermal Activity Monitor, Thermometrics, Sweden) in the same range of temperatures.

[1] M. V. Rekharsky, Y. Inoue, Chem. Rev., 1998, 98, 1875 - 1917.
[2] J. Szejtil, Chem. Rev., 1998, 98, 1743 - 1753.
[3] G. Wentz, Andegaw. Chem. Int. Ed. Engl., 1994, 33, 803-822.
[4] E. A. Castro, D. A. J. Barbiric, J. Arg. Chem. Soc., 2002, 90, 1-44.
[5] A. A. Rafati, N. Hamnabard, E. Ghasemian, Z. B. Nojini, Mat. Sci. Eng. C, 2009, 29791–795.

NMR STUDY OF WATER CONFINED IN IONIC LIQUIDS

Stasė Bielskutė

Department of General Physics and Spectroscopy, Vilnius University, Lithuania
stase.bielskute@gmail.com

Ionic Liquids (ILs) or Room Temperature Ionic Liquids (RTILs) are organic salts which melt below 100 °C. Sometimes RTILs are called tunable solvents because by varying the anion and cation subsystems their properties are changed dramatically. Recently a strange water clusterization process called water pocket formation in RTILS was observed applying SAX, SANS and NMR techniques [1, 2]. The purpose of present work was to analyse the dynamics of water pockets formation applying ^{1}H NMR and relaxation methods.

In present study six imidazolium based RTILs were used, namely 1-butyl-3-methylimidazolium nitrate/chloride/bromide/iodide/trifluoromethanesulfonate/tertafluoroborate ([bmim][NO3/Cl/Br/I/TfO/BF4]). NMR experiments were carried on Bruker AVANCE III HDNMR spectrometer operating at 400 MHZ frequency for ^{1}H at 298K using Bruker BBO probehead. Precise dilution curves were measured by changing the solutions compositions and measuring chemical shifts. Exact minima of water chemical shifts are present for all ILs except [bmim][BF4] (Fig 1.).

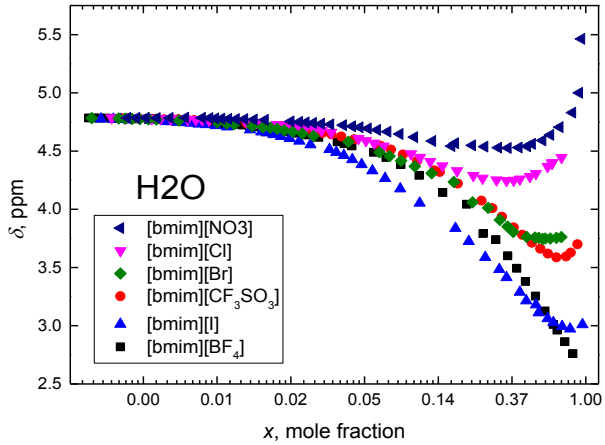

Fig. 1. H_2O spectral lines chemical shift dependency on the IL water system composition. More details in the figure.

The observed chemical shift is the average value of all water manifolds in the sample. In our case the smaller the water pocket is the smaller chemical shift should be because relatively it would be constructed from more non-hydrogen bonded molecules in other words the shell would be relatively larger. Such dependency gives a hint that the water pocket diameter reduces within the anion accordingly $d_{[NO3]}>d_{[Cl]}>d_{[Br]}>d_{[TfO]}>d_{[I]}$.

Spin-Lattice T_1 and Spin-spin T_2 relaxations measurements corroborate water pockets formation in RTILs water systems. The minima are present at the same concentration in T_1 dependency on concentration curves in all studied systems except [bmim][BF4]-water system. The next objective is to analyse inter- and intra- molecular parts of the relaxation process applying ^{2}H NMR relaxation experiments.

[1] H. Abe, T. Takahiro, M. Shigemi, Y. Yoshimura, S. Tsuge, T. Hanasaki, K. Ohishi, S. Takata and J. Suzuki, Open Journal of Physical Chemistry (2014).
[2] K. Saihara1, Y. Yoshimura, S. Ohta1 and A. Shimizu1, *Properties of Water Confined in Ionic Liquids*, Scientific Reports 5 (2015).

NMR CROSS-POLARIZATION IN AMMONIUM DIHYDROGEN PHOSPHATE

Laurynas Dagys[1], Vytautas Klimavičius[1], Vytautas Balevičius[1]

[1] Department of General Physics and Spectroscopy, Vilnius University, Lithuania
dagys.laurynas@gmail.com

Cross-polarization (CP) is a well-known solid-state nuclear magnetic resonance spectroscopy (SS NMR) technique. Originally it was developed for signal-to-noise ratio enhancement and experiment time reduction [1]. Considering the experiment involves a process between different spin species it is interesting area because information about these dipoles could be uncovered. In present work, CP kinetics of ammonium dihydrogen phosphate (ADP) is investigated. The physical reasoning for choosing ADP was: *i)* ammonia and phosphoric acid forms tetragonal crystal structure, hence it is easier to understand CP kinetics, *ii)* interrnolecular distances are known from X-Ray, Neutron diffraction analysis [2]. Thus the purpose of the work is to confirm that CP-MAS is a complementary method for solid-state crystallography.

The experiments were performed using Bruker AVANCE III HD SS NMR spectrometer. The resonant frequencies were 400 MHz and 162 MHz respectively for ^{1}H and ^{31}P. ^{1}H→^{31}P CP kinetics were obtained using 498 equidistance time domain points. 7 kHz Magic Angle Spinning (MAS) was applied. Temperature was varied from 233 K to 363 K.

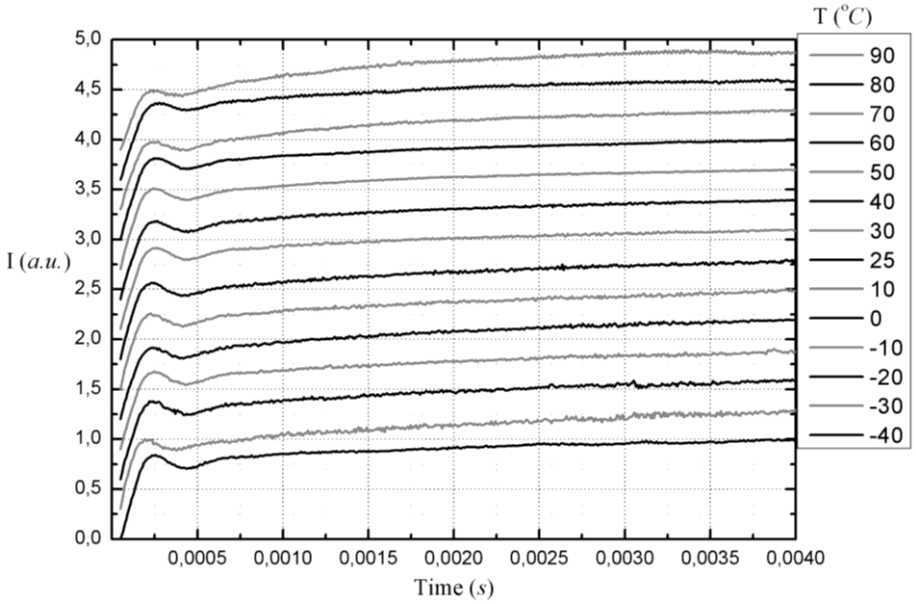

Fig. 1. ^{1}H→^{31}P CP kinetics in ADP. Temperature range of -40°C to 90°C. MAS rate – 7 kHz.

Obtained CP kinetics had certain type of curve shape. It has been seen, that the shape does not change in different temperatures and there is some sort of oscillations at the beginning. In NMR crystallography several models for CP are present. For compounds like ADP (that has high order in structure) I-I*-S model is used. In this model, I* and S spin pair (^{1}H and ^{31}P respectively) acts like two coupled pendulum in oscillatory manner [3]. Oscillations then are damped by subsequent spin-diffusion. This model results that signal dependency to time is given by Eq. (1):

$$I(t) = I_0 \exp\left(\frac{-t}{T_{1\rho}}\right) \times \left(1 - \lambda \exp\left(\frac{-t}{T_{df}}\right) - (1-\lambda)\exp\left(\frac{-3t}{2T_{df}}\right)\cos\left(2\pi\frac{b\cdot t}{2}\right)\right) \quad (1)$$

Enabling nonlinear curve fitting to this function, gives numerical results: diffusion time is around 3 ms and dipolar coupling – 3000 Hz respectively. Dipolar coupling is a function of distance, this would give that the distance between two spins is about 0.25 nm. In present work it has been shown, that in this temperature range, ADP crystal remains stable in the aspect of structural properties: spin-diffusion time T_{df} and dipolar coupling b are invariant to temperature.

[1] D. Apperley, R. K. Harris, P. Hodgkinson, *Solid-State NMR: basics principles and practice* (Momentum press, USA, 2012).
[2] D. Xu, D. Xue, Chemical bond analysis of the crystal growth of KDP and ADP, Journal of Crystal Growth, **286**, 108-113 (2006).
[3] W. Kolodziejski, J. Klinowski, Kinetics of Cross- Polarization in Solid-State NMR: A Guide for Chemists, Chemical Reviews **2002**, 613-628 (2000).

CHARAKTERIZATION OF DIAZO COMPOUNDS AS POTENCIAL ELECTRON TRANSFER MEDIATORS FOR CONJUGATED BIOCATALYTICAL SCHEMES

Ana Chaleckaja[1], Lidija Tetianec[1,2], Juozas Kulys[1,2], Liucija Marcinkeviciene[1], Jonita Stankeviciute[1], Rolandas Meskys[1*]

[1] Vilnius University, Institute of Biochemistry, Mokslininku 12, LT-08662, Vilnius, Lithuania
[2] Department of Chemistry and Bioengineering, Vilnius Gediminas Technical University, Faculty of Fundamental Sciences, Sauletekio al. 11, LT-10223, Vilnius, Lithuania
ana.chaleckaja@gmail.com

The application of dehydrogenases for bioconversion of organic compounds is very attractive due to their appropriate catalytic activity and substrate specificity. For successful use of dehydrogenases in bioconversion systems the effective regeneration *in situ* schemes of their expensive cofactors must be created [1,2,3].

Common mediator-dependent conjugated biocatalytical systems consist of a mediator reducing and a mediator oxidizing steps (Fig.1).

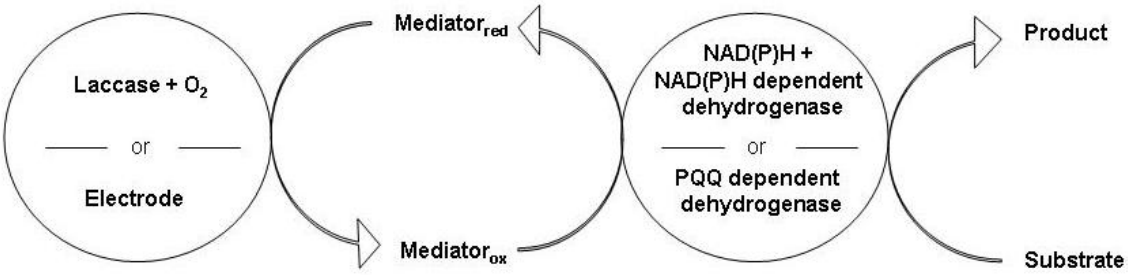

Fig. 1. Scheme of conjugated biocatalytical substrate conversion system in the presence of mediator.

The task of our investigation is to develop the possibility of use of a diazo compounds - 4-hydroxy-3,5-dimethoxybenzaldehydeazine (syringaldazine) and N,N'-dimethyl-4,4'-azopyridinium (MAZP), as electron transfer mediators for conjugated biocatalytical schemes.

Both the chosen mediators are of moderate redox potential and their redox conversion proceeds with participation of two electrons and two protons [4,5].

The reactivity of mediator and NAD(P)H is one of the factors defining the efficiency of the mediator in the cofactor regeneration process. The calculated bimolecular constant values (k_b) of cross reaction of oxidized syringaldazineand NAD(P)H are $(1.0\pm0.1)\times10^4$ $M^{-1}s^{-1}$ for NADH and $(1.0\pm0.2)\times10^4$ $M^{-1}s^{-1}$ for NAD(P)H at pH 8.0, whereas the k_b value of MAZP and NADH is $(2.2\pm0.1)\times10^5$ $M^{-1}s^{-1}$ at pH 7.2. This is a very high value comparing to other compounds used as mediators for NADH oxidation.

The activity of laccases from *Didymocrea sp*. (DsL) and *Trichaptum abietinum* (TaL) with syringaldazine as a substrate was investigated at different pH. These enzymes showed different pH profiles toward syringaldazine. DsL showed a maximum activity at pH 8.0 that is unusual for fungal laccases. The maximal activity of TaL was observed at pH 5.5. The rate constant of syringaldazine reactivity with DsL is $(4.2\pm0.5)\times10^4$ $M^{-1}s^{-1}$, at pH 8.0. Differently than syringaldazine the reactivity of MAZP with laccase was low. The rate constant of MAZP reduced form reactivity with laccase from *Polyporus pinsitus* (PpL) is $(5.4\pm0.3)\times10^3$ $M^{-1}s^{-1}$ at pH 5.5.

The efficiency of mediator in conjugated scheme was investigated using DsL laccase as oxidized enzyme and oxygen as a final electron acceptor in the case of syringaldazine, whereas in the case of MAZP mediator was oxidized at the electrode. In the case of laccase total turnover numbers (TTNs) was determined by the product of ethanol oxidation - acetaldehyde amount, whereas in the case of MAZP - by the number of electrons in the electrolysis. TTNs for cofactor using syringaldazine and MAZP as mediators are 4 and 8.5, respectively. The calculated TTNs were not high because of the enzyme (NAD^+-dependent alcohol dehydrogenase) inactivation and of the leakage of acetaldehyde, which is known as volatile and reactive compound.

Acknowledgements

The work was supported by European Social Foundation and the Government of the Republic of Lithuania, project No. VP1-3.1-ŠMM-08-K-01-001.The authors thank dr. Regina Jančienė for the MPD synthesis.

[1] S. W. May. Applications of oxidoreductases, Current Opinion of Biotechnology **10(4)**, 370-375 (1999).
[2] D. Monti, G. Ottolina, G. Carrea, S. Riva, Redox reactions catalyzed by isolated enzymes, Chemical Reviews **111,** 4111–4140, (2011).
[3] T. Ikeda, K. Kano, Bioelectrocatalysis-based application of quinoproteins and quinoprotein-containing bacterial cells in biosensors and biofuel cells, Biochimica et Biophysica Acta **1647**, 121– 126 (2003).
[4] P. Hapiot, J. Pinson, P. Neta, C. Rolando. Electrochemical behaviour of syringaldazine, a colorimetric redox reagent, Journal of Electroanalytical Chemistry **353(1-2)**, 225-235 (1993).
[5] A. Safavi, O. Moradlou,M. Saadatifar. Methylated Azopyridine as a New Electron Transfer Mediator for the Electrocatalytic Oxidation of NADH, Electroanalysis **22(10)**, 1072-1077 (2010).

TARTARIC ACID ASSISTED SYNTHESIS AND CHARACTERIZATION OF GADOLINIUM-DOPED CERIA (GDC)

Žygimantas Gricius[1], Artūras Žalga[1], Edvardas Kazakevičius[2]

[1] Department of Applied Chemistry, Faculty of Chemistry, Vilnius University, Naugarduko Str. 24, LT-03225 Vilnius, Lithuania

[2] Faculty of Physics, Vilnius University, Saulėtekio al. 9, LT-10222 Vilnius, Lithuania

hamilton@inbox.lt

During the last decade the solid oxide fuel cells (SOFC's) have been intensely investigated as a next generation green energy system as they exhibit high ionic conductivity, chemical and thermal stability and also have high efficiency and generate low pollution emissions [1]. Nowadays the high performance SOFC is limited to relatively high temperatures, it consists of three types of components: an electrolyte, an anode and a cathode. The electrochemical reaction involves oxygen which is reduced to oxide ions at the cathode and a fuel that is oxidized at the anode. The cathode is a perovskite-like material, the anode is a cermet (i.e., a composite material consisting of a ceramic constituent and a metal). In addition, an electrolyte used in this process is generally a doped solid ceramic oxide that eases the generation of oxygen vacancies and carries the charge between the cathode and the anode. The most widely used ceramic in SOFC is yttria stabilized zirconium (YSZ) ceramic. It is a traditional fuel cell electrolyte which exhibits the necessary ionic conductivity and low electrical resistance at high temperatures, but lacks all these properties at relatively low temperatures. Also this ceramic presents the metastable tetragonal phase which is essential for the structural hardening during cooling [2]. As a potential lower temperature replacement for YSZ electrolyte a gadolinium-doped ceria (GDC, $Ce_{0.9}Gd_{0.1}O_{1.95}$) is considered. Ceria-based electrolytes have relatively large unit cells compared to systems based on zirconia and, as a consequence, ceria-based systems have larger channels through which oxygen ions can pass during the conduction [3-5]. Moreover, decreasing the temperature of operation for Gd doped ceria to 600 ºC appears to minimize the reduction of the electrolyte; however, lower temperatures result in the greater loss of power density due to the decrease in the ionic conductivity. To address the significant problem with ceria based materials a number of approaches have been taken, such as finding the ideal doping level and ion to balance stability with adequate oxide ion conductivity, decreasing the operating temperature and improving materials processing etc [3]. The implement of these challenges could be successfully reached by using so-called solution-based synthetic methods, which play a crucial role in the design and production of fine ceramics and have been successful in overcoming many of the limitation of the traditional solid-state, high-temperature methods. For example, the metal complexes with organic ligands have been used for the preparation of ceramics and metal oxide thin films by both co-precipitation synthesis and sol–gel process, using metal nitrates, chlorides, acetates, and oxalates as starting materials.

In this study, we report the aqueous sol-gel tartaric acid assisted synthesis of Ce–Gd–O acetate–oxalate gel precursor for $Ce_{0.9}Gd_{0.1}O_{1.95}$ ceramic. In this case, we investigated the thermal behavior of as-prepared Gd–Ce–O nitrate–tartrate precursors and their affinity to the decomposition processes of the starting materials. Moreover, the influence of the temperature, heating atmosphere, and annealing time on both the morphology and crystallinity of the Ce–Gd–O gel precursor were additionally investigated in detail using a scanning electron microscopy (SEM), X-Ray diffraction (XRD) and Fourier transform infrared spectroscopy (FT–IR).

[1] J. H. Myung et al., Synthesis and characterization of NiO/GDCeGDC dual nano-composite powders for high-performance methane fueled solid oxide fuel cells, International Journal of Hydrogen Energy (2012), doi:10.1016/j.ijhydene.2012.04.140.

[2] M. Morales, J. J. Roa X.G. Capdevila, M. Segarra, S. Pinol. Mechanical properties at the nanometer scale of GDC and YSZ used as electrolytes for solid oxide fuel cells. DOI:10.1016/j.actamat.2009.12.036.

[3] M. G. Chourashiya, L. D. Jadhav, Synthesis and characterization of 10%Gd doped ceria (GDC) deposited on NiO-GDC anode-grade-ceramic substrate as half cell for IT-SOFC, International Journal of Hydrogen Energy (2011), doi:10.1016/j.ijhydene.2010.12.083.

[4] K. Tönsuaadu, A. Zalga, A. Beganskiene, A. Kareiva, Journal of Thermal Analysis and Calorimetry 110 (2012) 77.

[5] A. Zalga, Z. Moravec, J. Pinkas, A. Kareiva, Journal of Thermal Analysis and Calorimetry 105 (2011) 3.

RECOMBINANT PRODUCTION AND THERMODYNAMICS OF INHIBITOR BINDING TO HUMAN HISTONE DEACETYLASES 6 AND 8

Goda Milinavičiūtė, Justina Kazokaitė, Daumantas Matulis

Department of Biothermodynamics and Drug Design, Institute of Biotechnology, Vilnius University, Lithuania

goda.milinaviciute@chf.stud.vu.lt

The histone deacetylases (HDAC) are enzymes that deacetylate lysine residues in histones as well as in several other non-histone proteins. [1] The deacetylation of histones induces a condensed and transcriptionally inactive DNA. [2] There are 18 HDAC family members in human genome. They are divided into 4 different groups according to their catalytic pockets and mechanisms of action. [3] Several HDAC isoforms, such as HDAC6, potentially play a role in schizophrenia, cancer and Alzheimer's disease. Furthermore, alterations in acetylation have been implicated in neurodegenerative disorders, including Huntington's and Parkinson's diseases. [2]

HDAC6 deacetylates histones and many other substrates. For example, HDAC6 was shown to take part in the microtubule network by acting as a specific α-tubulin deacetylase. [1] HDAC8 is mostly expressed in smooth muscle and the function is related with muscle contractility. In addition, HDAC8 has been shown to be important for the growth of human tumor cell lines. [4] Therefore, both HDAC6 and HDAC8 are potential drug targets. Thus, the production of the recombinant HDAC6 and HDAC8 and the investigation of inhibitor binding affinity to them are important for the design of new compounds with desired affinity properties.

The gene of human recombinant HDAC6 was cloned into four different plasmids containing N-terminal His-tag, C-terminal His-tag and N-terminal GST-tag. All of the constructs were expressed in various *E. coli* strains. Unfortunately, efforts to purify the recombinant HDAC6 by affinity and ion exchange chromatographies have not yet succeeded. However, human recombinant HDAC8 with a C-terminal His-tag was expressed in *E. coli* strain and successfully purified by affinity chromatography. The thermodynamics of interaction between HDAC8 and inhibitors such as Tubastatin A and Belinostat, which is clinically used for the treatment of cancer, were determined by the fluorescent thermal shift assay (FTSA) and isothermal titration calorimetry (ITC). Tubastatin A exhibited a dissociation constant of 14.29 μM for HDAC8. Belinostat bound HDAC8 with 7.69 μM affinity. Furthermore, the thermal stability of HDAC8 was determined at various pH and in the presence of buffers and salts by FTSA. HDAC8 was the most stable in sodium phosphate buffer at pH 6.0-7.0. The recombinant human HDAC8 was successfully produced and characterized and the search for novel inhibitors is in progress.

[1] Claudia Simoes-Pires et al. HDAC6 as a target for neurodegenerative diseases: what makes it different from the other HDACs? Molecular Neurodegeneration, 8:7 (2013)

[2] Florence F. Wagner et al. Small molecule inhibitors of Zinc-dependent Histone deacetylases. Neurotherapeutics, 10:589-60 (2013)

[3] Olaf Witt et al. HDAC family: What are the cancer relevant targets? Cancer Letters, 277: 8-21 (2009)

[4] Jinhong Feng et al. Expression, purification, and S-nitrosylation of recombinant histone deacetylase 8 in *Echerichia coli*. BioScience Trends, 5(1):17-22 (2011)

SYNTHESIS OF THE CYCLOOCTYNE DERIVATIVES BEARING METALLOCARBONYL MOIETY FOR SITE-SPECIFIC PROTEIN LABELLING

Daria Lizińska, Elżbieta Gędek, Bogna Rudolf

Department of Organic Chemistry, University of Lodz, Lodz
daria.lizinska@gmail.com

The modifications of biomolecules is a key technology in the field of chemical biology. The plethora of functional groups present in bioactive molecules requires specific bioorthonal conjugation methods to introduce novel functionality to such systems. Most of reactions utilized in this aim are based on „click chemistry"[1]. The copper(I)-catalyzed azide alkyne cycloaddition (CuAAC) is the most used „click" reaction. However, the toxicity of copper is a concern for in vitro or in vivo applications. Therefore, there has been significant interest in developing alternative methods that do not require any metal catalyst. One of them is the strain promoted azide-alkyne [3+2] cycloaddition (SPAAC) reported by Bertozzi and co-workers [2]. SPAAC reactions rely on the use of strained cyclooctynes that possess a remarkably decreased activation energy in contrast to terminal alkynes and thus do not require an exogenous catalyst [3].

Over the past years we have explored the chemistry of metallcarbonyl complexes type $CpM(CO)_x(\eta^1$-*N*-maleimidato) (M= Fe, Mo; x= 2, 3). These complexes are easy to detect with the use of IR spectroscopy due to the presence of strong absorption bands in the 1800-2150 cm^{-1} (ν CO) spectral range, which is free of any biomolecule absorption. The ethylenic bond of the maleimidato ligand in these complexes is readily attacked by nucleophiles such as thiols, amines or imidazoles. These reactions can be used to introduce IR-detectable moieties into peptydes and proteins with potential applications in immunoassays.[4]

The aim of this study was to synthesize the cyclooctyne derivatives bearing metallocarbonyl moiety for site-specific protein labelling. Herein we report on the reaction of $CpM(CO)_x(\eta^1$-*N*-maleimidato) (M= Fe, Mo; x= 2, 3) with ADIBO-amine in presence of thiethyl amine.

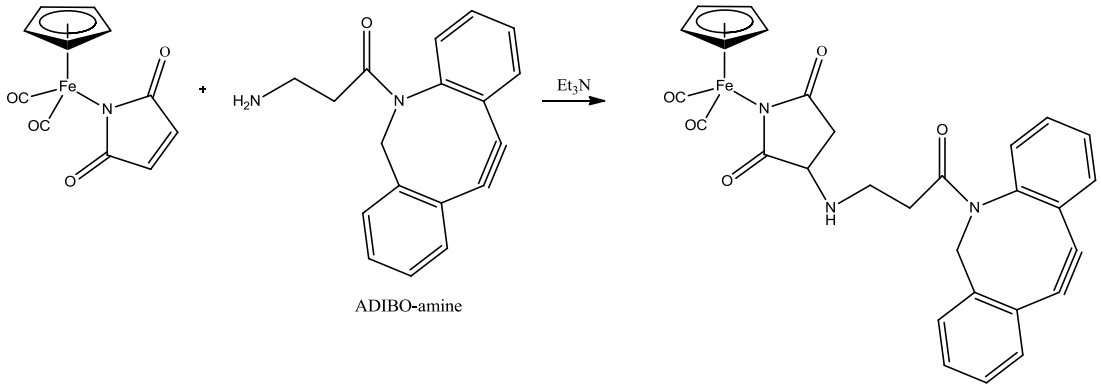

Scheme.1 Reaction of $CpFe(CO)_2(\eta^1$-*N*-maleimidato) with ADIBO-amine.

We found out that $CpM(CO)_x(\eta^1$-*N*-maleimidato) (M= Fe, Mo; x= 2, 3) complexes easly react with ADIBO-amine, to form metallocarbonyl-ADIBO conjugates (Scheme. 1). In the next step we investigate reactivity of obtained metallocarbonyl-ADIBO conjugates with model azides in catalyst-free iClick reaction.

[1] L. Henry, C. Schneider, B. Mutzel, P. V. Simpson, C. Nagel, K. Fucke, U. Schatzschneider, *Chem. Commun*., 2014, 50, 15692.
[2] J. M. Baskin, J. A. Prerscher, S. T. Laughin, N. J. Agard, P. V. Chang, I. A. Miller, A. Lo, J. A. Codelli, C. R. Bertozzi, *Proc. Natl. Acad. Sci,* USA 2007, 104, 16793-16797.
[3] C. Remzi Becer, R. Hoogenboom, U. S. Schubert, *Angew. Chem. Int. Ed*., 2009, 48, 4900-4908.
[4] B. Rudolf, M. Salmain, M. Palusiak, J. Zakrzewski, *J. Organomet. Chem*., 694, 2009, 908-915.

SYNTHESIS AND CYTOTOXIC PROPERTIES OF NEW FURAN-DERIVED AMINOPHOSPHONATES

Edyta Rzeszotarska[1], Jarosław Lewkowski[1], Agnieszka Matusiak[1], Marta Morawska[1], Renata Kontek[2], Gabriela Gajek[2*]

[1]Department of Organic Chemistry, Faculty of Chemistry, University of Łódź, Tamka 12, 91 403 Łódź, Poland
[2]Laboratory of Cytogenetics, Faculty of Biology and Environmental Protection, University of Łódź, Banacha 12/16, 90-237 Łódź, Poland
e.ladybas@gmail.com

Aminophosphonates, as analogues of natural amino acids constitute the very important group of compounds in various fields of pharmacology and agrochemistry. Their career started with the first applications of aminophosphonic acids as antibiotics (alaphosphaline) or herbicides (glyphosate) [1]. Many of them show very interesting antitumour properties [2].

However, known are furan derivatives used in pharmacy, they generally have antibacterial properties. Most of aminophosphonic derivatives containing furan moiety is already in literature. Some of N-arylamino(2-furyl)methylphosphonic acid esters were reported by us to be potential anticancer agents against squamous esophageal cancer [3,4].

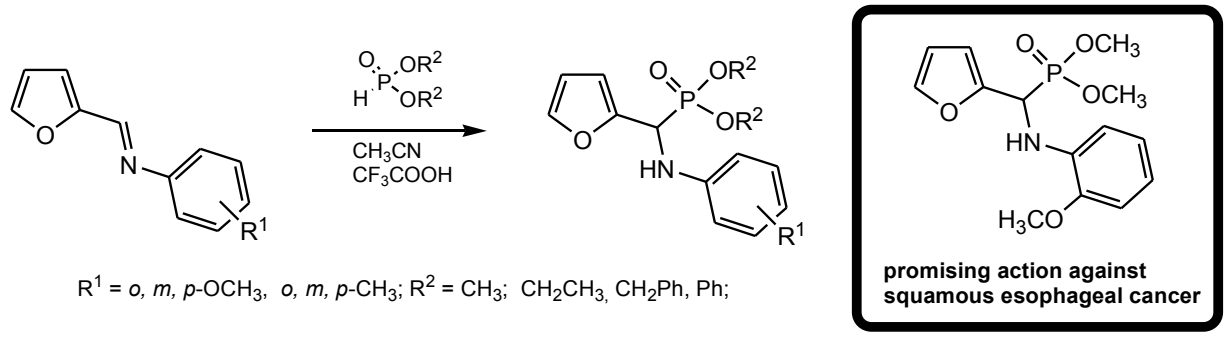

R^1 = *o, m, p*-OCH_3, *o, m, p*-CH_3; R^2 = CH_3; CH_2CH_3, CH_2Ph, Ph;

Fig. 1. Synthesis of aminophosphonates.

In this communication, we would like to present synthesis of some N-arylamino(2-furyl)-methylphosphonates and results of their action against several types of colon cancer.

Financial support of the Polish National Centre of Science (NCN), grant nr 2014/13/B/NZ9/02418 is kindly acknowledged. E.R. wishes to thank the Faculty of Chemistry, University of Łódź, Poland and the Łódź Division of Polish Chemical Society for covering the Conference expenses.

[1] P. Kafarski, B. Lejczak, Biological activity of aminophospchonic acids, Phosphorus Sulfur Silicon **63**, 193-215(1991).
[2] P. Kafarski, B. Lejczak, Aminophosphonic Acids of Potential Medical Importance, Curr. Med. Chem. Anti-Cancer Agents **1**, 301-312(2001).
[3] A.A. Klimczak, A. Kuropatwa, J. Lewkowski, J. Szemraj, Synthesis of new N-arylamino(2-furyl)methylphosphonic acid diesters, and in vitro evaluation of their cytotoxicity against esophageal cancer cells, Med. Chem. Res. **22**, 852-860(2013).
[4] A.A. Klimczak, A. Matusiak, J. Lewkowski, J. Bitner, J. Szemraj, R. Kontek, Dimethyl (2-Furyl)-N-(2-Methoxyphenyl)Aminomethylphosphonate Induces Apoptosis in Esophageal Squamous Cancer Cells. Structure Versus Activity of its Selected Analogs, Phosphorus Sulfur Silicon **190**, 1088-1099(2015).

SYNTHESIS AND INVESTIGATION OF BIOCATALYTIC NANODERIVATIVES

Justina Gruzauskaite[1], Liucija Marcinkeviciene[2], Lidija Tetianec[1,2]

[1] Department of Chemistry and Bioengineering, Vilnius Gediminas Technical University, Faculty of Fundamental Sciences, Sauletekio 11, LT-10223, Vilnius, Lithuania
[2] Vilnius University, Institute of Biochemistry, Mokslininku 12, LT-08662, Vilnius, Lithuania
justinagruzauskaite@gmail.com

This paper focuses on the synthesis of magnetic iron oxide nanoparticles (MNP) and silver-coated MNP (SMNP) and the investigation of direct electron transfer between bacterial glucose dehydrogenase (GDH) from *Ewingella americana* and laccase from *Didymocrea sp*. through MNP and SMNP (Fig. 1).

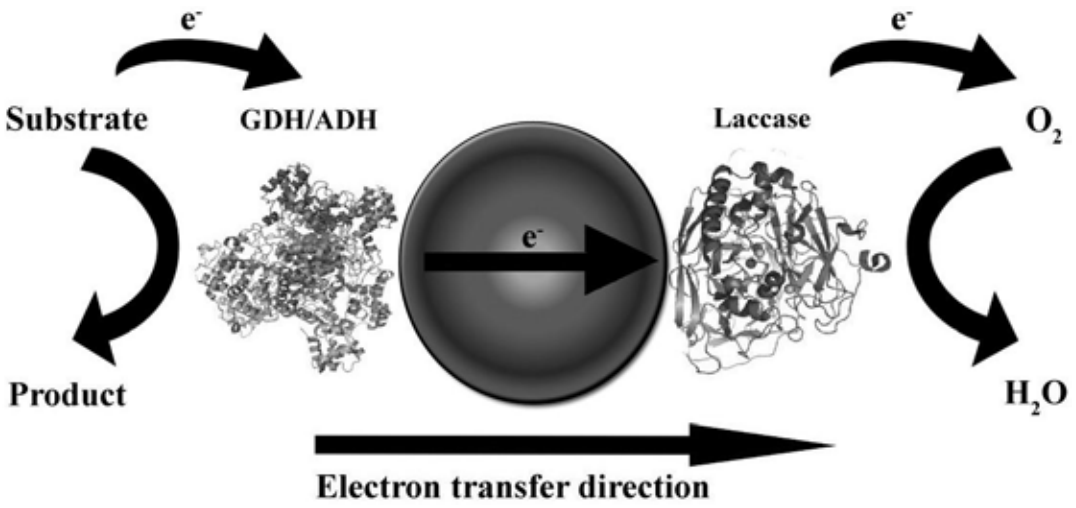

Fig. 1. Electron transfer in bienzymatic system

Magnetic iron oxide nanoparticles (MNP) were preapared by following the procedure described in the literature [1]. Ag-shell coating was performed by reduction of Ag^{+} on the surface of iron magnetic nanoparticles using citric acid [2]. UV/VIS spectroscopy were used for nanoparticles characterization.

Lowry method and bovine serum albumin (BSA) as model protein were used to test the adsorption characteristics of MNP or SMNP.

Laccase and GDH were imobilized on the surface of MNP or SMNP by simple adsorption. The enzymatic activity of imobilized laccase was assayed spectrofotometically by measuring increase of absorbance at 414 nm of wavelength resulting from oxidation of 2,2'-azino-bis(3-ethylbenzothiazoline-6-sulphonic acid) (ABTS) and of imobilized GDH by measuring decrease of absorbance at 600 nm of wavelength resulting from reduction of phenazine methosulfate (PMS) and 2,6-dichlorophenolindophenol (DCPIP) mixture in the presence of glucose.

Oxygen electrode was used to follow oxygen consumption by bienzymatic MNP or SMNP. The oxygen consumption rate in GDH/MNP/laccase system in the presence of glucose was $2.09 \cdot 10^{-5}$ μM/s. After addition of effective mediator ABTS, oxygen consumption rate increased and reached the value of $6.5 \cdot 10^{-5}$ μM/s. The increase of oxygen consumption rate after mediator addition shows that MNP is not effective electron transducer in the bienzymatic system. In order to increase the efficiency of the electron transducer in the system, silver-coated MNP were used. In GDH/SMNP/laccase system oxygen consumption rate in the presence of glucose was $3.26 \cdot 10^{-5}$ μM/s. After effective mediator ABTS addition, oxygen consumption rate almost unchanged and this shows that SMNP are more effective electron transducer than bare MNP.

[1] M. Magro, D. Baratella, G. Salviulo, K. Polakova, G. Zoppellaro, J. Tucek, F. Vianello. Core-shell hybrid nanomaterial based on prussian blue and surface active maghemite nanoparticles as stable electrocatalyst, Biosensors & Bioelectronics **52**, 159–65 (2014)
[2] K. Eskandari, H. Ghourchian. Performance of gold- and silver-coated magnetic nanoparticles as carriers for horseradish peroxidase, Journal of the Iranian Chemical Society **10(6)**, 1113-1121 (2013)

LIPOXYGENASE – FUTURE BIOCATALYST FOR POLYOL SYNTHESIS

Povilas Matusevičius, Rimantas Šiekštelė, Aurelija Sirvydaitė, Inga Matijošytė

Sector of Applied Biocatalysis, Institute of Biotechnology, Vilnius University
povilas.matusevicius@chf.stud.vu.lt

Biocatalysis is the use of enzymes (biocatalysts) to initiate or accelerate chemical reactions. Biocatalysts have several advantages over chemical catalysts, including the ability to carry out reactions under mild conditions with high stereo-, regioselectivity and to reduce enviromental waste. Thus, industrial interest in various enzymes as catalysts is constantly increasing [1, 2].

One of such industrially potential enzymes is lipoxygenase (LOX). It can be used in diverse industrial applications, such as food processing and synthesis of polyols from vegetable oil. Currently, LOX is widely used as co-oxidator of various carotenoid pigments. Additionally, lipoxygenase could be applied in the synthesis of biopolyols, which are commonly used in foam forms for mattresses and coatings, as well as in building insulations [3]. Besides possibility of comprehensive application, too little research have been done on LOXs. Lipoxygenase can be found in animals, plants, fungi and bacteria. However, currently only plant LOX is commercially available.

The aim of our work was to express LOX of bacterial origin in *E.coli*. We have extracted DNA from *P.aeruginosa* strain, which had LOX gene. LOX gene was amplified using PCR method, ligated with pLATE11 vector and transformed into *E.coli* DH5α and BL21(DE3) cells. Functional analysis on agar-starch plates indicated several clones with LOX activity. Analysis of protein expression by SDS-PAGE gel revealed that LOX was highly overexpressed, but in the insoluble fraction. Further research was focused on testing of other heterologous expression systems in order to obtain soluble enzyme. More detailed data will be presented during poster session.

[1] Illanes A. *Enzyme Biocatalysis. Principles and Aplications* (Springer Science, Chile, 2008).
[2] J. M. Choi et al., Industrial applications of enzyme biocatalysis: Current status and future aspects, Biotechnology Advances, 33, 1443-1454 (2015).
[3] R. Heshof et al., Industrial potential of lipoxygenases, Critical Reviews of Biotechnology, Jul 26, 1-10 (2015).

RECENT PROGRESS IN THE SYNTHESIS OF 7-MEMBERED SYSTEMS BY USING LITHIATED ALKOXYALLENES

Greta Utecht, Marcin Jasiński*

Faculty of Chemistry, University of Łódź, Tamka 12, 91-403 Łódź, Poland
gretautecht@gmail.com

Over the last decade lithiated alkoxyallenes have been demonstrated as an extremely versatile C3 building blocks for the preparation of various heterocyclic systems of biological importance.[1] For example, a series of enantiopure oxepane derivatives were prepared *via* [3+3] cyclisation of chiral nitrones and alkoxyallenes followed by Lewis acid-mediated cyclisation protocol.[2] Here we report on recent progress in the synthesis and structural studies on novel polyfunctionalized 7-membered systems, namely septanosides and septitols readily available in several steps starting with methoxyallene anion and carbohydrate-derived substrates as a chiral pool.[3]

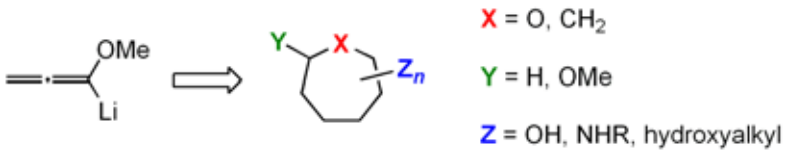

Fig. 1. Polyfunctionalized 7-membered systems

Financial support by the Ministry of Science and Higher Education (Republic of Poland; grant Iuventus Plus no IP2014 017173) is gratefully acknowledged.

[1] Zimmer, R.; Reissig, H.-U. Alkoxyallenes as building blocks for organic synthesis *Chem. Soc. Rev.* **43**, 2888-2903 (2014).
[2] (a) Bouché, L.; Kandziora, M.; Reissig, H.-U. Synthesis of new enantiopure poly(hydroxy)aminooxepanes as building blocks for multivalent carbohydrate mimetics *Beilstein J. Org. Chem.* **10**, 213-223 (2014); (b) Salta, J.; Reissig, H.-U. Synthesis of divalent carbohydrate mimetics by reductive amination with enantiopure 1,2-oxazines as precursors *Synthesis* **47**, 1893-1898 (2015).
[3] (a) Jasiński, M.; Utecht, G.; Fruziński, A.; Reissig, H.-U. Three-step synthesis of 3-aminoseptanoside derivatives by using lithiated methoxyallene and δ-siloxynitrones *Synthesis* doi:10.1055/s-0035-1560398 (2016); (b) Wojtala, K.; Utecht, G.; Jasiński, M. *unpublished results*.

SYNTHESIS AND EVALUATION OF CATALYTIC ACTIVITY OF 2-(AMINOALKYL)AZIRIDINE DERIVATIVES

Szymon Jarzyński, Stanisław Leśniak*, Michał Rachwalski

Faculty of Chemistry, University of Łódź, Tamka 12, 91-403 Łódź, Poland
szymonjarzynski@wp.pl

Enantiopure compounds are interesting for synthetic organic chemists due to the importance of chirality in industrial sectors (e.g. pharmaceuticals and food). So far, enantioselective carbon–carbon bond formation using organozinc reagents is commonly used in the synthesis of chiral non-racemic compounds. As an example, the asymmetric addition of alkynylzinc to carbonyl compounds is highly useful in the synthesis of chiral propargyl alcohols, which are important building blocks for the preparation of various natural and biologically active products.[1,2]

Here we presented the synthesis and applications of new optically pure 2-(aminomethyl)aziridine derivatives. These compounds were obtained from the corresponding chiral ester of aziridinyl-2-carboxylic acid. The next step of the proposed synthesis is the reaction with the corresponding amines in the presence of trimethylaluminum ($AlMe_3$) in order to synthesize tertiary amides. The desired optically pure 2-(aminomethyl)aziridine derivatives were obtained via reduction in the presence of triethoxysilane and zinc acetate. We examined a series of chiral aziridine catalysts in the stereocontrolled addition of diethyl- and phenylethynylzinc to various aldehydes and asymmetric 1,4-addition of diethylzinc to enones.

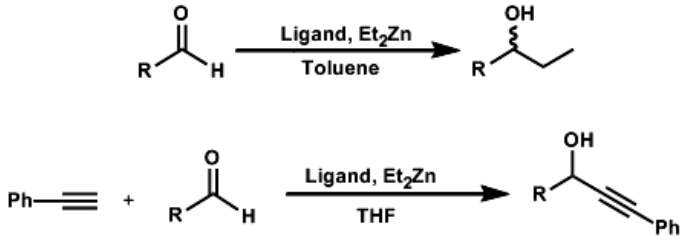

Fig. 1. Asymmetric addition of diethyl- and phenylethynylzinc to various aldehydes

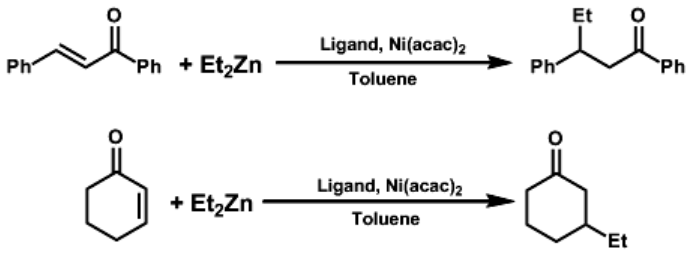

Fig. 2. Asymmetric 1,4-addition of diethylzinc to enones

Acknowledgement: *Financial support by the National Science Center (Poland; PRELUDIUM grant no. 2014/15/N/ST5/02897) is gratefully acknowledged.*

[1] S. Jarzyński, S. Leśniak, A. M. Pieczonka, M. Rachwalski, N-Trityl-aziridinyl alcohols as highly efficient chiral catalysts in asymmetric additions of organozinc species to aldehydes *Tetrahedron: Asymmetry* **2015**, *26*, 35–40.
[2] S. Jarzyński, M. Rachwalski, A. M. Pieczonka, Z. Wujkowska, S. Leśniak, Highly efficient conjugate additions of diethylzinc to enones promoted by chiral aziridine alcohols and aziridine ethers, *Tetrahedron: Asymmetry* **2015**, *26*, 924–927.

AMINOPHOSPHONATES BEARING PYRENE MOIETY SYNTHESIS, FLUORESCENT AND CYTOTOXICOLOGICAL PROPERTIES

Maria Rodriguez Moya[1], Anna Wrona Piotrowicz[1], Jarosław Lewkowski[1], Janusz Zakrzewski[1], Renata Kontek[2]

[1]Department of Organic Chemistry, Faculty of Chemistry, University of Lodz, Tamka 12, 91-403 Lodz
[2] Laboratory of Cytogenetics; Department of General Genetics, Molecular Biology and Plant Biotechnology, Faculty of Biology and Environmental Protection, University of Lodz, Banacha 12/13, 90-237 Lodz
mrm_chem@wp.pl

Derivatives containing aminophosphonate pyrene system substituted in position '1' have been described only twice in the chemical literature[1,2].
In this communication, we would like to report the preparation of a series of amino(1-pyrenyl)methylphosphonates, and to discuss fluorescence and cytotoxicological properties, which seem to be very interesting.

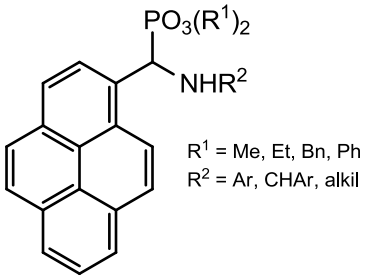

Fig.1. Derivatives containing aminophosphonate pyrene system

The influence of a series of derivatives on two colon cancer cell lines HT29 and HCT116 was investigated. For comparative reasons, the influence of these compounds on normal lymphocytes was studied too.
The most interesting results were obtained for *N*-4-methoxyphenyl derivative, which was found to be cytotoxic for these two colon cancer cell lines (IC_{50} ~ 20 μM), but gave nearly no toxicity towards lymphocytes (IC_{50} ~ 230 μM).

Studies were founded by the National Centre of Science (NCN), grant no.2014/13/B/NZ9/02418

[1] H.R. Hudson et al., Phosphorus, Sulfur, Silicon, **2004**, 179, 1691–1709
[2] S.H. Jayaprakash et al., Phosphorus, Sulfur, Silicon, **2015**, 190, 449–460

SINTHESIS AND CHARACTERIZATION OF BARIUM SUBSTITUTED LANTHANUM MOLYBDATE AS AN OXIDE ION CONDUCTOR

Emilija Užpurvytė[1], Artūras Žalga[1], Dalius Petrulionis[2], Edvardas Kazakevičius[2], Algimantas Kežionis[2]

[1] Department of Applied Chemistry, Faculty of Chemistry, Vilnius University, Naugarduko Str. 24, LT-03225 Vilnius, Lithuania

[2] Faculty of Physics, Vilnius University, Saulėtekio al. 9, LT-10222 Vilnius, Lithuania

e.uzpurvyte@gmail.com

Oxide ion conductors are technologically important materials, essential for applications including oxygen sensors and pumps, membranes for oxygen separation, and solid oxide fuel cells. Currently, the most commonly used materials are based on stabilized zirconia; however, one of the main limiting factors associated with their use is their relatively low oxide ion conductivity below 1000 °C [1]. As a consequence, the need for new materials with analogous conductivities, i.e., in the range of 10^{-1} S cm^{-1}, at lower temperatures (600-700 °C) is highly desirable in order to make them technologically useful. A strong contribution in this respect has been recently given by the discovery of a new oxygen ion conductor material of formula $La_2Mo_2O_9$, also known as LAMOX.

This compound exhibits a first-order phase transition from the nonconductive monoclinic phase (α) to the highly conductive cubic phase (β) at around 580 °C with the latter phase having an ionic conductivity of 6×10^{-2} S cm^{-1} at 800 °C [2]. However, pure $La_2Mo_2O_9$ presents some limitations for its potential application as solid electrolyte due to a phase transition that causes a drastic drop in the conductivity below 833 K and mechanical failure due to the high thermal expansion between the high and low-temperature polymorphs. In order to stabilize the β-polymorph, several series of compounds have been investigated, substituting La^{3+} by Bi^{3+}, Ca^{2+}, Ba^{2+}, K^{+}, and etc. [3]. Ba doping has resulted in both high temperature phase stabilization at room temperature and enhanced oxide ion conductivity compared to pure $La_2Mo_2O_9$ and hence could be a potential material for future applications [4].

In this work, the aqueous sol-gel synthesis method was successfully used for the preparation of Ba-La-Mo-O tartrate gel precursor using tartaric acid as a complexing agent. The crystalline compounds were calcined at 600, 800, 1000, 1200° C of temperatures. In order to investigate the surface morphology and crystal structure of the as-prepared Ba-La-Mo-O samples the SEM analysis and X-ray diffraction (XRD) were performed. Also to analyze thermal decomposition and vibrations of chemical bonds thermal analysis (TG/DTA) and Fourier transform infrared spectroscopy (FT-IR) were performed respectively.

[1] Ivana Radosavljevic Evans, Judith A. K. Howard, and John S. O. Evans, The Crystal Structure of r-$La_2Mo_2O_9$ and the Structural Origin of the Oxide Ion Migration Pathway, Chem.Matter 17, (2005) 4074-4077.

[2] Lorenzo Malavasi, HyunJeong Kim, Simon J. L. Billinge, Thomas Proffen, Cristina Tealdi, Giorgio Flor, Nature of the Monoclinic to Cubic Phase Transition in the Fast Oxygen Ion Conductor $La_2Mo_2O_9$ (LAMOX), J. AM. CHEM. SOC. 129, (2007) 6903-6907.

[3] D. Marrero-Lopez ´, D. Perez-Coll ´, J.C. Ruiz-Morales , J. Canales-Vazquez ´ , M.C. Mart´ ın-Sedeno, P. Nu ´nez , Synthesis and transport properties in $La_{2-x}A_xMo_2O_{9-\delta}$ (A = Ca^{2+}, Sr^{2+}, Ba^{2+}, K^{+}) series, Electrochimica Acta 52, (2007) 5219–5231.

[4] S. Basu, P. Sujatha Devi, H. S. Maiti, A potential low-temperature oxide-ion conductor: $La_{2-x}Ba_xMo_2O_9$, Applied Physics Letters 85, (2004) No. 16.

THE SYNTHESIS AND INVESTIGATION OF PYRAZOLE BETAINES

Laimdota Zizmare, Maris Utinans

Department of Applied Chemistry, Riga Technical University, Latvia
Laimdota.Zizmare_1@edu.rtu.lv

There is an ongoing search for new materials with nonlinear optical properties that could be applicable to microelectronics and optics. One of the approaches for obtaining such materials is to synthesize new chromophore with nonlinear optical features, effective second harmonics generation. We chose to look for such compounds in the row of pyrazole - pyridinium betaines.

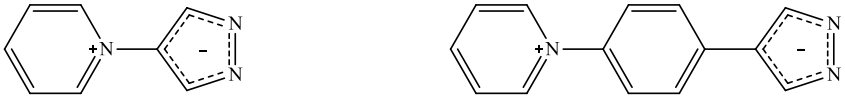

1 **2**

Fig. 1. Pyrazole - pyridinium inner salts without and with a phenylene bridge

Although quantum chemical calculations of such structures **1** and **2** were made earlier [1], the compounds had not been synthesized so far (we have found only some synthesis of similar pyridinium-pyrazole salts [2, 3], but not in betaine forms). Quantum chemical calculations show that compounds possess the necessary prerequisites for exhibiting efficient second harmonic generation - large dipole moment changes transitioning from the ground state to excited state, strong localization of HOMO and LUMO, small overlapping of the orbitals and considerable hyperpolarizabilities (β_{static}=19,8·10^{-30} esu (for **1**) and 114,4·10^{-30} esu (for **2**)).

The starting materials – 4-nitropyrazole, 3,5-dimethyl-4-nitropyrazole and 4-(4-nitrophenyl)pyrazole were synthesized by already known methods. The subsequent reduction of nitro- derivatives to amino- compounds were carried out with zinc in acetic acid, but the product yields were not quite high. Amino- derivatives were obtained by reduction with hydrogen in the presence of a palladium catalyst with almost quantitative yields.

The 4-aminopyrazole, 3,5-dimethyl-4-aminopyrazole and 4-(4-aminophenyl)pyrazole in reactions with 2,4,6-triphenylpyrilium perchlorate forms 2,4,6-triphenyl-1-(pyrazol-4-yl)pyridinium, 2,4,6-triphenyl-1-(3,5-dimethylpyrazol-4-yl)pyridinium and 2,4,6-triphenyl-1-(pyrazol-4-yl(1,4-phenylene))pyridinium perchlorates that further gives betaines **3**,**4** by treating them with base. A similar reactions takes place with 2,4,6-trimethylpyrilium tetrafluoroborate.

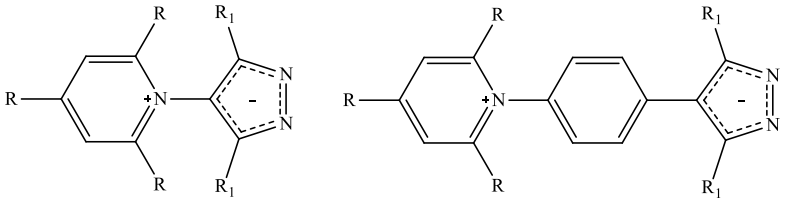

3 **4**

R = H, Me, Ph; R_1 = H, Me

Fig. 2. Target compounds

We also have investigated the 4-aminopyrazole, 3,5-dimethyl-4-aminopyrazole and 4-(4-aminophenyl)pyrazole reactions with 1-(2,4-dinitrophenyl)pyridinium bromide using Zincke reaction [4] and corresponding 1-(pyrazol-4-yl)pyridinium, 1-(3,5-dimethylpyrazol-4-yl)pyridinium and 1-(pyrazol-4-yl(1,4-phenylene))pyridinium bromides were obtained and converted to betaines **3**,**4**.

The synthesized betaines are orange to red colored crystalline substances, well soluble in alcohols and other polar solvents but scarcely soluble in hexane and other non-polar hydrocarbons. The NLO properties and influence of substituents and bridge in these betaines are under investigation.

[1] M. Utinans, O. Neilands. Quantum chemical calculations, synthesis and properties of novel organic materials with the photo induced intermolecular electron transfer and giant change of the electric dipole moment in the excited state, Advanced Materials for Optics and Electronics **9**, 19-25 (1999).
[2] A. R. Katritzky, B. Agha, G. Z. de Ville. Spectroscopic Elucidation of Pseudo-Base Formation from Benzo[8,9]quinolizino[4,5,6,7-*fed*]phenanthridridyliums, Organic Magnetic Resonance **vol.21, Nr.11**, 649-656 (1983).
[3] A. R. Katritzky, B. Agha, G. Z. de Ville, E. Lunt, M. I. Knyazanskii, Ya. R. Tymyanskii, A. I. Pyshchev. Phtocyclization of 1,2-diaryl- and Photobicyclization of 1,2,6-triarypyridinium cations, Chemistry of Heterocyclic Compounds N.Y. **vol.20, Nr.11**, 1245-1254 (1984).
[4] Sh. Kunugi, T. Okubo, N. Ise. A Study on the Mechanism of the Reaction of *N-(* 2,4-Dinitrophenyl)-3-carbamoylpyridinium Chloride with Amines and Amino Acids with Reference to Effect of Polyelectrolyte Addition, Journal of the American Chemical Society **vol.98, Nr.8**, 2282-2287 (1976).

A NOVEL AND BRIEF SYNTHESIS OF 1,7-DIOXASPIRO[5.5]UNDECANE (OLEAN)

Nektarios S. Kranidiotis, Konstantinos E. Grammatoglou and Ioannis K. Gallos

Department of Chemistry, Aristotle University of Thessaloniki, Greece
nkranidi@chem.auth.gr

The two enantiomeric spiroacetalic structures of 1,7-diaxospiro[5.5]undecane [(R)- and (S)- Olean] are the main components of the sex pheromone of the male and female olive fruit fly (*Bactrocera Oleae*), respectively [1]. Because of the economic, nutritional and social importance of olive oil for Mediterranean countries and the necessity of fighting against the olive fruit fly, the main enemy of its production, with efficient and ecological methods it is important, on the one hand, to develop advanced trapping and pest control using pheromones, on the other hand, to develop new, low cost and short synthetic methods –as far as possible enantioselective- of olean [2].

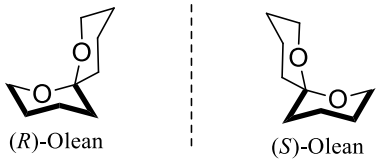

Fig. 1. Enantiomeric structures of Olean

With those in mind, our group developed a new method of synthesis of (±)-Olean. Key-reaction in the synthesis of carbon skeleton of the target molecule, is olefin cross metathesis between commercially available heptadienol **2** and excess of commercially also available unsaturated ester **3**. The product **4**, which is formed in satisfactory yield, is readily converted to pheromone **1**, by a sequence of three routine reactions: catalytic hydrogenation of the double bonds, oxidation of the hydroxyl-group to ketone, methanolysis of the ester groups and spontaneous spiro-cyclisation.

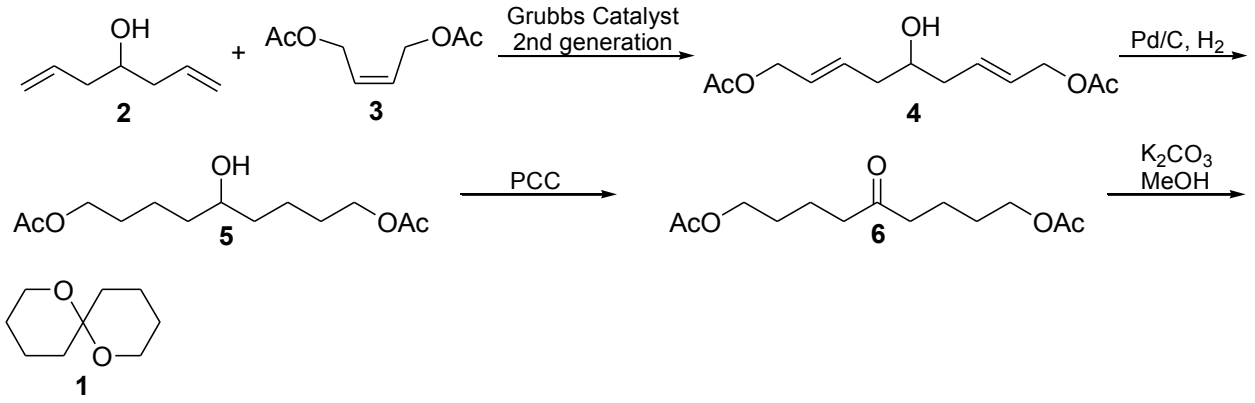

Fig. 2. Synthetic pathway of Olean

The advantages of the method are the brevity, overall yield and ease of the experimental synthetic procedures.

[1] Haniotakis, G., Francke, W., Mori, K., Redlich, H., Schurig, V. J. Chem. Ecol.,1986, 12, 1559.
[2] (a) Mori, K. Tetrahedron, 1989, 45, 3298. (b) Mori, K. Acc. Chem. Res, 2000, 33, 102..

B TRICHOTHECENE DISTRIBUTION IN LITHUANIA WHEAT GRAIN

Karina Stumbriene, Skaidre Suproniene, Simonas Sakalauskas, Povilas Svegzda, Renata Zvirdauskiene

Institute of Agriculture, Lithuania Reasearch Center for Agriculture ant Forestry
Instituto 1, Akademija, Kedainiai distr., Lithuania
Karina_stumbriene@yahoo.com

Fusarium head blight (FHB) is one of the major diseases of cereals causing quality reduction and yield losses. The situation has changed with *F. graminearum* establishing itself as a major FHB pathogen in Lithuania. Not so long time ago the major causal agents of FHB were *F. poae* and *F. avenaceum* in Lithuania and other Northern European countries. This species drift was accompanied by an increased contamination of grain with type B trichothecenes (TRI) - deoxynivalenol (DON), its acetylated derivatives (3ADON, 15ADON) and nivalenol (NIV). TRI are the main mycotoxins associated with (FHB) of wheat and other small-grain cereals with a worldwide economic and health impact. *Fusarium graminearum*, *F. culmorum*, *F. poae* and *F. sporotrichioides* are commonly identified as the cause of disease and trichothecene contamination. *Fusarium* fungi and mycotoxins studies are being carried out for about 10 years in the grain products in Lithuania. From the year 2010 observed bright *f. graminearum* kind of spread, and this spread is accompanied by the presence of DON, zearalenone increase in concentrations of toxins. The FHB appeared as the main disease of wheat in Lithuania in 2012. Until that time the chemotype diversity of FHB pathogens was not investigated.

The aim of the study is to detect *Fusarium* species which are able of producing B trichothecene (TRI) mycotoxins, determine their distribution in Lithuanian grain cereals. The study was conducted in 2014-2015. 118 spring wheat and 30 winter wheat samples collected in various locations all over Lithuania were tested for TRI and their producers. Of the species capable of producing DON, 3ADON, 15ADON and NIV, *F. graminearum, F. culmorum* and *F. poae* were detected. *F, graminearum* was dominant in spring wheat (found in 13.7% of grain, *F. poae* in 8.2% and *F. culmorum* in 0.4%), and *F. poae* – in winter wheat (2.9% of grain, *F graminearum* 2.2%, *F. culmorum* 0.2%). Species *F. graminearum* and *F. culmorum* were less common in organic than in conventional and extensive farms. The DNA quantity of these two species in grain had stronger correlational ties to DON quantity (*F.gr.* 0.414**, *F.c.* 0.783**) in grain internal infection determined by plating techniques (*F.gr.* 0.351**, *F.c.* 0.476**). This demonstrates the advantages of qPCR technique over the morphological plating method. FHB incidence and severity (scale acorting Engle et al., 2003) were evaluated at late milk – early dough (BBCH 77-83) stage in spring wheat fields all over Lithuania. DON concentration (ELISA method) and *Fusarium*-damaged (visual assessment) and -infected grain (agar plate method) were quantified after harvest.

Acknowledgments: The research was funded by the Lithuanian Research Council through the National Research Programme „Healthy and Safe FoodB, grant number SVE-09/2014 (TRICHEMOTIPAI)

PSEUDOMONAS SYRINGAE -PHYTOPATHOGENIC BACTERIA RESEARCH IN CEREALS

Kelpsiene J., Supronienе S.

[1] Institute of Agriculture, Lithuanian Researche Centre for Agriculture and Forestry
jurgita.kelpsiene@lzi.lt

Pseudomonas syringae pathovars are known to cause diseases of cereals: pathovars atrofaciens has been associated with the basal glume blotch, pv. syringae with dieback and leaf blight, and pv. japonica – with black node and stripe blight. Meteorological conditions, particularly low temperature and high humidity, play the major role in manifestation and severity of bacterial diseases of cereals. Under favorable conditions these bacterial diseases may amount for up to 50% of yield loss. Usually regarded as being of low importance in comparison to fungal diseases, *P. syringae* has not been studied in cereal crops of Lithuania, and the atypical for fungal diseases leaf spots and glume discolorations are found rather frequently on cereals in the fields.

Fig. 1,2. *Pseudomonas syringae* on damaged wheat leaf and grain

The disease affected plants were collected and isolation of *P*. syringae from damaged plant parts was attempted, with the resulting *Pseudomonas* isolates then classified by LOPAT tests: Levan production on sucrose medium, Kovacs' oxidase reaction, Pectolisity activity on potato slices or pectate gel, Arginine dihydrolase activity and hypersensitivity reacyion on Tobacco leaves.

Fig. 3,4,5 Arginine dihydrolase activity ,Pectolisity activity on potato slices and hypersensitivity reacyion on Tobacco leaves

From grain and leaf distinguish 168 isolates, they stored -80ºC to further research. There are currently performed biochemical studies with 149 (75% of spring wheat) bacterial isolates. The preliminary results indicate that approximately 14% of isolates are *Pseudomonas* spp. bacteria whose pathogenicity will be finally approved by the tobacco hypersensitivity test and infection of host plants.

Poster session 2

MICROMACHINING AND VALIDATION OF THE SCANNING ACOUSTIC MICROSCOPE SPATIAL RESOLUTION AND SENSITIVITY CALIBRATION BLOCK

Orestas Ulčinas[1], Tomas Tamulevičius[1,2], Linas Šimatonis[1], Sigitas Tamulevičius[1]
Egidijus Žukauskas[3], Regina Rekuvienė[3], Liudas Mažeika[3]

[1] Institute of Materials Science of Kaunas University of Technology, K. Baršausko St. 59, Kaunas LT-51423, Lithuania
[2] Department of Physics, Kaunas University of Technology, Studentų Str. 50, Kaunas LT-51368, Lithuania
[3] Prof. K. Baršauskas Ultrasound Research Institute of Kaunas University of Technology, K. Baršausko St. 59, Kaunas LT-51423, Lithuania
orestas.ulcinas@ktu.edu

Scanning acoustic microscopy (SAM) is used as a routine non-destructive test tool for different diagnostic examinations: detection of defects such as micro-cracks, delamination, disbonding, inclusions, subsurface features in materials such as pores and cracks. SAM can be operated in a wide frequency range from MHz to GHz. SAM measurement spatial resolution is diffraction limited by the wavelength of the acoustic wave and also depends on particular transducers geometry. Actual SAM spatial resolution can be determine by measuring calibrated lithographically formed microstructures in high acoustic impedance materials [1-3].

Laser micromachining is an attractive one step lithography technique for producing micro structures. Micromachining with ultrashort pulses (nanosecond, picoseconds, femtosecond) provides additional advantages, such as high flexibility and very small heat-affected zones, since the short pulse duration results in high peak power intensities and the material is removed by vaporization, instead of melting as in long-pulse or continuous laser material processing [4].

In this work the femtosecond laser micromachining technology that was applied to produce universal resolution and sensitivity calibration block for SAM is presented. Calibration block (Fig. 1) was micromachined in high acoustic impedance alumina ceramic substrates. Differently spaced (from 18 µm to 185 µm) lines of same widths and different widths (from 17 µm to 113 µm) but similar spacing lines were imposed in alumina ceramics employing Yb:KGW femtosecond laser ablation. The detailed analysis of the calibration block was performed employing optical and scanning electron microscopy as well as numerical simulation to show the feasibility of the device for calibration of SAM operating in a wide frequency range from 20 MHz to 230 MHz.

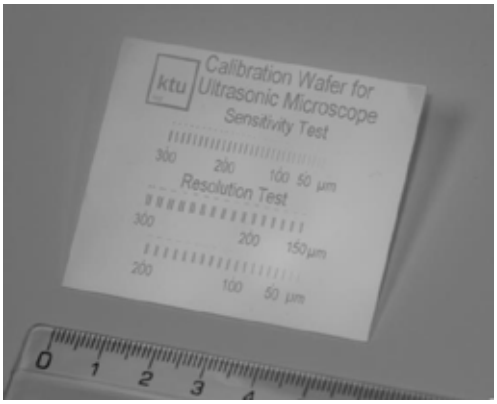

Fig. 1. Digital camera image of the prototype of the SAM resolution calibration block

This research was funded by Kaunas University of Technology interdisciplinary project

[1] Maev R., Fundamentals and Applications, 291 [ISBN 978-3-527-40744-6] (2008).
[2] Ramanathan et al., Conference paper: Electronic Components & Technology Conference, 1865 – 1868 [DOI: 10.1109/ECTC.2006.1645914] (2006).
[3] Ross R J., The materials Information Society, 653 [ISBN 978-1-61503-725-4] (2011).
[4] Hu W. et al., Journal of Manufacturing Science and Engineering, 132(1), 011009 7 p. [doi:10.1115/1.4000836] (2010).

IN SEARCH OF POLYMORPHISM: X-RAY ANALYSIS OF CRYSTAL STRUCTURES OF TOLUENE DERIVATIVES IN HIGH PRESSURE

Szymon Sutuła, Roman Gajda, Krzysztof Woźniak

Department of Chemistry, University of Warsaw, Poland
ssutula@chem.uw.edu.pl

Polymorphism can be described as the ability of substance to crystallize in different structures depending on the external conditions. More precise definition states that polymorphs are different in crystal structures, but melt giving identical liquids [1]. In our research we examined halogen derivatives of toluene in high pressure to determine how those compounds differ in their crystal structures and intermolecular interactions.

In our experiments we used Diamond Anvil Cell (DAC) to obtain high pressures. DAC creates homogeneous environment for an examined substance and requires very small quantities of the compound. This makes DAC an ideal tool for single-crystal X-ray diffraction experiments. However, as a consequence of reducing angular access to the sample, number of reflections that can be measured is reduced. Also, additional reflections coming from crystal structure of diamonds are collected.

Typical procedure of loading DAC (shown in Fig. 1) involves puting sample and a chip of ruby inside a small hole in a gasket. Then the sample is compressed by culets of two diamond anvils [2] that are pushed towards by screws that control the stability of pressure.

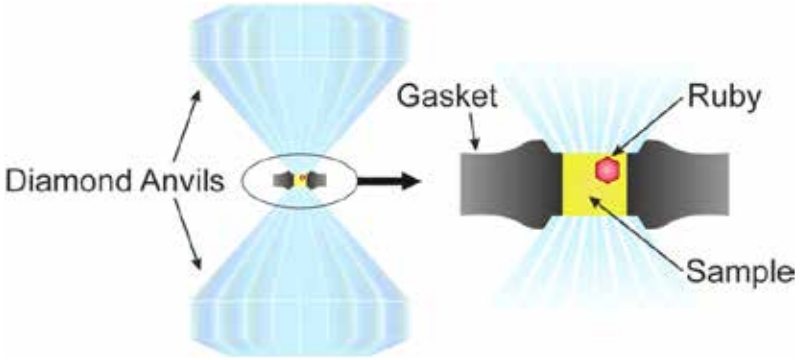

Fig. 1. Construction scheme of Diamond Anvil Cell

A chip of ruby that is loaded with a sample acts as a fluorescent pressure sensor. When illuminated by a laser, ruby fluoresces giving two R-line peaks. Shift of those peaks depends on the pressure inside the cell [3][4].

If sample is liquid under normal conditions, compressing results in polycrystallization of the sample. The next step is to raise the temperature up to the melting point so that there is only one crystallite left. Cooling the sample from that point results in growing a monocrystal inside DAC. Observing the sample between polarizer and analyzer gives a great insight into homogeneity of the crystals and allows for notification if any unwanted twinning occurs during cooling.

In our research we examined p-fluorotoluene, p-chlorotoluene, p-bromotoluene and p-iodotoluene behaviour in high pressure. We determined the structures they crystallize in sets of different pressures within the ranges of up to few GPa. Although in our research three of those compounds did not exhibit polymorphism, we managed to crystallize one of them in two different structures. We would like to discuss the results we obtained for the examined substances in high pressures with those that had already been achieved by low-temperature crystallization.

In all our experiments we used shorter wavelength (Ag Kα 0,56 Å) than those exploited in typical X-ray diffraction experiments (Mo Kα 0,71 Å and Cu Kα 1,54 Å). Shorter wavelength enables to collect more reflections in the reciprocal space and closer crystal planes may be measured, according to the Bragg's equation, Eq. (1).

$$n\lambda = 2d_{hkl}\sin\theta \tag{1}$$

[1] J. D. Dunitz, J. Bernstein, Disappearing Polymorphs, Acc. Chem. Res. **28**, 193-200 (1995)
[2] M. McMahon, High-Pressure Crystallography, Top Curr Chem **315**, 69-110 (2012).
[3] A. Chijioke, W. Nellis, A. Soldatov, I. Silvera, The ruby pressure standard to 150 GPa, J. Appl. Phys. **98** (2005).
[4] H. Yamaoka et al., Ruby pressure scale in a low-temperature diamond anvil cell, J. Appl. Phys. **112** (2012).

STRUCTURE OF PHENYL-TERMINATED SELF-ASSEMBLED MONOLAYERS WITH AMIDE GROUP REVEALED VIA SFG

Marija Špandyreva, Zenonas Kuodis, Ilja Ignatjev, Gediminas Niaura

Center for Physical Sciences and Technology, Lithuania
Marija.spandyreva@gmail.com

SAM on gold, resulting from the binding of thiols, are well-known examples of organized monolayers which enable one to functionalize surfaces and bind receptors in a controlled manner [1]. Sum frequency generation vibrational spectroscopy (SFG-VS) is powerful and versatile method for in-situ investigation of surfaces and interfaces. SFG was used to study self-assembled monolayers formed from 1-alkanethiols at Au surface. The resonant enhancement provides spectral information on surface characteristic vibrational transitions [2]. The results of the structural changes of MOPHE (N-(2-phenylethyl)-8-sulphanyloctanamide) (**Fig. 1.**) are presented and discussed. Data from the high-frequency spectral region, where C-H stretching vibrations take place, are discussed in this work.

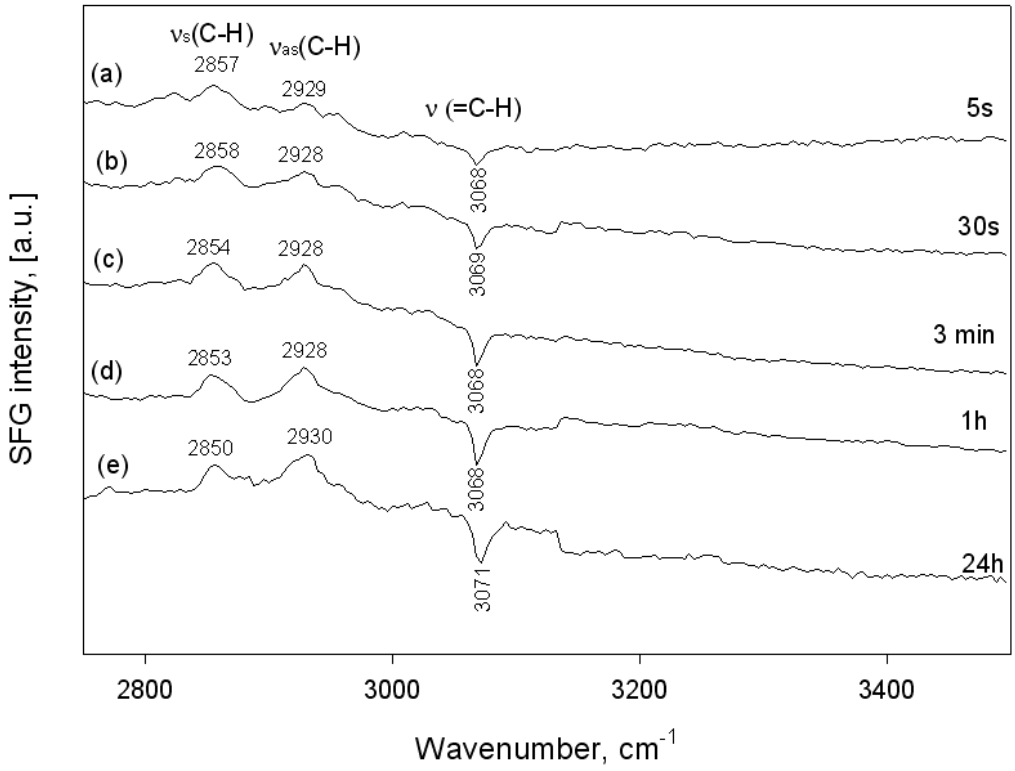

Fig. 1. Sum frequency generation vibrational spectroscopy spectra of self-assembled monolayers formed from MOPHE (N-(2-phenylethyl)-8-sulphanyloctanamide) by immersion of gold in ethanolic solution containing 1 mM MOPHE for (a) 5s, (b) 30s, (c) 3 min, (d) 1h, (e) 24h, at Au surface, revealing ordering of the phenyl rings C_6H_5 at interface as well as presence of hydrocarbon chain *gosh* defects.

MOPHE (N-(2-phenylethyl)-8-sulphanyloctanamide) monolayer on Au surfaces probed by SFG shows hydrocarbon chain *gauche* defects, which are characterized by the clearly observed band near 2850 due to the symmetric stretching vibration of methylene groups. An another band located at 2930 cm^{-1} corresponds to assymetric stretching vibration of CH_2. SFG spectra indicates that hydrocarbon chain defects remain after 24h of adsorption. Strong resonance near 3069 cm^{-1} belongs to stretching vibration ν(=C-H) of phenyl ring. Intensity of this band rapidly increases after 30 s of adsorption indicating formation of well-orederded structure at interface.

[1] M.Che, J.C.Vedrine, *Characterization of solid materials and heterogeneous catalysts. From structure to surface reactivity*. (Copyright Wiley-VCH Verlag GmbH & Co. KGaA, France, 2012)
[2] G.Vaicikauskas, G-J. Babonas, Z.Kuprionis, G.Niaura, V.Sablinskas., *Surface optical spectroscopy*. (TEV, Vilnius, 2008).

SIZE AND MORPHOLOGY DEPENDENCY ON UPCONVERSION OF $NaGdF_4$: Yb^{3+}, Er^{3+} NANOPARTICLES

Nadezda Traskina, Simas Sakirzanovas

Department of Applied Chemistry, Faculty of Chemistry, Vilnius University, Lithuania
nadezda.traskina@chf.stud.vu.lt

Upconversion nanoparticles (UCPNS) are a separate group of phosphors with a luminescence mechanism which is different from that of organic dyes and quantum dots [1]. The process consists of simultaneous emission of two or more photons and eventual emission of light in shorter wavelength than excitation wavelength [2]. Due to their potential for different applications varying from biological imaging to targeted drug delivery UCNS are a subject of a special interest in science. $NaGdF_4$: Yb^{3+}, Er^{3+} exhibits excellent upconversion fluorescence peaks in blue, green and red spectral areas under 980 nm IR laser excitation. Besides, as a Gd^{3+} -containing host, $NaGdF_4$ can be characterized by superior magnetic properties, making it a promising hmaterial for simultaneous optical and magnetic imaging [3].

For most applications in biological systems it is essential to produce the compounds with controllable size and narrow size distribution. It has been noted that synthesis conditions have a great influence on the physical properties of the final product [4]. The effects of reaction temperature and synthesis duration on the morphology and size were investigated. Luminescent properties of particles were determined by spectrofluorometer. Information about α and β(desired) phase composition was obtained through X-ray diffraction analysis. Size and dispersion of UCNPS was examined using scanning electron microscope. The luminescence intensity dependence on reaction temperature is illustrated in figure 1.

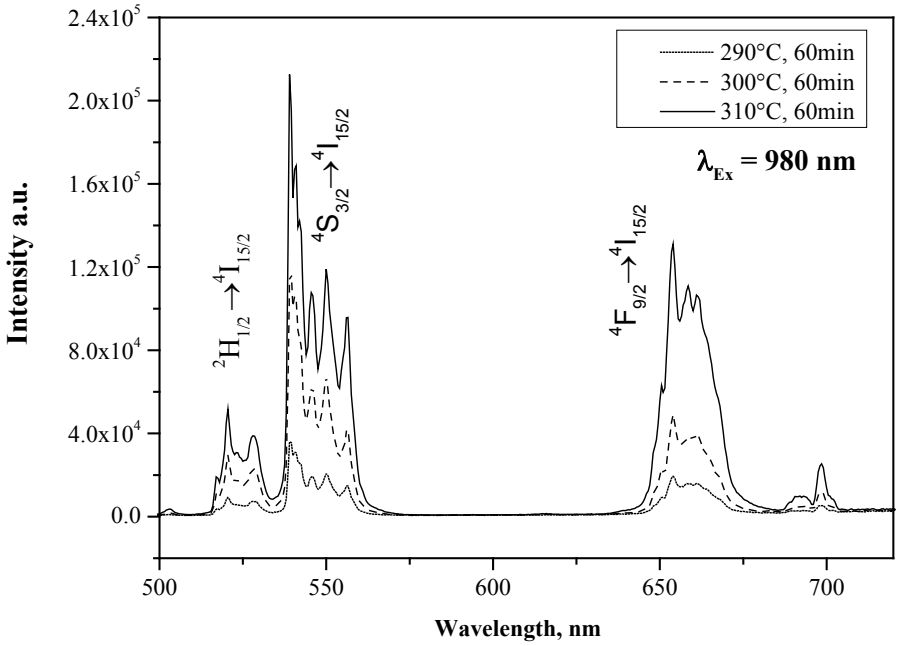

Fig. 1. $NaGdF_4$: Yb^{3+}, Er^{3+} luminescence intensity dependence on reaction temperature.

[1] Chao Zhang, Lingdong Sun et al., "Rare earth upconversion nanophosphors: synthesis, functionalization and application as biolabels and energy transfer donors". *Journal of Rare Earths* **28**, No. 6, p. 807 (Dec. 2010).
[2] Zhou, B.; et al. "Controlling Upconversion Nanocrystals for Emerging Applications". *Nature Nanotechnology* **10**: 924–936 (2015).
[3] Xu Wang, Jia-Tong Chen et al, "One-step solvotermal synthesis of targetable optomagnetic upconversion nanoparticles for in vivo bimodal imaging" *Anal. Chem*, ***85*** **(21)** 10225–10231 (2013)
[4]Fan Zhang "Photon Upconversion Nanomaterials", *Nanostructure Science and Technology* p.23 (2015)

ULTRAFAST TIME-RESOLVED STUDIES OF BETANIN PHOTOPHYSICS

Monika Wendel[1*], Stanislaw Nizinski[1], Dominika Szot[2], Dorota Prukala[3], Marek Sikorski[3], Slawomir Wybraniec[2], Gotard Burdzinski[1]

[1] Department of Physics, Adam Mickiewicz University in Poznan, Poland.
[2] Departmeny of Chemical Engineering and Technology, Cracow University of Technology, Poland
[3] Departmen of Chemistry, Adam Mickiewicz University in Poznan, Poland
monika.wendel@amu.edu.pl

Betanin (Fig. 1) is commonly used as a purple pigment (E-number E162) in pharmaceutical, food and cosmetic industries [1], located in plant vacuoles of *Caryophyllales*. Sun-screening function of betanin indicates its photoprotective role in plants [2]. Light absorption at λ ~ 535 nm results in the excitation of betanin to its first singlet excited S_1 state. Since betanin in the S_1 state is a short-lived species, and S_1 deactivation pathways are unknown, we applied femtosecond transient absorption spectroscopy to describe the mechanism and kinetics of betanin S_1 decay. Figure 1 shows that betanin in the S_1 state has distinctive $S_1 \rightarrow S_n$ and $S_1 \rightarrow S_m$ (n> m> 1) absorption bands at ca. 450 and 1220 nm, respectively [3]. The betanin S_1 state lifetime is very short (6.4 ps in water) due to highly efficient $S_1 \rightarrow S_0$ radiationless relaxation. Other S_1 state deactivation pathways as photoproduct or excited T_1 state formation are absent, while fluorescence of betanin is characterized by a very low quantum yield (0.0007 in H_2O) [3]. We suggest that the S_1 state decay is preceded by a strong change in geometry, since the S_1 lifetime is four times longer in viscous ethylene glycol (27 ps) in comparison to methanol (7.7 ps) [3]. Observed light-to-heat conversion in betanin supports its photoprotective role in plants.

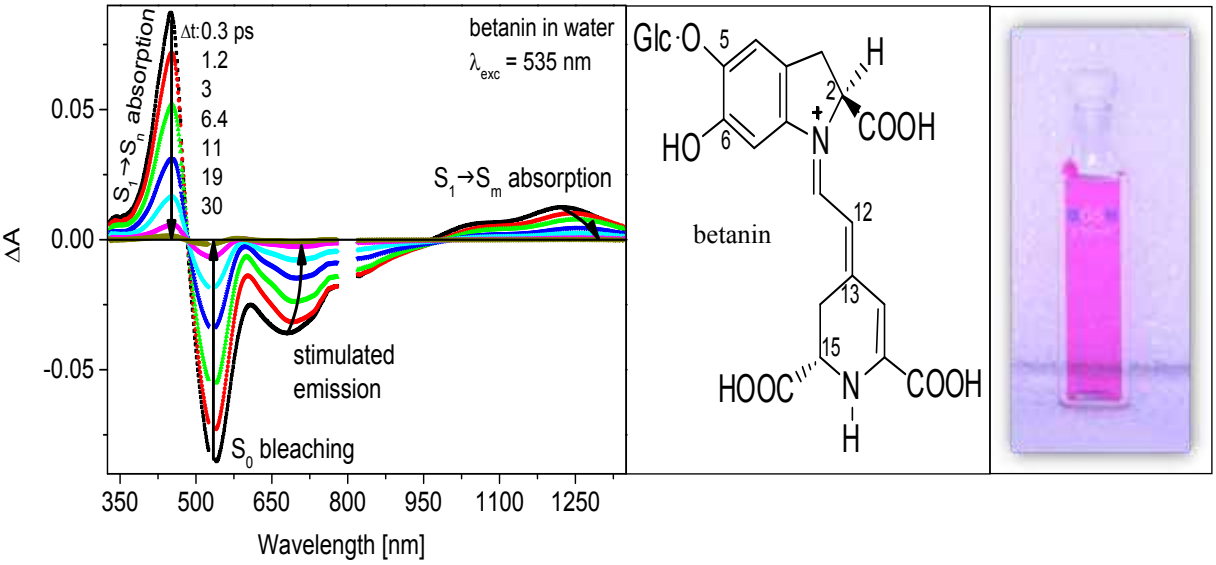

Fig. 1. UV-vis-NIR transient absorption spectra recorded for betanin in water over a 0.3 – 30 ps time window following photoexcitation at λ=535 nm.

[1] F. C. Stintzing and R. Carle, Functional properties of anthocyanins and betalains in plants, food, and in human nutrition, Trends in Food Science & Technology **15**, 19–38 (2004).
[2] G. Jain, K. S. Gould, Are betalain pigments the functional homologues of anthocyanins in plants?, Environmental and Experimental Botany **119**, 48–53 (2015).
[3] M. Wendel, S. Nizinski, D. Tuwalska et al., Time-resolved spectroscopy of the singlet excited state of betanin in aqueous and alcoholic solutions, Physical Chemistry Chemical Physics **17**, 18152-18158 (2015).

LUMINESCENCE AND LUMINESCENCE QUENCHING OF $K_2Bi(PO_4)(MoO_4):Sm^{3+}$ PHOSPHORS

Julija Grigorjevaite, Arturas Katelnikovas

Department of Analytical and Environmental Chemistry, Faculty of Chemistry, Vilnius University, Lithuania
arturas.katelnikovas@chf.vu.lt

$K_2Bi_{1-x}Sm_x(PO_4)(MoO_4)$ powder samples were prepared by conventional high temperature solid-state reaction. The stoichiometric amounts (Bi_2O_3, Sm_2O_3, MoO_3, K_2CO_3 and $NH_4H_2PO_4$) were mixed in the mortar employing acetone as grinding media. The obtained powder was transferred to the porcelain crucible and annealed at 600 °C for 12 h in air. The calcination procedure was repeated another two times. [1]

The structural, morphological and optical characteristics of the compounds were investigated by powder scanning X-ray diffraction (XRD), electron microscope (SEM) analysis and UV-Visible spectroscopy. The phase purity was confirmed by powder XRD measurements (Fig. 1a.). Isostructural compounds of $K_2Bi(PO_4)(MoO_4):Sm^{3+}$ are obtained at any Bi^{3+}/Sm^{3+} ratio what is in line with the Vegard's law.

The reflection, excitation and emission spectra of the single phase compounds were measured and analyzed (Fig. 1b). The temperature dependent emission spectra and decay curves in 77 – 500 K temperature interval were also recorded and discussed.

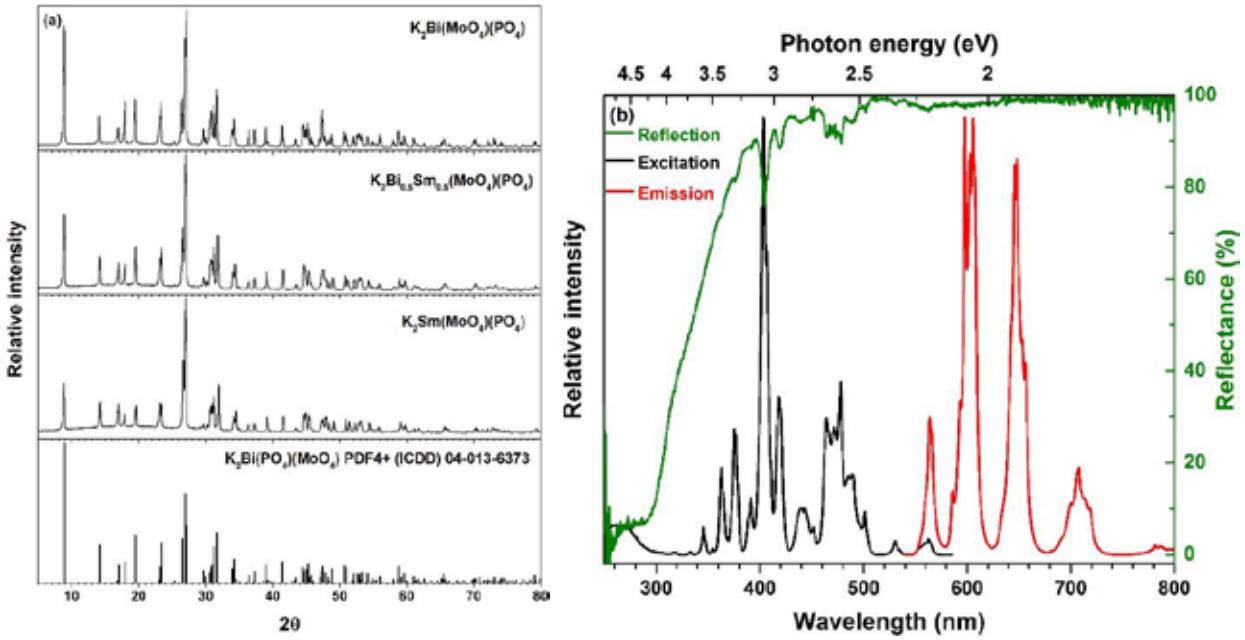

Fig. 1. (a) XRD patterns of samples with different Bi^{3+}/Sm^{3+} ratios; (b) reflection, emission (λ_{ex} = 404 nm) and excitation (λ_{em} = 598 nm) spectra of $K_2Bi(PO_4)(MoO_4)$: 5% Sm^{3+}.

Moreover, colour points, luminous efficacies (LE) and decay times were also calculated. The external quantum efficiency of the synthesized phosphors was calculated employing Eq. (1):

$$QE = \frac{\int I_{em,sample} - \int I_{em,BaSO_4}}{\int I_{abs,BaSO_4} - \int I_{abs,sample}} \times 100\% \qquad (1)$$

Samples were red emitting and showed moderate quantum efficiencies.

[1] H. Huang, G. Chen, S. Wang, L. Kang, Z. Lin, Y. Zhang. Mater. Res. Bull., 51 (2014) 455-459.

DETERMINING THE FLUORESCENCE QUANTUM YIELD OF A PERYLENEDIIMIDE DERIVATIVE BY THREE DIFFERENT METHODS

Austėja Bukauskytė[1,2], Renata Karpič[2]

[1] Faculty of Physics, Vilnius University, Saulėtekio Ave. 9-III, LT-10222 Vilnius, Lithuania
[2] Center for Physical Sciences and Technology, Savanorių 231, Vilnius LT-02300, Lithuania
bukauskyte.austeja@gmail.com

Organic materials with fluorescence in visible spectrum are investigated extensively due to their potential application in organic optoelectronics. For instance, perylenediimides (PDIs) are materials of high photo and thermal stability, high fluorescence quantum yields and chemical inertness. Therefore, they can be used in many organic optoelectronics devices like organic light emitting diodes, solid-state lasers and photovoltaic devices [1].

The fluorescence properties of a material may be characterized by determining the fluorescence spectra, lifetime and quantum yield. The fluorescence quantum yield is the ratio of the number of photons absorbed to the number of photons emitted through fluorescence. This parameter is important when choosing a material for organic optoelectronics applications. While measurements of the absolute quantum yield require sophisticated methods and instrumentation, one of the easiest ways to determine quantum yield is the comparative method [2]. The essence of this method is comparisonof absorption and fluorescence spectra between a test sample and a standard sample with known fluorescence quantum yield.

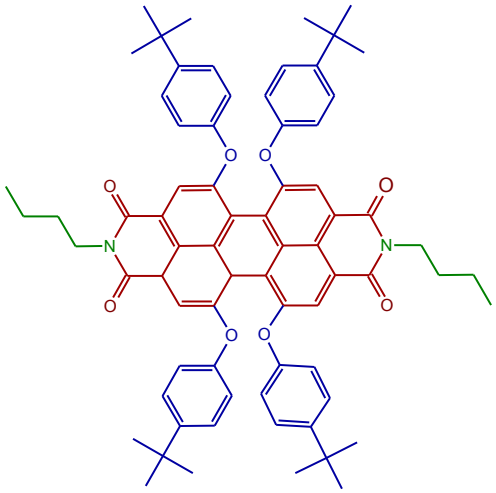

Fig.1 Molecular structure of PDI7

In this research, the fluorescence quantum yields of PDI7in two different solvents (ethanol and chloroform) were determined, employing three different methods. Molecular structure of this perylenediimide derivative is shown in Figure 1. Fluorescein, rhodamine 6G and sulforhodamine were used as standards. Furthermore, radiative and non-radiative fluorescence lifetimes of PDI7 in chloroform were determined and presented.

[1] E. M. Calzado, J. M. Villalvilla, P. G. Boj, J. A. Quintana, R. Go´mez, J. L. Segura, M. A. Dı´az-Garcı´a,Effect of Structural Modifications in the Spectral and Laser Properties of Perylenediimide Derivatives, J. Phys. Chem. C, **111**, 13595-13605 (2007).
[2] J. R. Lakowicz Principles of Fluorescence Spectroscopy 3rd ed., Springer Science+Business Media, LLC, (2006)

FLUORESCENCE DYNAMICS OF GLUCOSE OXIDASE

Raminta Mazėtytė[1,2], Renata Karpič[2], Urtė Bubnienė[3], Arūnas Ramanavičius[2,3]

[1] Faculty of Physics, Vilnius University, Saulėtekio Ave. 9-III, LT-10222 Vilnius, Lithuania
[2] Institute of Physics, Center for Physical Sciences and Technology, A. Goštauto Ave 11, Vilnius LT-01108, Lithuania
[3] Department of Physical Chemistry, Faculty of Chemistry, Vilnius University, Naugarduko Str. 24, LT-03225 Vilnius, Lithuania
raminta.mazetyte@ff.stud.vu.lt

Nowadays the best-known and the most common biosensing systems are glucose biosensors. They can accurately detect blood free glucose in a short period of time – it is very important for people with diabetes [1]. The active part of the biosensor is glucose oxidase (GOx) enzyme immobilized on surface of the electrode. GOx is a flavin adenine dinucleotide (FAD) containing glycoprotein. FAD is involved in enzymatic redox reactions and determines the enzyme's activity [2]. Glucose oxidase enzyme can exist in several different spatial conformations within its active site FAD can have "twisted" (stacked) or "planar" (open) structure [3]. In a planar configuration, flavins have a long lifetime (in nanoseconds), except for the stacked conformation of FAD, where intramolecular electron transfer between the flavin isoalloxazine ring and the adenine moiety takes shorter lifetime periods.

Spectroscopic properties of glucose oxidase (GOx) and flavin adenine dinucleotide (FAD) were investigated. The purpose of this research was to evaluate absorption and fluorescence spectra changes. The steady – state absorption and fluorescence spectra of GOx and FAD are shown in figure 1.

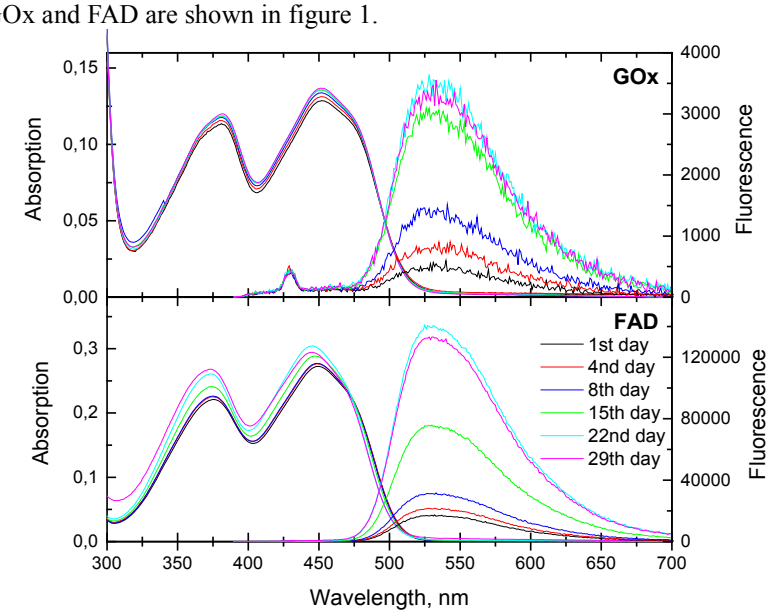

Fig.1. Fluorescence and absorption spectra of GOx and FAD.

GOx exhibits two absorption bands, which are attributed to FAD absorption bands, with peaks at 380 nm and 450 nm, which are assigned to the $S_2 \leftarrow S_0$ and $S_1 \leftarrow S_0$ and transitions, respectively. These transitions are ascribed to the π–π^* transition along the three cycles of the isoalloxazine ring in FAD.

GOx fluorescence spectra have two bands at 450 nm and 530 nm. During this study we found that GOx enzyme fluorescence band at 530 nm belongs to coenzyme FAD fluorescence [4]. The increase of GOx fluorescence, which is due to the fact that the enzyme has changed its structure and denatured [2], was visible in 29 day measurement period.

GOx fluorescence lifetimes have been measured at fixed 450 nm and 530 nm wavelengths. The fluorescence decay kinetics were well approximated by a two-exponential model. Average lifetimes of GOx and FAD at 530 nm were coincided and changed from 2,7 ns to 4,5 ns. This confirms that the GOx fluorescence at 530 nm wavelength is determined by FAD fluorescence.

[1] Eun-Hyung Yoo, Soo-Youn Lee, Glucose Biosensors: An Overview of Use in Clinical Practice, Sensors (2010), 10, 4558-4576.
[2] V. Leskovac, S. Trivic, G. Wohlfahrt, J. Kandrač, D. Peričin, Glucose oxidase from Aspergillus niger: the mechanism of action with molecular oxygen, quinones, and one-electron acceptors, The International Journal of Biochemistry & Cell Biology 37 (2005) 731–750.
[3] Y. Kao, Ch. Saxena, T. He, L. Guo, L. Wang, A. Sancar, D. ZhongA, Ultrafast Dynamics of Flavins in Five Redox States, J. Am. Chem. Soc., (2008), 130 (39), pp 13132–13139.
[4] A. Ramanavicius, N. Ryskevic, A. Kausaite-Minkstimiene, U. Bubniene, I. Baleviciute, Y. Oztekin, A. Ramanaviciene Fluorescence study of glucose oxidase self-encapsulated within polypyrrole, Sensors and Actuators B 171– 172 (2012) 753– 759.

SERS TECHNIQUE OPTIMIZATION FOR CULTURAL HERITAGE RESEARCH

Liudmila Trotsiuk, Yauheniya Korza, Anna Matsukovich

B.I.Stepanov Institute of Physics, National Academy of Science of Belarus, Belarus
l.trotsiuk@ifanbel.bas-net.by

Surface Enhanced Raman spectroscopy (SERS) offers efficient techniques for material science. In recent years, a new application of SERS for cultural heritage and art pigment studies was developed [1]. Due to the possibility to get information about chemical structure of the objects under investigation, SERS is a powerful tool for pigments and dyes identification and hence for dating definition in authenticating of artworks. Moreover, the identification of art components is particularly helpful for conservators who can use the information for national treasures preserve.

SERS techniques are widely used for organic dyes identification. Recently SERS have been successfully applied for inorganic pigment identification in the real objects of cultural heritage [2]. Paints represent themselves the multiphase system of binding media and pigment microcrystals. The following sample preparation technique was proposed early [2] to provide close interaction between pigment microcrystals and gold nanoparticles: to extract pigments from the binding media via washing of paints in alcohol and chloroform under the slight heating. To avoid this stage of sample preparation, organic sol of gold nanoparticles was proposed to use in the present study due to its ability to dissolve the binding media.

For the SERS-analysis we used the organic sol of gold nanoparticles in toluene which has been prepared via Brust-Shiffrin method [3]. Optical density spectrum of the obtained Au-sol is characterized with the maximum on 525 nm. The microfragments of paints (not more than 1 μg) safety taken from the canvas painting "Portrait of young man" was used in the experiment as the analyte.

SERS-spectrum obtained in 100-950 cm^{-1} spectral range (Figure 1) is characterized with the high signal-to-noise ratio, while the Raman spectrum in the absence of gold nanoparticles have not been recorded at all. The peaks at 223, 289, 406, 491, 603, 654 cm^{-1} could be ascribed to ochre (Fe_2O_3+clay minerals).

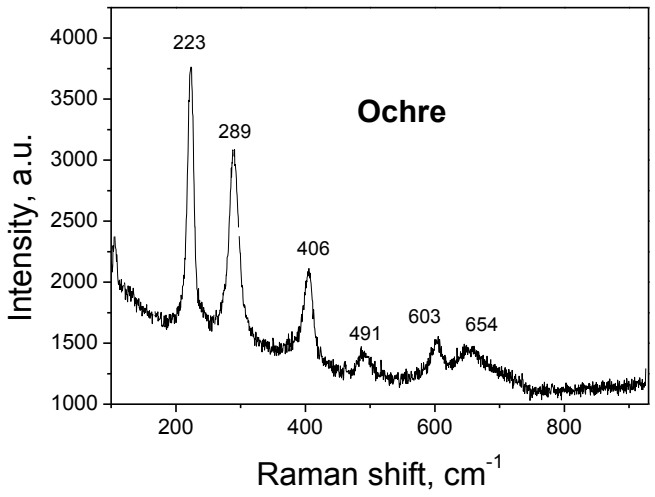

Fig. 1 – SERS spectrum of ochre taken from the canvas painting "Portrait of young man"

So, gold organic sol allows to simplify the sample preparation procedure for the SERS-identification of the art pigments in the Cultural heritage objects. The authors are grateful to Dr. E. Shabunya-Klyachkovskaya and Dr. O. Kulakovich for fruitful discussion as well as The National Art Museum of the Republic of Belarus for sample provided.

[1] K. Chen, M. Leona, T. Vo-Dinh, Surface-enhanced Raman scattering for identification of organic pigments and dyes in works of art and cultural heritage material, Sensor Review. 27(2), 109–120 (2007).
[2] E. Shabunya-Klyachkovskaya O. Kulakovich, Surface enhanced Raman spectroscopy as the ultrasensetive technique for inorganic art materials identification, ESRARC'15, Trnava, Proceedings book , 63-65 (2015).
[3] M. Brust, D. J. Schiffrin et al., Self-Assembled Gold Nanoparticle Thin Films with Nonmetallic Optical and Electronic Properties, Langmuir 14, 5425-5429 (1998).

DETECTION OF L–CYSTINE IN AQUEOUS SOLUTIONS BY MEANS OF SERS SPECTROSCOPY

Vida Daukšaitė, Milda Pučetaitė

Faculty of Physics, University of Vilnius, Lithuania
vida.dauksaite@ff.stud.vu.lt

Metal nanoparticles' (NPs) interactions with various molecules have become an attractive field of research in spectroscopy from both theoretical and practical view due to their adjustable properties and thus wide range of applications. In this work l-cystine molecule (Fig. 1) and its interactions with NPs were analyzed due to its importance in human body (it is necessary for the formation of hair, nails and skin). On the other hand, high cystine concentration in blood, kidneys could cause several pathological problems. The surface enhanced Raman scattering (SERS) spectroscopy was chosen as the main method to analyze l-cystine molecule as SERS is capable to detect molecules at low concentrations.

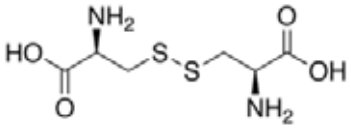

Fig. 1 Structural view of l-cystine molecule.

The main interest of this work was to find the best l-cystine detection conditions in aqueous solutions using three different colloidal solutions - Leopold-Lendl, Lee-Meisel silver and gold - as well as applying different metal NP of various shapes. Moreover, l-cystine samples were prepared in two ways – aqueous and dried.

From the carried out experiments it was found that in aqueous solutions the enhancement of Raman scattering of l-cystine molecule depends on solution concentration – the larger the concentration, the lower is the enhancement (Fig. 2). This could be explained by the fact that the higher the concentration of l-cystine molecules, the relatively less of them adsorb on the surface of metal NPs. Moreover, it was observed that S-S stretching band (between 490 cm^{-1} – 510 cm^{-1} Raman shift) exists in SERS spectra of aqueous solution samples, whereas in SERS spectra of dried solutions (Fig. 3), the S-S stretching band was not detected – cystine cleaved into cysteine molecules [1].

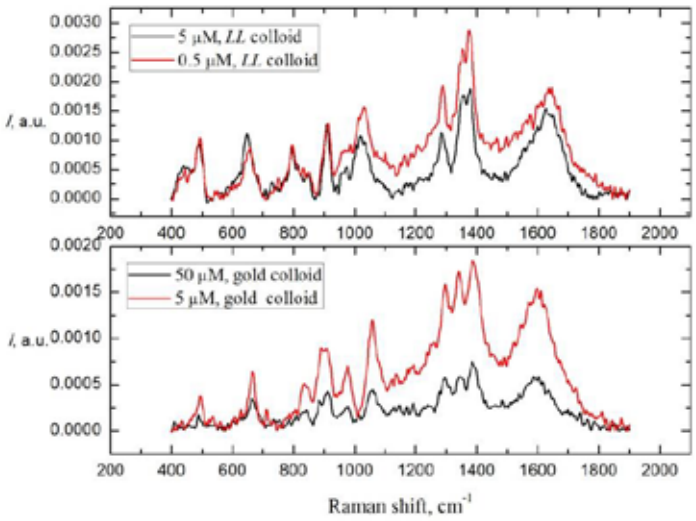

Fig. 2 SERS spectra of l-cystine solutions of 5 μM and 0.5 μM concentrations, recorded using Leopold-Lendl colloid (upper graph) and SERS spectra of l-cystine solutions of 5 μM and 5 μM concentrations, recorded using gold colloid (lower graph).

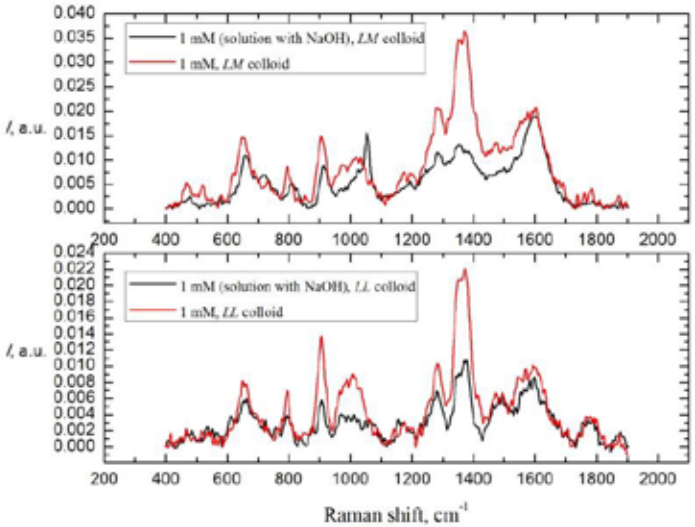

Fig. 3 SERS spectra of l-cystine solutions of 1 mM concentration, recorded using Lee-Meisel colloid with NaOH and without it (upper graph) and SERS spectra of l-cystine solutions of 1 mM concentration, recorded using Leopold-Lendl colloid with NaOH and without it (lower graph).

[1] E. Lo, M. Ghomi, and S. Sanchez-cortes, "Stability of the Disulfide Bond in Cystine Adsorbed on Silver and Gold Nanoparticles As Evidenced by SERS Data´ Herna n," *J. Phys. Chem. C*, vol. 117, 2012.

CONFORMATIONAL ANALYSIS OF TETRAHYDROFURAN BY MEANS OF FT-IR MATRIX ISOLATION SPECTRA – HOT NOZZLE EXPERIMENT

Joanna Lach, Rasa Platakytė, Justinas Čeponkus, Valdas Šablinskas

Department of General Physics and Spectroscopy, Vilnius University, Lithuania
joana.lach@university.com

Tetrahydrofuran (THF) is an organic heterocyclic compound with formula $(CH_2)_4O$. THF finds usage mainly as a precursor in polymerisation. Polar properties and wide liquid state temperature range makes THF a versatile solvent. The high-level ab initio calculations show that the global minimum of the THF molecule in a gas phase is an envelope (C_s) structure. [1, 2, 3] According to the latest benchmark calculations the absolute energy difference between the global minimum (C_s) and the first local minima, the twisted conformation (C_2), is only 1.77 kJ/ mol^{-1}.[4] Such low differences between global and local minima suggest a high flexibility of THF molecule at finite temperature and its barrierless adaptation to different conformations.

Matrix isolation comprises a category of experimental techniques in which guest molecules or atoms are trapped in rigid host materials. Because the species are embedded in a host material, the diffusion process is prevented and bimolecular reactions cannot take place except with the host material. After successful deposition of the matrix, the trapped guest species can be activated by irradiation and by low-temperature annealing.

Matrix isolation experiment was performed with concentration ratio of 0.5 THF and 500 nitrogen (matrix). In order to change the conformational equilibrium the temperature of the matrix mixture was varied during deposition in the large temperature range in different experiments by using hot nozzle matrix deposition technique.

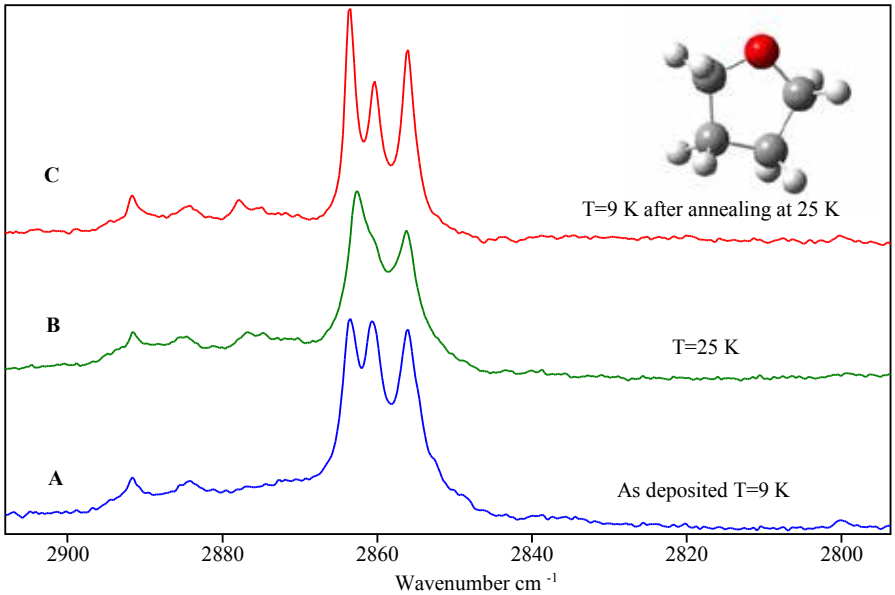

Fig. 1. THF@N_2 FT-IR spectra from matrix isolation experiment for A: 9K (blue), B: 25 K (green) and C:9K after 25 K (red) for deposition mixture in room temperature.

In the C-H stretch vibration range of the THF infrared absorption spectra we can observe the change of intensity of spectral bands associated with C_s and C_2 conformers with heating up and cooling down the matrix (A and C). Additionally we have observed changes of C_s and C_2 ratio when the sample is deposited at different hot nozzle temperatures. Detail analysis of the conformer structure and conformational dynamics will be in detail described on the poster.

[1]D. G. Melnik, S. Gopalakrishnan, T. A. Miller, F. C. D. Lucia, The absorption spectroscopy of the lowest pseudorotational states of tetrahydrofuran, J. Chem. Phys. 118 (2003) 3589.
[2] V. M. Rayon, J. A. Sordo, Pseudorotation motion in tetrahydrofuran: An ab initio study, J. Chem. Phys. 122 (2005) 204303.
[3] A. D. Boese, R. Boese, Tetrahydrothiophene and tetrahydrofuran, computational and x-ray studies in the crystalline phase, Cryst. Growth Des. 15 (2015) 1073.
[4] T. Yang, G. Su, C. Ning, J. Deng, F. Wang, S. Zhang, X. Ren, Y. Huang, New diagnostic of the most populated conformer of tetrahydrofuran in the gas phase, J. Phys. Chem. A 111 (2007) 4927.

INFLUENCE OF COBALTACARBORANE ANION CONFORMATION ON STRUCTURE AND VIBRATIONAL SPECTRA OF CHARGE TRANSFER SALTS

Anna Wójcik[1], Michał Walczak[1], Bolesław Barszcz[2], Vladimir Starodub[3]

[1] Faculty of Technical Physics, Poznan University of Technology, Poznań, Poland
[2] Institute of Molecular Physics, Polish Academy of Sciences, Poznań, Poland
[3]Department of Chemical Technology, The Jan Kochanowski University in Kielce, Poland
anna.s.wojcik@student.put.poznan.com

The ET (bisethylenedithio-tetrathiafulvalene or BEDT-TTF) molecule combined with anions creates a variety of organic salts (including organic superconductors). In such materials we can observe several different phases with various packing patterns of the BEDT-TTF molecules, depending on the anion type and the growth conditions. Important phases are the α-, β- , θ- and especially κ-phase, which are half-filled systems. This property drive them into superconductivity at higher temperatures than other phases. The neutral ET is nonplanar (boat structure) but when it forms the charge transfer complex, the molecule becomes more planar and the packing density can be increased. The charge transfer salts created from ET molecule are very popular because they are model low dimensional systems exhibiting fascinating physical properties.

This work is devoted to characterization of two salts: $(ET)_2[8\text{-I-Co}(C_2B_9H_{10})(C_2B_9H_{11})]$ [1] and $(ET)_2[Co(8\text{-Cl-}C_2B_9H_{10})(8'\text{-Cl-}C_2B_9H_{10})]$ [2] using the vibrational spectroscopy. The Raman spectra of the single crystals has been registered in the spectral range 50-2500 cm^{-1} using the excitation line 633 nm from the He-Ne laser while the IR spectra were registered in the range 400-7500 cm^{-1}. The Raman scattering spectra and complementary infrared (reflectance, absorption, and transmittance) spectra will give us information about average charge on ET molecule and anion conformation.

Received Raman spectra of investigated salts shows a few intense peaks, which could be related to the fully symmetric vibrational modes of the ET, and some less intense features. The polarized infrared reflectance spectra of the $(ET)_2[8\text{-I-Co}(C_2B_9H_{10})(C_2B_9H_{11})]$ crystal show distinct anisotropy of reflectance in contrast to the second salt. The IR spectra of presented salts (registered in KBr matrix) shows vibrational features specific for this class of materials. The information about the crystallographic structure will complete the spectral data and tell us how the change in the anion species influence the structure and the spectra of the salt.

[1] Olga N. Kazheva, Grigorii G Alexandrov, Andrey V. Kravchenko, Vladimir A. Starodub, Igor B. Sivaev, Irina A. Lobanova, Vladimir I. Bregadze, Lev I. Buravov, Oleg A. Dyachenko, Journal of Organometallic Chemistry **692** (2007) 5033-5043.
[2] Olga N. Kazheva, Grigorii G. Alexandrov, Andrey V. Kravchenko, Vladimir A. Starodub, , Irina A. Lobanova, Irina D. Kosenko, Igor B. Sivaev, Vladimir I. Bregadze, Lev I. Buravov, Oleg A. Dyachenko, Crystals 2012, **2**, 43-55.

STRUCTURE AND SPECTRAL PROPERTIES OF ET SALTS WITH CO, FE AND CR BIS(DICARBOLLIDE) ANIONS

Michał Walczak[1], Anna Wójcik[1], Bolesław Barszcz[2], Vladimir Starodub[3]

[1] Faculty of Technical Physics, Poznan University of Technology, Poznań, Poland
[2] Institute of Molecular Physics, Polish Academy of Sciences, Poznań, Poland
[3]Department of Chemical Technology, The Jan Kochanowski University in Kielce, Poland
michal.wl.walczak@student.put.poznan.pl

Recently ET salts became very popular materials among scientists. They are organic materials exhibiting superconductivity and other interesting phenomena. The ET molecules forms salts with various anions, often with 2:1 composition ratio as $(ET)_2X$ (where X is monovalent anion). Among them there are several quasi one-dimensional conductors, but most of them are quasi two-dimensional. The dimensionality of the salt determine its physical properties. For example in 2D salts the conductance is possible even despite the structural defects while 1D systems are more vulnerable to the breaks in the conductance pathway. ET salts have various electrical and optical properties but they are attracting attention because the small structural change in the anion can cause the dramatic change in physical properties of the salt (e. g. from semiconducting to metallic or even superconducting character). Moreover the entire potential of such materials has still not been sized.

In this study, to get information about four salts: $(ET)[Co(C_2B_9H_{11})_2)]$, $(ET)_2[Co(C_2B_9H_{11})_2)]$, $(ET)_2[Fe(C_2B_9H_{11})_2)]$ and $(ET)_2[Cr(C_2B_9H_{11})_2)]$[1-4] we use the vibrational spectroscopy techniques. Our aim is to describe structure and spectral properties of these salts using Raman scattering and infrared spectroscopies. The Raman spectra of the single crystals has been registered in the spectral range 50-2500 cm^{-1} using the excitation line 633 nm from the He-Ne laser while the IR spectra were registered in the range 400-7500 cm^{-1}. Both Raman and IR spectra will give information about ET molecule and anion, allowing to determine the influence of anion structure on salts properties.

The Raman spectra of the salts shows a few intense peaks (most probably related to the fully symmetric vibrational modes of the ET molecule) and some less intense features. The infrared reflectance of the $(ET)[Co(C_2B_9H_{11})_2)]$ and $(ET)_2[Cr(C_2B_9H_{11})_2)]$ crystals strongly depend on the polarization of the incident IR beam. On the other hand the reflectance spectra of the remaining crystals show weak or no anisotropy. The IR spectra of the samples registered in KBr matrix demonstrates vibrational features typical for low dimensional conductors. The dimensionality of the salts will be discussed from both spectroscopic and structural point of view.

[1] Olga N. Kazheva, Anatolii N. Chekhlov, Grigorii G Alexandrov, Lev I. Buravov, Andrey V. Kravchenko, Vladimir A. Starodub, Igor B. Sivaev, Vladimir I. Bregadze, Oleg A. Dyachenko, Journal of Organometallic Chemistry **691** (2006) 4225-4233.

[2] Olga N. Kazheva, Grigorii G Alexandrov, Andrey V. Kravchenko, Vladimir A. Starodub, Igor B. Sivaev, Irina A. Lobanova, Vladimir I. Bregadze, Lev I. Buravov, Oleg A. Dyachenko, Journal of Organometallic Chemistry **692** (2007) 5033-5043.

[3] Olga N. Kazheva, Grigorii G Alexandrov, Andrey V. Kravchenko, Igor B. Sivaev, Irina D. Kosenko, Irina A. Lobanova, Marcela Kajnakova, Lev I. Buravov, Vladimir I. Bregadze, Alexander Feher, Vladimir A. Starodub, Oleg A. Dyachenko, Inorganic Chemistry Communications **15** (2012) 106-108.

[4] Yaw-Kai Yan, D. Michael P. Mingos, David J. Williams, Mohamedally Kurmoo, Journal of the Chemical Society Dalton Transactions (1995), Paper **5**/01204J

ANALYSIS OF CELL ELECTROPORATION INDUCED BY ELECTRIC PULSE WITH THE DURATION FROM 40 ns TO 2 ms

Aiste Bitinaite[1,2], Rita Saule[1], Voitech Stankevic[2], Nerija Zurauskiene[2], Saulius Balevicius[2], and Gintautas Saulis[1,2]

[1]Department of Biology, Vytautas Magnus University, Lithuania
[2]Laboratory of High Power Pulses, Institute of Semiconductor Physics, Lithuania
Aiste.Bitinaite@gmf.vdu.lt

To optimize practical applications of electroporation, it is important to know whether and how many of cells have become electroporated under the influence of a particular electric field treatment. However, to determine whether the cell is porated or still intact is rather a complicated task. The matter is that different treatments create different pore populations: the size of the pores and their lifetime depend on the duration of the pulse.

Here, the size and lifetime of the pores created by a single electric field pulse of different durations have been evaluated. The fraction of electroporated mouse hepatoma MH-22A and Chinese hamster ovary cells was determined from the extent of the release of intracellular potassium ions and erythrocytes - from the extent of their hemolysis after 20-24 h-incubation in 0.63% NaCl solution at 4°C. The size of the pores was evaluated by studying membrane permeability to bleomycin and protective action of xylitol, mannitol, and sucrose against colloid-osmotic lysis.

In the case of a short pulse (square-wave with the duration 40 ns-100 μs), in the large portion (30–60%) of electroporated (permeable to potassium ions) cells, an electric pulse created only the pores, which were smaller than the molecules of bleomycin (radius ≈ 0.8 nm) or sucrose (radius 0.44–0.52 nm). In the case of a long pulse (duration 1-2 ms), in almost all cells, which were electroporated, there were the pores larger than the molecules of bleomycin and/or sucrose. Kinetics of pore resealing depended on the pulse duration as well and was faster after shorter pulses.

The results obtained here show that the methods based on measuring membrane permeability for rather large tracer molecules, e.g. propidium iodide or trypan blue, which are suitable for determination of cell electroporation by long pulses, can fail in the case of short pulses.

THERMALLY ACTIVATED DELAYED FLUORESCENCE IN DONOR-ACCEPTOR-BASED TRIAZINE AND PYRIMIDINE DERIVATIVES

Paulius Imbrasas[1], Karolis Kazlauskas[1], Sigitas Tumkevičius[2], Juozas V. Gražulevičius[3], Saulius Juršėnas[1]

[1]Institute of Applied Research, Vilnius University, Saulėtekio 9, LT-10222 Vilnius, Lithuania
[2]Department of Organic Chemistry, Faculty of Chemistry, Vilnius University, Naugarduko 24, LT-03225 Vilnius, Lithuania
[3]Department of Polymer Chemistry and Technology, Kaunas University of Technology, Radvilėnų pl. 19, LT-50254 Kaunas, Lithuania
paulius.imbrasas@ff.stud.vu.lt

Thermally activated delayed fluorescence (TADF) is a thermally-assisted process that allows triplet state harvesting with an efficiency of 100% via reverse intersystem crossing (RISC) to singlet states. Therefore, TADF-based organic light-emitting devices (OLEDs) are capable of delivering internal quantum efficiencies reaching unity [1]. They are serious competitors to the state-of-the-art phosphorescent OLEDs. Avoiding the utilization of triplet emitters makes TADF devices less expensive and longer-lasting than their phosphorescent counterparts. For the RISC process to be efficient, the energy gap ΔE_{ST} between S_1 and T_1 excited states must be as small as possible. Thus, one must ensure a small overlap of HOMO and LUMO in the emitter molecule. This is realized by spatially separating donor and acceptor moieties in the compound. However, since the separation weakens oscillator strength, there exists a trade-off between the fluorescence quantum efficiency and ΔE_{ST}. Therefore, it is highly challenging to find compounds demonstrating both high quantum efficiency and small ΔE_{ST}. Search of high-efficiency TADF materials is an important task for it could lead to the realization of new generation extremely efficient and cost-effective OLEDs.

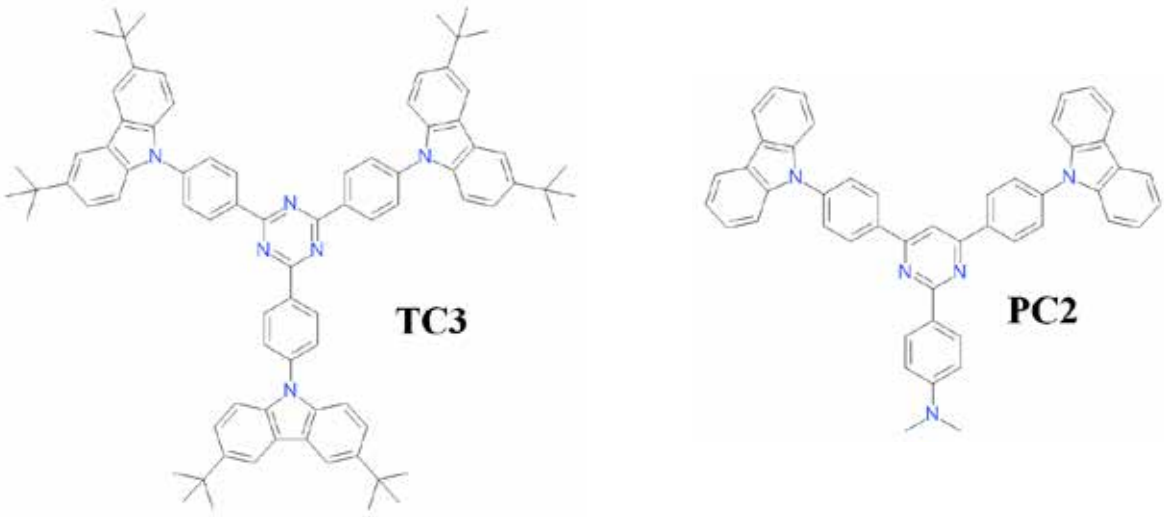

Fig. **1**. TADF compounds **TC3** and **PC2**.

In this work a thorough analysis of donor-acceptor-based TADF compounds with triazine (**TC3**) and pyrimidine (**PC2**) core (see Fig. 1) is presented. As expected, the efficiency of RISC was found to be strongly affected by the amount of oxygen in the sample, because oxygen is an effective triplet state quencher. Removal of O_2 by argon bubbling of toluene solutions led to an increase of quantum efficiency from 0.7 to 0.79 and from 0.08 to 0.11 for **TC3** and **PC2**, respectively. The removal of O_2 also prolonged the luminescence transients of compounds dissolved in solutions and dispersed in polymer films, because the unquenched triplet excitons populate singlet states via RISC and cause delayed fluorescence. By testing polymer film samples at 20 K thermally activated RISC was highly suppressed, which allowed the phosphorescence spectra to be measured and T_1 state energy to be determined. ΔE_{ST} values estimated from these measurements were 0.2 eV and 0.05 eV for **TC3** for **PC2**, respectively. The phosphorescence lifetime was much longer than 100 ms.

The results confirmed notable TADF contribution in the luminescence of **TC3** and **PC2**. High luminescence quantum efficiency and small ΔE_{ST} of **TC3** render the compound suitable for TADF OLEDs.

[1] H. Uoyama, K. Goushi, K. Shizu, H. Nomura, and C. Adachi, Nature **492**, 234 (2012).

LIGHT AMPLIFICATION IN BIFLUORENE SOLID STATE COMPOUNDS

Edvinas Radiunas, Gediminas Kreiza, Povilas Adomėnas, Karolis Kazlauskas, Saulius Juršėnas

Institute of Applied research, Vilnius University, Lithuania
eradiunas@gmail.com

Strong interest in laser sources based on low-cost organic semiconductors is provoked by their attractive electronic and optical properties combined with the mechanical flexibility and ease of processability [1-2]. Broad gain spectra offer wide emission-wavelength tunability across the entire visible range, whereas negligible temperature dependence of amplified emission threshold, output power and emission wavelength renders organic laser sources relevant for applications in spectroscopy as well as optical data communications, memory, sensing and displays [2]. Up to now, optically pumped lasers based on conjugated organic materials have been demonstrated in both solutions and thin films. With continuous efforts in pursuing electrically pumped organic lasing, organic semiconductors with improved stability, emissive as well as charge transport properties are constantly desired. Most of these properties are retained in organic crystals in which small size conjugated molecules are held together with long-range order via weak non-bonding interactions, such as van der Waals forces [3]. Moreover, in the last decade, organic crystals have played an important role in the development of organic solid state lasers.

In this work, light amplification properties of new bifluorene compound, shown in the inset of Fig. 1, were investigated. The properties were assessed for the compound dispersed in polystyrene (PS) matrix as well as for single crystals, which were grown from supersaturated chlorobenzene/water solution. Emission measurements of the bifluorene compound dispersed in PS matrix at different concentrations (0.5-100 wt%) indicated weak concentration quenching. In particular, fluorescence quantum yield (Φ_F) and fluorescence lifetime (τ) remained almost unchanged up to 50 wt% of compound in PS (see Fig. 2). Bifluorene crystals exhibited similar fluorescence lifetime (~0.7 ns) and radiative relaxation rate (~10^9 s^{-1}) values as compared to those estimated for compounds in PS matrix. Concentration dependence of amplified spontaneous emission (ASE) threshold (I_s) for studied molecules in PS matrix was investigated to reveal optimal conditions for laser operation. The lowest I_s (580 W/cm^2) was obtained for 6 wt% PS film. I_s remained unchanged by further increasing chromophore concentration (see Fig. 1). However, I_s in the compound crystal was couple orders of magnitude higher (67 kW/cm^2) mainly because of absorption losses in thick bifluorene crystals. Importantly, ASE threshold values achieved in PS matrix were similar or even lower as compared to the most of reported results and showed great potential for bifluorene compound as active media for lasing applications.

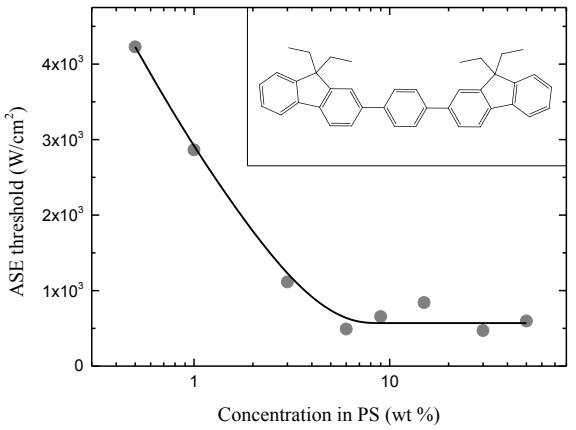

Fig.1. Amplified spontaneous emission threshold *vs.* compound concentration in polystyrene matrix.

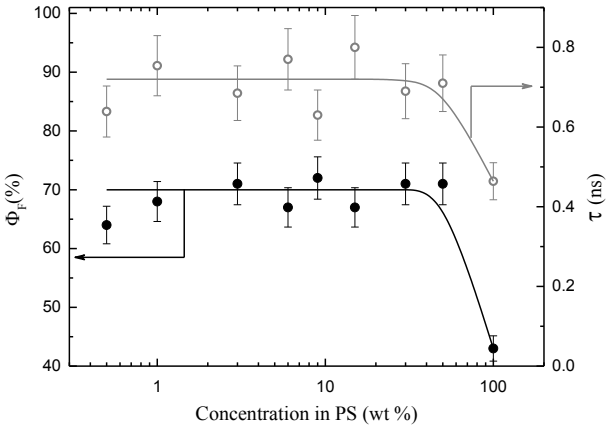

Fig. 2. Fluorescence quantum yields and average fluorescence lifetimes of the bifluorene compound as a function of its concentration in PS matrix.

[1] K. Kazlauskas, G. Kreiza, E. Radiunas, P. Adomėnas, O. Adomėnienė, K. Karpavičius, J.Bucevičius, V. Jankauskas and S.Juršėnas, Concentration effects on spontaneous and amplified emission in benzo[c]fluorenes, Phys.Chem.Chem.Phys. **17,** 12935-12948 (2015).
[2] I. D. W. Samuel and G. A. Turnbull, Organic semiconductor lasers, Chem. Rev. **107**, 1272-1295 (2007).
[3] H. Fang, J. Yang, J. Feng, T. Yamao, S. Hotta, and H. Sun, Functional organic single crystals for solid-state laser application, Laser Photonics Rev. **8**, 687-715 (2014).

THE CONTROL OF OPTICAL PROPERTIES OF 1,8-NAPHTHALIMIDE MODIFIED WITH (ALKYL)THIOPHENE

Gediminas Kyburys, Regimantas Komskis, Saulius Juršėnas

Institute of Applied Research, Vilnius University, Saulėtekio 9-III, LT-10222 Vilnius, Lithuania
gedasky@fidi.lt

The interest in semiconductor materials has been growing in the last decades and had a strong impact on the development of variety of electronic devices and modern technologies. The integration and utilisation of organic materials in technology has begun relatively recently. These materials have been used in different specific areas as well as various devices, such as metal detectors, OLEDs, OTFTs, organic solar cells. Naphthalimide derivatives are well known as an anticancer agent and are used for fluorescence sensors and are easily modified. This scientific study covers the topic of spectroscopic properties of naphthalimide derivatives (Fig. 1), modified with a different mass thiophene and alkylthiophene substitutes (Fig. 2), as well as control of optical characteristics in a different polarity and viscosity mediums.

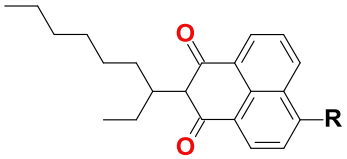

Fig. 1. Naphthalimide.

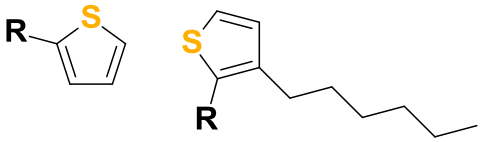

Fig. 2. Thiophene and alkylthiophene.

Two materials with different torsion effect have been chosen for this investigation. The torsion angle of thiophene substituent was controlled by introducing an alkyl chain in the 4th position. Both structures demonstrate local and charge transfer states in absorption and emission spectra. The emission of naphthalimide derivatives exhibits strong solvatochromic behaviour by increasing the polarity in medium from toluene (non – polar medium) to DMSO (polar medium). 1,8 – naphthalimide – thiophene compound demonstrates a typical red shift in the fluorescence spectra. Meanwhile, alkyl chain modifies torsion effect of thiophene substituent which affects the dynamics of charge transfer states and emission spectra. Dependence on solvent polarity and naphthalimide substituent massiveness showed that molecular twist is very important in optimizing the fluorescence quantum yield. It has been shown that photochemical reactions and the control of non-radiative relaxation speed is very strongly influenced by the molecular fragment twist. Naphthalimide with thiophene substituent has shown an increase of fluorescence quantum yield up to 6 times (from 10% to 60%) while the polarity of medium was increased. However naphthalimide with alkylthiophene substituent has shown a decreasing fluorescence quantum yield up to 12 times (from 6% to 0,5%).

In order to distinguish the influence of medium polarity and viscosity to optical properties of 1,8 – naphthalimide – thiophene derivatives were dissolved in four solvents increasing viscosity and constant polarity. Although both compounds show local and charge transfer states in absorption and emission spectra, the solvatochromic behaviour is insignificant. Moreover, naphthalimide with thiophene substituent shows minor changes in fluorescence quantum yield from 70% to 63% while alkylthiophene substituent slightly increases fluorescence quantum yield from 5,5% to 7,2%, on the condition that the viscosity of the medium was increased. That nontrivial effect is related to the competition between radiative and non radiative relaxation channel while the nature of charge transfer is changing. Radiative relaxation was very fast (2ns), for naphthalimide with lover mass thiophene substitute in comparison to the naphthalimide with higher mass alkylthiophene substitute (50ns) independent to the viscosity of the medium. However, polarity increase slows radiative relaxation process for naphthalimide with alkylthiophene substituent up to 2 times (from 30ns to 65ns).

1,8 – naphthalimide derivatives with thiophene substituents are promising materials for sensor technologies, due to their high sensitivity to the medium polarity up to 12 times.

Eu^{3+}-DOPED $Y_{3-x}Nd_xAl_3O_{12}$:SYMTHESIS AND STRUCTURAL INVESTIGATION

Lina Pavasaryte[1], Vytautas Klimavicius[2], Vytautas Balevicius[2],Andraz Krajnc[3], Gregor Mali[3],Janez Plavec[3], Aivaras Kareiva[1]

[1]Faculty of Chemistry, Department of Inorganic Chemistry, Vilnius University, LT-10223 Vilnius, Lithuania
[2]Faculty of Physics, Department of General Physics and spectroscopy, Vilnius University, LT-10223 Vilnius, Lithuania
[3]National Institute of Chemistry, NMR Center, SI-1001, Ljubljana, Slovenia
lina.pavasaryte@gmail.com

$Y_3Al_5O_{12}$ is commonly called yttrium aluminium garnet (YAG) and adopts the cubic garnet structure. Rare earth doped yttrium aluminium garnet has been thoroughly investigated for application in various fields, such as laser, scintillators, cathode ray tubes (CRT), field-emission displays (FEDs), plasmas display panels (PDPs,) and optical windows, due to its attractive optical property, outstanding chemical stability, low creep rate and high thermal resistance. Luminescent materials based on YAG are stable under conditions of high irradiation with an electron beam.When YAG is doped with Nd^{3+}, it is reported that the near-infrared (NIR) laser output with high power and high slope efficiency were obtained in single crystals and polycrystalline transparent ceramic. The Nd^{3+}- doped YAG is one of the most popular laser active materials [1-3].

In this work YAG garnetsamples doped with different amount of Nd^{3+} were prepared by sol-gel method. To our best knowledge, Nd:YAG garnets with various doping levels of europium have not been synthesized yet. Therefore, the main aim of this study was to fabricate these garnets and investigated their structural properties. The phase purity and crystallinity of synthesized samples were characterized by X-ray powder diffraction (XRD) analysis. The infrared spectroscopy (FTIR) was chosen as an additional tool to prove purity of garnets. The scanning electron microscope was used to study the surface morphology and microstructure of the obtained ceramic samples. The local structure of garnets was investigated by nuclear magnetic resonance spectroscopy (NMR ^{27}Al).

It was confirmed from the XRD data that monophasic garnets can be easily synthesized at 1000 °C using the proposed sol-gel chemical approach. The results obtained by FTIR method are in a good agreement with XRD data and proves monophasic garnet structure compound existence. Surface behaviour between samples of different doping level was shown by SEM.^{27}Al MAS NMR spectroscopy helped to investigate structural combination of garnets and allowed to compare dependence of peaks intensity on the concentration of dopant (Fig. 1).

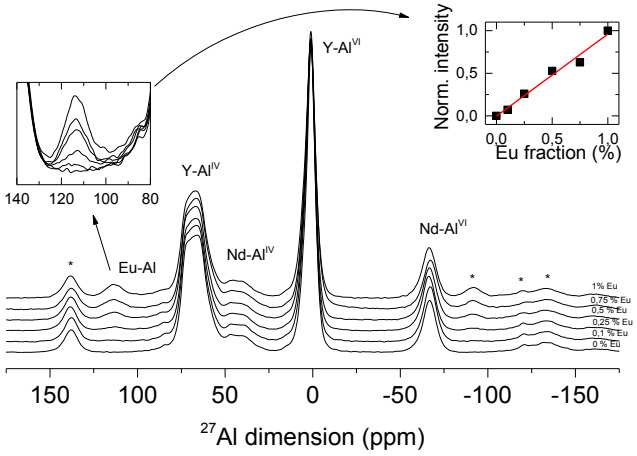

Fig. 1. 27Al NMR spectra of the $Y_{2,9}Nd_{0,1}Al_5O_{12}$:Eu gels annealed at 1000°C for 10 h.

One of our aims was to analyze the influence of Eu^{3+}in a garnet structure when concentration of neodymium ionswas permanent (0.1 molar part).This permanent amount of neodymium wasselected because ofthe sharpest and most intensive lines for all peakswith this doping level were observed. In Fig. 1 are seen the peaks which are attributed to the yttrium, neodymium and europium which are neighbours of tetrahedral and octahedral coordinated aluminium.The peaks attributed to Al-Eu increased proportionally with increasing doping level of europium.

[1] Y. Zhou, J. Lin, M. Yu, S. Wang, H. Zhang,Synthesis-dependent luminescence properties of Y3Al5O12: Re 3+(Re= Ce, Sm, Tb) phosphors,Materials Letters 2002, 56 628-636.
[2] E. Caponetti, D. Ch. Martino, M. L. Saladino, Preparation of Nd:YAG Nanopowder in a Confined Environment, Langmuir 2007, 23, 3947-3952
[3] X. J. Xu, X. D. Sun, H. Liu, J.-G. Li, X. D. Li, D. Huo, and S. H. Liu, Synthesis of Monodispersed Spherical Yttrium Aluminium Garnet (YAG) Powders by a Homogeneous Precipitation Method, Journal of the American Ceramic Society95(12), 3821-3826.

FUNCTIONALIZED GRAPHENE OXIDE AND ITS APPLICATION IN RAPESSEED OIL TRANSESTERIFICATION REACTION

Justina Gaidukevič[1], Jurgis Barkauskas[1], Paulina Rechnia[2], Aleksandra Miklaszewska[2], Mieczysław Kozłowski[2]

[1]Department of Inorganic Chemistry, Vilnius University, Lithuania
[2]Faculty of Chemistry, Adam Mickiewicz University in Poznań, Poland
Justina.daksevic@chf.stud.vu.lt

As the fossil fuels are depleting progressively, there is a need to find an alternative fuel to fulfill the energy demand of the world. One of the most promising propositions is biodiesel, which is defined as a mixture of mono-alkyl esters of long chain fatty acids (FAME), produced by the transesterification of vegetable oils with an alcohol in the presence of a homogeneous catalyst (NaOH or H_2SO_4) [1]. However, the use of such substances may cause corrosion and environmental problems, moreover, these catalysts are not recoverable and require more expensive equipment. Additionally, while these catalysts are partly soluble in the reaction mixture, the separation and purification of products become a more difficult task [2]. A solution of those problems could be the application of heterogeneous catalysts, e.g. modified carbon materials. In comparison with the conventional catalysts, carbon materials have many advantages: they are biocompatible, inexpensive, stable, environmentally friendly and readily available. Different carbon materials, including carbon black, activated carbon, carbon nanotubes and graphene, have been used as the effective catalysts or catalyst supports [3]. Amongst the carbon materials described above, graphene has recently gained some serious attention, as it has extraordinary properties, including high specific surface area (2630 m^2/g), good chemical stability, remarkable electrical, thermal and mechanical properties and it is an ideal platform to attach various functional groups. Accordingly, a derivative of graphene - graphene oxide (GO), offers a wide range of possibilities to synthesize the novel functional catalysts due to the abundant oxygen-containing functional groups on its basal planes (hydroxyl and epoxy groups) and edges (carboxylic groups) [4].

The aim of this work was to produce functionalized graphene oxide catalysts with acidic or basic sites on their surface and to investigate their catalytic activity in the transesterification reaction of rapeseed oil with methanol.

The graphite oxide (GrO) was prepared from the natural graphite by the protocol reported by Yan et al. [5]. In a typical experiment, graphite powder was treated with conc. H_2SO_4, $K_2S_2O_8$ and P_2O_5. Later, this pre-oxidized graphite was subjected to oxidation by Hummers method using $NaNO_3$, H_2SO_4 and $KMnO_4$ [6]. GO nanosheets were generated when GrO powder was dispersed in water with ultrasonic vibration under 25 kHz for 15 h. Finally, the GO suspension was dried at 100 °C to obtain the GO powder. To introduce acidic sites on GO surface, different sulphonation protocols with 4-aminobenzenesulphonic acid were applied [7, 8]. To introduce basic sites, GO was modified with 3-(N,N'-dicyclohexylguanidine)-propyltrimethoxysilane (GPMS) [9] or 1,5,7-triazabicyclo [4.4.0] dec-5-ene (TBD) as described in [10, 11]. The obtained catalysts were characterized by different methods (TG and elemental analysis, BET measurements, potentiometric titration and SEM investigations). The transesterification reaction of rapeseed oil with methanol was carried out at the temperature of 130 ºC under 1.3 MPa for 24 h. During the reaction four samples of the reaction mixture were collected (after 1, 3, 6 and 24 hours). The SRI 8610C gas chromatograph was used to determine the content of FAME in the post-reaction mixture.

The results show that acidic catalysts were more active in the transesterification reaction of rapeseed oil with methanol than basic ones. The best results were obtained using GO, which was modified by $SOCl_2$ and 4-aminobenzenesulphonic acid. The content of FAME after 24 hours was equal to 63 %. In the conditions used, this catalyst was more active than the commercial Amberlyst 15.

[1] I. M. Atadashi, M. K. Aroua, A. R. Abdul Aziz, N. M. N. Sulaiman, The effects of catalysts in biodiesel production: A review, J. Ind. Eng. Chem. **19** (1), 14–26 (2013).
[2] K. Narasimharao, A. F. Lee, K. Wilson, Catalysts in production of biodiesel: a review, J. Biobased Mater. Bioenergy **1** (3), 301–314 (2007).
[3] L. J. Konwar, J. Boro, and D. Deka, Review on latest developments in biodiesel production using carbon-based catalysts, Renew. Sustain. Energy Rev. **29**, 546–564 (2014).
[4] D. R. Dreyer, S. Park, C. W. Bielawski, R. S. Ruoff, The chemistry of graphene oxide, Chem. Soc. Rev. **39** (1), 228–240 (2010).
[5] X. Yan, J. Chen, J. Yang, Q. Xue, P. Miele, Fabrication of free-standing, electrochemically active, and biocompatible graphene oxide-polyaniline and graphene-polyaniline hybrid papers, ACS Appl. Mater. Interfaces **2** (9), 2521–9 (2010).
[6] J. William S. Hummers,R. E. Offeman, Preparation of Graphitic Oxide, J. Am. Chem. Soc. **80**, 1339 (1958).
[7] M. Toupin, D. Bélanger, Spontaneous functionalization of carbon black by reaction with 4 nitrophenyldiazonium cations, Langmuir **24** (12),1910–1917 (2008).
[8] V. Sadhu, N. a Nismy, D. T. Adikaari, S. J. Henley, M. Shkunov, S. R. P. Silva, The incorporation of mono- and bi-functionalized multiwall carbon nanotubes in organic photovoltaic cells, Nanotechnology **22**, 265 (2011).
[9] J. M. Balbino, E. W. de Menezes, E. V. Benvenutti, R. Cataluna, G. Ebeling, J. Dupont, Silica-supported guanidine catalyst for continuous flow biodiesel production, Green Chem. **13**, 3111 (2011).
[10] P. Kalita, R. Kumar, Immobilization of 1,5,7-triazabicyclo [4.4.0] dec-5-ene over mesoporous materials: An efficient catalyst for Michael-addition reactions under solvent-free condition, Applied Catalysis A: General **397**, 250–258 (2011).
[11] S. B. Muazu, A.Farook, The chemical fixation of carbon dioxide to propylene carbonate over triazabicyclodecenefunctionalized silica nano catalyst, International Journal of Scientific & Engineering Research **5**, 1045-1056 (2014).

CHARACTERIZATION OF Nb_2O_5 AND Ta_2O_5 COATINGS PRODUCED BY ELECTRON BEAM EVAPORATION WITH PLASMA SOURCE ASSISTANCE

Lina Grinevičiūtė, Audrius Valavičius, Tomas Tolenis, Ramutis Drazdys

State research institute Center for Physical Sciences and Technology, Savanorių ave. 231, Vilnius, Lithuania, LT-02300

grineviciute.lina@gmail.com

Optical and mechanical characterization is important in fabrication of optical components which are widely used in laser systems. Optical properties of materials are essential in modeling sophisticated elements which could be suited in various applications. In production of such elements many layers of different materials with high and low refractive indexes must be deposited on substrates. During coating processes inner stresses emerge in films due to defects, lattice mismatch, difference between the thermal expansion coefficients of substrate and thin layer and etc. Stresses can cause cracking, peeling off or substrate bending, so the possibility to handle inner stress is crucial in production of high quality optical elements.

In present work we report the applications of plasma source assistance in electron beam evaporation technique and its influence on optical and mechanical characteristics of materials with high refractive index - Nb_2O_5 and Ta_2O_5. Layers with three quarters optical thickness of each material were evaporated using optical monitoring control at 630 nm wavelength. Twelve different evaporation processes were accomplished by using different plasma source parameters. The power of plasma source was 1000 W and 2000 W, the energy of generated oxygen ions was varying approximately from 100 eV to 170 eV. All processes were started at 110 °C and in high vacuum of $p_0 = 1.0 \cdot 10^{-5}$ mbar. An oxygen flow was controlled during the process to maintain the pressure in chamber at $1.5 \cdot 10^{-4}$ mbar. The evaporation rate was 2 Å/s for both materials and controlled by crystal quartz monitoring.

The refractive indexes of Nb_2O_5 and Ta_2O_5 thin films were determined by modeling transmission spectra using "OptiLayer" program. The stresses in the films were calculated using Stoney formula, which evaluated the curvature of the 1 mm thickness fused silica substrate before and after material evaporation on it [1]. Profilometer and interferometer for determination of curvatures were employed.

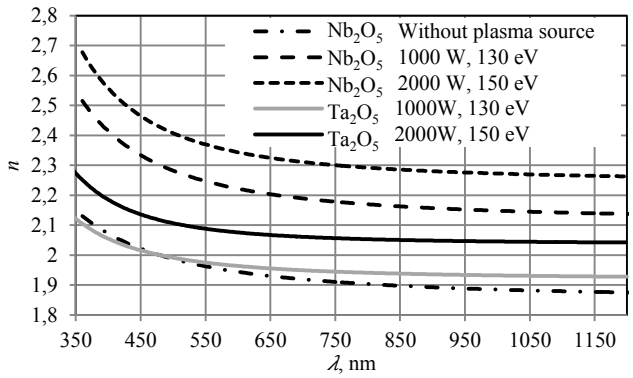

Fig. 1 Refractive index dispersions of Nb_2O_5 and Ta_2O_5, evaporated at different parameters of plasma source

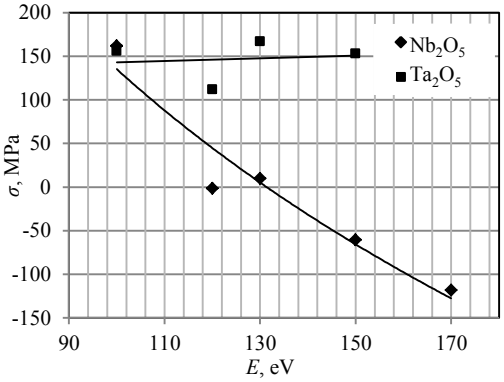

Fig. 2 Stress dependency on assisted ions energy for evaporated Nb_2O_5 and Ta_2O_5 coatings

The dispersions of characterized refractive indexes are represented in Fig. 1. If the plasma source is not used during electron beam evaporation, the refractive index of Nb_2O_5 is comparatively small – 2,0 for 500 nm wavelength. When the assisted plasma source is employed the refractive index can be raised due to the plasma generated ions which affect the material atoms to form denser layer. The values of 2,4 and 2.1 for 500 nm wavelength of Nb_2O_5 and Ta_2O_5 thin films respectively can be accomplished by optimizing the parameters of plasma source.

The inner stress in Nb_2O_5 thin film was changing uniformly from compressive to tensile when assisted plasma source was used during electron beam evaporation. Only compressive stress values were observed for Ta_2O_5 coatings. The stress dependency on ions energy is shown in Fig. 2. This relationship gives a possibility to manufacture good quality Nb_2O_5 multilayer optical elements with flat surface which makes no distortions for interacting wave front.

[1] M. R. Ardigo, M. Ahmed, A. Besnard, "Stoney Formula: Investigation of Curvature Measurements by Optical Profilometer", Advanced Materials Research, Vol. 996, pp. 361-366, Aug. 2014

VOLUME REFLECTION HOLOGRAPHIC GRATINGS IN COMPOSITE OF PHENANTHRENEQUINONE IN POLYMETHYLMETHACRYLATE

Maksim Malashko, Alexandra Trofimova, Uladzimir Mahilny

Department of Physical Optics, Belarusian State University, Belarus.
maksimalashko@gmail.com

This study describes the formation of effective reflection holograms in the glassy layers of polymethylmethacrylate (PMMA) with a high content of phenanthrenequinone (PQ).

Holograms were recorded using Denisyuk scheme (Fig. 1). A semiconductor laser with a wavelength of 532 nm was used in experiments, light beam was expanded and passed through the diaphragm to control its size.

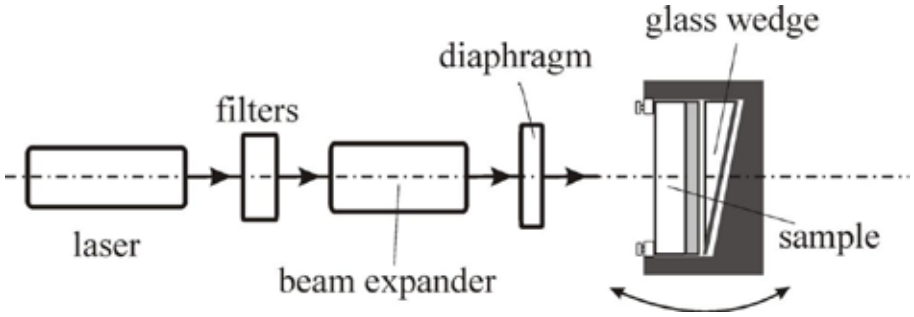

Fig. 1. Basic scheme of hologram recording.

The recording gratings were probed by laser radiation at λ=532 nm and the measurements of the diffracted beams intensities were performed. The diffraction efficiency (η) was determined as the ratio of the diffracted beam intensity to the intensity of the probing beam.

Upon laser radiation photosensitive PQ molecules attach to macromolecules. Under the influence of a sinusoidally modulated field of interfering beams an antiphase spatial distribution of concentrations of PQ and its photoproduct is formed [1]. Since the refractivities of PQ and photoproduct differ slightly, the hologram with a diffraction efficiency of 6% was achieved at the recording process. Further in the process of the dark relaxation at room temperature (18ºC), η increased up to 18%. Despite the low temperature, there was a diffusion of PQ molecules, whereas being attached to polymer matrix molecules of photoproduct remain fixed. Diffusion leads to spatial alignment of PQ concentration in the layer and consequently to a degradation of PQ contribution to the refractive index distribution, and the hologram efficiency increases.

Diffusion of PQ molecules obviously intensifies at elevated temperatures [2]. It has been experimentally revealed that the sample annealing at a temperature of 80 °C results in almost fourfold increase of hologram diffraction efficiency. To fix hologram after annealing it is enough to perform uniform light irradiation and the diffraction efficiency is revealed not to decrease in the process.

Analysis of the recorded gratings also included measurement of contour of angular selectivity (the dependence of the diffraction efficiency on the angle of incidence of probing beam). The angular selectivity value was calculated as a full width at half maximum of the contour:

We have also recorded gratings under the scheme in Fig. 1 for different incidence angles of probing beam, the same value of η is achieved, but the angular selectivity is changing – see Table 1.

Table 1.Values of angular selectivity at different angles of incidence

angle of incidence	angular selectivity
0º	≈2º
8º	1º
16º	36´

The results received indicate to possibility to use holographic materials investigated for multiplexing recording.

[1] A. V. Veniaminov, U. V. Mahilny. Holographic polymer materials with diffusion development: principles, arrangement, investigation, and applications. Optics and Spectroscopy **115**, 906–930, (2013)

[2] U.V. Mahilny, D. N. Marmysh, A. L. Tolstik, V. Matusevich and R Kowarchik. , Phase hologram formation in highly concentrated phenanthrenequinone—PMMA media, J Opt. A: Pure Appl. Opt. **10** , 085302-7pp (2008).

SYNTHESIS AND PROPERTIES OF 9-PHENYL CARBAZOLE DERIVATIVES CONTAINING INDOLE MOIETIES

Karolis Norvaisa, Dalius Gudeika

Department of Polymer Chemistry and Technology, Kaunas University of Technology, Radvilenu pl. 19, LT-50254 Kaunas, Lithuania
karolis.n.9@gmail.com

Compounds with electroactive moieties are widely studied due to their good processability and applications in various optoelectronic devices including organic light emitting diodes [1,2]. Their thin films on the different substrates can be fabricated by using simple techniques, i.e. casting or spin-coating from solutions. Such advantages are important in the fabrication of low cost, large area devices. In this work the synthesis and properties of carbazole and indole derivatives **1-3** will be presented (Fig 1).

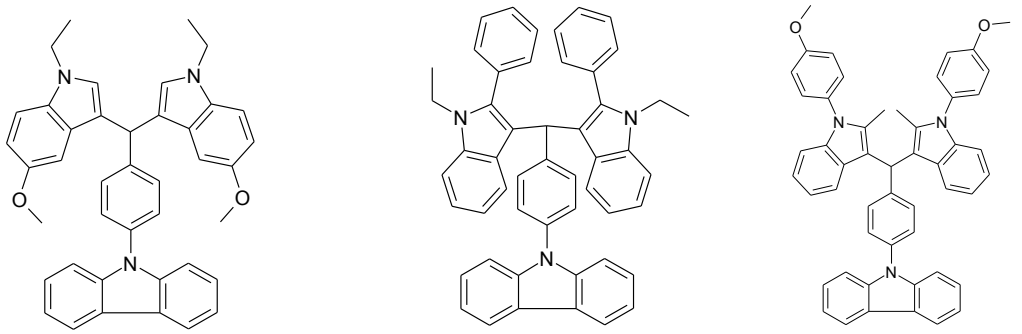

1 **2** **3**

Fig. 1. Structures of **1-3**.

All the compounds demonstrated high thermal stability: their 5% weight loss temperatures were found to be higher than 390 °C. The glass-transitions were observed in the range of 89-130 °C. The ionization potentials of the derivatives were estimated by cyclic voltammetry. They were found to be comparable and ranged from 5.59-5.66 eV. Photophysical properties of the synthesized compounds were studied.

[1] S. R. Forrest, M. E. Eds. Thompson, Organic electronics and optoelectronics. Chemical Review **107**, 923−1386 (2007).
[2] Y. Shirota, H..Kageyama, Charge carrier transporting molecular materials and their applications in devices, Chemical Review **107**, 953−1010 (2007).

SUB-60 FS YB:KGW OSCILLATOR PUMPED BY SINGLE-MODE LASER DIODE

Maciej Kowalczyk*, Jakub Boguslawski, Jan Tarka, Jaroslaw Sotor, Krzysztof M. Abramski

Laser & Fiber Electronics Group, Wroclaw University of Technology, Wybrzeze Wyspianskiego 27, 50-370, Wroclaw, Poland
*m.kowalczyk@pwr.edu.pl

Development of ultrafast lasers emitting radiation in the 1 μm spectral range is crucial for several applications. Amongst them, microfabrication is of the highest industrial importance generating the largest market concerning all laser implementations. Yet, such devices are also indispensable for the whole variety of applications which do not necessarily require very high power like e.g. biomedicine [1].

Here we present a passively mode-locked Yb:KGW laser pumped by a low power single-mode laser diode. A lot of effort was put into power scaling of Yb:KGW oscillators, however we are not aware of a demonstration of a single-mode diode pumped oscillator generating pulses with a duration close to the limit of the crystal performance. In contrary to high power operation, single-mode pumping enabled us to suppress parasitic thermal effects, while keeping the setup compact and its alignment straightforward.

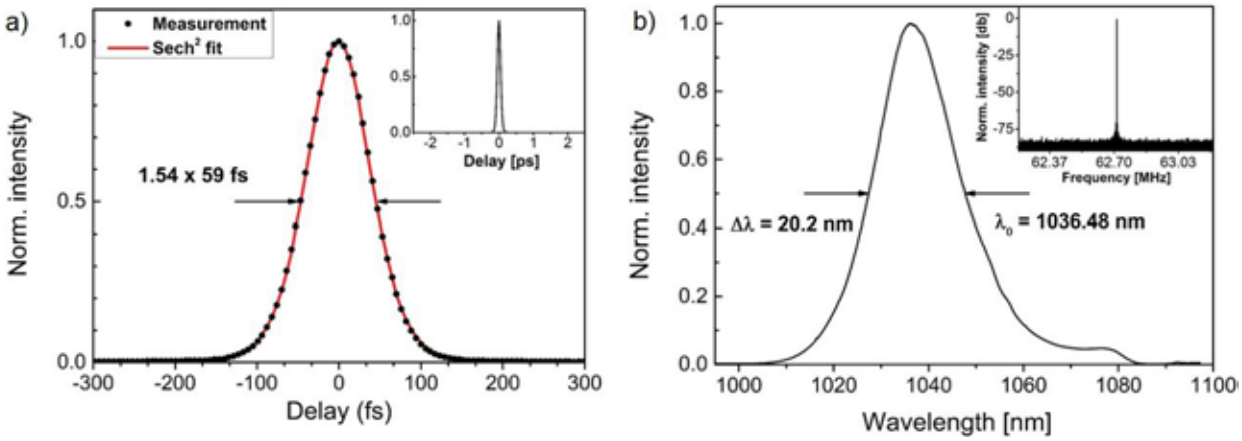

Fig. 1. Output characteristics of the laser in SESAM-assisted Kerr-lens mode-locked regime. (a) Autocorrelation trace with a corresponding sech2 fit (1.5 ps span). Inset: Autocorrelation trace with 5 ps span. (b) Optical spectrum of the pulse. Inset: Radio frequency spectrum of the fundamental beat note (RBW: 1 kHz).

We achieved two different pulsing regimes: the laser can be mode-locked only with semiconductor saturable absorber mirror (SESAM) generating 191 fs pulses with 160 mW of average power. By proper tuning of the same cavity we could exploit soft aperture Kerr-lensing assisted by SESAM. In this configuration the laser emitted almost transform-limited pulses as short as 59 fs with 62 mW of average output power. To our knowledge, these are the shortest pulses generated from an Yb:KGW laser. For such case we obtained 20.2 nm broad spectrum at 1036 nm which approaches the performance limit of the crystal [2]. Figure 1 presents output characteristics of the laser working in described SESAM-assisted Kerr-lens mode-locked regime. Undisturbed mode-locking stability was achieved without active cooling of the gain medium and the laser was entirely self-starting.

[1] J. M. Squirrell, D. L. Wokosin, J. G. White, and B.D. Bavister, "Long-term two-photon fluorescence imaging of mammalian embryos without compromising viability," Nat. Biotechnol. 17(8), 763-767 (1999).

[2] N. V. Kuleshov, A. A. Lagatsky, A. V. Podlipensky, V. P. Mikhailov, and G. Huber, "Pulsed laser operation of Yb-doped KY(WO4)2 and KGd(WO4)2," Opt. Lett. 22(17), 1317-1319 (1997).

BEAM-POINTING CONTROL IN LASER SYSTEMS

Šarūnas Straigis[1], Linas Karpavičius[2], Arūnas Varanavičius[1]

[1] Department of Quantum Physics, Vilnius University, Lithuania
[2]Light Conversion Ltd., Lithuania
sarunas.straigis@gmail.com

Laser beam-pointing stability and control is a topic of great interest in modern science due to the increasing complexity of laser systems [1]. Beam-pointing fluctuations, which are primarily caused by air circulation, convection, temperature and mechanical vibrations can have a negative impact on the operation of such laser systems [2]. High power ultrashort pulse laser system is being developed at Vilnius University Laser Research Center which will be used for high-order harmonics generation in the not too distant future. In order to achieve maximum generation efficiency, laser beam will have to hit a small hole in a needle with 10µm accuracy. Therefore an active beam-pointing stabilization system will be used. We present the design, capabilities and test results of the system that was developed for this task.

Beam-pointing stabilization system consists of position detectors and controllable mirror mounts connected in closed loop (Fig.1). Beam position is detected with cameras that were developed by Light Conversion Ltd. and are capable of calculating the position at 140Hz frequency. The direction of the beam is controlled by *Polaris*^{TM} (*Thorlabs*) mirror mounts with integrated linear piezo elements which offer 500µrad angular range with 0.5µrad precision. PI feedback controllers are integrated inside the cameras providing 0-140V signal to the mirror mounts with 16bit resolution.

Fig. 1 Camera and piezo mirror mount used for beam-pointing stabilization.

We investigated the beam-pointing stability of the laser system and the sources causing fluctuations. It was determined that short term stability of Yb:KGW laser which is the starting point of the laser system is around 1µrad in both axes and can deviate by as high as 60µrad after initial start. We also observed that air ventilation systems present in the laboratory can have a significant impact on the beam-pointing stability and equipment using active cooling can cause major fluctuations.

The active beam-position stabilization system was tested experimentally. We determined that it is capable of reducing fluctuations with frequencies of up to 14Hz (Fig. 2) while higher frequency fluctuations are being amplified by the active control. We also tested how it performs over a large distance when laser beam has to travel more than 10 meters and pass three separate tables. Two pairs of cameras and pieso mirror mounts were used in the experiment. The results with and without stabilization are presented in figure 3. Beam-pointing fluctuations reaching as high as 100µm were successfully reduced by active stabilization system which proved to be capable of keeping beam position with ±5µm precision and 1.2µm standard deviation.

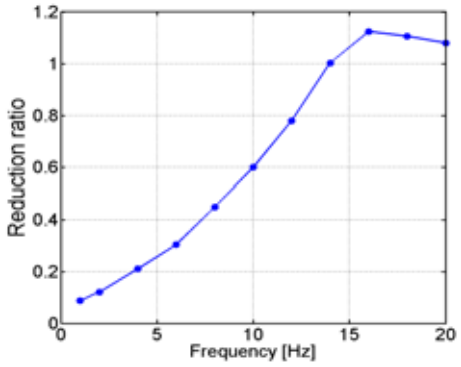

Fig. 2. Frequency response of the active beam-pointing stabilization system

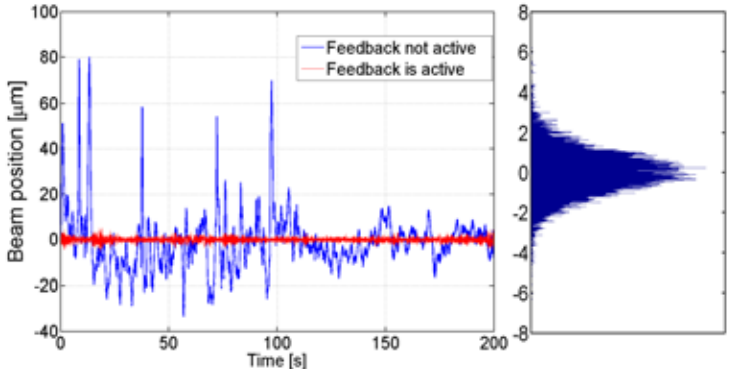

Fig. 3. Beam position stability over large distance with and without active beam-pointing stabilization.

[1] M. Mori, A. Pirozhkov, M.Nishiuchi, K. Ogura, A. Sagisaka et. al., "Development of Beam-Pointing Stabilizer on a 10-TW Ti:Al_2O_3 Laser System JLITE-X for Laser-Exited Ion Accelerator Research", ISSN 1054-660X, Laser Physics, 2006.
[2] G. Genoud, M.B.F. Wojda, A.Persson and C.G. Wahlstrom, "Active Control of the Pointing of a Multi-Terawatt Laser", Rev. Sci. Instrum. 82, 033102,Lund (2011).

RESEARCH ON FOCUSING LARGE DIAMETER BEAMS

Rimantė Jarockytė, Arūnas Varanavičius

Department of Quantum Electronics, Faculty of Physics, Vilnius University, Lithuania
rimante.jarockyte@ff.stud.vu.lt

High intensity laser research is a topic of great interest in modern sciences. These laser sources have various scientific applications. One of the most interesting examples is high-harmonic generation in gases, which requires intensity of a beam to be around 10^{15}W/cm^2. To reach such intensity with a laser system, which has energy of 10mJ and generates pulses with duration around 10fs, it is necessary to have beam focused to a spot, which diameter is smaller than 100μm.

Precise focusing requires careful selection of optical elements to be used. Avoiding aberrations is crucial for having high beam quality. That brings to the goal of this work – to measure aberrations, which can be caused by spherical and parabolic mirrors of large aperture.

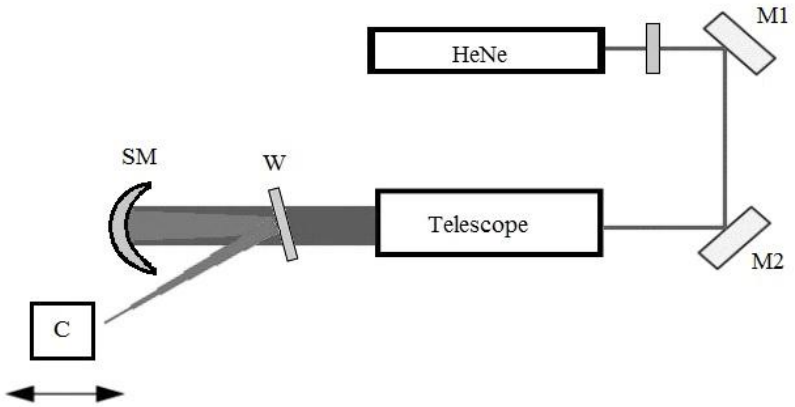

Fig. 1. Optical system, used for the measurements.
HeNe – Helium-Neon lazer, λ=632nm; L – lens, f=1000mm; M1, M2 - mirrors; W –wedge;
SM - spherical mirror, R=3000mm; C- PointGrey camera

During the research, there was made an optical system (Fig. 1), generating 20-23mm diameter collimated beam. Experiments for measuring beam aberrations were carried out and it was found that beam experiences mild astigmatism. Furthermore, characteristics of the beam, reflected from 75mm diameter and R=3000mm spherical mirror were measured. It was found, that astigmatism in a system depends on a pressing and a position of the mirror. Position of least astigmatism was found.

Also, by varying angle of incidence, changes of focus spot size and astigmatism were observed. All measured values were compared with theoretical ones.

Investigation will be continued on parabolic mirrors.

HIGH POWER FEMTOSECOND FCPA SYSTEM USING ROD-TYPE PHOTONIC CRYSTAL FIBER

Tadas Bartulevičius[1,3*], Saulius Frankinas[1,2] and Nerijus Rusteika[1]

[1] EKSPLA, Ltd., Vilnius, Lithuania
[2] Department of Laser Technology, Center for Physical Sciences & Technology, Vilnius, Lithuania
[3] Department of Quantum Electronics, Vilnius University, Vilnius, Lithuania
tadas.bartulevicius@gmail.com

Pulsed fiber lasers are widely used for micromachining applications because of their reliability, excellent beam quality and high output power. High peak power ultrashort pulse fiber lasers are usually realized using fiber chirped pulse amplification (FCPA) technique [1]. Before passing through the amplifier medium, the pulses are temporally stretched to a much longer duration by means of a strongly dispersive element. This reduces the peak power to a level where nonlinear pulse distortion effects in the gain medium are suppressed. After amplification laser pulses are compressed using a pair of diffraction gratings. FCPA technique using large mode rod-type photonic crystal fiber (PCF) benefits from large mode area which helps to reduce nonlinear effects and increase pulse energies from the amplifiers. Compressed pulse energy could reach the level of mJ in this configuration [2]. Maximum pulse energy and quality extremely depends of the intitial pulse parameters. Pulse duration and spectrum could be strongly affected by the seed source parameters. In this work we constructed FCPA system using rod-type Yb doped PCF amplifier and optimized seed source parameters to acheive highest pulse energy from the system. Schematic representation of laser is shown in Fig. 1(a).

Passively mode-locked picosecond all-in-fiber oscillator was used as a seed source in FCPA system. Near transform limited 1 ps pulses from fiber oscillator were stretched up to 430 ps duration, while their spectrum was broadened to 12 nm, by self-phase modulation in passive fiber. Broad spectrum enables to acheive femtosecond duration of the pulses in the output of the laser. Chirped pulses were amplified in a single mode fiber amplifier up to 1μJ energy. Finally the pulses were amplified in the power amplifier which was an 80 cm long single mode Ytterbium-doped polarization maintaining rod-type PCF with large mode area (NKT Photonics). A core diameter of the fiber was 55 μm and pump cladding diameter was 200 μm. Cladding pump configuaration was used in this work. The system was operated at different repetition rates from 250 kHz to 1 MHz. Output power 13-18 W was obtained at these repetition rates. Pulse energy up to 52 μJ was achieved at repetition rate of 250 kHz. A pulse duration of 300 fs was measured after pulse compression. The autocorrelation trace is shown in Fig. 1(b). Output beam quality at the output of the amplifier was evaluated. The best-fit M^2 values were close to 1.1.

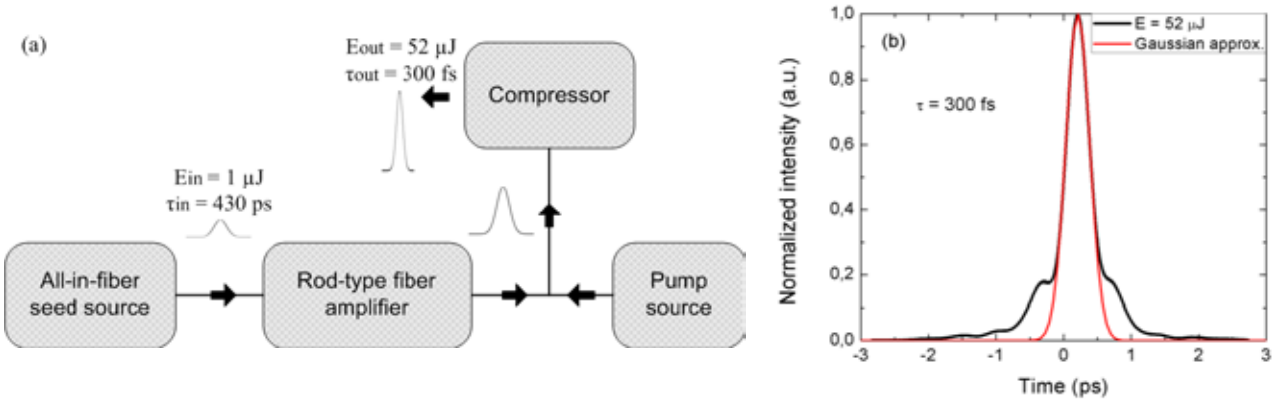

Fig. 1. (a) Schematic representation of laser and (b) experimentally measured intensity autocorrelation trace of amplified pulse at 52 μJ

[1] J. Želudevičius, R. Danilevičius, K. Viskontas, N. Rusteika, and K. Regelskis, Femtosecond fiber CPA system based on picosecond master oscillator and power amplifier with CCC fiber, Opt. Express 21, 5338–45 (2013).
[2] P. Wan, L. Yang, J. Liu, All fiber-based Yb-doped high energy, high power femtosecond fiber lasers, Opt. Express 21, 29854-59 (2013).

DYNAMICS AND SPECTRAL DEPENDANCE OF BIREFRINGENCE, INDUCED AT DIFFERENT WAVELENGTHS IN AZOPOLYMER FILMS

Deyan Ivanov[1,2], Lian Nedelchev[2,3], Dimana Nazarova[2]

[1]Faculty of Physics, Sofia University, Bulgaria
[2]Institute of Optical Materials and Technologies – Bulgarian Academy of Sciences, Bulgaria
[3]University of Telecommunications and Posts, Bulgaria
mr.ivanov@yahoo.com

Azopolymers have been intensively investigated as an efficient media for recording the polarization state of light. They have numerous applications in the field of polarization holography, such as data storage and diffractive optical elements with unique properties [1].

One of the most important optical parameters of the azopolymers is the value of the birefringence Δn induced in them by illumination with polarized light. Usually, laser beam at a single wavelength is chosen as a pump and the birefringence is measured at another single wavelength, different from the pump one. On the other hand, very rarely data about the spectral behavior of Δn are given [2,3]. Even in these cases, the birefringence is induced at a single wavelength. To our best knowledge, there are no reports about the influence of the recording laser wavelength on the photoinduced birefringence spectrum $\Delta n(\lambda)$. For this reason, in this work we present experimental data for the spectrum of birefringence, induced with pump lasers at different wavelengths: $\lambda_1 = 444$ nm, $\lambda_2 = 473$ nm, $\lambda_3 = 488$ nm.

The samples used in our experiments are thin films from an azopolymer shortly denoted as PAZO. Its chemical structure and spectrum of absorbance are shown in Fig. 1(a). The dynamics of the photoinduced birefringence – $\Delta n(t)$ is monitored in real time, measuring the Stokes parameters of a probe He-Ne laser beam ($\lambda = 633$ nm) passing through the sample. The recording continues until Δn reaches saturation. From this measurement the following key information can be obtained: the highest value of the birefringence – Δn_{max}, response time – τ and stability – r, as illustrated in Fig. 1(b).

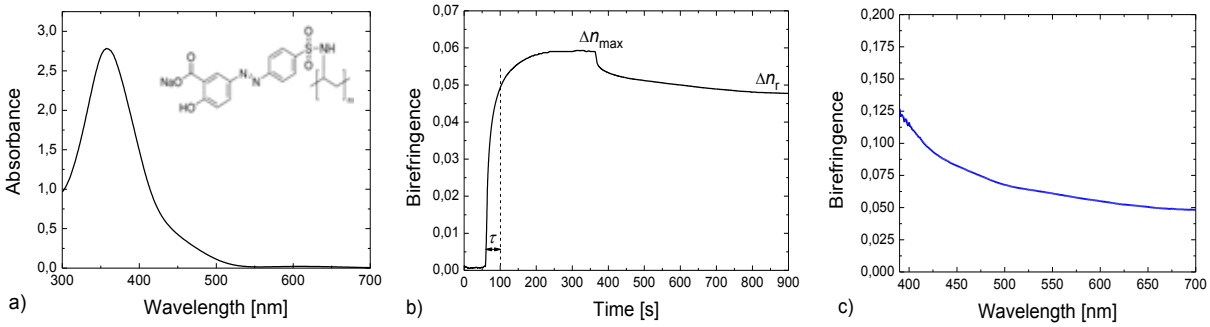

Fig. 1. a) Spectrum of absorbance and chemical structure of the polymer; b) Kinetics of the photoinduced birefringence; c) Spectral dependance of the birefringence, induced by pump laser with $\lambda_2 = 473$ nm.

After the recording, the spectral dependence of the photoinduced birefringence $\Delta n(\lambda)$ is determined, based on the transmittance of the azopolymer sample, placed between two crossed polarizers in a spectrophotometer compartment. As seen in Fig. 1(c), values of Δn vary from 0.05 at the longer wavelengths up to 0.12 close to 400 nm. Good coincidence is observed between the value of Δn obtained from the real-time measurement and $\Delta n(633$ nm) – from the spectral dependence.

As indicated by our experiments, these azopolymer films can be used for recording of polarization diffractive elements, operating in the entire visible range of the light spectrum.

[1] L. Nikolova, P. S. Ramanujam, *Polarization Holography* (Cambridge University Press, Cambridge, 2009).
[2] B. L. Lachut, S. A. Meier, H. A. Atwater, M. J. A. de Dood, A. Polman, R. Hagen, S. Kostromine, Large Spectral Birefringence in Photoaddressable Polymer Films, Advanced Materials **16**, 1746-1750 (2004).
[3] L. L. Nedelchev, D. I. Nazarova, P. Petrova, Large photoinduced birefringence observed over a wide spectral range in an amorphous azopolymer, Bulgarian Chemical Communications **45**, Special Issue B, 133-136 (2013).

OPTIMIZATION PROBLEM FOR LIGHT QUALITY CONTROL OF POLYCHROMATIC SOLID-STATE LIGHTING DEVICES

Ignas Dapsys[1,2]

[1]Department of Mathematics and Informatics of Vilnius University, Naugarduko St. 24, LT-03225 Vilnius
[2]Baltic Institute of Advanced Technology, Sauletekio Ave. 15, LT-10224 Vilnius
ignas.dapsys@mif.stud.vu.lt

Solid-state lighting (SSL) offers superior energy efficiency and control possibilities than traditional light sources such as incandescent and compact flourescent light bulbs [1]. Therefore, many groups of scientists around the world are interested in research and development of SSL. Among such research is the study of colorimetric properties of artificial light [2], its psychophysical effect to an observer and the control of light quality to maintain human needs [3]. Multiple ways have been devised to numerically define color rendering, such as CRI and CQS [4] for human vision, as well as TLCI [5] - for CCD sensors of digital cameras. Therefore, the color rendering is ambiguous, whereas lighting industry requires adaptive lighting fixtures with optimal rendering quality for not just human vision. Although SSL offers better energy savings, their color rendering and adaptive control of color temperature leave much to be desired. Yet, it may be overcome by the control capabilities offered by polychromatic SSL. By changing the electrical current driving a SSL device, we can modify the light output, i.e. illuminance E, correlated color temperature T. In this work, a mathematical model for a control of polychromatic SSL device, that will be used to maximize color rendering index R while changing the correlated color temperature T and maintaining constant illuminance E is going to be presented.

The modelled polychromatic SSL device consists of n light emitting diodes (LEDs), each of different color, and is driven by a pulse wave modulation (PWM) power source with n independently controllable channels. Each of the channels is described by the control parameter q, that is the pulse width in time scale. The light spectrum of each LED is represented by a Gaussian distribution

$$S(\lambda, q) = P(q) \exp\left\{ -\frac{(\lambda - \lambda_{max})^2 4 \ln 2}{\Delta\lambda^2} \right\}, \tag{1}$$

where $P(q)$ is the optical power of an each LED, λ_{max} is the peak wavelength and $\Delta\lambda$ is the spectral width at half-maximum. One can see that only the optical power depends on the q. The entire spectrum of this SSL device is given by a sum of the spectra of each LED.

The spectrum can then be used to calculate the illuminance E, color temperature T and color rendering index R. In this case, all depends on n variables: $E(q_1, q_2, \ldots, q_n)$, $T(q_1, q_2 \ldots, q_n)$ and $R(q_1, q_2, \ldots, q_n)$. $R(q_1, q_2, \ldots, q_n)$ is the objective function that we seek to maximize by changing the pulse widths $q_1, q_2, \ldots, q_n$, each for one of the n LEDs, with respect to following conditions: the illuminance and the correlated color temperature must remain constant to the preset values. Therefore, we formulate the following optimization problem

$$\max_{q_1, q_2, \ldots, q_n} R(q_1, q_2, \ldots, q_n) \tag{2}$$

such that the following constraints are met

$$E(q_1, q_2, \ldots, q_n) = E_0, \quad E_0 \in [0, 1], \tag{3}$$

$$T(q_1, q_2, \ldots, q_n) = T_0, \quad T_{min} \leq T_0 \leq T_{max}. \tag{4}$$

The optimization problem is solved by using the brute force algorithm. The grid with 10 points per control parameter is created. Then values of E, T, and R are calculated with all possible n-tuples of control parameters. That is 10^n number of values for each of the function. However only defined number of control parameters can meet the constrains of the optimization problem. The problem is solved with $n = 2, 3$, and 4. The relationship between the color temperature T and color rendering index R is determined. The results of the optimization problem for four LEDs using three polychromatic SSL configurations: RGBA, RGB[WW] and RGB[CW], where R is red, G - green, B - blue, A - amber, WW - warm white and CW - cool white LEDs, are compared.

[1] E. F. Schubert, J. K. Kim, Solid-state light sources getting smart, SCIENCE **308**, 12741278 (2005).
[2] A. Zukauskas, R. Vaicekauskas, F. Ivanauskas, R. Gaska, M. S. Shur, Optimization of white polychromatic semiconductor lamps, Appl. Phys. Lett. **80**(2), 234 (2002).
[3] M. Aldrich, N. Zhao, and J. Paradiso, Energy efficient control of polychromatic solid-state lighting using a sensor network, Proc. of SPIE **7784**, 778408 (2010).
[4] M. Wood, CRI and the Color Quality Scale, Part 2, Protocol 15(2), 1620 (2010).
[5] European Broadcasting Union, Television Lighting Consistency Index, https://tech.ebu.ch/tlci-2012, [accessed 2015-12-16] (2012).

INVESTIGATION OF THE LIGHT SOURCES USING VARIOUS FIELDS COLORIMETRIC FUNCTIONS

Justina Aglinskaitė, Andrius Petrulis[1]

[1] Institute of Applied Research, Vilnius University, Lithuania
justinaaglin@gmail.com

All visible colours for human can be described mathematically using colour mixing principles and human's eye characteristics. The eyes have three kinds of a cone cells if the vision is normal. These cone cells have different spectral sensitivities and according to that the colorimetric viewing functions were derived and standardized as *CIE 1931 2° Standard Observer*[1]. Colorimetric viewing functions relate physical and physiological light parameters. Rods and cones are responsible for human vision and have uneven spatial distribution in retina, so colorimetric functions depend not only on spectral sensitivity of different cones, but also on spatial distribution of rods and cones, so our vision depends on viewing angles. For this reason for larger viewing fields *CIE 1964 10° Standard Observer* was derived.

The main problem resulting from this colorimetric functions dependence on viewing angles is that it makes it more difficult to describe colours unambiguously. Nowadays almost every light and colours related institution uses only 2° viewing field functions which really contravene reality because people usually do not look at minor things. It turns out, that metameres can be calculated just for defined viewing angles and would appear different under other observer viewing angles. Spectral power distributions difference between metameres can be seen in figure 1. According to this graph 2° viewing field has stronger impact in short wavelength for our brightness perception. Hu and Houser[2] also showed that for more larger fields colour matching functions also differ. No other than *CIE 1931 2°* and *1964 10°* colour matching functions are officially created and approved.

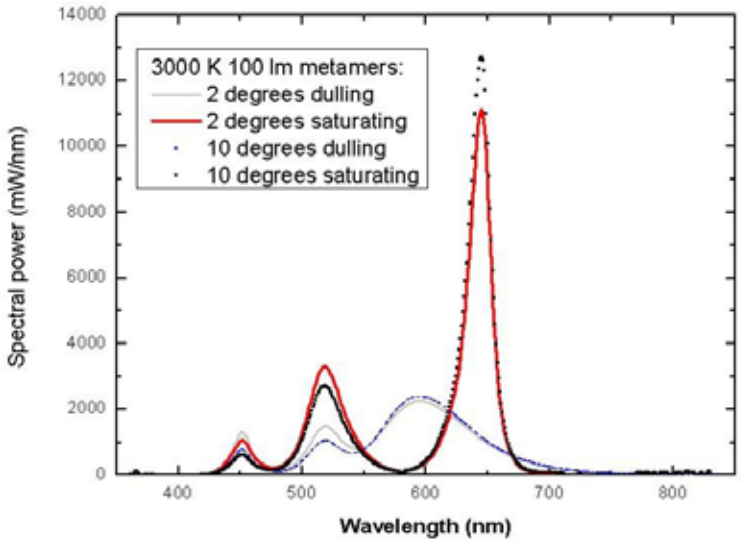

Fig. 1 Saturated and dulling spectral power distributions for 2° and 10° viewing fields and normalized to 100 lm

For example, huge difference between various viewing fields can be seen calculating luminous flux for 2° and 10° viewing fields of different light emitting diodes. Luminous flux increases when our viewing field increases up to *20°* so if we look at larger area illuminated with the same illuminator we will think that light is brighter. Luminous flux of royal blue light emitting diode (453 nm) increases more than 100% for 10° viewing field according to 2° viewing field while other colour LEDs has a lower increase in luminous flux. Yellow and green visible spectrum region has a lowest increase of perceived flux and brightness.

More studies are needed to fully understand viewing angle influence for our colour perception. Existing colour perception and luminous fluxes are investigated at known photometry for common and high-end light sources. In the future brightness dependence on spectral power distribution is going to be investigated.

[1] CIE (1932). Commission internationale de l'Eclairage proceedings, 1931. Cambridge: Cambridge University Press.
[2] Hu X., Houser KW Large-field colour matching functions. Colour Research and Application 2006; 31: 18-29.

THE CHARGE DENSITY ANALYSIS OF FERROCENE TAXOL ANALOGUE

Sylwia Pawlędzio, Anna Makal, Krzysztof Woźniak

Biological and Chemical Research Centre, Department of Chemistry, Univeristy of Warsaw, Poland
spawledzio@chem.uw.edu.pl

The ferrocene analogue of taxol (named TAX1) was investigated. The most important fragment in the investigated molecule is a β- lactam ring, which constitutes the core of the structure of many antibiotics families (for example penicillins, cephalosporins, carbapenems, and monobactams). The compound is also considered as a candidate for cancer treatment.

The structural and high resolution X-ray diffraction experiments were performed (on single crystal diffractometer in 100 K and 90 K, respectively) and analysis of the experimental electron density distribution was performed. Five different approaches were tested in order to characterize the distribution of the electron density. Modeled were electron density distributions for molecule with local symmetry imposed on atoms or without symmetry (while the iron atom was assigned an initial charge of either zero or plus two). For the last model in which the UBDB bank was applied, were calculated electron density distributions for a molecule with a local symmetry imposed on atoms when all multipole populations were allowed and iron atom has a neutral valance.

Preliminary results suggest that the model without imposed local symmetry, in which the iron atom has a zero valance population was the best. In all models the iron atom has positive charge, but the exact value of the charge is different in each model. It is worth to notice, that some of the populations of multipole parameters prohibited due to the local symmetry were statistically significant, when the model without imposed symmetry was tested. The atomic charges in the current best model are negative on both oxygen atoms and, on nitrogen atom, while the carbon atoms in the β-lactam ring have positive charges. The distribution of the electrostatic potential around the TAX1 molecule and the network of intermolecular hydrogen bonds will be presented.

THERMOANALYTICAL INVESTIGATION OF La–Bi–Mo–O NITRATE–TARTARE GEL PRECURSORS PREPARED BY THE AQUEOUS SOL-GEL SYNTHESIS METHOD

Jonas Gadeikis[1], Artūras Žalga[1]

[1] Department of Applied Chemistry, Faculty of Chemistry, Vilnius University, Naugarduko Str. 24, LT-03225 Vilnius, Lithuania
jonas.gadeikis@chf.stud.vu.lt

Ln_2MoO_6 (Ln= lanthanides and Y) compounds are of interests because of their potential applications in catalysis. They have been reported to crystallize in three polymorphs with monoclinic (α), cubic (β), or tetragonal (γ) symmetries, depending on the size of Ln and the synthesis conditions [1].

The lanthanum molybdate compounds form a group of ceramic materials whose properties are dependent upon the crystalline structure and on the molybdenum valence. The phase diagram of this system exhibits several phases with La_2O_3–MoO_3 molar ratios 1:1, 1:2, 1:3, 1:4, 1:6, 2:1, 3:1 and 9:4. Earlier crystallographic studies of the La_2MoO_6 mixed oxide have shown that it crystallizes in the tetragonal structure, space group I42m (no. 121). Neutron diffraction results revealed that the crystalline structure of the La_2MoO_6 phase might be described as constituted by two La_2O_2 layers intercalated between layers of MoO_4 tetrahedra. The lanthanum ions are coordinated by eight oxygen ions, whereas each molybdenum ion is fourcoordinated with oxygen ions, in the first coordination sphere [2].

Although the rare earth molybdates are important compounds for a wide range of applications, many different synthesis techniques for the preparation of such kind of materials are really desirable. For the most part, these materials are currently synthesized by solid-state reactions with the mixtures of rare earth oxides and MoO_3. This process takes generally several days of heating with intermediate grindings. In this instance, high temperatures, lengthy heating process, and especially subsequent grinding damage the substance surfaces, resulting in the loss of expected of both physical and chemical properties. Besides, the volatility of MoO_3 at elevated temperatures makes the synthesis of rare earth molybdates more difficult. These limitations of the traditional solid-state method motivated us to explore the searching of synthesis technique that could shorten, facilitate, and reduce the preparation way of the rare earth molybdates. In the past few decades, many researchers have carried out the studies on the formation of metal complexes with organic ligands. Furthermore, the metal complexes with organic ligands have been used for the preparation of ceramics and metal oxide thin films by a sol–gel process, using metal nitrates, chlorides, and acetates as starting materials. Besides, metal salts are very useful, inexpensive, and very easy to handle in comparison to metal alkoxides, and hence they are good alternatives for the conversion to oxides by thermal decomposition. They can be dissolved in many kinds of organic solvents in which metal complexes are formed. From this point of view, the wet synthesis route called an aqueous sol–gel method is really attractive and compared to other techniques, as it has the advantages of a good control of the starting materials and of the processing parameters, a high purity of the raw materials, and the low temperature of the process, which completely minimizes the volatility of molybdenum (VI) oxide by formation of double metal molybdates [3].

In this study the La–Bi–Mo–O nitrate–tartrate gels were prepared by an aqueous sol-gel synthesis method using tartaric acid as complexing agent. $La_{2-x}Bi_xMoO_6$ mixed oxides were obtained after annealing of the initial La–Bi–Mo–O nitrate–tartrate gel precursors at 600, 800, 1000 and 1200 ^oC temperatures. The main purpose of this work was to obtain dense ceramic materials. The thermal decomposition behavior of the metal complexes and residue of tartaric acid was studied by thermal analysis and Fourier transform infrared spectroscopy. A surface morphology and elemental analysis were estimated by scanning electron microscopy (SEM) and Energy-dispersive X-ray spectroscopy (EDX). X-ray diffraction measurements (XRD) were also performed in order to estimate the crystal phases of corresponding oxides annealed at different temperatures.

[1] J. S. Xue, Mark R. Antonio, and L. Soderholm, Polymorphs of Ln_2MoO_6: A Neutron Diffraction Investigation of the Crystal Structures of La_2MoO_6 and Tb_2MoO_6, Chemistry of Materials, 1995, 7, 333-340.

[2] R.A. Rocha, E.N.S. Muccillo, Characterization of La_2MoO_6 prepared by the cation complexation technique, Journal of Alloys and Compounds 400 (2005) 83–87.

[3] R. Stankeviciute, A. Zalga, Sol–gel synthesis, crystal structure, surface morphology, and optical properties of Eu_2O_3-doped $La_2Mo_3O_{12}$ ceramic, Journal of thermal analysis and calorimetry 118 (2), 925-935 (2014).

STUDIES ON PHOTODEGRADATION OF $CpFe(CO)_2(\eta^1$-*N*-imidato) COMPLEX

Aneta Kosińska[1], Emilia Fornal[2], Ewa Parfieniuk[2], Anna Gumieniczek[3], Bogna Rudolf[1], Grzegorz Celichowski[4]

[1] Department of Organic Chemistry, University of Lodz, Poland
[2] Laboratory of Spectroscopic and Separation Mehod Applications, The John Paul II Catholic University of Lublin, Poland
[3] Faculty of Pharmacy, Medical University of Lublin, Medical University of Lublin, Poland
[4] Department of Materials Technology and Chemistry, University of Lodz, Poland
kosinskaneta@wp.pl

Over the past few years we have explored the chemistry of metallocarbonyl maleimide complexes (η^5-cyclopentadienyl)$M(CO)_n(\eta^1$-*N*-maleimidato) (M=Fe, Ru, W, Mo, n=2,3), which can be applied as useful IR-detectable markers endowing labeled molecules with strong absorption bands in the 1800-2150 cm^{-1} spectral region which is free of any absorption by proteins or biological matrixes [1-3]. This feature makes them useful as IR-detectable markers for monitoring of biochemical processes such as hormone-receptor or antigen-antibody interactions. It was also found that these compounds can release carbon monoxide in therapeutic amounts upon irradiation with UV and visible light and can be used as CO-RMs (*Carbon Monoxide – Releasing Molecules*).

Herein we report the studies on photodegradation of $CpFe(CO)_2(\eta^1$-*N*-imidato) complexes exposed to the UV and visible light. The formation of degradation products was monitored by LC-MS and FTIR spectroscopy. In case of maleimide complex, it was found that one of the degradation products is the product of Diels-Alder reaction of (η^5-cyclopentadienyl)$Fe(CO)_2(\eta^1$-*N*-maleimidato) with cyclopentadiene release from the other molecule of complex (Scheme 1) [4].

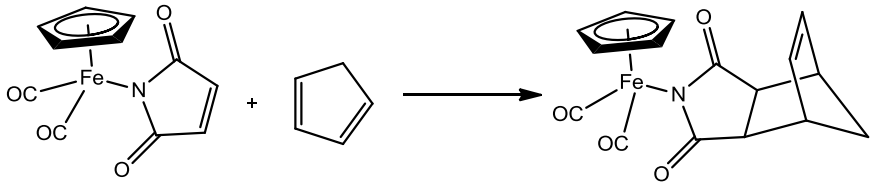

Scheme 1. The product of Diels-Alder reaction of $CpFe(CO)_2(\eta^1$-*N*-maleimidato) with cyclopentadiene.

[1] B. Rudolf, J. Zakrzewski, M. Salmain, G. Jaouen, Metallo-carbonyl complexes based on the $CpFe(CO)_2(\eta^1$-N-imidato) system as protein labeling reagents: Reactivity and selectivity studies using bovine serum albumin as a model protein, New J. Chem. **22**, 813-818 (1998).
[2] M. Salmain, N. Fischer-Durand et al., Transition metal-carbonyl labeling of biotin and avidin for use in solid-phase carbonyl metallo immunoassay (CMIA), Bioconjugate Chemistry **13**, 693-698 (2002).
[3] N. Fischer-Durand, M. Salmain, B. Rudolf et al., Design of a new multifunctionalized PAMAM dendrimer with hydrazide-terminated spacer arm suitable for metal-carbonyl multilabeling of aldehyde-containing molecules, Macromolecules **40**, 8568-8575 (2007).
[4] B. Rudolf, M. Palusiak, J. Zakrzewski, Diels-Alder reaction with cyclopentadiene and electronic structures of (η^5-cyclopentadienyl)$M(CO)_x(\eta$1-N-maleimidato) (M = Fe, Mo, W, x = 2 or 3), J. Organomet. Chem. **694**, 1354-1358 (2009).

SYNTHESIS AND CHARACTERIZATION OF Mn^{4+} DOPED INORGANIC FLUORIDES

Simonas Lialys, Simas Šakirzanovas

Department of Applied Chemistry, Faculty of Chemistry, Vilnius University, Naugarduko Str. 24, 03225 Vilnius, Lithuania
simonas.lialys@chf.stud.vu.lt

White light emitting diodes (WLEDs) are replacing incandescent and halogen lamps because of their energy saving and environment-friendly characteristics [1]. Nowadays commercial WLEDs are produced by combining yellow $Y_3Al_5O_{12}:Ce^{3+}$ phosphor and blue InGaN chip [2]. However, this combination lacks red colour emission and thus emits cool white light with high correlated colour temperature. In order to achieve warm white light for indoor lighting we need to employ a phosphor with emission in the red spectral region.

Recently, studies of inorganic fluoride phosphors doped by tetravalent manganese (Mn^{4+}) ions attracted much attention [3]. Mn^{4+} ions in fluoride hosts exhibit broadband absorption ($^4A_{2g} \rightarrow {}^4T_{2g}$ and $^4A_{2g} \rightarrow {}^4T_{1g}$) overlapping InGaN electroluminescence band and sharp emission lines due to the forbidden electron transition ($^2E_g \rightarrow {}^4A_{2g}$). Moreover, the position of Mn^{4+} emission lines depends on the distance between Mn-F in a host crystal. These characteristics lead to exploration of a practical red phosphor with desired optical and thermal properties.

In this study, we synthesized series of Mn^{4+} doped fluorides $A_2XF_6:Mn^{4+}$ (A = K or Na; X = Si or Ti) by convenient co-precipitation method. The preparation was carried out by dissolving SiO_2 or TiO_2 in 40% hydrofluoric acid solution and mixing it with K_2MnF_6 and KF or $NaSO_4$ at ambient conditions. Dopant concentration was controlled by adjusting the quantity of K_2MnF_6. Phase purity and surface morphology of obtained samples were measured using X-ray powder diffractometer and scanning electron microscope respectively. Photoluminescence properties (excitation, emission, temperature-dependent emission, quantum efficiency) and UV-vis reflectance spectra of Mn^{4+} in different host lattices were recorded on a spectrofluorometer.

The results showed that abovementioned hosts fluorides are suitable for Mn^{4+} doping because of the similar ionic radius between Mn^{4+} and Si^{4+} or Ti^{4+}. The maximum photoluminescence emission peaks were found to be situated at 626 nm ($Na_2TiF_6:Mn^{4+}$), 627 nm ($Na_2SiF_6:Mn^{4+}$), 630 nm ($K_2SiF_6:Mn^{4+}$) and 631 nm ($K_2TiF_6:Mn^{4+}$). The intensity of emission and excitation strongly depends on the concentration of the dopant (Fig. 1).

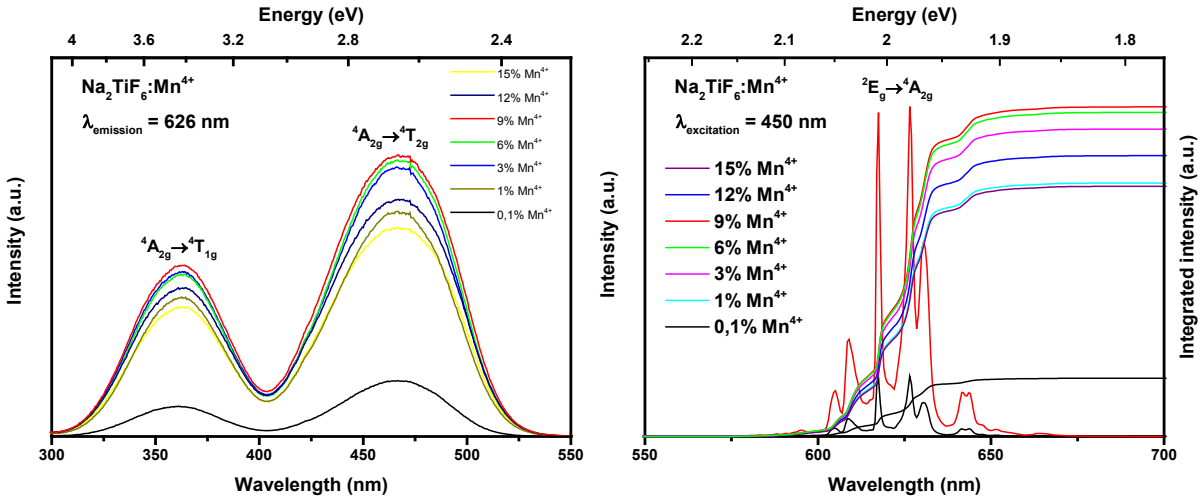

Fig. 1. Experimental excitation and emission spectra of $Na_2TiF_6:Mn^{4+}$.

[1] Zhu, H., et al., *Highly efficient non-rare-earth red emitting phosphor for warm white light-emitting diodes.* Nat Commun, 2014. **5**: p. 4312.
[2] Shen, X., et al., *Fabrication and characterization of YAG:Ce phosphor films for white LED applications.* Journal of Materials Science: Materials in Electronics, 2015: p. 1-6.
[3] Brik, M.G. and A.M. Srivastava, *On the optical properties of the Mn4+ ion in solids.* Journal of Luminescence, 2013. **133**: p. 69-72.

SYNTHESIS AND OPTICAL PROPERTIES OF Er^{3+} AND Yb^{3+} CO-DOPED La_2BaZnO_5

Artur Lyskoit, Simas Sakirzanovas

Department of Applied Chemistry, Faculty of Chemistry, Vilnius University, Lithuania
Artur.lyskoit@chf.stud.vu.lt

In the last 10 years photon upconversion materials have undergone significant expansion and have become one of the most active research fields. These kinds of materials can emit ultraviolet, visible and near-infrared wavelengths under near-infrared radiation (anti-Stokes emission presence) (for example Fig.1). In addition, lanthanide doped upconverting materials have the following characteristics: narrow emission spectrum, fluorescence stability, low background fluorescence and light scattering from bio-systems. The unique properties of novel photon upconversion materials have a wide range of applications from traditional fields, for example, solid-state lasers to novel 3-D display technology, biotechnology, security labeling and solar cells [1].

Up to now, many halides are reported as the most efficient crystal structures to observe upconversion process, but often shows poor chemical stability (hygroscopy) limiting their industrial applicability [2]. In this work Er^{3+} and Yb^{3+} co-doped tetragonal La_2BaZnO_4 powders were prepared via a high temperature solid-state and combustion synthesis methods. La_2BaZnO_5 can be an excellent host for doping with various ions, provide good chemical, thermal and mechanical stability and it is promising materials for practical applications. The phase purity and crystal structure were characterized by X-ray powder diffraction method (XRD), the surface morphology was determined by scanning electron microscopy (SEM) and luminescence properties were measured with spectrofluorometer.

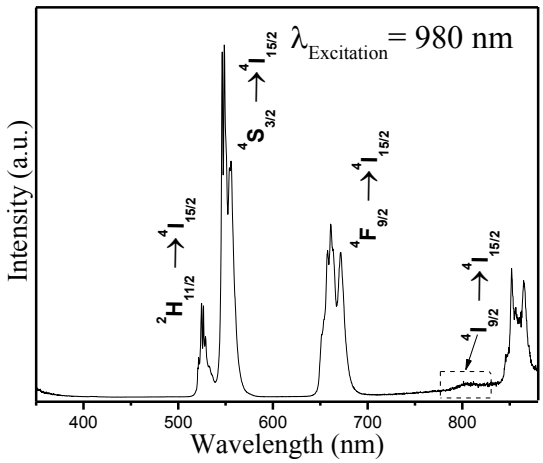

Fig. 1. Luminescence photon upconversion spectrum of 0,4% Er^{3+} and 4% Yb^{3+} doped La_2BaZnO_5.

[1] Fan Zhang, Photon upconversion nanomaterials, **428**, 1-2 (2015)
[2] I. Etchart, Metal oxides for efficient infrared to visible upconversion, Summary of doctoral dissertation, University of Cambridge, Cambridge, 2010.

STUDY OF COMPONENTS DIFFERENT CONCENTRATION INFLUENCE TO FORMATION OF STRONTIUM YTTRIUM FLUORIDE

L.Bereiša, D.Sakalauskas, S.Šakirzanovas

Department of Applied Chemistry, Vilnius University, Naugarduko 24, LT-03225 Vilnius, Lithuania
bereisa.lukas@gmail.com

Nowadays is increasing demand to find a new techniques for the facile synthesis of nanosized phosphors. Ultrasmall monodispersed light-emitting nanomaterials have real and potential applications in solid-state lasers, bioimaging, optical data storage and three-dimensional flatpanel display. Resent publications have reported that colloidal $NaYF_4$ hosts in either α- or βphase doped with RE (RE = Er, Yb, Ho or Tm) are the best candidates for biological applications [1]. However, there are only a few reports on a series of alkali-earth–rare-earth complex fluoride, xMF_2–$yRREF_3$ (M = Na,Ba, Sr), (R = Y, Gd), (RE = Er, Yb, Ho or Tm) ternary compounds [2]. It is believed that the alkali-earth–rare-earth complex fluorides have cubic and trigonal phase structure and might possess highly efficient UC emission [3].

Firstly we decided to start from creating a host material which would be suitable for biological applications, one of requirements for nanoparticles is their size. As mentioned above alkali-earth– rare-earth complex fluoride are promising host material for UCNPs. $SrYF_5$ have been selected as the research object. $SrYF_5$ particle are dependent on the nucleation rate, which, in turn, was governed by the reagents concentration, molar ratio, choice of capping ligand and viscosity of reaction mixture. Temperature of synthesis was kept as constant.

$SrYF_5$ samples were synthesized using co – precipitation method. All samples were analyzed using X-Ray diffraction (XRD), scanning electron microscopy (SEM), dynamic light scattering (DLS), infrared spectroscopy (FTIR) methods. By changing respectively the ratio of all components (from 90-10 mol %), we got nanoparticles of different size and shape. TRITON X100 and TWEEN 80 were selected as capping agents. Synthesis conditions and surfactant concentration influents to particle size and shape will be discussed.

---

[1] Ma, M., et al., *Solvothermal synthesis and tailored upconversion emission of monodisperse ultrasmall face-centered cubic Sr2YF7 nanocrystals.* Journal of Alloys and Compounds, 2012. **525**(0): p. 97-102.

[2] Fedorov, P.P., et al., *Nanofluorides.* Journal of Fluorine Chemistry, 2011. **132**(12): p. 1012-1039.

[3] Xia, Z., P. Du, and L. Liao, *Facile hydrothermal synthesis and upconversion luminescence of tetragonal Sr2LnF7:Yb3+/Er3+(Ln = Y, Gd) nanocrystals.* physica status solidi (a), 2013: p. n/a-n/a.

SYNTHESIS AND PROPERTIES OF HEPTACENE ANALOGS - 8*H*-16,17-EPOXYDINAPHTO[2,3-*c*:2',3'-*g*]CARBAZOLES

Renaldas Rimkus[1], Tomas Serevičius[2], Regimantas Komskis[2], Povilas Adomėnas[2], Alytis Gruodis[3], Vygintas Jankauskas[2], Karolis Kazlauskas[2], Saulius Juršėnas[2] and Sigitas Tumkevičius[1]

[1] Department of Organic Chemistry, Vilnius University, Lithuania
[2]Institute of Applied Research, Vilnius University, Lithuania
[3]Department of General Physics and Spectroscopy, Vilnius University, Lithuania
renaldas.rimkus@chf.stud.vu.lt

Higher acenes are highly demanded in field of organic electronics, due to their high hole drift-mobility properties. However, higher acenes suffer from at least few drawbacks, such as low solubility in organic solvents that aggravates processing via printing technologies, photodimerization and oxygen addition reactions that occur at ambient conditions and lead to degradation of materials. Few design strategies were successfully introduced to increase stability of these molecules. First and the most successful of them, is replacement of some benzene rings with heterocyclic moieties, second, edge-cutting modification is non-linear arrangement of rings in the molecule. The introduction of heteroatoms to polyacene scaffold increases stability of the materials without loss or even with an increase of charge mobility [1]. Adjustment of aromatic ring annulation with introduction of heteroatoms has already showed some promising results [2]. Herein we present a novel V-shaped and two heteroatoms enriched heptacene analogs - 8*H*-16,17-epoxydinaphto[2,3-*c*:2',3'-*g*]carbazoles (EDNC), as potential materials for organic electronic devices. The results of investigation of their optical and photoelectric properties will be presented, as well.

Synthesis of EDNC derivatives was carried out using 2,7,9-trisubstituted carbazoles as initial materials. Few steps synthetic protocol allowed to introduce solubilizing side-substituents into 6, 8 and 10 positions of the molecule, reducing solubility issues of the materials to negligible levels. The synthesized EDNC derivatives are stable under ambient conditions in a solid state and solutions.

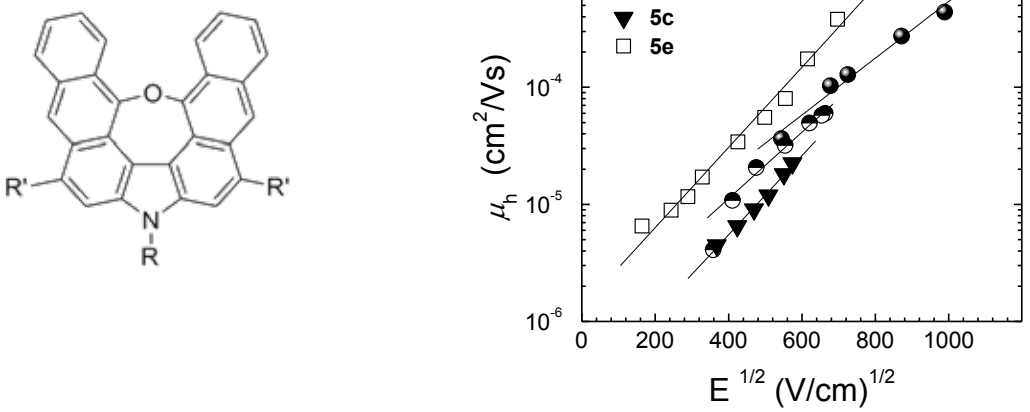

Fig. 1. General structure of EDNCs and hole drift-mobilities of its derivatives as a function of applied electric field.

Optical properties of the synthesized compounds were assessed by absorption and fluorescence spectroscopy. Fluorescence spectra for most derivatives were observed at about 545 nm in solutions and in the range of 560 - 595 nm in solids. Hole drift-mobility of synthesized compounds was measured by XTOF method and reached up to $8 \cdot 10^{-4}$ cm^2/(V s), which is enhanced for compounds possessing aryl side-substituents at 6 and 10 positions.

[1] T.V. Pho, J. D. Yuen, J. A. Kurzman, B. G. Smith, M. Miao, W. T. Walker et al., *N* -Alkyldinaphthocarbazoles, Azaheptacenes, for Solution-Processed Organic Field-Effect Transistors, J. Am. Chem. Soc. **134**, 18185-18188 (2012).
[2] T. Okamoto, C. Mitsui, M. Yamagishi, K. Nakahara, J. Soeda, Y. Hirose et al., V-Shaped Organic Semiconductors With Solution Processability, High Mobility, and High Thermal Durability, Adv. Mater. **25**, 6392-6397 (2013).

STUDY OF WATER-ACETYLACETONE COMPLEXES BY THE MEANS OF MATRIX ISOLATION INFRARED ABSORPTION SPECTROMETRY

Rasa Platakytė[1], Joanna Lach[1], Justinas Čeponkus[1], Claudine Crepin-Gilbert[2], Alejandro Gutierrez[2], Michele Chevalier[2], Valdas Šablinskas[1]

[1]Vilnius University, Faculty of Physics, Department of General Physics and Spectroscopy, Saulėtekio al. 9, Vilnius
[2]CNRS and Paris Sud University, Institute o Moecular Sciences, 91405 Orsay, France
rasa.platakyte@ff.stud.vu.lt

Acetylacetone (AcAc) is a relatively simple organic compound whose structure is determined by an internal hydrogen bond. This molecule has been analyzed before but not all of its structural and dynamic properties have been fully researched [1]. In this experiment, acetylacetone molecules formed intermolecular hydrogen bonds with water molecules. Analysis of such complexes is a good way to study the influence of hydrogen bond formation on properties such as complex structure, charge and energy transfer mechanisms.

Theoretical calculations (using density functional theory (DFT) at the B3LYP/6-311++G(3df,3dp) level) gave information about the possible molecular complex geometry (fig. 1) and the theoretical IR spectra.

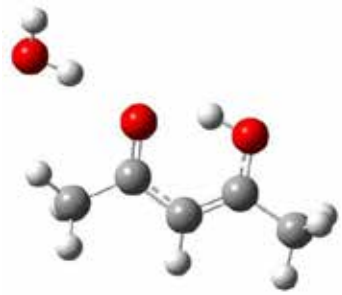

Fig. 1. Optimal structure of AcAc and H_2O molecular complex as determined by theoretical calculations.

IR spectra were registered after isolating sample molecules in a host gas and depositing them on a low-temperature spectral window. We registered the spectra of both pure substances and their mixture. From the new bands in the mixture spectra (fig. 2) at 3520 cm^{-1} and 3420 cm^{-1} we can conclude that stable complexes do form from one acetylacetone and one or two water molecules. Acetylacetone bands themselves are not very sensitive to the formation of hydrogen bond. The greatest changes can be witnessed at 960 cm-1 (band resulting from the out-of-plane bending vibration of OH).

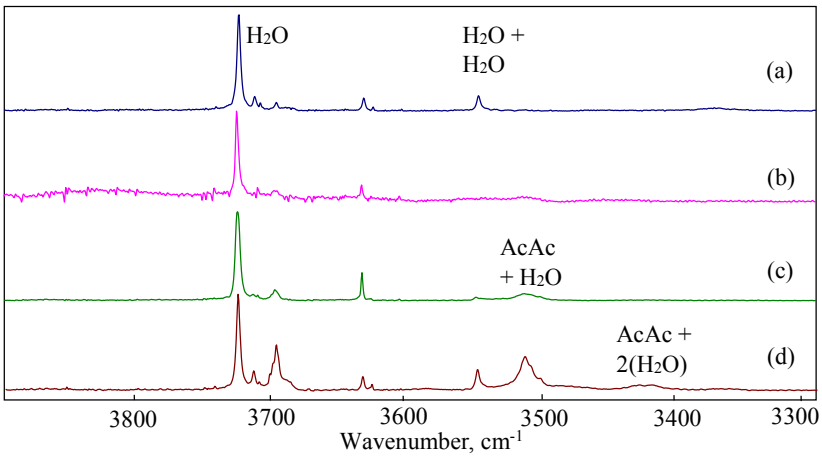

Fig. 2. (a) Experimental spectra of water in nitrogen at 25 K, (b) acetylacetone in nitrogen at 9 K, (c) acetylacetone and water in nitrogen (1:1:500) at 9 K and (d) at 25 K.

The obtained results were enough to determine that the water molecule is attached to the carbonyl group in acetylacetone. We also carried out experiments with argon as matrix gas and with deuterated acetylacetone and heavy water to better understand the dynamics of this complex.

[1] R.R. Lozada-Garcia et al., Chem. Phys. Lett. 504, 142 (2011)

PARAMETRIC AMPLIFICATION OF BROADBAND CHIRPED PULSES AT 2 μm

Agnė Marcinkevičiūtė, Marius Guščia, Rytis Butkus

Vilnius University, Faculty of Physics, Saulėtekio al. 10, LT-10223 Vilnius, Lithuania

agne.marcinkeviciute@ff.stud.vu.lt

Generation of broadband laser pulses, especially in the near and mid-infrared spectral range, is receiving increased amounts of attention from the scientific community due to its quickly developing applications in strong-field physics [1], [2]. Such broadband signals are mostly achieved using nonlinear parametric interactions, while the energy of the signal is generally increased via optical parametric chirped pulse amplification (OPCPA) [3].

We present experimental results of generation and parametric amplification of broadband pulses at 2 μm using methods of difference frequency generation (DFG) and OPCPA. A broadband chirped signal was generated by implementing DFG technique and amplified using a two-stage optical parametric amplifier (OPA).

The whole system was based on Ti:sapphire oscillator providing femtosecond pulses at around 800 nm. It acted as a seed source for pump amplifiers and the broadband infrared signal thus providing optical synchronization between the two. In order to boost the energy of pulses generated by the oscillator, a parametric chirped pulse amplifier was employed. The signal of the oscillator was split into two parts. The first one was frequency-shifted and injected into Nd:YAG regenerative laser amplifier. By using additional amplifiers two parallel channels were set-up, each providing 50 ps long pulses and energy of up to ∼2 mJ. In order to obtain reasonable efficiency of the parametric process, the second part of the oscillator signal was stretched in time up to more than 10 ps in bulk flint (SF57) glass. Initially, theoretical modelling was performed and gain bandwidth was estimated for all OPA stages utilizing noncollinear interaction and certain crystal length. Experimentally, the chirped pulse was parametrically amplified in two successive visible OPA stages based on BBO crystals using a noncollinear setup and the second harmonic of Nd:YAG amplifier as a pump. Afterwards, DFG was realized when the amplified stretched pulse was mixed with the fundamental frequency radiation of Nd:YAG amplifier in a thin BBO crystal using noncollinear geometry. Consequently, a broadband chirped signal with energy of up to 1 μJ and a spectral range of 1.9 - 2.5 μm was generated. Lastly, the generated broadband infrared signal was amplified in two OPA stages, first of which acted as a preamplifier and was pumped by the fundamental frequency of Nd:YAG amplifier's first channel. The second channel served as a pump for the last OPA stage. Noncollinear interactions were implemented in both stages and the final signal with ∼250 nm spectral bandwidth at FWHM (see Fig. 1) and maximum energy of 0.5 mJ at 1 kHz repetition rate was achieved.

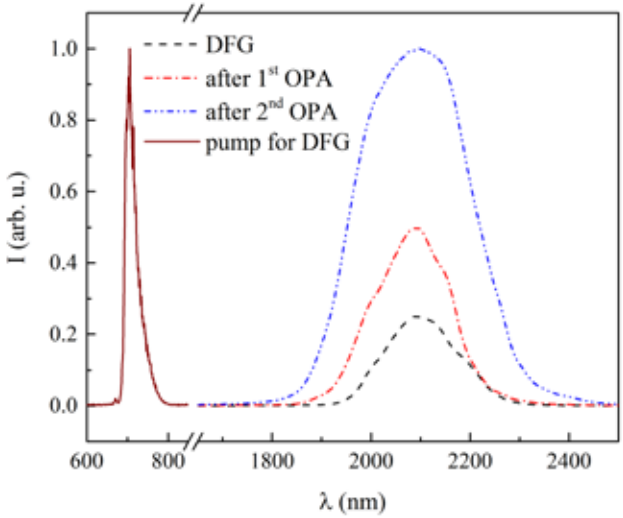

Fig. 1. Normalized spectra of the DFG pump signal (solid line), DFG signal (dashed line, scaled by a factor of 0.25), amplified signal in the first OPA (dash-dot line, scaled by a factor of 0.5), amplified signal after second OPA (dash-dot-dot line)

[1] K. Zhao, H. Zhong, P. Yuan, G. Xie, J. Wang, J. Ma, L. Qian, Generation of 120 GW mid-infrared pulses from a widely tunable noncollinear optical parametric amplifier, Opt. Lett., **38**, 2159-2161 (2013).

[2] Y. Shamir, J. Rothhardt, S. Hädrich, S. Demmler, M. Tschernajew, J. Limpert, A. Tünnermann, High-average-power 2 μm few-cycle optical parametric chirped pulse amplifier at 100 kHz repetition rate, Opt. Lett., **40**, 5546-5549 (2015).

[3] A. Dubietis, G. Jonušauskas, A. Piskarskas, Powerful femtosecond pulse generation by chirped and stretched pulse parametric amplification in BBO crystal, Opt. Lett., **88**, 437 (1992).

DYNAMICS OF QUANTUM DOTS SEMICONDUCTOR LASERS UNDER THE INFLUENCE OF DOUBLE CAVITY FEEDBACK

Tatiana Oloinic, Spiridon Rusu, Vasile Tronciu

Department of Physics, Technical University of Moldova Chisinau MD-2004, Republic of Moldova
oloinic_tatiana@mail.utm.md

During recent years, the phenomena of self-organization and chaos have received considerable attention due to its fundamental and applied interests. In optical chaos-based communications, the chaotic waveform is generated by using semiconductor lasers with either all-optical or electro-optical feedback loops [1]. It is well known that optical feedback can considerably influence the dynamical behavior of a semiconductor laser. Due to the influence of the feedback, under the appropriate conditions, the system displays chaotic behavior appropriate for chaos-based communications. The quantum dots integrated cavity laser under the influence of optical feedback could be a key element for chaos-based communications systems. Here we consider a configuration of quantum dots laser under the influence of optical feedback from an integrated double cavity. We focus on the investigation of the dynamics of semiconductor lasers with quantum dots active medium shown in Fig. 1. The setup consists of a semiconductor laser operating under the influence of an external optical feedback from double cavity. The first mirror is located at distance l from the laser front facet. The distance between first and second mirrors is L. The phase φ in the air gap can be changed by a piezo-element. On the other hand, the feedback phase ψ can be tuned, by the change in the delay time between the two mirrors.

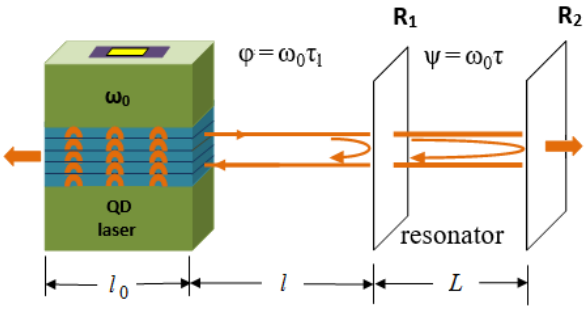

Fig. 1. Laser setup

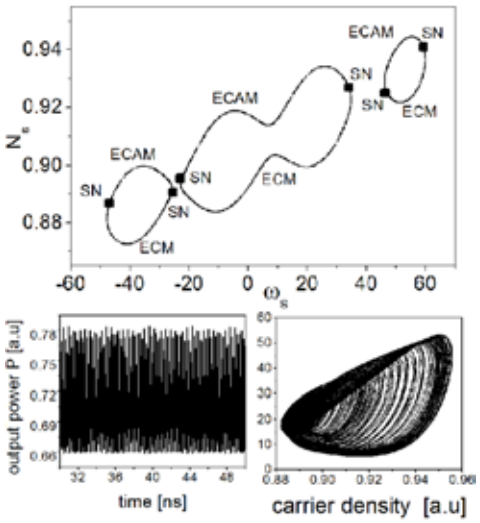

Fig. 2. Top: stationary. Bottom: dynamics.

For modeling of the dynamics of quantum dots laser under the influence of double optical feedback we use the following equations for the complex amplitude of the electric field E, the occupation probability in the quantum dot ρ, and for the carrier density in the quantum well N with the feedback strength Γ_1 and Γ_2 [2]

$$\frac{dE}{d\tau}=\frac{1}{2}(1+i\alpha)\left[-\gamma_{np}+g(2\rho-1)\right]E+\Gamma_1 e^{-i\varphi}E(\tau-\tau_l)+\Gamma_2 e^{-i(\varphi+\psi)}E(\tau-(\tau_l+\tau_L)), \quad (1)$$

$$\frac{d\rho}{d\tau}=-\gamma_{ns}\rho-(2\rho-1)|E|^2+(CN^2+BN)(1-\rho), \quad (2)$$

$$\frac{dN}{d\tau}=J-N-2\left[(CN^2+BN)(1-\rho)\right]. \quad (3)$$

We have examined the stationary states (see Fig. 2 top) and dynamical behavior (see Fig 2 bottom) of semiconductor lasers shown in Fig. 1 using the set of equations (1) – (3) and the following main parameters $\tau_1 = 0.2$, $\tau_2 = 0.5$, $\alpha = 2.0$, $\gamma_{np} = 500$, $C = 40$, $g = 1200$, $J = 20$ [3]. Figure 2 (top) shows the panel distribution of external cavity modes and anti-modes i.e. stationary solutions of equations (1) – (3) in the plane of two parameters: N_s versus ω_s. SN denotes saddle-node bifurcation. Figure 2 (bottom) presents the time evolution of the emerging power (left) and phase portrait (right) for the chaotic behavior appropriate for chaos-based communications. We show that the advantage of the proposed system compared to the conventional optical feedback is that the chaotic behavior occurs for short lengths of cavities, which makes more compact device. On the other hand, we show that under certain conditions two such laser systems could be synchronized when they operate under chaotic emitter-receiver configuration. We believe that our work provides a good basis for further research to optimize quantum dots semiconductor lasers with feedback for chaos based communications.

[1] Apostolos Argyris, Dimitris Syvridis, Laurent Larger, Chaos-based communications at high bit rates using commercial fibre-optic links, Nature **438**, 343-346 (2005).
[2] Huyet G, O'Brien D, Hegarty S P et al. Quantum dot semiconductor lasers with optical feedback, Physica status solidi (a) **201**, 345-352 (2004).
[3] Oloinic T., Rusu S.S., and Tronciu V.Z., Communication with chaos using semiconductor lasers with an air gap, Moldavian Journal of the Physical Sciences, **14**, N1-2, 113-118 (2015).

3D OPTICAL PRINTING AND CUSTOM MADE RESINS

Edvinas Skliutas[1], Sigita Kašėtaitė[2], Jolita Ostrauskaitė[2], Mangirdas Malinauskas[1]

[1]Department of Quantum Electronics, VU, Saulėtekio Ave 9, Vilnius LT-10222, Lithuania
[2]Department of Polymer Chemistry and Technology, KTU, Radvilėnų Rd. 19, Kaunas LT-50254, Lithuania
edvinas.skliutas@ff.stud.vu.lt

Stereolithography (SLA) allows rapid and accurate materialization of computer aided design (CAD) models into real objects out of photoreactive resin. Nowadays this technology has evolved to a widespread simple and flexible personal tabletop devices – 3D optical printers. However, lithography process involves wet developing and the commercially available resins are relatively not cheap and of limited applicability. For instance, 3D SLA printer offers spatial structuring resolution and throughput sufficient for tissue engineering research at a pre-clinical level, yet for such purpose there is no suitable biocompatible and biodegradable material available on the market [1, 2]. Furthermore, the accessible resins are often of unknown chemical ingredients and fixed to certain mechanical properties, which in principle would be beneficial to tune them according to specific object or its function [3]. Thus, despite technology's 3D microstructuring flexibility the material remains a restricting factor for the applicability of the made objects. Lastly, recent advances have shown that linseed oil-based polymers can be applied as photoresins [4]. These two reasons encouraged us to study synthesis and photostructuring of organic biomaterial applicable for 3D printing (3DP) technologies.

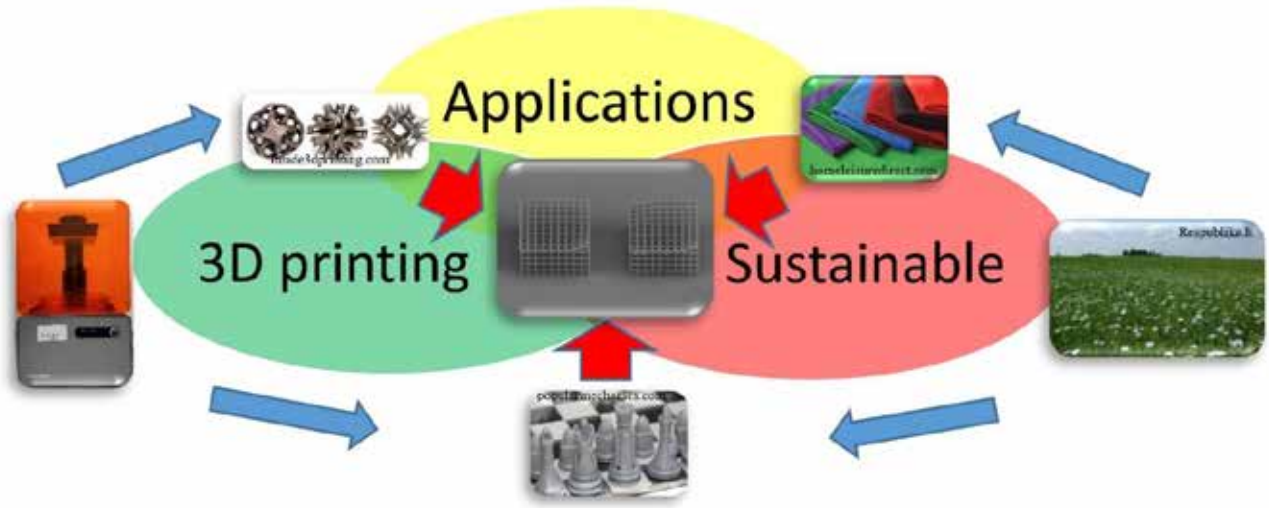

Fig. 1. Additive value for applications combining 3DP and sustainable materials.

In our study, the primary chosen substance for photosensitive material synthesis was linseed oil, one of the cheapest and most abundant, non-toxic, annually renewable natural resources available in large quantities, with a high content of double bonds making it an ideal for the preparation of bio-based resins. UV mask lithography was employed to determine its photocross-linking performance and processed material properties, it was compared to FormLabs Form 1+ standard material Form Clear. Next to it, photosensitized polyethylene(glycol) diacrylates (PEG-DA) of diverse molecular weights were used as standard biodegradable materials [5]. Exposing to UV diode of 365 nm wavelength through a micro-patterned amplitude mask the materials were classified according to their: photoreactivity (cross-linking efficiency determining required exposure dose), photomodification selectivity (structuring spatial resolution limiting the finest reproducible feature), mechanical rigidity, developing and adhesive properties (shrinkage and CAD shape preservation, wettability, etc.).

These results motivate to continue studies on epoxidized linseed oil based photoresins towards their optical printing applications. Further research covers applying tabletop SLA printer Form 1+ for the manufacturing of 3D objects. The custom made biomaterials could be further functionalized doping them with biologically active compounds, for instance nano-hydroxyapatites which are well known inorganic substance for bone tissue engineering. Such organic-inorganic nanocompounds would possess improved mechanical properties and even gain shape memory features [6].

[1] M. Malinauskas, et al., Appl. Phys. A **108**, 751 (2012).
[2] J. Mačiulaitis, et al., Biofabrication **7**(1), 015015 (2015).
[3] D. Mizeras, et al., Proc. SPIE **9505**, 95050P (2015).
[4] A. Remeikytė, et al., J. Appl. Pol. Sci., **129**(3), 1290 (2013).
[5] A. Ovsianikov, et al., Acta Biomaterialia **7**(3), 967 (2011).
[6] F. S. Senatov, et al., Jrnl. of the Mech. Behavior Biomed. Mat. **57**, 139 (2016).

IN-VOLUME MODIFICATION OF SODA-LIME GLASS WITH PICOSECOND BESSEL-GAUSSIAN BEAMS

Juozas Dudutis

Center for Physical Sciences and Technology, Savanoriu Ave. 231, LT-02300, Vilnius, Lithuania
juozas.dudutis@ftmc.lt

The zeroth order Bessel beams are exact solutions of the Helmholtz wave equation and are invariant along the propagation direction. The intensity pattern of such beams can be considered as the interference product of plane waves propagating on a conical surface. As a result, Bessel beams consist of the high-intensity central lobe surrounded by the infinite number of concentric rings. Therefore, such non-diffractive beams carry the infinite amount of energy and cannot be generated experimentally. The approximation of such beams, called quasi-Bessel or Bessel-Gaussian beams, can be obtained for the finite spatial extent using the finite amount of energy [1]. Such beams have a greater depth of field compared to the Gaussian beam and can be applied to the formation of high aspect ratio structures in transparent materials. Another important property of Bessel-Gaussian beams is the self-reconstruction after an obstruction which reduces non-uniformities caused by perturbed beam propagation during processing [2].

Bessel-like beams were successfully applied for glass cutting applications [3, 4], micro and nano-channels formation in transparent materials [2, 5]. Even drilling of non-transparent materials, such as thin stainless steel [6] and copper foils [1], silicon [7] was demonstrated using such beams.

The aim of this research was to investigate the in-volume modification of soda-lime glass sheets using picosecond Bessel-Gaussian beams. Experiments were carried out using the fundamental harmonic of the diode-pumped solid-state lasers with a pulse duration of 10 ps and 300 ps. A conical lens with an apex angle of 170 deg together with a 4F optical system was used to transform the incident Gaussian beam into the preferred Bessel-Gaussian beam. Samples were characterized using an optical microscope and a stylus profiler.

In this research, the laser-induced modification size dependence on the laser pulse energy and 4F optical system demagnification was measured. The maximum axial length of defects was defined by the available laser pulse energy. In the case of 300 ps pulse duration, 3.4 mm-length modifications were achieved when 2.1 mJ laser pulses were applied. The formation of the unmodified zone in the volume of glass was observed and depended on the sample position in the vertical direction. The length of this zone was related to the front surface damage and was suppressed as the scanning speed was increased.

In this work, we demonstrated the formation of high aspect ratio laser induced modifications in the bulk of soda-lime glass (Fig. 1) and the possibility to vary the position of defects in the vertical direction.

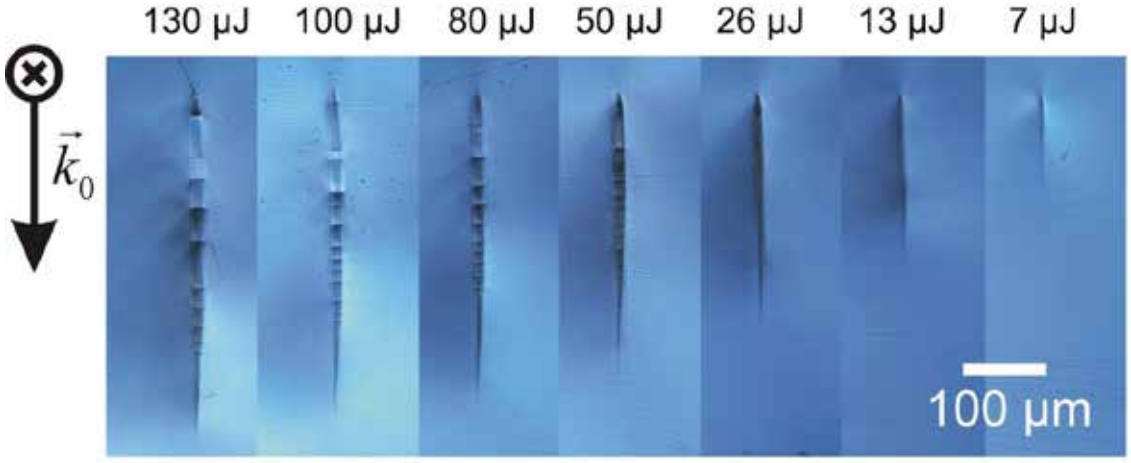

Fig. 1. A cross-section of the laser induced modifications in the bulk of glass using different pulse energy.

[1] I. Alexeev, K.-H. Leitz, A. Otto and M. Schmidt, Application of Bessel beams for ultrafast laser volume structuring of nontransparent media, Phys. Procedia **5**, pp. 533–540 (2010).
[2] M. Duocastella and C. B. Arnold, Bessel and annular beams for materials processing, Laser Photonics Rev. **6**(5), pp. 607–621 (2012).
[3] M. K. Bhuyan, O. Jedrkiewicz, V. Sabonis, M. Mikutis, S. Recchia, A. Aprea, M. Bollani and P. Di Trapani, High-speed laser-assisted cutting of strong transparent materials using picosecond Bessel beams, Appl. Phys. A, **120**(2), pp. 443–446 (2015).
[4] J. Lopez, K. Mishchik, B. Chassagne, C. Javaux-Leger, C. Honninger, E. Mottay and R. Kling, Glass Cutting Using Ultrashort Pulsed Bessel Beams, Int. Congr. Appl. Lasers Electro-Optics, pp. 60–69 (2015).
[5] M. K. Bhuyan, F. Courvoisier, M. Jacquot, P.-A. Lacourt, L. Froehly, R. Salut, L. Furfaro and J. M. Dudley, Femtosecond non-diffracting Bessel beams and controlled nanoscale ablation, in 2011 XXXth URSI General Assembly and Scientific Symposium, pp. 1–3 (2011).
[6] Y. Matsuoka, Y. Kizuka and T. Inoue, The characteristics of laser micro drilling using a Bessel beam, Appl. Phys. A Mater. Sci. Process. **84**(4), pp. 423–430 (2006).
[7] R. Inoue, K. Takakusaki, Y. Takagi and T. Yagi, Micro-ablation on silicon by femtosecond laser pulses focused with an axicon assisted with a lens, Appl. Surf. Sci. **257**(2), pp. 476–480 (2010).

Production of selective self-assembly monolayer (SAM) patterns using laser direct writing

Airidas Žukauskas[1,2], Bogdan Voisiat[1], Tomas Rakickas[3], Ramūnas Valiokas[3], Gediminas Račiukaitis[1]

[1] Department of Laser Technologies, Center for Physical Science and Technology, Lithuania
[2]Faculty of Natural Science, Vilnius University, Lithuania
[3] Department of Nanoengineering, Center for Physical Science and Technology, Lithuania
a.zukauskas@ftmc.lt

Biofunctional patterning technologies such as dip-pen nanolithography or micro-contact printing are used for patterning of selectively graft proteins, peptides and other biomolecules on solid supports, which are mostly used in the biomedical field. However, patterning of biomolecules efficiently without losing their functionality and structure is a difficult task. Furthermore, it gets more challenging if multi-biomolecular patterns, which are more preferred for biomedical applications, are needed to be produced.

This work represents the technology of self-assembly monolayer (SAM) pattern production which is based on direct laser writing (DLW) technology. Firstly SAM matrix is grown on the gold surface; then nanosecond laser pulses are used to interrupt the bond between the SAM molecule and the gold coating, which is deposited on silicon sample. The laser irradiation creates a selective surface for another type of SAM to be grafted thus forming a new pattern of multiples types of SAM (Fig. 1). Newly created patterns can be joined with proteins and other biomolecules for biochip production.

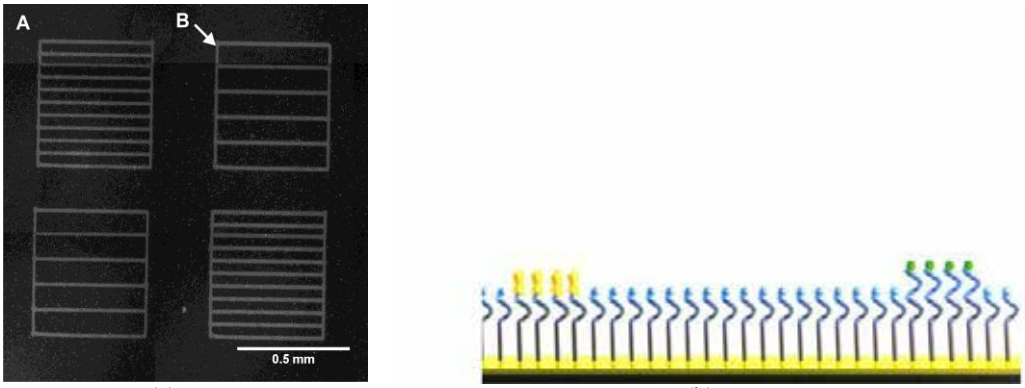

(a) (b)

Fig. 1 (a) SAM pattern sample visualized with a fluorescent microscope. A: background SAM with -OH radical group, B: Changed SAM using DLW (this SAM's radical group -biotin is bound with streptavidin conjugated QDots (sv-Qdots)). (b) SAM pattern 2D model.

This technology is very advantageous for forming multi-biomolecular patterns [1,2]. It reduces the cost and time of pattern production, as it does not require costly mask development and provides an easy way of the pattern architecture adjustment. Also, due the usage of the high-speed beam scanning equipment, this technique provides fast and accurate (in micrometric scale) patterning.

[1] Afara, N., Omanovic, S., Asghari-khiavi, M., 2012. Functionalization of gold surface with fibronectin (FN) covalently bound to mixed alkanethiol self-assembled monolayers (SAMs): The influence of SAM composition on its physicochemical properties and FN surface secondary structure. Thin Solis Films 522, 381-389. Doi 10.1016/l.tsf.2012.08.025

[2] Shadnam, M.R., Kirkwood, S.E., Fedosejevs, R., Amirfazli, A., 2004. Direct Patterning of Self-Assembled Monolayers on Gold Using a Laser Beam. Langmuir 20, 2667-2676. Doi:10.1021/la0354584

SUPERCONTINUUM GENERATION WITH PICOSECOND LASER PULSES

Enrika Keblytė[1], Ieva Gražulevičiūtė[1], Justinas Galinis[1], Gintaras Tamošauskas[1], Vytautas Jukna[2], Audrius Dubietis[1]

[1] Department of Quantum Physics and Laser Research Center, Vilnius University, LT-10223 Vilnius, Lithuania
[2] Centre de Physique Theorique, CNRS, Ecole Polytechnique, F-91128 Palaiseau, France
enrika.keblyte@ff.stud.vu.lt

One of the most remarkable and visually observed effects produced by filamentation in dielectric media is supercontinuum (SC) generation, resulting in a broadband radiation with high spatial and temporal coherence [1]. The spectral extent of SC strongly depends on the linear and nonlinear optical properties of the medium and the pump wavelength [2]. In the bulk solid-state dielectric media the practical scheme for SC generation is as compact as efficient: under suitable low numerical aperture focusing conditions filamentation and spectral superbroadening are achieved in few millimeters of propagation without the onset of the optical damage of material [3]. Nowadays this broadband coherent radiation is used in many applications such as ultrafast spectroscopy, generation of few-optical-cycle pulses and modern nonlinear optics. So far SC was generated by femtosecond laser pulses in wide bandgap dielectric media, but the development of compact chirped pulse amplification (OPCPA)-based systems prompted experimental investigations of the SC generation in solid-state media using longer, sub-picosecond and picosecond pump pulses [4,5].

In this study we have experimentally and numerically investigated the filamentation and SC generation in YAG crystal, pumped by picosecond infrared laser pulses. The important details of Nd:glass laser system (Twinkle, Light Conversion Ltd.): 1.3 ps pulse duration, 1055 nm wavelength, energy up to 5 mJ at 10 Hz repetition rate. Using three YAG crystals of 3, 6, 10 mm length we experimentally measured spatiotemporal intensity distributions of the pulse at relevant stages of spectral broadening. With the input pulse energy of 8.8 μJ, the measured SC spectra in 10 mm long crystal covered wavelength range from 480 nm to 2 μm. Our measurements uncovered a complex temporal structure of the pulse, however, we found out that the red-shifted and blue-shifted spectral broadenings are associated just with propagation of two distinct sub-pulses with different durations and traveling with different group velocities.

The experimental data was accurately reproduced by the numerical simulations of the wave packet at various stages of propogation through YAG crystal.The numerical simulations based on solving the unidirectional propagation equation revealed that picosecond laser pulse spatiotemporal dynamics is governed by free electron plasma and markedly differs from femtosecond laser pulse dynamics which is due to multiphoton absorbtion. Free electron plasma defocuses and absorbs rear parts of pulse, resulting in formation of several sub-pulses of femtosecond duration which afterwards experience peculiar spatiotemporal dynamics and have different contributions to spectral superbroadening.

[1] M. Bradler, P. Baum, E. Riedle, Femtosecond continuum generation in bulk laser host materials with sub-μj pump pulses, Applied Physics B 97(3), 561–574 (2009).
[2] A. Brodeur and S. L. Chin, Ultrafast white-light continuum generation and selffocusing in transparent condensed media, J. Opt. Soc. Am. B, 16(4), 637–650 (1999).
[3] J. B. Ashcom, R. R. Gattass, C. B. Schaffer, E. Mazur, Numerical aperture dependence of damage and supercontinuum generation from femtosecond laser pulses in bulk fused silica, J. Opt. Soc. Am. B 23(11), 2317–2322 (2006).
[4] A.-L. Calendron, H. Cankaya, G. Cirmi, and F. X. Kartner, White-light generation with sub-ps pulses, Opt. Express 23, 13866 (2015).
[5] J. Galinis, G. Tamošauskas, I. Gražulevičiūtė, E. Keblytė, V. Jukna, and A. Dubietis, Filamentation and supercontinuum generation in solid-state dielectric media with picosecond laser pulses, Phys. Rev. A 92, 033857 (2015).

THREE-DIMENSIONAL SELF-FOCUSING AND CONTROL OF SUPERCONTINUUM GENERATION IN BBO CRYSTAL WITH COMPETING QUADRATIC AND CUBIC NONLINEARITIES

Rosvaldas Šuminas, Gintaras Tamošauskas, Gintaras Valiulis, Audrius Dubietis

Vilnius University, Faculty of Physics, Saulėtekio al. 10, LT-10223 Vilnius, Lithuania
rosvaldas.suminas@ff.stud.vu.lt

Femtosecond filamentation is a phenomenon arising from the nonlinear interaction between the intense ultrashort laser pulse and transparent dielectric medium, which modifies the spatial, temporal and spectral properties of the incident radiation and induces temporary or permanent modification of the optical properties of the medium itself [1]. A particularly interesting regime of filamentation occurs in solid-state dielectric media with anomalous group velocity dispersion (GVD), where the input wave packet undergoes space-time focusing leading to generation of self-compressed spatiotemporal light bullets [2] and ultrabroadband, several octave-spanning supercontinuum (SC) [3]. However, so far filamentation phenomena were almost exclusively studied in isotropic materials, where the nonlinear effects arise from the intrinsic cubic (Kerr) nonlinearity, therefore limiting control over the filamentation dynamics. On the other hand, it is well known that phase mismatched second-harmonic generation (SHG) in anisotropic crystals possessing quadratic nonlinearity leads to recurrent energy exchange (cascading) that imprints large nonlinear phase shifts on the interacting waves [4]. The cascading effect produces an effective nonlinear index of refraction, which can readily be controlled by setting an appropriate phase mismatch between the interacting waves.

In this work we demonstrated that competing cascaded-quadratic and intrinsic cubic nonlinear responses may be used for control of filamentation and supercontinuum generation dynamics in a birefringent nonlinear medium with anomalous GVD (see Fig. 1). The experiments were performed using 90 fs, 1.8 μm wavelength pulses in a β-BBO crystal cut for type-I SHG within a broad range of positive and negative phase mismatch parameters, which were varied by simply changing the angle θ between the incident wave and the optical axis of the crystal. In particular, we found that in the case of large negative phase mismatch, the filamentation threshold is markedly reduced due to the enhancement of the effective nonlinear refractive index, leading to SC generation at sub-critical powers for self-focusing. In contrast, positive phase mismatch yields strong negative cascaded nonlinearity which competes with the intrinsic one, resulting in a lower effective nonlinear refractive index and SC generation at elevated intensities. By the use of three-dimensional imaging, we verified that in both cases the SC generation is facilitated by three-dimensional self-focusing of the input pulses, which transform into the self-compressed spatiotemporal light bullets with more than four-fold compression factors. Giant spectral shifts of the second harmonic radiation observed in the region of negative phase mismatch were attributed to a light bullet-induced second harmonic self-phase matching condition.

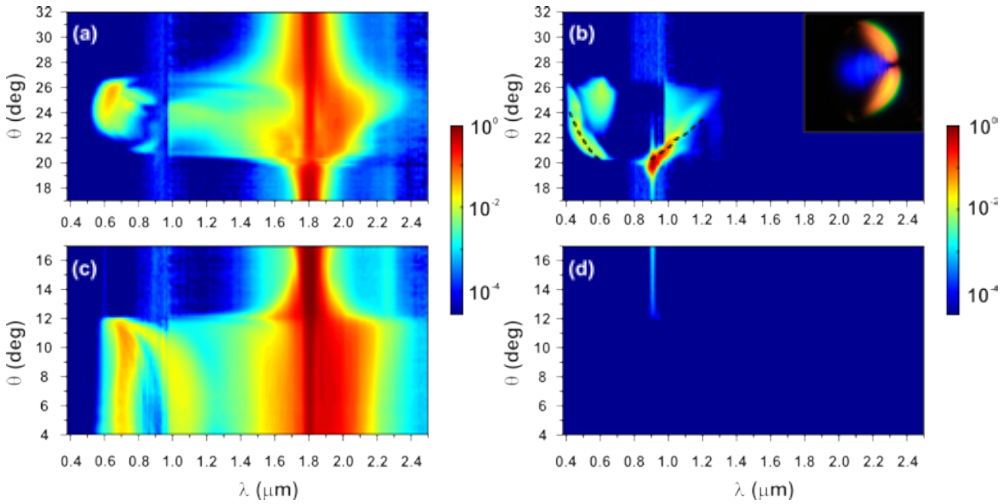

Fig. 1. Experimentally measured spectra as functions of angle θ at ordinary (a), (c) and extraordinary (b), (d) polarizations. The input pulse energy: (a), (b) $E = 0.36$ μJ, (c), (d) $E = 1.35$ μJ. The self-phase matching curve for SHG is depicted by the black dashed curves shown in panel (b). Inset: photo of the second harmonic radiation at $\theta = 24.3°$.

[1] A. Couairon, A. Mysysrowicz, Femtosecond filamentation in transparent media, Phys. Rep. **441**, 47–189 (2007).
[2] D. Majus, G. Tamošauskas, I. Gražulevičiūtė, N. Garejev, A. Lotti, A. Couairon, D. Faccio, A. Dubietis, Nature of spatiotemporal light bullets in bulk Kerr media, Phys. Rev. Lett. **112**, 193901 (2014).
[3] F. Silva, D. R. Austin, A. Thai, M. Baudisch, M. Hemmer, D. Faccio, A. Couairon, and J. Biegert, Multi-octave supercontinuum generation from mid-infrared filamentation in a bulk crystal, Nature Commun. **3**, 807 (2012).
[4] G. I. Stegeman, D. J. Hagan, L. Torner, $\chi^{(2)}$ cascading phenomena and their applications to all-optical signal processing, mode-locking, pulse compression and solitons, Opt. Quantum Electron. **28**, 1691–1740 (1996).

BROAD SPECTRUM PULSE GENERATION IN MULTI-COMPONENT CONTINUUM GENERATORS

Dainius Kučinskas, Rimantas Budriūnas, Arūnas Varanavičius

Department of Quantum Electronics, Faculty of Physics, Vilnius University, Sauletekio Ave. 9, Vilnius LT-10222, Lithuania

dainius.kucinskas@ff.stud.vu.lt

High-power, few-cycle femtosecond laser sources require high energy, coherent phase pulses with broad spectra [1]. Continuum generation is widely used to obtain octave-spanning spectra by focusing the laser beam into one 3-5mm thick sapphire or YAG plate, but destructive nonlinear processes, which lead to pulse breakup, limit its energy to a few μJ.

Recently, a new method of generating high-energy continua was proposed, utilising several thin plates positioned one after the other near the beam focus [2]. For a beam focusing in a nonlinear medium, spectral broadening precedes multiple filamentation and damage, thus allowing a thin plate to broaden the spectrum of a high-energy pulse while avoiding unwanted spatial and temporal modulations [3].

We have assembled a multi-component continuum generator using 0.2mm thick sapphire (Al_2O_3) and 0.5mm thick fused silica (SiO_2) plates. The plates were positioned at the Brewster's angle to minimise energy losses due to reflections. The generated continuum pulses were measured using visual and near-infrared spectrometers and the XFROG (Cross-corelation frequency resolved optical gating) pulse characterisation method.

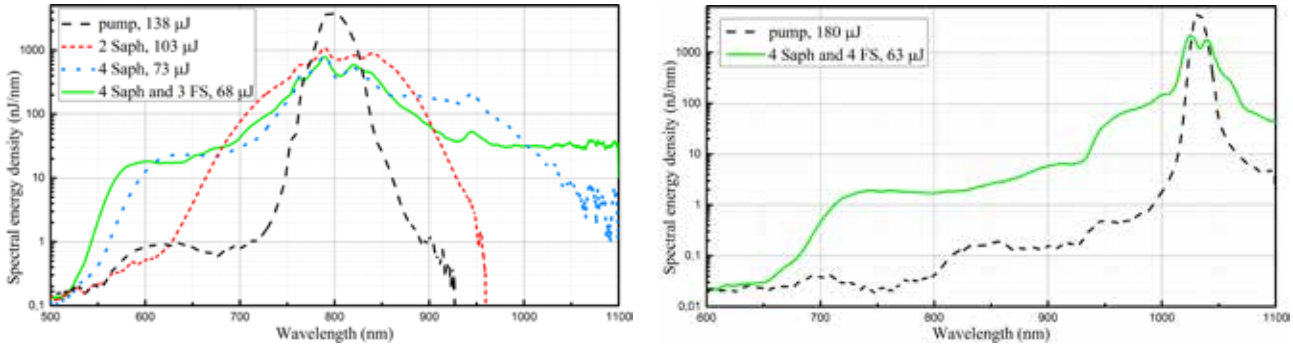

(a) (b)

Fig. 1. Continuum spectra: a) pumped by a 800nm pulse, with different number of plates; b) pumped by a 1030nm pulse.

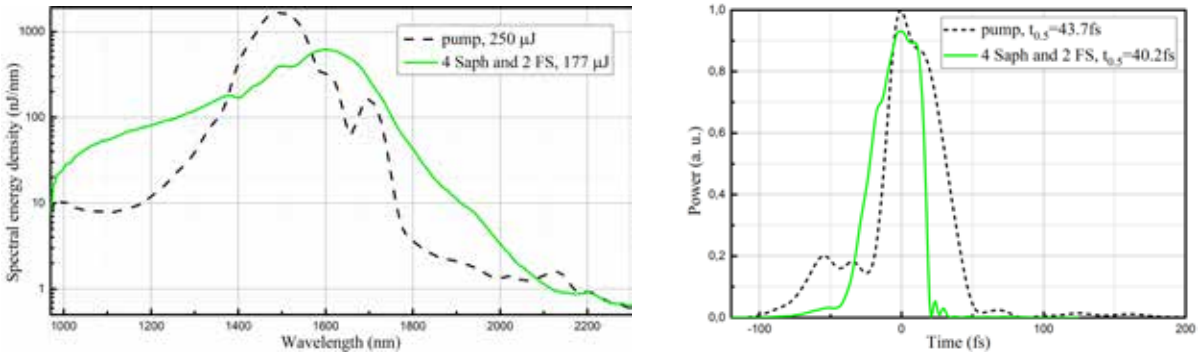

(a) (b)

Fig. 2. Continuum pumped by a 1500nm pulse: a) spectrum; b) temporal profile (retrieved from XFROG measurements).

Using a 800nm, 138μJ pump pulse, a 68μJ continuum pulse with a wavelength range of 570-1100nm above the spectral energy density value of 10 nm/nJ was generated. Using a 1030nm, 180μJ pump pulse, a 63μJ continuum pulse with wavelengths extending from 715nm to at least 1100nm above 1 nJ/nm was produced. Using a 1500nm, 250μJ pump pulse, a 177μJ continuum pulse was achieved, with an octave-spanning wavelength range of 980-1910nm exceeding 10 nJ/nm, coherent spectral phase and a transform-limited length of 5 fs. In all the cases the resulting values of spectral energy density exceed a few hundres times those achieved by generating continua using only one 3-5mm thick plate.

[1] A. Dubietis, G. Jonušauskas, A. Piskarskas, Powerful femtosecond pulse generation by chirped and stretched pulse parametric amplification in BBO crystal, Optics Communications **88**(4), 437-440 (1991).

[2] C. H. Lu, Y. J. Tsou, H. Y. Chen, B. H. Chen, Y. C. Cheng, S. D. Yang, M. C. Chen, C. C. Hsu, A. H. Kung, Generation of intense supercontinuum in condensed media, Optica **1**(6), 400-406 (2014).

[3] M. Kretschmar, C. Brée, T. Nagy, A. Demircan, H. G. Kurz, U. Morgner, M. Kovačev, Direct observation of pulse dynamics and self-compression along a femtosecond filament, Optics Express **22**(19), 22905-22916 (2014)

SUPERCONTINUUM GENERATION IN PHOTONIC CRYSTAL FIBER USING FEMTOSECOND FIBER LASER

Dovilė Mackevičiūtė[1,2], Nerijus Rusteika[1,2]

[1] Department of Quantum Electronics, Vilnius University, Saulėtekio Ave. 9, Vilnius LT-102222, Lithuania
[2] EKSPLA, Ltd, Vilnius, Lithuania
dovile.mackeviciute10@gmail.com

Supercontinuum (SC) generation is a phenomenon governed by many nonlinear effects such as self-phase modulation, Raman scattering, four-wave mixing, soliton formation and others [1, 2]. SC as a light source has its own unique characteristics like a very broad spectrum and a large brightness, which cannot be offered by any other technology. Therefore it is widely applied in various fields such as spectroscopy, optical coherence tomography, metrology, optical telecommunications, etc [3].

For a long time SC was generated in bulk materials – solids, liquids or gasses. In this case peak power required for SC generation is governed by self-focusing and is of the order of a few MW for most common transparent materials. This translates in the pulse energy for 100fs pulses of the order of hundreds nJ. Alternatively, one may send pulses with much lower energy through an optical fiber with much higher nonlinearity. A photonic crystal fiber (PCF) allows generating a broad SC using laser pulse energies of the order of a few nJ which has many practical advantages [4].

PCF is based on a two-dimensional photonic crystal, where the third dimension is not constrained, forming a fiber. The solid core of PCF is surrounded by an array of air holes and the guiding properties of this type of PCF works on the same principle as the step-index fibers.

In this work we present experimental study of SC generation in photonic crystal fiber. The chosen PCF combines a high nonlinear coefficient (11 $(W \bullet km)^{-1}$) with zero dispersion wavelenght shifted to 1040 nm. Two laser sources with 1064 nm central wavelenght but different pulse energies were used. First, by fussion splicing an optical fiber from the laser output (~100 fs, 6 nJ pulses) to a PCF, monolitical SC source was produced generating broadband radiation in the 800 - 1400 nm range. When higher pulse energy (~40 nJ) free space couple laser was used, SC spectrum covered more than octave – from 600 nm to 1700 nm.

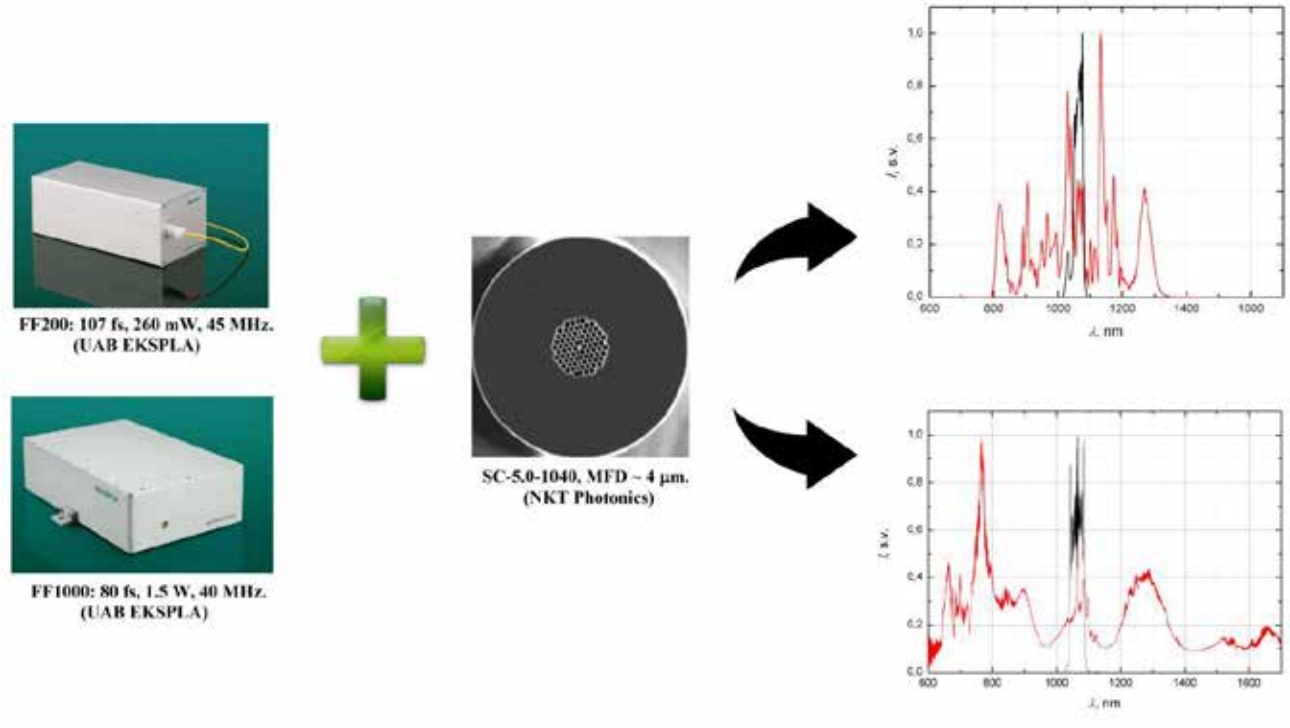

Fig. 1. Comparison of measured supercontinuum spectra in PCF using two different femtosecond fiber lasers

[1] J. M. Dudley, G. Genty, S. Coen, Supercontinuum generation in photonic crystal fiber, Rev.Mod.Phys. **78**, 1135-1184 (2006).
[2] J. M. Dudley, J. R. Taylor, Supercontinuum Generation in Optical Fibers, Cambridge Univ. Press (2010).
[3] T. Ganz, Supercontinuum Generation by Chirped Pulse Compression for Ultrafast Spectroscopy and Broadband Near-field Microscopy, dissertation, Munich(2011).
[4] J. K.Ranka, R. S. Windeler, A. J. Stenz, Visible continuum generation in air-silica microstructure optical fibers with anomalous dispersion at 800 nm, Opt. Lett. **25**(1), 25-27 (2000).

CREATION OF PHOTOGONIOMETER USING LABVIEW PROGRAMING ENVIRONMENT

Vladislovas Čižas, Laurynas Dabašinskas, Pranciškus Vitta

Vilnius University, Institute of Applied Research, Lithuania
vladislovas.cizas@ff.stud.vu.lt

Nowadays, when luminaires based on light – emitting diode (LED) technology are becoming more and more popular a lot of different standards were created to make the quality of luminaires better and prevent damage to users. For different uses of light sources (e.g. luminaires used on roads) there are several requirements (standards) for light distribution. Technique that is used to measure that distribution is called goniophotometry and the device is goniophotometer.

The main drawbacks of this method are that photogoniometers are quite expensive and requires huge room for big luminaires. Our task was to create an inexpensive goniophotometer which can be used in long rooms without essential loses of accuracy. Another task was to minimize the whole measurement time as much as possible.

Goniophotometers usually have two rotating axes, which depend on the configuration used for measurement. There are three possible configurations (A, B and C) and for each special construction of photogoniometer is required[1]. Our created photogoniometer consists of the goniometer (fig 1.) and the luxmeter. As the goniometer rotates the luminaire, luxmeter measures the illuminance. At the end created software sorts out the date and returns a txt file that can be used in a special photometric programs to plot graphical distribution of light. It was decided to create a photogoniometer with two (B and C) configurations as they are most recently used. Rotation by x and y axes were introduced by high precision motors and rotation by z axis was simulated using mathematical formulas considering the shape of luminaire[2]. Software part was created using LabVIEW programing environment[3].

Fig 1. The created goniophotometer

As a result, totally autonomous photogoniometer with B and C configuration measuring ability was created. Tests showed that the accuracy of measurement is high enough (maximum errors < 1%). An integrated ability of automatic creation of IES files helped to decrease the time required for measurement.

[1] A.Žukauskas „Puslaidininkiniai šviestuvai“
[2] LM 75-01 Goniophotometer Types and Photometric Coordinates
[3] Jeffrey Travis, Jim Kring. LabVIEW For Everyone. Graphical Progamming Made Easy and Fun. (2006)

THERMAL LENSING IN YAG ROD WITH TEMPERATURE DEPENDENT PARAMETERS AND DIFFERENT PROFILES OF PUMP BEAM

Dominykas Bričkus[1,2], Alexander S. Dement'ev[1]

[1]Center for Physical Sciences and Technology, Savanorių av. 231, Vilnius 02300, Lithuania
[2] Department of Quantum Electronics, Vilnius University, Saulėtekio av. 9, Vilnius 10222, Lithuania
dominykus@gmail.com

Thermally induced lens in high power solid state lasers is one of the main issues for high average power scaling possibilities. At high temperature gradients it becomes important to take into account the temperature dependence of the thermal, mechanical and optical parameters of the crystal. We discuss a case of steady-state radial heat flow in YAG cylindrical rods with radially symmetric heating distribution. This allows to simplify the problem enough to obtain simple solution for radial temperature distribution for various heat load distributions $q(r)$:

$$T(r)=T_R\left[1+\frac{(1-\xi)q_2(r)}{k(T_R)T_R}\right]^{\frac{1}{1-\xi}},\quad T_R=T_a+\frac{q_1(R)}{hR},\quad q_1(r)=\int_0^r q(\rho)\rho d\rho,\quad q_2(r)=\int_r^R\frac{q_1(\rho)d\rho}{\rho}, \qquad (1)$$

where R is the radius of the rod, T_R and T_a are the temperatures at the cylindrical surface of the rod and cooling liquid respectively, h is the heat transfer coefficient, $k(T)=k_0(T_r/T)^{\xi}$ is the coefficient of thermal conductivity, T_r is the reference temperature. The case $\xi=0$ is that of a constant conductivity. Sometimes $\xi=0.7$ is used [1]. $\xi=1.0$ is more validated experimentally. For this case $T(r)=T_R\exp(q_2(r)/k_0T_r)$. Formulae (1) are very convenient for numerical calculations of temperature distributions. We investigate 4 different pump distributions with the same total loading power $P_h=60$ W for the YAG rod with $R=2$ mm and length $L=10$ mm (Fig. 1a). Temperatures were

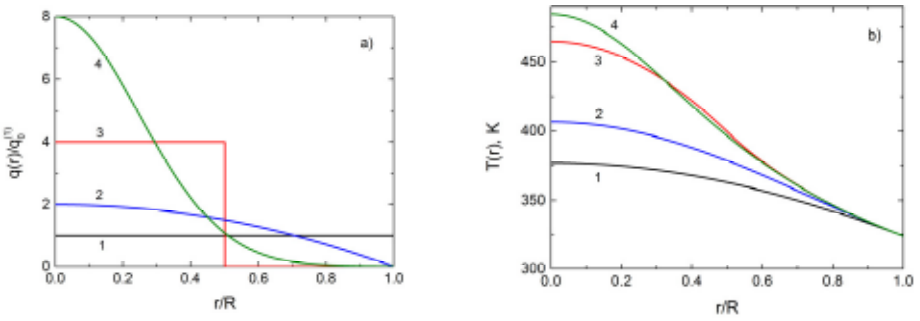

Fig. 1. Normalized heat loading distributions for uniform (1), parabolic (2), top-hat (3) and Gaussian (4) beam shape (a) and respective temperature distributions (b).

calculated using parameters $\xi=1.0$, $k_0=0.105$ W/(cm K), $h=2.0$ W/(cm^{2}K). It should be noted that the expansion method used in [1] is not applicable for Gaussian beam with radius $w_p=1$ mm used here. For temperature independent thermo-optic coefficient dn/dT and expansion coefficient α the optical path difference may be calculated using corresponding formulae from [2] which take into account the change of refractive index by temperature gradient induced stresses. In this work, we generalized these formulae for temperature dependent parameters dn/dT and α [3]. Paraxial radial and tangential focal lengths calculated using temperature independent ($f_{r,\theta}(T_r)$) and temperature dependent ($f_{r,\theta}(T)$) YAG parameters are presented in Table 1. It is seen that its values depend strongly on pump distribution used and temperature dependence of parameters. For each pump shape temperature dependence of parameters decreases the value of the focal length by a factor of at least 1.5.

Table 1: The ratios of focal lengths for temperature independent to temperature dependent YAG parameters

	Uniform	Parabolic	Top-Hat	Gaussian
$f_r(T_r)/f_r(T)$, mm	448/301	224/132	106/48	59/28
$f_\theta(T_r)/f_\theta(T)$, mm	531/355	265/155	127/57	70/33

[1] M.H.M. Dindarlu, M.K. Tehrani, H. Saghafifar, and A. Maleki, Analytical model for thermal lensing and spherical aberration in diode side-pumped Nd:YAG laser rod having Gaussian pump profile, Chin. Phys. B, 24(124205 (2015).
[2] A.S. Dement'ev, Relatioships between different expressions of thermo-optic and photoelastic coefficients of YAG crystal, Laser Phys. **29**(9), 095004 (2015).
[3] H. Furuse, R. Yasuhara, and K. Hiraga, Thermo-optic properties of ceramic YAG at high temperatures, Opt. Mater. Express, **4**(9),1794-1799 (2014).

INVESTIGATION OF LIGHT PROPAGATION THROUGH PERIODIC SUB-WAVELENGTH APERTURES

Jonas Berzins, Simonas Indrisiunas, Bogdan Voisiat, Gediminas Raciukaitis

Department of Laser Technologies, Center for Physical Sciences and Technology,
Savanoriu Ave. 231, LT-02300 Vilnius, Lithuania
jonas.berzins@ftmc.lt

Light propagation through sub-wavelength structures has a huge potential in many applications: frequency selective surfaces [1], metal-enhanced fluorescence [2], chemical and biomedical sensors [3], and thus have been intensively researched. Direct Laser Interference Patterning (DLIP) technique using the interference of several beams to directly ablate the material can be used to form such periodic arrays of subwavelength structures [4]. This method is capable of producing two-dimensional periodic structures in an effective way on relatively large area with just a single laser shot and has been successfully used in the Center for Physical Sciences and Technology, but a strong theoretical basis of light passing through these sub-wavelength apertures has to be built in order to machine specific structures for the development of future applications.

In periodically formed metallic apertures Enhanced Optical Transmission (EOT) is observed [5]. The unique transmission spectra (Fig. 1) have a periodic grating-like modes, while the enhancement phenomena is explained by Surface Plasmon Polaritons (SPP), a wave emerging due to the so called plasmons, coupling of electromagnetic wave to oscillations of free electrons, and propagating at the interface of dielectric and metal [6].

Modelling of EOT is critically connected to a proper setting of boundary conditions, properties of materials and description of propagating electromagnetic wave. Simulations were carried out by using Finite Element Method (FEM). Main goal of this work was to understand and apply COMSOL Multiphysics program package, which is an interactive user interface for solving partial differential equations, for the above mentioned problem. Analysis of dielectric functions were made in parallel with the modelling objectives. The optical transmission of periodic apertures was investigated mostly in the range of the visible light, while observing EOT dependence on different materials, periodic arrangements, size and form of the apertures, incidence angle of the light and the surrounding environment.

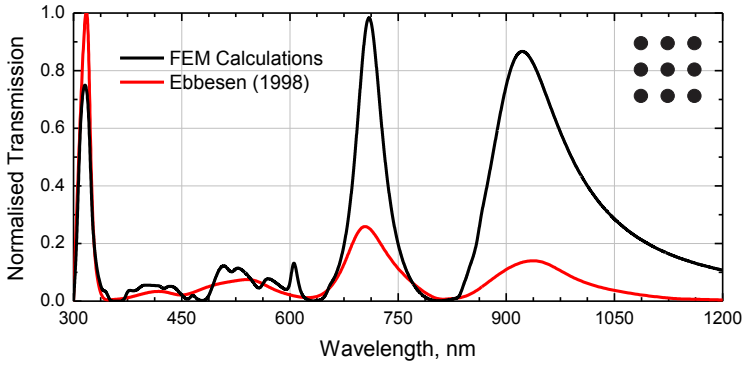

Fig. 1. Normalised transmission spectra of periodic sub-wavelength apertures in thin film of silver. FEM calculations using COMSOL Multiphysics are compared to approximated experimental data taken from [5]. The apertures are 300 nm in diameter, have a period of 600 nm and are 200 nm thick.

Results are comparable to the experimental data from various publications as a clear spectral line identity can be notified (Fig. 1). Basing on this, we can state that COMSOL Multiphysics program package can be successfully used for the modelling of light propagation through periodic sub-wavelength apertures. Current results will be used for the micromachining of real periodic subwavelength apertures.

[1] M. Beruete et al., Enhanced Millimeter Wave Transmission Through Quasioptical Subwavelength Perforated Plates, Ieee Trans. Antennas Propag. **53**(6), 1897-1903, 2005.
[2] D. Gérard et al., Nanoaperture-Enhanced Fluorescence: Towards Higher Detection Rates with Plasmonic Metals, Phys. Rev. B - Condens. Matter Mat. Phys. **77**, 1-8, 2008.
[3] R. Gordon et al., A New Generation of Sensors Based on Extraordinary Optical Transmission, Acc. Chem. Res. **41**(8), 1049-1057, 2008.
[4] S. Indrišiunas et al., Direct Laser Beam Interference Patterning Technique for Fast High Aspect Ratio Surface Structuring, Proc. of SPIE **9350**, 935003, 1-7, 2015.
[5] T. Ebbesen et al., Extraordinary Optical Transmission through Sub-Wavelength hole arrays, Nature **139**, 667-668, 1998.
[6] S. A. Maier, *Plasmonics: Fundamentals And Applications* (Springer, Bath, 2007).

AN ENHANCED KERR NONLINEARITY FOR CLOSED LOOP QUANTUM SYSTEMS

Hamid Reza Hamedi and Gediminas Juzeliunas

Institute of Theoretical Physics and Astronomy, Vilnius University, A. Go˘stauto 12, Vilnius LT-01108, Lithuania
hamid.r.hamedi@gmail.com

The third order susceptibility [1] is investigated in a five- level atomic system in which the laser beams couple the ground state to a four level closed loop system (Fig. 1).

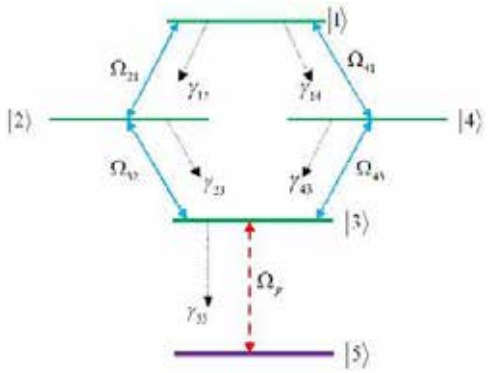

Fig. 1.Schematic diagram of the five level quantum system. Here, the atomic states are denoted by $|1\rangle,|2\rangle,|3\rangle,|4\rangle$ and $|5\rangle$, the Rabi- frequencies are Ω_{ij}, and the spontaneous decay rates of upper level $|i\rangle$ to the lower level $|k\rangle$ are denoted by γ_{ik}.

The equation of the motion for the density operator describing an atomic system can be written as

$$\dot{\rho} = -\frac{i}{\hbar}[H_{5Levels}, \rho]. \qquad (1)$$

where $H_{5Levels}$ is the total Hamiltonian of the system. Applying the rotating wave approximation and under the weak probe field approximation, the first and third order nonlinear susceptibility of the atomic medium for the weak probe laser field has been obtained. Subsequently it was used to investigate the linear and nonlinear evolution of the system.

It is found that under the condition of the multi-photon resonance, one can enhance the Kerr nonlinearity of such a medium by properly adjusting the amplitudes and phases of the applied fields. In this case, the linear and nonlinear absorption reduce considerably in a region with a positive group velocity. It is demonstrated that the third order susceptibility is very sensitive to a relative phase of the applied fields. An analytical model is presented to elucidate such phase control of the Kerr nonlinearity [2].

[1] Hai Wang, David Goorskey, and Min Xiao, *Enhanced Kerr Nonlinearity via Atomic Coherence in a Three-Level Atomic System*, Phys. Rev. Lett. **87**, 073601 (2001)
[2] H. R. Hamedi and G. Juzeliūnas, *Phase-sensitive Kerr nonlinearity for closed-loop quantum systems,* Phys. Rev. A **91**, 053823 (2015)

CALCULATION OF FORCES ACTING ON LEVITATING PYROLYTIC GRAPHITE ILLUMINATED BY LASER

Robertas Samavičius, Virgilijus Minialga

Department of Physics, Kaunas University of Technology
robertas.samavicius@ktu.edu

Diamagnetism is the property of a substance to induce a magnetic field opposite to the applied external magnetic field and thus be pushed in the direction of the weaker magnetic field. Pyrolytic graphite (PG) is a synthetic material with a structure much like of graphite. It has the strongest diamagnetic properties of all known materials at room temperature. Pyrolytic graphite and other diamagnetic materials are described by negative magnetic susceptibility χ. PG is anisotropic material, so its magnetic susceptibility value depends on crystallographic direction: perpendicular to the crystallographic planes $\chi_{\perp} = -450 \cdot 10^{-6}$, parallel to the crystallographic planes $\chi_{=} = -85 \cdot 10^{-6}$.

Pyrolytic graphite placed in magnetic field will levitate under certain conditions. Levitation height of diamagnetic material will depend on the material density, magnetic susceptibility and magnetic field. PG plate, illuminated by a laser beam, will change its magnetic susceptibility. This change will decrease levitation height of pyrolytic graphite. PG will move towards direction of laser illumination point if laser beam is directed towards the edge of the plate. This movement can be explained by the appearance of an unbalanced forces. The aim of this work was to calculate the forces acting on pyrolytic graphite. FEMM 4.2 software was used to calculate such forces. Using this software we simulated pyrolytic graphite levitation above neodymium magnet system comprising quad pole (Fig. 1). PG plate (thickness - 25 µm, diameter – 3 mm) is levitating 0.60 mm above four 500mT NdFeB magnets (3 mm x 3 mm x 10 mm). Changes of magnetic field at the plate edges were observed with the change of material magnetic susceptibility. Using this data the magnetic force dependence on temperature and unbalanced force magnitude was calculated.

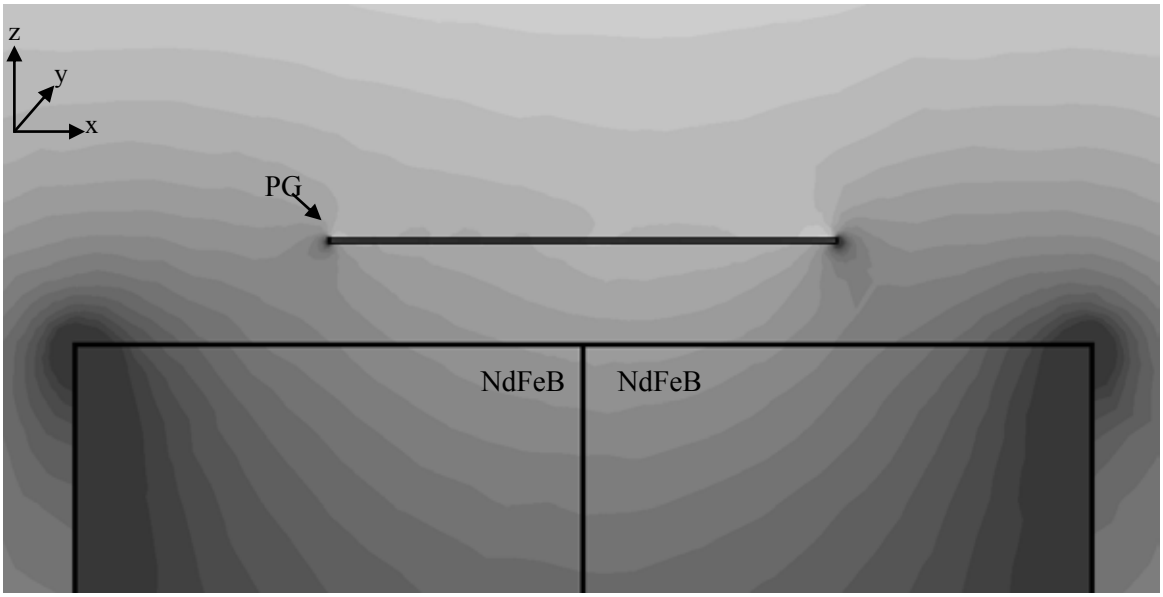

Fig. 1. Simulation of pyrolytic graphite plate (PG) levitating above neodymium magnets (NdFeB) obtained by FEMM 4.2 software

Magnetic force acting on pyrolytic graphite depends on the magnetic susceptibility of PG which varies with changes in temperature. Different magnetic susceptibility values in the material causes appearance of unbalanced forces. Vertical unbalanced force acting on PG can be described as follows

$$\Delta F = \left(\frac{V \cdot (a \cdot \Delta T - b)}{\mu_0}\right) \cdot B \cdot \frac{dB}{dz}, \quad (1)$$

where V is PG plate volume, ΔT is temperature difference at PG plate edges, coefficients $a = 4.293 \cdot 10^{-7}$ 1/K and $b = 4{,}563 \cdot 10^{-4}$, $\mu_0 = 1.26 \cdot 10^{-6}\ {}^{H}/_{m}$, B is magnetic field induction at levitation height z, $\frac{dB}{dz}$ is magnetic field induction gradient at levitation height z.

Program FEMM 4.2 allows us to calculate magnetic field values around diamagnetic material, unbalanced forces increase linearly with increasing temperature difference on the different edges of PG plate.

[1] Masayuki Kobayashi, Jiro Abe., Optical Motion Control of Maglev Graphite, J. Am. Chem. Soc. (2012).
[2] FEMM 4.2, http://www.femm.info/wiki/HomePage (2015.01.25)

Poster session 3

CHINOLINE DERIVATIVES WITH AMINO SUBSTITUENTS: AN INVESTIGATION OF PHOTOLUMINESCENCE AND ELECTROLUMINESCENCE PROPERTIES IN THE OLEDs

Dovydas Banevičius[1], Bronė Lenkevičiūtė-Vasiliauskienė[1], Sigita Višniakova[2], Albinas Žilinskas[2]

[1]Department of Solid State Electronics, Vilnius University, Lithuania
[2]Department of Organic Chemistry, Vilnius University, Lithuania
dovydas@fidi.lt

Organic Light Emitting Diodes (OLEDs) manufacturing industry needs new more effective in terms of high photoluminescence (PL) quantum yield (QY), more stable in terms of emissive layer (EL) lifespan in working OLEDs and less expensive in terms of fewer reactions to obtain the organic materials which are suitable for the OLED production. New chinoline derivatives with amino substituents are promising materials for these applications due to their chemical stability and PL QY up to 17% [1]. In this work we have made OLEDs using chinoline derivatives with amino substituent (5a, 5b, 5f, 5g) in the EL and investigated *j*-V characteristics, photoluminescence (PL) and electroluminescence properties of these devices. Chinoline derivatives have been synthesized at Vilnius University Faculty of Chemistry.

Using the method of thermal evaporation in the vacuum chamber all the organic layers (hole transporting layer (HTL) of material N,N′-Bis(3-methylphenyl)-N,N′-diphenylbenzidine (TPD), EL of chinoline derivatives with amino substituent, hole blocking layer (HBL) of material 1,3,5-Tris(3-pyridyl-3-phenyl)benzene (TmPyPB), electron transporting layer (ETL) of material Tris-(8-hydroxyquinolinato)aluminum (Alq_3) and electrode of LiF/Al were manufactured. Then the spectra of PL and electroluminescence were registered and *j*-V characteristics were measured. According to *j*-V characteristics all devices have double injection mode which starts from 1 V to 10 V input voltage. With respect to band gap energy values of EL materials the electroluminescence peak should be at 620 nm (5f), 590 nm (5b) and 560 nm (5a, 5g). Recorded PL and electroluminescence spectra showed that emissive peaks of the OLEDs are from 400 nm to 550 nm that means the emissive center of OLEDs are the interlayers of two materials. The comparison of photo- and electroluminescence spectra showed that material 5b is fluorescent type material and all the others are mixed fluorescence and phosphorescent type materials.

In this work we showed that chinoline derivatives with amino substituent can be used as the ELs in the ITO/TPD/El/TmPyPB/Alq_3/LiF/Al type OLED structure emitting light from 400 nm to 600 nm range. This type of structure is optimal for these devises according to *j*-V curve double injection regime values. However the electroluminescence peaks in 420 nm region in OLED ITO/TPD/5a/TmPyPB/Alq_3/LiF/Al, OLED ITO/TPD/5f/TmPyPB/Alq_3/LiF/Al and OLED ITO/TPD/5g/TmPyPB/Alq_3/LiF/Al show that excitons can diffuse from the EL to the HTL. Additional hole blocking layer is needed. We have also showed that small chemical structure changes of the EL using chinoline derivatives with amino substituent (5a, 5b, 5f, 5g) provoke light emission of the OLEDs in different spectral regions from blue to green. Also close to white emission of the OLED ITO/TPD/5g/TmPyPB/Alq_3/LiF/Al was observed due to intermolecular and intramolecular excitations in the EL.

[1] Sigita Visniakova, Indre Urbanaviciute, Lauryna Dauksaite, Matas Janulevicius, Brone Lenkeviciute, Ilya Sychugov, Kestutis Arlauskas, Albinas Zilinskas. Luminescent benzo- and naphthoquinolines: Synthesis and investigation of photophysical properties. Journal of Luminescence 167 (2015) 261–267 p.

OLEDS WITH QUINOLINE DERIVATIVES AS EMISSIVE LAYER: AN INVESTIGATION OF LUMINESCENCE AND ELECTRICAL PROPERTIES

Ernesta Bužavaitė[1], Sigita Višniakova[2], Bronė Lenkevičiūtė - Vasiliauskienė[1]

[1]Department of Solid State Electronics, Vilnius University, Lithuania
[2]Department of Organic Chemistry, Vilnius University, Lithuania
Ernesta.buzavaite@ff.stud.vu.lt

Quinoline derivatives are popular in medicine to treat cancer, malaria, tuberculosis and other parasitic infections [1]. As well they are used in organic photovoltaic electronics as cell dyes because of their fluorescent properties [2]. Good fluorescent properties of quinoline derivatives with EQE ~ 15% [3] can be exploited as emissive layer in the organic light emitting devices (OLEDs).

Driven by this idea we decided to explore luminescence and electrical properties of the OLEDs with quinolone derivatives as emissive layer. These quinolone compounds with chlorine substituent were synthesised in Faculty of Chemistry of Vilnius University.

OLEDs were formed using thermal evaporation in the high vacuum. A principal structure of these organic devices is shown in Fig. 1 on the left. Energies of all formed OLED layers are known from literature [4, 5, 6] and are shown in Fig. 1 on the right. OLEDs were formed on a glass with transparent indium tin oxide (ITO) electrode as follows. First, 15 nm hole transporting layer (HTL) was formed from N,N‘-Bis(3-methylphenyl)-N,N‘-diphenylbenzidine (TPD). After that the emissive layer (EL) of one quinoline derivative with chlorine substituents was evaporated. The hole blocking layer (20 nm) was evaporated of 1,3,5-tris(m-pyrid-3-yl-phenyl) benzene (TmPyPB) to prevent holes leakage in the EL. Then electron transporting layer (ETL) was formed using 15 nm of aluminium 8-hydroxyquinolinate (Alq_3) material. Lastly, cathode (LiF with Al) was formed. The *j-V* characteristics, electroluminescence and photoluminescence (*PL*) properties of these made devices were measured.

.

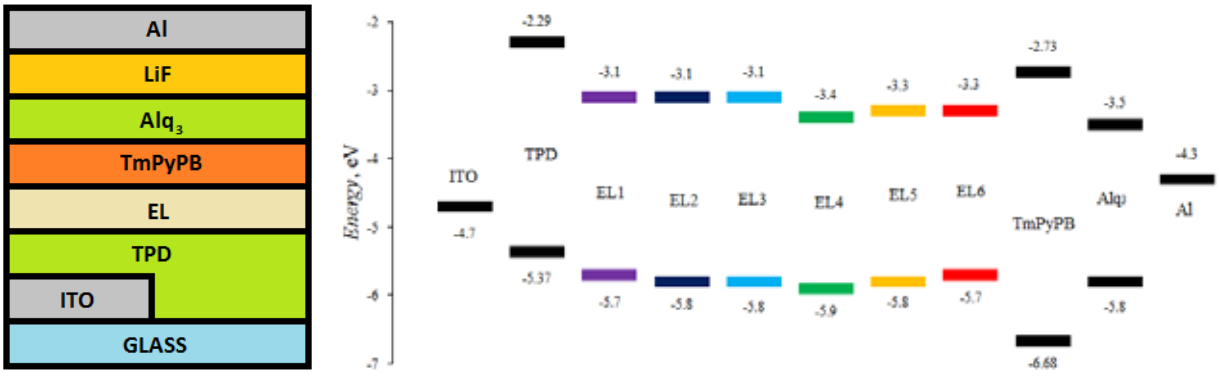

Fig. 1. A structure of OLED’s (left) and energy diagram of used emissive layers (right).

The investigation of electroluminescence spectra allowed us to evaluate, which materials are appropriate for OLED’s fabrication. The *PL* and electroluminescence of all ELs with the quinoline derivatives varied from 470 nm to 500 nm. These results satisfy the values of the optical band gap (E_{g_opt}) of the quinoline derivatives except material **EL6.** The E_{g_opt} for **EL6** material is 2.4 eV which corresponds to luminescence at 516 nm range. But OLED with **EL6** layer electroluminescated in 490 nm. Some of results were not as expected due to charge transport singularities and different thicknesses of the ELs in the formed OLED structures.

All in all we investigated *j-V* characteristics, *PL* and electroluminescence properties of OLED devices with the ELs of the quinoline derivatives with chlorine substituent and showed that EL properties depend on chemical structure of the chlorine substituent as well on charge transport peculiarities in the OLEDs.

[1] A. Marella et al. Quinoline: A versatile heterocyclic. *Saudi pharmaceutical Journal* Vol. 21, Issue 1, (2013): 1 - 12.
[2] P. C. Kao et al. Improves efficiency of organic photovoltaic cells using tris(8-hydroxy-quinolone) aluminum as a doping material. *Thin Solid Films* Vol. 517, Issue 17, (2009): 5301 - 5304.
[3] J. Ding et al. Highly efficient phosphorescent bis-cyclometalated iridium complexes based on quinolone ligands. *Synthetic Metals* Vol. 155, Issue 3, (2005):539 - 548.
[4] S. Višniakova et al. Luminescent benzo-and naphthoquinolines: Synthesis and investigation of photophysical properties. *Journal of Luminescence* 167, (2015): 261 - 267.
[5] S. Juršėnas. *Organinės optoelektronikos prietaisai*, Vilnius: Progretus (2008), 174p.
[6] Shi - Jian Su et al. Pyridine-Containing Triphenylbenzene Derivatives with High Electron Mobility for Highly Efficient Phosphorescent OLEDs, *Adv. Mater.* (2008): 2125 - 2130.

ORGANIC SOLAR CELLS WITH UP-CONVERTERS: LAYER BY LAYER FABRICATION AND INFLUENCE OF THE UP-CONVERSION LAYER TOWARDS SOLAR CELL EFFICIENCY

Karolis Gesevičius[1], Bronė Lenkevičiūtė-Vasiliauskienė[1], Ieva Mikalauskaitė[2]

[1] Department of Solid State Electronics, Faculty of Physics, Vilnius University, Lithuania
[2] Department of Inorganic Chemistry, Faculty of Chemistry, Vilnius University, Lithuania
gesevicius.karolis@gmail.com

Organic Solar cells are suffering from thermal and transition photonic losses. Thermal losses are obtained through absorption of higher than semiconductors band gap energy photons and transition losses are acquired by photons which have lower energy (IR zone) than band gap of the Solar Cell and are not absorbed. In order to lower transition losses in Solar Cells up-conversion is used [1].

Inspired with this idea we synthesized $NaYF_4$:Yb^{+3} (20%), Er^{+3} (2%) up-converters in Vilnius University Faculty of Chemistry. These up-converters were deposited onto glass substrate covered with Indium Tin Oxide (ITO) and can improve cell efficiency. In fabrication process we used spin-casting and drop-casting methods to deposit $NaYF_4$:Yb^{+3} (20%), Er^{+3} (2%) up- converters with different concentrations of up-converters in the solutions. These solutions were made from powder of $NaYF_4$:Yb^{+3} (20%), Er^{+3} (2%) up-converters which were dissolved in toluene solvent. Best result is shown in figure 1.

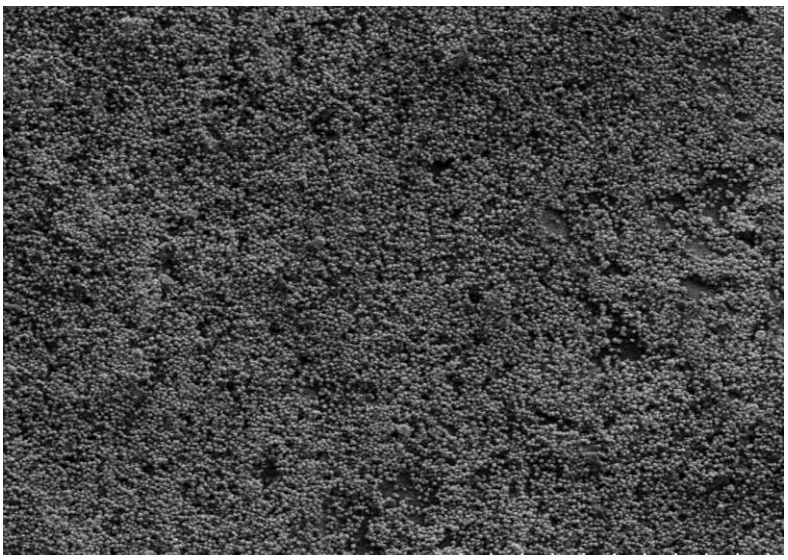

Fig. 1. ITO surface coated with IM0072 up-converters of 10 mg/ml solution concentration using drop-casting method

SEM images indicates that higher concentration (c_t = 5; 10;15 mg/ml) solutions cover substrate surface more densely in wider area. Using both methods was found out that drop-casting method is more efficient way to cover substrate surface.

[1] T. Trupke, A. Shalav, B. S. Richards, P.W€urfel and M. A. Green, Sol. Energy Mater. Sol. Cells, **90**, 3327–3338 (2006)

IMPROVED ABSORPTION PROPERTIES OF NANOCARBON/MAGNETITE COMPOSITES IN 26-37 GHZ

Gleb Gorokhov[1], Anton Moiseenko[2], Dzmitry Bychanok[1], Polina Kuzhir[1]

[1] Institute for Nuclear Problems, Belarusian State University, Belarus
[2] Physical-Technical Institute of National Academy of Sciences of Belarus, Belarus
glebgorokhov@yandex.ru

There is a strong need in artificial materials with a specific set of electromagnetic and mechanical properties, that cannot exist in nature. The development of a material with high absorption of microwave radiation is extremely important for industrial needs. The so-called nonresonant metamaterials (MMs) are able to solve these problems. They can give an advance in the development of electromagnetic protection due to constantly high absorption and extremely low transmission of electromagnetic radiation in wide range (at least in Ka-band[1] and THz ranges).

The most common materials for composites production are epoxy resin[2], thermoplastic natural rubber (TPNR) [3], polyethylene (PET) and other widely used polymers. Usually only one type of filler is used to achieve the necessary electromagnetic properties[1]. Additional fillers, such as clay, has been used to increase spatial dispersion of nanoparticles in the dielectric matrix[4] The development of nanocomposites with two or more electromagnetically active fillers is prospective. For example, the carbon nanotubes (CNT) increases permittivity and Fe_3O_4 (magnetite) nanoparticles increases composite permeability.

The composites based on CNT and Fe_3O_4 (magnetite) were prepared and investigated in 26-37 GHz frequency range. The combination of conducting (CNT) and magnetic (Fe_3O_4) fillers allows to increase the absorption coefficient up to perfect.

[1] S. Bellucci, S. Bistarelli, A. Cataldo, F. Micciulla, J. Macutkevic, I. Kranauskaite, J. Banys, P. Kuzhir, N. Volynets, A. Paddubskaya, D. Bychanok, S. Maksimenko, V. Fierro, A. Celzard, Microwave response properties of epoxy resin composites filled with graphitic fillers, Proceedings of IEEE International Conference on Numerical Electromagnetic Modeling and Optimization for RF, microwave, and terahertz applications (NEMO 2014), (2014)
[2] J.K.W. Sandler, J.E. Kirk, I.A. Kinloch, M.S.P. Shaffer, A.H. Windle, Ultra-low electrical percolation threshold in carbon-nanotube-epoxy composites, Polymer 44, 5893–5899 (2003)
[3] Ing Konga , Sahrim Hj Ahmada, Mustaffa Hj Abdullaha, David Huib, Ahmad Nazlim Yusoffc, Dwi Puryantia, Magnetic and microwave absorbing properties of magnetite–thermoplastic natural rubber nanocomposites, Journal of Magnetism and Magnetic Materials 322, 3401–3409 (2014)
[4] D.Bychanok, M.Yakovleva, P.Kuzhir, V.Ksenevich, R. Kotsilkova, Broadband electromagnetic characterization of ternary polypropylene-MWCNT-clay composites, Book of abstracts of International Conference «FANEM'15», Minsk 2015

LUMINESCENCE PROPERTIES OF EUROPIUM AND DYSPROSIUM CO-DOPED OXYFLUORIDE GLASSES

Meldra Kemere*, Janis Sperga, Uldis Rogulis, Jurgis Grube

Institute of Solid State Physics, University of Latvia, Kengaraga Street 8, Riga, Latvia
meldra.kemere@gmail.com

A wide range of luminescent materials are used in lighting devices and diodes, displays, optical communication, sensors, etc. Rare-earth (RE) doped glasses and glass-ceramics are considered as promising luminescent materials due to mechanical and chemical stability and long-lasting performance. Oxyfluoride glasses and glass-ceramics are characterized with low phonon energy, good optical properties and therefore have been widely investigated in the last decades. [1, 2] RE activator pair – Dy^{3+} and Eu^{3+}- can be used in white light luminophores.[3] In addition, energy transfer processes between both ions in aluminoborate and zinc-aluminium-sodium-phosphate glasses have been announced. [3,4] In the present work, we have investigated luminescence of Eu^{3+} and Dy^{3+} -doped aluminosilicate glasses with CaF_2, the interaction and energy transfer mechanisms between both activator ions.

Transparent oxyfluoride glasses with composition SiO_2-Al_2O_3-CaO-CaF_2, co-doped with Eu^{3+} and Dy^{3+} (concentration ~1 mol%), have been synthesized by the melt quenching method in air atmosphere. In order to investigate the interaction between the activator ions, different concentration ratios of activators Dy^{3+} : Eu^{3+} (1:0,1:1,1:0.5,0:1) were chosen.

The photoluminescence (PL) and photoluminescence decay measurements were performed on grinded samples using a tunable laser. The PL excitation spectra of glass samples were recorded using the excitation range 300-480 nm.

In the co-doped samples, interaction between Eu^{3+} and Dy^{3+} ions was observed. Luminescence spectra show that emission intensity of Dy^{3+} ions in co-doped samples is much lower with respect to Dy^{3+} single-doped sample. The excitation spectra of Eu^{3+} show excitation peaks at the characteristic excitation wavelengths of Dy^{3+} (350 nm and 453 nm) which indicates, that energy transfer from Dy^{3+} to Eu^{3+} occurs. Furthermore, changes in luminescence decay curves are also observed. Using the luminescence lifetimes of single doped and co-doped samples, the energy transfer rate was estimated and energy transfer mechanism was discussed.

[1] P. P. Fedorov, A. A. Luginina, and A. I. Popov, Transparent oxyfluoride glass ceramics, Journal of Fluorine Chemistry 172, 22 (2015)

[2] C.C. Lin, R.S. Liu, Advances in phosphors for light-emitting diodes, The Journal of Physical Chemistry Letters 2(11), 1268-1277 (2011)

[3] J.L.Cai, R.Y. Li,C.J. Zhao,S.L. Tie, X. Wan, J.Y. Shen, White light emission and energy transfer in Dy^{3+}/Eu^{3+} co-doped aluminoborate glass, Optical Materials 34(7), 1112-1115 (2012)

[4] .D. Rajesh, K. Brahmachary, Y. C. Ratnakaram, N. Kiran, A.P. Baker, G.G. Wang, Energy transfer based emission analysis of Dy^{3+}/Eu^{3+} co-doped ZANP glasses for white LED applications, Journal of Alloys and Compounds 646, 1096-1103 (2015)

INVESTIGATION OF POSSIBILITIES OF DETERMINATION OF LONG-CHAIN HYDROCARBONS IN CARBON-BASED DUST FROM FUSION REACTOR

Dāvis Čonka, Roberts Zariņš, Līga Avotiņa, Gunta Ķizāne

Institute of Chemical Physics, University of Latvia, Riga, Latvia
davis.conka@lu.lv

Carbon fibre composite materials (CFC) have been used as divertor and plasma facing materials in the vacuum vessel of the Joint European Torus (JET) until 2009 and as substrate for tungsten-coated tiles in the JET ITER-like wall (ILW) divertor [1]. These materials can be used for the fusion applications due to low Z and good thermal-conductivity.

Operation of plasma in fusion reactors causes plasma-wall interactions (PWI): like erosion, formation of co-deposited layers and dust and flakes, fuel retention, formation of fullerenes [2], causing decrease in amount of fusion fuel and shortening lifetime of divertor materials. Formation of long-chain hydrocarbons and fullerene like compounds also can take place in plasma-wall interactions.

During PWI tritium can be captured in erosion products, deposited layers. Chemical reactions, like formation of long-chain hydrocarbons, can take place [3]. Therefore, it is important to investigate possibilities of determination of such hydrocarbons in dusts and flakes from a fusion reactor.

Long-chain hydrocarbons with and without addition of carbon-based dusts (C-dust) prepared from CFC are analyzed, in order to understand ways of tritium accumulation and formation mechanisms of various compounds including long-chain hydrocarbons in materials collected from a fusion reactor.

To characterize structure and chemical composition of the plasma exposed and non-exposed materials, Raman, Fourier transformation infrared spectroscopy (FT-IR) and Scanning electron microscopy together with energy dispersion X-ray spectroscopy (SEM-EDX) were used.

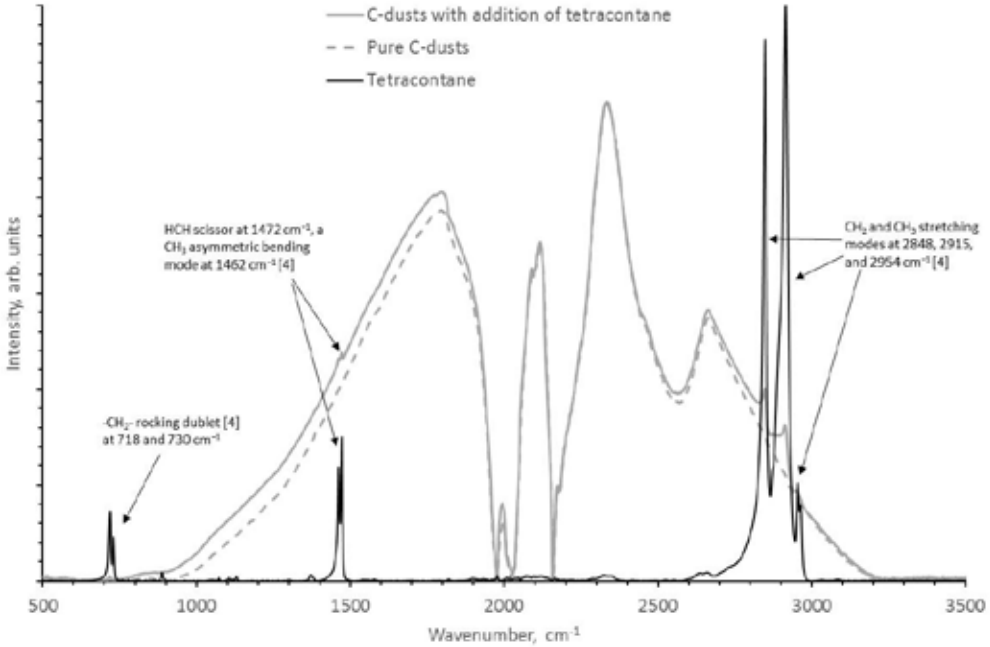

Fig. 1. FT-IR spectra of long chain hydrocarbon (tetracontane), CFC with addition of tetracontane and pure CFC

It was obtained, that presence of <5 wt.% hydrocarbons in non-irradiated C-dust can be determined by using FT-IR spectroscopy, by CH_2 and CH_3 stretching modes at 2848, 2915 and 2954 cm^{-1} and by weaker signal HCH scissor at 1472 cm^{-1} [4]. FT-IR and other above mentioned methods can be successfully used to determine chemical composition of carbon based dust and flakes from a fusion reactor.

[1] G.F. Matthews et al., Plasma operation with an all metal first-wall: Comparison of an ITER-like wall with a carbon wall in JET, Journal of Nuclear Materials, 438 (2013), S2-S10
[2] N. Bekris et al., Characterisation of flakes generated in JET after DD and DT plasma operations, Journal of Nuclear Materials, 337–339 (2005), 659–663
[3] S. Grünhagen Romanelli et al., Gas analyses of the first complete JET cryopump regeneration with ITER-like wall, Phys. Scr., T159 (2014) 014068 (4pp)
[4] S. J. Seltzer et al., Investigation of Anti-Relaxation Coatings for Alkali-Metal Vapor Cells Using Surface Science Techniques, Journal of Chemical Physics, 133, 144703 (2010)

TRITIUM ACCUMULATION IN JOINT EUROPEAN TORUS BERYLLIUM WALL MATERIALS

Ieva Igaune[1], Elīna Pajuste[1], Gunta Ķizāne[1], JET Contributors[2]

[1]Institute of Chemical Physics, University of Latvia, Riga, Latvia
[2] EUROfusion Consortium, JET, Culham Science Centre, OX14 3DB, Abingdon, UK
Ieva.igaune18@gmail.com

ITER – Like Wall project has been launched at Joint European Torus to test plasma facing materials relevant to International Thermonuclear Experimental Reactor – ITER. Beryllium will be used as plasma facing material for first wall and neutron multiplier in blanket zone. This material was selected due to low Z, good thermal conductivity and high oxygen gettering characteristic.[1]

Erosion and tritium accumulation are the main issues related to performance of the plasma facing materials in the vacuum vessel of fusion reactors. Thermal transiet loads cause heating of beryllium surface and can result in significant changes – material loss, melting, cracking evaporation, formation of dust and hydrogen isotopes retention in the wall materials and dust.[2,3]

During the shut down in 2012, beryllium tiles were removed from three positions in the vacuum vesel. Tiles were from the iner wall (Inner Wall Guard Limiter), outer wall (Wide Poloidal Limiter) and upper region (Upper Dump Plate) (Fig.1).

To assess changes in the surface, beryllium tiles were studied with scanning electron microscopy and energy dispersive X-ray spectroscopy. A beryllium dissolution method under controlled conditions was used to determine tritium concentration and its bulk distribution in the sample. During dissolution tritium and hydrogen was released (1) and both measured.

$$Be(s) + 2H^{+}(l.) \rightarrow Be^{2+}(l.) + H_2\uparrow(g) \quad (1)$$

Results revealed that tritium was localized in 80 µm of the tile surface with highest concentration in the first 2-10µm. SEM and EDX analysis demonstrated that surface structure modifications and chemical composition of the deposited layer strongly depends on the location of the sample in the vacuum vessel.

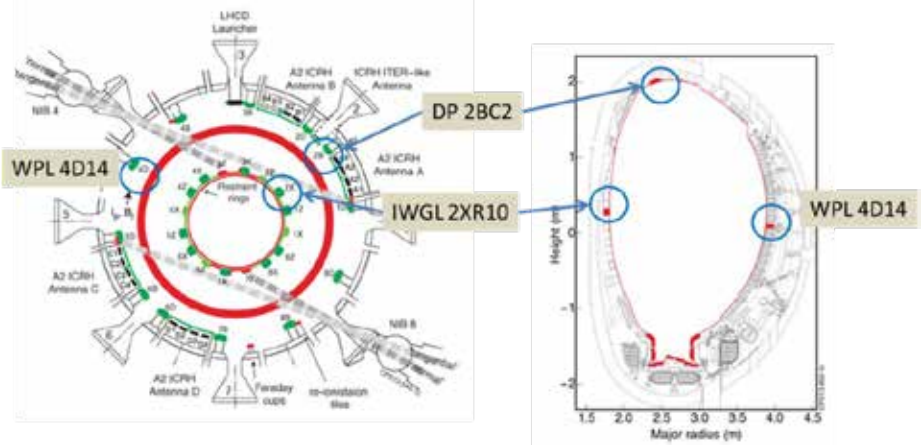

Fig. 1 Position (approximate) of analysed tiles in the vacuum vessel

[1] Khomutov, A., Barabash, V., Chakin, V. et.al. Beryllium for fusion application – recent results. *Journal of Nuclear Materials,* **2002.,** 630-637.
[2] Chakin, V., Reimann, J., Moeslang, A. et.al. Thermal conductivity of highly neutron-irradiated beryllium in nuclear fusion reactors. *Progress in Nuclear Energy.* **2012.,** 57, 2-7.
[3] Kupriyanov, I.B., Nikolaev, G.N., Kurbatova, L.A., et al. Erosion of beryllium under ITER – Relevant transient plasma loads. *Journal of Nuclear Materials.* **2015.,** 1-6.
* See the Appendix of F. Romanelli et al., Proceedings of the 25th IAEA Fusion Energy Conference 2014, Saint Petersburg, Russia

RADIOLYSIS OF LITHIUM ORTHOSILICATE PEBBLES WITH ADDITION OF TITANIUM DIOXIDE

Oskars Valtenbergs[1], Arturs Zarins[1], Gunta Kizane[1], Arnis Supe[1], Larisa Baumane[2]

[1] University of Latvia, Institute of Chemical Physics, 1 Jelgavas Street, LV-1004, Riga, Latvia.
[2] Latvian Institute of Organic Synthesis, 21 Aizkraukles Street, LV-1006, Riga, Latvia.
oskars.valtenbergs@lu.lv

Lithium orthosilicate (Li_4SiO_4) pebbles with addition of titanium dioxide (TiO_2) are suggested as an alternative tritium breeding ceramic for the fusion reactors. Under exploitation conditions, the Li_4SiO_4 pebbles will be subjected to neutron and ionizing irradiation, high temperature and magnetic field. The radiolysis will take place in the Li_4SiO_4 pebbles where radiation-induced defects (RD) and radiolysis products (RP) can form and accumulate. The aim of this work is to analyse the formation and accumulation of RD and RP in the Li_4SiO_4 pebbles with different content of TiO_2.

The Li_4SiO_4 pebbles with addition of TiO_2 were irradiated with accelerated electrons (E=5 MeV) up to 5 GGy absorbed dose at 300-730 K in dry argon atmosphere. The formation, accumulation and annihilation of paramagnetic RD and RP were analysed by electron spin resonance (ESR) spectroscopy.

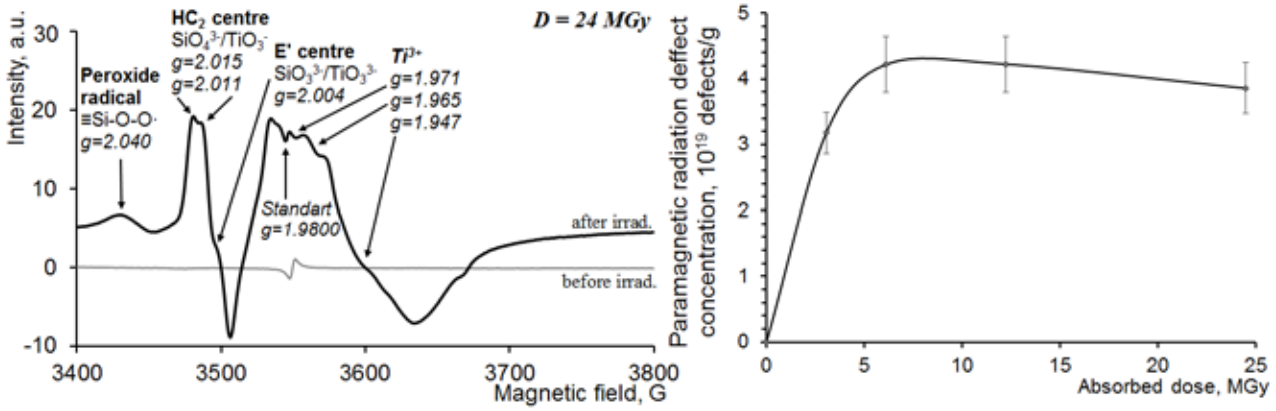

Fig. 1. The ESR spectra of the modified Li_4SiO_4 pebbles with addition of TiO_2 before and after irradiation (D=24 MGy, $T_{(aver.)}$=320 K) (left) and total concentration of the accumulated paramagnetic RD (right).

Using ESR spectroscopy, the formation and accumulation of paramagnetic RD in the Li_4SiO_4 pebbles with addition of TiO_2 was detected (Fig. 1, left). The total concentration of paramagnetic RD was calculated using double integration method of the first derivative ESR signals and by comparison with the standard signal (Fig. 1, right). In comparison with previous researches [1], it was shown that the Li_4SiO_4 pebbles with addition of TiO_2 have a good radiation stability and the initial radiation chemical yield (G) is below 0.5 defects per 100 eV. It was determined that up to 95% of accumulated paramagnetic RD annihilated before reaching 650 K.

Acknowledgment:

The authors greatly acknowledge the technical and experimental support of Regina Knitter, Matthias Kolb and Oliver Leys (Karlsruhe Institute of Technology, Institute for Applied Materials (IAM-KWT), Germany).

[1] J. Tiliks et al. Fusion Eng. Des. 69 (2003) 519-522.

PLASMON-ENHANCED RAMAN SCATTERING BY ZnO NANOCRYSTALS

Alina Muravitskaya[1]

[1] B. I. Stepanov Institute of Physics, National Academy of Sciences of Belarus, Belarus
alina.muravitskaya@ifanbel.bas-net.by

ZnO-based materials in the low dimensional regime have attracted considerable attention owing to a wide bandgap of 3.4 eV, large excitonic binding energy of 60 meV and their size-dependent optical and electronic properties, based on the quantum confinement effect of the electronic states. Raman scattering allows investigating the internal properties of material, phonon modes, and electron-phonon interactions. Surface enhanced Raman scattering of light by ZnO nanostructures was previously reported by several groups [1,2]. An increase of Raman scattering for nonresonant excitation was obtained for ZnO NCs coupled with colloidal silver nanoparticles [1], ZnO nanorods and nanocrystals covered with silver clusters by vacuum deposition [2]. The enhanced modes were A_1 (LO) and E_2 (high). In this work we report on significant surface enhanced nonresonant Raman scattering of light by ZnO NCs coupled with silver nanostructures.

Colloidal ZnO nanocrystals solution in ethanol were synthesized by hydrolysis of zinc acetate (reagent grade) with sodium hydroxide (pure) at 0 ^{o}C, as described in more details elsewhere [1]. After the synthesis solution was kept at 55–60 ^{o}C for 2 h to promote ZnO particles crystallization. The molar zinc oxide concentration in solution was 0.01 M corresponding to about 10^{-5} M in terms of NC concentration. Raman scattering experiments were performed on ZnO NCs deposited by drop-casting onto the glass substrate. As the source of plasmonic enhancement a nanostuctured silver thin films were deposited by means of the vacuum evaporation technique. Two sorts of samples were prepared: with silver film deposited on glass before ZnO NCs casting or by deposition of the nanostructured metal film on top of the ZnO NCs preliminary applied onto the pure glass surface. In both cases, deposition of ZnO NC film was performed by dropping a 10 μL of ZnO NCs solution onto the substrate and drying for at least 1 hour. The reference sample was prepared in the same way but without metal deposition. Raman spectra were collected in backscattering geometry using Jobin-Yvon Labram confocal spectrometer with He-Ne laser source (λ_{exc}=632.8 nm).

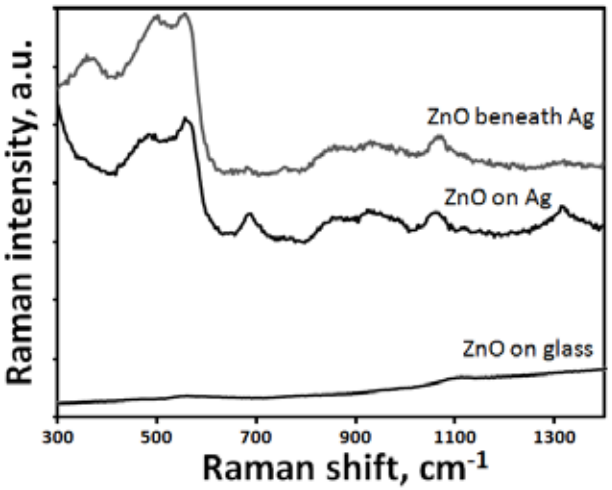

Fig. 1. Raman spectra of ZnO NCs on Ag-coated glass substrate, ZnO NCs beneath a Ag-coating, reference spectra for ZnO NCs on glass substrate.

The Raman spectra of the ZnO NCs on and beneath the silver coating are shown in Fig. 1. The most intensive component at about 560 cm^{-1} coincides with previously obtained mode for ZnO nanocrystals [1,2]. According to the results of Ref.[2], the modes at 490–500 cm^{-1} and 560 cm^{-1} can be attributed to the surface optical (SO) phonons formed from phonons of the symmetry A_1 or the symmetry E_1. Spectrum for ZnO beneath silver nanoparticles shows the additional peak at 373 cm^{-1}, which also have surface nature. The modes in the range 600-1500 cm^{-1} can be attributed to zinc acetate. Both SERS configurations demonstrated comparable enhancement efficiency and can be used in further experiments.

[1] A.Rumyantseva, S.Kostcheev, P.-M.Adam, S.V. Gaponenko, S.V.Vaschenko, O.S.Kulakovich, A.A.Ramanenka, D.V.Guzatov, D.Korbutyak, V.Dzhagan, A.Stroyuk, and V. Shvalagin, Nonresonant Surface-Enhanced Raman Scattering of ZnO Quantum Dots with Au and Ag Nanoparticles, ACS Nano 7(4), 3420-3426 (2013).

[2] A. G. Milekhin, N. A. Yeryukov, L. L. Sveshnikova, T. A. Duda, E. I. Zenkevich, S. S. Kosolobov, A. V. Latyshev, C. Himcinski, N. V. Surovtsev, S. V. Adichtchev, Z.C. Feng, C. C. Wu, D. S. Wuu, D. R. T. Zahn, Surface enhanced Raman scattering of light by ZnO nanostructures, JETP 113(6), 983-991 (2011).

SUPERCONDUCTIVITY ON THE EDGE OF FERROMAGNETISM – PHYSICAL PROPERTIES OF La_3Co COMPOUND

Marta Roman, Judyta Strychalska, Tomasz Klimczuk

Faculty of Applied Physics and Mathematics, Gdansk University of Technology, Poland
roman.marta92@gmail.com

Numerous intermetallic compounds containing ferromagnetic elements like Ni, Fe or Co exist, but only few of them exhibit superconducting properties. Generally, compounds consisting of strongly magnetic atoms do not exhibit superconducting behaviour. However, superconductivity in the intermetallic compound La_3Co, which contains a ferromagnetic element of the d block (Co), was reported [1], [2], [3]. This unexpected result motivated us to carry out a detailed experimental examination of the properties of this material, which is the subject of this presentation.

The superconducting transition ($T_c \approx 4.57$ K) of La_3Co was studied by measuring the magnetic susceptibility, resistivity and specific heat using the experimental system PPMS (*Physical Property Measurement System*) and the highlights of our results are presented. We also describe the procedure of preparation of the La_3Co compound (arc melting under an atmosphere of highly purified argon; subsequent annealing in vacuum at 500 °C), the crystallographic structure of this material (orthorhombic, space group Pnma, number 62) and results of powder X-ray diffraction, which enabled the determination of the phase composition of the sample. Values of relevant physical parameters, recovered as a result of our experiments, and their implications for our understanding of the mechanism of superconductivity in this compound, will also be discussed.

---

[1] K. Sato, K. Maezawa, T. Fukuhara, Y. Isikawa, K. Mori., Superconductivity in intermetallic compound La_3Co, J. Appl. Phys. 73 (10), 1992.
[2] H. Talik, J. Heimann, J. Szade, A. Chełkowski, Temperature dependence of magnetic susceptibility and electrical resistivity of La_3Co and Lu_3Co, J. Less-Common Met., 155, 241-246 (1989).
[3] C.S. Garde, J. Ray, G. Chandra, Resistivity and thermopower studies on La3X (X: Al, Sn, In, Ru, Ir, Co, Ni, Ge, Ga) systems, 1993.
[4] D. T Cromer., A. C Larson., The Crystal Structure of La_3Co, Acta Cryst. 14 1226-1228 (1961)

DIRECTED ASSEMBLY OF MICRO PARTICLES INTO WELL-ORGANIZED ARRAYS

Mindaugas Juodėnas[1], Dainius Virganavičius[1], Tomas Tamulevičius[1,2], Viktoras Grigaliūnas[1], Morten Madsen[3], Sigitas Tamulevičius[1,2]

[1]Institute of Materials Science, Kaunas University of Technology, Lithuania
[2]Department of Physics, Kaunas University of Technology, Lithuania
[3]Mads Clausen Institute, University of Southern Denmark, Denmark
mindaugas.juodenas@ktu.edu

Recent advances in nanoscience developed elaborated synthesis of nanoparticles of various shapes, sizes and materials. Most applications of nano and micro particles demand their precise stacking into one, two or three dimensional assemblies. Such applications involve novel biosensors [1], nanoelectronic [2], nanophotonic devices [3], drug delivery [4], fluorescence biological labels [5], etc.

One of the techniques for achieving such particle positioning is capillary force assisted assembly. Its basic principle is as follows: a drop of suspension with nanoparticles is confined between a template with surface structures designed for the specific application and a clamping glass slide. These parallel surfaces are translated with respect with each other. Because of evaporation at computer controlled template temperature a particle accumulation zone forms at the three phase contact point i.e. at the edge of liquid meniscus. As it passes over particular size surface structures it deforms and directs particles into predesigned traps. Once the meniscus depins from the structure, the particle stays in the trap. This method offers high arrangement precision, selectivity, throughput and scalability. Several investigations of assembly speed, template temperature and trap geometry have been performed by other authors [6, 7], however the mechanism leading to particle assembly is not quite fully understood.

Here we present results achieved employing custom built capillary force assisted particle assembly setup. Holographic and electron beam lithographies in combination with dry etching of crystalline silicon and soft lithography replication in temperature curable polymer were employed to form 4 cm^2 area templates. Arrays of fluorescent particles (Fig. 1) and ordinary polystyrene beads (Fig. 2) were assembled into ordered 2D patterns and investigated using optical and scanning electron microscopy. Such regular micro and nano particles arrays are expected to be used for anti-counterfeiting applications and surface enhanced Raman scattering (SERS).

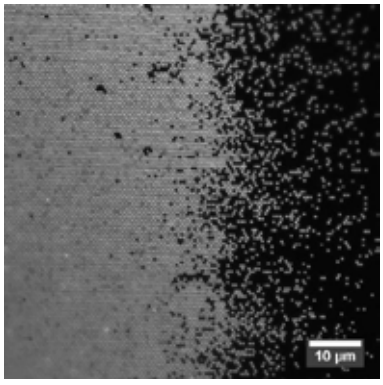

Fig. 1. Fluorescent microscope micrograph of transition zone between assembly areas (left) and non-assembly (right) of 270 nm particles assembled into poly-dimethylsiloxane (PDMS) template pits of 300 nm diameter. Scale bar 10 µm

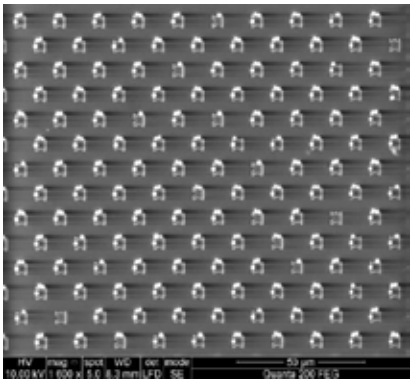

Fig. 2. SEM micrograph of 1.5 µm beads assembled into geometric traps on a PDMS template. Scale bar 50 µm

Lithuanian–Japan bilateral cooperation partnership programme project (No. LJB-1/2015) was financed by Research Council of Lithuania.

[1] R. L. Edelstein, C. R. Tamanaha, P. E. Sheehan et al., The BARC biosensor applied to the detection of biological warfare agents, Biosensors Bioelectron. 2000; 14:805–813.
[2] M. Homberger, U. Simon, On the application potential of gold nanoparticles in nanoelectronics and biomedicine, Phil. Trans. R. Soc. A. 2010; 368:1405-1453.
[3] I. Venditti, I. Fratoddi, C. Palazzesi et al., Self-assembled nanoparticles of functional copolymers for photonic applications, Journal of Colloid and Interface Science. 2010; 348(2):424–430.
[4] S. Biffi, R. Voltan, E. Rampazzo et al., Applications of nanoparticles in cancer medicine and beyond: optical and multimodal in vivo imaging, tissue targeting and drug delivery, Expert Opin Drug Deliv. 2015; 12(12):1847-1849.
[5] M. Bruchez, M. Moronne, P. Gin et al., Semiconductor nanocrystals as fluorescent biological labels, Science. 1998; 281:2013–2016.
[6] L. Malaquin, T. Kraus, H. Schmid et al., Controlled particle placement through convective and capillary assembly, Langmuir: The ACS Journal of Surfaces and Colloids. 2007; 23(23):11513–11521.
[7] N. Songbo, J. Leemann, H. Wolf et al., Insights into mechanisms of capillary assembly, Faraday Discuss. 2015; 181:225-242.

OXYGEN GAS SENSING PROPERTIES OF AlN NANOPOWDER

Paula Jankovska, Valdis Korsaks, Baiba Berzina

Institute of Solid State Physics, University of Latvia
paula.jankovska@fizmati.lv

Oxygen gas sensing properties based on defect induced luminescence of AlN nanopowder were studied. Spectral characteristics of AlN nanopowder with 60 nm average grain size were examined. Photoluminescence (PL) spectra and its excitation spectra (PLE) measured at room temperature (RT) are depicted on Fig.1, a and b, correspondingly. It was observed that for AlN a wide luminescence band at 420 nm (blue luminescence - BL) is characteristic (Fig. 1, a), which can be excited either through exciton processes (215 nm) or by direct defect excitation with ultraviolet light forming two separated spectral bands at 260 nm and 315 nm (Fig. 1,b). This luminescence is distinct from those observed in AlN materials with bulk structure [1]. It was found, that the 420 nm luminescence is sensitive to oxygen gas surrounding the material, resulting in quenching of luminescence intensity as it is demonstrated on Fig. 1, a, where four PL spectra are depicted obtained under sample excitation with 265 nm light. The first and the second PL curves were measured when sample is surrounded with vacuum (~10^{-5}mBa) or nitrogen gas. On contrary, the third and fourth PL curves, which were measured, when sample was put into dry air or pure oxygen gas, are with considerably reduced intensity demonstrating luminescence quenching.

From the results of spectral characterization of hBN material it follows, that the F-centers, formed from the nitrogen vacancies with trapped electrons, could be the possible defects responsible for the BL. In this case the defects, which are close to the material surface, are interacting with environmental oxygen gas.

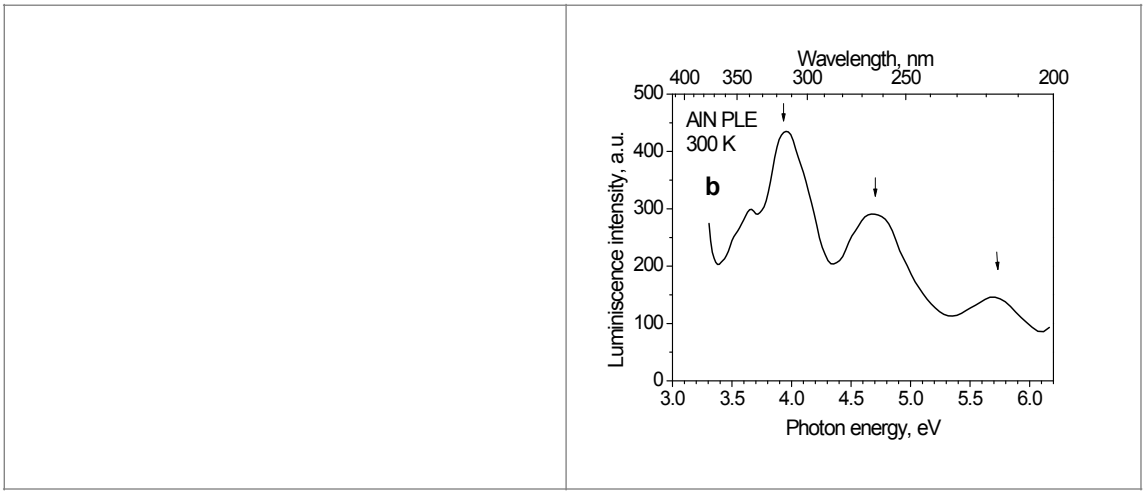

Fig. 1. AlN nanopowder, RT; a – PL spectra under 265 nm excitation, when sample is surrounded with vacuum (1), nitrogen gas (2), dray air (3), and oxygen gas (4); b – 420 nm luminescence excitation spectrum. Arrows show separated excitation bands.

BL characteristics demonstrating oxygen gas sensing properties of AlN materials were investigated. They are: *i)* gas sensing parameter of material measured as ratio of BL intensity when sample is in vacuum or in gas, *ii)* repeatability of measurements, *iii)* oxygen sensitivity graduation curve obtained at different oxygen gas concentrations in gas mixture.

The results obtained allow joining AlN nanopowder to the material class prospective for application as luminescent sensors of oxygen gas.

[1] B.Berzina, L.Trinkler, D.Jakimovica, V.Korsaks, J.Grabis, I.Steins, E.Palcevskis, S.Bellucci, L.-C.Chen, S.Chattopadhyay and K.Chen, Spectral characterization of bulk and nanostructured aluminum nitride. Journal of Nanophotonics, Vol. 3, 031950-031950-16 (2009),DOI: 10.1117/1.3276803.

EFFECT OF ADDITIVES ON THE HYDROTHERMAL SYNTHESIS OF MANGANESE FERRITE NANOPARTICLES

Simonas Ramanavičius, Arūnas Jagminas

State Research Institute Center for Physical Sciences and Technology, Savanorių 231, LT-02300 Vilnius, Lithuania
simonas.ramanavicius@chf.stud.vu.lt

In recent years, considerable interest has been devoted to fabrication of various ferrite nanoparticles (*Nps*) with the aim of developing the convenient method for synthesis of uniform *Nps* with predictable size, morphology and homogeneity [1]. This need is dictated by the increasing interest in application of superparamagnetic nanoparticles and ferrofluids in catalysis, waste water treatments and nanomedicine, in particular, diagnostics, magnetic hyperthermia, drug delivery systems, etc. [2].

This study is focused on the synthesis of manganese ferrite ($MnFe_2O_4$) *Nps* by most commonly used chemical way pursuing better control of their size, purity and magnetic properties. Co-precipitation syntheses were performed using aqueous alkaline solutions of Mn(II) and Fe(III) salts and NaOH within a wide pH range using various hydrothermal treatment regimes. Different additives, such as cysteine, glycine, chitosan, polypropylene glycol, etc., were tested on purpose to obtain good yield of pure phase and monodispersed *Nps* with average size of ≤20 nm. X-ray diffraction (XRD), Mössbauer spectroscopy down to cryogenic temperatures and magnetic measurements were utilized in this study.

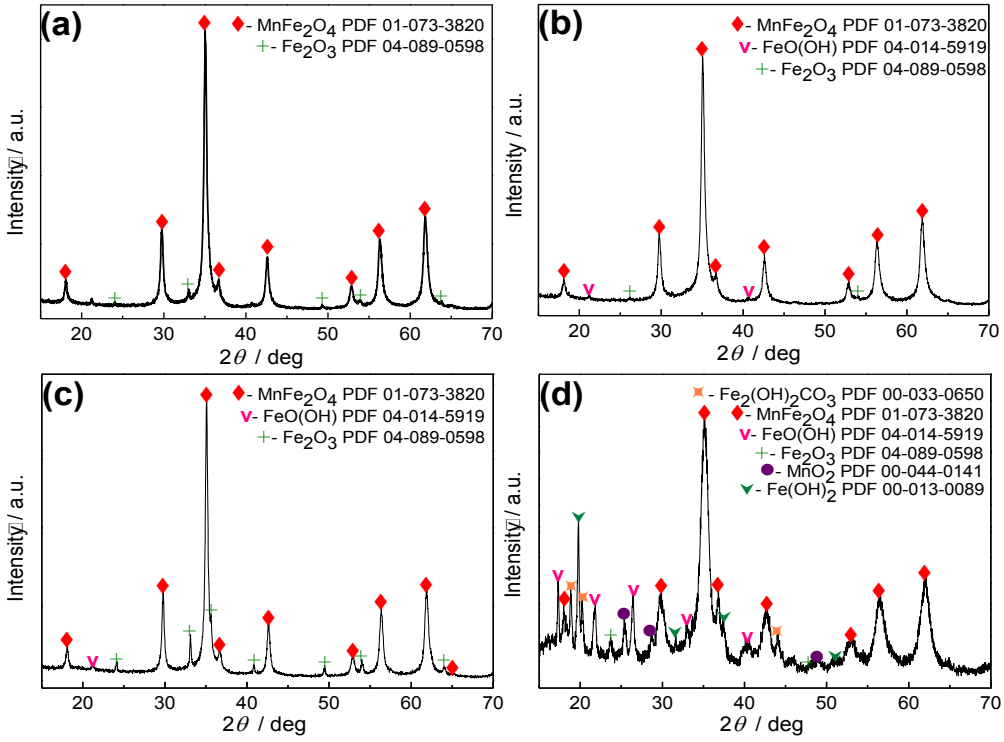

Fig. 1. XRD patterns of the products synthesized in a 25 mmol/L $MnCl_2$ and 50 mmol/L $FeCl_2$ solution at pH = 11,5 by hydrothermal treatment at 120˚C for 10h with glycine (a), PPG 425 (b), chitosan (c), and cysteine (d) addition.

It was determined that the majority of tested chelating and Me^{z+} complexing additives, besides the expected control of the particle size and size dispersity, also have a strong effect on the purity of the product obtained by hydrothermal as well as microwave-assisted synthesis by co-precipitation reaction of Mn(II) and Fe(III) ions. Therefore, the application of such additives as cysteine, glycine, chitosan and their salts for the synthesis of pure phase $MnFe_2O_4$ nanoparticles is not suitable. On the other hand, the influence of the tested additive PPG, on the purity of the synthesized *Nps* is significantly weaker, therefore PPG can be used for the production of superparamagnetic $MnFe_2O_4$ *Nps* with a good yield.

[1] C Kumar, F. Mohammed, Magnetic nanomaterials for hyperthermia-based therapy and controlled drug delivery, Advanced Drug Delivery Reviews 63 (2011) 789–808
[2] A. K. Gupta, M. Gupta, Synthesis and surface engineering of iron oxide nanoparticles for biomedical applications, Biomaterials 26 (2005) 3995–4021

CARRIER DYNAMICS IN InGaN QUANTUM WELLS WITH GROSS WELL WIDTH FLUCTUATIONS

D. Dargis

Institute of Applied Research and Faculty of Physics, Vilnius University
Donatas.Dargis@ff.stud.vu.lt

Over the last decade, performance of InGaN-based light emitting diodes (LEDs) has improved considerably to the point where they are now penetrating the outdoor and indoor general lighting. One of the key issues in the manufacture of high efficiency nitride-based heterostructures is the control of the In-composition in the $In_xGa_{1-x}N$ quantum wells (QWs). One common approach is to grow the GaN barriers between the QWs at a higher temperature than the InGaN QWs themselves. This high temperature barrier growth has two potential impacts: reducing the density of defects in the barrier material and altering the morphology or composition distribution of the InGaN QW itself. In this work, there was investigated a matrix of four samples which was designed to separate the two effects: quality of GaN barrier and gross well-width fluctuations.

It was noticed, that samples with gross well-width fluctuations has lower coefficient of diffusion. It can be explained by the width of the QW reducing to zero in several places, leaving a "gap" which is filled with GaN. Larger PL peak position shift in samples with gross well-width fluctuations is due to lower density of localized states. It was supported by the calculated localization parameter σ value which is equal to zero in samples with gross well-width fluctuations [1]. The higher activation energy E_a indicates that in samples with gross well-width fluctuations deeper localization states are formed during QW's growth process.

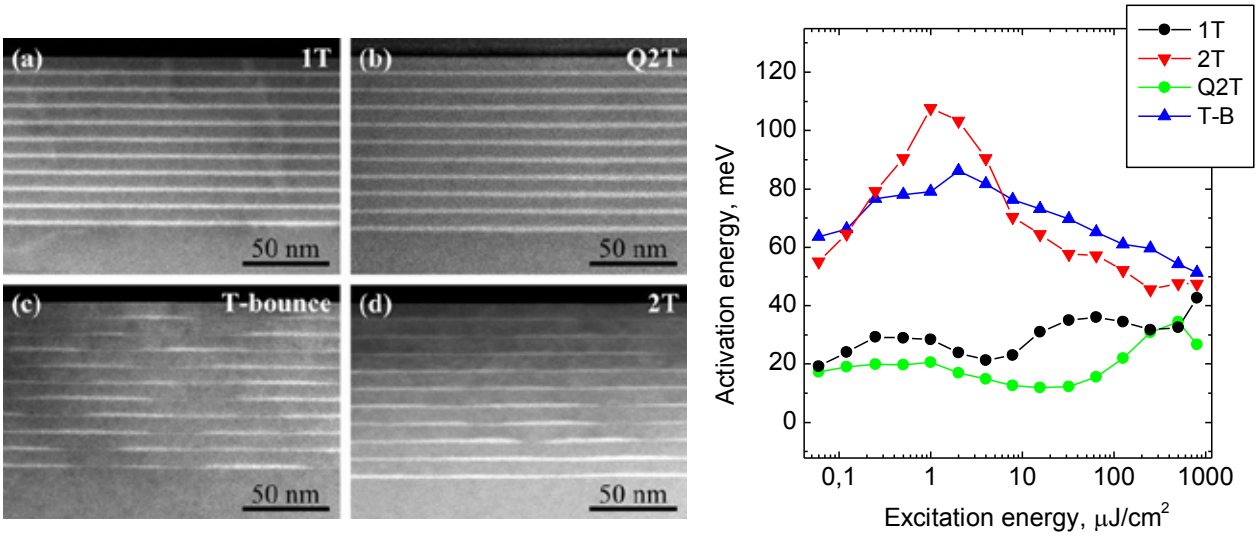

Fig. 1. STEM images of MQWs grown by four different methods:(a) 1T, (b) Q2T, (c) T-bounced, (d) 2T [2]. Activation energies dependence of excitation energy are shown in (e).

[1] S. Hammersley, D. Watson-Parris, P. Dawson, M. J. Godfrey, T. J. Badcock, M. J. Kappers, C. McAleese, R. A. Oliver, and C. J. Humphreys, "The consequences of high injected carrier densities on carrier localization and efficiency droop in InGaN/GaN quantum well structures," *J. Appl. Phys.*, vol. 111, no. 8, p. 083512, 2012.

[2] R. A. Oliver, F. C.-P. Massabuau, M. J. Kappers, W. A. Phillips, E. J. Thrush, C. C. Tartan, W. E. Blenkhorn, T. J. Badcock, P. Dawson, M. A. Hopkins, D. W. E. Allsopp, and C. J. Humphreys, "The impact of gross well width fluctuations on the efficiency of GaN-based light emitting diodes," Appl. Phys. Lett., vol. 103, no. 14, p. 141114, 2013.

TRIPLET ANNIHILATION AND THERMALLY ACTIVATED DELAYED FLUORESCENCE IN PYRROLE PYRIMIDINE DERIVATIVES

Tadas Bučiūnas[1], Lina Skardžiūtė[1], Jelena Dodonova[2], Sigitas Tumkevičius[2], Saulius Juršėnas[1]

[1] Institute of Applied Research, Vilnius University, Saulėtekio al. 9-III, LT-10222 Vilnius, Lithuania
[2] Department of Organic Chemistry, Vilnius University, Naugarduko 24, LT-03225 Vilnius, Lithuania
tadas.buciunas@gmail.com

Nowadays, the technology of organic light emitting devices undergoes a breakthrough due to introduction of novel emission mechanisms adopting delayed florescence generated by triplet-triplet annihilation (TTA) [1] or thermal activation (TADF) [2]. In this work, the ability to control the characteristics of photoluminescence of donor-acceptor pyrrole pyrimidine derivatives with intramolecular charge transfer features are investigated as potential delayed fluorescence emitters.

The pyrrole pyrimidine molecule is identified as an efficient blue emitter, exhibiting antitumor, antiviral and antibacterial attributes [3]. Here we analyze the optical characteristics of three pyrrole pyrimidine derivatives with acceptor-like (**1**), donor-like (**3**) substituents and without a substituent (**2**) at pyrrole nitrogen atom position.

The analysis of emission in an extensive time range reveals three radiative relaxation pathways intrinsic to all of the pyrrole pyrimidine derivatives: fluorescence of charge transfer states, delayed emission of molecular aggregates and molecular phosphorescence. Studies of spectral and transient properties of fluorescence lead to conclusion that intramolecular charge transfer character is enhanced by increasing polarity of the substituent. It is evident by the decrease of the oscillator strength (by factor 2,4), increase in relaxation decay times (from 0,38 ns to 10,56 ns) and bathochromic shift (from 3,2 eV to 2,79 eV) registered from the most acceptor-like compound to the most donor-like compound. The photoluminescence properties measured in 15 K temperature reveals the independence of triplet energy state (positioned at 2,455 eV) from polarity of the substituent, due to excitation localization on the pyrrole pyrimidine core.

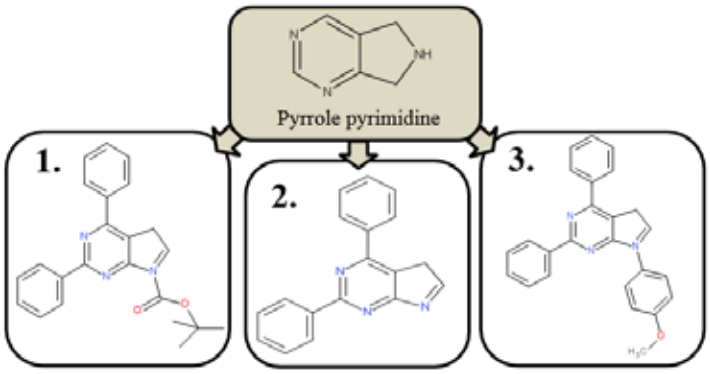

Fig. 1. Chemical structures of Pyrrole pyrimidine derivatives analysed in this work.

The constant intensity of photoluminescence in extensive temperature range (15 K – 300 K) displayed by **3** derivative leads to an absence of thermally activated delayed fluorescence process. Meanwhile, a decrease in intensity is demonstrated by **1** derivative. It is assumed that energy relaxation pathway is not prevailed by thermal activation also and dominated by non-radiative mechanisms, unrelated to triplet energy state. This argument is supported by the wide singlet-triplet energy state gap (ΔE varying in range of 0,705 eV - 0,52 eV). The quadratic dependence of the intensity of photoluminescence on excitation fluency implies presence of triplet-triplet annihilation process, although, the effect is non-dominant. Thus, the radiative properties of pyrrole pyrimidine derivatives are dominated by the intramolecular charge transfer character and its effect is enhanced by the increase of the polarity of the substituent.

[1] C. Mayr, T. D. Schmidt, and W. Brütting, "High-efficiency fluorescent organic light-emitting diodes enabled by triplet-triplet annihilation and horizontal emitter orientation," Appl. Phys. Lett., vol. 105, no. 18, p. 183304, 2014.
[2] F. B. Dias, K. N. Bourdakos, V. Jankus, K. C. Moss, K. T. Kamtekar, V. Bhalla, J. Santos, M. R. Bryce, and A. P. Monkman, "Triplet harvesting with 100% efficiency by way of thermally activated delayed fluorescence in charge transfer OLED emitters," Adv. Mater., vol. 25, no. 27, pp. 3707–3714, 2013.
[3] J. Dodonova, L. Skardziute, K. Kazlauskas, S. Jursenas, and S. Tumkevicius, "Synthesis of 4-aryl-, 2,4-diaryl- and 2,4,7-triarylpyrrolo[2,3-d] pyrimidines by a combination of the Suzuki cross-coupling and N-arylation reactions," Tetrahedron, vol. 68, no. 1, pp. 329–339, 2012.).

POLYAMORPHSIM IN METALLIC GLASSES ASSESSED BY EXAFS METHOD

Przemyslaw Dziegielewski[1], J. Antonowicz[1], A. Pietnoczka[1], O. Mathon[2], I. Kantor[2], S. Pascarelli[2], T. Shinmei[3], T. Irifune[3]

[1]Faculty of Physics, Warsaw University of Technology, Koszykowa 75, 00-662 Warsaw, Poland
[2]European Synchrotron Radiation Facility, BP 220, F-38043 Grenoble, France
[3]Geodynamics Research Center, Ehime University, 2-5 Bunkyo-cho, Matsuyama 790-8577, Japan
pdziegielewski@if.pw.edu.pl

EXAFS (Extended X-ray Absorption Fine Structure) method based on analysis oscillations X-ray absorption coefficient as a functions of energy, which contain information about interatomic distances, coordinations numbers and structural disorder. The method is useful to study local atomic structure in crystals and in materials so-called *metallic glasses*. Metallic glasses are obtained by rapidly quenched metallic alloys retaining their amorphous structure on solidification. As a interesting metallic glass selected Ce-Al alloy of the composition $Ce_{55}Al_{45}$.

Amorphous alloys Ce-Al in high pressure conditions are characterized by polyamorphism (an analogue of crystalline polymorphism), which is consequence of changes in electronic structure (f-electrons delocalization) of the cerium atoms caused by high pressure[1][2]. The EXAFS studies Ce-Al alloys indicates, that as the pressure increases Ce-Ce distances split into two sub-shells atoms with different radii (Fig. 1). It was found that partial cerium sub-shell coordinations numbers change with the pressure and the change is not fully reversible. Furthermore, it is shown, that Ce-Ce pairs are more pressure resistant than Ce-Al pairs (bulk modulus for Ce-Ce: $K \approx 90$GPa and for Ce-Al:$K \approx 50$GPa). An absorption spectra of Ce K-edge were collected in-situ during hydrostatic compression/decompression in the pressure range 0-30 GPa.

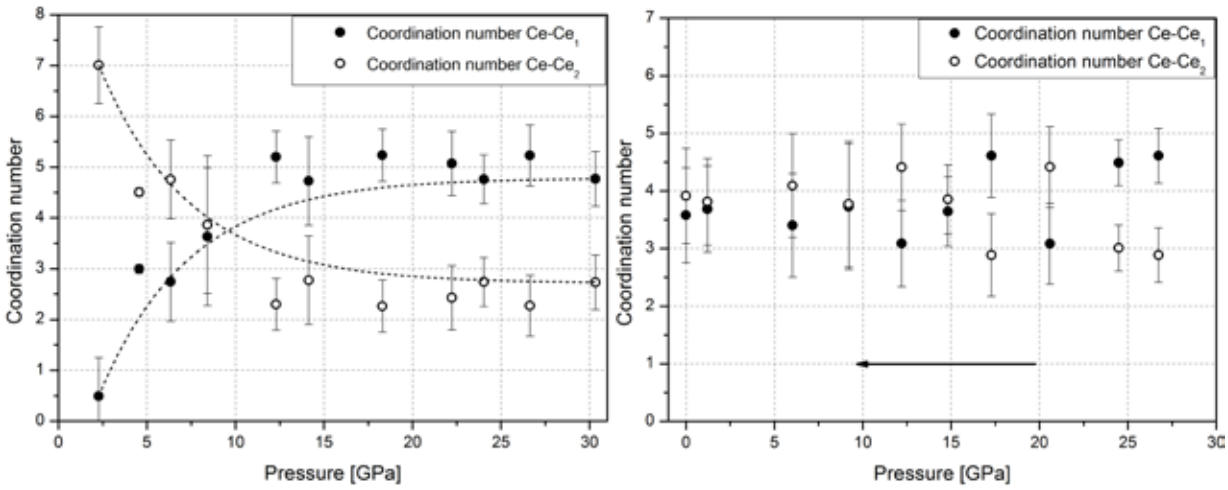

Fig. 1. Coordination numbers for Ce-Ce sub-shells during compression and decompression of $Ce_{55}Al_{45}$.

[1] H.W. Sheng, H.Z. Liu, Y.Q. Cheng, J. Wen, P.L. Lee, W.K. Luo, S.D. Shastri, E. Ma, Nature Mater. **6**, 192 (2007).
[2] L. Belhadi, F. Decremps, S. Pascarelli, L. Cormier, Y. Le Godec, S. Gorsse, F. Baudelet, C. Marini, and G. Garbarino, Appl. Phys. Lett. 103 (2013) 111905

GROWTH KINETICS OF NON-POLAR GaN GROWN ON SI SUBSTRATE WITH AN ERBIUM OXIDE INTERLAYER

Agnė Kalpakovaitė[1], Tomas Grinys[1], Rytis Dargis[2], Andrew Clarck[2], Kazimieras Badokas[1], Tadas Malinauskas[1]

[1] Institute of Applied Research, Vilnius University, Saulėtekio Av. 10, 10223 Vilnius, Lithuania
[2]Translucent Inc., 952 Commercial St, Palo Alto CA 94303, USA
agne.kalpakovaite@ff.stud.vu.lt

A strong internal electric field in a polar GaN leads to band bending. The consequences of this effect include decreased efficiency and spectral instability of InGaN LEDs. Lately, there has been found an increasing interest in non-polar and semi-polar GaN in order to resolve these fundamental problems and improve the performance of the devices. Due to the absence of the large scale and cheap GaN substrates the homo-epitaxy is still limited up to date. The foreign substrates such as Si may be an option for a cost-effective GaN growth in non-polar and semi-polar directions.

We investigated the non-polar crystalline GaN structures prepared by metal-organic chemical vapour deposition (MOCVD) technique on Si (100) substrates with rare-earth erbium oxide interlayer. The X-ray diffraction studies showed that non-polar GaN (11-20) tends to grow on Si (100) with Er_2O_3 interlayer because of very low 1,7% lattice mismatch between oxide and nitride in this direction. The semi-polar GaN (10-13) tends to form, if the growth is performed by introducing an additional AlN buffer layer. The scanning electron microscope analysis revealed that semi-polar GaN structures exhibit the hexagonal pyramid-shaped islands (Fig. 1a). Surface of the pyramids terminates with crystallographic planes (0001), (10-12), (10-11), (10-10), (10-1-1). The polar GaN <0001> direction is inclined by 33° to the Si<100> direction. For given MOCVD growth parameters (T=1030°C, V/III=1423) growth rate is greater in semi-polar [10$\bar{1}$2] direction due to lowest required activation energy. Such semi-polar GaN samples exhibit an optical rotation effect due to birefringence and optical dicroism of the crystal. These semi-polar structures showed a strong photoluminescence (PL). The near band edge PL peak position of semi-polar GaN shows a good agreement with a polar GaN, whereas the non-polar maximum is shifted to a longer wavelength (see Fig 1 b). The presented findings are important for the further regrowth process to obtain high quality non/semi-polar GaN layers by MOCVD.

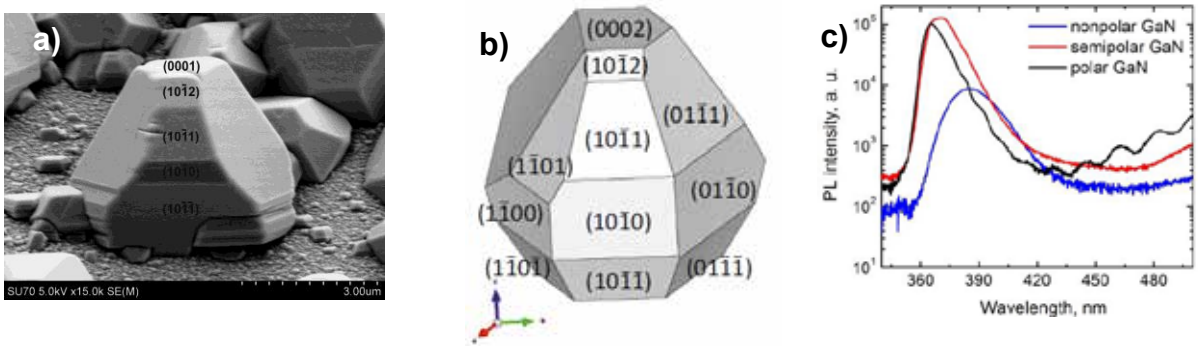

Fig. 1. Semi-polar GaN island with identified crystal planes (a), 3D model of an island (b) and photoluminescence spectra of different polarity GaN samples (c).

GROWTH OF NON-POLAR GaN ON Si WITH RARE-EARTH OXIDE INTERLAYERS

Kazimieras Badokas[1], Tadas Malinauskas[1], Tomas Grinys[1]

[1] Institute of Applied Research, Vilnius University, Saulėtekio av. 10, LT-10223 Vilnius, Lithuania
badokas.k@gmail.com

Group-III nitrides are widely used for optoelectronic devices such as light emitting diodes and laser diodes. However, most epitaxial nitride layers are grown on foreign substrates such as sapphire and silicon carbide because native ones are currently expensive. One problem associated with III-nitrides is spontaneous polarisation that appears when growing along *c*-direction, due to the lack of inversion symmetry in hexagonal crystal structure. This leads to energy band bending and efficiency decrease as well as spectral instability of LEDs. Silicon (100) substrates are suitable for gallium nitride (GaN) growth in non-polar and semi-polar directions. Rear-earth oxide interlayers could be used to solve problems related to high lattice mismatch, thermal expansion coefficient differences as well as to prevent gallium reactions with silicon.

We have used slightly miscut Si (100) substrates coated with 300 nm erbium oxide (Er_2O_3) interlayers for GaN heteroepitaxy. The aim of this work was to find optimal growth conditions for GaN formation in non-polar directions. Growth of III-nitrides was performed in close-coupled showerhead metalorganic chemical vapour deposition reactor (MOCVD). Growth conditions such as temperature, V/III ratio and carrier gases were varied. Aluminium nitride (AlN) interlayers as well as various GaN layers were used for stress management. Grown epitaxial structures were investigated using X-ray diffraction (XRD), scanning electron microscopy (SEM) and photoluminescence (PL) techniques. Investigation of grown structures showed that nitrogen atmosphere during GaN growth prevents it from forming towards polar [001] direction as well as helps to obtain smoother epitaxial layers (Fig. 1). In hydrogen atmosphere polycrystalline island-like GaN growth was observed (Fig. 2).

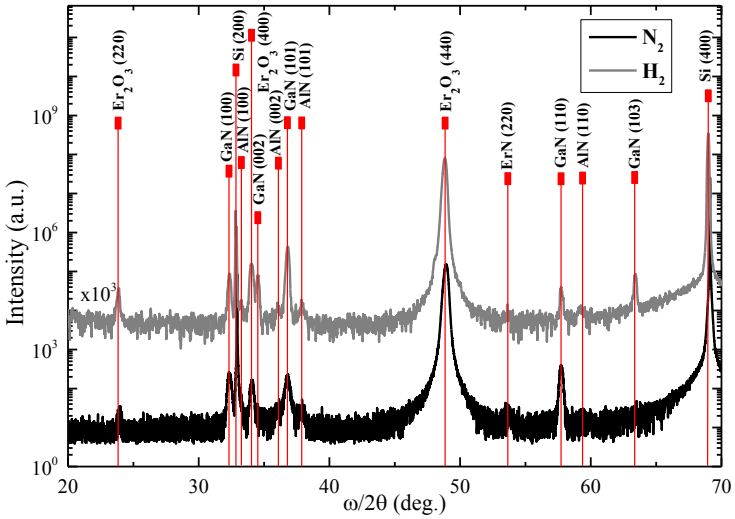

Fig. 1. XRD ω/2θ scans.

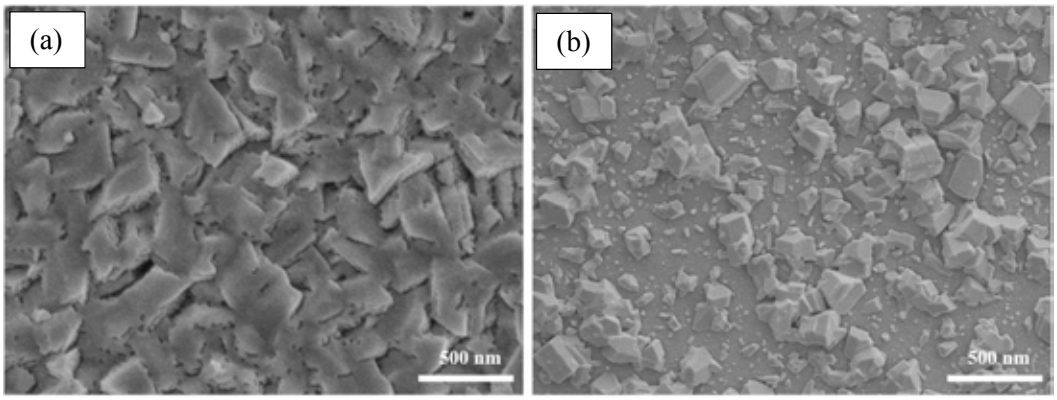

Fig. 2. SEM images of GaN layers grown in nitrogen (a) and hydrogen (b) atmospheres.

SPATIAL DISTRIBUTION OF PHOTOLUMINESCENCE IN GAN NANORODS WITH INGAN/GAN MULTIPLE QUANTUM WELLS

Henrikas Svidras, Darius Dobrovolskas

Institute of Applied Research and Semiconductor Physics Department, Vilnius University, Saulėtekio av. 9, building III, 10222 Vilnius, Lithuania
henrikas.svidras@ff.stud.vu.lt

Currently InGaN/GaN based light-emitting diodes (LEDs) continuously strengthen their footprint in the market of general lighting. However, their performance is far from the ultimate efficiency. Nanorod-based LEDs are believed to be one of the most promising concepts for efficiency enhancement. Specifically, GaN nanorods are found to dramatically reduce the dislocation density in the upper part of nanorods. Moreover, nanorods with a small area of contact with the substrate tend to relieve the strain induced by thermal expansion mismatch. However, it is necessary to fully understand the properties of nanorods, before they can be widely applied.

In this work, the photoluminescence (PL) properties of GaN nanorods with InGaN/GaN core-shell multiple quantum wells (MQWs), grown by metal-organic vapour phase deposition with different trimethylindium (TMIn) gas flow rates (80, 160, 320 sccm), were studied using a confocal microscope. Three different samples of nanorods were excited with a 405 nm laser focused through a NA=0.9 100× objective. The PL signal was directed to a spectroscope coupled with CCD camera through an optical fiber. Spatial distributions of PL parameters were measured at three areas on each nanorod: the top, middle and base. Additionally, polarization-dependent PL measurements were performed. Average degrees of polarization (DOP) and DOP spatial distributions were obtained for each area.

Results show that all PL spectra consist of two bands, one of which is associated with the QWs emission, while the other is a defect-related GaN yellow-band. As TMIn flux rate is increased, the PL peak position redshifts from 450 to 530 nm. The spatial PL intensity distribution measurements show that intensity is distributed non-uniformly; a larger density of bright dots at the top than at the bottom part of nanorod was observed. It implies that quantum wells are deposited inhomogeneously on the GaN rod. The increase of excitation intensity by an order of magnitude did not change the PL peak positions (Fig. 1). These results suggest that QWs are grown on non-polar planes.

In order to ensure that the planes are non-polar, polarization measurements were carried out. The emission band that is associated with QWs, proved to be significantly more intense when the polarizer is oriented perpendicularly to the c-direction rather than parallely. This proves that QWs are grown on non-polar planes. Additionally, it was found that DOP decreases from the top (up to 0.5) to the base (~0.1) of nanorod. By comparing spatial PL intensity and spatial DOP distributions it was found that areas of higher intensity correspond to areas of higher DOP. The GaN yellow-band's position and peak intensity did not change when the orientation of polarizer was changed.

Moreover, periodical oscillations of PL spectra were observed. Calculations of cavity thickness proved these local peaks to correspond to Fabry-Perot interference maxima. It shows that Fabry-Perot modes occur between opposite facets of the nanorod.

To conclude, high spatial resolution measurements of GaN nanorods showed that PL intensity distribution is inhomogeneous. This suggested that QWs are deposited non-uniformly on the GaN rod. Results of PL measurements at different excitation power densities and different polarization angles suggest that QWs are grown on non-polar planes. The degree of polarization was higher at top and decreased at the base of the nanorod due to peculiarities of QW growth.

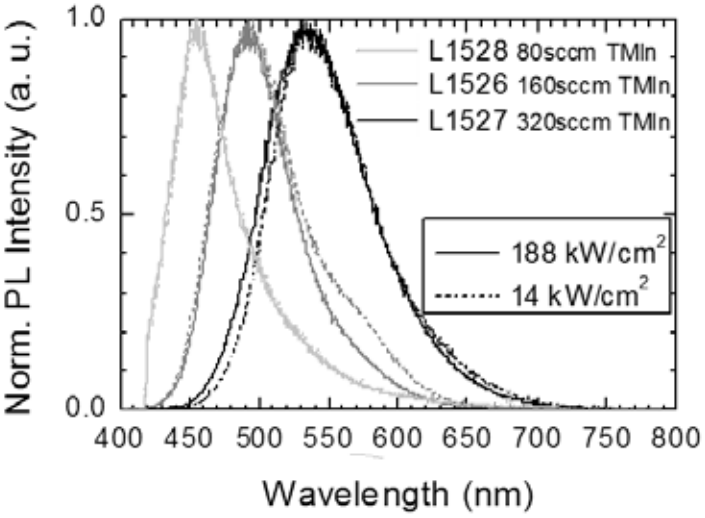

Fig. 1. Normalized PL spectra of nanorods at different PL excitation intensities.

BGaN GROWTH ON 6H-SiC AND AlN BY MOVPE AND CHARACTERIZATION

Marek Kolenda, Tadas Malinauskas, Jūras Mickevičius, Jonas Jurkevičius, Darius Dobrovolskas, Arūnas Kadys

Institute of Applied Research and Semiconductor Physics Department, Vilnius University, Saulėtekio al. 9-III, Vilnius 10222, Lithuania
mkolendaus@gmail.com

Characteristics of BGaN alloys are expected to be similar to those of InGaN and AlGaN materials with the additional advantage of a better lattice-matching to AlN and SiC substrates [1]. The boron-based nitride compounds could be used as active regions for UV optoelectronic devices, as barriers in high electron mobility transistors [2] and for the direct detection of thermal neutrons due to a large neutron capture cross section of boron atoms [3].

The main goal of this work was to obtain high crystalline quality BGaN epilayers with different B concentration.

The growth of BGaN layers on AlN/sapphire templates was carried out in H_2 ambient and the reactor pressure of 100 mBar (75 Torr). The TMGa flow was maintained at 1.8×10^{-4} mol min^{-1} during the growth of all the samples, the NH_3 flow was varied in the range from 0.134 to 0.223 mol min^{-1}, while the TEB flow was varied from 3.12×10^{-6} to 2.5×10^{-5} mol min^{-1}. Thus, the TEB/(TEB+TMGa) ratio was varied from 1.7% to 12.2%. The growth temperature was varied in the range from 770 to 870 °C. The BGaN layer growth time was 900 s, which resulted in the layer thicknesses of 240–480 nm, as estimated by *in situ* reflectometry.

The growth of BGaN layers on 6H-SiC substrates was carried out in H_2 ambient and the reactor pressure of 100 mBar (75 Torr). BGaN layers were grown on Si-face of the substrates. The TMGa and NH_3 flows were fixed at 1.8×10^{-4} mol min^{-1} and 0.178 mol min^{-1}, respectively. The TEB flow was varied from 3.12×10^{-6} to 2.5×10^{-5} mol min^{-1}, resulting in the TEB/(TEB+TMGa) ratio in the range from 1.7% to 12.2%. The growth temperature was varied in the range from 700 to 900 °C. The growth time was varied from 900 s to 2425 s, and the resulting layer thicknesses were in the range from 360 to 1200 nm, as estimated by *in situ* reflectometry.

The crystal quality of BGaN layers and B concentration on the different substrates has been evaluated using high resolution X-ray diffraction measurements (HRXRD) (Fig. 1 a, b).

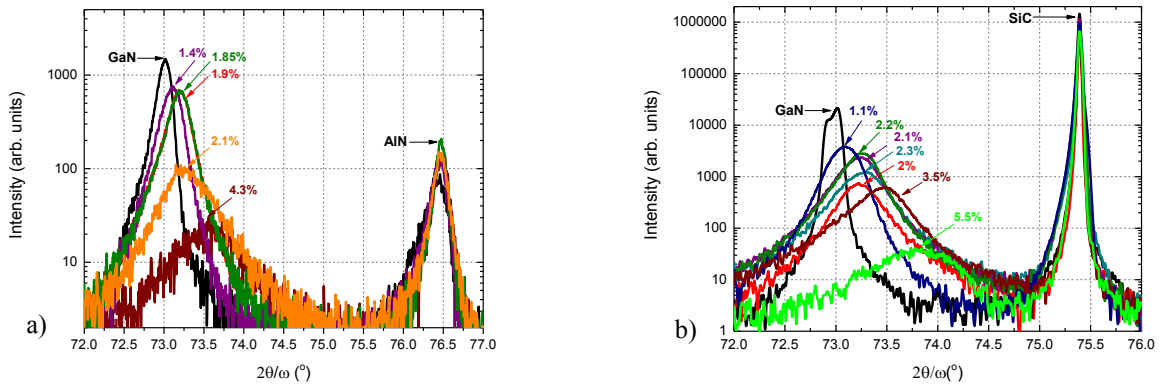

Figure 1. XRD scans along (0 0 4) direction for BGaN layers grown on AlN/sapphire (a) and SiC (b) substrates

As expected, the increase of TEB/III ratio results in a BGaN peak shift to higher angles, indicating an increase in boron content in the layers up to 4.3% on the AlN/sapphire substrate and up to 5.5% on the SiC substrate. The shift of the BGaN peak is accompanied by decreasing intensity and increasing width indicating the deteriorating structural quality of the BGaN layers.

The surface roughness of BGaN layers grown on AlN/sapphire templates was in the range from 40 nm to 8 nm, decreasing with the increase in boron content of up to 2.7%. On the other hand, two of the samples had a very rough surface (100 ÷ 165 nm) with large crystallites with polygonal shape on the surface.

The surfaces of BGaN layers grown on SiC substrates were rougher than the surfaces of the samples deposited on sapphire with AlN templates. Only a couple of samples had a rather smooth surface with the roughness in the range of 8–25 nm. large crystallites are evident on the surfaces of most of the samples grown on SiC, and the surface roughness varies in the range from 50 nm to 280 nm.

The optical properties of BGaN layers have been investigated by room temperature photoluminescence. With the introduction of increasing amount of boron into GaN, the PL band shifts to lower energies. A bowing parameter *b* of ~4eV was obtained from the band gap variations as a function of B composition.

[1] Ougazzaden A, Gautier S, Sartel C, Maloufi N, Martin J and Jomard F 2007 J. Cryst. Growth **298** 316
[2] Ravindran V, et al. 2012 Appl. Phys. Lett. **100** 243503
[3] Atsumi K, Inoue Y, Mimura H, Aoki T and Nakano T 2014 APL Mater. **2** 032106

LOW-FREQUENCY NOISE SPECTROSCOPY AND THRESHOLD CHARACTERISTICS OF LASER DIODES

Justinas Glemža, Jonas Matukas, Sandra Pralgauskaitė

Department of Radiophysics, Faculty of Physics, Vilnius University, Lithuania
justinas.glemza@ff.stud.vu.lt

Nowadays semiconductor laser diodes (LDs) are widely used in the high-speed optical communication and data transmission systems. Researches on reliability of laser diodes can help to avoid system breakdowns due to LD failure. Compared to the other methods, low-frequency noise spectroscopy is non-destructive and very sensitive diagnostic tool for optoelectronic device quality evaluation and identification of nature of the degradation sources [1, 2]. Understanding of physical processes that occur in the vicinity of the lasing threshold requires a special attention, too [3].

The investigated devices are multiple-quantum-well distributed feedback (DFB) InGaAsP 250 μm channel length laser diodes radiating at 1.55 μm. They were fabricated for operation as light source in optical communication systems.

Spectra of optical and electrical fluctuations are $1/f^{\alpha}$-type. The cross-correlation coefficient between optical and electrical fluctuations is very sensitive to the LDs quality: for some samples at the lasing threshold there is negative correlation range while for others – only positive. Leakage current channels at the active region interface leads to the negatively correlated fluctuations in LD and it is shown that such LDs are unreliable and tend to degrade. A positive cross-correlation coefficient at currents above the threshold is considered as typical for the good quality DFB LDs [1].

The power spectral density of either electrical or optical fluctuations of LD at low frequencies can be presented as a sum of independent components of $1/f$, $1/f^{\alpha}$, Lorentzian type (with characteristic time τ) and shot noise. Such presentation means that noise sources are statistically independent. An example is presented in Fig. 1. Actually, not all electrical low frequency fluctuations completely correlate with the optical ones (e. g., contact noise or noises in the passive layers of LD do not correlate) [2]. Total and correlated parts of the variance of current fluctuation are approximately proportional to the forward current in LED mode. Radiative recombination occurs in the active layer, so correlated fluctuations are related with the active layer, too. In the LD mode dependence of variance on forward current is very weak.

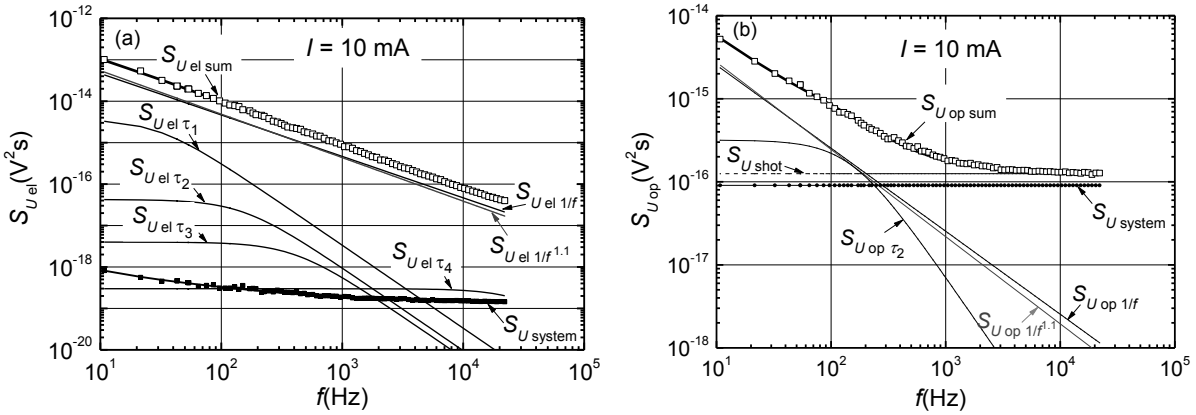

Fig. 1. Decomposition of electrical (a) and optical (b) noise spectrum into independent noise components (symbols represent experimental data; $S_{U\,\mathrm{system}}$ is own noise of the measuring system).

Many other characteristics have sudden changes in the threshold region, e. g., the $I\mathrm{d}U/\mathrm{d}I$ curve that is derivative current-voltage characteristic drops abruptly at the onset of lasing. Curves of conductance and junction capacitance dependencies on forward current jump simultaneously at the lasing threshold: conductance increases and capacitance decreases. There was observed negative capacitance effect which is stated related with the increase of the rate of charge carrier recombination, when spontaneous emission turns into the stimulated emission [3].

In conclusion, it is shown that negative cross-correlation factor between electrical and optical fluctuations at the threshold indicates presence of defects at the active region interface that forms leakage current channels and accelerates LD degradation. Decomposition of noise spectral density into independent noise component enables evaluation of correlated (that are located in the active region) and uncorrelated (that are in the passive layers of LD) optical and electrical noise sources. Also it is shown that electrical characteristics (derivative of current-voltage characteristic, conductance and capacitance) can be used for the threshold current identification.

[1] S. Pralgauskaitė, J. Matukas, V. Palenskis, G. Letal, R. Mallard, and S. Smetona, Low-frequency Noise and Quality Prediction of MQW Buried-heterostructure DFB Lasers, Proc. SPIE Advanced Optical Devices, Technologies, and Medical Applications, **5123**, 85-93 (2003).

[2] V. Palenskis, J. Matukas, and B. Šaulys, A Detailed Analysis of Electrical and Optical Fluctuations of Light-emitting Diodes by Correlation Method, Lithuanian J Phys, **49**, 1–9, (2009).

[3] L. F. Feng, C. D. Wang, H. X. Cong, et al., Sudden Change of Electrical Characteristics at Lasing Threshold of a Semiconductor Laser, IEEE J Quantum Electron., **43**, 458–461 (2007).

INVESTIGATION OF MORPHOLOGY AND PERFOMANCE IN TQ1:[60]PCBM:[70]PCBM STANDARD GEOMETRY SOLAR CELLS

Austėja Galvelytė[1], Zheng Tang[2], Olle Inganäs[2]

[1]Department of Solid State Electronics, Vilnius University, Lithuania
[2]Department of Physics, Chemistry and Biology, Linköping University, Sweden
austeja.galvelyte@gmail.com

The nanoscale morphology of bulk heterojunction solar devices has a great impact on the performance [1]. Weight ratio between donor:acceptor (D:A) and between acceptors ([60]PCBM and [70]PCBM), mixing non-halogenated solvents and thermal annealing were tested in *Poly[[2,3-bis(3-octyloxyphenyl)-5,8-quinoxalinediyl]-2,5-thiophenediyl]* (TQ1), [60]PCBM and [70]PCBM solar devices, with ITO/PEDOT:PSS/active layer/LiF/Al structure. Active layer was spin-coated from solution (20 mg/ml, solvent—o-xylene (except solvent testing part)). Photovoltaic characteristics were obtained by illumination with white light from solar spectrum simulator (AM1.5G). Morphology evaluation was done from Atomic Force Microscope (AFM) images and from Photoluminescence (PL) signal (425 nm exciting wavelength).

Devices with D:A ratio 1:2 (and 4:1 ratio of [60]:[70] PCBMs) had larger average short circuit current density (J_{SC}=5.12 mA/cm^2), the average fill factor (FF=0.54) and the average power conversion efficiency (PCE=2.51 %) than 1:1 devices (4.30 mA/cm^2, 0.52 and 2.07 %). PL and AFM data implied 1:1 (Fig. 1a) samples having fewer pure material domains, but too homogenous morphology might have led to poorer percolation of materials and less efficient charge transport than in 1:2 (Fig. 1b) blend.

1:0, 4:1, 1:1, 1:4 and 0:1 weight combinations of [60]PCBM:[70]PCBM were tested, keeping 1:2 (D:A). Nanoclusters grew bigger with the increase of the [70]PCBM amount (Fig 1c, d) leading to phase separation abd thus decrease of D:A interface area followed by loss of J_{SC}, FF and PCE (2.80 mA/cm^2, 0.48 and 1.18 % in devices without [60]PCBM). The possible reason is worse sollubility of [70]PCBM than of [60]PCBM in o-xylene. Despite 1:0 blend having largest J_{SC}, FF and PCE, the ratio 4:1 was chosen for further improvement because of its thermal stability [2], which is important for printing process.

The small amount of additives with different vapour pressure than the main solvent may improve sollubility of fulerenes [3], so TQ1:[60]PCBM:[70]PCBM with the weigth ratio 5:8:2 were dissolved in o-xylene:toluene with the following proportions: 1:0, 10:1, 1:1, 1:10 and 0:1. Toluene favoured demixing of the materials into separate phases (Fig. 1e, f), J_{SC}, FF and PCE were reduced with increasing toluene concentration in the blend.

In the last part devices were heated at 80 °C, 100 °C, 120 °C, 140 °C and 160 °C temperatures for 10 minutes before deposition of the electrodes. Heating promotes reorganization of materials into separate phases. The open-circuit voltage decreased with heating and stabilized at 120 °C (0.9 V at room temperature and 0.8 V at 120-160 °C). Annealing reduced J_{SC} as well, leaving not annealed samples with the best perfomance. The morphology probably was already optimal under the chosen preparation conditions; annealing possibly would have improved performance of 1:1 (D:A) blend [2], which had less demixed phase and thus more complicated paths for charge transport than 1:2 blend.

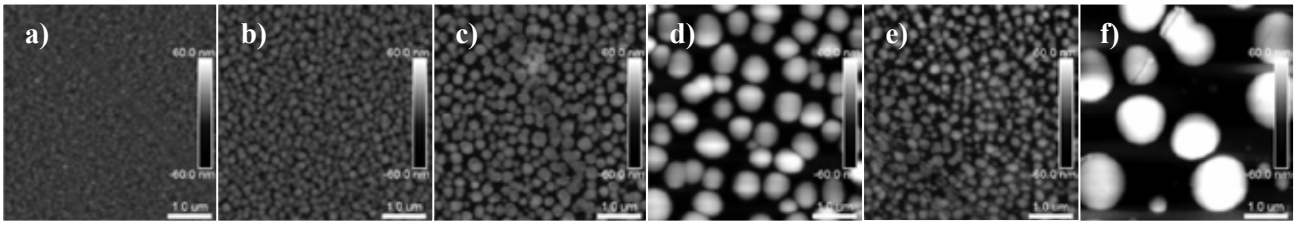

Figure 1 AFM images (5 μm × 5 μm) of TQ1:[60]PCBM:[70]PCBM devices, a)5:4:1, b) 5:8:2, c) 5:5:5, d) 5:0:10, e) 5:8:2 dissolved in o-xylene:toluene 1:1, f) 5:8:2 dissolved in toluene; the height scale is from -60 nm (black) to 60 nm(white), the size of horizontal bar in the bottom-right corner is 1 μm.

[1] HOPPE, Harald; SARICIFTCI, Niyazi Serdar, Journal of Materials Chemistry, 2006, 16.1: 45-61.
[2] LINDQVIST, Camilla, et al., Applied Physics Letters, 2014, 104.15: 153301.
[3] CHUEH, Chu-Chen, et al, Energy & Environmental Science, 2013, 6.11: 3241-3248.

TRANSPORT PROPERTIES OF BISMUTH POLYCRYSTALLINE FILMS

Alexander Fedotov[1], Sergey Perevoznikov[2]

[1] Department of Energy Physics, Physics Faculty of Belarusian State University, Belarus
[2] Research Institute for Physical Chemical Problems, Belarusian State University, Minsk, Belarus
fedotov.alehandro@gmail.com

The goal of this work is to study influence of grain size of polycrystalline Bi films on charge carriers scattering mechanisms, resistivity ρ, relative magnetoresistance MR, Hall coefficient R_H and Seebeck coefficient S. Bi films were fabricated by melt spinning and electrochemical deposition (with further annealing). Microstructure of samples investigated by scanning electron microscopy (SEM), X-ray difrcation analysis and electron diffraction analysis. Temperature and magnetic field dependeces of ρ(T,B) (fig1.a), MR(T,B) (fig1.b), R_H(T,B) and S(T,B) were measured in cryogenless system CHNF (Cryogenics Ltd) on the basis of close-cycle in temperature range $4 < T < 310$ K under magnetic fields up to $B < 8$ T. Experimental setup allowed to measure and stabilize temperature with accuracy up to 1 mK, determine resistivity and Hall coefficient with measuring error less 0,1 % and Seebeck coefficient with error less than 10 % at temperatures lower than 20 K and less than 0,5 % at T > 100 K.

On the base of solution 3D initial-boundary problem for partial differential equation system describing coupled transport of charge and heat [1] method for computation of Seebeck coefficient of film is proposed. The only inputs required for the method are tensor transport coefficients for single-crystal and experimentally obtained crystalline texture mapping of the film. Numerical processing of experimentally measured ρ(T,B), MR(T,B), R_H(T,B) and S(T,B) allowed to calculate temperature dependences of mobilities and concentration for electrons and holes using approach described in [2] (fig. 1c), which helped to explain changing of charge carriers mechanisms with increase of grain size.

Performed study enabled to develop technology for synthesis of polycrystalline Bi films with controllable properties for their usage as thermometer and heater for experimental implementation of thin film thermal conductivity measuring technique known as 3-ω method.

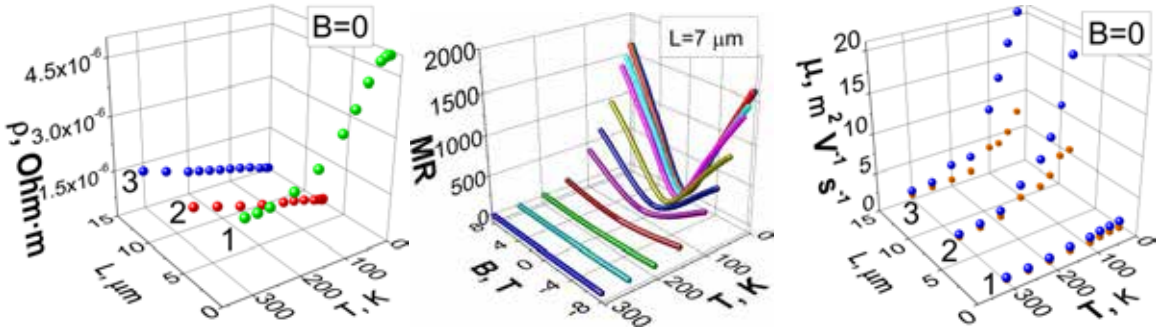

(a) (b) (c)

Fig. 1. Experimental dependences ρ(T,L) (a) and MR(T,B) (b). Calculated mobilities μ(T,L) (c) for electrons (blue spheres) and holes (orange cubes) for bismuth films with grain sizes $L \approx 1$ μm (1), $L \approx 9$ μm (2) and $L \approx 25$ μm (3).

[1] L.D. Landau, E.M. Lifshitz, *Electrodynamics of Continuous Media.* V.8 (1st ed.) (Pergamon Press, 1960).
[2] D. Nakamura, M. Murata, H. Yamamoto et al., Mean free path limitation of thermoelectric properties of bismuth nanowire, Journal of Applied Physics **110**, P. 053702 (2011).

CORRELATION BETWEEN SPATIAL DISTRIBUTION OF PHOTOLUMINESCENCE AND SURFACE MORPHOLOGY IN GaBiAs EPITAXIAL LAYERS AND QUANTUM WELLS

Justinas Aleknavičius, Darius Dobrovolskas, Gintautas Tamulaitis

Institute of Applied Research and Semiconductor Physics Department, Vilnius University, Saulėtekio Ave. 9-III, LT-10222 Vilnius, Lithuania
ju.aleknavicius@gmail.com

Semiconductor compound GaBiAs is a promising material for ultrafast infrared light emitters and detectors for optical fiber systems and terahertz applications. Introducing a small content of bismuth into gallium arsenide significantly reduces the band gap of the compound. However, the growth of high quality GaBiAs is still a challenge. GaBiAs epitaxial layers with Bi content of up to 10% can be grown at low temperatures (~240-380°C).

In this work, the photoluminescence (PL) properties of GaBiAs epitaxial layers and GaBiAs/GaAs quantum wells were investigated with spatial resolution. To investigate the correlation of the surface morphology to the PL images, the same areas were additionally scanned by an atomic force microscope (AFM). The GaBiAs structures used in this study were grown by molecular beam epitaxy (MBE) technique on semi-insulating GaAs substrates at the Center for Physical Sciences and Technology, Vilnius, Lithuania. Six low-temperature grown samples were investigated: three epilayers and three multiple quantum well (MQW) structures with different Bi content. The approximate percentage of Bi in the epitaxial layers was determined according to the position of optical absorption edge while the Bi content in the MQW structures was found from the PL emission peak wavelength.

The PL spatial distribution of the samples was investigated using *WITec Alpha 300S* confocal microscope coupled to *Andor* spectrometer equipped with *iDus* InGaAs CCD. The spatial distributions of PL parameters were investigated by raster scanning randomly selected areas on the sample top surface. A red CW laser diode (emission wavelength at 660 nm) manufactured by *Integrated Optics* was used for excitation. The surface morphology of the samples was studied by an atomic force microscope (AFM) integrated in the *WITec* system. All the measurements were performed at room temperature.

The epitaxial layers exhibited PL bands peaked at 1088 nm, 1164 nm, and 1321 nm in the epilayers containing 5.4%, 6.3% and 7.0% of Bi, respectively. The highest PL intensity was recorded in the sample with the lowest Bi content. The PL spectrum of the epilayer with Bi content of 7.0% consists of two highly overlapping peaks at 1274 and 1321 nm, which is most probably related to microscale phase separation. The PL band undergoes a red shift and a decrease in intensity with increasing Bi content. All of the epilayers have a striped pattern of PL intensity spatial distribution. Such patterns are related to the corresponding structures in surface morphology, as it was observed by AFM. The patterns originate from thick layer relaxation. The epilayer with 6.3% of Bi showed a spotted pattern of PL intensity distribution in the smaller-scale images. This epilayer also exhibited the largest density of dislocation-related pits.

The MQW structures with approximate Bi content of 5.6%, 6.8% and 8.0% exhibited PL bands peaked at 1039 nm, 1112 nm, and 1191, respectively. The dependences of intensity and spectral position of the PL bands on Bi content are similar to those observed in the epilayers. However, the PL intensity degradation with increasing Bi fraction is not as abrupt for the MWQs. Most probably, the strained layers in the MQW structure are more resistant to the formation of point defects than the epitaxial layers are.

All of the MQW structures exhibited a modest density of dislocation related pits in the surface images. PL imaging revealed spots of lower emission intensity, which are associated with the dislocations. The MQW sample with the lowest Bi content exhibits a red shift of PL band at the pits. Therefore it is feasible that the dislocation threads are originating from the Bi-rich clusters inside quantum wells. On the contrary, for the rest of the MQW samples, a blue shift is observed at the dislocation pits. The shift in this case might be related to the decrease of quantum well width at the pits.

The MQW structure with the largest Bi content (8.0%) exhibits a smaller density of dislocation related pits than the sample with the moderate Bi percentage (6.8%), as opposed to the expectations. The reduction of dislocation density might be related to the decreased quantum well width and improved strain. Nevertheless, the PL intensity in this sample is lower, due to the influence of a larger density of point defects. Our results indicate that the increased density of point defects is in correlation with the defective notches on the surfaces of the MQW samples.

MAGNETOTRANSPORT PROPERTIES OF RARE-EARTH-BEARING HALF-HEUSLER PHASES

Daniel Gnida[1], Kamil Ciesielski[1,2], Dariusz Kaczorowski[1]

[1] Institute of Low Temperature and Structure Research, Polish Academy of Sciences, Poland
[2] Gdansk University of Technology, Poland
kamciesi@student.pg.gda.pl

Polycrystalline samples of several ternaries with the chemical formula RTSb (R = Er, Lu, Y, Tb, Gd; T = Ni, Pd, Pt), crystallizing with the cubic MgAgAs-type structure, were investigated by means of magnetic susceptibility, electrical resistivity and magnetoresistivity measurements, carried out from 2 to 300 K. The nonmagnetic compounds LuNiSb, LuPdSb and YPdSb were found to exhibit negative temperature coefficients of the resistivity in the whole temperature range studied. In contrast, the resistivity of antiferromagnetic ErPdSb, GdPtSb and TbPtSb was found to decrease with lowering the temperature down to the onset of the ordered state. In turn, the resistivity of nonmagnetic YPtSb and antiferromagnetic ErNiSb was established to vary with temperature in a more complex non-monotonic manner. All the materials studied were classified as semimetals or narrow band-gap semiconductors, in line with the results of electronic band structure calculations, reported in the literature.

Remarkably, the low-temperature electrical resistivity of LuNiSb, ErNiSb, YPdSb and YPtSb, measured in zero and finite applied magnetic fields, was found to increase proportionally to the square-root of temperature, in a manner characteristic of structurally disordered metals, in which the low-temperature transport is notably influenced by electron-electron interactions. The scenario of quantum interference effects is supported by the observed large magnitude of the electrical resistivity and small values of the residual resistivity ratio, which both imply that the electrical transport in these materials is likely dominated by scattering conduction electrons on crystal structure imperfections.

PHOTOELECTRIC PROPERTIES MEASUREMENT OF THIN FILM HYDROGENATED AMORPHOUS SILICON WITH VANADIUM PENTOXIDE WINDOW LAYER

Augustas Nekrošius, Vaidotas Kažukauskas

Semiconductor Physics Department and Institute of Applied Research, Vilnius University, Saulėtekio al. 9/3, Vilnius LT-10222, Lithuania
nekrosius.augustas@gmail.com

Hydrogenated amorphous silicon (a-Si:H) has a sufficiently low amount of defects to be used within devices such as solar photovoltaic cells, particularly in the protocrystalline growth regime.[1][2] However, hydrogenation is associated with light-induced degradation of the material, termed the Staebler–Wronski effect.[3]

pin-type hydrogenated amorphous silicon (a-Si:H) solar cells are potential renewable solar energy sources due to their low fabrication cost. On the other hand, the device efficiency of a-Si:H solar cells is still relatively low compared to poly-Si solar cells. One method of improving device performances in a-Si:H solar cells is to insert a transition metal oxide, such as vanadium pentoxide (V2O5-x) window layer.

In order to determine the difference in performance and capabilities of such solar cells I-V characteristics and temperature dependencies of electrical dark and photo-conductivity were measured in the temperature range from 80 K to 320 K.

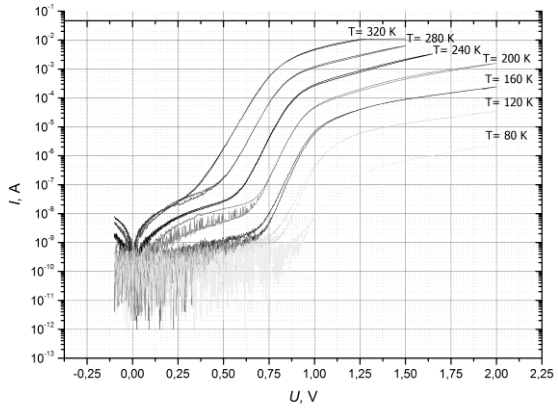

Fig.1. I-V characteristics of electrical dark conductivity.

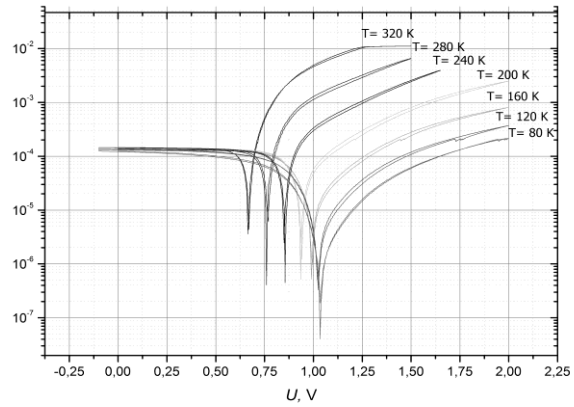

Fig.2. I-V characteristics of photo-conductivity.

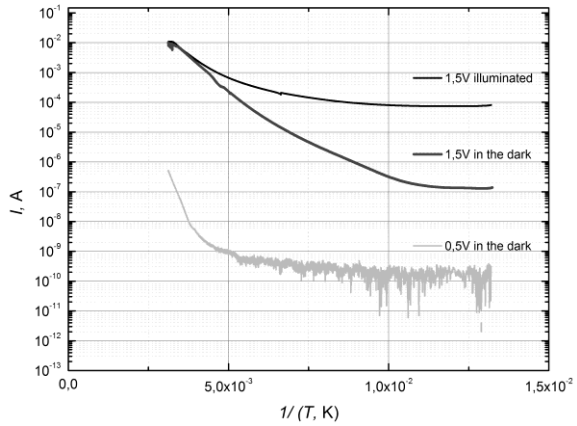

Fig.3 Temperature dependencies of electrical dark and photo-conductivity.

Further measurements must be done to confirm the systematic reiteration of measurements for reliable data that could be applied in theoretical calculations and conclusions.

[1] R.W. Collins, et al., "Evolution of microstructure and phase in amorphous, protocrystalline, and microcrystalline silicon studied by real time spectroscopic ellipsometry", *Solar Energy Materials and Solar Cells*, 78(1-4), pp. 143-180, 2003.
[2] S. Y. Myong, S. W. Kwon, J. H. Kwak, K. S. Lim, J. M. Pearce, and M. Konagai, "Good stability of protocrystalline silicon multilayer solar cells against light irradiation originating from vertically regular distribution of isolated nano-sized silicon grains", *4th World Conference on Photovoltaic Energy Conversion Proceedings*, p. 492, 2006.
[3] C. R. Wronski, et al., "Intrinsic and Light Induced Gap States in a-Si:H Materials and Solar Cells - Effects of Microstructure", *Thin Solid Films*, 451-452 pp. 470-475, 2004

SINGLE- AND MULTI–PHONON ABSORPTION IN $LiGaO_2$

P. Mackonis, S. Tumėnas

Semiconductor Optics Laboratory, Center for Physical Sciences and Technology,
A. Goštauto 11, 01108 Vilnius, Lithuania
paulius.mackonis@ff.stud.vu.lt

In recent years, lithium gallate ($LiGaO_2$) has attracted wide interest in both academia and industry as a lattice-matched substrate for an epitaxial growth of optoelectronic semiconductors such as ZnO, GaN and InN [1]. Large ~70 mm wafers and good quality (less than $4.6 \times 10^4/cm^2$ defects) single crystals can be grown by the Czochralski method. The structure of $LiGaO_2$ crystal is orthorhombic with space group $Pna2_1$ and with lattice parameters a = 5.402 Å, b = 6.372 Å and c = 5.007 Å. The unit cell contains four molecules, and every atom is tetrahedrally coordinated with the arrangement of the wurtzite-like structure. $LiGaO_2$ show high phonon-mediated thermal conductivity, which is more than 1 W/cm·K, and knowledge of optical and vibronic properties and phonon interactions are of importance.

In this work we present results of polarized-transmittance and -reflectance spectroscopy study which was combined with Raman measurements. An employment of all three spectroscopic techniques allow us to determine optical phonons modes and distinguish transverse and longitudinal phonon's frequencies. Experimental measurements were performed on set of samples which were grown by Czochralski method. Samples were cut from grown bulk crystal and oriented along principal crystallographic planes (001), (010) and (100). Normal incidence transmittance and specular reflectance measurements were performed in the 100 – 7500 cm^{-1} spectral range with a resolution of 2 cm^{-1} using Vertex 70v vacuum FT-infrared spectrometer. The polarizer was oriented in the light path to make electromagnetic wave vector parallel to along crystallographic directions **E** || *a*, **E** || *b* and **E** || *c*. To obtain the absolute reflectivity, the reflectance of the evaporated gold film was taken. The FT-infrared Raman scattering measurements were performed in a backscattering configuration on a RAM II module which is attached to Vertex spectrometer. Raman scattering measurements were carried out using 1064 nm excitation wavelength.

The polarized reflectivity spectra along *a*, *b* and *c* axis shown in Fig. 1. The reflectance in all three directions are dominated by the contribution from the phonons. According to group theory analysis, $LiGaO_2$ should have the Brillouin zone center modes at the Γ point with $\Gamma = 11A_1(c) + 11B_1(a) + 11B_2(b) + 12A_2$. The B_1, B_2 and A_1 modes are infrared active, corresponding to the polarization directions **E** || *a*, **E** || *b* and **E** || *c*, and the A_2 mode is only Raman active. Combining reflectivity and Raman data we identified 30 optical phonons modes and determined longitudinal and transverse frequencies. Experimental IR reflectance data were analyzed using complex dielectric function $\varepsilon(\omega)$ which was modeled by sum of Lorentz's oscillators. Frequencies of transverse optical phonons were calculated from imaginary part of dielectric function Im[$\varepsilon(\omega)$] and longitudinal frequencies from energy loss function Im[$-1/\varepsilon(\omega)$]. Experimental transmittance data above 800 cm^{-1} revealed optical features which can be assigned to multi-phonon absorption.

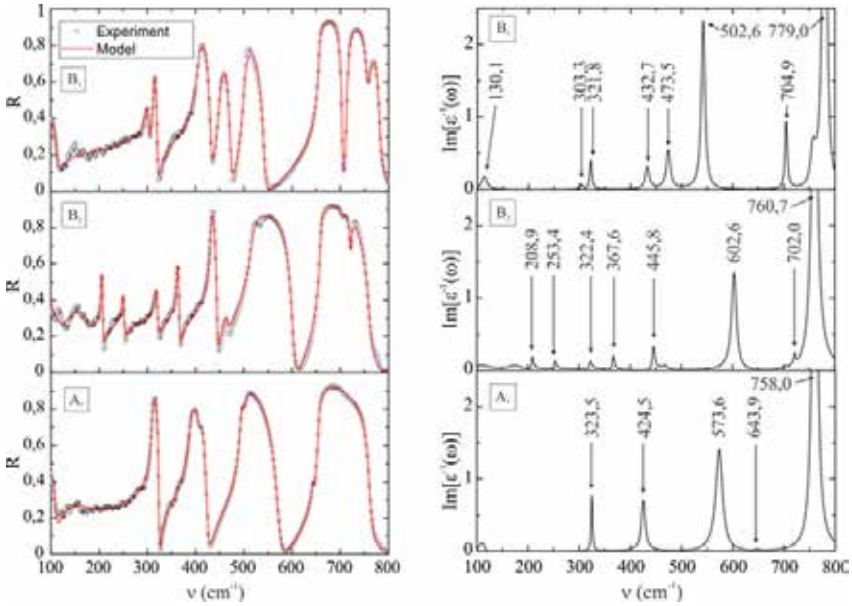

Fig. 1. a) Experimental (dots) and best fit (solid line) reflectance spectrum along *a*, *b* and *c* axis; b) determined energy loss function Im[$-1/\varepsilon(\omega)$] spectrum.

[1] W. A. Doolittle, S. Kang, T. J. Kropewnicki, S. Stock, P. A. Kohl, and A. S. Brown, *MBE growth of high quality GaN on LiGaO2*, J. Electron. Mater. **27**, L58 (1998).

PHOTOLUMINESCENCE DECAY DYNAMICS OF INGAN MQW STRUCTURES REVEALED BY FREQUENCY DOMAIN TECHNIQUE

Rolandas Kudžma[1], Ignas Reklaitis[1], Saulius Miasojedovas[2], Roland Tomašiūnas[1]

[1] Institute of Applied Research, Vilnius University, Lithuania
[2] Faculty of Physics, Vilnius University, Lithuania
rolandas.kudzma@gmail.com

In this work we demonstrate the use of frequency domain lifetime measurement (FDLM) technique to measure the lifetime of light emitting diode (LED) samples. The samples were excited using harmonically modulated light, in the wide frequency range – from 1 Hz to 100 MHz, which enables the measurement of long and stretched decay dynamics giving deep insight into carrier recombination processes.

Using 405 nm resonant excitation enabled the excitation of carriers in quantum well region only, leaving cladding layers unaffected. In order to reveal origin of recombination and delocalization processes, experiments were carried out in a wide temperature (from 10 to 300 K) and excitation power density (from 0,001 to 15 W/cm^2) range,. The samples, used in experiment, luminesce with peaking wavelengths at 450 and 530 nm and are referred as “blue” and “green” samples in the figure 1. The decay times were evaluated using Fast Fourier-transform (FFT) analysis. This study revealed three exponential decay channels, with components in sum-µs, µs and ns timescale range, for the “blue” sample while “green” can be characterized by two decay channels in sum-µs and ns timescale range.

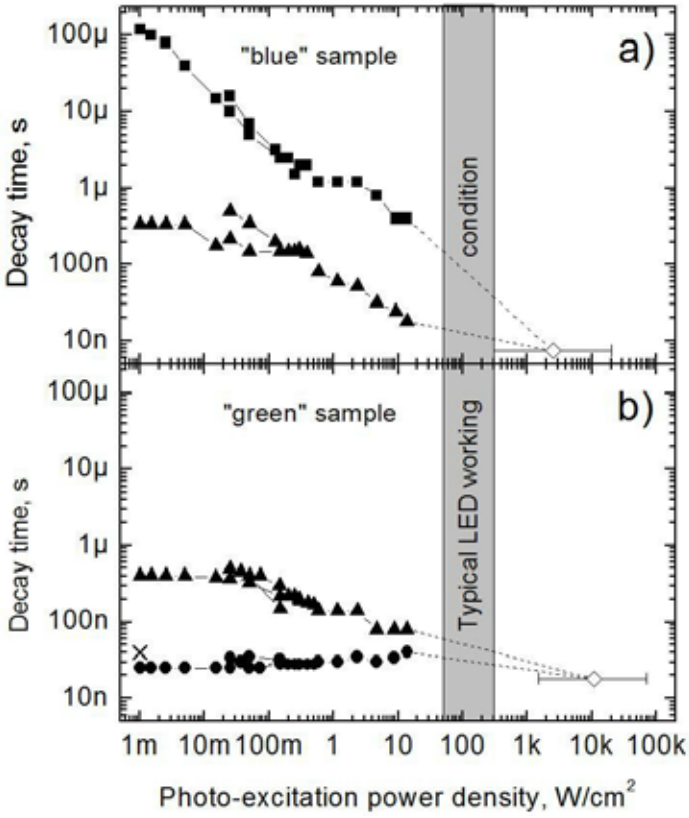

Fig. 1. Samples’ decay time as function of excitation power density, measured at room temperature, using FDLM (filled points) and time domain (open diamonds).

PHOTOELECTRIC PROPERTIES OF $Tl_{1-x}In_{1-x}Sn_xSe_2$ ALLOYS

Vilius Vertelis

Department of Semiconductor phys., Vilnius University, Lithuania
Viliusvertelis@gmail.com

$Tl_{1-x}In_{1-x}Sn_xSe_2$ compounds might be promising materials for the engineering of radiation detectors of different types of radiation, ranging from neutron to gamma rays. This group of alloys has not been extensively studied, so its properties are not fully analyzed yet. The objective of this work was to study photoelectrical properties of these compounds. We have studied two samples: one of $Tl_{0,9}In_{0,9}Sn_{0,1}Se_2$ and one of $Tl_{0,75}In_{0,75}Sn_{0,25}Se_2$. Measurements of current-voltage characteristics (I-V curves), photoconductivity spectra, photocurrent relaxation and thermally stimulated current (TSC) were made. We have concluded that the space charge limited currents with a notable influence of trapping states take place in both samples. The samples of $Tl_{0,9}In_{0,9}Sn_{0,1}Se_2$ were proved to be the single crystalline ones, having the optical bandgap of 1.2 eV; meanwhile $Tl_{0,75}In_{0,75}Sn_{0,25}Se_2$ was most probably the two-phase material with the "fingerprints" of both $TlInSe_2$ and $SnSe_2$. We have determined that the excess carriers recombine via three recombination channels, having different recombination time constants that depend on temperature. From TSC analysis, we determined that shallow traps with the effective thermal activation energies of 0.1-0.2 eV are present in both crystals.

INVESTIGATION OF THERMAL AND PLASMONIC EMISSION FROM GaN/AlGaN GRATING GATED HIGH ELECTRON MOBILITY TRANSISTORS

Vytautas Janonis, Vytautas Jakštas, Irmantas Kašalynas

Semiconductor Physics Institute of Center for Physical Sciences and Technology
vytautas.janonis@ftmc.lt

Gallium nitride (GaN) is one of the most promising semiconductor materials for high frequency and high power electronics applications, where silicon faces fundamental challenges. High electron mobility, high saturation velocity and breakdown voltages, also very high thermal and mechanical stability are the main parameters that encouraged rapid GaN-based devices development during recent years [1]. Normally two dimensional electron gas (2DEG) forms at GaN/AlGaN heterojunction interface without any intentional doping of materials. High carrier mobility and density of 2DEG are suitable for development of the field effect transistors (FETs) used in radiofrequency power electronics [1]. It was predicted that parameters of 2DEG in GaN/AlGaN would allow the fabrication of plasmonic THz emitters for efficient operation at room temperature [2]. THz frequency plasmonic oscillations originate in the HEMT channel and couple out to free space via the grating gate, which in addition is used to modulate the resonant frequency via modulation of carrier density in the channel.

The aim of this work was to investigate THz radiation spectra of the grating gate HEMT with aim to observe plasmonic emission at room and liquid nitrogen temperatures. AlGaN/GaN structures were grown on Al2O3 substrate in the Institute of Applied Research of Vilnius University (VU TMI) MOCVD reactor and Institute of High Pressure Physics (UNIPRESS), Warsaw, Poland. Samples with different grating gate geometries were used. The structures were fabricated in Semiconductor Physics Institute of Center for Physical Sciences and Technology employing recently developed procedures [3].

Constant current stimulated THz emission was investigated in normal room environment using setup based on two parabolic mirrors telescope and pyroelectric THz detector which signals were measured using Lock-In amplifier. Optical chopper was used in DC regime, electrical modulation was used in AC regime. Measurements in AC regime revealed high correlation between optical THz power and electrical power supplied to the emitter. Results obtained in DC regime and normalised by supplied electrical power (12-44 mW) and open surface area (30-60 %) reviled that emission power of all samples is very similar and independent from the grating structure without error of the experiment. Emission power decreased around three times upon sample cooling to cryogenic temperatures, which is also consistent with thermal emission through cryostat window.

In the next step, radiation spectra of the sample in DC and AC regime were recorded using vacuumed Fourier spectrometer. Emission spectra in DC regime was found similar to black body thermal radiation [4] without notable plasmonic THz peaks. Intensity of the AC modulated spectra was in level with the noise of the spectrometer and no plasmonic signatures were observed. Plasmonic emission amplitude needed to be observed in our research must be over one tenth of the thermal emission. Our results are in agreement with newest published literature, which suggests that realisation of AlGaN/GaN HEMT THz emitters requires more sophisticated contact structures [5] and further research of structures growth and preparation – electron drift velocities in current geometry must be enhanced by two orders of magnitude [6].

[1] Trew, R. J., SiC and GaN transistors - is there one winner for microwave power applications?, Proc. IEEE 90, 1032–1047 (2002).
[2] Shur M., AlGaN/GaN plasmonic terahertz electronic devices, Journal of Physics: Conference Series, 486, 012025 (2014).
[3] Jakštas, V. et al., Schottky diodes and high electron mobility transistors made of 2DEG AlGaN/GaN structures on sapphire. Lith. J. Phys. 54, 227–232 (2014).
[4] Laužadis, J. et al., THZ EMISSION FROM LARGE ALGAN/GAN HEMTS WITH GRATING ELECTRODES, Open readings 2015: 58th scientific conference for students of physics and natural sciences, ISSN 2029-4425, Vilnius University, 121 (2015).
[5] Zheng Zhongxin et.al., Broadband terahertz radiation from a biased two-dimensional electron gas in an AlGaN/GaN heterostructure, Journal of Semiconductors, Vol. 36, No. 10, 10.1088/1674-4926/36/10/104002 (2015).
[6] Sung-Min Hong, Numerical Simulation of Plasma Oscillation in 2-D Electron Gas Using a Periodic Steady-State Solver, IEEE TRANSACTIONS ON ELECTRON DEVICES 10.1109/TED.2015.2489220, 2015.

FOURIER-TRANSFORM IR SPECTROSCOPY OF SEMICONDUCTORS: INTRINSIC AND DOPANT-RELATED EFFECTS

Giedrius Tušinskis[1], Henk Vrielinck[2]

[1] Department of Theoretical Physics, Vilnius University, Lithuania
[2] Department of Solid State Sciences, Ghent University, Belgium
giedrius.tusinskis@ff.stud.vu.lt

Due to the ever rapidly growing industry of semiconductor materials there is increase in demand for techniques to analyze the quality and properties of the semiconductors. These properties are such as the chemical composition, dopant concentration, level of impurities, sample thickness, etc. [1, 2]. Fourier Transform Infrared Spectroscopy (FT-IR) is a powerful technique in such analysis. It allows to obtain information about properties of the material in a non-destructive way, although it does have its limitations. One of the problems occurring in the measurements of thin samples is the appearance of interference (fringes). To be more precise, the occurrence of these fringes is determined by the value of $2nd$, here n is the real part of the refractive index of the sample, d is the thickness of the sample [1]. Since the interference is caused by multiple reflections inside the sample it is possible to derive the dependence of the interference pattern by using Fresnel's relations Eq. (1). The equation is obtained with the hypothesis that the coherence length of the incident electromagnetic wave is infinite. This in fact is not true.

$$T = \frac{(tt')^2 e^{-\alpha d}}{1 + r'^4 e^{-2\alpha d} - 2e^{-\alpha d} r'^2 \cos(\frac{2\pi}{\lambda} 2nd)}. \quad (1)$$

Here $t = \frac{2}{1+n}$; $t' = \frac{2n}{1+n}$; $r = \frac{1-n}{1+n}$; $r' = \frac{n-1}{1+n}$, λ is the wavelength of the incident electromagnetic wave and α is the absorption coefficient at a given wavelength. This interference pattern appearing in the spectra makes it difficult to evaluate exact peak positions and heights, thus also the integrated intensity.

There are several ways of dealing with the interference pattern. One of them makes use of Brewster's angle [3], in order to avoid reflections. The second method is to generate a function that mimics the interference pattern Eq. (1), while the last one is based on removing the echo peaks from the interferogram [3]. The result of such manipulation can be seen in Fig. 1.

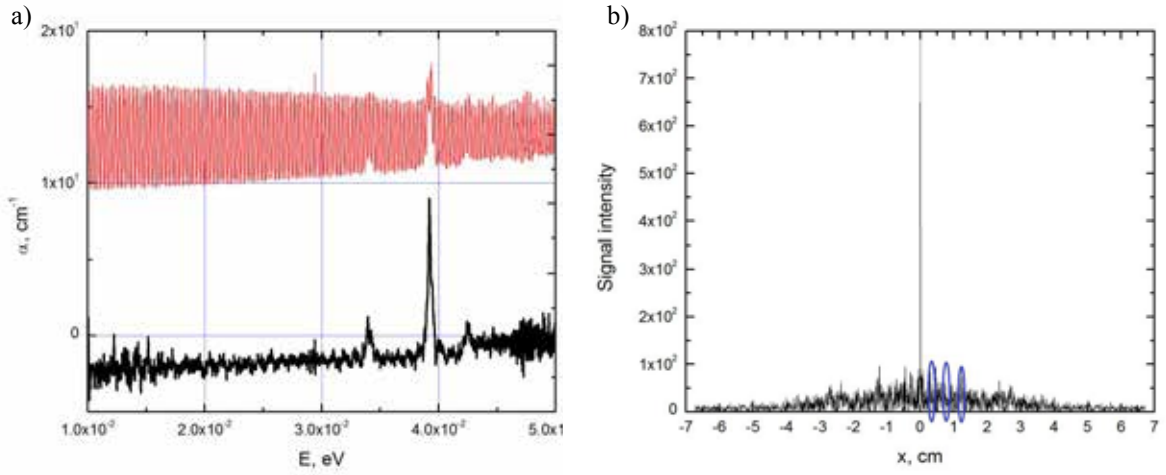

Fig. 1. Phosphorus doped (n-type) silicon sample absorption coefficient dependency unprocessed (left-top curve/right α axis) and processed (left-bottom curve/left α axis) along with its interferogram (b) and indicated echo peak positions (circled), $d = 0{,}62mm$. Spectra recorded at 6K.

As seen in the Fig. 1 by manipulating the interferogram it is possible to obtain good results in the reduction of the interference pattern within samples with low values of $2nd$. More thorough studies need to be performed to obtain information on the reliability and limitations of this method.

[1] Werner Herres and Joern Gronholz, 'Understanding FT-IR Data Processing'.
[2] M. Porrini, M. G. Pretto, R. Scalla, A. V. Batunina, H. C. Alt, R. Wolf, 'Measurement of boron and phosphorus concentration in silicon by low-temperature FTIR spectroscopy', App. Phys. A (2004).
[3] Hiroshi Shirai Yoshihata Yanase: 'Measurements of phosphorus and boron concentrations in Czochralski silicon wafer-thick samples by p-polarized Brewster incidence far-infrared transmission', Appl. Phys. A, 120:927–931 (2015).

CHARACTERISATION OF IMPURITIES IN DIAMOND AND GALLIUM NITRIDE MATERIALS BY ESR SPECTROSCOPY

Laimonas Deveikis, Tomas Ceponis, Eugenijus Gaubas

Institute of Applied Research, Vilnius University, Sauletekio av. 9-III, LT-10222, Vilnius, Lithuania
laimonas.deveikis@ff.stud.vu.lt

Synthetic diamond and GaN are promising wide band-gap materials for fabrication of the solar-blind photo-sensors and radiation tolerant particle detectors applied in high energy physics, radiation monitoring and other fields [1,2]. Wide band-gap determines low leakage current and proper radiation hardness of devices made of these materials. High carrier mobility determines fast charge collection of devices made of diamond. High luminescence efficiency is an attractive characteristic of GaN. Diamond and GaN materials of large thickness (300-600 μm) and high resistivity ($\geq 10^6$ Ωcm) can also be used for manufacturing of the capacitor type particle sensors with high sensitivity [3]. Diamond crystals of such thickness can be synthesised by high pressure and high temperature (HPHT) while GaN – by hydride vapour phase epitaxy (HVPE) and ammono-thermal (AT) techniques. Additionally, acceptor type impurities are often introduced during growth of GaN to reach high resistivity of the material. However, technological defects and impurities introduced during crystal growth process affect functional characteristics of devices made of diamond and GaN materials. The knowledge of parameters of the technological defects is very important in prediction of operational characteristics (leakage current determined by recombination defects, charge collection efficiency affected by trapping centres, etc.) of detectors, and the spectroscopic methods are highly effective tools for the investigation of these defects.

In this work electron spin resonance (ESR) technique has been applied for characterisation of defects and impurities introduced in HPHT diamond, HVPE and AT grown GaN samples during the growth process. Four diamond wafer samples with surface normal being of <001> direction and two GaN wafer samples of HVPE and AT grown technology with surface normal being parallel to hexagonal lattice c axis have been investigated. Measurements were performed in the temperature range of 100-300 K using Bruker Elexsys E580 spectrometer.

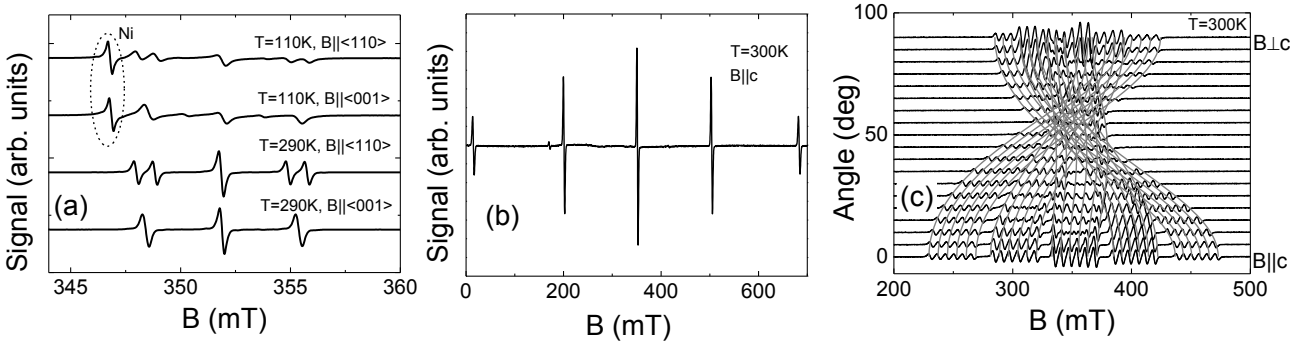

Fig. 1. (a)-Comparison of ESR spectra measured in HPHT diamond at room and at T=110 K temperatures and different crystal orientations relative to magnetic field. (b)-ESR spectrum measured in HVPE GaN at magnetic field orientation B||c. (c)-Angular variations of ESR spectra in AT-GaN. Grey lines illustrate the simulated variations of resonance positions.

Analysis of ESR spectra measured at different temperatures and microwave power levels, as well as using different magnetic field orientations relative to crystal axis (Figure 1) allowed us to determine the spin-Hamiltonian parameters of spin system and to identify the dominant spin-active defects and impurities in materials under investigation. The density of defects has been evaluated using Bruker software. Substitutional nitrogen and substitutional negatively charged nickel (Ni_S^-) paramagnetic centres ascribed to P1 and W8 defects, respectively, have been identified in HPHT diamond samples. Densities of the predominant paramagnetic impurities in HPHT single crystal diamond wafer samples were evaluated to be up to 2×10^{19} cm^{-3} and 2×10^{17} cm^{-3} of nitrogen and of nickel impurities, respectively. In the HVPE grown semi-insulating GaN samples the intentionally introduced Fe^{3+} impurities have been detected and concentration of 2×10^{17} cm^{-3} has been evaluated. Meanwhile, Mn^{2+} impurities have been identified in the AT grown GaN sample. The concentration of Mn^{2+} impurities has been evaluated to be of 10^{19} cm^{-3}. The analysis of the ESR spectra and procedure for identification of spin-active defects and impurities will be discussed.

[1] S. J. Pearton, *GaN and related materials II*, (Gordon and Breach Science Publishers, Amsterdam, 2000).
[2] D. R. Kania, M. I. Landstrass, M. A. Plano, L. S. Pan, and S. Han, Diamond radiation detectors, Diam. Relat. Mater. **2**, 1012-1019 (1993).
[3] E. Gaubas, T. Ceponis, V. Kalesinskas, J. Pavlov, and J. Vysniauskas, Simulations of operation dynamics of different type GaN particle sensors, Sensors **15**, 5429-5473 (2015).

MODERN WINDOWS TRANSMISSION AND REFLECTIVITY RESEARCH IN MICROWAVE FREQUENCIES

Evaldas Bilotas, Paulius Ragulis, Žilvinas Kancleris, Rimantas Simniškis

Microwave Laboratory, Department of Physical Technologies, Center for Physical Sciences and Technology, Lithuania
Evaldas.Bilotas@ff.stud.vu.lt

For the last century, microwave usage has become more and more relevant. Microwaves are not only used in narrow fields like military radars or scientific cosmic background detectors but also they are seen in our everyday lives, for example, mobile phones, wireless network routers and microwave ovens. And, as usual, everything has its darker side. The more electronics develop, the more vulnerable they become to various electromagnetic attacks, such as, electromagnetic pulse (EMP) and microwave radiation [1]. Therefore, now we have another form of terrorism, which doesn't require a person to be near electronic devices or even in the same building in order to interrupt their work or irreversibly damage them. This is accomplished by using portable high power microwave generators and directional antennas [2]. That being the case, there are several projects in Europe which purpose is to find out countermeasures for such electromagnetic attacks [3]. My purpose of this work is investigation of the weakest part of every building – window. I will show and explain the results of four measured glasses which are used in modern window panes.

In my research I measured four aforementioned glasses in semi anechoic chamber, shown in Fig. 1 (a), while following far field conditions [4]. Investigation of transmission was done by calculating shield effectiveness (SE) parameter, which shows objects ability to shield from electromagnetic waves. SE is defined as ratio between power of incident signal and power of propagated signal through the object. SE is measured in dB and you can see its formula below in Eq. (1):

$$SE = 10 * \log\left(\frac{P_{inc}}{P_{glass}}\right) \tag{1}$$

It is required to do logarithmic expression to calculate in dB. These units are easier to use than just the ratio itself because ratio may differ in several orders.

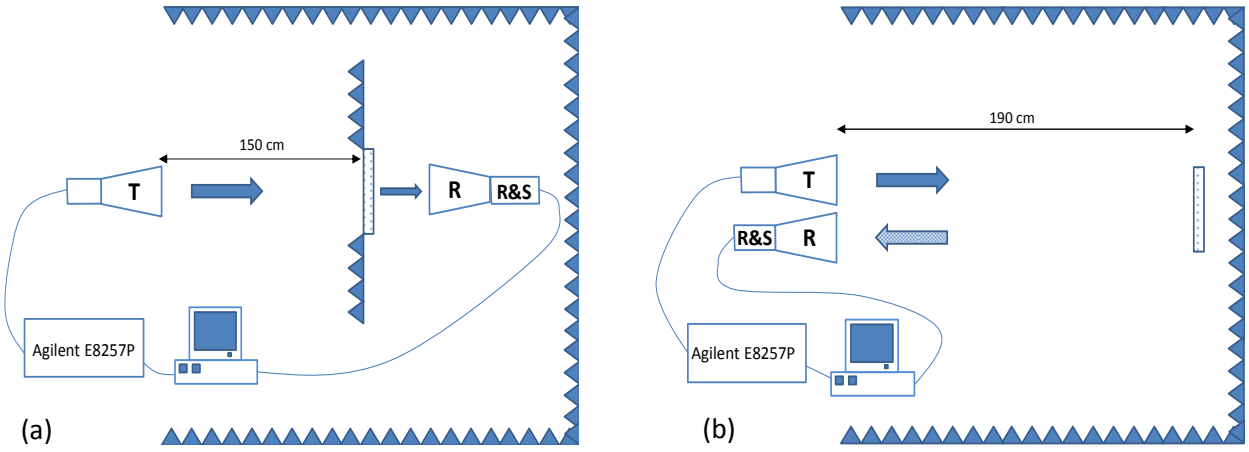

Fig. 1. Layouts of different measurements: (a) transmission, (b) reflectivity.

Second part of my research is measurements of reflectivity. They are done in the same conditions as transmission measurements, only antennas and sample layout differs, as you can see in Fig. 1 (b). Both antennas are parallel to each other and perpendicular to the sample in order to get almost 0 degree angle of incidence. Reflectivity (R) is a ratio between reflected power from the glass and reflected power from the metal plate. In this case reflectivity has values between 0 and 1. And the formula is shown in Eq. (2):

$$R = \frac{P_{from\ glass}}{P_{from\ metal}} \tag{2}$$

[1] M. Camp and H. Garbe, "Susceptibility of personal computer systems to fast transient electromagnetic pulses," Electromagnetic Compatibility, IEEE Transactions on, vol. 48, pp. 829-833, 2006.
[2] E. Hanada, K. Kodama, K. Takano, Y. Watanabe, and Y. Nose, "Possible electromagnetic interference with electronic medical equipment by radio waves coming from outside the hospital," Journal of medical systems, vol. 25, pp. 257-267, 2001.
[3] P. Angskog, M. Backstrom, and B. Vallhagen, "Measurement of radio signal propagation through window panes and energy saving windows," in Electromagnetic Compatibility (EMC), 2015 IEEE International Symposium on, pp. 74-79, 2015.
[4] C. A. Balanis, Antenna theory: analysis and design vol. 1: John Wiley & Sons, 2005.

OLEDS WITH CHINOLINE DERIVATIVES USING TETRAZOLE AND IMINOPHOSPHORANE SUBSTITUENTS: A LUMINESCENCE STUDY

Miglė Stebrytė[1], Bronė Lenkevičiūtė-Vasiliauskienė[1], Sigita Višniakova[2], Albinas Žilinskas[2]

[1] Department of Solid State Electronics, Faculty of Physics, Vilnius University, Lithuania
[2] Department of Organic Chemistry, Faculty of Chemistry, Vilnius University, Lithuania
migle.stebryte@ff.stud.vu.lt

Organic light emitting diodes (OLEDs) with five different chinoline derivatives using tetrazole and iminophosphorane substituents were prepared using thermal vacuum evaporation technology. These materials were synthesized in Vilnius University Faculty of Chemistry and worked as an emission layer in a structure of layers formed on a glass/ITO substrate. Structure consisted of anode (ITO), hole transfer layer (TPD), emission layer (chinoline derivatives with tetrazole and iminophosphorane substituents), hole blocking layer (TmPyPB), electron transporting layer (Alq_3) and cathode (LiF/Al). Energy values of HOMO (Highest Occupied Molecular Orbital) and LUMO (Lowest Unoccupied Molecular Orbital) for newly synthesized organic materials were taken from the article [1]. The other HOMO and LUMO values were taken from literature [2-5].

After formation of OLEDs with the structure mentioned above, examination of photoelectric properties followed. Photoluminescence and electroluminescence spectra were measured using AvaSpec spectrometer. Electroluminescence was noticed in OLEDs starting with 9V threshold voltage. Measurements showed that EL was obtained in 400 nm and 600 nm wavelength range.

Photoluminescence spectra were measured upon excitation at 369 nm using UV light. In all OLEDs PL spectra had few peaks in range of 400 nm to 600 nm.

We have also measured Volt-Ampere Characteristic (j-V) of OLEDs in which double injection regime was noticed.

Due to structural defects in some emissive chinoline derivative layers multicrystaline OLED structures were formed. As a result, EL was not observed in these OLEDs.

In summary, small peculiarities in the chemical structure of the substituent in chinoline derivatives can cause not only spectral PL and EL emission changes but also structural defects in the OLED structure.

[1] S. Višniakova, I. Urbanavičiūtė, L. Daukšaitė, M. Janulevičius, B. Lenkevičiūtė, I. Sychugov, K. Arlauskas, A. Žilinskas. Luminescent benzo- and naphthoquinolines: Synthesis and investigation of photophysical properties. Journal of Luminescence 167 (2015) 261–267.
[2] L.M. Yee, W.M.M. Yunus, Z.A. Talib, A. Kassim, Effect of thickness of Tris (8- hydroxyquinolinato) aluminum on the photoluminescence and I–V characteristic of organic light emitting structure, Am. J. Appl. Sci. 7 (2010) 1215–1218.
[3] S.J. Yoo, H.J. Yun, I. Kang, K. Thangaraju, S.K. Kwon, Y.H. Kim. A new electron transporting material for effective hole-blocking and improved charge balance in highly efficient phosphorescent organic light emitting diodes. J. Mater. Chem. C. 1 (2013) 2217-2223.
[4] Y. Song, S. Lv, X. Liu, X. Li, S. Wang, H. Wei, D. Li, Y. Xiao and Q. Meng. Energy level tuning of TPB-based hole-transporting materials for high efficient perovskite solar cellsChem. Commun., 2014.
[5] M.-F. Lin, L. Wang, W.-K. Wong, K.-W. Cheah, H.-L. Tam, M.-T. Lee, and C. H. Chen. Highly efficient and stable sky blue organic light-emitting devices, Appl. Phys. Lett. 89 (2006) 121913.

PROFILING OF CURRENT TRANSIENTS IN GALLIUM NITIRIDE SENSORS

Kornelijus Pūkas, Tomas Čeponis, Eugenijus Gaubas

Institute of Applied Research, Vilnius University, Lithuania
kornelijus.pukas@ff.stud.vu.lt

Gallium nitride (GaN) is a promising material for application to particle and solar-blind photo-detectors, due to high radiation hardness and relevant operational characteristics [1]. In this study, the structures of the capacitor and Schottky diode type detectors have been fabricated on MOCVD, HVPE and ammono-thermal GaN materials using plasma etching and metal deposition technology. The operational characteristics of detectors have been investigated by pulsed current techniques using experimental regimes of the perpendicular and parallel profiling.

The experimental current transients, shown in Fig.1a, have been correlated with simulated current transients by employing the dynamic models [2] derived using Shockley-Ramo's theorem. Cross-sectional profiling of the carrier injection location within boundary of HVPE GaN capacitor type detectors, illustrated in Fig.1b, enabled us to separate the bipolar and the monopolar charge drift components. Carrier mobility values attributed to the HVPE GaN material have been estimated as μ_e= 1000±200 cm^2/Vs for electrons and μ_h= 400±80 cm^2/Vs for holes, respectively. Current transients under injection of the localized and bulk packets of excess carriers have been examined in order to determine formation of the depleted layers of surface charge and to examine polarization effects.

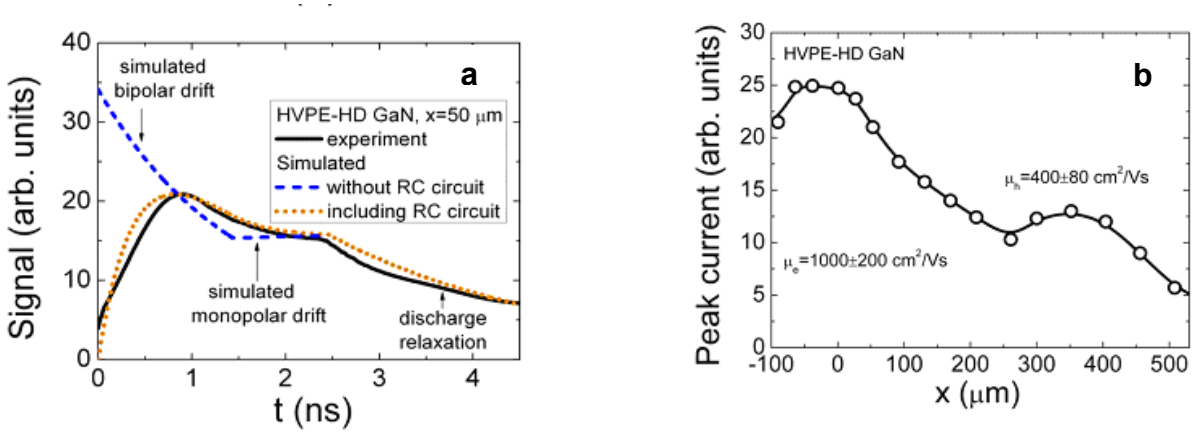

Fig. 1. Profiling of current transients by varying location of the initial injection of e-h domain in HVPE GaN. In figure (a): the solid curve represents the transient as recorded within cross-sectional scan for carrier injection location at x= 50 μm, the dashed curve represents the simulated current transient without including the impact of external circuit, the dotted curve simulated with including delays within external circuit. In figure (b): two current peaks appear within a profile of bipolar drift transient ascribed to induction current formation through electron (the first peak) and hole (the second peak) approaching to an electrode.

The carrier capture, diffusion and drift components as well as polarization effect have been revealed in different GaN sensors. Relaxation of the peak current values due to polarization effect has been examined using a set of the excitation pulses. For the HVPE GaN capacitor type sensors, the relaxation curve shape and its duration depends on doping of material. The polarization effect exhibits the components of the static (slow) and of the dynamic (fast) polarization. The charge collection efficiency at low voltages can be considerably limited due to screening of the external electric field caused by the polarization effects in such structures under injection of the bulk charge within inter-electrode gap. It has been shown that the role of the polarization effect decreases with enhancement of the applied voltage. The drift component can be well discriminated by varying a location of a focused injection beam within the inter-electrode gap when the local e-h domains are injected. The drift distance for drift of each sub-domain and their transit times can then be discriminated and evaluated. Using the parameters of the drift paths and of the transit times, carrier mobility has been extracted.

[1] M. Moll, Radiation tolerant semiconductor sensors for tracking detectors, Nucl. Instr. Meth. Phys. Res. A **565,** 202 (2006).
[2] E. Gaubas, T. Ceponis, D. Meskauskaite and N. Kazuchits, Profiling of current transients in capacitor type diamond sensors, Sensors **15,** 13424. (2015).

FLUENCE DEPENDENT CARRIER RECOMBINATION LIFETIME IN GALLIUM NITRIDE GROWN BY DIFFERENT TECHNLOGIES

Kornelijus Pūkas, Veslava Rymaš, Tomas Čeponis, Eugenijus Gaubas

Institute of Applied Research, Vilnius University, Lithuania
kornelijus.pukas@ff.stud.vu.lt

Carrier lifetime is one of the most sensitive parameters to defects formed in semiconductor materials and devices. Thus, contact-less examination of carrier recombination, trapping and thermal emission rates is a proper tool for evaluation of pristine material quality and for monitoring of the evolution of the radiation defects introduced during irradiation.

In this study, fluence dependent variations of carrier recombination and trapping lifetime have been examined by means of microwave probed photoconductivity (MW-PC) transients. The epitaxial layers of GaN grown by MOCVD technology on sapphire substrates, HVPE grown self-standing GaN samples as well as wafer pieces of bulk GaN fabricated by the ammono-thermal (AT) technology were investigated. These materials contained different density of threading dislocations, varied in the range from 10^4 to 10^{11} cm^{-2}. Also, the undoped pristine GaN material and samples containing intentionally introduced impurities of Fe^{3+} and Mn^{2+} were researched. These sets of samples were irradiated with different fluences, ranging 10^{11} - 5×10^{16} cm^{-2} diapason, of penetrative (by using the samples of relevant thickness) protons of 1.7 MeV protons and reactor neutrons.

The excess carrier transients recorded by MW-PC technique exhibit a two-componential, non-exponential decay for the as-grown MOCVD GaN epitaxial material, as illustrated in Fig. 1a for VU sample. The very initial carrier decay MW-PC component (top-scale curve in Fig 1a) correlates with photoluminescence (PL) decay rate. The asymptotic MW-PC relaxation component, which covers a time scale from tens of ns to tens of ms, can be only fitted by a stretched-exponent approximation: $\exp[-(t/\tau_{se})^{\alpha}]$. An initial fast decay component is determined by the radiative and non-radiative recombination as well as carrier capture processes, and its partial amplitude decreases with irradiation exposure time. The long-tail component is also transformed with irradiation fluence, as can be deduced from Fig. 1a, causing changes of stretched-exponential fractional index α. The long-tail component is ascribed to the excess carrier trapping processes at dislocations that comprise a disordered network within the epi-layer.

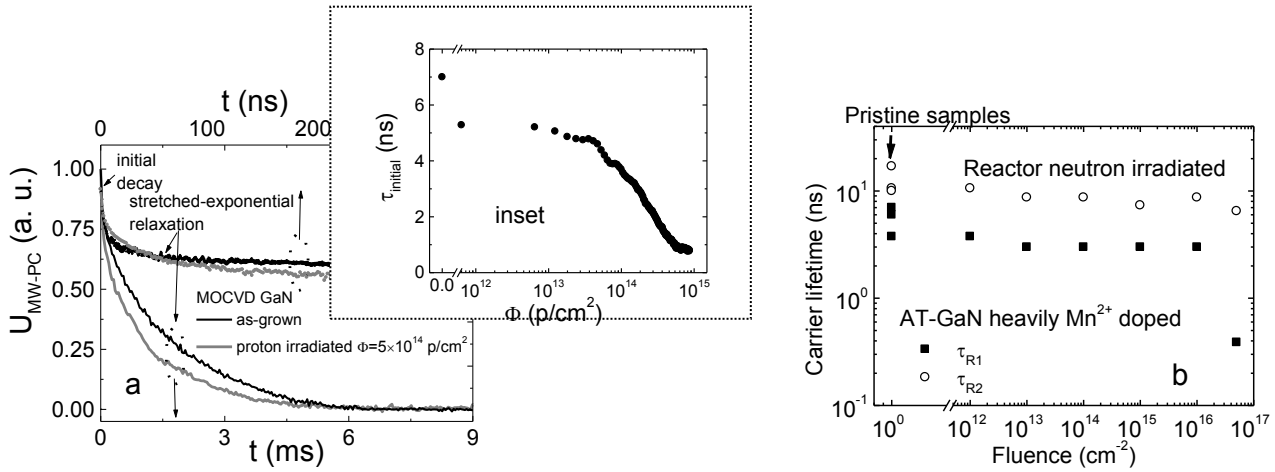

Fig.1. a- MW-PC transients measured in the as-grown (black curves) and proton irradiated (grey curves) MOCVD GaN epi-layers, while fluence dependent variations of carrier lifetime are shown in the inset. b- Reactor neutron fluence dependent carrier lifetime in heavily doped AT-GaN bulk crystal samples.

The lifetime, as an indicator of the concentration of the recombination centres, decreases non-linearly with proton fluence > 10^{14} p/cm^2. This implies that the enhanced concentration of the fast radiation induced centres prevails within carrier decay processes in MOCVD GaN epi-layers, while trapping effect is less expressed. Large capture cross-sections (>10^{-13} cm^2) can be deduced from the short lifetime values obtained for MOCVD GaN. Lifetime variations in pristine AT-GaN samples indicate lateral inhomogeneity of dopant distribution. Two decay components (τ_{R1} and τ_{R2}) imply two species of recombination centres ascribed to growth defects and to dopants. Nevertheless, the longer recombination lifetime values are obtained in bulk crystal AT-GaN samplers relative to dislocations-rich MOCVD GaN. The AT-GaN is rather tolerant (the clear decrease of carrier lifetime is obtained only for fluences > 10^{16} n/cm^2) to neutron irradiations, relative to the MOCVD and HVPE GaN samples. The role and transforms of different radiation and technological defects in fluence dependent carrier lifetime variations will be discussed.

ELECTRON PARAMAGNETIC RESONANCE STUDY OF Gd^{3+} IONS IN OXYFLUORIDE GLASS CERAMICS

Andris Antuzevics, Meldra Kemere, Reinis Ignatans

Institute of Solid State Physics, University of Latvia
andris.antuzevics@gmail.com

Oxyfluoride glass ceramics are composite materials consisting of tiny crystallites inside a glass matrix. When doped with rare earth ions they serve as attractive materials for applications in optical devices [1]. It is necessary to study the structure of luminescence centres in order to improve optical properties of such materials.

Electron paramagnetic resonance (EPR) spectroscopy is a structure sensitive method for point defect study. If the host material is doped with paramagnetic probes (point defects with unpaired electrons), we can study the local structure of impurities. In this work EPR is used to detect the surrounding environment of Gd^{3+} impurities in fluorite structure nanocrystals (CaF_2, SrF_2, BaF_2) embedded in the glass matrix. The formation of crystallites is controlled with X-ray diffraction (XRD) measurements.

The EPR measurements of the glass samples show that Gd^{3+} in located in a disordered environment, however, in glass ceramics for each crystallite a characteristic fine structure emerges. Fine structure parameter analysis indicates that the cubic, tetragonal and trigonal Gd^{3+} centres have been observed in the studied glass ceramics.

This work was supported by Scientific Research Project for Students and Young Researchers Nr. SJZ2015/1 realized at the Institute of Solid State Physics, University of Latvia.

[1] P. P. Fedorov, A. A. Luginina, A. I. Popov, Transparent oxyfluoride glass ceramics, Journal of Fluorine Chemistry **172**, 22-50 (2015).

STRUCTURE OF PHOTOVOLTAIC DERIVATIVES PROBED BY RAMAN SPECTROSCOPY

Laurynas Čekanavičius[1*], Ieva Matulaitienė[2], Remigijus Juškėnas[2], Gediminas Niaura[1]

[1] Faculty of Physics, Vilnius University, Lithuania
[2] Center for Physical Sciences and Technology, Institute of Chemistry, Lithuania
laurynas.cekanavicius@ff.stud.vu.lt

Thin film $Cu_2ZnSnSe_4$ (CZTSe) absorber for solar cells is a promising alloy to boost a progress in photovoltaic (PV) materials industry. Kesterites as CZTSe contain chemical elements that are easy and cheap to obtain from Earth's crust. Researchers have found that CZTSe optoelectronic properties are strongly dependent on the structural properties, crystalline quality and presence of secondary phases in the absorber layer [1]. In order to recognize spectroscopically secondary phases we have made five different CTSe (Cu_2SnSe_3) precursors by using different amount of selenium, annealing temperature and annealing time, as properties of kesterites are dependent on their precursors properties. CTSe photovoltaic derivatives were probed by Raman spectroscopy with 633 nm excitation wavelength (Fig. 1).

The dominant feature near 182 cm^{-1} and broad band at 76 cm^{-1} belongs to A′ mode of CTSe. Comparing Raman spectra we observed that CTSe-3 sample demonstrates intense Raman band at 236 cm^{-1} wavelength, which is assigned to ν(Se-Se) and belongs to trigonal Se (t-Se) [2]. Raman band characterized at 216 cm^{-1} is not observed at CTSe-3 Raman spectra. This indicates that Raman spectroscopy is able to probe subtle structural changes of CTSe dependent on annealing time and temperature.

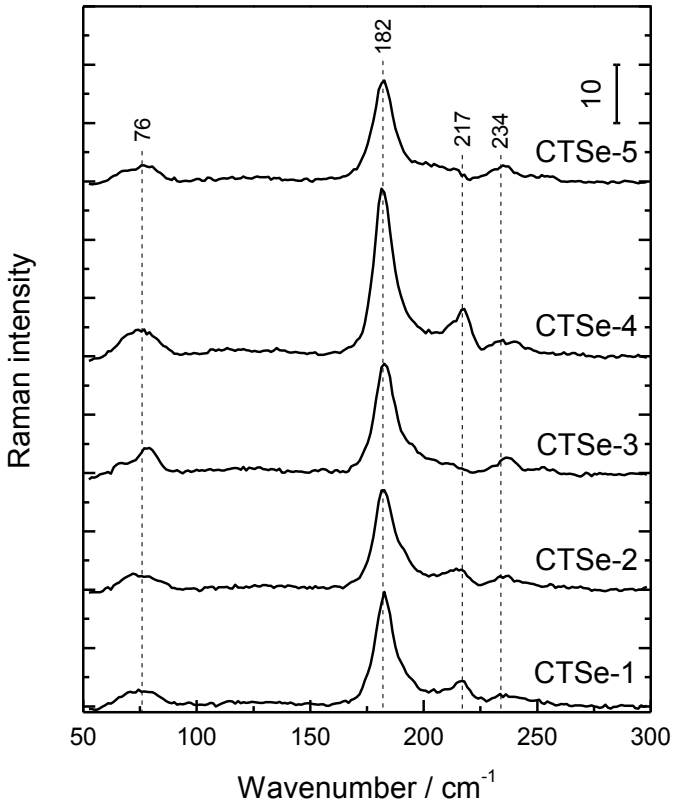

Fig. 1. Raman spectra of Cu_2SnSe_3 secondary phases, using 633 nm excitation wavelength, where CTSe-1 – T = 450 °C, m(Se) = 5 mg, t = 20 min; CTSe-2 – T = 450 °C, m(Se) = 2 mg, t = 20 min; CTSe-3 – T = 450 °C, m(Se) = 2 mg, t = 40 min, T = 560 °C, t = 40 min, CTSe-4 – T = 500 °C, m(Se) = 5 mg, t = 20 min, CTSe-5 – T = 450 °C, m(Se) = 5 mg, t = 20 min.

[1] M. Dimitrievska, A. Fairbrother, A. Perez-Rodriguez, E. Saucedo, V. Izquierdo-Roca, Raman scattering crystalline assessment of polycrystalline Cu_2ZnSnS_4 thin films for sustainable photovoltaic technologies: Photon confinement model, Acta Materialia **70**, 272–280 (2014).
[2] S.Y. Zhang, C.X. Fang, Y.P. Tian, K.R. Zhu, B.K. Jin, Y.H. Shen, J.X. Yang, Synthesis and characterization of hexagonal CuSe nanotubes by templating against trigonal Se nanotubes, Crystal Growth & Design **6,** 2809–2813 (2006).

OPTICAL ABSORPTION AND TRANSMISSION OF NANOCARBON THIN FILMS

Klaudia Żerańska, Anna Wróblewska, Mariusz Zdrojek

[1]Faculty of Physics, Warsaw University of Technology, Poland
zeranska.k@gmail.com

There is a growing interest in elastic and transparent materials, capable of conducting current, used for example as electrodes in organic solar cells, or touch screens as ITO replacements. Lightweight and nontoxic carbon nanomaterials, like graphene [1], or carbon nanotubes seem be suitable for those purposes [2]. What is more, some of nano carbon materials electromagnetic wave attenuation properties may lead to their utilization as EMI (electromagnetic interference) shields, or eye protection [3].

Although carbon nanomaterials have been thoroughly studied in many fields of physics and chemistry, we have noticed a lack of a comparative study of those materials regarding their attenuation of electromagnetic waves. Such work is vital in understanding possible applications of aforementioned nanostructures.

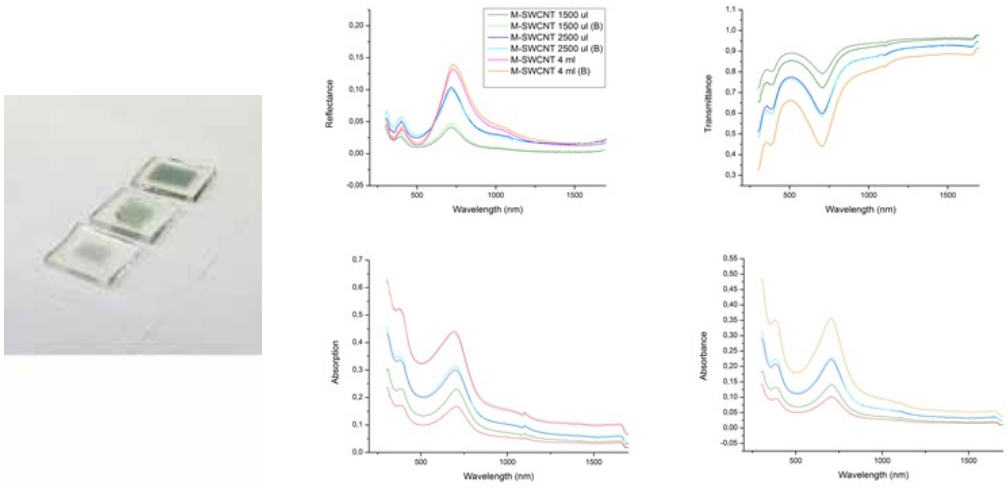

(a) (b)

Fig. 1. a) Image of M-SWCNT thin films on glass with different thickness (50, 100, 200nm) b) Sample measurements of those thin films

We present a complex review on optical properties of selected carbon nanomaterials. Samples transmittance, reflectance and as a result – absorption and absorbance, are measured in the visible light spectrum as well as IR and UV (300 -1700nm), using an integrating sphere. Materials used in this study include graphene (both mono- and multilayer), GO (graphene oxide), rGO (reduced graphene oxide) and carbon nanotubes – semiconducting, metallic and mixed. Those materials are further processed to recieve homogenous thin films using various methods like vacuum filtration, drop-casting or electrochemical delamination. The study includes measuring those nanocomposites in respect to their thickness (from 50nm to 1μm).

[1] Cooper, Daniel R., et al.; Experimental review of graphene.; ISRN Condensed Matter Physics 2012 (2012).
[2] Hecht, David S., Liangbing Hu, and Glen Irvin. "Emerging transparent electrodes based on thin films of carbon nanotubes, graphene, and metallic nanostructures." Advanced Materials 23.13 (2011): 1482-1513.
[3] Mizuno, Kohei, et al. "A black body absorber from vertically aligned single-walled carbon nanotubes." Proceedings of the National Academy of Sciences 106.15 (2009): 6044-6047.

$SiO_2@Ag^0$ NANOPARTICLES' PLASMONIC RESPONSE OPTIMIZATION BY SiO_2 SHELL'S TREATMENT IN <1nm THICKNESS

Anastasios Koutsogiannis[1], Yiannis Delligiannakis[2]

[1]Aristotle University of Thessaloniki, Greece
[2] Department of Physics, University of Ioannina, Greece
koan@auth.gr

Plasmonic response of noble metal nanoparticles (NPs) depends on size –shape as well as the immediate dielectric environment of the particles [1].

Hybrid core-shell nanoparticles $SiO_2@Ag^0$ synthesized by Flame Spray Pyrolysis, tend to decrease aggregation and Ag^{+-} ions release due to hermetic SiO_2 coating [2], thus shielding the Ag^0 nanoparticles vs effects (redox, pH, ionic strength).

In the present study, the plasmonic response for $SiO_2@Ag^0$ colloid nanoparticles was optimized by controlled decreasing the SiO_2 shell thickness, via wet chemistry . This allowed a sub-nanometer control of the SiO_2 shell thickness . After optimization vs pH, temperature and dispersion, the so-treated particles used as plasmonic sensors for Pb^{2+} ions in aqueous solution. To support the discussion, it is presented UV-Vis characterization and ions release quantification data.

Fig.1. Core-shell $SiO_2@Ag^0$ NPs before (a) and after (b) treatment. The so-treated colloid NPs used as plasmonic sensors for Pb^{2+} ions in aqueous solution(b).

[1] Kelly, K. L.; Coronado, E.; Zhao, L. L.; Schatz, G. C., The Optical Properties of Metal Nanoparticles: The Influence of Size, Shape, and Dielectric Environment, *J. Phys. Chem. B* , ***107***, 668-677, 2003.

[2] G. A. Sotiriou , T. Sannomiya , A. Teleki , F. Krumeich , J. Vörös , S. E. Pratsinis , Non-toxic, dry-coated nanosilver for plasmonic biosensors, Adv. Funct. Mater. 2010 , **20** , 4250.

INVESTIGATION OF ZIGBEE COMMUNICATION PROTOCOLS FOR LIGHTING APPLICATIONS

Miglius Budriūnas[1]

[1] Institute of Applied Research, Vilnius University, Lithuania
miglius.budriunas@ff.stud.vu.lt

Light - emitting diodes (LED) based lighting can offer a lot of unique opportunities for lighting, such as instantaneous and efficient dimming, excellent color rendering, selectable saturation/dulling ratio and also variable correlated color temperature from very low “firelight” up to bluish “starlight” as well as color tints. Furthermore, Human Centric Lighting paradigm and integration of lighting into the smart house or energy grid requires flexible, reliable and simple control options. A ZigBee ™ communication protocol can offer safe, effective, affordable, wireless (wired solution would require investment in data and electrical wiring infrastructure) and reliable communication system between luminaires and controlling devices such as smartphones and computers. The most famous lighting manufacturers are considering wireless controls based on ZigBee architecture.

Two slightly different ZigBee protocols have been examined: ZigBee Light Link (ZLL) and ZigBee RF4CE. Both offer basic ZigBee characteristics: very low power consumption, wireless data transfer rate of 250 kbit/s (more than enough for control commands) and secure 128 bit AES encryption.

ZigBee Light Link has mesh network topology, which ensures high reliability and accessibility. It also offers standardized commands for control of almost all light parameters. Commanding from a smart device is very convenient. The downside is that ZLL-capable module’s programming is quite complicated; besides, adding commands for new functions leaves these commands manufacturer specific.

ZigBee RF4CE supports multiple-star network topology. Command structure is very easy to use with a remote controller, but many of more advanced lighting control commands will be manufacturer specific. In addition, module programming is not complicated.

Both ZigBee protocols offer similar possibilities. ZigBee Light Link is easier to control with a smart device and has more advanced built-in light control functionality. ZigBee RF4CE is more convenient for controlling from remote controller and is able to control basic light parameters.

Fig. 1. Atsamr21 ZigBee module for wireless communication.

PROTEIN NANOPATTERN FABRICATION VIA LIPID DIP-PEN NANOLITHOGRAPHY

Vytautas Navikas, Martynas Gavutis, Ramūnas Valiokas

Department of Nanoengineering, Center for Physical Sciences and Technology, Vilnius, Lithuania
vytautas.navikas@ftmc.lt

This study has been focusing on the development and optimization of a biochip architecture by means of lipid dip-pen nanolithography (DPN). This scanning probe fabrication technique allows direct writing or arraying variety of biomolecules including lipids. As compared to other molecular inks, lipid DPN displays unusually high process speeds and yields micro/nanopatterns over ~mm2 surface areas within minutes. Lipid DPN technique has been successfully tested in screening of cellular membrane receptor-mediated interactions and in studies of protein crystals. Based on these observations we have employed lipid DPN for arraying proteins on pre-structured self-assembled monolayer surfaces.

Protein domain formation was a two-step process. First, structured self-assembled monolayer surface containing hydrophilic (tri-(ethylene glycol)-terminated thiol) and hydrophobic (methyl-terminated eicosane thiol) areas were fabricated using micro-contact printing technique. Surfaces, containing such microdomains were further used to guide lipid spreading during DPN process using 1, 2-dioleoyl-sn-glycero-3-phosphocholine (DOPC) and biotin labeled 1,2-dioleoyl-sn-glycero-3-phosphoethanolamine (Bt-PE) lipid mixture (100:1) as an ink. This process was characterized in a great detail using scanning probe microscopy analysis [1] and revealed the formation of multilamellar lipid assemblies. Lipid patterns remained present during transfer of the sample through the air/water interphase. Finally, lipid structures containing biotinyl functional groups were successfully tested in aqueous environment for selective streptavidin protein immobilization by means of fluorescence microscopy.

Based on these observations we were able to guide DPN lipid spreading and form lipid domains of pre-defined shape and size for selective protein immobilization. These results promote further development of micro and nano-patterned lipid domains which can be further utilized for lipid membrane mimetics in microarray and lab-on-a-chip device formats.

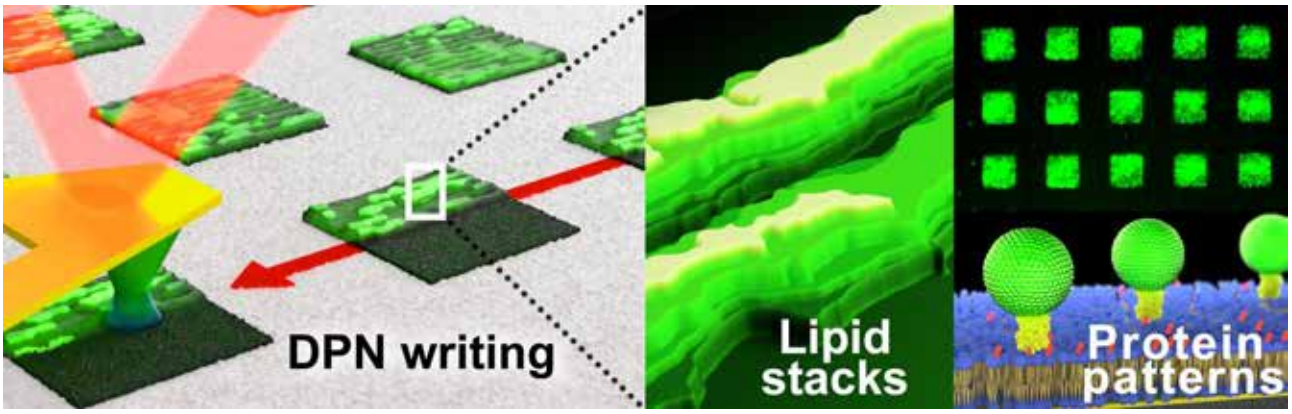

Fig.1 Schematic explanation of the protein pattern formation by lipid dip-pen nanolithography.

[1] M. Gavutis, V. Navikas, T. Rakickas, Š. Vaitekonis and R. Valiokas, Lipid dip-pen nanolithography on self-assembled monolayers. J. Micromech. Microeng., **26** (2016).

DAMMANN GRATING FOR THZ RANGE.

Karolina Wegrzynska*, Martyna Rachon[1], Jaroslaw Suszek[1], Dmytro But[2], Agnieszka Siemion[1], Wojciech Knap[2] and Maciej Sypek[1]

[1]Facoulty of Physics, Warsaw University of Technology, Koszykowa 75, 00-662 Warsaw, Poland
[2]Charles Coulomb Laboratory , University of Montpellier 2, 34095 Montpellier, France
*Corresponding author: wegrzynska@if.pw.edu.pl

At the turn of the current and previous century may be noted increased interest THz range that mean range from 100GHz to 3Thz. The main reason for this ever-growing interest is the fact that the radiation in this area is non-ionizing and therefore harmless to humans, unlike the X-ray radiation. In addition, many of hazardous substances has a characteristic spectrum in this regard. Given this and the fact that it is able to penetrate through non-metallic, dry substances the amount of possible applications that we receive is enormous.

To fully exploit the potential of the THz range it is necessary to examine the possibilities of shaping the beam. Aim of this study is to investigate the performance and capabilities of separating the light emitted from the source to the specified number of beams. Such division can be achieved by using a Dammann grating [1].

This diffractive structure is not only able to create the desired array of beams, moreover, unlike the conventional diffraction grating, the beams have the same power. With such distribution, this structure can be used both in THz scanners[2], multi-point communication[3], as well as in astronomical observations and much more.

Due to the diffractive nature of the Dammann grating was easily possible to add diffractive lens in the final optical element. As the source emits diverging wave, lens gives us a wave of parallel necessary for most applications. As a result of the combination of this two structures there is possibility to eliminate the additional optical element which introduces energy loss, generate costs and require adjustment.

This type of structure can be designed with the use of Light Sword program. Presented in this poster structure was designed on the array 4096x4096, with sampling 117 μm x 117 μm. The structure was designed for the wavelength of 282 GHz (DWL 1,064 mm) and is able to divide one beam into matrix of 3 x 3 – 9 points. Focal length of lens is 495 mm.

Since many plastics are transparent to the wavelength in THz range, designed components can be easily printed on 3D printers [4] with sufficient accuracy. It is very cheap and effective way of production such diffractive structures. As a result of such a production process, they are tough, lightweight and less costly than the complex refractive structures. In this particular structure due to the very good transparency and low loss PA12 material was used.

Acknowledgment. The authors would like to thank Orteh Company for providing LS 6.0 Software for designing and modelling diffractive optical elements and also for manufacturing investigated structures.

[1] H. Dammann and K. Go¨rtler, “High-efficiency in-line multiple imaging by means of multiple phase holograms,” Opt. Commun. **3,** 312–315 ~1971;
[2] *Proc. SPIE* 3464, Optical Devices and Methods for Microwave/Millimeter-Wave and Frontier Applications, 95 (October 2, 1998); doi:10.1117/12.323133
[3] Journal of Reinforced Plastics and Composites (Impact Factor: 1.5). 07/2015; 34(19
[4] 3-D-printed flat optics for THz linear scanners, :IEEE Transactions on Terahertz Science and Technology, vol. 5, nr 2, 2015, 314-316

INCREASING EFFICIENCY OF THZ DETECTORS BY USING MATRICES OF LENSES.

Martyna Rachon[1*], Karolina Wegrzynska[1], Agnieszka Siemion[1] , Jaroslaw Bomba[1] , Artur Sobczyk[1,2], Wojciech Knap [3], Dominique Coquillat[3] , Dmytro But[3], Jaroslaw Suszek[1] and Maciej Sypek[1]

[1]Faculty of Physics, Warsaw University of Technology, 75 Koszykowa Str. 00-662 Warsaw, POLAND
[2]Faculty of Geodesy and Cartography, Warsaw University of Technology, 75 Koszykowa Str. 00-662 Warsaw, POLAND
[3]University Montpellier 2 – CNRS, Place E. Batallion, 34095 Montpellier, FRANCE
rachon@if.pw.edu.pl

Imaging with waves of the range between 100 Ghz to 3THz is a very promising field of development of the present photonics. It is so because of no-ionizing THz radiation nature and unique spectral fingerprints that have a number of dangerous substances in this range [1]. In order to achieve fast and accurate imaging in the THz range intensive efforts are undergoing to create efficient THz cameras.

Currently, many factors are causing problems in creating an efficient active imaging system. Commercially available sources of THz radiation have relatively low power. Radiation beam is further attenuated by the water vapor present in the atmosphere. Adding the poor performance of existing uncooled detectors that are sensitive to radiation in THz range, a very low system performance is obtained.

Therefore there is need of sophisticated optical elements that would increase an efficiency of such imaging system. To achieve this goal we introduced a matrix of lenses. Each component is associated to a single detector and has large aperture, low absorption and Fresnel reflections as well as high focusing efficiency. The structure must be thin, lightweight and cost-effective in production to be in the future aplicable in real devices hence we choosen the diffractive structures. To get very good performance designed structures were printed on a 3D printer [2] using PA12 material.[3]

Fig. 1. Matrix of 49 lenses with focal length 5mm and size 5mm

The response of the detectors were measured and compared with and without the matrix of lenses. The performance was improved approximately 6 times in the case of matrix from Fig. 1.

---

[1] M.R. Leahy-Hoppa , M. J. Fitch, R. Osiander, "Terahertz spectroscopy techniques for explosives detection"' Analytical and Bioanalytical Chemistry, September 2009, Volume 395, Issue 2, pp 247-257
[2] http://mcortechnologies.com/3d-printers/iris/
[3] Suszek, J. Siemion, A. ; Bieda, M.S. ; Blocki, N. ; Coquillat, D. ; Cywinski, G. ; Czerwinska, E. ; Doch, M. ;Kowalczyk, A. ; Palka, N. ; Sobczyk, A. ; Zagrajek, P. ; Zaremba, M. ; Kolodziejczyk, A. ; Knap, W. ;Sypek, M.' "3-D-Printed Flat Optics for THz Linear Scanners", :IEEE Transactions on Terahertz Science and Technology, vol. 5, nr 2, 2015, 314-316

STUDIES OF SURFACE MORPHOLOGY AND MAGNETIC PROPERTIES OF CO/PD ANTIDOTS ON NANOPOROUS AL_2O_3 MEMBRANES

Juliusz Chojenka[1], Alexey Maximenko[2], Marta Marszałek[2]

[1]Department of Physics, Cracow University of Technology, Poland
[2]Institute of Nuclear Physics, Polish Academy of Sciences, Poland
chojenka@wp.pl

Magnetic thin films with periodic arrays of holes (antidots) show promising results as elements of various spintronics devices (sensors, magnetic field transistors etc.) and as a media for high density magnetic recording (storage density >1 Tbit/in^2) [1]. In this work the technology of magnetic antidot fabrication with different pore diameters (10 – 135 nm) is presented and the dependence of antidot parameter on their magnetic properties is discussed.

Co/Pd antidots were fabricated by deposition of Co/Pd multilayers on nanoporous Al_2O_3 templates [2, 3]. Anodic Aluminium Oxide (AAO) templates were fabricated by anodizing of aluminium film deposited on silicon wafers. The template porosity was controlled by parameters of anodization. To determine the contribution of antidot morphology to magnetic properties of the system Co/Pd multilayers on flat Si substrate were also prepared.

SEM imaging confirmed antidot formation and indicated that deposited material is concentrated in the form of small grains between the pores. XRR and XRD measurments revealed a presence of Co_xPd_{1-x} alloy at Co/Pd MLs interface.

Magnetization curves (Fig. 1) demonstrated perpendicular magnetic anisotropy for continuous multilayers and its conservation for antidots.The value of magnetic anisotropy constant for antidots is inversely proportional to antidot diameter. A twofold enhancement of coercive field was detected for antidots below 100 nm and it was explained by pinning of magnetic moments on the pore borders. MFM imaging of antidots showed complicated magnetic contrast with small magnetic domains and areas with magnetic moments distorted from perpendicular direction in comparison to continuous films. It was associated with complex distribution of magnetic material due to developed surface morphology of antidots.

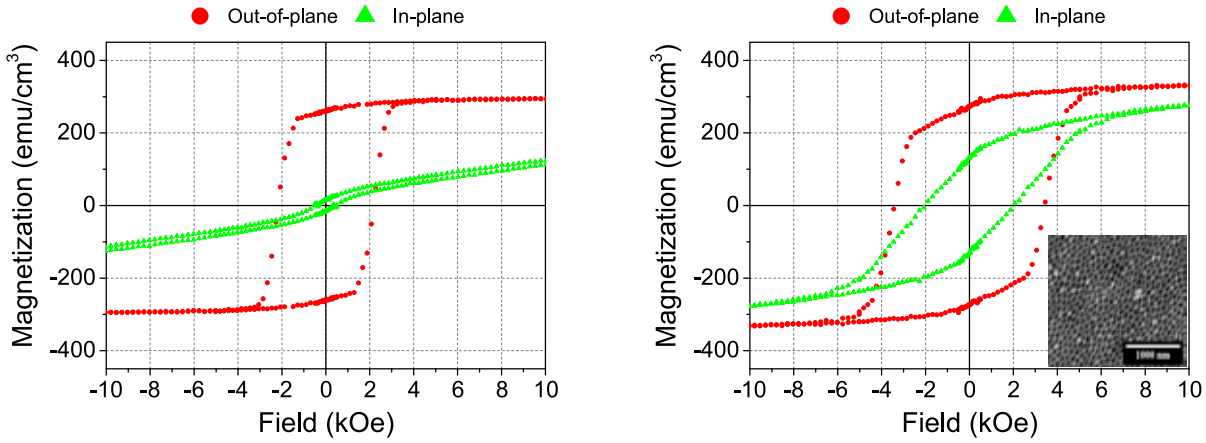

(a) Flat sample (b) Antidots

Fig. 1. Histeresis loops of Co/Pd continuous multilayers (a) and antidots with pores diameter D_p=35 nm (b). The inset shows SEM image of the antidots.

[1] J.M. Shaw, H.T. Nembach, T.J. Silva, S.E. Russek, *Effect of microstructure on magnetic properties and anisotropy distributions in Co/Pd thin films and nanostructures*, Phys. Rev. B 80, 184419, 2009
[2] A. Maximenko, J. Fedotova, M. Marszałek, A. Zarzycki, Y. Zabila, *Magnetic characteristics of CoPd and FePd antidot arrays on nanoperforated Al_2O_3 templates*, J. Mag. Mag. Mat. 400, 200205, 2016
[3] G.E.J. Poinern, N. Ali, D. Fawcett, *Progress in Nano-Engineered Anodic Aluminum Oxide Membrane Development*, Materials, 4, 487-526, 2011

THE FLUORESCENT SPECTRAL TECHNIQUE FOR DETERMINATION THE AFFINITY OF ARYL-PORPHYRINS TO BIOLOGICAL STRUCTURES

Yakovets Ilya[1,2,3*], Yankovsky Igor[1,2,3], Bezdetnaya Lina[2,3], Zorin Vladimir[1]

[1] Department of Biophysics, Belarussian State University, Minsk, Belarus
[2] Centre de Recherche en Automatique de Nancy, CNRS, Université de Lorraine, Nancy, France
[3] Institut de Cancérologie de Lorraine, Vandoeuvre-lès-Nancy, France
viprorok@gmail.com

An evaluation of drugs affinity to different biological structures (serum proteins, membranes and others) is very important to understand their pharmacokinetics features. In spite of the fact, there are a large number of physico-chemical methods for direct determination of the characteristics of affinity; most of them meet with difficulties when dealing with non-polar compounds. In the current work we present a new spectral fluorescent method which allows to quantify of relative affinity of aryl-porphyrins to biomolecules and biomembranes.

Aryl-porphyrins (AP) are widely used in photodynamic diagnostic and therapy of oncological diseases. Most of them are hydrophobic molecules and form aggregates in aqueous surroundings, which complicates their biodistribution after injection in blood. Additionally, the aggregation process is accompanied by loss of the fluorescent properties of porphyrins, the formation of aggregates influences the processes of interaction with the main plasma protein transport and cell membranes Furthermore, the aggregation leads also to the loss of fluorescent ability of porphyrins and affects to their affinity to biological structures.

In our study we used cyclic oligosaccharides (cyclodextrns, CDs) to prevent the aggregation of AP and to estimate the relative partition coefficients of aryl-porphyrins to the biological membranes and serum proteins. It is widely known that CDs readily form inclusion complexes with many drugs by incorporating a drug molecule or more commonly a lipophilic moiety of the molecule into the central cavity. It has been shown, that CDs efficiently form an inclusion complexes with AP and can be vehicles of photosensitizers via complexation [1].

As object to study we used following APs: 5,10,15,20-Tetra(*m*-hydroxyphenyl)chlorin (mTHPC), 5,10,15,20-Tetra(*o*-sulfophenyl)porphyrin (TSPP) and 5,10,15,20-Tetra(*o*-carboxyphenyl)porphyrin (TCPP). The processes of complex formation between listed above aryl-porphyrins and Methyl-β-cyclodextrin (Me-β-CD) have been studied and the spectral techniques to determine of stoichiometry and quantitative parameters of complexation have been developed [2]. According to the data obtained, the complexes between aryl-porphyrins and Me-β-CD have a stoichiometry 1:2 and can be characterized by the binding constants values over 10^{12} M^{-2}.

To determine the AP affinity to biological structures we have analyzed the processes of AP binding to Me-β-CD in serum proteins solutions (human serum albumin, low and high density lipoproteins) and in suspensions of lipid vesicles. The obtained titration curves and previously determined values of binding constants for Aps association with Me-β-CD were used to estimate relative affinity of porphyrins to biological structures. In the case of mTHPC obtained the following values of the distribution coefficient: 2.6 $(mg/ml)^{-1}$ for human serum albumin, $4.8x10^2$ $(mg/ml)^{-1}$ for low density lipoproteins and $1.0x10^3$ $(mg/ml)^{-1}$ for high density lipoproteins. The ratios of mTHPC distribution coefficients in plasma compounds are in good accordance to the data obtained by gel-chromatography [3].

Acknowledgements. This study was supported by Belarussian Republican Foundation for Fundamental Research, the Ministry of Education of the Republic of Belarus and French "Ligue National contre le Cancer". We thank Biolitec (Jena, Germany) for providing us with mTHPC.

[1] Mosinger, J., Deumie, M., Lang, K., Kubat, P., Wagnerova, D.M. Supramolecular sensitizer: complexation of meso-tetrakis(4-sulfonatophenyl)porphyrin with 2-hydroxypropyl-cyclodextrin, Journal of Photochemistry and Photobiology A: Chemistry **130**, 13-20 (2000).

[2] Yakavets, I., Yankovsky, I., Bolotine, L., Zorin, V. Spectral characteristics of meta-tetra(hydroxyl-phenyl)chlorin in biological systems, J. BSU Herald Series 1 Physics 2, 39-45 (2015).

[3] Reshetov, V., Zorin, V., Agnieszka, S., D'Hallewin, M.-A., Guillemin, F., Bezdetnaya, L. Interaction of liposomal formulations of meta-tetra(hydroxyphenyl)chlorin (temoporfin) with serum proteins: protein binding and liposome destruction. Photochem. Photobiol. **88** (5), 1256-1264 (2012).

THERMAL ANALYSIS OF InP-BASED TYPE-II QUANTUM-WELL LASERS

Simona Paurazaitė[1,2], Hannes Schmeiduch[2], Stephan Sprengel[2] and Markus-Christian Amann[2]

[1] Semiconductor optics laboratory, Center for Physical Sciences and Technology, Vilnius, Lithuania
[2] Walter Schottky Institute, Technische Universität München, Germany
simona.paurazaite@gmail.com

Lasers operating in the wavelength range above 2μm have many applications: contactless highly sensitive gas sensors, biosensing, medical sensing and medical devices, etc. A novel approach to cover this wavelength range is InP-based lasers [1]. These utilize the type-II band alignment between GaInAs and GaAsSb, to create transition energies below the band gap of the constituent materials [1].

The lasers are based on *n*-InP substrate with active region and cladding layers grown on top. The structures were grown with Molecular Beam Epitaxy (MBE). The active region consists of quantum wells with W-shaped based structure. These are made of two 2.6 nm thick layers of $Ga_{0.32}In_{0.68}As$ surrounding a 2.9 nm thick $GaAs_{0.3}Sb_{0.7}$ layer. The active region consist of different number W-shaped QW. The band structure is depicted in Fig. 2.

Thermal properties of laser devices are very important for later applications, since they are required to provide lasing at room temperature or at higher temperatures. The main loss mechanisms in semiconductor lasers are non-radiative recombination mechanism, free carrier absorption and interband absorption. Those three are strongly depend on temperature. Since most of the input power below laser threshold is lost due to radiative recombination, one of the most important characteristics of a laser is the threshold current desnity.

Fig. 1. shows dependence of threshold current density plotted against temperature. The optical output was measured by an liquid nitrogen cooled InSb. For increasing temperature, loss mechanisms get stronger and are causing higher threshold currents. Such behavior was also reported for GaSb-based lasers and could indicate different loss mechanism, like a resonant absorption. [2]. As can be seen in Fig. 3(b) the characteristic temperature of the laser is strongly increasing with higher numbers of QWs. The temperature dependence of the modal gain Γg_0 however seems to be independent of the number of QWs (Fig. 3(a)). Therefore, higher number of QWs offer a higher thermal stability, due to lower filling of the QWs, the total threshold current densities, however, are still lowest for small number of QWs.

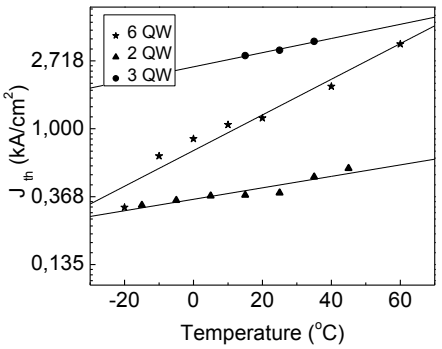

Fig. 1. Threshold current density per temperature.

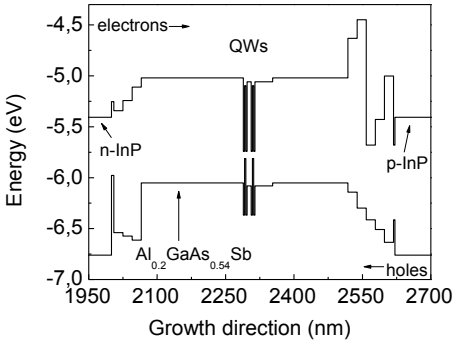

Fig. 2. Schematic band structure of an InP type-II laser, injection directions for electrons and holes are indicated.

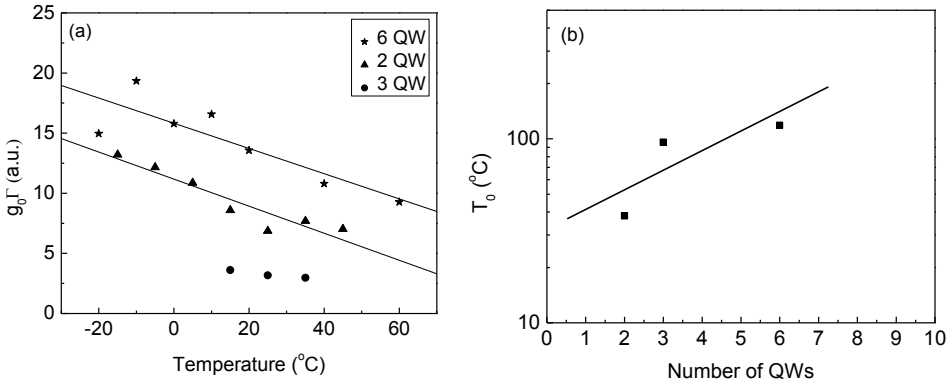

Fig.3. (a) Gain as a function of temperature showing degradation with temperature; (b) Characteristic temperature plotted against the number of QWs.

[1] S. Sprengel, A. Andrejew, K. Vizbaras, T. Gruendl, K. Geiger, G. Boehm, C. Grasse, M.-C Amann, Type-II InP-based lasers emitting at 2.55 μm, Appl. Phys. Lett, **4** , 041109 (2012).

[2] K.Vizbaras and M.-C. Amann, , 3.6 μm GaSb-based type-I lasers with quinternary barriers, operating at room temperature, Electron. Lett., **42**, 980 (2011).

FORMATION OF SILVER NANOPARTICLES AND THEIR INFLUENCE ON OPTICAL PROPERTIES OF ORGANIC MATERIALS

Simona Streckaitė[1], Marius Franckevičius[1], Domantas Peckus[2], Vidmantas Gulbinas[1]

[1] Institute of Physics, Center for Physical Sciences and Technology, A. Goštauto Ave 11, Vilnius LT-01108, Lithuania,
[2] Institute of Materials Science of Kaunas University of Technology, K. Baršausko Ave 59, Kaunas LT-51423, Lithuania
simona.streckaite@ftmc.lt

Metal nanoparticles and nanostructured metal films excited by electromagnetic radiation exhibit collective oscillations of their conduction electrons, known as localized surface plasmon resonance (LSPR), that give these materials a number of interesting and useful optical properties. Possible manipulations of these properties lead to various applications of silver nanoparticles (AgNPs) in optoelectronics [1], biosensing [2], catalysis, metal enhanced optical spectroscopies (metal enhanced fluorescence (MEF) [3], surface enhanced Raman scattering (SERS) [4]), as antimicrobials [5] and other. One of active research fields using AgNPs, which exhibit LSPR in a visible region, is altering emission properties of dyes. For optimized applications of these metal nanostructures and their unique features, it is important to understand the dependence of spectral properties of metal-fluorophore complex on their individual optical behavior.

In this work, layers of AgNPs of different sizes were formed and their influence on absorption and fluorescence properties of low fluorescent conjugated polymer RZ11 and highly fluorescent organic dye Uranin was investigated. Spherical AgNPs were formed by thermal evaporation and annealing: Ag layer was deposited on glass and heated until AgNPs have formed. Samples with AgNPs of approx. 50 nm, 100 nm and 150 nm diameter (which were made from 5 nm, 10 nm and 15 nm of deposited Ag layer respectively) were used for the investigations. Organic materials on layers of AgNPs were spin-coated of few hundred nanometers thickness. Samples were studied by using steady-state and time-resolved absorption and fluorescence spectroscopy.

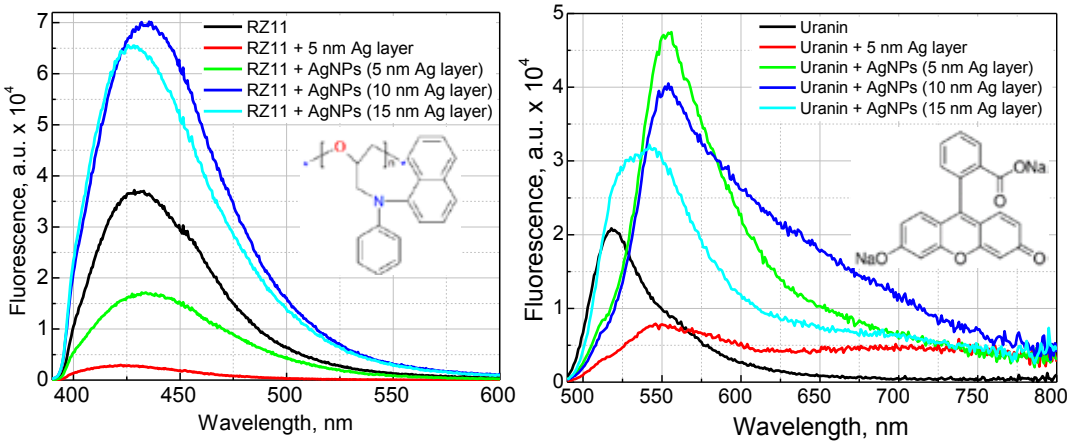

Fig. 1. Fluorescence spectra of polymer RZ11 (left) and dye Uranin (right) on layers of AgNPs formed from 5, 10 and 15 nm thickness thermally evaporated silver

Steady-state absorption spectra showed strongest interaction between fluorophores and AgNPs occurring, when absorption spectrum of organic material overlaps with plasmon resonance band or when it is redshifted compared to the plasmon resonance. Fluorescence studies revealed double fluorescence intensities of organic materials with nanoparticles of approx. 50-150 nm diameter (Fig. 1) and faster decay times than for the samples without nanoparticles. These results indicate fluorescence enhancement effect due to enhanced and confined local electromagnetic fields near the surface of metal nanoparticles and increased radiative decay times. Strongest interaction is observed, when excitation light matches absorption of fluorophore as well as plasmon resonance band. We conclude, that for achieving fluorescence changes or enhancement, absorption and fluorescence spectra of fluorophores and plasmon resonance overlap must be ensured and wavelength of the excitation light is of great importance too.

[1] C.W. Hsu, B. Zhen, W. Qiu et al., Transparent displays enabled by resonant nanoparticle scattering, Nat. Commun. **5**, 3152 (2014).
[2] B. Abel, S. Coskun, M. Mohammed et al., Metal-Enhanced Fluorescence from Silver Nanowires with High Aspect Ratio on Glass Slides for Biosensing Applications, J. Phys. Chem. C **119(1)**, 675-684 (2015).
[3] X. Wang, F. He, X. Zhu et al., Hybrid silver nanoparticle/conjugated polyelectrolyte nanocomposites exhibiting controllable metal-enhanced fluorescence., Sci. Rep. **4**, 4406 (2014).
[4] W. Wu, L. Liu, Z. Dai et al., Low-Cost, Disposable, Flexible and Highly Reproducible Screen Printed SERS Substrates for the Detection of Various Chemicals, Sci. Rep. **5**, 10208 (2015).
[5] S. Agnihotri, S. Mukherji, S. Mukherji, Size-controlled silver nanoparticles synthesized over the range 5-100 nm using the same protocol and their antibacterial efficacy, RSC Adv. **4**, 3974-3983 (2014).

Poster session 4

ELECTRON-IMPACT IONIZATION CROSS SECTIONS FOR W^{25+} ION

Saulius Pakalka, Aušra Kynienė, Šarūnas Masys, Valdas Jonauskas

Institute of Theoretical Physics and Astronomy, Vilnius University, Lithuania
s.pakalka@gmail.com

Various atomic and ionic characteristics of tungsten ions are of great concern being the subject of experiments and of numerical simulations. The data required involve mainly electron-ion collisions, and include excitation, recombination and ionization processes.

We have investigated electron-impact ionization cross sections from the threshold to 20000 eV for the ground configuration of the W^{25+} ion. The ground configuration of the W^{25+} ion ($[\mathrm{Ni}]4s^2 4p^6 4d^{10} 4f^3$) consists of 41 levels. Main attention has been focused on influence of the increasing principal and orbital momentum quantum numbers to the excitation-autoionization (EA) process and its contribution to full ionization cross sections. The calculations were carried out using the Flexible Atomic Code (FAC) [1], which employs Dirac-Fock-Slater method. The subconfiguration-average and level-to-level distorted-wave (LLDW) approximations are utilized to describe the electron excitation and ionization processes.

The total electron-impact single-ionization cross sections from the level i of A^{q+} ion to the level j of $A^{(q+1)+}$ ion can expressed by direct and indirect processes as following:

$$\sigma_{ij}(\varepsilon) = \sigma_{ij}^{\mathrm{DI}}(\varepsilon) + \sum_k \sigma_{ik}^{\mathrm{exc}}(\varepsilon)\, B_{kj}, \qquad (1)$$

where $\sigma_{ij}^{\mathrm{DI}}(\varepsilon)$ is the direct ionization (DI) cross section at the electron energy ε, $\sigma_{ik}^{\mathrm{exc}}$ is the electron-impact excitation cross section to the level k of the A^{q+} ion, B_{kj} is autoionization branching ratio. The study includes excitations up to the shells with the principal quantum numbers $n \leq 25$ and orbital quantum numbers $l \leq 6$. All possible electric dipole and Auger transitions from the generated excited configurations are calculated.

Figure 1 shows that excitations to the high-nl shells ($9 \leq n \leq 25$) increase electron-impact cross sections of indirect ionization process by about a factor of 2 compared to the excitations to the lower shells ($n \leq 8$). This conclusion is in agreement with recent works [2, 3]. Current results demonstrate that the contribution of the EA channels originating from the excitations to the high-nl shells has to be estimated in the analysis of the electron-impact ionization process for the highly charged ions. In order to estimate the contributions from the high-nl shells, the convergence of the cross sections of the EA process must be checked. Furthermore, the obtained results demonstrate that the radiative damping has a large impact on the ionization cross sections. Also, it is established that the greatest contribution to the EA gives the excitations to the shells with the orbital quantum number $l = 4$. The EA channel for the excitations from the $4d$ shell is predicted to show the largest contribution for the LLDW results with $n > 8$ compared to the EA channels from $4p$ but in the case $n \leq 8$. This can be explained by the fact that large amount of configurations produced by excitations from the $4d$ shell are below the ionization threshold.

Maxwellian rate coefficients derived from our calculated cross sections for the ground state are compared with the previous values obtained using configuration-average distorted-wave (CADW) rate coefficients. The rate coefficients for DI cross section are smaller than CADW rates while EA rate coefficients are larger than CADW rates. The total DI+EA rate coefficients are about 16% larger than the CADW rate coefficients.

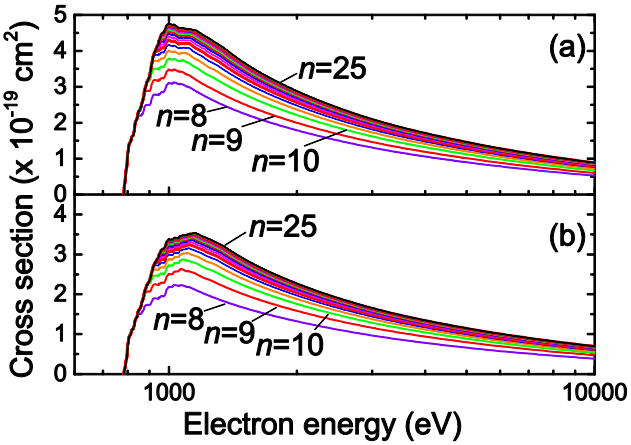

Fig. 1. EA channels to the high-nl shells for W^{25+}: (a) without radiative damping and (b) with radiative damping.

[1] M. F. Gu, Can. J. Phys. **86**, 675 (2008).
[2] V. Jonauskas, A. Kynienė, G. Merkelis, G. Gaigalas, R. Kisielius, S. Kučas, Š. Masys, L. Radžiūtė and P. Rynkun, Phys. Rev. A **91**, 012715 (2015).
[3] A. Kynienė, Š. Masys and V. Jonauskas, Phys. Rev. A **91**, 062707 (2015).

PLASMON DISPERSION RELATION IN GATED TWO DIMENSIONAL ELECTRON GAS

Dovilė Čibiraitė[1], Alvydas Lisauskas[1,2], Jonas Matukas[1]

[1] Department of Radiophysics, Faculty of Physics, Vilnius University Sauletekio av. 9-III, LT-10222 Vilnius, Lithuania
dovile.cibiraite@ff.stud.vu.lt
[2] Physikalisches Institut, Johann Wolfgang Goethe-Universität, DE-60438 Frankfurt (Main), Germany
lisauskas@physik.uni-frankfurt.de

Technologies of high frequency electronic devices experience permanent developments, which allow for higher operation frequency, higher power and etc. One strategy for extension of the applicability of semiconductor devices beyond their transit-time-limited cut-off frequencies proposes to exploit the collective motion of charge carries - plasma waves [1]. The authors used comparably simple hydrodynamic transport concept to describe carrier motion within the channel of a field-effect transistor and proposed series of novel devices including terahertz detectors, frequency mixers and radiation sources. To illustrate the role of plasmons, the local carrier density in 2-DEG plane of a field-effect transistor was described using gradual channel approximation and by employing a planar capacitor formula: $n = CV_{sv}(x,t)/q$. Here C is the capacitance between 2-DEG plane and gate, V_{sv} – a gate to channel voltage swing minus transistor threshold voltage.

The task of this work is further development of the hydrodynamic description by accounting high frequency dielectric properties of 2-DEG [2]. Similar device geometry as [1] (shown in Fig. 1) is used in our considerations. The necessity of improvement in hydrodynamic transport description comes into consideration when the wavelength of excited plasmons becomes comparable to gate-to-2-DEG separation.

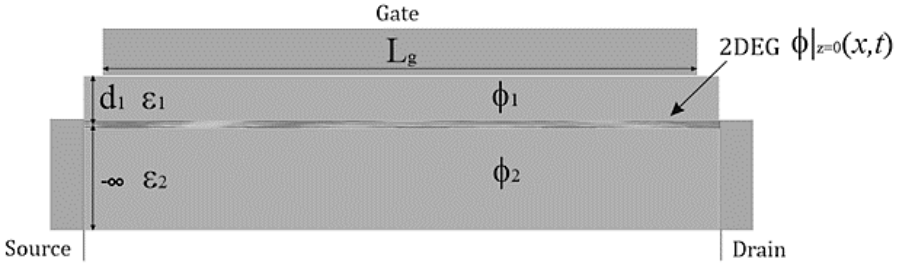

Fig. 1. THz FET with a 2 DEG channel.

In order to find a response of two-dimensional electron gas to electromagnetic fields, at first a dependence of potential in the 2-DEG plane on carrier density is needed to be found. Therefore, we solve the Poisson equation and apply appropriate boundary conditions.

The improved model allows to derive potential function to the response of perturbation by external charge q_{ext} :

$$\varphi_1(k)|_{z=0} = -\frac{q_{\mathrm{ext}}}{\varepsilon_0\left(k\varepsilon_1 \coth(kd)+k\varepsilon_2+k_{\mathrm{s}}(\varepsilon_1+\varepsilon_2)\right)} \quad (1)$$

Here k_{s} is a screening wavevector, $k_{\mathrm{s}} = \frac{e}{\varepsilon_0(\varepsilon_1+\varepsilon_2)}\frac{\mathrm{d}}{\mathrm{d}\varphi}n(\varphi)|_{\varphi=\varphi_0}$. The resulting dispersion relation for plasmons:

$$\omega^2 - i\frac{\omega}{\tau} - \frac{\mathrm{e}^2\, k^2 n_0}{\varepsilon_0 m\left(k\varepsilon_1 \coth(kd)+k\varepsilon_2+k_{\mathrm{s}}(\varepsilon_1+\varepsilon_2)\right)} = 0 \quad (2)$$

For $kd >> 1$ and $\omega\tau >> 1$ it reduces to well-known dispersion for ungated 2D plasmons:

$$\omega^2 = \frac{\mathrm{e}^2 n_0}{\varepsilon_0 m(\varepsilon_1+\varepsilon_2)}k \quad (3)$$

In this work, we derived dispersion relation for plasmons in gated two dimensional electron gas that can be used for a wide range of plasmon wavevectors. The theory allows improving existing plasma-wave-based terahertz detector models.

[1] M. Dyakonov, M. S. Shur, Plasma wave electronics: Novel terahertz devices using two dimensional electron fluid, IEEE Trans. Electron. Dev., **43**(10), p. 1640 (1996).
[2] T. Ando, A. B. Fowler, F. Stern, Electronic properties of two-dimensional systems, Reviews of Modern Physics, **54**(2), p. 437 (1982).
[3] M. Dyakonov, M. Shur, Detection, mixing and frequency multiplication of terahertz radiation by two-dimensional electronic fluid, IEEE Transactions on electron devices, 43(3), 380–387 (1996).

DYNAMICS OF CARRIER RECOMBINATION IN InGaN/GaN QUANTUM WELLS: KINETIC MONTE-CARLO STUDIES

Monika Bijeikytė[1,2], Audrius Alkauskas[2]

[1]Vilnius university, Faculty of Physics, Vilnius
[2]Center for Physical Sciences and Technology, Vilnius
monika.bijeikyte@gmail.com

Light-emitting diodes (LEDs) made from InGaN are considered to be the most promising next-generation lighting sources. Nevertheless, many puzzles remain regarding the physics of these devices. One of the unanswered questions is related to the potential fluctuations in InGaN/GaN quantum wells. More specifically, it remains unclear what is the influence of these fluctuations on radiative and non-radiative carrier recombination [1], and how they affect quantum efficiencies of LEDs.

In this study we have investigated carrier dynamics in InGaN quantum wells. Five programs have been written in order to simulate different components of carrier dynamics: diffusion, drift, non-radiative and radiative recombination, as well as carrier distribution in a quantum well. In addition, one program has been written to create a realistic model of InGaN potential fluctuations. A random-walk algorithm was used to simulate diffusion. Once the spatial scale is fixed, the temporal scale is then determined so that the actual diffusion constant is reproduced. The kinetic Monte Carlo algorithm was used to simulate drift. In both diffusion and drift we monitored the trajectories of particles; these were found to agree with theoretical predictions. Einstein's relationship was shown to hold when electric fields are not too strong. Simulations of non-radiative and radiative recombination were also in agreement with theoretical expectations.

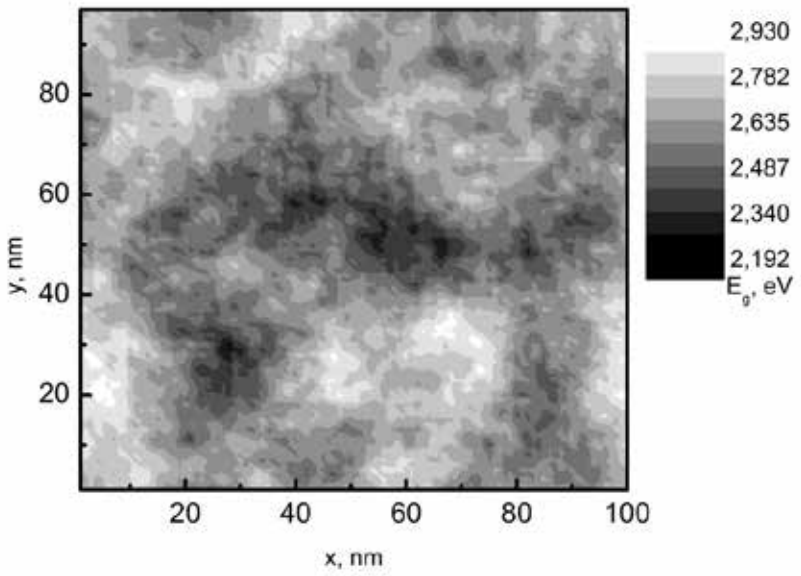

Fig. 1. InGaN band gap fluctuation model.

In this study a realistic model of InGaN potential fluctuations (Fig. 1) was created. We will use it further in order to explain physical effects which determine efficiency of LED.

[1] S. Marcinkevicius, K. Gelzinyte, Y. Zhao, S. Nakamura, S.P. DenBaars, and J.S. Speck. Carrier redistribution between different potential sites in semipolar 2021 InGaN quantum wells studied by near-field photoluminescence. *Applied Physics Letters*, **105**, 111108 (2014).

VECTOR ELECTROMAGNETIC FIELDS IN ABSORBING MEDIUM FOR LASER MICROFABRICATION APPLICATIONS

Alfonsas Juršėnas[1,2], Sergejus Orlovas[2], Gediminas Račiukaitis[2]

[1]Department of Theoretical Physics, Faculty of Physics, Vilnius University
[2] Center for Physical Sciences and Technology, Savanoriu ave 231, Vilnius Lithuania
alfonsas.jursenas@ff.stud.vu.lt

Despite decades of progress laser microfabrication has not achieved the flexibility required by industrial applications such as silicon (Si) photonics. 3D laser micromachining of silicon is a complex task and it is targeted by several groups worldwide [1, 2]. The difficulties of bulk Si microfabrication arise due to high absorption of light in visible, near-IR, UV spectral regions and its indirect bandgap. Propagation of the beam is deformed by free charges generated during microfabrication. This leads to the spreading of focal region [1] and inability to form structures with required dimensions. Therefore the spatial formation of laser light at the microscale is an essential step for laser microfabrication in the volume of semiconductors.

One way of spatial structuring of light in absorbing media is to construct superpositions of many beams with the same wavelength but different longitudinal wave vectors [3]. If the distribution of field in the axis of propagation is described by harmonic functions then truncated discrete Fourier series can be formed by superposition of such beams. These superpositions are called - frozen waves, due to their property of stationary longitudinal intensity pattern [4]. In this work we construct vectorial frozen waves of Bessel beams.

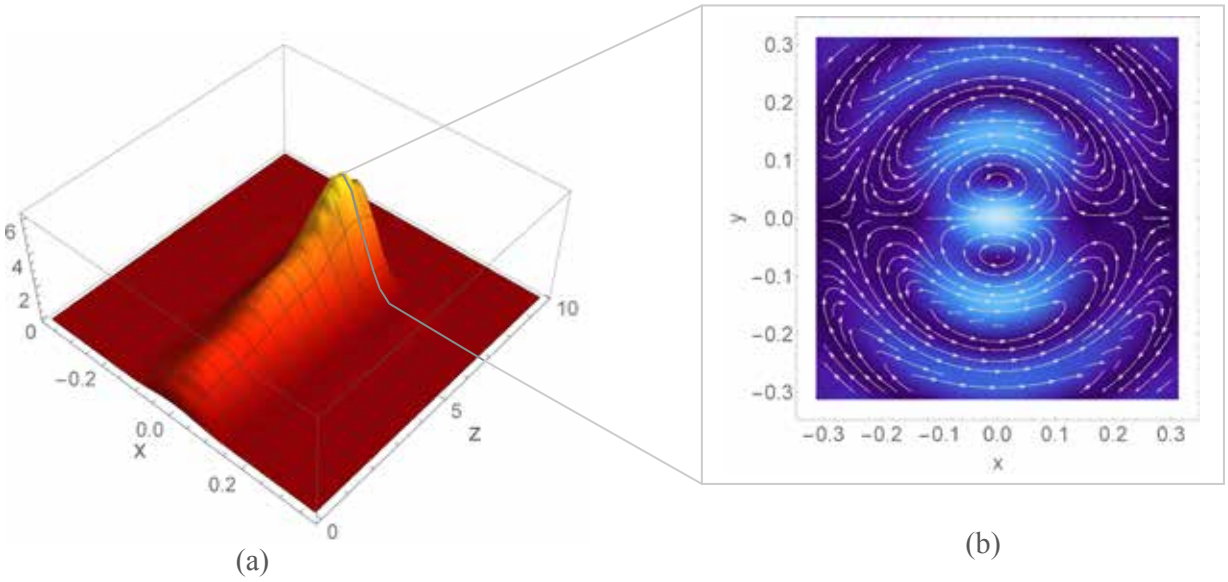

Fig. 1. Longitudinal intensity (a) and transverse magnetic field (b) distributions of vectorial frozen wave inside Si medium. Laser beam wavelength is $\lambda = 600nm$, length is measured in units of λ.

We investigate a new class of vectorial Bessel beams, which can overcome linear absorption and reach the microfabrication intensities inside the volume of a semiconductor material. We demonstrate that in case of these beams the behavior of either longitudinal or transverse component of electric field can be controlled on the axis of propagation.

[1] EV Zavedeev, VV Kononenko, VM Gololobov, and VI Konov. Modeling the effect of fs light delocalization in si bulk. *Laser Physics Letters*, 11(3):036002, 2014.
[2] PC Verburg, GRBE Römer, et al. Two-photon–induced internal modification of silicon by erbium-doped fiber laser. *Optics express*, 22(18):21958–21971, 2014.
[3] Michel Zamboni-Rached. Diffraction-attenuation resistant beams in absorbing media. *Optics Express*, 14(5):1804–1809, Mar 2006.
[4] Michel Zamboni-Rached, Erasmo Recami, and Hugo E. Hernández-Figueroa. Theory of "frozen waves": modeling the shape of stationary wave fields. *Journal of the Optical Society of America A*, 22(11):2465–2475, Nov 2005.

NEURONAL EXCITABILITY CHANGES UNDER ACH MODULATION IN A MULTI-COMPARTMENTAL HIPPOCAMPAL CA1 PYRAMIDAL NEURON MODEL

Domas Linkevičius[1], Aušra Saudargienė[2], Bruce Graham[3]

[1]Faculty of Natural Sciences, Vilnius University, Lithuania
[2]Departament of Applied Informatics, Vytautas Magnus University, Lithuania
[3]Divison of Computing Science and Mathematics, University of Stirling, Scotland, United Kingdom
domas.linkevicius@fsf.stud.vu.lt

Modeling parts of the central nervous system is a complex task. It requires capturing the essential characteristics and mechanisms of the phenomenon or structure being modeled, model itself being as simple as possible for various practical reasons (difficulty of analysis, unknown relevant parameters, long computation time). The building block of the nervous system, the neuron, insofar as modeling goes, has generally been considered as an ever-expanding collection of ion channels described by Hodgkin-Huxley type equations, inserted in to dendritic structures of varying complexity. However, in vivo and in vitro studies have shown that this picture of the neuron is, at best, incomplete and additional variables must be included to achieve a more precise view of how the neuron functions. Hence the goal of this study is to modify an existing model of a hippocampal CA1 pyramidal neuron by adding the effects of neurotransmitter acetylcholine on such ion channels as R-type calcium as well as potassium channels responsible for AHP and A currents [2,3]. The effects of acetylcholine in the central nervous system have been shown to be critical in consolidation of memory, prominent in reward circuits and Alzheimer's disease [1].

We used a compartmental model of a CA1 hippocampal pyramidal neuron, consisting of soma, three compartments of apical dendrites, basal dendrite, and modified R-type calcium, I_A, I_{AHP} channels to include ACh modulation. We measured the alterations in neuron excitability and calcium concentration in an apical dendritic spine as a result of the increased ACh concentration from low (0.001μM) to high (10μM). The neuron was stimulated by a sinusoidal current injection into proximal apical dendrite and AMPA/NMDA synapse activation.

We found that, at high ACh concentrations, the CA1 hippocampal pyramidal neuron fires more spikes, has a larger Ca^{2+} influx in the dendritic spine. The increased excitability and firing rate, for the most part, can be attributed to inhibition of I_{AHP} and I_A, which hyperpolarize and stabilize the cell. By increasing conductance of R-type Ca^{2+} channels, ACh works to increase dendritic spine Ca^{2+} levels, confirming that ACh, via its effect on calcium, is critical in circuits that play a role in memory formation and consolidation. Having modified CA1 hippocampal pyramidal neuron to include ACh modulation, we see its utility being the further elucidation of how autoassociative networks function under different neurotransmitter concentrations and signals.

[1] M. E. Hasselmo, The role of acetylcholine in learning and memory, Current Opinion in Neurobiology **16**, 710 – 715 (2006).
[2] C. Tai, J. B. Kuzminski, B. A. MacVicar, Muscarinic enhancement of R-Type calcium currents in hippocampal CA1 pyramidal neurons, The Journal of Neuroscience **26(23)**, 6249 - 6258 (2006)
[3] E. D. Menshcik, L. H. Finkel, Neuromodulatory control of hippocampal function: towards a model of Alzheimer's disease, Artificial Intelligence in Medicine **13**, 99 – 121 **(**1998)

RENORMALIZATION OF PROPAGATORS OF WEYL SPINORS IN THE SEESAW EXTENSION OF THE STANDARD MODEL

Vytautas Dūdėnas, Thomas Gajdosik

Department of Theoretical Physics, Vilnius University, Lithuania
vytautas.dudenas@tfai.vu.lt

Despite the tremendous success of the Standard Model (SM), there is no doubt that it cannot be a complete theory due to numerous experimental evidences for which the SM fails to find an explanation. One part of these experimental evidences are the observations of neutrino oscillations (for a short review of these experiments see [1]). This proves that at least two of the neutrinos have masses. But the original assumptions of the SM forbid these mass terms. Hence an extension of the SM to explain the masses of neutrinos is needed.

Extending the model means adding new particles to the model. Particles fall into representations of the Lorentz group. The Lorentz group can be decomposed into two $SU(2)$ subgroups, which are conventionally called the left subgroup ($SU(2)_L$) and the right subgroup ($SU(2)_R$). The Dirac spinor is a direct sum of fundamental representations of these two subgroups ($SU(2)_L \oplus SU(2)_R$). However, it is possible to describe a fermion with an even smaller representation, which is the fundamental representation of only one $SU(2)$ subgroup. This representation is called a Weyl spinor and is widely used in model building (for more detailed explanations about the difference between Dirac, Majorana and Weyl spinors see [2]). But Dirac spinors are preferred over Weyl spinors in practical calculations. This is due to the fact that in the SM, all fermions are Dirac fermions and the transformation from one formalism to the other is rather trivial. However, if we have more complicated cases, for instance, when we have fermions with mixed mass terms of Majorana and Dirac type, this transformation might pose some difficulties. This kind of fermionic mass structure can be found in the seesaw extension of the SM (for an overview see [3]), which is used to explain the masses of the neutrinos. In this case, choosing Weyl spinors over Dirac spinors as a basis to calculate correlation functions seems more reasonable. However, this approach is somewhat absent in the literature. Hence, in our work we try to fill this gap and present the usage of Weyl spinors in the seesaw extension of the SM.

After setting up the definitions and Feynman rules for using Weyl spinors to construct correlation functions (we followed [4], where the definitions and the usage of Weyl spinors for supersymmetric models are presented), we continue the development of this formalism concentrating on the subject of renormalization. For simplicity, we take one family of the seesaw extension of the SM and look at the one loop corrections for the propagators of heavy and light neutrinos. We express counterterms starting from multiplicative renormalization and translate the renormalization constants into additive counterterms, that are sufficient at one loop order. Using the arguments of Lorentz covariance we extract the scalar part of the self energy functions. With this preparation we can conveniently resum these functions together with their corresponding counterterms into the denominators of the propagators. By using the on-shell prescription we define the counterterms in terms of these scalar self energy functions in Weyl spinor notation.

Acknowledgements: The authors thank the Lithuanian Academy of Sciences for the support (the project DaFi2015).

[1] K. M. Heeger, "Evidence for neutrino mass: A Decade of discovery," arXiv:hep-ex/0412032.
[2] P. B. Pal,"Dirac, Majorana and Weyl fermions," Am. J. Phys. **79** (2011) 485 arXiv:1006.1718 [hep-ph].
[3] G. Senjanovic, "Neutrino mass: From LHC to grand unification," Riv. Nuovo Cim. **34** (2011) 1.
[4] H. K. Dreiner, H. E. Haber and S. P. Martin, "Two-component spinor techniques and Feynman rules for quantum field theory and supersymmetry," Phys. Rept. **494** (2010) 1

THREE-DIMENSIONAL SPIN HALL EFFECT

Jogundas Armaitis and Gediminas Juzeliūnas

Institute of Theoretical Physics and Astronomy, Vilnius university, Lithuania
jogundas@gmail.com

The physics of charge and spin transport constitutes a basis of current consumer devices. Recent discoveries in solid-state physics have highlighted the importance of the coupling of the electron's motion to its spin for transport phenomena. One of these phenomena related to spin-orbit coupling is the spin Hall effect, in which density currents generate transverse spin currents [1]. Recently, the spin Hall effect has been detected experimentally in a wide variety of materials. This stimulates advances in the field of spintronics [2], including both condensed-matter systems and also ultracold atoms [3]. Building on a novel possibility to generate a three-dimensional spin-orbit coupling in ultracold-atom systems [4], we propose a protocol to generate and observe for the first time a three-dimensional version of the spin Hall effect. Our proposal highlights unique tools available in ultracold-atom experiments for generation of spin-orbit coupling and subsequent detection of chiral spin currents.

[1] J. Sinova et al., Universal Intrinsic Spin Hall Effect, Phys. Rev. Lett. **92**, 126603 (2004).
[2] J. Sinova et al., Spin Hall effects, Rev. Mod. Phys. **87**, 1213 (2015).
[3] M. C. Beeler et al., The spin Hall effect in a quantum gas, Nature **498**, 201–204 (2013).
[4] B. M. Anderson et al., Synthetic 3D Spin-Orbit Coupling, Phys. Rev. Lett. **108**, 235301 (2012).

TWO HIGGS DOUBLET MODELS AS EXTENSIONS TO THE STANDARD MODEL: DIFFERENT BASIS CHOICES

Anton Kunčinas, Thomas Gajdosik

Department of Theoretical Physics, Vilnius University, Lithuania
Anton.Kunchin@protonmail.com

The Higgs mechanism [1] as a part of the electroweak theory [2] forms the core of the Standard Model. Most of its predictions are experimentally verified with the Higgs boson as the last missing piece detected in 2012 with a mass $m_h = 125.09 \pm 0.21(\text{stat.}) \pm 0.11(\text{syst.})$ GeV [3].

Nevertheless several theoretical questions are not answered yet, allowing for extensions of the Standard Model. The two-Higgs-doublet model is one of the simplest extensions of the Standard Model Higgs sector. It consists of two complex $SU(2)$-doublet scalar fields, while in the Standard Model there is only one complex scalar Higgs field. The addition of the second Higgs doublet leads to the generation of the five physical Higgs bosons: two neutral CP-even Higgs bosons, h and H, with $m_H > m_h$, a neutral CP-odd or pseudoscalar Higgs boson A, and a pair of charged Higgs bosons $H^{\pm}$. So far only the Standard Model like Higgs boson h was found. The Higgs Hunter's Guide [4] lays out search strategies for the other Higgs bosons. The program 2HDMC [5] helps the prospective Higgs hunter to calculate the properties of the studied two-Higgs-doublet model theoretically.

Haber and collaborators noticed, that there is an arbitrariness left in the choice, how we distribute the physical Higgs fields among the two complex $SU(2)$-doublet scalar fields and described a basis independent formulation for the potential of the two-Higgs-doublet models [6]. Their notation is advantageous in new implementations of the two-Higgs-doublet model together with the seesaw mechanism as an extension of the Standard Model [7]. But this notation is not implemented in the 2HDMC.

Historically people distinguish different two-Higgs-doublet models by their fermion couplings. In the type I models the Higgs doublets can be defined in such a way that all fermions couple only to a single Higgs doublet. In type II the down-type fermions couple to one Higgs doublet and the up-type fermions to the other. The parameter $\tan\beta$ relates the vacuum expectation values of the two doublets.

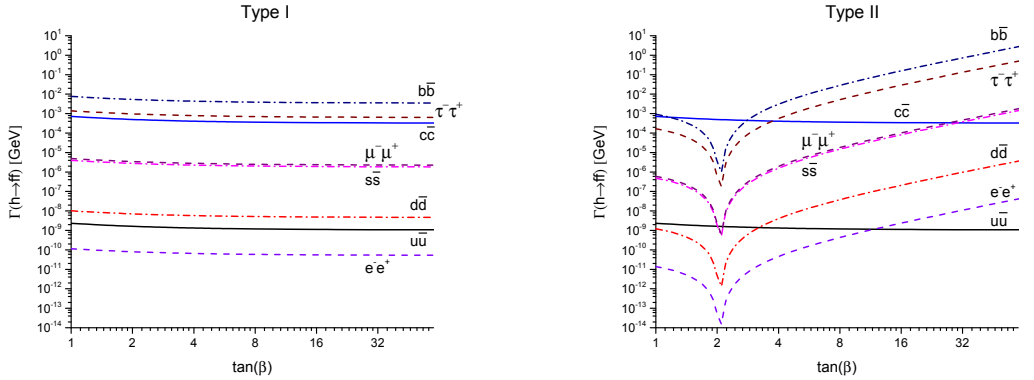

Fig. 1. Partial decay widths of the SM-like Higgs boson into fermions for different types of Yukawa couplings.

We derive the connection between the input for 2HDMC and the notation of the general formalism of [6]. With this connection we compare the results from 2HDMC with our general decay width calculations [8] and confirm the correctness of the code.

[1] F. Englert and R. Brout, Phys. Rev. Lett. **13** (1964) 321. doi:10.1103/PhysRevLett.13.321
P. W. Higgs, Phys. Rev. Lett. **13** (1964) 508. doi:10.1103/PhysRevLett.13.508
G. S. Guralnik, C. R. Hagen and T. W. B. Kibble, Phys. Rev. Lett. **13** (1964) 585. doi:10.1103/PhysRevLett.13.585
[2] S. L. Glashow and S. Weinberg, "Natural Conservation Laws for Neutral Currents", Phys. Rev. D **15** (1977) 1958. doi:10.1103/PhysRevD.15.1958
[3] G. Aad *et al.* [ATLAS and CMS Collaborations], "Combined Measurement of the Higgs Boson Mass in pp Collisions at $\sqrt{s} = 7$ and 8 TeV with the ATLAS and CMS Experiments", Phys. Rev. Lett. **114** (2015) 191803 doi:10.1103/PhysRevLett.114.191803 [arXiv:1503.07589 [hep-ex]].
[4] J. F. Gunion, H. E. Haber, G. L. Kane and S. Dawson, "The Higgs Hunter's Guide" Front. Phys. **80** (2000).
[5] D. Eriksson, J. Rathsman and O. Stal, "2HDMC: Two-Higgs-Doublet Model Calculator Physics and Manual", Comput. Phys. Commun. **181** (2010) 189 doi:10.1016/j.cpc.2009.09.011 [arXiv:0902.0851 [hep-ph]].
[6] S. Davidson and H. E. Haber, Phys. Rev. D **72** (2005) 035004 [Phys. Rev. D **72** (2005) 099902] doi:10.1103/PhysRevD.72.099902, 10.1103/PhysRevD.72.035004 [hep-ph/0504050].
H. E. Haber and D. O'Neil, Phys. Rev. D **74** (2006) 015018 doi:10.1103/PhysRevD.74.015018 [hep-ph/0602242].
H. E. Haber and D. O'Neil, Phys. Rev. D **83** (2011) 055017 doi:10.1103/PhysRevD.83.055017 [arXiv:1011.6188 [hep-ph]].
[7] T. Gajdosik, A. Juodagalvis, D. Jurčiukonis and T. Sabonis, Acta Phys. Polon. B **46** (2015) 11, 2323. doi:10.5506/APhysPolB.46.2323 ... and references in this paper ...
[8] A. Kunčinas, "A second Higgs doublet as an extension to the Standard Model", semester practice work, VU (2016)

MONTE CARLO SIMULATION STUDIES OF THE τ LEPTON POLARISATION IN THE Z and H BOSON DECAYS IN PP COLLISIONS

Jonas R. Umaras[1], Adrian Perieanu[2], Andrius Juodagalvis[3]

[1]Department of Physics, Vilnius University, Lithuania
[2]Institute of Experimental Physics, Hamburg University, Germany
[3]Institute of Theoretical Physics and Astronomy, Vilnius University, Lithuania
jonas.umaras@ff.stud.vu.lt

The Large Hadron Collider (LHC) based at the laboratory of the Conseil Européen pour la Recherche Nucléaire (CERN) near Geneva, Switzerland, resumed its operations after the planned shutdown. In April 2015 the accelerator reached the center-of-mass energy level of proton-proton collisions of 13 TeV.

After the discovery of the new particle around 125 GeV/c^2 [1, 2], which was announced as the Higgs boson, experimental research will further investigate Higgs mechanism [3, 4]. A few decay channels of the Higgs boson are still to be confirmed by reaching the statistical significance of five standard deviations (5σ), including $H \to \tau^- + \tau^+$, for which the main background is the Drell-Yan process $Z/\gamma^* \to \tau^- + \tau^+$. The purpose of this study is to develop a cut-based analysis algorithm that would help to discriminate these events with the Compact Muon Solenoid (CMS) detector and would allow researchers to reach the required statistical significance for confirmation of the decay channel, without a need for an additional large amount of data. The focus is on the property of τ leptons called polarisation as it differs in the signal and background events. The difference in polarisation reflects in energy distribution among the decay products of τ leptons, which themselves are not observed in the detector because of their short lifetime of (290.6 ± 1) fs [5]. τ leptons are reconstructed from their decay products, but as neutrinos are not detected and carry a part of the energy away, the τ lepton candidate has a lower measured energy, called the visible energy E_{vis}. The decaying τ lepton has the total energy $E_{tot} > E_{vis}$.

The production of the Higgs boson through gluon-gluon fusion in a proton-proton collision as well as the production of the Z boson through a quark-antiquark annihilation and their decay to τ leptons were simulated using *Pythia 8* [6], a generator for high-energy physics based on principles of Monte Carlo method. The simulated events were processed with *GEANT4* [7, 8], a software package which emulates the response of the CMS detector to the particles produced in an event and which pass through the detector. The simulated detector response was further processed with the standard CMS event reconstruction software CMSSW. Simulated data provides two layers of information on the same event. The generator (GEN) level possesses information about all particles simulated in the event - their relations to each other, energies, momenta, etc. The second layer is the reconstructed (RECO) level, which is purely an emulation of what can be reconstructed from this event with the detector.

The simulated samples were analysed using *ROOT* [9]. By looking at the energy fractions of τ leptons, $z = E_{vis}/E_{tot}$, an effect of polarisation in these events was observed, which provides basis for further development of the analysis algorithm and its implementation in the standard analysis chain of CMS.

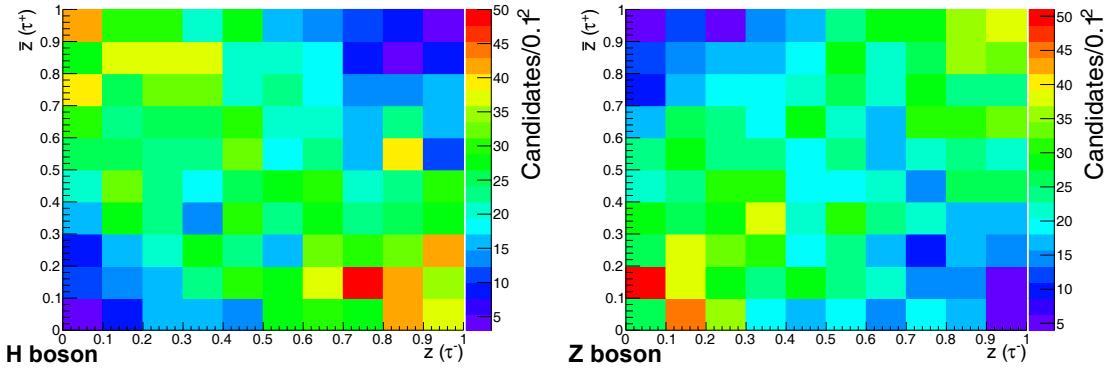

Fig. 1. Influence of τ lepton polarisation to energy fractions ($z = E_{vis}/E_{tot}$) at GEN level. The case of the Higgs (Z) boson decay to τ leptons is shown on the left (right). $\tau(\bar{\tau})$ lepton decay to $\pi^-(\pi^+) + \nu_\tau(\bar{\nu}_\tau)$.

[1] Serguei Chatrchyan et al. Observation of a new boson at a mass of 125 GeV with the CMS experiment at the LHC. Phys. Lett., B716:30–61, 2012.
[2] Georges Aad et al. Observation of a new particle in the search for the Standard Model Higgs boson with the ATLAS detector at the LHC. Phys. Lett., B716:1–29, 2012.
[3] F. Englert and R. Brout. Broken Symmetry and the Mass of Gauge Vector Mesons. Phys. Rev. Lett., 13:321–323, 1964.
[4] Peter W. Higgs. Broken symmetries, massless particles and gauge fields. Phys. Lett., 12:132–133, 1964.
[5] K. A. Olive et al. Review of Particle Physics. Chin. Phys., C38:090001, 2014.
[6] Torbjrn Sjstrand, Stefan Ask, Jesper R. Christiansen, Richard Corke, Nishita Desai, Philip Ilten, Stephen Mrenna, Stefan Prestel, Christine O. Rasmussen, and Peter Z. Skands. An Introduction to PYTHIA 8.2. Comput. Phys. Commun., 191:159–177, 2015.
[7] S. Agostinelli et al. GEANT4: A Simulation toolkit. Nucl. Instrum. Meth., A506:250–303, 2003.
[8] John Allison et al. Geant4 developments and applications. IEEE Trans. Nucl. Sci., 53:270, 2006.
[9] R. Brun and F. Rademakers. ROOT: An object oriented data analysis framework. Nucl. Instrum. Meth., A389:81–86, 1997.

SPHERICAL TRIANGLE TO FIND THE COORDINATES OF CELESTIAL BODIES

Alexey Pavlov, Maxim Belov

Department of Physics, Belarusian State University, Belarus
alex.neal.moz@gmail.com

Practical astronomy is the part of astronomy, which deals with methods of observations and appropriate related tools used to find the geographical coordinates, the coordinates of celestial bodies, the exact calculation of local time and azimuth location. Spherical astronomy calculations are routinely used while doing these calculations. Besides, routines of spherical astronomy are often used at the astronomy course, and the calculation usually takes considerable time.

Evidently, there are software that deal with some of these issues, we can point out Stellarium [1]. Unfortunately, most of the software is designed for personal computers. This puts some difficulties for both on-site applications and classroom usage.

A software with continuous availability and mobility makes one able to overcome these inconveniences. We decided to do a first step and create an application that can run on a variety of electronic devices: desktops, phones, tablets. Our software has the following availability features:

1. Maximum compatibility across different platforms,
2. The adaptive design, which can be conveniently used on various platforms.

We have chosen a popular cross-platform API to provide the:

1. HTML+ CSS + SVG [2] provides maximum adaptability of the application,
2. JavaScript provides a powerful mathematical tool.

The result is a cross-platform application that solves spherical geometry problems, namely, allows to determine unknown sides and angles of a given spherical triangle (Fig. 1).

Fig. 1. Application design

[1] http://www.stellarium.org/
[2] https://developer.mozilla.org/en-US/docs/Web/SVG

THE EVOLVED PULSATING CEMP STAR HD 112869

Laimons Začs[1,2], Julius Sperauskas[1], Aija Grankina[2], Viktoras Deveikis[1], Bogdan Kaminskyi[3], Yakiv Pavlenko[3], and Faig A.Musaev[4]

[1] Vilnius University Observatory, Čiurlionio 29, Vilnius 2009, Lithuania
[2] Laser Center, University of Latvia, Raiņa bulvāris 19, LV-1586 Rīga, Latvia
[3]Main Astronomical Observatory of Academy of Sciences of Ukraine, Zabolotnoho 27, Kyiv, 03680, Ukraine
[4]Special Astrophysical Observatory of the Russian AS, Nizhnij Arkhyz, 369167, Russia
aija.laure@gmail.com

Radial velocity measurements, $BV R_C$ photometry, and high-resolution spectroscopy in the wavelength region from blue to near infrared are employed in order to clarify the evolutionary status of the carbon-enhanced metal-poor star HD 112869 with unique ratio of carbon isotopes in the atmosphere. An LTE abundance analysis was carried out using the method of spectral synthesis and new self consistent 1D atmospheric models. The radial velocity monitoring confirmed semiregular variations with a peak-to-peak amplitude of about 10 km s^{-1} and a dominating period of about 115 days. The light, color and radial velocity variations are typical of the evolved pulsating stars. The atmosphere of HD 112869 appears to be less metal-poor than reported before, [Fe/H] = -2.3±0.2 dex. Carbon to oxygen and carbon isotope ratios are found to be extremely high, C/O ≃ 12.6 and $^{12}C/^{13}C \gtrsim 1500$, respectively. The s-process elements yttrium and barium are not enhanced, but neodymium appears to be overabundant. The magnesium abundance seems to be lower than the average found for CEMP stars, [Mg/Fe] < +0.4 dex. HD 112869 could be a single low mass halo star in the stage of asymptotic giant branch evolution [1].

The European Union FP7-PEOPLE-2010-IRSES program is acknowledged for funding exchange visits in the framework of the project POSTAGBinGALAXIES (grant agreement No. 269193).

[1] Začs, L., Sperauskas, J., Grankina, A., Deveikis, V., Kaminskyi, B., Pavlenko, Y.,Musaev, F.A., The evolved pulsating CEMP star HD 112869, The Astrophysical Journal **803**, 17 (2015)

HOT EXOPLANETS ON NON-CIRCULAR ORBITS

Sylwia Plenzner[1], Gracjan Maciejewski[2]

[1] Faculty of Physics, Astronomy and Informatics , Nicolaus Copernicus University, Poland
[2]Toruń Centre for Astronomy, Nicolaus Copernicus University, Poland
258286@stud.umk.pl

Hot exoplanets have been shown to orbit their host stars on highly circularized orbits. It is however not always so. Some planetary systems containing massive exoplanets on short orbits show curious eccentricities, suggesting external effects. With recent progress on exoplanetary research, this issue can be further looked into.

During this work planets whose orbits appeared eccentric were investigated, focusing on the possibility of their systems hosting additional objects on larger orbits. To this end, a sample of exoplanets was chosen along specific criteria, so as to make certain to filter out planets that do not fall into the ‚hot exoplanet' definition. Thus, the objects had to be transiting ones – to make certain their orbits are short, their transit depth had to be greater than 10 mmag, which defined the size of the exoplanets. In addition, convenience criteria were chosen, such as that the host star's brightness had to be lesser than 13.5 magnitudes, and the objects declination greater than 0^{o}. This was so that objects with none (or highly innacurate) radial velocity measurements would be excluded, and that the resulting selection would be of use to the observatories on the northern hemisphere respectively.

Using radial velocity measurements of the host stars, as well as recorded moments of transit, orbits were fitted (Fig.1.) through the SYSTEMIC [1] software which calculated precise eccentricity factors. From these, a catalogue was prepared, containing 73 objects showing non-circularity in their orbits. .

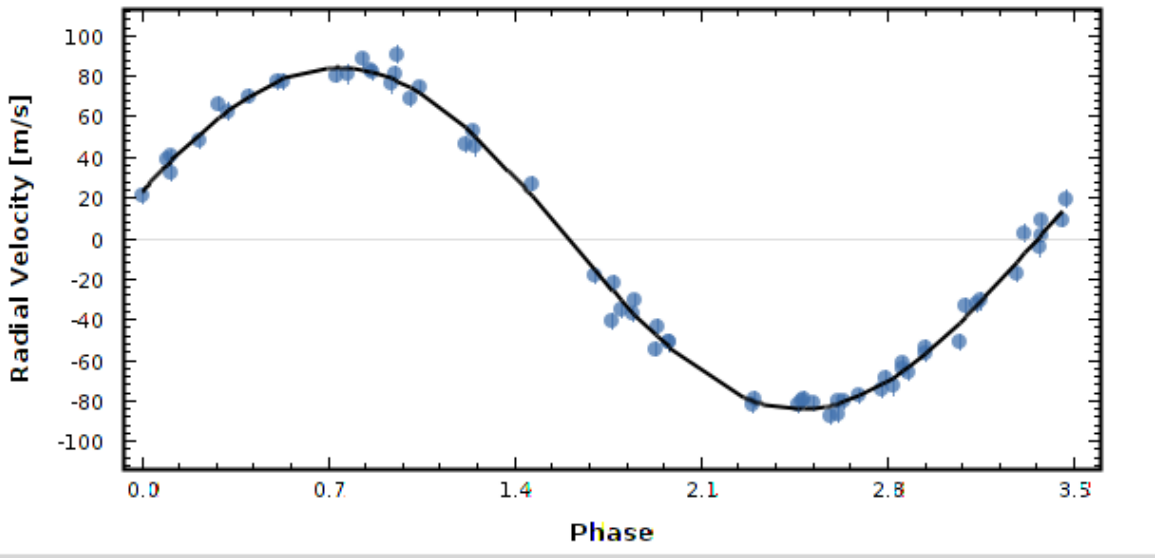

Fig. 1. An exemplary radial velocity fit for system HD209458, displaying measured radial velocities (dots) and the fitted orbit (line).

Following, a 'goodness' factor was determined as the relation of eccentricity to its uncertainty, whereas if the factor was higher than 3, it was considered that the system most likely hosts another – yet undetected object.

As a result, 24 objects with a goodness factor of over 2 were found, in 18 of which the factor exceeded 3, which in turn nearly guarantees presence of an accompanying object. This marks the selected 18 systems as good candidates for further observation with a high chance of exoplanetary discovery.

[1] Stefano Meschiari. *Synthetic Worlds*. [ONLINE] Available at: http://www.stefanom.org/systemic/. [Accessed 04 February 2016]

DEVELOPMENT AND TESTING OF CUBESAT ROCKET ENGINE TEST STAND

Algimantas Bikulčius[1], Liudas Tumonis[2]

[1] Department of Solid State Electronics, Vilnius University, Lithuania
[2]Space Technology Center, Vilnius University, Lithuania
algimantas.bik@gmail.com

The use of nanosatellites (artificial satellites with mass between 1 and 10 kg) for space missions is significantly increasing due to relatively simple design and launch process compared to bigger satellites. CubeSat, one of the nanosatellite standards, is often used for research and education purposes, as well as for experiments that may be too risky to perform using bigger satellites.

Orbital decay caused by Earth's atmospheric drag greatly limits the mission time of small artificial satellites. In order to extend the orbital lifetime, miniaturized propulsion systems are being researched and developed by academic and industrial institutions.

CubeSat LituanicaSAT-2 is being developed by Vilnius University and NanoAvionika, JSC. This joint team is a member of QB50 project, meant to launch 50 satellites simultaneously into orbit and perform coordinated research of lower layers of Earth's thermosphere, measuring concentration of atomic oxygen [1]. Another objective of LituanicaSAT-2 is to test new rocket engine, using ADN-based monopropellant fuel blend [2].

The aim of this work is to prepare the equipment for measuring thrust force produced by the engine and heat generated by catalyst heater. Since the atmospheric pressure significantly decreases produced thrust force and convection decreases performance of the catalyst heater, the engine tests must be performed in vacuum chamber. Thrust force was measured using pendulum, shown in Fig. 1. The swing (1) and a frame – on which the swing is placed (8, 10), were balanced to touch the load cell (2). The engine was placed on the plate (9) so that the thrust force would push the swing onto the load cell. The S-beam load cell used in the experiments can measure forces up to 1N. Additionally, K-type thermocouple was used to monitor the temperature of the engine. The hardware and software to acquire the experimental data were developed and callibrated using high-precision tools. The pressure in the vacuum chamber was monitored using factory-callibrated pressure gauge. Vacuum pressure dynamics were used to determine engine characteristics such as mass flow.

It was concluded that the response time of sensors is quick enough to perform accurate measurements. Initial tests confirmed that this test stand is suitable to perform firing tests of various small rocket engines in vacuum environment.

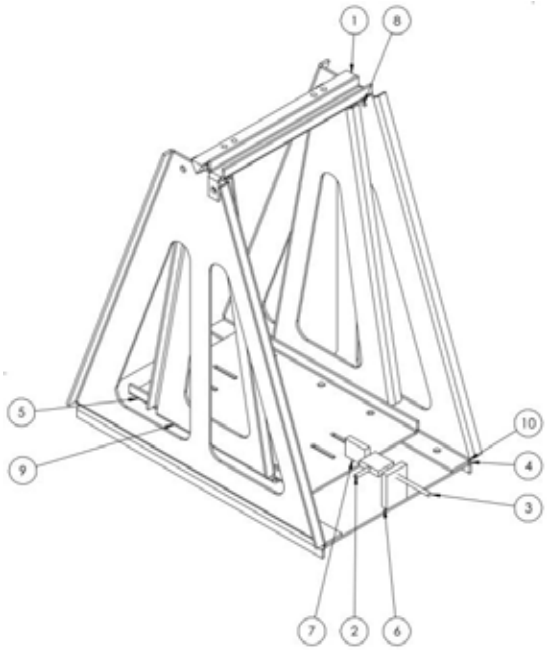

Fig. 1: Drawing of thrust force measurement scales.

1. **QB50 consortium.** QB50 mission objectives. [Online] https://qb50.eu/index.php/project-description-obj/mission-objectives.

2. **Nanoavionika, UAB.** Chemical Propulsion system, project brochure. 2015.

MODELLING BIOSENSORS UTILIZING ALLOSTERIC ENZYME ACTIVITY

Liutauras Ričkus, Romas Baronas

Faculty of Mathematics and Informatics, Vilnius University, Lithuania
liutauras.rickus@mif.vu.lt

Biosensors are analytical devices used mainly for the recognition of the chemical substances in solution to be analyzed [1]. The biosensors usually utilize specific biochemical reactions catalyzed by enzymes immobilized on electrodes. Allosteric enzymes are unique compared to other enzymes because of its multiple interacting active sites. These enzymes are very attractive in different applications, e. g. for detecting disease [2]. Mathematical modelling is one of the most attractive solutions to understanding the peculiarities of the biosensors and optimizing their configuration [3].

The purpose of this work was to develop a mathematical as well as the corresponding computational models of a biosensor based on an allosteric enzyme and to investigate the influence of the allosteric effect on the biosensor response. The developed mathematical model of the biosensor is based on non-stationary diffusion equations and involves a model of the allosteric reaction network [4]. The model comprises two compartments: a layer of the enzyme entrapped on the electrode surface and an outer diffusion layer modelled by the Nernst approach [1, 3]. The governing equations in the dimensionless form read as follows:

$$\frac{\partial S_e}{\partial T} = \frac{\partial^2 S_e}{\partial X^2} - \sigma^2 \frac{S_e(K'_m + kS_e)}{K'_m + K'_m S_e + S_e^2},$$
$$\frac{\partial P_e}{\partial T} = D_{P_E} \frac{\partial^2 P_e}{\partial X^2} + \sigma^2 \frac{S_e(K'_m + kS_e)}{K'_m + K'_m S_e + S_e^2} \qquad (1)$$

where X is space, T – time, $S_e(X,T)$ and $P_e(X,T)$ are the concentrations of the substrate and product, respectively, K'_m is normalized Michaelis constant, k is the allosteric ratio, and σ^2 is the diffusion module. The governing equations (1) together with appropriate initial, boundary and matching conditions form an initial boundary value problem, which was numerically solved by applying the finite difference technique [3].

By varying the input parameters, the output results were numerically analyzed with a special emphasis to the influence of the model parameters on the allosteric effect of the biosensor response. Numerical experiments showed that the allosteric effect nonlinearly increases with decreasing the enzyme concentration as well as decreasing the thickness of the enzyme layer.

[1] F. W. Scheller, F. Schubert, *Biosensors* (Elsevier Science, Amsterdam, 1992).
[2] A. Villaverde. Allosteric enzymes as biosensors for molecular diagnosis. FEBS Letters **554**, 169–172 (2003).
[3] R. Baronas, F. Ivanauskas, J. Kulys, *Mathematical Modeling of Biosensors* (Springer, Dordrecht, 2010).
[4] J. D. Murray. *Mathematical Biology*, *I. An Introduction* (Springer-Verlag, New York, 2002).

RADIONUCLIDES DISPERSION MODELING IN LIGHT WATER REACTOR BUILDING COMPARTMENTS DURING HYPOTHETICAL NUCLEAR INCIDENT

Ignas Kazakevičius[1], dr. Evaldas Maceika[2]

[1] Faculty of Physics, Vilnius University
[2] Center for physical sciences and technology
ignas.kazakevicius@ff.stud.vu.lt

Nuclear energy performs a significant role in a world energy demand. By using this energy source we are able to ensure large capacity, diversified energy supply with stable baseload, low carbon electricity. However, for further nuclear energy development we need to ensure nuclear and radiological safety, which will overweight the cons and solve the problems related with this energy source. One of these methods is a radioactive contamination incident simulation and modeling, where the most important aspect is radionuclides dispersion into environment.

For this purpose we are using ASTEC (Accident Source Term Evaluation Code) program to simulate and to evaluate potential consequences of nuclear incident or accident. We are using one of several ASTEC modules CPA (Containment Part of the integral code Astec). This module calculate thermal hydraulics and aerosol behaviour in LWR (Light water reactor) technological channels and compartments. CPA module is composed of two parts: THY and AFP. First one calculates temperature and pressure variations and distributions, as well as heat exchange with compartment walls. Second, CPA-AFP module calculates aerosols dispersion and depletion. CPA principle is based on FIPLOC (Fission Product Localisation) code. By using this code we are able to model up to eight different aerosol component size classes. All relevant agglomeration processes, natural deposition processes and the droplet growth by fog formation are included. The aerosol retention by filters, water pools (pool scrubbing), and containment sprays is modeled. In the aerosol module all essential interactions thermal hydraulic phenomena, iodine behaviour, and decay heat are taken into account [1]. CPA modeling includes aerosols simulated phenomena behaviour of non-soluble and hygroscopic aerosols, fission product transport. Processes modeled for the simulation of aerosol behaviour: agglomeration, condensation on aerosols, sedimentation, diffusiophoresis, thermophoresis, diffusion and aerosols removal by spray [1].

We are using this code to evaluate fission radionuclide dispersion in Advanced Boiling Water Reactor (ABWR) building compartments due to some hypothetical incident.

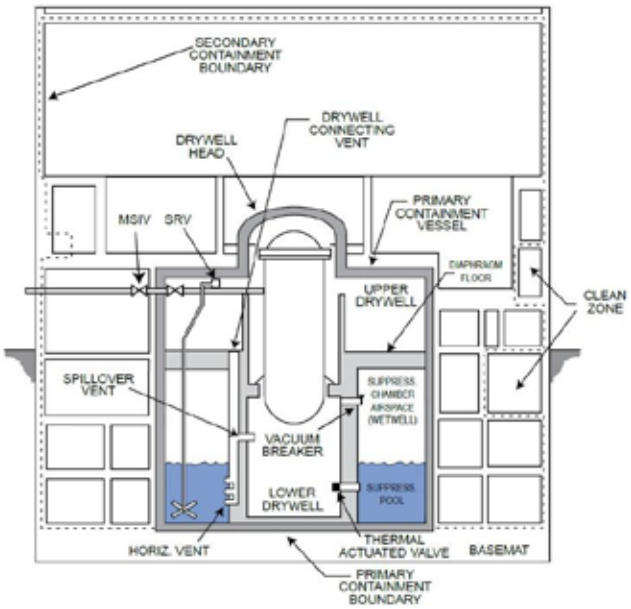

Fig. 1. ABWR reactor block scheme of modeled compartments [2].

[1] G. Weber, *ASTEC V0 Description of Aerosol Models in the Containment Part of ASTEC (CPA).*

[2] The ABWR Plant General Description, *GE Energy Nuclear Marketing* (2006)

IDENTIFICATION OF THE ENERGY SPECTRUM OF AUTOIONIZING STATES OF BARIUM EXCITED BY ELECTRON IMPACT

Gintaras Kerevičius

Department of the Theory of Atom, Institute of Theoretical Physics and Astronomy, Vilnius University, Saulėtekio Ave. 3, LT-10222, Vilnius, Lithuania
gintaras.kerevicius@tfai.vu.lt

Investigation of the energy spectrum of $5p^5 n_1 l_1 n_2 l_2 n_3 l_3$ J autoionizing states (AS) of Ba I is a complex task. Barium is a heavy alkaline metal atom ($Z = 56$), thus relativistic effects play a significant role. In light atoms one can ignore fine structure splitting and describe the states by using uncoupled total orbital L and spin S angular momenta, whereas in heavier atoms it is necessary to couple L and S to a total angular momentum J. The splitting is so apparent in Ba I, that the energy positions of particular AS from different terms ^{2S+1}L are interchanged, thus breaking the normal ordering. One of the reasons for this is the abscence of pure $(LS)J$ coupling in the AS of Ba I. The correlation effects between electrons in different states of heavy atoms are important, as gaps between the states become more narrow and in some cases unresolvable. This applies to Ba I also, because the gaps between AS with a sufficient excitation cross section σ and branching ratio B ($\sigma \cdot B \geq 0.05$ Mb) are of the order of $(10-100)$ meV in the investigated energy region of $(15.6-22.3)$ eV, except for a few states in the lowest energy region. The AS excited by electron impact are aligned, so there is an angular anisotropy in a measured ejected electron spectra observed with respect to the beam of incident electrons. There is a more specific complication to the problem, when some states of a particular configuration can have a corresponding potential with an inner and outer well. When an electron has a higher probability to be localized in the inner well of the potential, a so called collapse of the wave function occurs. This phenomenon is apparent for states of some configuration with the nf or (and) nd shell included. In the case of Ba I, this is observed for specific AS in configurations of type $5p^5 n_1 d n_2 l_2 n_3 l_3$, e. g. $5p^5 5d6s^2$. As a result, specific AS originating from the parent term ^{1}P, e. g. $5p^5(^2P)5d(^1P)6s^2\ ^{2S+1}L_J$, have much higher energy than AS with the parent term ^{3}P. Difficulties mentioned in this paragraph were also encountered in the previous work on Rb I [1] and Cs I [2]. Complications associated only with AS of Ba I, are described in the next paragraph.

Previous work [1, 2] on $mp^5 nln'l'$ J Auger states of alkali metal atoms Rb I ($m = 4$) and Cs I ($m = 5$) was more simple. The Auger states could only autoionize via one decay channel, i. e. $mp^6 \varepsilon\lambda$, leaving the ion in the ground state $mp^6\ ^1S_0$. Other excited states of the ion were energetically forbidden, thus only the width of an Auger line was proportional to the decay probability, but not the intensity value itself. Situation is different in the Ba I case. The $5p^5 n_1 l_1 n_2 l_2 n_3 l_3$ J AS can autoionize via $5p^6 n_4 l_4 \varepsilon' \lambda'$ decay channels, leaving Ba II in the ground or an excited state. Furthermore, if the AS of Ba I has a sufficiently high energy (more than 21 eV) it can decay to the $5p^5 nln'l'$ J Auger states of Ba II. The latter decay path is about an order of magnitude more probable than the former. This somewhat separates high energy AS from other AS in an ejected electron spectrum. Our preliminary calculations show, that $5p^5 nln'l'$ J Auger states of Ba II populate a wide ejected electron energy region, including the region of $5p^5 n_1 l_1 n_2 l_2 n_3 l_3$ J AS of Ba I. The Auger states of Ba II can be excited from Ba I ground state $5p^6 6s^2\ ^1S_0$ by a direct (simultaneous ionization-excitation) and indirect (two-step ionization and excitation) process. The processes have sufficient and in some cases very high excitation cross sections, e. g. 33 and 44 Mb, 1.1 and 1.7 Mb (with 912 Mb ionization to $5p^5 6s\ ^2S_{1/2}$ ground state) for $5p^5 6s^2\ ^2P_{1/2,3/2}$, respectively. Keep in mind, that $5p^5 nln'l'$ J Auger states of Ba II atoms can be populated by the autoionization of high energy $5p^5 n_1 l_1 n_2 l_2 n_3 l_3$ J AS of Ba I atoms. Therefore, a full treatment of the problem would require to solve time-dependent kinetic equations.

Fortunately, there is a one simplification to all investigations mentioned above. Our calculations show, that radiative decays of $5p^5 n_1 l_1 n_2 l_2 n_3 l_3$ J AS of Ba I and $mp^5 nln'l'$ J Auger states of Rb I ($m = 4$), Cs I and Ba II ($m = 5$) are 3 to 4 orders of magnitude less probable than autoionizing decays. Then the corresponding branching ratios B depend only on the autoionization probabilities of all decay paths of a particular state.

Calculations of excitation energies, electron impact excitation cross sections and autoionization probabilities of the $5p^5 n_1 l_1 n_2 l_2 n_3 l_3$ J AS of Ba I were performed by using the Flexible atomic code [3]. Relativistic radial orbitals were calculated by solving the self-consistent field Dirac-Fock-Slater equations. The potential was optimized on singly excited $5p^5 6s n_0 l_0$ J states of Ba I and the exchange part was approximated by the Slater potential. The latter, $5p^5(5d, 6s)^2 n_3 l_3$ J and $5p^5(5d, 6s) n_2 l_2 n_3 l_3$ J states were used to take into account the correlation effects. Cross sections were calculated by using the distorted-wave, autoionization probabilities – distorted-wave and isolated resonance approximations. The angular part of wave functions was transformed from the $(jj)J$ to $(LS)J$ coupling scheme of angular momenta.

A paper on identification of the experimental energy spectrum of $5p^5 n_1 l_1 n_2 l_2 n_3 l_3$ J AS of Ba I excited by electron impact was submitted [4]. Theoretical methods described in the previous paragraph were used for the identification [4].

[1] A. Kupliauskienė and G. Kerevičius, Theoretical study of the $4p^5 nln'l'$ autoionizing states of Rb excited by electron impact, Phys. Scripta **88**, 065305(7pp) (2013).

[2] G. Kerevičius and A. Kupliauskienė, Classification of the $5p^5 nln'l'$ LSJ energy levels of Cs excited by 30 eV electrons, Lith. J. Phys. **55**, 84-91 (2015).

[3] M.-F. Gu, The flexible atomic code, Can. J. Phys. **86**, 675-689 (2008).

[4] V. Hrytsko, G. Kerevičius, A. Kupliauskienė, O. Zatsarinny and A. Borovik, The 5p autoionization spectra of Ba atoms excited by electron impact: Identification of lines, submitted to J. Phys. B: At. Mol. Opt. Phys. (2016).

CALCULATION OF FIVE PARTICLE HARMONIC-OSCILLATOR TRANSFORMATION BRACKETS IN TRANSLATIONAL INVARIANT BASIS

Augustinas Stepšys[1], Saulius Mickevičius[2], Darius Germanas[3], Ramutis Kazys Kalinauskas[3]

[1]Department of Theoretical Physics,Faculty of Physics of Vilnius University, Saulėtekio Avenue 9,build. 3, 10222, Vilnius , Lithuania

[2]Vytautas Magnus University, K. Donelaičio str. 58, LT-44248, Kaunas, Lithuania

augustinas.stepsys@ff.stud.vu.lt

A basis of harmonic-oscillator functions is extremely useful and efficient in describing compact quantum systems, such as nucleons. The traditional applications, such as the nuclear shell model, are based on model Hamiltonian with individual one-particle variables. As a result, the corresponding model wave functions are not translational invariant and such model system is not properly represented because of center of mass (c.m.) motion[1]. One of the possible solutions for c.m. motion elimination is based on direct construction of the many-fermion wave function, which is independent from c.m. coordinate[2]. In this case, the harmonic-oscillator basis set in terms of intrinsic (Jacobi) coordinates is necessary. The set of HO functions can be chosen in a such manner than the transformation from one set of Jacobi coordinates to another results in expansion with a finite number of terms. This approach requires the Talmi-Moshinsky transformation[3, 4] and corresponding brackets.

In ab-initio many body system calculation it is useful to use coupled cluster models. The N identical particle system could be divided in two subclusters with N_1 and $N_2 = N - N_1$ particles respectively. If the each subcluster has its own intrinsic antisymmetrization the two body transposition operator $P_{N_1 N}$ is useful to secure the antisymmetry of the whole system[5]. This operator transforms Jacobian coordinates depending on clusterization and the initial antisymetrization of N particle system.

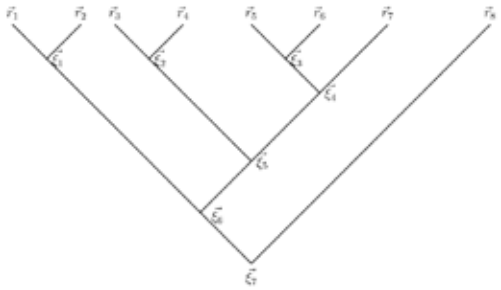

Fig. 1. Example of Jacobi tree for 8 particles composed of subsystems of 7 and 1 particle.

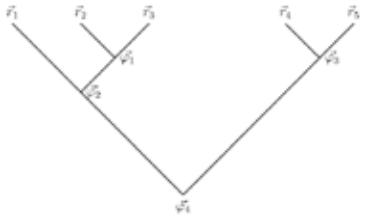

Fig. 2. Example of Jacobi tree for 5 particles composed of subsystems of 3 and 2 particles.

We present an independent scheme of transformations suitable for the N particle system consisting of subsystems composed of $N-1$ and 1 (Fig.1) or $N-2$ and 2 (Fig.2) particles, where the subsystems have intrinsic clusterization. Expressions for corresponding harmonic oscillator transformation brackets for five particles (5HOB) are presented and the examples of few body fermion systems where 5HOB can be applied are shown.

[1] G.P Kamuntavicius, R.K. Kalinauskas, B.R. Barrett, S. Mickevicius, D. Germanas, The general harmonic-oscillator brackets: compact expression, symmetries, sums and Fortran code, Nucl. Phys. A **695**, 191-201 (2001).

[2] P. Navratil, G.P. Kamuntavičius, B.R. Barrett, Few-nucleon systems in a translationally invariant harmonic oscillator basis, Phys. Rev. C, **61**, 044001 (2000).

[3] I. Talmi, Nuclear spectroscopy with harmonic-oscillator wave-functions, Helv. Phys. Acta, **25**, 185-234 (1952).

[4] M. Moshinsky, Transformation brackets for harmonic-oscillator functions, Nucl. Phys., **13**, 104-116 (1959)

[5] S. Mickevičius, D. Germanas, R.K. Kalinauskas Method simplifying Calculation of Coefficients of Fractional parentage for Translationally Invariant Shell-Model, 2013

THEORETICAL STUDY OF NEW TYPE OF VECTOR BESSEL BEAMS

Ada Gajauskaitė[1,2], Sergej Orlov[2], Gediminas Račiukaitis[2]

[1] Department of Quantum Electronics, Faculty of Physics, Vilnius University
[2] Center for Physical Sciences and Technology, Savanoriu ave 231, Vilnius Lithuania
ada.gajauskaite@ff.stud.vu.lt

Bessel beams belongs to a class of nondiffracting beams which transverse intensity profile does not change in free space propagation. Nondiffracting beams were found as a solution to the scalar Helmholtz wave equation in cylindrical coordinates [1] and for the first time experimentally showed by Durnin in 1987 [2]. Beam solutions to the scalar wave equation do not represent the polarization state of beam. Also, in a paraxial approximation electric field has nonzero divergence and therefore does not satisfy Maxwell's equations in the exact sense [3]. Contrary to scalar beams, vector beams exactly fulfill Maxwell's equations and can be formed with various polarizations (radial, azimuthal, circular or linear).

In our work vector Bessel beam solution was found using method described by Stratton [1]. By using the scalar Bessel beam function ψ, three vectorial fields **L**, **M**, **N** were obtained with the following definitions:

$$\mathbf{L} = \nabla\psi\,,\ \mathbf{M} = \mathbf{L}\times\mathbf{a}\,,\ \mathbf{N} = \frac{1}{\mathrm{k}}\nabla\times\mathbf{M}$$

where k – wavenumber of the beam, **a** – arbitrary vector. Vectors **M** and **N** represent fields **E** and **H** respectively. In our case arbitrary vector is **a** = (*x*,*y*,*z*). This novel type of vector Bessel beam has a spherical 3D doughnut placed in its distinct focal line (fig. 1). In this work, we also analyze how the curvature of produced 3D doughnut can be controlled and discuss the far field structure of such vector beams.

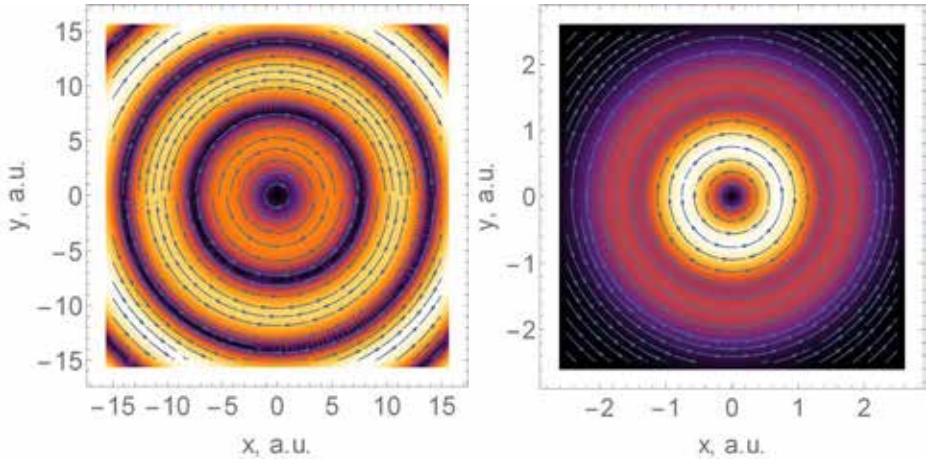

a) b)

Fig. 1. Transverse intensity profile of vector Bessel beam (a) and vector Bessel-Gauss beam (b) (x,y scale in arbitrary units)

This type of vector Bessel beam as well as vector Bessel-Gauss beam has dark focus in the center of beam surrounded by region with higher intensity. However, vector Bessel beam has infinite number of intensity rings and has infinite energy thus can not be experimentally realized. Intensity profile in fig. 1 (b) has the structure of so called optical bottle beam, which has potential application in guiding and binding of micro-particles [4] and in optical tweezers system [5].

[1] J.A. Stratton, IEEE Antennas, and Propagation Society. Electromagnetic Theory. An IEEE Press classic reissue. Wiley, 2007.
[2] J. Durnin. Exact solutions for nondiffracting beams. I. The scalar theory. Journal of the Optical Society of America A, 4(4):651, 1987.
[3] P. L. Greene and D. G. Hall. Properties and diffraction of vector Bessel-Gauss beams. Journal of the Optical Society of America A, 15(12):3020-3027, Dec 1998.
[4] T. Čižmár, L. C. Dávila Romero, K. Dholakia, and D. L. Andrews. Multiple optical trapping and binding: new routes to self-assembly. Journal of Physics B: Atomic, Molecular and Optical Physics, 43(10):102001, 2010.
[5] V. G. Shvedov, C. Hnatovsky, A. V. Rode, and W. Krolikowski. Robust trapping and manipulation of airborne particles with a bottle beam. Optics Express, 19(18):17350-17356, Aug 2011.

ANOMALOUS DIFFUSION AND POWER LAW STATISTICS

Rytis Kazakevičius, Julius Ruseckas

Institute of Theoretical Physics and Astronomy, Vilnius University, Lithuania
rytis.kazakevicius@tfai.vu.lt

One of the fundamental aspects of complex systems are the transport properties. Transport properties in complex systems are usually characterized by anomalous scaling, that is by a non-linear time dependency in the growth of the variance, $\sigma^2(t) \sim t^\mu$, where t is the elapsed time. This condition is known as an anomalous diffusion. In contrast to the anomalous diffusion, in a typical diffusion process the variance of the particle position (or mean squared displacement) is a linear function of time. Anomalous diffusion is classified by its power law exponent μ. If $\mu > 1$, the phenomenon is called super-diffusion. Super-diffusion has been experimentally observed in a study of tracer particles in a two-dimensional rotating flow [1]. If $\mu < 1$, the particle undergoes sub-diffusion. Sub-diffusion has been proposed as a measure of macromolecular crowding in the cytoplasm [2]. Experimental studies shows that anomalous scaling of variance and power law statistics (power law spectral density (PSD) and power law steady state probability densities (PDF)) can occur together[3]. Usually, these processes are modeled as separate and independent. So there is a need for model describing a system with bought anomalous diffusion and power law statistics.

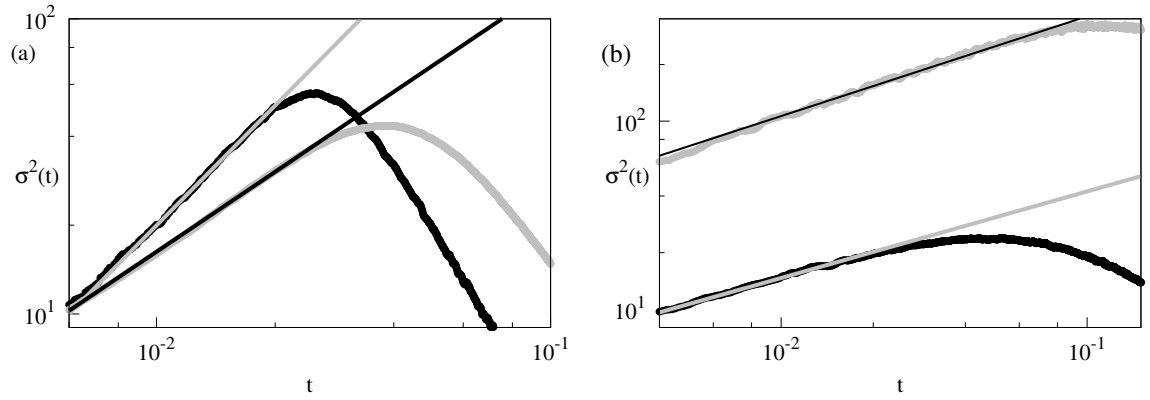

Fig. 1. Dependence of the variance $\sigma^2(t)$ of the signal generated by Eq. (2) on time t. The stability index of Lévy noise $\alpha = 1$ and power law exponent $\lambda = 3$. Gray and black strait lines show the power law dependence of the variance on time, $\sigma^2 \sim t^\mu$. (a) Black curve corresponds to $\eta = 2.8$, gray curve to $\eta = 2.9$. The numerically determined values of the index μ are $\mu = 1.35$ and $\mu = 0.9$, respectively. (b) Black curve corresponds to $\eta = 2.4$, gray curve to $\eta = 2.1$. The numerically determined values of the index μ are $\mu = 0.5$. Eq. (2) is solved with reflective boundary conditions $x_{min} = 1$, $x_{max} = 10^4$.

Stochastic differential equation (SDE) that generate signals with power law statistical properties have been proposed

$$\mathrm{d}x = \left(\eta - \frac{1}{2}\lambda\right) x^{2\eta-1}\mathrm{d}t + x^\eta \mathrm{d}W(t)\,. \tag{1}$$

However, proposed SDE generated signals variance do not exhibit anomalous power law growth [4]. The simplest known model of super-diffusion is Lévy α stable process L_t^α. We modified Eq. (1) by replacing Wiener W_t process to Lévy stable process L_t^α

$$\mathrm{d}x = \gamma(\eta,\lambda,\alpha) x^{\alpha(\eta-1)+1}\mathrm{d}t + x^\eta \mathrm{d}L_t^\alpha\,. \tag{2}$$

Proposed SDE generate signals with power law PDF ($P(x) \sim x^{-\lambda}$) and spectral density $S(f)$

$$S(f) \sim \frac{1}{f^\beta}\,, \qquad \beta = 1 + \frac{\lambda - 3}{\alpha(\eta-1)}\,. \tag{3}$$

In addition, numerical results show that due to presence of the multiplicative Lévy α stable noise process in Eq. (2) both sub-diffusion and super-diffusion can occur (see Fig. 1). This is in contrast to the SDEs with additive stable stochastic process, when only sub-diffusion is possible unless more complex non-Markovian models are used [5].

In conclusion, we have proposed nonlinear stochastic differential equations driven by Lévy α stable process that generate signals exhibiting power law statistical properties. In addition, such nonlinear SDEs can lead to Lévy flights with anomalous diffusion, both sub-diffusion and supper-diffusion.

[1] T. H. Solomon, E. R. Weeks, H. L. Swinney, Observation of anomalous diffusion and Lévy flights in a two-dimensional rotating flow, Phys. Rev. Lett. **71** 3975 (1993).
[2] M. Weiss, M. Elsner, F. Kartberg et al., Anomalous subdiffusion is a measure for cytoplasmic crowding in living cells, Biophys. J. **87** 3518 (2004).
[3] C. Scalliet, A. Gnoli, A. Puglisi et al., Cages and Anomalous Diffusion in Vibrated Dense Granular Media, Phys. Rev. Lett. **114**, 198001 (2015).
[4] A. G. Cherstvy and R. Metzler, Nonergodicity, fluctuations, and criticality in heterogeneous diffusion processes, Phys. Rev. E **90**, 012134 (2014).
[5] R. Metzler and J. Klafter, The random walk's guide to anomalous diffusion: a fractional dynamics approach, Phys. Rep. **339**, 1-77 (2014).

ABSORPTION ENHANCING OF ELECTROMAGNETIC WAVE IN GRAPHENE BY PERIODIC GRATING

Yakovleva Marina

Department of Physics, Belarusian State University, Belarus
yakovlevmarin@gmail.com

Since the discovery of graphene, its remarkable properties make this 2D material and graphene based structures very promising for material-based applications and nanoelectronics. The unusual electronic properties of graphene are the result of high electron mobility and, consequently, high conductivity which are very important for different applications [1]. As a result graphene has a high absorption in microwave and terahertz that may be used for shielding in this range which is important for graphene practical application. For some applications it is required absorption rather than reflection. High absorption of graphene can be used for sensing and shielding applications [2].

The present work considers effect of absorption enhance in graphene by using of periodic metallic grating. The grating couples incident wave with graphene plasmons [3].

Interaction of plane electromagnetic waves with metallic grating (as shown in Fig. 1) was calculated depending on the frequency of the radiation and the angle of its incidence.

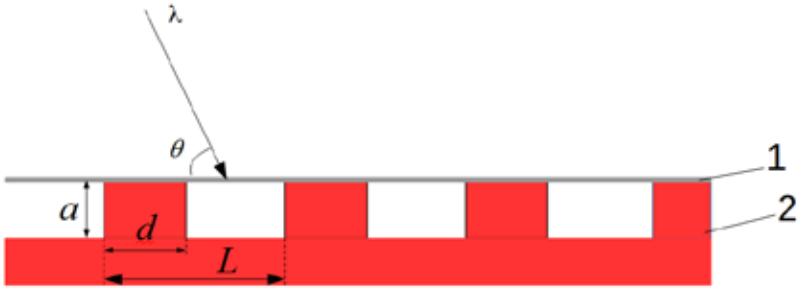

Fig. 1. Schematic representation of the study system: 1 – graphene monolayer, 2 – periodic metallic grating, where L is the grating periodicity, a is the groove height, and $L - d$ is its length.

The Floquet EM functions for this structure were calculated using boundary conditions for fields on the metal edges and graphene sheet. The calculations revealed for some combinations of wavelengths and angles of incidence such system absorbs more than 70% of the incident electromagnetic radiation in the graphene film which absorbs ~ 25% without grating [2].

This effect can be applied different branches of science and technic.

[1] K. Batrakov, P.Kuzhir, N. Valynets, S.Voronovich, T. Kaplas, Y.Svirko, Ph. Lambin, Terahetrz propertiez of graphene sandwich srtuctures, Physics Chemistry and Applications of Nanostructures Proceedings of International Conference Nanomeeting-2015, pp 218-221.
[2] K. Batrakov, P. Kuzhir, S. Maksimenko, A. Paddubskaya, S. Voronovich, Ph Lambin, T. Kaplas & Yu Svirko, Flexible transparent graphene/polymer multilayers for efficient electromagnetic field absorption Scientific Reports 4 : 7191 (2014).
[3] Bo Zhao and Zhuomin M. Zhang, Strong Plasmonic Coupling between Graphene Ribbon Array and Metal Gratings, ACS Photonics, 2 (11), pp 1611–1618 (2015).

HALOGEN BOND, HYDROGEN BOND – NONCOVALENT INTERACTIONS IN THE Cl-, Br-COMPLEXES

Aneta Lutyńska, Małgorzata Domagała, Marcin Palusiak

Department of Theoretical and Structural Chemistry, Faculty of Chemistry, University of Lodz
anetas@uni.lodz.pl

Since last a few years the halogen bond (X-bond) became one of the most thoroughly investigated noncovalent interaction [1,2]. This type of interaction is acting between the electron-acceptor fragment (Lewis acid) and electron-donor fragment (Lewis base). The cooperativity between H-bond and X-bond can be expected in systems shown in Figure 1. We analized complexes (RX)(HNC)(NCH), where R=CH_3, CF_3 and X=Cl, Br are schematically illustrated in Figure 1. The complexes of molecules are stabilized by two different noncovalent interactions, which can be classified as halogen bond and hydrogen bond.

The geometries of studied systems were optimized at ωB97XD/aug-cc-pVTZ using the Gaussian 09 program [3]. The energetic and structural properties of all complexes were tested against the topological parameters of the electron density distribution obtained by means of a Quantum Theory of „Atoms in Molecules" (QTAIM) [4]. Finally, we establish the influence of CP-corrected optimization the geometries and interaction energies of the trimmers. If the X=Cl or X=Br will be called Cl-complex and Br-complex, respectively. The CP procedure was also taken into account during optimization [5,6], which means that the resulting geometry may be different from that obtained by the standard optimization.

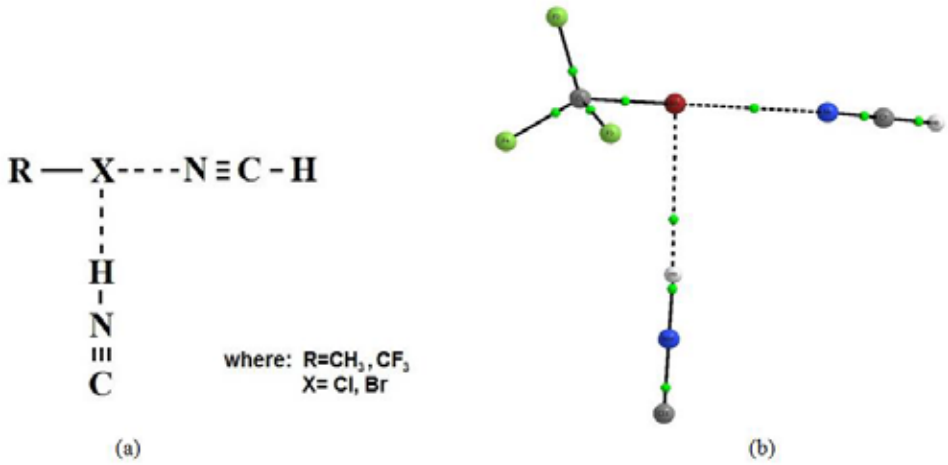

Fig. 1. Spatial arrangement of interacting fragments (monomers) in complexes (trimmers) of halogen atom (a). The Br-complex is shown as an example (b). In the case of the Cl-complex the spatial arrangement was practically the same.

[1] P. Politzer, J.S. Murray, T. Clark, Halogen bonding: an electrostatically-driven highly directional noncovalent interaction, Phys. Chem. Chem. Phys. **12**, 7748–7757 (2010).
[2] A.C. Legon, The halogen bond: an interim perspective, *Phys. Chem. Chem. Phys.* **12**, 7736–7747 (2010).
[3] M.J. Frisch, et. al., *Gaussian 09; Gaussian, Inc*.: Wallingford, CT, (2009).
[4] R. F. W. Bader, *Atoms in Molecules: A Quantum Theory*, Oxford University Press: New York, (1990).
[5] S. Simon, M. Duran, J.J. Dannenberg, How does basis set superposition error change the potential surfaces for hydrogen-bonded dimers?, J Chem. Phys. **105,** 11024–11032 (1996).
[6] W.-Z. Wang, X.-M. Pu, W.-X. Zheng, N.-B. Wong, A.-M. Tian, On the importance of CP-corrected gradient optimization in the study of hydrogen bonded systems, Chin. J. Chem. **21**, 1586–1590 (2003).

RELATIVE RAMAN LINE INTENSITIES OF BENDING HOH VIBRATIONS AS IMPORTANT FACTOR OF LOCAL WATER STRUCTURE.

Maryia Zhuk[1], Irina Doroshenko[2],Valery Pogorelov[2],Valdas Sablinskas[3],Vitas Balevicius[3], Lars G. M. Pettersson[4], George Pitsevich[1].

[1] Department of Physical Optics, Belarusian State University,Minsk, Belarus
[2]National Taras Shevchenko University, Kyiv, Ukraine
[3]Vilnius University, Vilnius, Lithuania
[4]Department of Physics, AlbaNova University Center, Stockholm University, Stockholm, Sweden
zhuk_maryia@mail.ru

Water is an interesting and important object for spectroscopic investigations. The local structure of water is still under debate [1], and any alternative new way to estimate it is very useful. Having this in mind, extensive Raman studies of bulk water in different phases and temperatures were made. It was found that the relative Raman line intensities of bending H-O-H vibrations are very sensitive to the phase structure of water. In Fig.1 one can see strong changes of relative intensities of this band during going from the liquid to solid phase (Fig. 1).

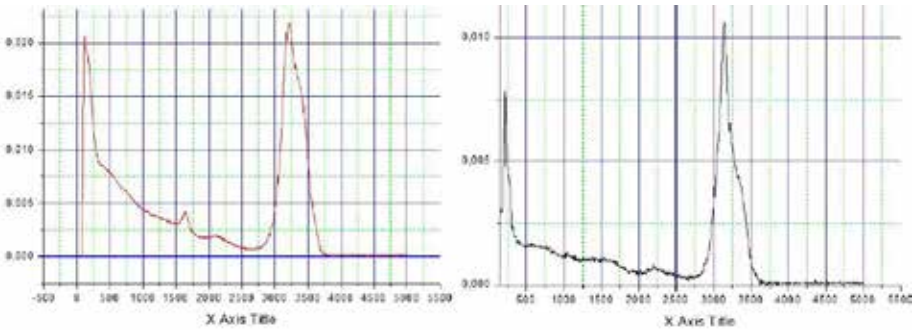

Fig.1. Raman spectra of water in (left) liquid (T=3^0 C) and (right) solid (T= - 4^0 C).

To find the reason for these changes some quantum-chemical calculations were made. The structure of a pentamer water cluster was optimized under tetragonal conditions using B3LYP/cc-pVTZ level of theory.

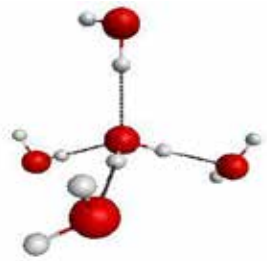

Fig.2. Structure of pentamer water cluster optimized under “tetragonal” condition.

In this model (see Fig. 2) we have one (central) molecule with two acceptor and two donor H-bonds, two molecules with only one donor H-bond and two molecules with only one acceptor H-bond. The Raman spectrum for this cluster was calculated. As one can expect the frequency of the bending vibration of water molecule increases when the number of donor H-bonds increases. For the Raman intensities of this mode the situation is different. The calculated intensity for this vibration is 10 times smaller in the case of double donor H-bonds and 5 times smaller in the case of single donor H-bond when comparing with molecules without donor H-bonds. Now we can analyze how the observed spectral changes are associated with the local structure of water. According to [2] liquid water is a mixture of HDL and LDL with 3:1 proportion. LDL has similar to ice at ambient condition a local structure where every water molecule has double acceptor and donor H-bonds. HDL has broken tetragonal structure where the water molecules on average have only one donor H-bond. So it is clear that the appearance of the 1630 cm^{-1} line in liquid water is mostly due to HDL. On the other hand, the near-absence of this line in solid water (in ice) is due to the fact that only molecules with double donor H-bonds are in this case. We hope that this approach can be developed for estimation of the LDL/HDL ratio at different temperatures and pressures.

[1] A. Nilsson, L.G.M. Pettersson Chem.Phys., **389** 1-38 (2011).
[2] Tokushima et al., Chem. Phys. Lett. **460** 387-400 (2008).

TWISTED INTERNAL CHARGE TRANSFER IN 1,8-NAPHTHALIMIDE DERIVATIVES WITH DIMETHYLAMINOBENZENE MOIETIES

Rokas Skaisgiris[1], Arūnas Miasojedovas[1], Alytis Gruodis[2],
Dalius Gudeika[3], Juozas V. Gražulevičius[3], Saulius Juršėnas[1]

[1]Institute of Applied Research, Vilnius Univeristy, Saulėtekio 9-III, LT-10222 Vilnius, Lithuania
[2]Department of General Physics and Spectroscopy, Vilnius Univeristy, Saulėtekio 9-III, LT-10222 Vilnius, Lithuania
[3]Department of Organic Technology, Kaunas University of Technology, Radvilenu pl. 19, LT- 50254, Kaunas, Lithuania
rokas.skaisgiris@ff.stud.vu.lt

1,8-Naphthalimide derivatives are widely used for various applications. They were applied in such fields as laser active media, anticancer agents, analgesics in medicine, fluorescent markers in biology, fluorescence switchers and sensors, as electron-transporting and emitting materials in light emitting diodes [1, 2]. Derivatives of 1,8-naphthalimide compounds generally have high electron affinity due to the existence of an electron-deficient center and can be easily functionalized. Meanwhile dimethylaminebenzene (DMAB) moieties are electron-rich and mostly known for they unusual dual fluorescence [3].

In this work we investigate photophysical properties of donor-acceptor systems composed of 1,8-naphthalimide (NI) with dimethylaminebenzene (DMAB) moiety linked through single C-C (NI1) and acetylene (NI2) bonds in the 4th position. The naphthalimide derivatives were synthesized by D. Gudeika from prof. J. V. Gražulevičius group at Kaunas University of Technology (KTU).

Theoretical DFT calculations revealed that in the ground state NI1 compound shows rotation angle of 51° between naphtalimide and DMAB and 9° dihedral angle between benzene ring and dimethylamine, while NI2 possess flat configuration (Fig. 1.). For both molecules the electron density is distributed between naphtalimide and DMAB moieties in ground state. The electron density for HOMO is mostly localized in DMAB moieties for both compounds. In the excited state both complexes rotate up to 90° and the charge density is localized on the naphthalimide moieties, thus showing twisted internal charge transfer (TICT). When molecules twist perpendicular oscillator strength for the lowest energy transitions becomes 0, hence restricting transitions.

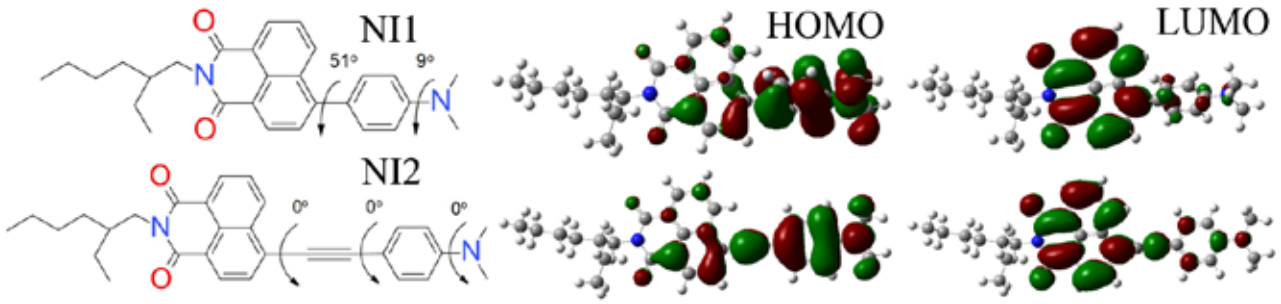

Fig. 1. Structural models with optimized dihedral angles indicated and electron density distributions for highest occupied molecular orbital (HOMO) and lowest unoccupied molecular orbital (LUMO) of 1,8-naphthalimide compounds.

The solvatochromic investigation of absorption and fluorescence spectra in medium of various polarity (0–3.96 D) approved a formation of twisted internal charge transfer states. Absorption spectra shows a broad structureless band at around 425 nm typical to charge transfer state. Also a small peak is observed at 350 nm typical for 1,8-naphthalimide locally excited (LE) state. The TICT state of NI2 absorbs twice as much light as NI1 supporting theoretical oscillator strength calculations. The color of fluorescence varies in the visible range of spectrum from 470 nm in non-polar solvent to 770 nm in the most polar solvent while the quantum yield is quenched from 82 % to 0.3 % respectively which is consistent with theoretical calculations. Strong fluorescence dependency on solvent polarity can be applied in medium polarity sensors.

Further investigation showed that some specific cations (such as Hg^{2+}) can change photophysical properties drastically. Absorption and fluorescence typical for TICT is quenched meanwhile peaks at 350 nm for absorption and 405 nm for fluorescence emerge. New bands exhibit similar properties in both molecules which are typical for 1,8-naphthalimide locally excited state. This means that cations interact with dimethylamine (DMA) moiety and disables its electron-donating properties prohibiting twisted internal charge transfer. This effect can be used to sensitively detect specific cations.

[1] H. Ulla, M. R. Kiran, B. Garudachari, M. N. Satyanarayan, G. Umesh, A. M. Isloor, Blue emitting halogen–phenoxy substituted 1,8-naphthalimides for potential organic light emitting diode applications, Optical Materials **37**, 311–321 (2014).
[2] J. Xie, Y. Chen, W. Yang, D. Xu, K. Zhang, Water soluble 1,8-naphthalimide fluorescent pH probes and their application to bioimagings, Journal of Photochemistry and Photobiology A: Chemistry **223**, 111–118 (2011).
[3] A. Ito, S. Ishizaka, N. Kitamura, A ratiometric TICT-type dual fluorescent sensor for an amino acid, Physical Chemistry Chemical Physics **12**, 6641–6649 (2010).

OPTIMISATION OF BIOSENSOR UTILIZING SYNERGISTIC SUBSTRATES CONVERSION

Linas Litvinas[1], Romas Baronas[1], Antanas Žilinskas[2]

[1]Faculty of Mathematics and Informatics, Vilnius University, Lithuania
[2]Institute of Mathematics and Informatics, Vilnius University, Lithuania
linas.litvinas@mif.vu.lt

Biosensors are relatively cheap and reliable devices capable to resolve a large number of analytical problems in clinical diagnostic, environmental and industrial fields. The biosensor response is determined by the catalytical substrate conversion to a reaction product. In a case of amperometric biosensors the response is a result of the oksidation-reduction reaction on a surface of electrode. The concentration of the analyte is usually proportional to the measured current and can be determined by the calibration curve. In the simplest Michaelis-Menten scheme the substrates are directly converted to the products. In a more complex synergistic scheme, an enzyme catalyzes the parallel conversion of substrates into the products, with the concomitant cross reactions of the substrates and the products [1].

A biosensor must meet user requirements for a range of the analyte concentrations - $K_M^{calc.}$, a level of the saturation current - $I\left({K_M}^{calc.}\right)$ and an enzyme amount - Ad_1E_0. The measurement range and saturation current should be high enough, while the enzyme amount should be low as enzyme usually is expensive. The biosensor utilizing synergistic substrates conversion involves multiple changeable parameters: the thicknesses of enzyme and dialysis membranes, the concentrations of the enzyme and two reaction mediators [1]. By varying these parameters multicriteria Pareto optimal solutions can be achieved. A digital model based on a mathematical model of the biosensor facilitate this. It has been used to fine-tune the analytical characteristics of the biosensors. An optimisation algorithm uses the Chebyshev scalarization technique to transform a multicriteria problem into the single criteria optimisation problem [2]. The Hooke-Jeeves single criteria optimisation algorithm was used due to fast convergence like gradient descent algorithms and it requires no gradient of the optimised function [3]. The achieved Pareto optimal results are depicted in Fig. 1 and can be used by experts in a design phase of a practical biosensor utilizing synergistic substrates conversion.

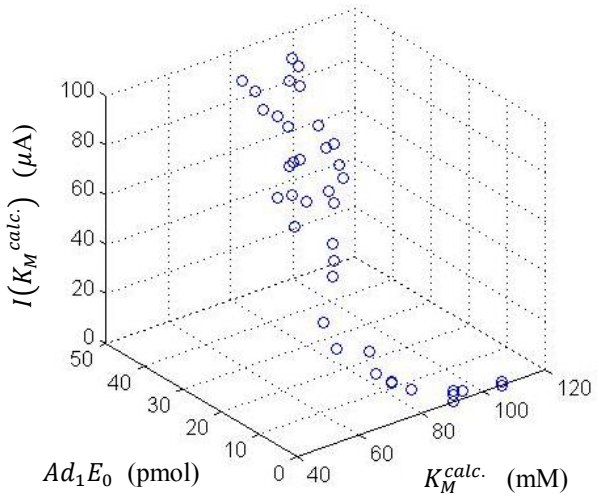

Fig. 1. Multicriteria Pareto optimal front.

[1] V. Ašeris, E. Gaidamauskaitė, J. Kulys et al., Modelling glucose dehydrogenase-based amperometric biosensor utilizing synergistic substrates conversion, Electrochimica Acta **146**, 752–758 (2014).

[2] G. Eichfelder, *Adaptive Scalarization Methods in Multiobjective optimization* (Springer-Verlag, Berlin, Heidelberg, 2008).

[3] R. Hooke, T.A. Jeeves, "Direct search" solution of numerical and statistical problems, Journal of the Association for Computing Machinery **8**, 212–229 (1961).

11THEORETICAL MODELLING OF OPTICALLY DETECTABLE MAGNETIC RESONANCES IN NITROGEN - VACANCY CENTRES IN DIAMOND

Laima Busaite, Reinis Lazda, Marcis Auzinsh, Janis Smits, Linards Kalvans, Agris Spiss

Laser Centre, University of Latvia, Rainis blvd. 19, Riga, Latvia, LV-1586
laima.busaite@lu.lv

The nitrogen vacancy (NV) center is a point defect in a diamond crystal lattice consisting of a carbon atom substituting nitrogen atom (N) and a vacancy (V) pair, see Fig. 1 (left) [1]. The energy level scheme (information used from [2]) used is shown in Fig. 1 (right)

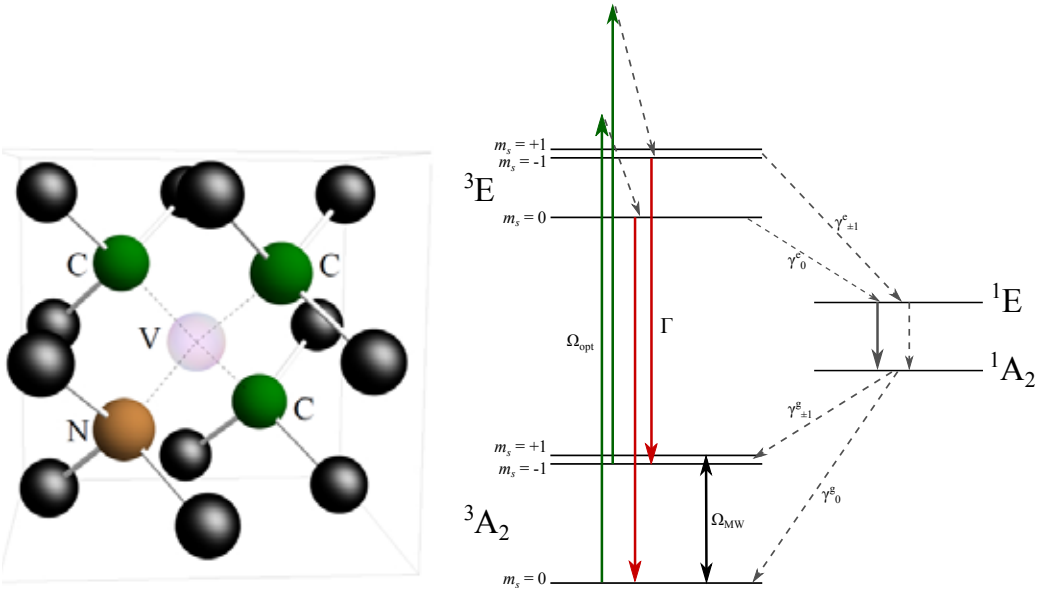

Fig. 1. Left - Schematic image of a NV center in a diamond lattice, black - carbon atoms, orange - nitrogen atom, white (transparent) - vacancy. Right - Considered energy level scheme of a NV center, where Γ, γ - relaxation rates, Ω_{opt} - pump laser Rabi frequency, Ω_{MW} - scanned microwave Rabi frequency.

The aim of the research is to create a theoretical model describing optically detectable magnetic resonances, using density matrix formalism. The model is based on Liouvile equation for density matrix evolution (1):

$$\dot{\rho} = \frac{1}{i\hbar}[H,\rho] - \frac{1}{2}\{\Gamma,\rho\} + \Lambda, \tag{1}$$

where the system Hamiltonian is described as

$$H_0 = g_e \mu_b \boldsymbol{BS} + \boldsymbol{S}\hat{\boldsymbol{D}}\boldsymbol{S}, \tag{2}$$

where the first term describe the Zeeman interaction of the spin **S** of the center with an external magnetic field **B** and second term takes into account the spin-spin interaction between two uncoupled electrons of the NV center [3].

The modelling of ODMR spectra is first done just taking into account the ground state levels, looking at population leaving and returning to these levels.

The model which takes into account also excited state levels, describing full interaction with light, is in progress.

Acknowledgements
This study was supported by the M-ERA.NET project MyND no. Z/15/1366.

[1] Lloyd C.L. Hollenberg et al., Physics Reports **528** 1, 1-46 (2013).
[2] Dumeige et al., Phys. Rev. B **87**, 155202 (2013).
[3] A. P. Nizovtsev et al., Opt. Spectrosc. **108** (2), 230-238 (2010).

SIMULATION OF STRUCTURE AND ELECTRONIC SPECTRA OF 1,3,4-OXADIAZOLE CHROMOFORES

Ignas Gaižiūnas, Juozas Šulskus

Department of Theoretical Physics, Faculty of Physics, Vilnius Universety, Saulėtekio al. 9-III, LT-10222 Vilnius, Lithuania
ignas.gaiziunas@ff.stud.vu.lt

1,3,4-oxadiazoles are a class of significant heterocyclic compounds used in medicinal and pesticide chemistry, asymmetric organic synthesis, and polymer and materials science. 2,5-Diaryl-1,3,4-oxadiazoles are important materials used as red luminescent emitters with carrier-transporting ability, efficient electron transporting and hole blocking materials in organic light-emitting diodes (OLEDs)[1] The 1,3,4- and 1,2,4-oxadiazole moieties have been incorporated to many series of organic compounds due to their interest as electron transporting materials or their application in emission layers for OLEDS and in biology. Oxadiazole units have been extensively incorporated in dendrons and dendrimers to study their luminescent properties in nonmesomorphic materials. The highly branched structure of the dendrimer may improve the luminescence efficiency of the materials in films since their globular shape reduces intermolecular interactions. The well-defined architecture of dendrimers enables for the specific and controlled location of the oxadiazole moieties in the dendritic scaffold, and this feature favors the supramolecular organization required to obtain mesomorphic properties [2].

In this work we simulate spectral properties of 1,3,4-oxadiazole monomers and dimers (Fig. 2) by means of quantum chemical methods in order to explain the experimental spectra results of oxadiazole in chloroform solution and in thin films. Experimental spectra were provided by prof. V. Gulbinas group from Lithuanian Center of Physical Sciences and Technology.

Molecular ground-state structures of photochromic monomer and dimer were obtained by optimizing geometric parameters of investigated compounds. All optimizations were performed using electronic structure modeling suite *Gaussian09* [3]. DFT method [4-6] with hybrid functionals B3LYP, CAM-B3LYP, LC-BLYP and PBE1PBE and 6-31(2,p) basis set were used for optimization. Electronic excitation energy calculations were then carried out at the optimized geometries using TD-DFT and 6-31(2,p) basis set as implemented in *Gaussian09*. Vilnius University Faculty of Physics supercomputer [7] was used in this work.

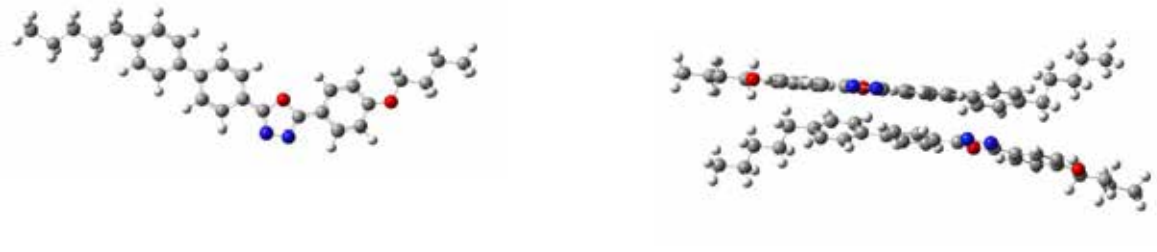

a **b**

Fig. 1 Investigated (a) monomers and (b) dimers of chromophores.

The TD-DFT calculations at b3lyp/631G(d,p) level reproduces the experimental absorption and fluorescence spectra of monomers and dimers in chloroform solutions (337 nm in absorption spectra and about 400 nm in fluorescence spectra in solutions). Experimental maximums at 400 nm and 550 nm in fluorescence spectra in PEI polymer thin films were not achieved by modeling chromophore dimers at equilibrium positions. The fluorescence spectra of PEI polymer thin films were reproduced when thin film was modelled by placing two separately optimized dimers in S0 and S1 states at closer distances (about 2 Å). On the ground of our theoretical simulations we can conclude that 550 nm band in fluorescence spectrum of polymers is caused by interaction of π electronic systems of chromophores in S0 and S1 states.

[1] Yun-Nan Yan, Wen-long Pan, Hua-Can Song , *The synthesis and optical properties of novel 1,3,4-oxadiazole derivatives containing an imidazole unit*, School of Chemistry and Chemical Engineering, Sun Yat-Sen University, Guangzhou 510275, China, Dyes and Pigments **86** (2010), 249.
[2] Silvia Hernandez-Ainsa, Joaquín Barbera, Mercedes Marcos and Jose Luis Serrano, *Liquid Crystalline Ionic Dendrimers Containing Luminescent Oxadiazole Moieties*, Macromolecules **45** (2012), 1006.
[3] Frisch M. J. et all. *Gaussian 09, Revision D.01* (2013), Gaussian, Inc., Wallingford CT.
[4] P. Hohenberg, W. Kohn, *Phys. Rev.* **136** (1964), B864.
[5] W. Kohn, L. J. Sham, *Phys. Rev.* **140** (1965), A1133.
[6] R. G. Parr, W. Yang, *Density-functional theory of atoms and molecules*, Oxford Univ. Press, Oxford, 1989.
[7] http://supercomputing.ff.vu.lt

3D STUDY OF OH AND CH_3 INTERNAL ROTATIONS COUPLING WITH LOW FREQUENCY BENDING C-C-O VIBRATION IN ETHANOL MOLECULE

Anastasiya Kapskaya[1], Alex Malevich[1], George Pitsevich[1]

[1]Department of Physical Optics, Belarusian State University, Minsk, Belarus
kapskaya.anastasiya@mail.ru

Kinematic and force interactions of hydroxyl and methyl tops in ethanol molecule were studied recently [1]. Good agreement between calculated and experimental frequencies of torsional vibrations was obtained. During the calculation of 2D PES for γ and φ internal rotation angles (see Fig. 1) optimization of the molecular structure on all remaining vibrational coordinates in each node of the mesh was made. This showed that most sensitive structure parameter to the γ and φ changes is C-C-O angle. To improve the results of calculations of torsional levels for hydroxyl and methyl tops the 3D PES for γ, φ and θ (where θ - natural bending coordinates for C-C-O angle) was calculated using B3LYP/cc-pVQZ level of theory. Just like in [1] we use Wilson's $\vec{s}$ vectors [2] for transformation of Schrödinger equation from Cartesian to natural coordinates. In doing so one can get following kinetic energy operator for internal rotations of two tops and bending C-C-O vibration in ethanol molecule if we neglect the first derivative of the wave function for torsion coordinates:

$$\begin{aligned}
&\left[-B_H\left[\left(\vec{s}^{\,\varphi}_{r7}\right)^2+\left(\vec{s}^{\,\varphi}_{r8}\right)^2+\left(\vec{s}^{\,\varphi}_{r9}\right)^2+\left(\vec{s}^{\,\varphi}_{r2}\right)^2+\left(\vec{s}^{\,\varphi}_{r3}\right)^2\right]-B_C\left[\left(\vec{s}^{\,\varphi}_{r6}\right)^2+\left(\vec{s}^{\,\varphi}_{r1}\right)^2\right]-B_O\left(\vec{s}^{\,\varphi}_{r4}\right)^2\right]\frac{\partial^2}{\partial\varphi^2}+\\
&\left[-B_H\left[\left(\vec{s}^{\,\gamma}_{r5}\right)^2+\left(\vec{s}^{\,\gamma}_{r2}\right)^2+\left(\vec{s}^{\,\gamma}_{r3}\right)^2\right]-B_C\left[\left(\vec{s}^{\,\gamma}_{r6}\right)^2+\left(\vec{s}^{\,\gamma}_{r1}\right)^2\right]-B_O\left(\vec{s}^{\,\gamma}_{r4}\right)^2\right]\frac{\partial^2}{\partial\gamma^2}+\\
&\left[-B_H\left[2\left(\vec{s}^{\,\gamma}_{r2}\cdot\vec{s}^{\,\varphi}_{r2}\right)+2\left(\vec{s}^{\,\gamma}_{r3}\cdot\vec{s}^{\,\varphi}_{r3}\right)\right]-B_C\left[2\left(\vec{s}^{\,\gamma}_{r1}\cdot\vec{s}^{\,\varphi}_{r1}\right)+2\left(\vec{s}^{\,\gamma}_{r6}\cdot\vec{s}^{\,\varphi}_{r6}\right)\right]-B_O 2\left(\vec{s}^{\,\gamma}_{r4}\cdot\vec{s}^{\,\varphi}_{r4}\right)\right]\frac{\partial^2}{\partial\gamma\partial\varphi}+\\
&\left[-B_C\left[\left(\vec{s}^{\,\theta}_{r6}\right)^2+\left(\vec{s}^{\,\theta}_{r1}\right)^2\right]-B_O\left(\vec{s}^{\,\theta}_{r4}\right)^2\right]\frac{\partial^2}{\partial\theta^2};
\end{aligned}\qquad (1)$$

where φ and γ torsional coordinates for CH_3 and OH internal rotations respectively, $B_H = 16.7346\ \text{см}^{-1}$, $B_C = 1.4043\ \text{см}^{-1}$, $B_O = 1.0544\ \text{см}^{-1}$, $\vec{s}^{\,\varphi}_{\gamma_i}$, $\vec{s}^{\,\gamma}_{\gamma_j}$, $\vec{s}^{\,\theta}_{\gamma_k}$ - Wilson $\vec{s}$ for φ, γ and θ coordinates, *i,,j,k*- atoms numbers according with Fig. 1

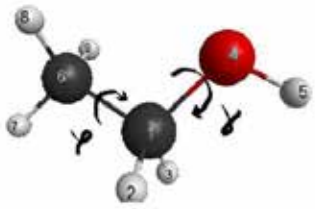

Fig. 1. Ethanol molecule with indication of atoms numbering and some vibrational coordinates.

Energy was calculated at the nodes of 3D uniform grid with sides $0 \le \gamma \le 2\pi;\ 0 \le \varphi \le 2\pi/3;\ 1.19 \le \theta \le 2.57$ with steps $\pi/6$, $\pi/12$ and $\pi/36$ respectively. Representing (1) in form:

$$F^{\gamma\gamma}(\gamma,\varphi,\theta)\frac{\partial^2\psi(\gamma,\varphi,\theta)}{\partial\gamma^2}+F^{\gamma\varphi}(\gamma,\varphi,\theta)\frac{\partial^2\psi(\gamma,\varphi,\theta)}{\partial\gamma\partial\varphi}+F^{\varphi\varphi}(\gamma,\varphi,\theta)\frac{\partial^2\psi(\gamma,\varphi,\theta)}{\partial\varphi^2}+F^{\theta\theta}(\gamma,\varphi,\theta)\frac{\partial^2\psi(\gamma,\varphi,\theta)}{\partial\theta^2};\qquad (2)$$

and expanding the kinematic coefficients and potential energy $U(\gamma,\varphi,\theta)$ in a three-dimensional complex Fourier series one can get the expression for elements of Hamiltonian matrix:

$$H_{(m'n'k')(mnk)} = -m^2F^{\gamma\gamma}_{m'-m,n'-n,k'-k}-9n^2F^{\varphi\varphi}_{m'-m,n'-n,k'-k}-3mnF^{\gamma\varphi}_{m'-m,n'-n,k'-k}-k^2F^{\theta\theta}_{m'-m,n'-n,k'-k}+U_{m'-m,n'-n,k'-k}\quad (3)$$

During calculations of energies and wavefunctions according with [1] better agreement between calculated and experimental frequencies was obtained.

[1] G. Pitsevich, A. Malevich, Ab initio determination of the far infrared spectra of some isotopic varieties of ethanol, Journal of Applied Spectroscopy, **82**, 540-553 (2015).
[2] E.B.Wilson,J.C.Decius,P.C.Cross Molecular Vibrations. Dover Publications Ink, New York, 1955

SIMULATION OF THE INTENSITY DISTRIBUTION OF THE VIBRONIC TRANSITIONS TO THE GROUND STATE FROM THE LOWEST EXITED STATES OF THE YbCs MOLECULE

Darya N. Meniailava, Maksim B. Shundalau

Department of Physics, Belarusian State University, Belarus
darhon.yo@gmail.com

Nowadays polar diatomic molecules comprising atoms of different alkali metals offer prospects for the realization of new forms of quantum matter with possible applications to quantum information [1]. The YbCs molecule is a heteronuclear polar diatomic dimer which has unpaired electron. This gives the molecule paramagnetic properties and opportunity to be manipulated by magnetic fields. An experimental search for a permanent electric dipole moment of the electron and for constructing lattice-spin models for quantum computing is also among possible applications of such a molecule. In this case it is necessary to know the exact forms of the potential energy curves (PECs) of the electronic states, as well as the spectral, energetic and dynamic characteristics of their rovibronic states. To predict the most probable vibronic transitions it is necessary to know its intensity. The intensity of vibronic transitions is proportional to the product of the Franck-Condon factors (FCFs) and fourth power of the transition frequencies. Thus FCFs are crucial for the simulation of the spectrum. The system of electronic states of the molecule YbCs has not been investigated experimentally and therefore calculations of the Franck-Condon factors are the actual task.

In this work we study the terms of the YbCs molecule corresponding to 2 asymptotic limits: Yb($6s^2$) + Cs(6s) which comprises ground state $X^2\Sigma^+$ and Yb($6s^2$) + Cs(6p) comprising $2^2\Sigma^+$, $1^2\Pi$. After applying the spin-orbit coupling (SOC) the states are altered into $X^2\Sigma^+_{1/2}$, $2^2\Sigma^+_{1/2}$, $1^2\Pi_{1/2}$ and $1^2\Pi_{3/2}$ respectively (Fig. 1). The terms of the molecule were obtained at SA-CASSCF(3,12)/XMCQDPT2 level of theory, taking into account the SOC by using the one-electron Pauli-Breit operator.

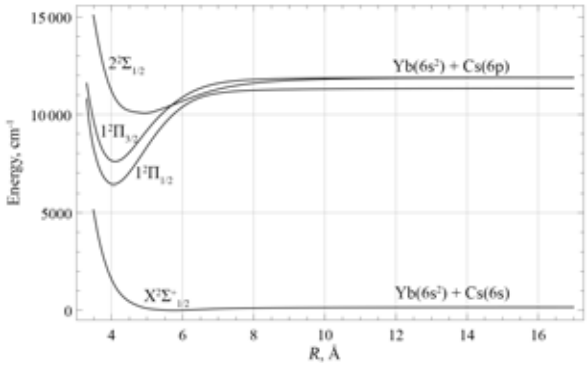

Fig. 1. Calculated at CASSCF(3,12)/XMCQDPT2 + SOC level of theory low-lying terms of the YbCs molecule.

The FCFs were calculated for the vibronic transitions between relevant ab initio states. These calculations were performed between the fixed vibrational level v' of the upper electronic state and the sequence of vibrational levels v'' of the ground electronic state (applying the selection rules $\Delta\Omega = 0$ or $\Delta\Omega = \pm 1$). The FCFs for $2^2\Sigma^+_{1/2} \rightarrow X^2\Sigma^+_{1/2}$, $1^2\Pi_{1/2} \rightarrow X^2\Sigma^+_{1/2}$ and $1^2\Pi_{3/2} \rightarrow X^2\Sigma^+_{1/2}$ transitions are shown in Fig. 2.

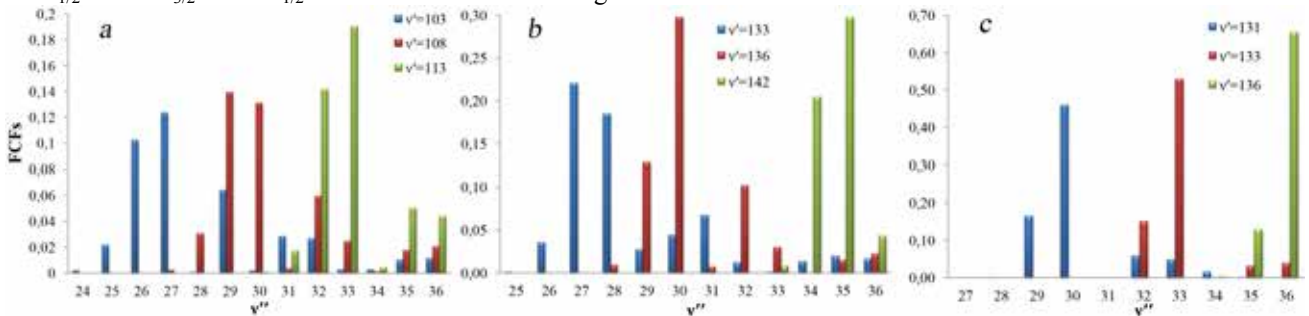

Fig. 2. The Franck–Condon factors for $2^2\Sigma^+_{1/2} \rightarrow X^2\Sigma^+_{1/2}$ transition (*a*): v'=103, 108, 113→ v''=24…36; $1^2\Pi_{1/2} \rightarrow X^2\Sigma^+_{1/2}$ transition (*b*): v'=133, 136, 142→ v''=25…36; $1^2\Pi_{3/2} \rightarrow X^2\Sigma^+_{1/2}$ transition (*c*): v'=131, 133, 136→ v''=27…36.

The equilibrium internuclear distances for $X^2\Sigma^+_{1/2}$, $2^2\Sigma^+_{1/2}$, $1^2\Pi_{1/2}$, $1^2\Pi_{3/2}$ are 5.775 Å, 4.950 Å, 4.025 Å and 4.100 Å respectively. From FCFs distribution (Fig. 2) it is seen that the most probable vibronic transitions are for states near the dissociation limits. For the $1^2\Pi_{3/2} \rightarrow X^2\Sigma^+_{1/2}$ transitions the nonzero FCFs have a distribution with larger values than for the other transitions under consideration.

[1] O. Dulieu, C. Gabbanini, The formation and interactions of cold and ultracold molecules: new challenges for interdisciplinary physics, Rep. Prog. Phys. **72**, 086401-1-086401-10 (2012).

MODELLNG OF ABSORPTION PROFILE OF THE PUMP RADIATION AND OUTPUT BEAM PARAMETERS FOR Nd:YAG MASTER OSCILLATOR IN MOPA-CONFIGURATION FOR SPACE LIDAR

Viktoryia Vatutsina, Konstantin Orexov

Department of Physics, Belorussian State University, Belarus
fiz.vatutina@bsu.com

Today, LIDARs are used for mapping the 3-D structure of Earth's from space [1]. The use of the laser in space at an altitude of 500 km has strict requirements for output power and beam quality. The aim of this study were the simulation of the profile of the absorption of the pump energy by diode one-side pumping in a cylindrical active element as well as the calculation of the quality of the laser beam taking into account thermo-optical effects for further experimental assembly.

The pump absorption profile was obtained using software Optichamber 2. There was a trade-off between efficiency and uniformity of the pumping profile. For a more uniform pumping profile is known to use non-cylindrical reflectors [2,3]. During the study of the absorption profile of the pump have been identified some trends in the choice of reflector for a more uniform beam.

For multiple configurations of the quantrons the total optical pumping efficiency reaches more than 65% at a satisfactory beam quality (see Fig.1) the uniformity of absorbtion profile increases if we use diffuse cavity reflector and wide placed diode bars.

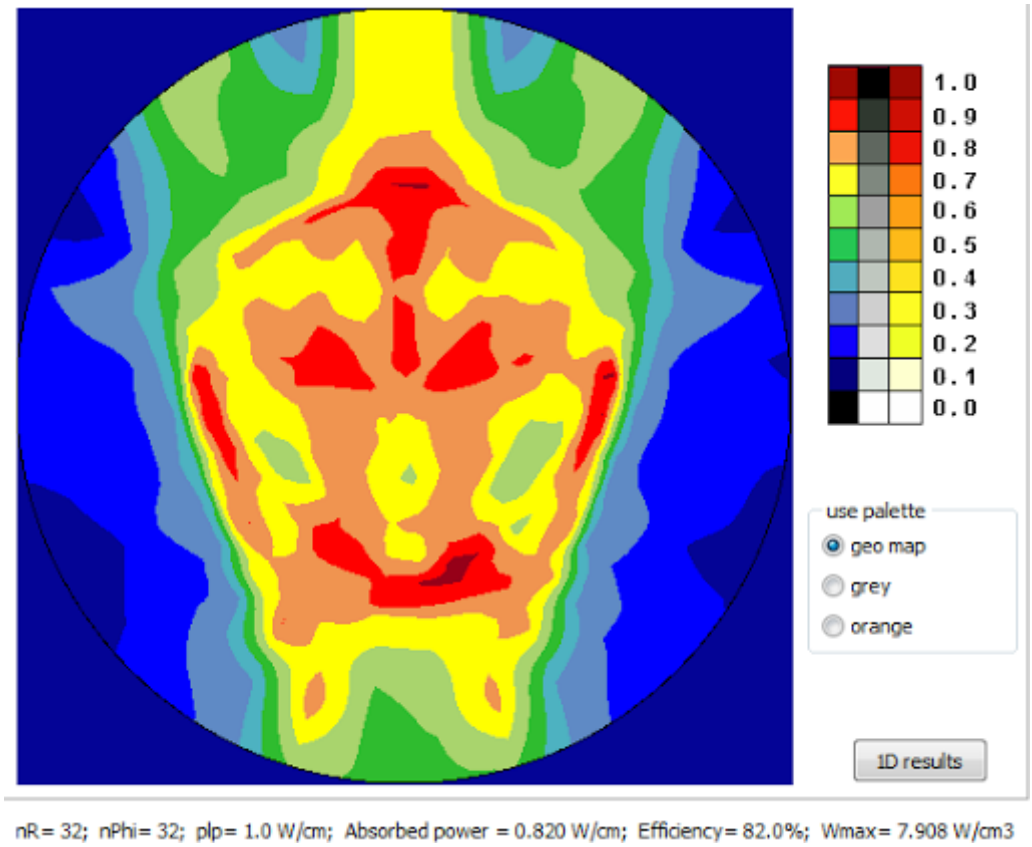

Fig. 1. Absorbed pump radiation profile for one of laser cavity configurations.

The beam parameters were calculated using Matrix Formalism and ABCD law. Effect of heating the rod, leading to a change in the refractive index in the parabolic approximation, is reduced to take into account the positive thin lens in cavity.

[1] Xiaoli Sun, James B. Abshire, Jan F. McGarry et al., Space Lidar Developed at the NASA Goddard Space Flight Center—The First 20 Years, IEEE Journal of selected topics in appl. earth observations and remote sensing, 1939-1404 (2013).
[2] Y.Hirano, T. Yanagisawa, S. Ueno et al., All-solid-state high-power conduction-cooled Nd:YLF rod laser, Optics Letters, Vol.25, 1168 (2000).
[3] K. Du, J. Zhang, M. Quade et al., Neodymium:YAG 30-W cw laser side pumped by three diode laser bars, Applied Optics, Vol. 37, 2361 (1998).

INVERSE FILTERING OF DEFOCUSED IMAGES USING CUDA TECHNOLOGY

Robert Chudek, Maciej Sypek

Faculty of Physics, Warsaw University of Technology, Poland
robert.chudek@student.fizyka.pw.edu.pl

With the introduction of easy graphic-card-based computing, new possibilities have emerged for image prossessing programists, with a new area of real-time image improving regardless of users technical background. Thanks to miniaturization of components, rise of a computing power, and unification of graphic card architectures real-time computing applications are available for masses. At the forefront of this process it is Nvidia with theirs CUDA Technology which enables easy multi-thread graphic card computing[1].

One of the fields that could benefit from that technology is optical analysis of defocused images. That is currently main area of interest of our group. Defocused image is formed when the observation plane (or the screen or camera matrix) is moved slightly ahead or behind the focus plane. A focus plane is an imaginary plane where the sharp image is formed for a given optical system. Because most of optical systems consist of a combination of lenses, the distance from the system to focus plane can be given with Eq. (1)[2].

$$\frac{1}{f} = \frac{1}{x} + \frac{1}{y} \tag{1}$$

With certain assumtions it is possible to depict every single linear optical system with the convolution integral (Eq. (2)), where all capital letters functions are Fourier Transform of appropriate function as shown on Eq. (3)), which gives us an opportunity to obtain the original image fast with only knowledge of the final image and optical system parameters[3]. Using Fourier Transform creates a possibility of further acceleration of the process by multi-thread computing and use of fast and optimized algorithms.

Despite the fact that theoretical work on this topic had been done long time ago, we do not hear about the development in the area of real-time defocused image improvement. In this project, we focus on creating an application that will be able to compute the original image with given optical system parameters and known output image in real time with camera connected to the computer, and will operate in real time.

$$F(\nu_x, \nu_y) = G(\nu_x, \nu_y) \cdot H(\nu_x, \nu_y) \tag{2}$$

$$G(\nu_x, \nu_y) = \mathscr{F}\{g(x,y)\} \tag{3}$$

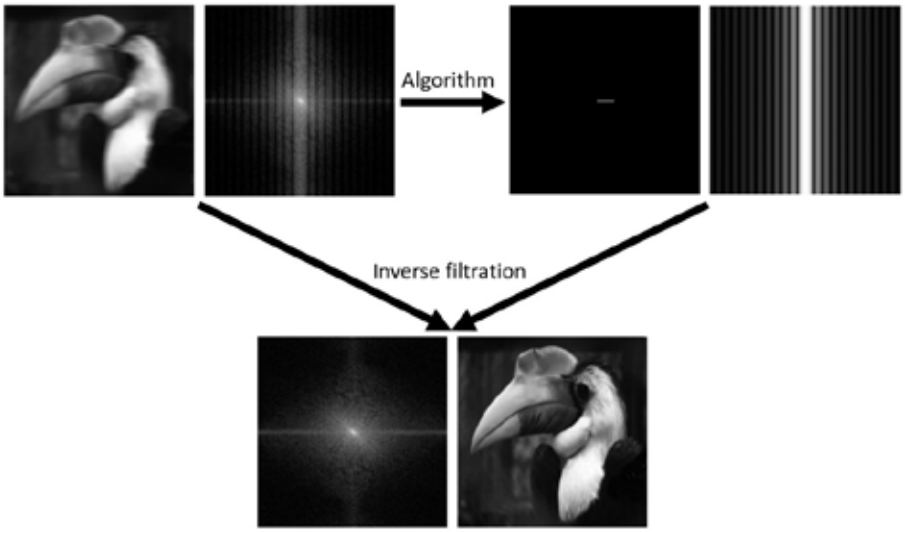

Fig. 1. Simulated process of inverse filtering.

[1] J. Russ, *The Image Processing Handbook 6th Ed.*,CRC Press, 2011.
[2] E. Hecht, *Optics, 4th Ed.*, Pearsons, 2002.
[3] J. Goodman, *Introduction to Fourier Optics 2nd Ed.*, McGraw-Hill, 1996.

STRONG SYMMETRIC H-BOND IN PROTONATED WATER DIMER. STRUCTURE AND VIBRATIONAL SPECTRA ANALYSIS PERFORMED USING B3LYP/acc-pVQZ AND MP4/acc-pVTZ LEVELS OF THEORY

Ekaterina Mahnach[1], Alex Malevich[1], Ekaterina Kozlovskaya[1], George Pitsevich[1], Valdas Sablinskas[2], Vytautas Balevicius[2]

[1]Belarusian State University, Minsk, Belarus
[2]Vilnius University, Vilnius, Lithuania
ekaterina.maxnach@mail.ru

Water is a key element of life, consequently it draws vast amounts of attention from the scientists. Its unique structure and properties are being constantly investigated and discussed, but yet they are not entirely understood. Water has two remarkable properties, which are responsible for its unique role in chemistry: first, water forms strong hydrogen bonds, which are the reason why water is a liquid at ambient conditions. Second, water has the ability to dissociate by forming a hydronium (H_3O^+) and a hydroxide ion (OH^-). On a large scale, aqueous media are believed to be an ensemble of different kinds of clusters, positively and negatively charged. Protonated water clusters $H_3O^+\cdot(H_2O)_n$ are among the most important species of such clusters. Studies of the hydrated proton in water bulk or in water solutions are important for many chemical and biological areas. A special place among $H_3O^+\cdot(H_2O)_n$ species belongs to the protonated water dimer (PWD) $H_5O_2^+$. This system is the simplest protonated water cluster and it is of considerable importance both because of the interest in proton mobility from a biochemical point of view as well as the interest in the strong hydrogen bonding that takes place in these clusters. Consequently, PWD is subject of many theoretical and experimental investigations. It was stated that due to the large anharmonicity of the vibrational modes of this system, the infrared spectrum is quite complex. Therefore, further theoretical investigations are needed in order to make convincing assignment of the bands in experimental spectrum.

Structure of PWD was analyzed using B3LYP/acc-pVTZ; B3LYP/acc-pVQZ; MP4/cc-pVTZ and MP4/acc-pVTZ levels of theory. For all of these cases geometry optimization was performed for C_2, C_S cluster symmetries as well as without symmetry restrictions (see Fig.1).

Fig. 1. Equilibrium structures of the PWD with C_2 (left) and C_S (right) symmetries.

It is worth noting that due to C_2 symmetry restriction (Fig.1 left) H-bonded proton located at the center of the hydrogen bridge. Different situation takes place for the C_S symmetry. H-bonded proton is closer to one of the H_2O molecules and it is more correctly to say that rather forms the structure $H_3O^+\cdot H_2O$. It is important to point out that only while using MP4/acc-pVTZ level of theory the H_3O^+ fragment becomes rather tetragonal than flat structure for all other levels of theory. Structural parameters and relative energies of equilibrium structures with different symmetries were discuss. IR spectra in harmonic and for some cases in anharmonic approximation were calculated. For detailed study of the anharmonic behavior of H-bonded proton vibrations 1D, 2D and 3D potential energy surfaces (PES) were constructed.

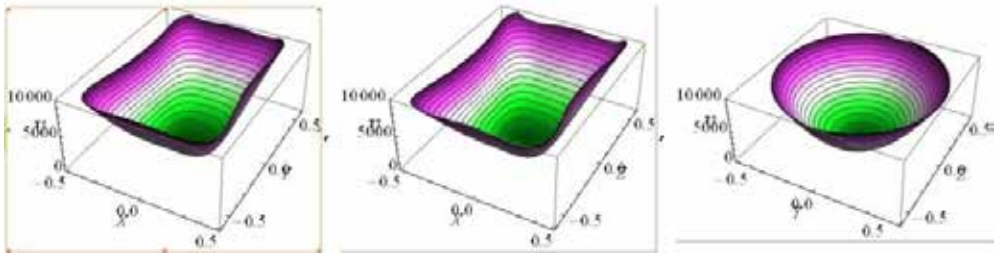

Fig. 2. 2D PES for stretching and bending vibrations of H-bonded proton in PWD: XY plane – left, XZ plane – center, YZ plane– right.

One can see that due to stretching motion (Fig. 2 – left and central) PES become strongly anharmonic. Frequencies of H-bonded proton vibrations were found by numerical solution of the multidimensional Schrödinger equations using Fourier [1] and DVR [2] methods. Strong coupling between normal modes is discourse.

[1] G. Pitsevich, A. Malevich, Simple method of the formation of the Hamiltonian matrix for some Schrodinger equations describing the molecules with LAM. Optics and Photonics Journal, **2**, 332-337 (2012).
[2] G. Pitsevich, A. Malevich, Comparison of the Fourier and DVR methods in the numerical solution of multidimensional Schrodinger equations. Journal of Applied Spectroscopy, **82**, 893-900 (2015).

SPECTRAL AND STRUCTURAL CHARACTERISTICS OF THE WEAK HYDROGEN BOND IN WATER DIMER

Nikita Tsimbrovsky[1], Alex Malevich[1], Ekaterina Kozlovskya[1], George Pitsevich[1], Valdas Sablinskas[2], Vytautas Balevicius[2]

[1] Belarusian State University, Minsk, Belarus
[2]Vilnius University, Vilnius, Lithuania
tsin-1995@yandex.by

Hydrogen bonds play a crucial role in chemistry and biology. Numerous experimental and theoretical studies have been devoted to the explanation of the structures and the energetics of hydrogen bonds [1-4]. Water is the prototypical molecule which forms hydrogen bonds easily with most other molecules, including itself. The absorption frequencies of a single water molecule in the vapor phase are well known. In contrast the vibration spectra of liquid water is much more difficult to interpret, since in water a single molecule can be associated with other molecules through hydrogen bond formation. The neighboring molecules change the absorption frequencies of the isolated molecule and also introduce new frequencies due to intermolecular interactions. Since the normal modes of vibration of liquid water are generally unknown the absorption bands are difficult to assign. Besides its fundamental importance in chemical and biological processes, water dimer is the simplest model system for intermolecular interactions. Therefore it has been the subject of numerous experimental and theoretical studies. As often happens when a variety of research groups examine the same molecular system using a wide assortment of ab initio techniques, the system evolves into a testbed for new methods. Among these systems relatively few generate sustained interest over a long enough period of time. However, the H_2O-H_2O system certainly falls into this category.

In present research structure of the water dimer was calculated using B3LYP/cc-pVTZ, B3LYP/acc-pVQZ, MP2/cc-pVTZ and MP4/cc-pVTZ levels of theory. Equilibrium geometry of the water dimer presented in Fig.1.

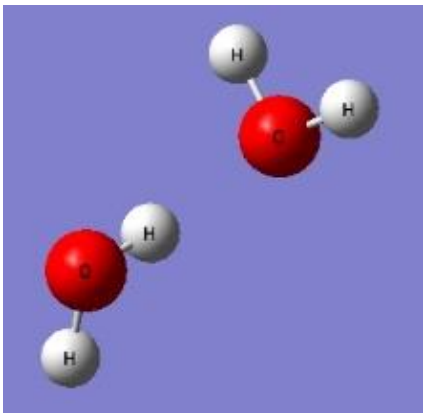

Fig. 1. Equilibrium geometry of the water dimer.

As known, vibrations of the hydroxyl groups involved in the hydrogen bond formation is strongly anharmonic. Therefore, vibrational spectra of the water dimer were calculated both in harmonic and anharmonic approximations for some levels of theory. Besides, multidimensional potential energy surfaces, associated with the motion of the H atom of the hydrogen bridge were computed, and their form confirm the suggestion about the presence of anharmonicity. In order to establish frequencies of the H-bonded hydroxyl group vibrations, the multidimensional Schrödinger equations were solved numerically using Fourier and DVR methods[5,6].

[1] G.M. Florio, C.J. Gruenloh, R.C. Quimpo, T.S. Zwier, The infrared spectroscopy of hydrogen-bonded briges: 2-pyridone-(water)n and 2-hydroxypyridine-(water)n clusters, n=1,2. Journal of Chemical Physics, **113**, 11143-11153 (2000).
[2] R. Laenen, K. Simeonidis, R. Ludwig, Investigation of an H-bonded dimer: Calculations of bonding structures and temperature dependence of the librational substructure of the O-H stretching band. Journal of Chemical Physics, **111**, 5897-5904 (1999).
[3] P. Jedlovszky, The local structure of various hydrogen bonded liquids: Voronoi polyhedral analysis of water, methanol and HF. Journal of Chemical Physics**, 113**, 9113-9121 (2000).
[4] J. Ceponkus, B. Nelander, Water dimer in solid neon. Far-infrared spectrum. J.Chem.Phys., **108**, 6499-6502 (2004).
[5] G. Pitsevich, A. Malevich, Simple method of the formation of the Hamiltonian matrix for some Schrodinger equations describing the molecules with LAM. Optics and Photonics Journal, **2**, 332-337 (2012).
[6] G. Pitsevich, A. Malevich, Comparison of the Fourier and DVR methods in the numerical solution of multidimensional Schrodinger equations. Journal of Applied Spectroscopy, **82**, 893-900 (2015).

LATTICE AS INTERDISCIPLINARY MEDIUM

Klaidas Grigaravicius[1], Audrius Jutas[1]*

[1] Department of Mechanical Engineering, Kaunas University of Technology, Lithuania
klaidas.grigaravicius@ktu.edu.lt

There lattice distortion modeling is presented in the theory of computation of elastic constant Poisson's ratio from the atomic perspective in close connection with experiment data obtained at macro-scale. This study is made in so named "analytical atom lab". Parallel to development in solid state physics and basic principles of statistical mechanics, atomistic modeling is shown as a maturing and perspective tool in materials science and for the fine investigations of physical properties of crystal materials. In order to render the present study more comprehensive, there basic principles and equations of infinitesimal strain field were applied.

To study patterning of atom motion in three dimensions, it was considered an idealized crystal of Vanadium deformed in spatial strain field f(x,y,z). In the bulk system, the reordering of atoms was chosen as "inevitable fellow traveller" to evaluate limits of elastic strains in bcc-lattice package. Also, as the procedure for verification and calibration of modelled quantity the *prior* and *posterior* probabilities were used. The averaged value of Poisson's ratio related directly with number of resonances (quantum jumps) was used as virtually controlled physical characteristic influenced by parameter of geometrical heterogeneity ξ for cooperating bcc-lattices (see Fig.1).

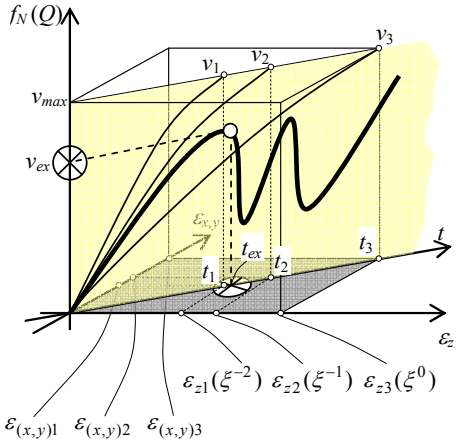

Fig.1. Surjective function of modeled Poisson's ratio ν_{ex} at "flat" space-time axes system

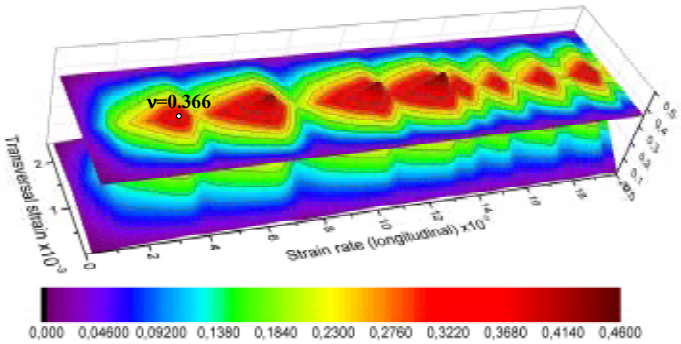

Fig.2. Virtual evolution of Poisson's ratio during tensile test. Vanadium: modelled 0.366 (reference 0.37)

Evolution of quantities used for data transfer described as wave function with resonances occurring stochastically along to direction of deformation (see Fig.2.). It's difficult to prevent fine number of resonances because each differently oriented lattice group cooperates with different gradient and impacts multi-directionally to other neighbour lattice groups for which this gradient during stretched system differs too. At the moment of total resonances, Poisson's ratio should reach some value Q and objective function then may be written recursively

$$f_N(Q,t) = \max \frac{1}{N}\left\{\nu(\varpi_N) + \nu_{N-1}(Q-\varpi_N)\right\}, \varpi_N \le 0 \text{ and } f_1(Q) = \nu_1(Q) \tag{1}$$

where ϖ_i is individual value caused by feature number i $(i = 1...N)$ before Poisson's ratio ν reaches its modelled value, t is scale related time.

Also it should be mentioned that difference in the gradient of atom motion around another atom was calculated in real time of deformation of material specimen using related scaling methods. This allows us to create conditions for virtual atom lab and to write objective function presented in the text above. The plastic deformation of bcc-lattice also exists as inevitable fact but it isn't explained explicitly because of complexity of this problem related with large number of methodological comparisons and explanations that could rebound on volume of this abstract [1-4].

[1] L. Kubin, J. P. Hirth, Dislocations in solids, Volume 15, Elsevier, UK (2009).
[2] I. Prigogine, I. Stengers, The end of certainty: time, chaos and the new laws of nature, Simon & Shuster Inc., New York (1997).
[3] D. Raabe, M. Sachtleber, Z. Zhao, F. Roters, S. Zaefferer, Micromechanical and macromechanical effects in grain scale polycrystal plasticity experimentation and simulation *Acta Materialia* 17, 3433-3441 (2001).
[4] Y. N. Osetsky, D. J. Bacon, An atomic-level model for studying the dynamics of edge dislocations in metals *Modelling Simul. Mater. Sci. Eng.* 11, 427-446 (2003).

CALCULATION OF THE EFFECTIVE DIFFUSION COEFFICIENT IN A PERIODIC POTENTIAL

Vlada Vysotskaya, Irina Shapochkina

Department of Physics, Belarusian State University, Belarus
vladavysockaya@mail.ru

Models based on the theory of Brownian motion are widely used to describe a number of phenomena in various field of modern science. One of the most impressive applications of the theory of diffusion transport are the so-called Brownian motors that simulate the directional motion of particles in a fluctuating periodic potential [1]. These models have found wide application both in description of motor proteins [2] and in the creation of artificial nanoscale devices [3]. On the other hand, in the theory of Brownian motors a number of specific problems appear which can enrich the theory of diffusion transport at all [4]. One of the ways of modeling Brownian motion is based on solving, by computer simulation (molecular dynamics method), the Langevin equation

$$m\ddot{x}(t) = -\zeta \dot{x}(t) - U'(x(t),t) + \xi(t) \qquad (1).$$

Here $-U'(x,t)$ is the force working on the particle in the potential field $U(x,t)$, $\zeta = \mu^{-1}$ is the viscous friction coefficient (inverse static mobility), $\xi(t)$ is the unbiased δ-correlated Gaussian noise ($\langle \xi(t) \rangle = 0, \langle \xi(t)\xi(t') \rangle = 2k_B T \zeta \delta(t-t')$, k_B is Boltzmann constant, T is the absolute temperature). This numerical technique makes it possible to simulate conditions close to real experiment. The basic idea of modelling is to integrate numerically the equation of motion with the random (Langevin) force simulated on a computer [5]. Then the required characteristics of the process are calculated by taking the average for a large number of realizations.

In this way, we have revealed the regularities of overdamped ($m \to 0$) Brownian motion in the following cases: free diffusion ($U(x,t) = 0$), diffusion under the influence of a stationary homogeneous (tilting) force ($U(x,t) = -Fx$), diffusion in a periodic potential ($U(x,t) = V(x)$ with $V(x+L) = V(x)$), and diffusion in a periodic potential under the influence of a stationary and homogeneous force ($U(x,t) = V(x) - Fx$). For these models, the effective diffusion coefficients and the particle effective mobilities have been calculated as the quantities of foremost interest. It is worthy to note, that under suitable conditions, the last case (diffusion in a tilted periodic potential) can demonstrate the giant acceleration of free diffusion [6, 7] so this effect could be of great interest from Brownian motors point of view as well. The results of statistical tests have been related to the available analytical data (namely, to results of Lifson and Jackson [8], Stratonovich [9] as well as to more resent results [6, 7]). The time dependencies of average particle characteristics as well as histograms of coordinate values and their distribution function have been given. The proposed model can be expanded by the time dependence of the potential energy of the particles (Brownian motor) and inertial effects to be taken into account (so we consider our results as a start position for our future motor experiments).

[1] P. Reimann, Brownian motors: noisy transport far from equilibrium, Phys. Rep. **361,** 57 – 265 (1990).
[2] J. Howard, *Mechanics of Motor Proteins and the Cytoskeleton* (Sinauer, Sunderland, MA, 2001).
[3] P. Hänggi and F. Marchesoni, Artificial Brownian motors: Controlling transport on the nanoscale, Rev. Mod. Phys. **81**, 387 - 442 (2009).
[4] V. M. Rozenbaum, Y. A. Makhnovskii, I. V. Shapochkina et al, Diffusion of a massive particle in a periodic potential: Application to adiabatic ratchets, Phys. Rev. E **92**, 062132-1 – 0621321-10 (2015).
[5] H. Riskin, *The Fokker-Plank Equation* (Springer-Verlag, Berlin, 1984).
[6] P. Reimann, C. Van den Broeck, H. Linke et al, Giant Acceleration of Free Diffusion by Use of Tilted Periodic Potentials, Phys. Rev. Letters, **87**, 010602-1 – 010602-4 (2001).
[7] P. Reimann, C. Van den Broeck, H. Linke et al, Diffusion in tilted periodic potentials: Enhancement, universality, and scaling, Phys. Rev. E, **65**, 031104-1 – 031104-16 (2001).
[8] S. Lifson and J. L. Jackson, On the Self Diffusion of Ions in a Polyelectrolyte Solution, J. Chem. Phys. **36**, 2410 - 2414 (1962).
[9] R. L. Stratonovich, Radiotekh. Elektron. **3**, 497 (1958).

EXTRACTING ENERGETIC LANDSCAPES AND DIFFUSION COEFFICIENTS VIA STUDYING MOTION BLUR

Michal Bogdan[1]

[1] Department of Engineering, University of Cambridge, United Kingdom
mjb271@cam.ac.uk

Numerous experimental strategies of reconstructing energetic landscapes in complex environments, such as microfluidic devices, biological systems and colloids, are based on measuring behaviour of Brownian particles moving in these environments.

Most of these methods rely on extracting information from measured particle trajectories and theoretical efforts were aimed in recent years at developing these and assessing their limitations.

However, an alternative strategy of recovering potentials based on observing distributions of particle positions can be also used, based on the assumption that they are related to the underlying energetic landscape via an exponential function (Boltzmann distribution).

This method has attracted considerable attention recently. However, theoretical developments are required to evaluate the effects of motion blur on the scope of validity of this method.

We have derived and tested with Brownian dynamics simulations a precise analytical formula evaluating the effects motion blur has on measuring potentials with this method. Interesting phenomenological effects include the appearence of false maxima in DLVO potentials and of a false apparent spring constant in quadratic potentials.

We also discuss how the results of this derivation imply that using motion blur by varying shutter times in measuring particle positions can actually be a useful tool in recovering local diffusion constants and curvatures and slopes of the energetic landscape in complex environments.

3D SIMULATIONS OF NANO-SIZED SQUID-ON-TIP

Abul Hasnat Rubel[1, 2,*], Milorad V. Milosevic[1]

[1]Department of Physics, University of Antwerp, Groenenborgerlaan 171, B-2020 Antwerp, Belgium
[2]Department of Physics, Jagannath University, Dhaka, Bangladesh
abul.hasnatrubel@uantwerpen.be, milorad.milosevic@uantwerpen.be*

SQUID-on-tip (SOT) is the most sensitive magnetometry device to date [1]. We study the performance of such nano-sized SOT, as a function of its geometric parameters (see Fig.1a), in the presence of magnetic field, using the state-of-the-art three dimensional (3D) simulations within the phenomenological Ginzburg-Landau (GL) theory. Based on the observed behavior of the superconducting order parameter in the SOT, its magnitude (related to Cooper-pair density) and phase (related to circulating supercurrents), we propose engineering solutions at the nanoscale to improve the sensitivity of the device. For example, if we introduce the constriction in the arms of the SQUID loop (Fig.1b), we observe that the gradient of phase of the order parameter is largely enhanced in the constriction of the SOT in the Meissner and first vortex state, which is expected to facilitate the interference pattern of the critical current of the SOT and reduce the noise. We further discuss the other realizations of the SOT with engineered 3D shapes of the SQUID itself [2], and show the relation of those geometries to sensitivity to 3D magnetic field.

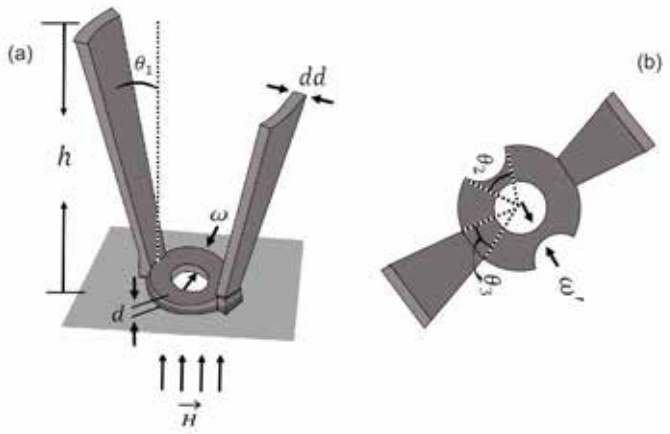

Fig. 1. Oblique view of SQUID-on-tip (SOT) device, (a) without and (b) with constriction in the pick-up loop, with indicated relevant geometric parameters and applied magnetic field.

[1] D. Vasyukov, Y. Anahory et al., A scanning superconducting quantum interference device with single electron spin sensitivity, Nature Nanotech **8**, 639-644 (2013).
[2] C. Granata, & A. Vettoliere, Nano Superconducting Quantum interference device: A powerful tool for nanoscale investigations, Physics Reports, In press (2015).

SURVEY AND GEOMETRIC CLASSIFICATION OF NUCLEOBASES DIMERS IN CRYSTALLINE STATE

Małgorzata K. Cabaj, Paulina M. Dominiak

Department of Chemistry, University of Warsaw, Poland
mcabaj@chem.uw.edu.pl

Cambridge Structural Database (CSD) [1] is a repository containing results of X-ray and neutron diffraction data of organic small molecules or metal-organic crystal structures. It enables easy search through many different structures with combined queries, taking into account search terms as molecule parts, names, elements or name of author that deposited the data[2]. It is a part of The Cambridge Crystallographic Data Centre (CCDC), dedicated to development of crystallographic knowledge all over the world.

My study is based on stored in CSD data, concerning existing in DNA and RNA nucleobases – adenine, guanine, cytosine, thymine and uracil.

There is no need to justify importance of those molecules for living organisms, therefore it's only natural that scientists all over the world, including myself, would approach them and try to investigate from different angles.

Molecules can interact differently in living organisms and in vial, and as most previous surveys were done from more 'biological' [3] or theoretical [4] point of view, I tried to check how nucleobases interact in more 'chemical' environment – inside a crystal. To have some insight into those interactions, I went through Cambridge Structural Database searching for occurrences of various possible homodimers of nucleobases, resembling those appearing in nucleic acids. That means two identical nucleobases interacting through multiple hydrogen bonds formed in plane. I tried to include every possible interaction in my survey, therefore not only Watson-Crick edge can be involved in interaction, but Hoogsteen and Sugar Edge as well. Even if searched interaction was rather unlikely to occur (like those involving hydrogen bonds with C as donor), I still included it in my survey.

Frequency of occurrence of particular dimers and comparing them with conditions of crystallization may give some insight into nature and driving force for investigated interactions.

[1] F. H. Allen, "The Cambridge Structural Database: A quarter of a million crystal structures and rising," *Acta Crystallogr. Sect. B Struct. Sci.*, vol. 58, no. 3 PART 1, pp. 380–388, 2002.

[2] R. A. Sykes, P. McCabe, F. H. Allen, G. M. Battle, I. J. Bruno, and P. A. Wood, "New software for statistical analysis of Cambridge Structural Database data.," *J. Appl. Crystallogr.*, vol. 44, no. Pt 4, pp. 882–886, Aug. 2011.

[3] A. S. Abu Almakarem, A. I. Petrov, J. Stombaugh, C. L. Zirbel, and N. B. Leontis, "Comprehensive survey and geometric classification of base triples in RNA structures," *Nucleic Acids Res.*, vol. 40, no. 4, pp. 1407–1423, 2012.

[4] D. Bhattacharyya, S. C. Koripella, A. Mitra, V. B. Rajendran, and B. Sinha, "Theoretical analysis of noncanonical base pairing interactions in RNA molecules.," *J. Biosci.*, vol. 32, no. 5, pp. 809–825, 2007.

PHYTOTOXICOLOGICAL PROPERTIES OF NOVEL AMINOPHOSPHONATES BEARING 2-PYRROLE MOIETY

Marta Morawska[1], Jarosław Lewkowski[1], Edyta Rzeszotarska[1], Piotr Rychter[2], Diana Rogacz[2]

[1] Department of Organic Chemistry, Faculty of Chemistry, University of Łódź, Tamka 12, 91-403 Łódź
[2] Institute of Chemistry, Environmental Protection and Biotechnology, Faculty of Mathematics and Natural Science, Jan Długosz University of Częstochowa, 42-200 Częstochowa, al. Armii Krajowej 13/15
martaem88@gmail.com

In the framework of a project financed by NCN, we perform studies concerning the synthesis, general phytotoxocity and selectivity of action on given plants [1] as well as the controlled release from biodegradable polymers.

The group of compounds, which seems to have the interesting properties are (2-pyrrole)aminophosphonates and in order to investigate them, we performed the synthesis of a series of such compounds using the modified aza-Pudovik reaction.

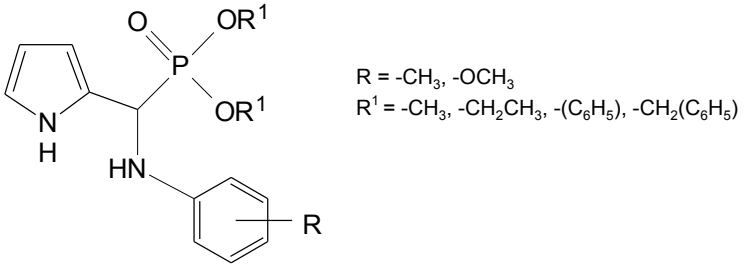

Fig.1. General scheme of aminophosphonate.

Compounds were investigated in the point of view of their influence on growth of higher plants belonging to two classes: monocotyledonous oat (Avena sativa) and dicotyledonous radish (Raphanus sativus).

Studies were founded by the National Centre of Science (NCN), grant no. 2014/13/B/NZ9/02418

[1] A. Matusiak, J. Lewkowski, P. Rychter, R. Biczak, "Phytotoxicity of New Furan-derived Amino-phosphonic Acids, N-Aryl Furaldimines and 5-Nitrofuraldimine", J. Agric. Food Chem., 61(32), 7673–7678 (2013).

NAVIGATION ALGORITHM FOR UNMANNED AERIAL VEHICLES USING AERIAL PHOTOGRAPHS

Lomako Aleksey, Kozadaev Konstantin

Department of Radio Physics and Computer Technologies, Belarusian State University, Belarus
alekseylomako@gmail.com

Today according to UVS International (the leading international association of pilotless systems) unmanned aerial vehicles (UAVs) make in 52 countries of the world. Tens big enterprises and small firms compete in this market.

One of the major elements for the UAV is the system of navigation. Now there is a set of the navigation systems working independently from each other, including, satellite navigation, inertial navigation systems, navigation with use of data of a video series. The systems transforming data of a video series to so-called contour maps on which the UAV has opportunity to be guided are developed. But, as often we have no physical capacity of storage onboard the UAV of large volume of data, we decided to go further away and instead of creation of the card to create a database of specific objects.

Development of algorithm of navigation according to a video series for return of the UAV to the place of basing in case of the emergency which caused malfunctions in systems of navigation of the aircraft or a blackout of its systems of navigation was the purpose of this work.

At creation of a database of specific objects we face a problem of preliminary processing of the image. It consists in allocation of objects necessary for us in a shot or, in other words, underlinings of contours of objects. There is a set of versions of solutions of this problem. On the solution chosen by us the first step is segmentation of the image. [1]

In our task we will use splitting the image into uniform areas. Namely, we will divide the image into 25 fixed parts equal by the size each other. It allows to solve the problem connected with various levels of brightness in various areas of the image. Besides, such segmentation allows to use further information on location of a segment with object in a shot for navigation of the UAV.

The following step when processing the image is the binarization of its segments with allocation of contours. There is a set of methods of a binarization, but not all conform to our requirements, namely, to the speed and quality of underlining of contours. After the analysis of the existing methods of binarization the decision was made that the most optimum for our task is Otsu's method. [2] Its main advantages are simplicity of realization, high level of adaptation to different images by a choice of the most optimum threshold, fast time of performance. Shortcomings of a method are blocked by preliminary segmentation of the image.

After we allocated a contour of objects in a shot, we need to define what of contours as much as possible conforms to our requirements. We accept as the best the contour with the longest border which is entirely within a segment.

Having allocated the best contour, so, and object in a segment, we are obliged to write down parameters of this contour in a database. Resistance to scaling has to be one of criteria of a choice of parameters of objects. Besides, it is obvious that at shift of object in a shot its parameters shouldn't change. So, there has to be no binding to coordinates in the image. In other words, parameters of object have to be steady against linear movements of object. Object parameters also have to be steady against different turns of system of coordinates. We found four parameters conforming to these requirements.

Except the parameters necessary for recognition of object, we need the parameters necessary for making decision on location of the UAV. A segment arrangement in a shot, the direction of the movement UAV concerning a shot, indications of inertial (in particular, the magnetometer) and navigation satellite systems, attached to shots will be such parameters.

Thus, we have sets from eight parameters for each object that we can write down in a database. Actually, the dynamic array by the 8xn size, where n – amount of the written-down objects is stored in cells of memory. Recognition is conducted only in the first four parameters from eight. Other parameters are used for making decision on the current location of the UAV in case of emergencies.

Record of objects in a database has to be kept constantly when flying the UAV in the set point. In case of break of communication, existence of hindrances, passes losses of one of the main UAVs navigation systems into emergency operation. The system of navigation on a collected database joins. The UAV is unwrapped on 180 degrees and makes preliminary processing of the image.

Further search of objects in algorithm of making decisions on existence of object in a database is carried out. In case of detection of the object existing in base the algorithm will use 4 additional parameters of object which are stored in a database for determination of the current location.

The developed navigation system is a good additional method for determination of location of the UAV. Using this system as the additional level of protection against emergency situations, we have an opportunity considerably to increase probability of not crash landing of the UAV and consequently, and to keep the expensive equipment.

[1] R. M. Haralick, L. G. Shapiro, “Image Segmentation Techniques,” Computer Vision, Graphics, and Image Processing, Vol 29, No 1, 1985

[2] Otsu, N., «A Threshold Selection Method from Gray-Level Histograms» IEEE Transactions on Systems, Man, and Cybernetics, Vol. 9, No. 1, 1979, pp. 62-66.

SOFTWARE COMPLEX FOR PROCESSING HYPERSPECTRAL DATA

Anton Martenov, Anhelina Shyrayeva, Victor Ivanov, Dimitry Ivanov, Aliaksandr Paseniuk, Leanid Katkouski

A. N. Sevchenko Institute of Applied Physical Problems of Belarusian State University, Belarus
antonmartenov@gmail.com

Spectroscopy is widely used in remote sensing for obtaining complete information about the Earth's surface. Hyper Spectroscopy with high spatial resolution results in obtaining spectral characteristics of all surface points under study allows investigating the state of the objects. The obtaining three-dimensional array of points is called "Spectral hypercube" and shows dependence of the recorded radiation on two spatial coordinates and wavelength.

The software complex (SC) under development is intended for processing hyperspectral images obtained by air-borne or space-borne shooting. SC is connected to specific remote sensing equipment (Fourier transform hyperspectrometer), takes all features of it into account and therefore provides alternative to universal commercial software packages.

The development of program modules is performed in C++ with QT framework. Structure of SC represents a set of plugins that can be divided into two groups: data reading modules and mathematical computations and transformations modules.

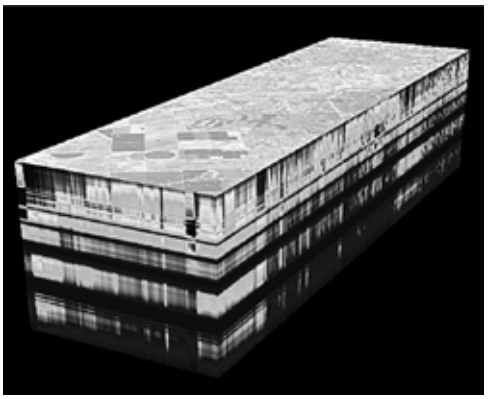

Fig. 1. 3D Visualization of hyperspectral data.

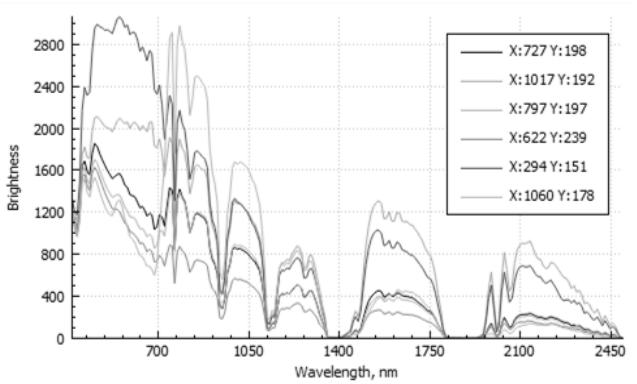

Fig. 2. Spectral profiles

The modules implemented at the moment:

- loading of AVIRIS hyperspectral data [1];
- graphic representation of hypercube in the form of 3D object (Fig. 1.) with tools for manipulating of hypercube visualization. 3D module is intended for preliminary data analysis;
- data representation as a set of separate channels. 2D module is intended for more convenient work with the separate channels of the hypercube and provides advanced functionality;
- selection of regions of interest for further processing and calculating of different statistics;
- graphic representation of the spectral curves (Fig. 1.) for any selected spatial pixels at the hypercube;
- graphic representation of spatial profiles along any line at the image for each spectral channel;
- synthesis and displaying of color(R, G, B) and pseudocolor images including image formation with a predetermined spectral profile;
- noise reduction in images as well as in spectral profiles;
- contrasting images in spectral and spatial domains;
- histogramming [2];
- comparison between spectral curves and calculating of the degree of their proximity. Searching pixels having close spectrograms with defined confidence interval and allocation them at the image;
- formation and operation with the set of spectral libraries [3].

These plugins are independent and can be run from other modules with corresponding initial preferences.

SC under development can be effectively used in scientific researches as well as for solving applied problems. Further investigations will be performed in order to create atmospheric correction techniques and object classification.

The work is done with the financial support of BRFFR (№ F15RM-064)

[1] Airborne Visible InfraRed Imaging Spectr. Available at: http://aviris.jpl.nasa.gov/aviris/index.html (accessed 25 January 2016).
[2] Kumar, N. Contrast Stretching / Remote sensing-digital image processing, IISc, Bangalore.
[3] Aster Spectral Library. Available at: http://speclib.jpl.nasa.gov/search-1 (accessed 25 January 2016).

THE DEVICE DRIVEN BY SOUND (HOW RESONANCE CAN BE USEFUL)

Author Nina Mazurewicz

Department of Mechatronics, Warsaw University of Technology, Poland
nina1996@wp.pl

Results presented by the Living Planet Report WWF, one of the most important scientific publications about the Earth's condition, are extremely alarming. It seems that until 2030, we will need two planets to fulfill growing humans' needs. Therefore, scientists should focus their research on seeking alternative energy sources and innovative ways of making our life's quality better. My work concentrates on building an acoustic engine which construction is based on a Helmholtz resonator. I have made an invention, a vehicle which uses only sound wave's energy to move. In my experiments, I have focused on creating an optimal model and on discovering the nature of such an engine. My work presents inventive solutions which could be used to maximize the efficiency of the acoustic engine, too. However, my work also points out how prospective and enormous for medicine, air and automotive industries could be using the resonance phenomena and in fact, my invention.

ESTIMATION OF HUMAN EMOTIONAL STATE BY ANALYZING HIS FACIAL IMAGES

Siarhei Sadau, Alena Kazlova

Department of Radio Physics and Computer Technologies, Belarusian State University, Belarus
seregasadov@gmail.com

It was found [1, 2] that in personal communication about 35% of the information is transmitted verbally, while the majority (over 60%), information is transmitted by non-verbal means - facial expressions, gestures, postures, etc. It was also found [1] that the expressions of basic emotions on the faces of the people do not depend on racial, cultural, gender or age of human origin. Emotions on the human face are equally well recognized by people in all corners of the Earth. This allows you to set the task of creating the intelligence system, which can recognize emotions and the true intentions of the person in his appearance and behavior in the communication process.

The aim of this work is to construct the algorithm for determining the emotional state of the person by analyzing the images of his face. To achieve the aim we need to solve the following tasks: 1. Obtaining of the human image and recognizing his face; 2. Image processing; 3. Creating image masks and performing brightness analysis of pixels; 4. Classification of the image (the definition of the emotions).

We consider the ideal case in which the original data are human photographs made from the front, and reflecting his various emotional states. An obligatory condition is the presence of human photos with neutral emotional background, which is taken as a template.

Researched emotions are anger, surprise, fear. Figure 1 shows a block diagram of the test algorithm. Figure 2 shows the original image and its mask.

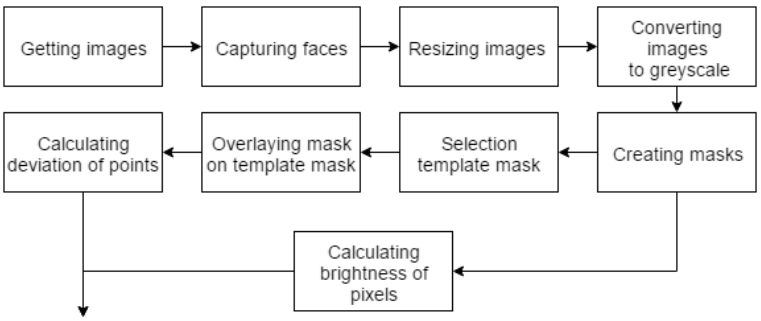

Fig. 1. Block diagram of the test algorithm

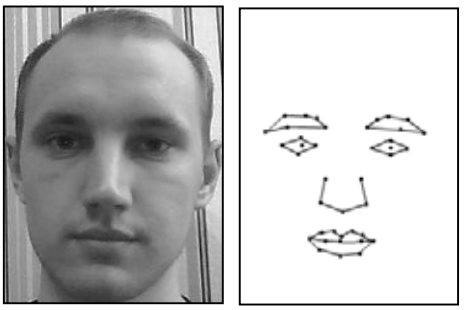

a b

Fig. 2. Original image (a) and its mask (b)

The chosen development software is package of computer mathematics Matlab. The choice is not random, as Matlab already has algorithms image processing, as well as packages for working with neural networks and fuzzy logic.

Currently, the main ways of expressing emotions of human are studied, the initial version of the algorithm for estimating the emotional state of a person analyzing facial images is developed, the database of images for later analysis is collected.

Further objectives are: recognition of a person's face, standing at different angles to the camera; using of additional criteria for the evaluation (brightness, contrast images, the comparison circuits); capturing images from a video stream; using of 3D - facial recognition; accounting entity of small details, specific facial expressions (increasing the number of mask points); an adaptation system to operate in realtime; recognition complex emotions; скуфештп an integrated system for determining emotion gestures, speech, gait, face.

[1] Ekman P., Unmasking the Face, Piter (2015).

[2] Pease A., The Definitive Book of Body Language. Extended Version, Eksmo (2014).

UNSUBSTITUTED POLYFLUOROALKYLATED PHOSPHONATES – THE GATE TO THE POLYFUNCTIONAL COMPOUNDS

Paweł Tokarz[1*], Piotr M. Zagórski[1], Jarosław Lewkowski[1], Bartłomiej Gostyński[2], Mieczysław W. Płotka[1]

[1] Department of Organic Chemistry, Faculty of Chemistry, University of Lodz, Poland
[2] Department of Computer Modelling, Centre of Molecular and Macromolecular Studies, Polish Academy of Sciences
paweltokarz.chem@gmail.com

The fluorine atoms in an organic molecule are responsible for essential changes in the physiochemical properties of the substance. They alter reactivity, enhance biological properties, increase volatility, improve lipophilicity and change many other parameters of the polyfluorinated compounds in comparison with their non-fluorinated analogues. All those facts together are sometimes attributed to as the *fluorine magic* [1].

Despite the importance of the polyfluorinated polyfunctionalyzed compounds their synthesis remains a challenging task. The presence of the perfluorinated fragments in the molecule changes the reaction mechanisms due to inductive effects. It also responsible for the specific form of the hyperconjugation [2]. Both effects dramatically decrease the electron density in the molecular neighborhood.

Recently, our team has focused on the synthesis and studies of the reactivity of the simplest possible polyfluoroalkylated phosphonates (compound 1, Fig. 1). First, we have noticed that this class of compounds is represented by just one example [3] which was rather surprising for such a simple molecules. We did the systematic research of the possible pathways of the synthesis of the mentioned phosphonates, going through the several unsuccessful attempts – including standard Arbuzov, Michaelis-Baker of Ruppert-Prahash protocols.

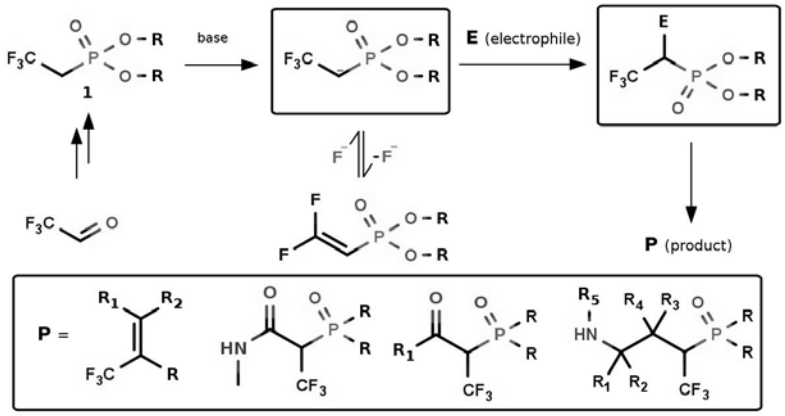

Fig. 1. The general idea behind the exploitation of the polyfluoroalkylated phosphonates in organic synthesis.

In this presentation we would like to show that the synthesis of these seemingly trivial compounds requires rather non-trivial methodology. The multi-step procedure starting from fluoral or its hydrate and dialkyl phosphonate was the first practically useful we have developed. Next, we will show the broad applicability of the synthesized phosphonates in reactions with the electrophilic substrates, which gives rise to a large library of the polyfluoroalkylated products, including yet undescribed compounds, which could be of high importance.

The work is financially supported by Polish National Centre of Science. Grant No. 2014/13/N/ST5/01532.

[1] K. Peikert, F. Hoffman, M. Fröba, Fluorine magic: one new organofluorine linker leads to three new metal–organic frameworks, CrystEngComm **17**, 353-360 (2015).
[2] D. Holtz, A critical examination of fluorine hyperconjugation in aromatic systems, Chem. Rev. **71**, 139-145 (1971).
[3] A. A. Kadyrov, E. M. Rokhlin, Hexafluoroisopropylidene and pentafluoroisopropenyl derivatives of phosphorus. Communication2. Electrophilicity pentafluorophenylphosphonate esters and the reactions of phosphorylhexafluoroisopropyl anions, B. Acad. Sci. USSR Ch+, 1224-1230 (1983).

THE SIMPLEST POLYFLUOROALKYLPHOSPHONATES AND THEIR NON TRIVIAL SYNTHESIS

Piotr M. Zagórski[1], Paweł Tokarz[1], Bartłomiej Gostyński[3], Jarosław Lewkowski[1], Mieczysław W. Płotka[1], Sławomir Domagała[2]

[1]Department of Organic Chemistry, University of Łódź, Poland
[2] Department of Inorganic and Analytical Chemistry, University of Łódź, Poland
[3] Department of Computer Modelling,Centre of Molecular and Macromolecular Studies Polish Academy of Sciences, Sienkiewicza 11, 90-363 Łódź, Poland.
zagorek@op.pl

Contemporary organic synthesis exploits a number of methods to introduce polyfluoroalkylated chains and even more to incorporate phosphonate groups into a molecule. On this background it came as a surprise to us to learn, that the synthesis of the unsubstituted polyfluoroalkylphosphonates (Fig. 1) is not as simple, as their structures are. For example: dimethyl 2,2,2-trifluoroethylphosphonate ($R_f = CF_3$) was reported only once [1] and was obtained as a product of hydrolysis of a more complex structure with very low yield (10%), while diethyl 3,3,3-trifluoropropylphosphonate was synthesized by means of Arbuzov reaction with 9% yield [2]. Here we present two methods for the synthesis of the simplest polyfluoroalkylphosphonates starting from commercially available di- and trialkyl phosphites.

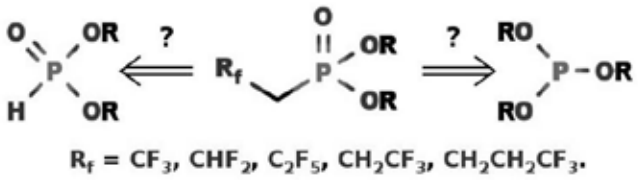

Fig. 1. Retrosynthetic analysis of the synthesis of the desired compounds.

We also tested the reactivity of a series of polyfluoroalkyliodides with trialkyl phosphites in Arbuzov reaction. For the derivative with $R_f = CF_3$, we did not observe the formation of target product; while the trimethyl phosphite underwent a rearrangement to methylphosphonate. We support these data with the quantum mechanical calculations of reaction pathways.

The work is financially supported by National Centre of Science. Grant No. 2014/13/N/ST5/0153

[1] A. A. Kadyrov, E. M. Rokhlin, B. Acad. Sci. USSR Ch+, 1224 (1983)
[2] J. A. Bennett, E. G. Hope, K. Singh, A. M. Stuart, J. Fluorine Chem., **130**, 615 (2009)

Author index

H

I

J

K

L

M

N

O

P

R

S

T

U

V

W

Y

Z